



**University of  
Nottingham**

UK | CHINA | MALAYSIA

# **Advanced Characterisation of Internal Diesel Injector Deposit Molecular Compositions**

**Joseph Lamb**

School of Engineering

Supervisors: Dr. David Scurr, Prof. Colin Snape, Dr. Jim Barker

Thesis submitted to the University of Nottingham for the degree of Doctor of  
Engineering

March 2022

# Abstract

Diesel engines remain widely used in a range of applications throughout the world, the clean operation of which is imperative for minimising their environmental impact during the transition towards a decarbonised energy system. The negative impact of insoluble internal diesel injector deposit (IDID) formation on emissions is well documented, and their incidence and severity has increased over the past two decades due to reasons thought to include the higher temperatures and pressures of newer injector systems and the uptake of biodiesel blending. Prevention and mitigation of such deposit formation requires an understanding of the formation process which requires the identification of detrimental fuel and additive components, their mechanisms of contributing to deposit formation, and how new mitigation strategies could prevent them.

Previous investigations have characterised IDIDs with a range of techniques, with ToF-SIMS proving itself effective for the analysis of insoluble carbonaceous deposit components and its ability to depth profile demonstrating a layered structure. However, characterisation with this technique was limited to non-diagnostic assignments due to high fragmentation of sputtered ions and low mass resolving power. This thesis builds on these studies with the recently developed technique of OrbiSIMS, which combines SIMS's ability to access insoluble material with the high mass resolving power of the Orbitrap<sup>TM</sup> mass analyser and preservation of chemistry through the softer Ar<sub>3000</sub><sup>+</sup> GCIB. Through this technique, detailed characterisation of deposit components is achieved, including chemistries not seen before that provide new insights into IDID formation processes. Examples include species originating from lubricant oil additives such as alkylbenzene sulfonates (C<sub>18</sub>H<sub>29</sub>SO<sub>3</sub><sup>-</sup>) and polyaromatic hydrocarbons derived from the carbonisation of fuel such as circumovalene (C<sub>66</sub>H<sub>20</sub><sup>+</sup>). In view of SIMS's limitation in being semi-quantitative, XPS is applied in support for elemental quantification that validates and provides context to the OrbiSIMS data, finding deposits that are generally over 70

relative atomic percent carbon but with significant contributions from other elements, including inorganic salts of sodium and calcium.

With OrbiSIMS and XPS depth profiling, the location of the detailed deposit chemistries of interest as well as elemental quantification with depth is observed all the way down to the needle substrate. The IDIDs showed an increase in inorganic content in the sub-surface, however XPS shows that carbon is the dominant element throughout the full thickness of the IDIDs analysed. Using a multivariate analysis approach, depth profile trends were identified and each sample characterised as four pseudo-layers. Each sample's organics and polyaromatics are found towards the surface, above inorganic and carbonaceous material, the latter suggesting a carbonisation of the surface organic material over time. Finally, the substrate is identified in all samples. This method achieves the most comprehensive IDID characterisation to date and the chemistries responsible for the nascent deposit formation can be suggested from the lower pseudo-layers' characterisations, for example indicating lubricant oil contamination or sodium contamination with a source of sulfate and carbonate.

To assess the effects of fuel, additive and contaminant chemistries in a controlled environment on diesel deposit formation, a laboratory bench test (the JFTOT) was applied to generate samples of known origin that can be analysed using the same methods. The deposit composition formed from a range of fuel, additive and contaminant components, including biodiesel, additives of interest and lubricant oil. The same chemistries identified are present in the IDIDs from real-world failures, and the JFTOT investigations demonstrate the possible origins of these components. For example, biodiesel and lubricant oil are indicated as a source of sulfur and phosphorus while LMW PIBSI is indicated as a source of nitrogen, all of which become integrated into carbonaceous material that is seen in both JFTOTs and real-world IDIDs. The findings from these investigations can inform the industry and future investigations to help mitigate deposition and ensure the efficiency and longevity of diesel engines.

## **Publications**

Edney, M.K., Lamb, J.S., Spanu, M., Smith, E.F., Steer, E., Wilmot, E., Reid, J., Barker, J., Alexander, M.R., Snape, C.E. and Scurr, D.J., 2020. Spatially Resolved Molecular Compositions of Insoluble Multilayer Deposits Responsible for Increased Pollution from Internal Combustion Engines. *ACS Applied Materials & Interfaces*, 12(45), pp.51026-51035.

Lamb, J.S., Barker, J., Wilmot, E., Scurr, D.J., Snape, C.E., Smith, E.F., Alexander, M.R. and Reid, J., 2020. Internal Diesel Injector Deposit Chemical Speciation and Quantification Using 3D OrbiSIMS and XPS Depth Profiling. *SAE International Journal of Advances and Current Practices in Mobility*, 3(2020-01-2098), pp.349-364.



## **Declaration**

I hereby declare that this thesis has been composed by myself and has not been submitted for any other degree previously. Acknowledgements of specific procedures not performed by myself are stated; otherwise, the work described is my own.

A handwritten signature in black ink, appearing to read 'J. Lamb', written in a cursive style.

Joseph Lamb

## Acknowledgements

Firstly I wish to gratefully acknowledge the funding that made this work possible from the EPSRC Centre for Doctoral Training in Carbon Capture and Storage and Cleaner Fossil Energy, the EPSRC Strategic Equipment grant ‘3D OrbiSIMS: Label free chemical imaging of materials, cells and tissues’ (grant no. EP/P029868/1) and Innospec Ltd.

I would like to thank my supervisors Dr. David Scurr, Prof. Colin Snape and Dr. Jim Barker for sharing their technical expertise and for their patience and thoughtful input into this project over the years. I am grateful to everybody at the University of Nottingham and Innospec who offered their technical skills and training. Thank you to Dr. Emily Smith and Dr. Craig Stoppiello for performing the XPS experiments and helping with data interpretation, Stefanie Kern for help with 3D OrbiSIMS experiments, Nicola Weston and Dr. Elisabeth Steer for SEM training and help, Dr. Gustavo Trindade and Dr. Andrew Hook for help with their MVA software packages, Kerry Burnett for performing the JFTOT experiments, Dr. Ed Wilmot for mass spectrometry help, Dr. Jacqueline Reid for her input into the project and publications, and Prof. Morgan Alexander for reviewing publications. Special thanks to Max Edney and Dr. Matteo Spanu for their hard work on our group publication and again to Max for carrying out the AP-MALDI experiments.

Thank you to my family and friends without whose support and advice I would not have reached this stage of finishing this thesis. Lastly, thank you to friends from the CDT, the office and the laboratory for their interesting and entertaining conversations and perspectives on a range of topics.

# Contents

Advanced Characterisation of Internal Diesel Injector Deposit Molecular	
Compositions .....	i
Abstract.....	i
Publications .....	iii
Declaration .....	iv
Acknowledgements .....	v
Contents .....	vi
Figures .....	x
Tables .....	xviii
Abbreviations .....	xx
Chapter 1: Introduction.....	1
1.1    Background: Diesel Fuel and Engines .....	1
1.1.1    The Diesel Engine .....	1
1.1.2    The Diesel Injector .....	2
1.1.3    Diesel Fuel.....	3
1.1.4    Biofuels: Biodiesel and HVO .....	4
1.1.5    Diesel Additives .....	5
1.1.6    The Status and Future of Diesel .....	7
1.1.7    Diesel Engine Deposits.....	7
1.2    Internal Diesel Injector Deposits: Types, Causes and Formation	
Mechanisms.....	8
1.2.1    Types of IDIDs .....	8
1.2.2    Causes and Formation Mechanisms of IDIDs .....	9
1.3    Chemical Analysis of IDIDs .....	20
1.3.1    Microscopy Techniques.....	20
1.3.2    Spectroscopy Techniques .....	23
1.3.3    Mass Spectrometry Techniques.....	28
1.3.4    Jet Fuel Thermal Oxidation Tester .....	36
1.4    Scope and Aims of this Thesis .....	37
Chapter 2: Materials and Methods .....	39

2.1	Injector Samples .....	39
2.1.1	Sourcing.....	39
2.1.2	Table of Injector Samples.....	39
2.2	Jet Fuel Thermal Oxidation Test .....	40
2.2.1	Experimental.....	41
2.2.2	Materials .....	41
2.2.3	JFTOT Samples .....	43
2.2.4	JFTOT Heater Tube Analysis: General .....	43
2.3	Analytical Methods .....	44
2.3.1	SEM-EDS .....	44
2.3.2	XPS .....	45
2.3.3	Orbitrap <sup>TM</sup> -Secondary Ion Mass Spectrometry .....	50
2.3.4	Atmospheric pressure matrix-assisted laser desorption/ionization high-resolution mass spectrometry (AP-MALDI-MS) .....	62
2.3.5	Optical Profilometry for Measurement of GCIB Craters .....	62
2.3.6	Optical Microscope .....	63
2.4	Graphs and Charts .....	63
Chapter 3: OrbiSIMS and XPS Characterisation of Internal Diesel Injector		
	Deposits .....	64
3.1	Introduction .....	64
3.2	Results and Discussion.....	65
3.2.1	Appearance and Morphology using Microscopy.....	65
3.2.2	Elemental Analysis using SEM-EDS .....	66
3.2.3	Evidence of Carbonisation in IDIDs by OrbiSIMS and XPS.....	67
3.2.4	Evidence of Fuel and Lubricant Additive Chemistries in IDIDs by OrbiSIMS and XPS .....	76
3.2.5	Inorganic Salt Chemistries in IDIDs by OrbiSIMS and XPS.....	87
3.2.6	Characterisation of Marine Injector Deposit Sample .....	90
3.3	Conclusions .....	96
Chapter 4: Towards a Comprehensive Characterisation of Chemical Variation with Depth of IDIDs.....		
		99

4.1	Introduction .....	99
4.2	Results and Discussion.....	100
4.2.1	Estimating deposit thickness from profilometry of OrbiSIMS depth profiling GCIB craters.....	100
4.2.2	Manual Depth Profile Interpretation of Needle 6 and 8 to Probe Chemical Variation with Depth .....	102
4.2.3	Multivariate Analysis to Understand IDID Layering Effects...	109
4.3	Conclusions .....	127
Chapter 5: Simulating Diesel Deposit Formation Using the Jet Fuel Thermal Oxidation Test for Chemical and Mechanistic Insights into IDID Composition .....		130
5.1	Introduction .....	130
5.2	Results and Discussion.....	132
5.2.1	Hydrocarbon and Carbonaceous Deposit Chemistries in JFTOTs and an IDID using OrbiSIMS and XPS .....	132
5.2.2	Nitrogen-Containing Deposit Chemistries in JFTOTs and IDIDs using OrbiSIMS and XPS .....	140
5.2.3	Sulfur and Phosphorus-Containing Deposit Chemistries in JFTOTs and IDIDs using OrbiSIMS and XPS .....	150
5.2.4	DDSA and Sodium Carboxylate Deposit Chemistry in JFTOTs and IDIDs using OrbiSIMS and XPS.....	155
5.2.5	Carboxylates and Triglycerides from Biofuels in JFTOT Deposits using OrbiSIMS .....	162
5.2.6	Heavy Metals in JFTOT and IDID Deposits by OrbiSIMS and XPS: Zinc and Molybdenum.....	165
5.2.7	Optimising JFTOT Temperature for Simulation of IDID Formation by OrbiSIMS and XPS Analysis .....	166
5.3	Conclusions .....	172
Chapter 6: Conclusions and Future Work .....		175
6.1	Research summary .....	175
6.2	Conclusions .....	175
6.3	Future Work .....	178

6.3.1	Use of Novel SIMS and XPS Methods .....	178
6.3.2	Validation of GCIB Depth Profiling .....	179
6.3.3	Expansion of JFTOT IDID Simulation Investigation.....	179
6.3.4	Determination of IDID Formation Mechanisms .....	180
6.3.5	Expansion of AP-MALDI-MS Methodology.....	181
6.3.6	Automation of Orbitrap™ Noise Treatment .....	182
6.3.7	Future Analytical Workflow Recommendations.....	182
References .....		183
Appendix .....		196

## Figures

Figure 1.1: Annotated ideal diesel cycle diagram, adapted from Winterbone <i>et al.</i> (8).	2
Figure 1.2: Schematic of Bosch diesel injector where the nozzle with needle housed inside can be seen on the far left. Taken from Crua, C. and Heikal, M.R. (2014), originally from Robert Bosch GmbH (13).	3
Figure 1.3: Examples of chemical structures typically seen in diesel fuel (7, 14, 15).	4
Figure 1.4: Reaction schemes for the production of HVO (saturated alkenes) via hydrogenation and biodiesel (FAME) via transesterification from a vegetable oil triglyceride feedstock (7, 19, 25).	5
Figure 1.5: Formation process of carbonaceous deposits adapted and extended from Barker <i>et al.</i> (2009) and Michelson <i>et al.</i> (2020) (50, 57).	11
Figure 1.6: Metal carboxylate deposit formation. DDSA corrosion inhibitor mode of function by a) metal surface adhesion, or b) inverse micelle solvation. c) Acid-base reaction of DDSA and other carboxylic acids with sodium forms a metal carboxylate inverse micelle. d) Micelle disassembly to precipitate the sodium carboxylates (2, 28).	12
Figure 1.7: Lubricant oil additives notable in this thesis (80, 85).	15
Figure 1.8: Reaction of PIBSI with different carboxylic acid species to form amides (58, 60). X = unidentified group.	18
Figure 1.9: SEM images of IDIDs from a-b) Venkataraman <i>et al.</i> (2008) (48), c).	22
Figure 1.10: TEM images of IDIDs from a-b) Venkataraman <i>et al.</i> (2008) (48), c) Barker <i>et al.</i> (2015) (46), and d) Barker <i>et al.</i> (2017) (108).	23
Figure 1.11: The photoelectric (a-b) and Auger (d) effects. Adapted from Jenkins <i>et al.</i> (111).	25
Figure 1.12: High-resolution carbon XP spectra for IDIDs in the literature. a) From Venkataraman <i>et al.</i> with additional annotations (48). b) From Dallanegra <i>et al.</i> (40).	26
Figure 1.13: Map of ordered and disordered carbon with Raman from Barker <i>et al.</i> (2015) (46).	27

Figure 1.14: Schematic diagram of the principle of ToF-SIMS. Primary ion bombardment of sample surface, emitting sputtered material of secondary particles, some of which are ionic. Adapted from Vickerman and Briggs (2013) (126). .....	30
Figure 1.15: A schematic of the layers identified by depth profiling of the IDID, from Barker <i>et al.</i> (2012) (47).....	31
Figure 1.16: ToF-SIMS spatial information from an IDID sample from Barker <i>et al.</i> .....	31
Figure 1.17: Results from PCA of static ToF-SIMS data from 8 injector needle IDIDs for showing PC 1 vs PC 2 scores for a) Positive polarity, b) Negative polarity. Adapted and annotated from Barker <i>et al.</i> (128).....	33
Figure 1.18: 3D OrbiSIMS example data. a) Mass spectra overlay using ToF analyser (black) and Orbitrap <sup>TM</sup> analyser (blue). b) 3D OrbiSIMS imaging of an animal cell. Adapted from Passarelli <i>et al.</i> (2017) (135).....	35
Figure 1.19: a) Internal and external temperature measurements for different positions along the JFTOT tube for different set temperature runs from Sander <i>et al.</i> (140). b) temperature profile of fuel in JFTOT calculated by CFD for a set-point of 260 °C from Lacey <i>et al.</i> (139). .....	36
Figure 2.1: a) Image of Alcor JFTOT Mk II. b) Schematic of Alcor JFTOT Mk II functionality. ....	40
Figure 2.2: JFTOT heater tube with dimensions (149). ....	40
Figure 2.3: Photograph of post-treatment a) JFTOT LMW PIBSI and b) JFTOT RME with analysis positions identified.....	44
Figure 2.4: Examples of noise artefacts at typical fuzzy site regions in sample JFTOT 9.....	53
Figure 2.5: Partial ringing artefacts surrounding PO <sub>3</sub> <sup>-</sup> peak in sample JFTOT 9, a) partial ringing that has the appearance of real peaks found neighbouring the saturating peak, b) depth profiles of partial ringing peaks and saturating PO <sub>3</sub> <sup>-</sup> ion, c) partial ringing “fuzzy” peaks around PO <sub>3</sub> <sup>-</sup> . ....	54
Figure 3.1: Optical microscope images (left) and SEM close-up images (right) for a) Needle 6 (with general OrbiSIMS analysis positions labelled), b) Needle 7 and c) Needle 8. ....	65



Figure 3.2: Normalised OrbiSIMS spectra for a) Needle 8 analysis position 4, and b) Needle 6 position 3. c) Spectra (normalised peak area) after filtering for hydrocarbon ions. ....	68
Figure 3.3: a) DBE v $m/z$ and C/N v $m/z$ plots for hydrocarbon and N1 and N2-containing ions in positive polarity for needle IDID samples. b) High-resolution C 1s XPS $\pi$ - $\pi^*$ component percentage area. ....	70
Figure 3.4: OrbiSIMS secondary ion overlaid normalised peaks for two positions of injector needle IDID samples. a) PAHs and b) N-PACs. ....	72
Figure 3.5: O-PAC-type ions OrbiSIMS data. a) O1 and O2-containing ions' DBE as a function of $m/z$ . b) O1 and O2-containing polyaromatic ion normalised peaks for Needles 6-8. ....	73
Figure 3.6: Needle 8 hydrocarbon OrbiSIMS ion depth profiles for a) a range of PAH sizes, and b) ions of the same C number with decreasing H number..	74
Figure 3.7: OrbiSIMS chemical images (two scans) for the IDID with the most intense and largest mass polyaromatics (Needle 8) at position 4, normalised to total ion image. 300×300 $\mu\text{m}$ images for inorganic salt, substrate, PAH, N-PAC and carbonaceous OrbiSIMS ions. ....	76
Figure 3.8: Succinimide OrbiSIMS ion normalised spectra for IDID samples, with varying sizes of alkyl groups. a) Succinimide head ion. b) Succinimide with 1 PIB unit ion. c) Derivative ion of succinimide with 6 PIB units.....	78
Figure 3.9: Kendrick mass defect (base $\text{CH}_2$ ) for Needle 12 position 3 depth profile (75-1125 $m/z$ range) filtered for organic ions of minimum normalised intensity $3.3\text{E-}6$ , N1-2, O2-5, DBE < 6. ....	79
Figure 3.10: a) Structure of PIBSI. b) Suggested structures for the highest mass ions of key homologous ion series (C, D, B, I, H, E, J and G) from the KMD (base $\text{CH}_2$ ) analysis.....	80
Figure 3.11: Fragmentation ions with suggested structures from an MS/MS experiment of a high intensity ion from series D ( $\text{C}_{29}\text{H}_{50}\text{NO}_3^+$ ). ....	81
Figure 3.12: Sodium-DDS related OrbiSIMS data. a) OrbiSIMS spectrum from a central position of Needle 13, b) MS/MS fragmentation schematic for Na-DDS ions in Needle 14. ....	82
Figure 3.13: DDSA OrbiSIMS and XPS data. a) Normalised spectra for Na-DDS and Na carbonate OrbiSIMS ions. b) XPS data for sodium atomic	

concentration and high-resolution C 1s spectra carboxyl component percentage area. ....	83
Figure 3.14: ABS data for Needles 6-9. a) ABS OrbiSIMS secondary ions normalised intensities for multiple positions (note Needle 6 only has four positions, labelled 2-5), b) S and Ca XPS atomic concentrations .....	86
Figure 3.15: Inorganic salt material in IDID samples at multiple positions from low on the needle shaft (position 1) to the end of the needle, of Needles 6, 8, 7, 9, 14. a) Positive polarity data. b) Negative polarity data. ....	89
Figure 3.16: Optical microscope images of marine injector plunger sample (Marine 1). a) View of metal surface and heavily deposited groove (7.8× zoom) with general analysis position marked. b) Zoomed in (51.1×) view of groove position. c) SEM image (36× zoom) of groove. d) SEM image (154× zoom) of groove. ....	91
Figure 3.17: a) Phenolate and salicylate OrbiSIMS normalised peaks in Marine 1 and IDID samples. b) High-resolution XPS C 1s C-O components for the same samples. ....	92
Figure 3.18: Organophosphate OrbiSIMS ions in sample Marine 1. MS/MS analysis of a) $C_{28}H_{42}PO_4^-$ , b) $C_{42}H_{64}PO_4^+$ and c) $C_{29}H_{52}PO_4^-$ . ....	94
Figure 3.19: Hydrocarbon distributions in Marine 1 from AP-MALDI (using TCNQ matrix with laser power of 6.2% or 19%) and OrbiSIMS (using $Ar_{3000}^+$ GCIB). a) DBE as a function of carbon number. b) Hydrogen number as a function of carbon number. ....	96
Figure 4.1: Profilometry 3D images of craters from OrbiSIMS positive and negative polarity depth profiles. a) Needle 6, b) Needle 8 and c) Needle 7...	101
Figure 4.2: Depth profiles of selected key ions for Needle 8 a) negative polarity, and b) positive polarity. Published in Lamb <i>et al.</i> (2020) (78). ....	103
Figure 4.3: Depth profiles of selected key ions for Needle 6 a) negative polarity, b) .....	104
Figure 4.4: O 1s XPS depth profile for Needle 8. a) O 1s spectrum at surface. b) O 1s spectrum at 2725s etch time. c) 3D graph of O 1s spectra vs. etch time, showing growth of metal oxide shoulder. ....	106
Figure 4.5: XPS depth profile of Needle 8 excluding substrate elements and substrate oxygen. Published in Lamb <i>et al.</i> (2020) (78). ....	106

Figure 4.6: XPS depth profile of Needle 6 showing all detected elements. Published in Lamb <i>et al.</i> (2020) (78).....	109
Figure 4.7: NMF results for Needle 6 negative polarity depth profile. a) OrbiSIMS spectrum over the full depth profile range. b) Endmember scores (normalised point-to-point). c) Original loadings for each endmember.....	111
Figure 4.8: Example ions' loadings for Needle 6 in negative polarity. a) Original loadings from simMVA NMF results. b) Relative loadings after normalisation in Equation 6.....	114
Figure 4.9: Loadings plots for each endmember after filtering to remove ions that have a higher loading in another endmember.....	115
Figure 4.10: OrbiSIMS depth profile NMF scores for negative and positive polarity and XPS atomic percentage depth profiles for Needles 6-8. ....	118
Figure 4.11: Summary of OrbiSIMS-NMF (from both polarities) and XPS key results for Needles 6-8 depth profiles, with deposit thickness estimate from profilometry of OrbiSIMS depth profile average crater depth. XPS element concentrations are marked with ▲ where there is an increase from the previous pseudo-layer and ▼ where there is a decrease (with 2 arrows marking a more significant increase/decrease and no arrow where no significant change occurs). ....	119
Figure 4.12: Schematic summarising key chemistries from Figure 4.11, with estimates for the thickness of each layer averaged from profilometry measurements (Table 4.1) for positive and negative depth profiles with error from the standard deviation, assuming constant sputter rates throughout each depth profile.....	127
Figure 5.1: Hydrocarbon data for JFTOT samples and Needle 8. a) OrbiSIMS principal component 1 (mass filtered <0.7) in positive polarity scores and loadings. b) C 1s XP spectrum components model example for JFTOT RF-06. c) Overlay of C 1s XP spectra from positions 1, 3 and 5 for JFTOT CME and JFTOT Lubricant. d) Overlay of C 1s XP spectra for position 3 of JFTOT RF-06, JFTOT Zinc and JFTOT Na + DDSA. e) C 1s $\pi$ - $\pi^*$ percentage area for key JFTOT and IDID samples.....	134
Figure 5.2: JFTOT OrbiSIMS principal component 6 (positive polarity, mass filtered <0.7), separating higher H-number hydrocarbons (negative loadings) from lower (positive).....	136

Figure 5.3: PAH/carbonaceous data from key JFTOT samples. a) Normalised secondary ion intensities of key PAH ions with high loadings for samples that had high scores in PC 1 (positive polarity, <0.7 mass filter), all data from position 3 except HVO which is position 5, b) normalised intensities of those ions for Needle 8, c) DBE vs. $m/z$ plots with intensity $>1 \times 10^{-5}$ normalised to total of ions with decimal masses <0.5 for each position of JFTOT RF-06, Needle 8, and JFTOT Zinc (using a higher cycle time and mass range).....	138
Figure 5.4: OrbiSIMS depth profile data for hydrocarbon secondary ions in JFTOT RF-06. Depth profiles of PAHs of a) increasing size and b) decreasing H/C ratio. c) H number as a function of C number for all hydrocarbons ( $>2.5 \times 10^{-5}$ normalised intensity) at positions 3 and 4 with colourmap for sputter time at which each ion reaches its maximum intensity. ....	140
Figure 5.5: Principal components describing nitrogenous ions, a) PC 4 positive polarity with <0.7 mass filtering, b) PC 1 negative polarity with <0.7 mass filtering. ....	142
Figure 5.6: Key OrbiSIMS and XPS data for LMW PIBSI and nitrogenous chemistries in JFTOTs and IDIDs. Normalised OrbiSIMS secondary ion peaks for a) Succinimides and b) N-PACs. Normalised secondary ion intensities along JFTOT LMW PIBSI positions 1-5 for c) LMW PIBSI marker ions and d) N-PAC and N-carbonaceous ions. e) XPS relative atomic concentrations of C, O and N.....	144
Figure 5.7: DBE or C/N as a function of $m/z$ for hydrocarbon and N-containing secondary ions at five positions of JFTOT and IDID samples. Calculated using the Formula_calculator script ( $1 \times 10^{-5}$ minimum intensity normalised to sum of ions with decimal mass <.5). ....	146
Figure 5.8: OrbiSIMS depth profiles showing nitrogen-containing secondary ions for JFTOT LMW PIBSI a) position 2, b) position 3. c) Needle 6 and d) Needle 10.....	147
Figure 5.9: Suggested mechanism of N-carbonaceous JFTOT deposit formation from diesel and LMW PIBSI (typical PIB length shown), based on Choudhary's succinimide pyrolytic decomposition and proposed integration of nitrogenous products into diesel carbonisation via N-PACs based on evidence from OrbiSIMS depth profiling (199). ....	149

Figure 5.10: OrbiSIMS and XPS data for phosphorus and sulfur-containing ions. ....	151
Figure 5.11: Depth profiles of key S- and P-containing OrbiSIMS secondary ions at central positions of a) JFTOT RME, b) JFTOT Lubricant, c) JFTOT CME and d) Needle 9. e) Schematic summary of S- and P-carbonaceous deposit formation.....	154
Figure 5.12: OrbiSIMS positive polarity PC 2 scores (>0.7 mass filtered) and loadings, identifying sodium inorganic salts in JFTOT Na + DDSA and JFTOT CME. ....	157
Figure 5.13: DDSA-related OrbiSIMS and XPS results. 3D OrbiSIMS normalised intensities along JFTOT Na + DDSA of a) sodium DDS and b) sodium inorganic secondary ions. c) C, O and Na relative atomic concentrations from XPS for JFTOT Na + DDSA (surface) and two IDIDs (surface and bulk from 0-1850s region of depth profiles). d) Normalised OrbiSIMS peak comparisons for key secondary ions. ....	158
Figure 5.14: DDSA-related high-resolution C 1s XPS data for JFTOT Na + DDSA position 3, JFTOT RF-06 position 3, Needle 6 and Needle 7. a) C 1s spectra overlay. b) Quantification of carboxyl and carbonate components. c) Ratios of carboxyl:carbonate components.....	159
Figure 5.15: Depth profiles of Na-DDS and key related ions for a) JFTOT Na + DDSA position 1, b) JFTOT Na + DDSA position 3, c) Needle 6 and d) Needle 7. ....	161
Figure 5.16: Mechanism of a) deposition and b) subsequent thermal decomposition suggested by OrbiSIMS depth profiles of JFTOT Na + DDSA. ....	162
Figure 5.17: JFTOT calcium carboxylate data. a) Scores and loadings for PC 5 (positive polarity, <0.7 mass filtering). b) Normalised peaks of secondary ions of interest found by PC 5. c) Calcium atomic percentage from XPS quantification for position 1 and the position of most deposition (position 3 for all samples except HVO, position 5). ....	163
Figure 5.18: Distribution of carboxylics in JFTOT CME (position 3) as free carboxylate, Na-carboxylate, and TAG secondary ions, compared to the Caballero <i>et al.</i> 's reported range for coconut oil's acids distribution normalised to lauric acid (12:0) (207). ....	164

Figure 5.19: Zinc and Molybdenum OrbiSIMS data for relevant JFTOTs and for Needle 8 from 0-25,000 seconds etch time, a) PC 2 (>.7 mass filtering, negative polarity) results and b) normalised peaks of key ions comparing affected samples. ....	166
Figure 5.20: Images of a) JFTOT 200 °C, b) JFTOT 250 °C and c) Needle 8 with analysis positions labelled. Position of thermocouple (position of heating) is marked for JFTOT samples. ....	168
Figure 5.21: PAH data for Needle 8 and JFTOT 200 °C and JFTOT 250 °C. a) Hydrocarbon distributions of DBE as a function of $m/z$ , b) PAH intensities normalised to $C_{12}H_8^+$ . c) C 1s XPS $\pi$ - $\pi^*$ component percentage area contributions. ....	169
Figure 5.22: GCIB-Orbitrap <sup>TM</sup> 300×300 $\mu$ m images of PAH ions, a carbonaceous ion, N-PAC ions and a calcium hydroxide ion at position 8 of JFTOT 200 °C (the position of highest deposition). All normalised to the total ion image. ....	171

## Tables

Table 1.1: A summary of the additives commonly used for diesel fuel (28). ....	6
Table 1.2: Types of IDIDs seen in the literature with details (4, 38, 39). ....	9
Table 2.1: IDID samples and marine injector deposit sample with thesis ID derived from the previous work by Angel-Smith (2017) (127, 128), ID supplied by Innospec and known geographical origins and information about the failure in service. ....	39
Table 2.2: JFTOT samples with fuel/dopant combination, temperature and run-time. ....	43
Table 2.3: Compiled references for binding energy and full-width-height-maxima expected for carbon's chemical states in XPS (156-158). ....	49
Table 2.4: Mass ranges of “fuzzy site” Orbitrap™ noise. ....	53
Table 2.5: Peak search parameters for creating peak lists in SurfaceLab for NMF of negative and positive polarity OrbiSIMS depth profiles for Needles 6-8. ....	60
Table 3.1: Needle 6 EDS data from position 1, before the DLC. ....	66
Table 3.2: Needle 6 EDS data from position 4, on the DLC and deposit. ....	66
Table 3.3: Largest hydrocarbon and N-containing (N <sub>1</sub> or N <sub>2</sub> ) positive polarity polyaromatic-type ions. Minimum intensity $1 \times 10^{-5}$ normalised to the total intensity for ions with decimal mass <.5. ....	70
Table 3.4: Homologous PIBSI-related ion series with highest intensity and mass ions from KMD. ....	79
Table 3.5: OrbiSIMS data for non-DDS carboxylate secondary ions. ....	84
Table 3.6: Zinc-containing OrbiSIMS secondary ions (all deviations <2.5 ppm) for multiple positions of Needle 8. ....	87
Table 3.7: MS/MS results for high mass O6 series ion. NCE = 40. ....	93
Table 3.8: Salicylate, O6 and O7 homologous series of OrbiSIMS ions, with colourmap for each series' intensities. ....	93
Table 4.1: Profilometry step height data for Needles 6-8 OrbiSIMS and XPS depth profiling craters using average of ten cross sections across each crater. ....	101
Table 4.2: Needle 6 negative polarity depth profile NMF results for key ions with ID numbers from Figure 4.9, loadings and relative loadings, separated by	

which endmember their loading is highest for. Additional ions shown at the bottom which are highly distributed across multiple endmembers. Heat map applied to each column: for original loadings green = maximum value and red = minimum, for relative loadings green = 100 and red = 0.....	116
Table 4.3: OrbiSIMS depth profile NMF score interfaces for Needle 6, Needle 8 and Needle 7 in both polarities. ....	117
Table 5.1: Motivation for the investigation of each JFTOT sample in this chapter. ....	131
Table 5.2: MS/MS results for N-PAC type ion $C_{24}H_{10}N^+$ ( NCE = 70 and width = 0.9).....	142
Table 5.3: MS/MS results for sodium adducted trilaurin ion in JFTOT CME position 3. ....	164
Table 5.4: PAH secondary ion intensities in JFTOT 200 °C, JFTOT 250 °C and Needle 8 normalised to intensity of $C_{12}H_8^+$ , then normalised to the largest intensity position for each respective ion in either JFTOT 200 °C or Needle 8, with heat map applied to relevant sample positions. Heat map applied to all table where red = 0 and green = 1, with the exception of JFTOT 250 °C position 4 which is excluded due to its much larger values. ....	170



## Abbreviations

<b>ABS</b>	Alkylbenzene sulfonate
<b>AP-MALDI</b>	Atmospheric pressure matrix-assisted laser desorption ionisation
<b>DBE</b>	Double bond equivalents
<b>DCA</b>	Deposit control additive
<b>DDS</b>	Dodecenyl succinate
<b>DDSA</b>	Dodecenyl succinic acid
<b>DLC</b>	Diamond-like carbon
<b>EDID</b>	External diesel injector deposit
<b>EDS</b>	Energy dispersive x-ray spectroscopy
<b>EM</b>	Endmember
<b>FAME</b>	Fatty acid methyl ester
<b>FIE</b>	Fuel injection equipment
<b>FTIR</b>	Fourier transform infrared
<b>GCIB</b>	Gas cluster ion beam
<b>GC-MS</b>	Gas chromatography-mass spectrometry
<b>GDI</b>	Gasoline direct injection
<b>HMW</b>	High molecular weight
<b>HVO</b>	Hydrotreated vegetable oil
<b>IDID</b>	Internal diesel injector deposit
<b>JFTOT</b>	Jet fuel thermal oxidation tester
<b>KMD</b>	Kendrick mass defect
<b>LMW</b>	Low molecular weight
<b>MALDI</b>	Matrix-assisted laser desorption ionisation
<b>MoDTC</b>	Molybdenum Dithiocarbamates
<b>MVA</b>	Multivariate analysis
<b>MW</b>	Molecular weight
<b>N-PAC</b>	Nitrogen-containing polyaromatic compound
<b>NMF</b>	Non-negative matrix factorisation
<b>O-PAC</b>	Oxygen-containing polyaromatic compound
<b>PAH</b>	Polyaromatic hydrocarbon
<b>PC</b>	Principal component
<b>PCA</b>	Principal component analysis
<b>PDMS</b>	Polydimethylsiloxane
<b>PIBSI</b>	Polyisobutylenesuccinimide
<b>SEM</b>	Scanning electron microscopy
<b>SIMS</b>	Secondary ion mass spectrometry
<b>TAG</b>	Triacylglyceride
<b>TEM</b>	Transmission electron microscopy
<b>ToF</b>	Time-of-flight
<b>XPS</b>	X-ray photoelectron spectroscopy
<b>ZDDP</b>	Zinc dialkyldithiophosphate

## Chapter 1: Introduction

A diesel injector's role in the combustion cycle is to deliver the correct quantity of fuel at the correct time in the ideal manner for efficient fuel dispersion and combustion (1). Deposit formation within the injector can affect its moving parts, leading to over fuelling or under fuelling which can cause operational issues with the engine, reduced fuel economy, power of the engine, and increased emissions (2). With a number of changes to diesel fuel and injector design over recent years, internal diesel injector deposits (IDIDs) have become increasingly common and a significant issue. Understanding their structure and composition is crucial for the development of effective mitigation strategies, such as through the development new deposit control additives (DCA) or changes to fuel composition or injector design (3, 4).

### 1.1 Background: Diesel Fuel and Engines

#### 1.1.1 The Diesel Engine

Rudolf Diesel's 1892 patent outlined an efficient engine which used higher air compression to reach a temperature above the fuel's ignition point and achieve automatic combustion as the fuel is gradually introduced. After 1945, the diesel engine's improved fuel economy was recognised and rapid uptake and development followed, especially in the commercial vehicle sector, which they dominate today (1, 5-7). Most modern diesel engines operate on a four-stroke cycle (intake, compression, power and exhaust strokes) and utilise direct injection (7, 8). The ideal diesel cycle's pressure-volume diagram is shown in Figure 1.1, showing the process of air compression, injection to produce ignition and expansion, and finally exhaust of the combustion products (8).

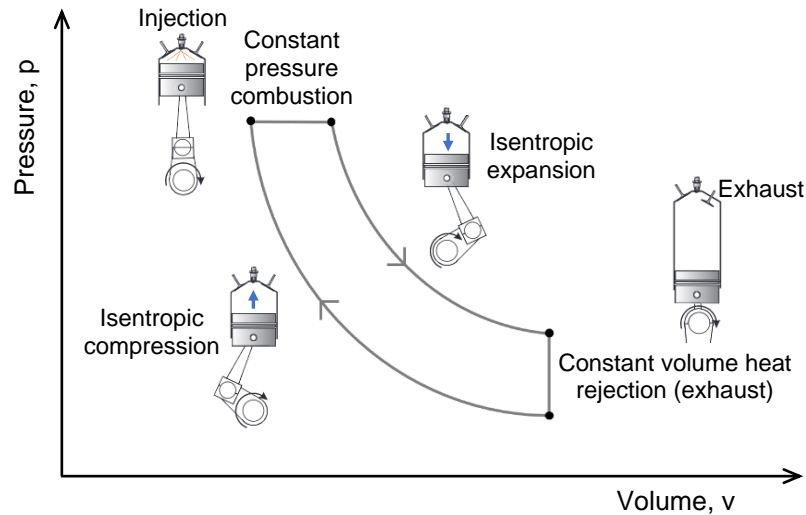


Figure 1.1: Annotated ideal diesel cycle diagram, adapted from Winterbone *et al.* (8).

### 1.1.2 The Diesel Injector

Figure 1.2 shows a schematic of a diesel injector in which the injector tip (nozzle) can be seen on the left which protrudes into the combustion chamber and houses the injector needle. The inlet, where high pressure fuel flows, is seen on the right and the fuel flows towards the outlet via the needle, which is actuated by a solenoid valve and moves to allow the fuel to flow through the nozzle holes into the combustion chamber (9). The pressures used in diesel injectors in commercial passenger car fuel injector equipment (FIE) is typically 2000 bar, however new developments are increasing this to over 3000 bar to improve efficiency (10, 11). A diesel injector tip is estimated to reach close to 370 °C during operation. Further from the tip, this temperature reduces as the distance from the heat source is larger, thus much of the injector needle likely reaches temperatures of 200-300 °C (12).

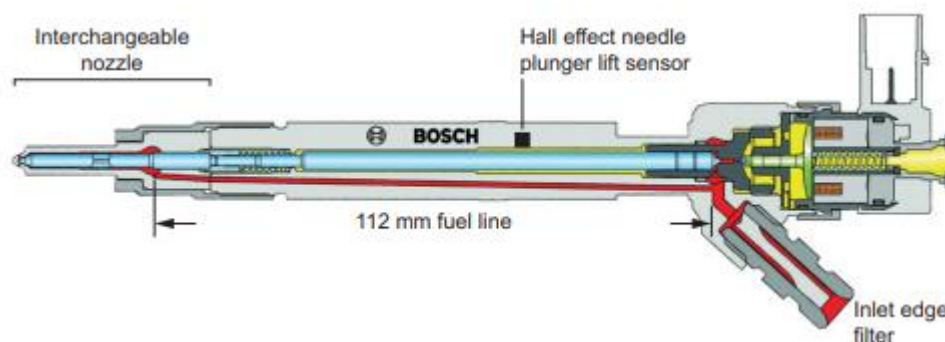


Figure 1.2: Schematic of Bosch diesel injector where the nozzle with needle housed inside can be seen on the far left. Taken from Crua, C. and Heikal, M.R. (2014), originally from Robert Bosch GmbH (13).

### 1.1.3 Diesel Fuel

Diesel fuel is a fraction from the distillation of crude oil and its composition therefore varies depending on the composition of the hydrocarbons of the oil from which it is derived. After removal of impurities in “de-salting”, crude oil is distilled to separate the respective fractions of the oil based on boiling point; other fractions include petrol (a lighter fraction) and fuel oil used for marine engines (a heavier fraction). Further processing is then performed to fine-tune the fuel’s properties based on standard measures such as octane number, cetane number, flash point, viscosity and volatility (7).

Commercial diesel is a complex mixture of mostly aliphatic hydrocarbons (~64%) with carbon numbers mostly in the range of  $C_9$ - $C_{20}$ , as well as significant aromatic hydrocarbon content (~35%) including benzene and polycyclic aromatic hydrocarbons and small amounts (~1-2%) of olefinic hydrocarbons (14). Examples of some of these compounds are shown in Figure 1.3 (7). The main polycyclic aromatics in diesel fuel are phenanthrene, pyrene, naphthalene and fluorene, though newer diesel contains lower concentrations of aromatics in order to reduce pollutants (15).

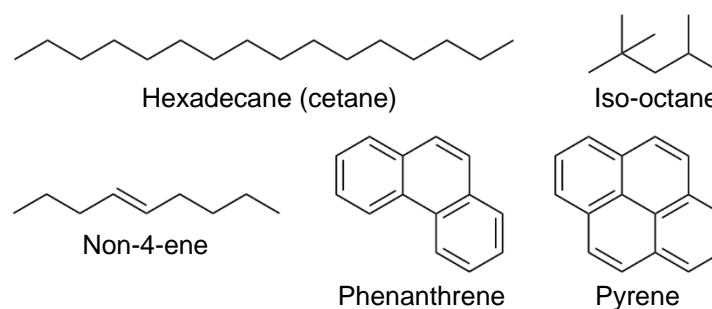


Figure 1.3: Examples of chemical structures typically seen in diesel fuel (7, 14, 15).

#### 1.1.4 Biofuels: Biodiesel and HVO

Biofuels are fuels derived immediately from living matter. This can be from a food crop (first generation biofuels) or a non-food source such as biowaste (second generation) (16). Legislation has been introduced requiring the inclusion of a certain percentage of renewable fuel in diesel blends to reduce carbon emissions. In the EU Renewable Energy Directive (RED) II, a 14% share of renewables is required in all member states' transport sectors by 2030, as part of a wider goal of a 32% renewables share across all energy consumption (17). Other motivations for increasing the share of biofuels include geopolitical energy security advantages and economic advantages from mitigating the impacts of oil price fluctuations (18).

The term biodiesel refers to traditional fatty acid methyl ester (FAME) biodiesel. This is produced by the transesterification of the triglyceride feedstock using a catalyst, which can be an acid, base or enzyme (Figure 1.4) (19). Biodiesel's properties depend upon the triglyceride feedstock as this dictates the specific FAME product but generally provides higher lubricity, good combustion characteristics and lower sulfur and aromatic content (20-22). Highly unsaturated feedstocks are a concern, as their FAME products have low cetane number and oxidation stability (21). To avoid stability and operational issues, blending of biodiesel with conventional diesel generally does not exceed 7-10% (B7-B10) (16).

Hydrotreated vegetable oil (HVO), also known as hydroprocessed esters and fatty acids (HEFA) or hydrogenation derived renewable diesel (HDRD), is a newer alternative biofuel to traditional biodiesel (23). It is produced by hydrogenating the triglyceride feedstock, which can be from a range of sources, to give saturated (paraffinic) hydrocarbons (Figure 1.4) (24, 25). Since HVO is purely hydrocarbon and free of aromatics, sulfur and oxygen, it can be very high quality fuel with very similar composition to petrodiesel and advantageous properties including a high cetane number and good cold properties, providing good combustion and low temperature performance (24, 26). The process of hydrogenation decouples the HVO's properties from its feedstock, so poorer quality feedstocks such as waste animal fats can be utilised (24).

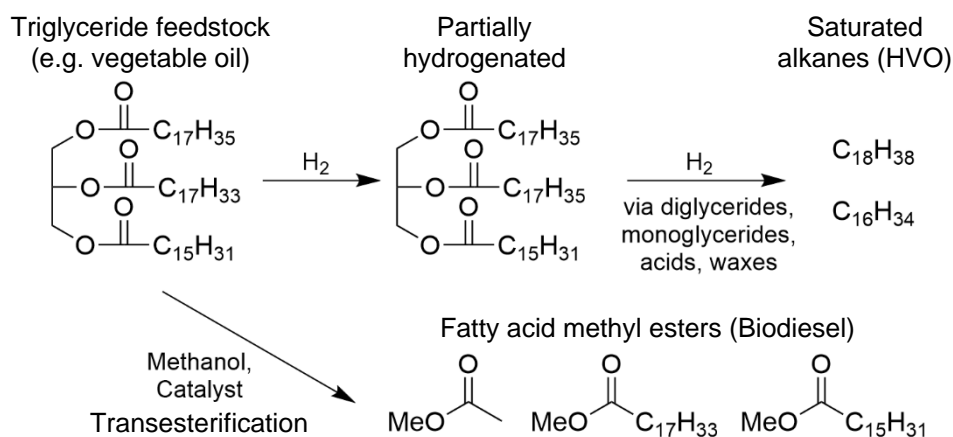
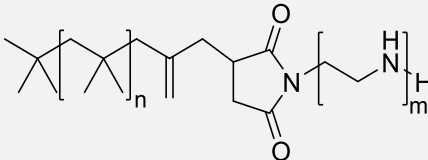
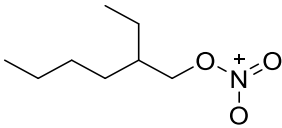
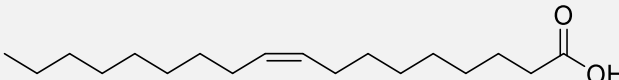
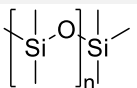
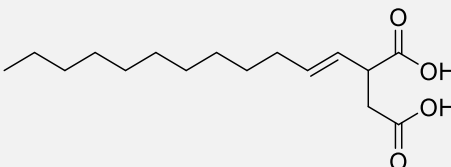
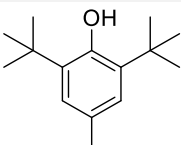


Figure 1.4: Reaction schemes for the production of HVO (saturated alkenes) via hydrogenation and biodiesel (FAME) via transesterification from a vegetable oil triglyceride feedstock (7, 19, 25).

### 1.1.5 Diesel Additives

Additivation in commercial diesel is more extensive than in the past and is becoming more so to improve properties, minimise costs and avoid engine damage/fouling. Additives perform specific functions to improve properties and characteristics of the fuel. This includes reducing harmful emissions, reducing deposit formation, improving stability, improving viscosity, improving ignition and reducing wear of pipelines (27). Table 1.1 provides an overview of the types of additives used in diesel fuel that are notable in this work, their purposes, modes of action and examples of their chemical structures (28).

Table 1.1: A summary of the additives commonly used for diesel fuel (28).

Type of Additive	Purpose	Mode of Action	Example
<b>Deposit Control Additive (DCA)</b>	Keeps the fuel system clean and free of deposit build-up, particularly at the injectors.	Solubilise polar deposit precursors; forms protective film on metal surfaces.	
<b>Cetane Number Improver (CNI)</b>	Increase cetane quality so the diesel ignites more easily and ignition delay is reduced.	Break down during combustion to form free radicals, which accelerate fuel decomposition.	
<b>Lubricity Improvers</b>	Lubricate the injector's moving parts to prevent wear.	Form a coating on metal surfaces providing a cushion between surfaces.	
<b>Anti-Foam Additives</b>	Reduce foam formation during re-fuelling, which can lead to premature fuel cut off or fuel splashing.	Reduce the surface tension of the walls of the air bubbles that form the foam, collapsing the bubble.	
<b>Corrosion Inhibitors</b>	Prevent surface corrosion of metallic components.	Forms a protective film on metal pipeline surface; solubilises water in the fuel.	
<b>Stability Improvers (Including Antioxidants)</b>	Prevent reactions of unstable compounds in the fuel that reduce its lifetime.	Preferentially react with unstable compounds to form soluble products and prevent sediment formation.	

### 1.1.6 The Status and Future of Diesel

Diesel vehicles once dominated the European car market following a push from both industry and government to lower carbon dioxide emissions but are increasingly disfavoured due to their harmful NO<sub>x</sub> and particulate matter emissions (29, 30). The market share of new diesel passenger cars in the UK fell from around 50% in 2015 to just 7.1% in July 2021, being overtaken by electric vehicles at 9%, plug-in hybrids with 8% and hybrid electric vehicles with 12% (31). The EU is following similar trends with decreasing numbers of internal combustion engine vehicles and increasing electric and hybrid vehicles, but diesel retains more of its historically high share in the union, representing 42.8% of passenger vehicles in 2022 (32, 33). The UK plans to ban sales of new petrol and diesel cars by 2030 and the EU has proposed a similar ban for 2035 (31, 34). Diesel maintains its dominance of commercial vehicles, representing 91.2% of light commercial vehicles and 96.3% of heavy commercial vehicles in the EU in 2022 (33). While diesel vehicles remain in use, their clean operation is imperative for limiting emissions of carbon and other harmful pollutants. To ensure this, emissions legislation continues to tighten, with the latest Euro 5 and Euro 6 standards further limiting the concentration of pollutants including carbon monoxide, hydrocarbons, nitrogen oxides, and particulate matter (35). Meeting these stringent emissions targets requires development of injection technology to improve combustion. This uses higher pressure, variable injection timing and metering, multiple injection events during each cycle and redesigned nozzles (36).

### 1.1.7 Diesel Engine Deposits

Since the 1940s, the propensity for deposit formation has been a criterion for engine performance testing, specifically on the combustion chamber and fuel injection valves. Fuel characteristics were recognised to contribute to the degree of deposition, which was of a soot-like nature. The manifestation of deposit issues depends upon the engine type and engine technologies; in today's engines, the fuel injection equipment (FIE) is particularly vulnerable (7). Other engine parts affected by deposits that have received research attention include filters and fuel tanks (7, 37). IDIDs are associated with FIE



operational issues such as loss of engine power, increased emissions, rough-idling, misfiring, stalling or, in the most severe cases, engine failure (3). The causes of internal diesel injector deposits today are broad and will be reviewed in the next section.

## **1.2 Internal Diesel Injector Deposits: Types, Causes and Formation Mechanisms**

The phenomena of IDID formation are complex, implicating fuel and additive components as well as contaminants and the engineering of the injector itself. This section covers the progress of research in understanding IDIDs, describing what has been learned about their composition and formation, their causes and mechanisms of formation.

### **1.2.1 Types of IDIDs**

The literature describes IDIDs of different structural and chemical types, with different causes and compositions identified. These types have been placed in six categories outlined in Table 1.2, all having been implicated in IDID-induced injector issues (38, 39). These deposits vary based on chemistry, exhibiting visual differences and different compositions when analysed. They range from carboxylate soaps to black carbonaceous coke-like material to inorganic salts. The compositional classification of diesel deposits is complicated by the observation of layered IDIDs, in which these different deposit types may exist together in layered structures (3, 38-40). Deposit layering may develop from the presence of different deposit-inducing components over multiple fuelling cycles.

Table 1.2: Types of IDIDs seen in the literature with details (4, 38, 39).

Type	Appearance	Chemistry	Origin
<b>Soaps</b>	White	Carboxylate salts	Soft metals reacting with carboxylics such as DDSA or others
<b>Inorganic</b>	Off-white	Inorganic salts such as sulfates	Contamination from many possible sources
<b>Amide</b>	Brown, often lacquer	Polymeric featuring amide bonds	Conversion of (mainly LMW) PIBSI succinimide to amide
<b>Aged fuel</b>	Sticky	Oxygen-containing species: carboxylics, aldehydes	Oxidation of fuel (often biodiesel)
<b>Lacquer</b>	Film, different colours	Possible carbonaceous precursor, often polymeric	Precipitation and deposition of various chemistries
<b>Coke/Carbonaceous</b>	Black	Carbonaceous, coke-like, possibly containing extended polyaromatics	Degradation, aromatisation, carbonisation of fuel and deposit over time

### 1.2.2 Causes and Formation Mechanisms of IDIDs

A number of causes of IDIDs have been identified and suggested in previous studies, though the field continues to develop as more deposit information is collected from new analytical developments. These are summarised in this section, with key known mechanistic details discussed.

#### 1.2.2.1 Ultra-low Sulfur Diesel

ULSD has been discussed as a factor behind the surge in frequency and severity of IDID cases, which shortly followed its introduction (2, 3, 38, 41, 42). Beginning in June 2006 for 80% of diesel fuel sold and expanding to 100% in December 2009, the US EPA enacted rules that cut the level of sulfur allowed in diesel to 15 ppm, a reduction of 97% (43). ULSD is less polar than higher sulfur diesels and contains less aromatic content which may lead to precipitation of deposit that would otherwise remain solvated in the fuel (4, 42, 44).

### 1.2.2.2 Degraded/Oxidised Fuel

Aged fuel components, such as via oxidation, are thought to be related to IDID formation (4). Many IDIDs show evidence of degraded fuel, primarily as oxygen-containing compounds (carboxylic acids and aldehydes) that have a sticky appearance. These deposits are suspected to be linked to biodiesel, discussed in Section 1.2.2.5.1 (37, 38). Such products in the fuel may trigger the initial deposition processes and progress to carbonaceous forms of deposit.

### 1.2.2.3 Aromatisation and Carbonisation

It is thought that after initial fuel degradation, precipitation and deposition, this early-stage deposit will continue to degrade and aromatise towards a coke-like or graphitic carbonaceous deposit comparable to other carbonaceous materials such as coal-tar pitch (3, 39, 45-47). Other types of deposit also likely degrade towards similar carbonaceous material due to the high pressure and temperature of the fuel injector. In the case of external diesel injector deposits (EDIDs), larger polyaromatic structures have been seen than in IDIDs, thought to be due to the higher temperatures and exposure to the combustion flames (48).

The processes that result in a carbonaceous deposit from the original organic fuel will be referred to in this thesis as “carbonisation”, a term which describes the conversion of organic material (in this case the diesel fuel and organic additives) to carbon materials (49, 50). This involves the loss of heteroatom-containing functional groups and hydrogen and the formation and growth of polyaromatic compounds, similar to the formation of soot (49-53). Such processes have been studied for flames, from the formation of the first aromatic ring through further growth into PAHs by the hydrogen abstraction-carbon addition (HACA) of acetylene (54). There are likely a myriad of other reactions occurring during carbonaceous deposit formation, such as phenyl addition/cyclisation (55). A recent review by Reizer *et al.* summarises current understandings of these mechanisms (56). The theory of how this occurs in an IDID is portrayed in Figure 1.5, proceeding via cyclic alkanes that can aromatise through hydrogen abstraction, the products of which can extend to

form large PAHs, becoming archipelago structures and then graphitic particles that may aggregate into a carbonaceous deposit (3, 50, 57). It is also theorised that these processes could integrate nitrogen to form nitrogen-containing polyaromatic hydrocarbons (N-PACs), however this has not been directly evidenced (3).

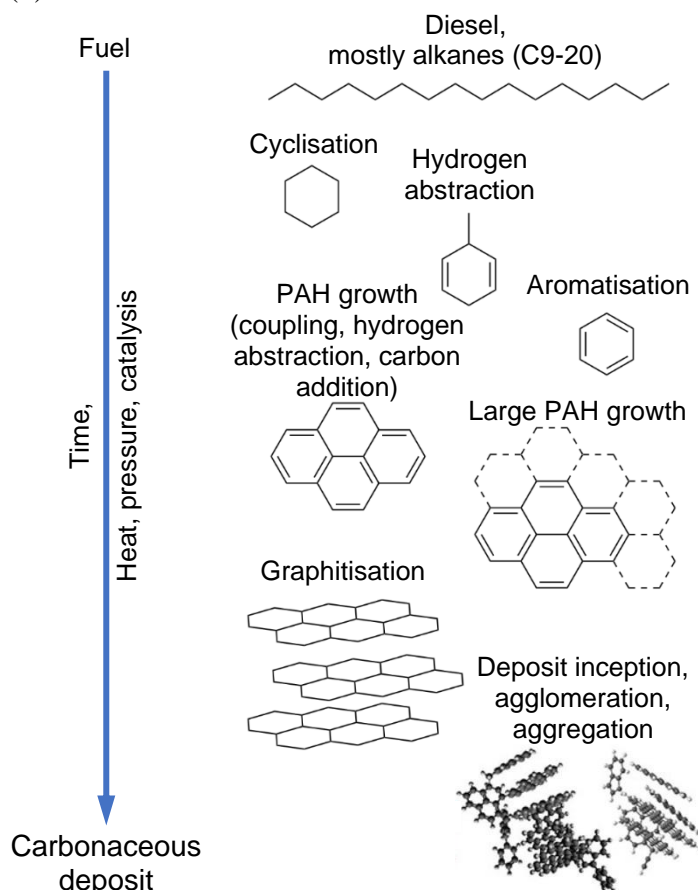


Figure 1.5: Formation process of carbonaceous deposits adapted and extended from Barker *et al.* (2009) and Michelson *et al.* (2020) (50, 57).

Heating of n-hexadecane (a typical straight chain alkane in diesel) to 160 °C at 450 psi (3.1 MPa) showed that this temperature could cause aromatisation, followed by polycondensation of the aromatic ring to form aromatic solids. This temperature is within the range experienced inside a diesel injector (200–300 °C) (12). The presence of oxygen was thought to be important, causing hydrogen abstraction of the cycloalkane by alkylperoxy/alkoxy radicals. In the absence of oxygen, these reactions would be expected to require temperatures above 400 °C (44, 48). Though multiple investigations have identified products of aromatisation in IDIDs, there remains uncertainty around the degree to which these processes occur within an injector environment.

### 1.2.2.4 Contamination

#### 1.2.2.4.1 Sodium

IDIDs caused by sodium are well documented in the literature and the element is detected in many studies (2, 40, 58, 59). Many cases involve interactions of sodium and carboxylic acids, which may be present in fuel from many sources, to form sodium carboxylate soaps with poor solubility in diesel. The most documented carboxylates are of the pipeline corrosion inhibitor additive dodecenylsuccinic acid (DDSA), a dicarboxylic acid species. The issue can also occur with any other carboxylic species in the fuel, such as impurities that may remain from FAME biodiesel production, be produced in auto-catalytic breakdown of FAME or be introduced as a contaminant (45, 58, 60-62). Other acids that can be involved include stearic, palmitic and oleic acids, which are also used as corrosion inhibitors in oil pipelines and are minor components in mono-acidic lubricity additives (63). Figure 1.6a-b shows how acid corrosion inhibitors work, by protecting surfaces or solvating water in micelles. Described by Trobaugh *et al.*, these micelles can solvate some sodium (and other) ions/polar species, but upon heating can disassemble to precipitate the soap deposit (2, 28).

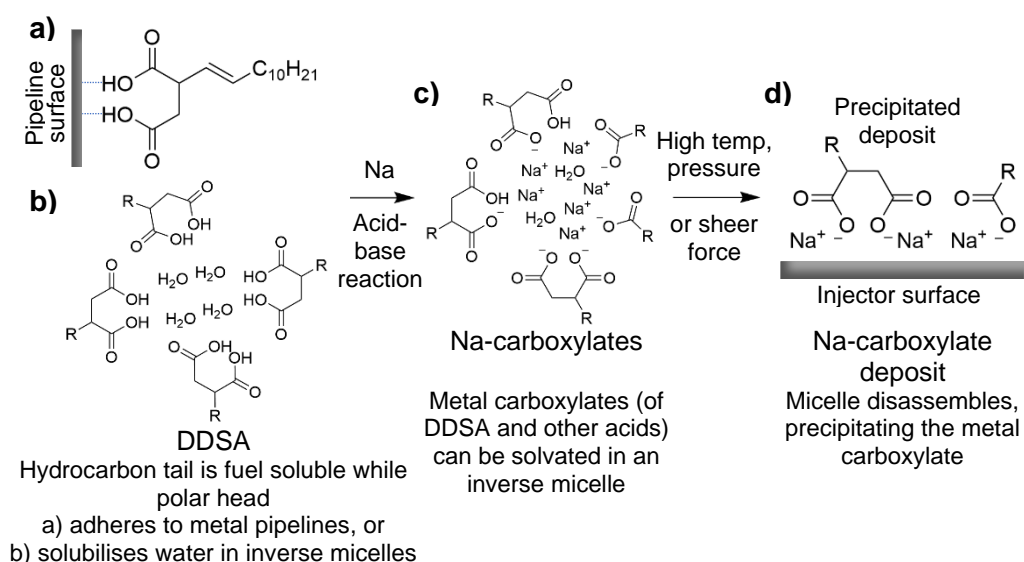


Figure 1.6: Metal carboxylate deposit formation. DDSA corrosion inhibitor mode of function by a) metal surface adhesion, or b) inverse micelle solvation. c) Acid-base reaction of DDSA and other carboxylic acids with sodium forms a metal carboxylate inverse micelle. d) Micelle disassembly to precipitate the sodium carboxylates (2, 28).

Inorganic sodium salts are also often observed, including hydroxides, cyanides, cyanates, carbonates, sulfates and chlorides (2, 59, 61). Some of these sodium sources, such as chloride and sulfate, appear less reactive than others for soap formation with carboxylic acids (61). Sodium contamination can enter the fuel system in many ways. Barge transportation and ballast water contamination from sea transportation of fuel can introduce sodium chloride (60, 64). Water bottoms can contribute sodium and other salts into fuel (65). Sodium chlorides and other sodium salts are used as drying agents. Contamination at refineries can introduce sodium sulfate and sodium hydroxide is used as a catalyst in the transesterification process that produces biodiesel (19, 60, 62). As biodiesel can contribute acid, this can exacerbate soap formation issues. Sodium nitrites were used as corrosion inhibitor additives which were problematic and replaced (62). As well as initiating deposit formation, sodium contaminated diesel in a diesel injector test is correlated with increased deposit thickness (64).

#### **1.2.2.4.2 Calcium**

Calcium is seen in many IDID samples (45, 58, 60, 66), including as a range of inorganic salts including oxides, carbonates, sulfates and chlorides (2, 59). Though fewer studies have focused on calcium than sodium, there are similar concerns surrounding it as with sodium as it is known to form insoluble carboxylate soaps (2, 41, 67). As with sodium, there is evidence that different types of calcium salt contaminants have different reactivity with acid species (67). Calcium can originate from water bottoms (61) and lubricant oil, which is a commonly cited source as for IDIDs that contain other lubricant components such as phosphorus (66).

#### **1.2.2.4.3 Zinc**

Zinc is known to promote injector deposit formation (45, 68, 69) and is used, generally as zinc neodecanoate, in engine testing (standardised test CEC F-98-08) for simulating injector nozzle fouling that reduces fuel flow and engine power (70-72). Testing of fuel from the field found that a diesel associated with deposit formation contained elevated levels of zinc (73).

An investigation has shown zinc may promote a more grainy type of deposit morphology visible with scanning electron microscopy (SEM) (74). However, the chemistry of the deposits that zinc causes is not well documented and the mechanism is unknown. Different studies suggest it may act to form carboxylate soaps like sodium and calcium, precipitate from fuel as a zinc oxide or act as a catalyst (60, 64, 75, 76). Ikemoto *et al.* found zinc carbonate in injector nozzles, which was suggested to originate from a reaction of zinc carboxylate with carbon dioxide from the combustion gases (76).

#### 1.2.2.4.4 Lubricant oil

Contamination with lubricant oil within an injector system can be problematic for the FIE, whether from deliberate fuel adulteration (as has been reported in some cases) or from accidental contamination such as from flow of blow-by gases or leakage within the engine (37, 44, 77, 78). Contamination of the injector has been suggested to be more likely with modern higher pressure FIE (77). Degradation of lubricant oil when remaining in its intended locations, such as piston rings, can form carbonaceous deposit (79). Lubricant oil contains many additives that are not designed for injector use, some of which are shown in Figure 1.7. Notably, they contain zinc in the form of the anti-wear additive zinc dialkyldithiophosphate (ZDDP) and calcium, often as calcium carbonate to form the core of an over-based detergent particle (70, 80). These two elements, as discussed above, are known to contribute to IDID formation and have been found in IDIDs from field samples (64, 81). Products of ZDDP degradation have also been seen in diesel engine piston deposits (82). Other lubricant additives have been indicated in IDIDs, such as alkylbenzene sulfonates (59). Some types of PIBSI, a family of chemistries discussed in depth in Section 1.2.2.6.1 which are used as deposit control additives (DCA) in diesel fuel, are also used as dispersant additives in lubricant oil (83). These are likely to be lower quality and lower mass than those used as DCAs, potentially contributing to IDID issues (84).

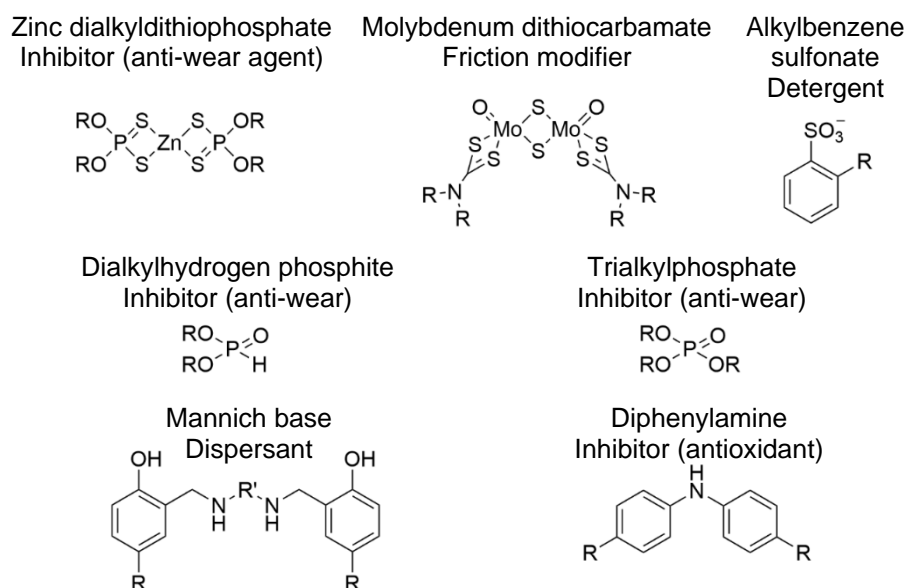


Figure 1.7: Lubricant oil additives notable in this thesis (80, 85).

#### 1.2.2.4.5 Other Contamination

Other contaminants can be found mentioned in the literature as possible contributors to IDID formation. As well as the metals discussed, copper, magnesium and iron are noted in various IDID analyses (2, 4, 40). In the case of iron, it is thought that carboxylic species in the fuel can corrode iron to form insoluble ferric carboxylate salts, similar to those described for sodium in Section 1.2.2.4.1 (4).

#### 1.2.2.5 Biofuels

##### 1.2.2.5.1 Biodiesel

Biodiesel has known IDID-promoting properties and its introduction in several regions has coincided with an increase in sodium salt deposits (64). Like the use of zinc in engine testing for injector deposit simulation, the reference fuel can also be doped with rapeseed methyl ester (RME) at 10% by volume to promote deposit formation, which results in loss of power (72). As discussed in the sections on sodium and calcium, insoluble soaps that precipitate in the injector to form IDIDs can form in reactions with acids; biodiesel, especially after ageing, has been shown to be a source of such acids (67, 86). It has been suggested that the metal ions can also auto-catalytically cleave the FAME to form the metal carboxylate soap (60). Lower quality biodiesel tends to have



higher concentrations of leftover acids from its production so is more of a concern (87). Further, as mentioned in Section 1.2.2.2, biodiesel is susceptible to ageing during fuel storage via oxidation, which can lead to soap formation (4). This is due to its unstable functionalities of unsaturated bonds and oxygen-containing groups (4, 88).

The catalysts used in biodiesel production, such as sodium hydroxide, can be highly reactive, potentially contributing another source of metals that can form soaps (87). Being of biological origin, biodiesel can introduce other diverse chemistries that may cause injector issues, such as triglycerides, sterol glucosides or phosphorus-containing compounds (7, 59, 89). To prevent issues, phosphorus is removed from petrodiesel during refining and is limited in biodiesel to 10 mg kg<sup>-1</sup> (90, 91). Its minor presence in coconut biodiesel has been suggested to contribute to diesel engine deposits (92). FAME and its decomposition products can be a nutrient medium for microbiological organisms, the growth of which is a concern for diesel quality (93). Both anaerobic and aerobic microorganisms are thought to contribute to IDIDs, possibly forming acetic acid and other undesired compounds (3, 45).

While biodiesel is generally considered detrimental for injector deposits, contrary evidence also exists suggesting that it may reduce deposits. It is more polar than petrodiesel and can therefore increase the ability to solubilise deposits that would otherwise precipitate (84). The quality of biodiesel is of significant importance, with low quality fuel shown to require less sodium to trigger IDID issues (64). Biodiesel's relationship to IDIDs is more documented than HVO's, however is not well understood beyond its potential soap-forming components.

#### **1.2.2.5.2 Hydrotreated Vegetable Oil**

Testing with buses has shown 100% HVO to reduce NO<sub>x</sub>, PM, CO, total hydrocarbon (THC) and PAH emissions, though less so with the newest common rail FIE systems. This success suggests there is no upper limit for HVO blending (94). The tendency to form internal injector deposits has been

claimed to be lower than petrodiesel, however there is little coverage of this in studies (24). However, HVO's properties have also been suggested from injector tests to increase the likelihood of injector blocking (95). A near-zero aromatic fuel similar to HVO was found to be unable to solvate zinc in the CEC F-98-08 engine test, leading to increased deposition (41). Like with biodiesel, the biological feedstock can introduce contaminants including metals. Pre-treatment is required to remove these but it is likely for impurities to exist in the final product (96)

### 1.2.2.6 Additives

#### 1.2.2.6.1 Low Molecular Weight PIBSI

Polyisobutylene succinimide (PIBSI) refers to a range of chemical structures following the form of Figure 1.8a, consisting of a polyisobutylene tail group bound to an *N*-polyaminesuccinimide head (39, 60, 84). They are therefore amphiphilic detergents and used as deposit control additives (DCAs) in diesel to solubilise polar species and as dispersants in lubricant oil to prevent agglomeration of polar contaminants that would increase friction and wear (97). PIBSI products are a mixture of different PIB and polyamine chain lengths; the molecular weight (MW) distribution of different PIBSIs determines their characteristics (84). High MW PIBSIs, associated with higher quality (DCA-grade) products, have MWs around 1200 (with the PIB component being around 1000 Da). Barker *et al.* found these to be effective DCAs in both engine and bench testing (84). Low molecular weight (LMW) PIBSIs (with average PIB MW around 600 Da) are associated with low quality DCAs or dispersants in engine lubricant oils and have been shown to promote deposition (84, 98). This is thought to be due to the lower solubility in the fuel of their shorter PIB chains (4).

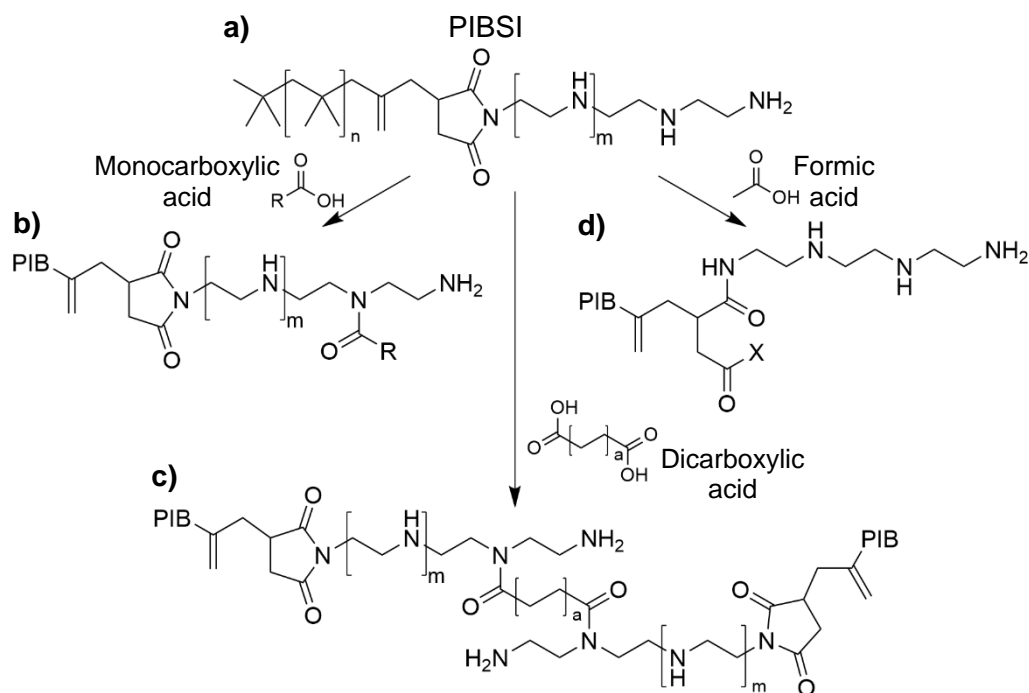


Figure 1.8: Reaction of PIBSI with different carboxylic acid species to form amides (58, 60). X = unidentified group.

The deposits resulting from PIBSI species are usually described as lacquers and characterised as amides using FTIR (discussed further in Section 1.3.2.3). The amide functionality can form from a reaction with an acid (84). Some acids, such as formic acid, which can form in diesel fuel blends from degradation of biodiesel, have been shown in testing to cleave the succinimide to form an amide (Figure 1.8c) (58, 60, 99). Other larger carboxylic acids form a product with both an imide and amide (Figure 1.8a), indicating a reaction at an amine site to form an amide while leaving the imide group of the succinimide unchanged (58, 99). Ullmann *et al.* proved the amine to be the group undergoing transformation to the amide by observing the same reaction with a polyamine, therefore a high primary amine content is suggested to promote this type of deposit (60, 99). Of particular concern, dicarboxylic acids can form bridges between the polyamine chains of PIBSI molecules (Figure 1.8b) (58, 60, 87). Finally, in the absence of a carboxylic acid to form an amide, ammonium salts of PIBSI have been suggested (58).

While studies demonstrate how amide chemistry can form, a deposit will only form if the fuel is unable to solubilise such products. As the PIBSI's solubility

relates to its mass distribution, this makes PIBSI quality very important to avoid issues with LMW PIBSI side-products (64, 84, 98). Whilst amides have been consistently identified in IDIDs in the literature, their detailed chemistry has not been characterised. Generally, the only chemical information gathered is confirmation of the amide functionality.

#### **1.2.2.6.2 2-Ethylhexylnitrate**

2-Ethylhexylnitrate (2-EHN) is a cetane improver used in diesel fuel to improve the “ease” of fuel auto-ignition (28). 2-EHN is an organic nitrate radical precursor which improves combustion characteristics by decomposing at relatively low temperatures (120-150 °C) (64, 100). Rancimat fuel testing indicates it has an impact on oxidative stability and would hence contribute to the formation of acids (62). 2-EHN has also been indicated to exacerbate issues with PIBSI-type deposits (64). Testing has shown higher concentrations of the additive to result in thicker deposits however analysis revealed no characteristics of 2-EHN in the deposit, suggesting that it only acts catalytically, likely via radical initiation, without affecting the deposit composition (64).

#### **1.2.2.7 Injector Design**

In the development of new diesel FIE, higher efficiency is sought-after in order to meet emissions regulations (37). Thus, new FIE technology uses increasingly higher temperatures and pressures in order to improve atomisation and the efficiency of fuel-air mixing. This creates a harsher environment for the fuel, and these systems are correlated with deposit formation and operational issues (4, 37). Diesel deposits generally require heat to form, with higher temperatures shown to produce thicker deposits (64, 74). To improve fuel-air mixing in the combustion chamber, as well as higher temperatures and pressures, newer FIE uses smaller nozzle holes and smaller moving parts that are more affected by a deposit build-up, resulting in more severe operational issues due to IDID build-up .

The injector substrate may also play a role in IDID formation. The effect of iron has been studied and its oxidation state found to be significant, potentially having catalytic effects on fuel breakdown (101). Diamond-like carbon (DLC) coatings are commonly placed on injector parts by the manufacturer, partially to improve wear characteristics but also to prevent deposit build-up, which they have been shown to be effective for (88, 102). FIE manufacturers have introduced modifications to injector design and continue to work on new changes to mitigate their deposit-promoting effects while maintaining modern FIE's higher efficiency (4). An example is the inclusion of cavities which can reduce nozzle hole deposit build-up (64).

### 1.3 Chemical Analysis of IDIDs

This section reviews previous work that has either made developments in the field of IDID analysis, discovered breakthroughs in IDID structure and/or composition, or uses effective techniques common for IDID analysis.

IDID research has focused on analysis of fouled injector parts from real-world field failures or from engine tests, as well as deposits created in controlled laboratory settings. Failure analysis reveals the chemistries that are causing these deposits in real-world settings, while engine and laboratory testing can investigate the effect of the fuel and additive components' chemistries that lead to deposit formation. A review by Edney *et al.* broadly covers the techniques used in injector deposit analysis, including the techniques discussed as well as others such as X-ray diffraction, thermogravimetric analysis and atomic force microscopy.

#### 1.3.1 Microscopy Techniques

Microscopy techniques provide images from which deposit structure, morphology and sample coverage can be assessed. This thesis aims for a chemical characterisation of IDIDs, therefore the utility of microscopy is limited however visualisation of IDIDs can be of value to understand their distribution, topography and structure.

### 1.3.1.1 Scanning Electron Microscopy (SEM)

In scanning electron microscopy (SEM), a finely focused electron beam is scanned across a surface and either secondary or backscattered electrons are detected at each point to generate images with up to nanometre-scale resolution. Secondary electrons are emitted when inelastic scattering of incident electrons emits low energy electrons from the specimen's outer electron shells while backscatter electrons are emitted when incident electrons are sufficiently scattered to entirely reverse their direction. Due to their low energy, SEs from only within a few nm of the surface can be emitted while BSEs can originate from depths of up to thousands of nm (103). The contrast of secondary electron images depends upon topography and backscattered images on the mean atomic number of the area, thus relating to the average atomic weight (104).

SEM has been applied to IDIDs by a number of researchers as it is useful for providing images of the deposits that can show morphology and topographical features (2, 40, 41, 48, 105, 106). Some examples of images are shown in Figure 1.9 and demonstrate the rough, porous, often grainy nature of diesel deposits.

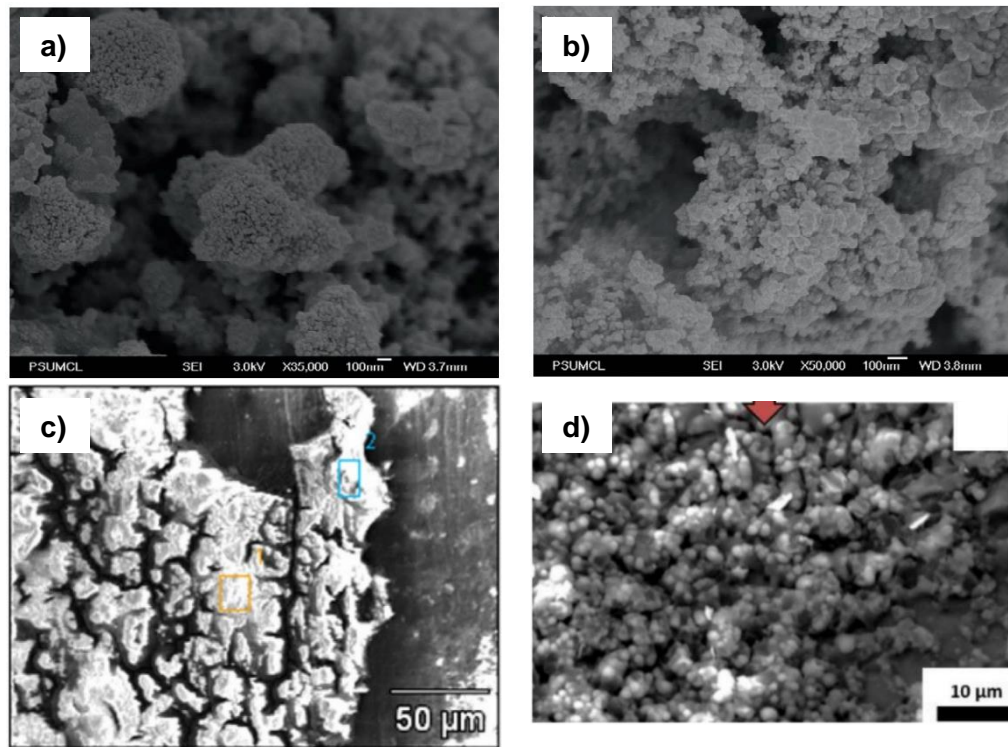


Figure 1.9: SEM images of IDIDs from a-b) Venkataraman *et al.* (2008) (48), c) Trobaugh *et al.* (2013) (2), and d) Rounthwaite *et al.* (2017) (106).

### 1.3.1.2 Transmission Electron Microscopy (TEM)

Transmission Electron Microscopy (TEM) is an electron microscopy technique that can achieve spatial resolutions on the Angstrom scale ( $\sim 0.2$  nm) (107). A very thin sample is irradiated with a very high energy electron beam, and the scattering of the electrons is measured (104). As electrons must pass through the sample, it cannot analyse IDIDs *in-situ*; the deposit must first be removed from the injector. If this challenging sample preparation is successful, the order of carbon ( $sp^2$  vs.  $sp^3$ ) and hence type of material in a carbonaceous deposit can be visually inspected.

Venkataraman *et al.* (2008) used TEM to show that an IDID deposit consisted of condensed structures made up of aggregated particles (48). It also showed that these particles appeared to contain more disordered structures than deposits formed from jet fuel degradation (Figure 1.10a-b). Barker *et al.* (2015) found an IDID to have similar graphitic components to diesel filter deposits (Figure 1.10c). Further, looking at a thin slice of IDID nano-milled with a focused ion beam (FIB), Barker *et al.* (2017) could identify two layers using

TEM (Figure 1.10d) (108). The upper layer was homogeneous with a liquid-like appearance, indicating that it was in a liquid state under the high temperature and pressure of the injector while the lower layer had both nanosized carbon crystals and amorphous/pseudo-graphitic carbon, indicating more ordered carbon.

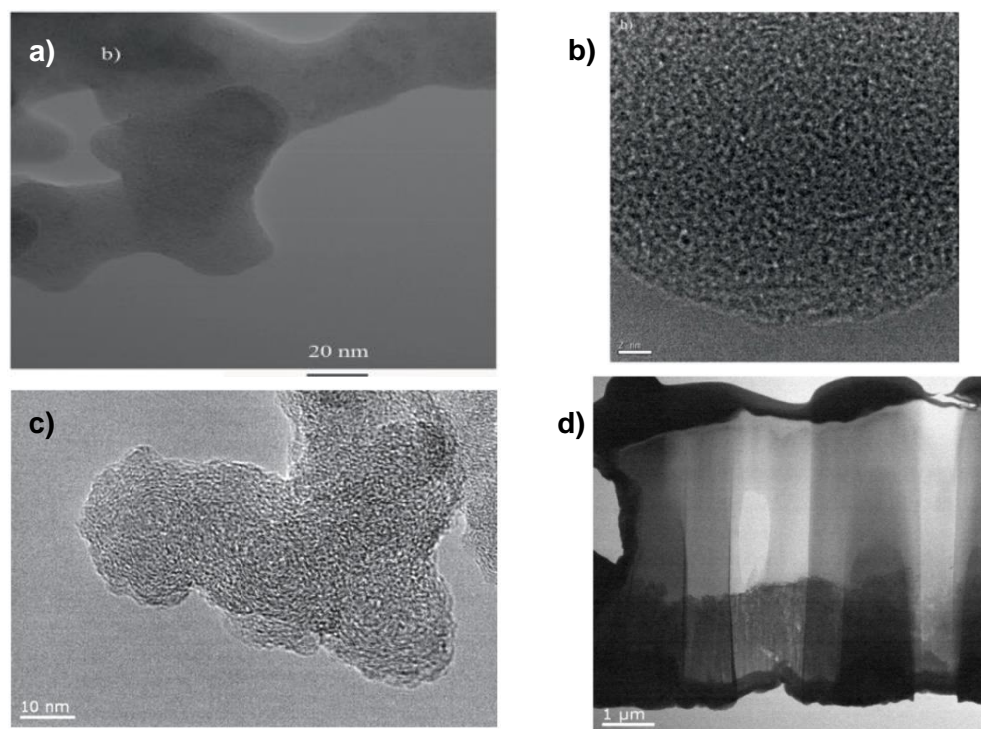


Figure 1.10: TEM images of IDIDs from a-b) Venkataraman *et al.* (2008) (48), c) Barker *et al.* (2015) (46), and d) Barker *et al.* (2017) (108).

### 1.3.2 Spectroscopy Techniques

Spectroscopy techniques are those that utilise electromagnetic radiation. They are able to provide often quantitative elemental information as well as detail about the chemical bonds present in a sample. For these reasons, they are widely adopted in IDID analysis.

#### 1.3.2.1 Energy Dispersive X-ray Spectroscopy

Energy Dispersive X-ray Spectroscopy (EDS) is a technique used typically in conjunction with SEM for elemental analysis. In EDS, a beam of electrons of sufficient energy (over twice the binding energy of the element and electron shell in question) is focused on the sample which can induce the emission of an X-ray with a frequency characteristic of the element and shell. This occurs via



emission of an electron and therefore ionisation of the element leaving an electron hole, with the subsequent transition of an outer shell electron to occupy the hole releasing the X-ray with a characteristic frequency corresponding to the energy difference between the two shells involved (103). EDS is widely used for IDID analysis as it is quick and provides semi-quantitative elemental information which is complementary to SEM micrographs (2, 40, 41, 105, 106). Thus, morphological information is gained from SEM alongside elemental information of the deposit's features. Almena *et al.* (2012) showed that a failing, fouled injector's surface was composed, on a mass basis, of 37% carbon, 23% iron, 10% oxygen and 11% tungsten, while a new injector's surface was 63% iron, 23% tungsten, 7% carbon and 3% oxygen, demonstrating the build-up of carbonaceous deposit (105).

### 1.3.2.2 X-ray Photoelectron Spectroscopy

X-ray photoelectron spectroscopy (XPS) is an analytical technique in which X-rays of defined energy irradiate a surface. By the photoelectric effect (Figure 1.11), an inner-shell electron is ejected by the incident photon, the kinetic energy of which is measured and is dependent upon only the electron's binding energy, the kinetic energy of the incident photon and the work function of the instrument. As the latter are two known values, the binding energy can be determined and is characteristic of the element, electron shell and the chemical environment of the element. Following photoemission, an electron of a higher energy orbital can fill the hole left by the photoelectron, emitting an x-ray in the same manner as in EDS (Section 1.3.2.1); another outer electron can then absorb the energy of this x-ray, resulting in its emission as an Auger electron, the energy of which is also measured and appears as a peak in XP spectra. (109). XPS can be one of the most accurate surface analysis techniques for quantitative analysis as it is highly surface sensitive and suffers no matrix effects (110).

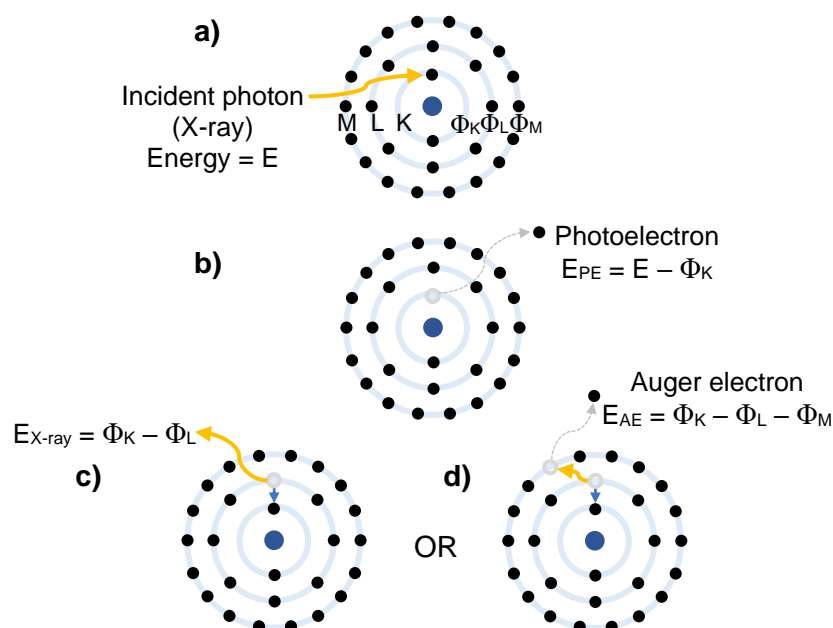


Figure 1.11: The photoelectric (a-b) and Auger (d) effects. Adapted from Jenkins *et al.* (111).

XPS has seen less use for IDID analysis, but there are studies applying it to IDIDs, as well as gasoline injector deposits and diesel piston deposits (40, 48, 82, 112). Venkataraman *et al.* (2008) used XPS for the analysis of an IDID and found only carbon and oxygen present on the surface. The O/C ratio in the deposit was found to be around 0.2, which was noted to be similar to that of the deposits seen with jet fuel thermal oxidative degradation. The high-resolution carbon 1s spectrum, shown in Figure 1.12a, indicated components for C=C (suggested to be aromatic carbon from polyaromatics), C-O (such as a phenol, furan, alcohol or other group) and O-C=O (such as a carboxyl, anhydride or lactone) (48). Dallanegra *et al.* (2014) applied XPS to three IDIDs, finding all were mostly carbon, oxygen and nitrogen with small concentrations of sodium, copper, zinc, sulfur and chlorine. The curve-fittings (example in Figure 1.12b) indicated amide functionalities as well as some alkoxy, carboxylate and possibly amine. One sample had a  $\pi$ - $\pi^*$  satellite peak, indicating aromatic content which was attributed to greater degradation by hydrogen loss and/or loss of functionality, i.e. a more carbonised deposit sample (40).

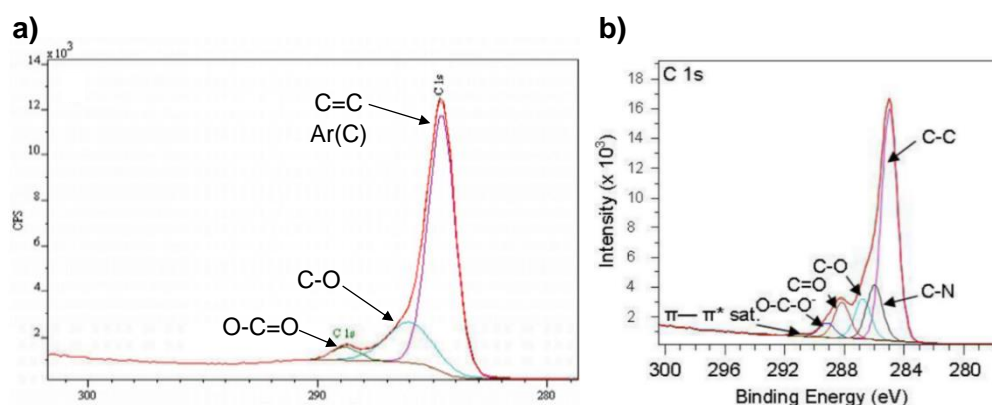


Figure 1.12: High-resolution carbon XP spectra for IDIDs in the literature. a) From Venkataraman *et al.* with additional annotations (48). b) From Dallanegra *et al.* (40).

### 1.3.2.3 Fourier Transform Infrared (FTIR) Spectroscopy

Fourier transform infrared (FTIR) spectroscopy allows identification of the chemical functionalities that have permanent dipole moments in a sample based on the wavelengths of infrared radiation they absorb. FTIR is a highly versatile technique that can analyse gases, liquids or solids (109).

FTIR is able to identify soap-type IDIDs via the  $\text{COO}^-$  stretching frequencies ( $1550\text{ cm}^{-1}$  and  $1440\text{ cm}^{-1}$ ) (2). This band is used in many investigations to confirm the presence of such carboxyl-containing deposits (2, 58, 59, 61, 65). FTIR is also very useful for amide-type deposits, often from PIBSI, as it is able to identify amide functionalities, the imide of the PIBSI's succinimide group and the PIB section's aliphatic chemistry (39, 40, 58-60, 84, 99, 113). If the imide expected for PIBSI is absent or reduced while an amide is detected, ring-opening succinimide cleavage to an amide is indicated. If both an amide and the original imide are present, conversion of an amine site to an amide is instead indicated (60). Laboratory testing on PIBSI mixed with di-fatty acid has shown the same FTIR band as in field IDID samples, confirming this as a problematic combination in the field (60). FTIR is also often used to identify the presence of generic aliphatic hydrocarbons (2, 59), with other groups such as esters and hydroxy groups (40). Other chemistries can be indicated, especially when compared to reference samples, such as identifying a similar structure to Kaolinite ( $\text{Al}_2\text{Si}_2\text{O}_5(\text{OH})_4$ ) (2).

FTIR is quick and very useful in some circumstances, however IDIDs can be heavily carbonaceous which the technique cannot identify due to the C-C bond lacking a permanent dipole. Further, it is not appropriate for analysis of IDID layering as its ability to probe chemistry as a function of depth is very limited.

#### 1.3.2.4 Raman Spectroscopy

Raman spectroscopy detects molecular vibrations of a sample by measuring the energy lost by incident photons due to the Raman effect, a phenomenon where a dipole moment is induced in a chemical bond by incident electromagnetic radiation. The duration of this dipole moment is dependent upon the atoms in the bond and no permanent dipole is required. Raman scattering is a weak process, therefore requires powerful lasers. The technique can be applied to a wide range of materials to map the surface in terms of the bonding present (109, 114).

Barker *et al.* (2015) used Raman to map the carbonaceous order present across an IDID surface. Application of HyPy, a technique in which a sample is heated under a stream of high-pressure hydrogen gas, to the IDID was a prerequisite for acquiring useful Raman data to remove volatile compounds that cause fluorescence. Deconvolution of the ordered (G) and disordered (D) spectrum bands and their ratio indicates how ordered/graphitic the carbon in the material is, shown mapped across the surface of an injector part as seen in Figure 1.13 (46, 115). This is therefore an important technique to measure how the deposit has progressed along the carbonisation process, though is limited by the HyPy pre-treatment and the lack of ability to measure the sub-surface to assess deposit layering.

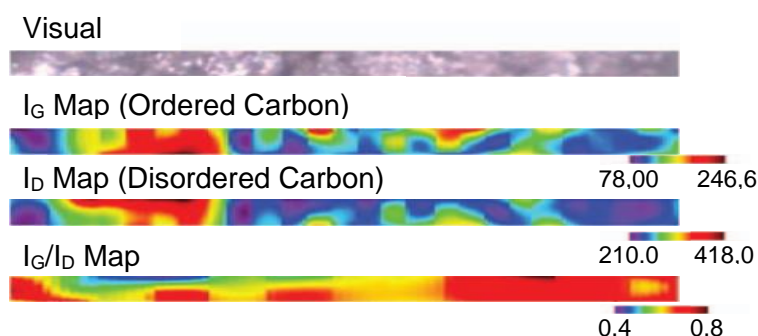


Figure 1.13: Map of ordered and disordered carbon with Raman from Barker *et al.* (2015) (46).

### 1.3.3 Mass Spectrometry Techniques

#### 1.3.3.1 Gas Chromatography-Mass Spectrometry

Gas chromatography-mass spectrometry (GC-MS) is a widely used technique that utilises a gas chromatograph coupled to a mass spectrometer, allowing complex chemical mixtures to be separated, identified and quantified. For effective GC-MS analysis, the compounds analysed must be sufficiently volatile and thermally stable. *In-situ* analysis of IDIDs on their injector component is not possible as the sample must be solvent extracted before analysis (116).

GC-MS has been used in many IDID investigations to identify the presence of specific compounds. These include carboxylate salts (palmitic and oleic), straight chain and branched alkanes consistent with petrodiesel, FAME consistent with biodiesel, aromatics and small polyaromatics thought to be from early-stage carbonisation via aromatisation (37, 48, 57, 117). Different sample preparations have been explored with GC-MS. Analysis from hexane washing could identify alkanes, while GC-MS with pyrolysis or hydropyrolysis (HyPy), a technique in which a sample is heated under a stream of high pressure hydrogen gas, were successful methods for evolving lightly cross-linked material including small polyaromatics (37, 48, 57, 115). It is thought that larger polyaromatics of a semi-graphitic nature would also be present in IDIDs but could not be released using pyrolysis or HyPy (57). Such material would be further along the deposit carbonisation process discussed in Section 1.2.2.3 and is of high interest, therefore GC-MS is a limited technique as this material is difficult to access for analysis. An *in-situ* technique is desired for measuring highly insoluble and non-volatile carbonaceous deposits. Additionally, GC-MS cannot probe deposit layering as provenance is lost upon dissolution of the deposit.

#### 1.3.3.2 Time-of-Flight Secondary Ion Mass Spectrometry

Time of flight-secondary ion mass spectrometry (ToF-SIMS) is an analytical technique in which a pulsed primary ion beam bombards a sample, producing a secondary cloud of particles from the target surface. Some of these particles are

ionised and can potentially be preserved up to masses of 10,000 Da. A schematic of this process is shown in Figure 1.14. The ions of a certain polarity are accelerated into a ToF analyser with the same kinetic energy towards an ion detector, which heavier ions take more time to reach due to the relationship between kinetic energy, velocity and mass shown in Equation 1. Several chemical species may be detected simultaneously and mapped over the analysed surface (3). ToF-SIMS is highly surface specific (nanometre scale), highly sensitive (ppm to ppb scale) and is advantageous compared to other techniques for the analysis of chemically heterogeneous samples (118, 119). Depth profiling can also be achieved by employing a separate “sputter” beam to gradually erode the surface in between measurements. Thus, the intensity of a mass signal can be seen as a function of time, corresponding to sample depth (3). Some of this technique’s main applications are in biological fields such as tissue imaging, and in the development of semiconductor materials where it is used to measure dopants (120).

$$E_K = \frac{1}{2}mv^2 \quad \text{Equation 1}$$

Compared to other mass spectrometry techniques, fragmentation features are extremely common in SIMS spectra due to the high energy collisions during sputtering (121). Indeed, SIMS can be highly destructive and can accumulate damage in the underlying material. This is particularly the case with atomic primary ion beams (e.g.  $\text{Ar}^+$ ,  $\text{Ga}^+$ ), with which SIMS analysis is limited static conditions; static conditions refers to limiting analysis to 1% of sample surface area to ensure only virgin material is analysed (121-123). Liquid metal cluster ion beams, developed in the 2000s, produce less fragmentation but are still destructive and require static conditions. Buckminster fullerene ( $\text{C}_{60}^+$ ) beams first took SIMS beyond the static limit, enabling dynamic depth profiling and 3D imaging, but gas cluster ion beams (GCIB) using argon (e.g.  $\text{Ar}_{2000}^+$ ) are now widely used for their very low destruction and fragmentation (124). Larger argon clusters show less fragmentation and damage due to their low energy per atom, though have lower resolution (120, 125, 126). Currently, GCIBs are the main depth profiling sputter beams and are common analysis beams alongside liquid metal ion guns (LMIG) (123, 126).

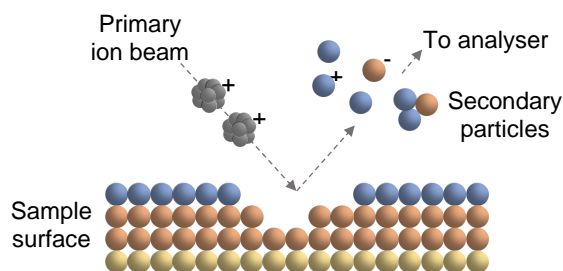


Figure 1.14: Schematic diagram of the principle of ToF-SIMS. Primary ion bombardment of sample surface, emitting sputtered material of secondary particles, some of which are ionic. Adapted from Vickerman and Briggs (2013) (126).

SIMS is at best a semi-quantitative technique due to the different ionisation probabilities of different materials. Further, SIMS suffers from matrix effects, whereby the analyte matrix partakes in the electronic processes that generate ions. Thus, the sample matrix composition significantly impacts the secondary ion yield, either enhancing or suppressing it. The same concentration of the same species can produce different signal strengths in different environments, even potentially being entirely suppressed. An example of a matrix effect is the availability of protons limiting  $[M + H]^+$  ion formation (124, 126).

#### 1.3.3.2.1 Application to IDIDs

ToF-SIMS has been utilised in several IDID investigations as a versatile technique for *in-situ* chemical analysis with spatial information from depth profiling or imaging (3, 38-40, 47, 59, 127, 128). Barker *et al.* introduced the technique for IDID analysis in a 2012 study for both surface analysis and depth profiling. Unlike the challenging sample preparation for GC-MS, ToF-SIMS could access polyaromatic and carbonaceous material, however in the fragmented form of carbonaceous clusters ( $C_6^-$ ) and nitrogen-containing clusters ( $C_3N^-$ ) which suggested N-PAC presence. Other chemistries measured included small inorganics such as sodium hydroxide, sodium sulfate, calcium, and chlorine. From a thick deposit's depth profile, a model of distinct deposit layering was constructed (Figure 1.15). It featured four layers: a surface inorganic "coating", a lower deposit layer of both inorganic and carbonaceous material, a penultimate layer thought to represent either crystalline carbon deposit or a DLC coating and a final steel substrate layer (47).

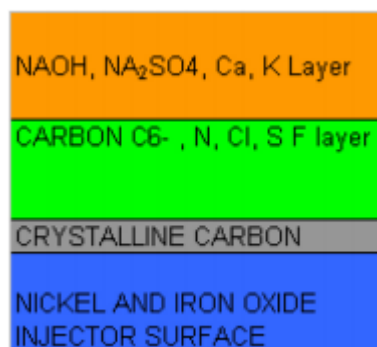


Figure 1.15: A schematic of the layers identified by depth profiling of the IDID, from Barker *et al.* (2012) (47).

Further work from Barker *et al.* (2014) expanded on the polyaromatics, comparing an IDID to coronene ( $C_{24}H_{12}$ ) and coal-tar pitch (CTP) reference samples. In coronene, structures close to the parent ( $C_{23}H_{11}^-$  and  $C_{24}H_{11}^-$ ) were identified, while CTP reached larger masses ( $>250$  m/z), as expected due to its larger PAH structures than coronene. Both coronene and CTP showed carbonaceous clusters ( $C_{2-10}H^-$ ), likely fragments of PAHs. The IDID had a similar distribution to CTP with ions over 250 m/z, indicating presence of PAH structures larger than coronene. Depth profiling was again utilised (Figure 1.16a) alongside imaging (Figure 1.16b), finding carbonaceous PAH-associated ions towards the surface and iron oxide substrate emerging later (3). Barker *et al.* (2015) also performed a ToF-SIMS depth profile with a PIBSI-type IDID, identifying an upper N-containing carbonaceous ion ( $C_3N^-$ ) above a suspected amide ion ( $CNO^-$ ) with the lowest deposit layer being a succinimide ( $C_4H_2NO_2^-$ ) consistent with a LMW PIBSI reference sample (39).

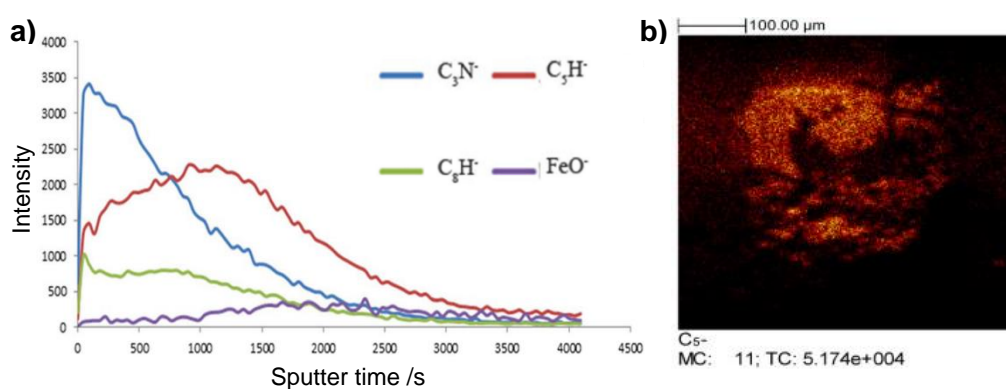


Figure 1.16: ToF-SIMS spatial information from an IDID sample from Barker *et al.*  
a) Depth profile for carbonaceous and substrate related ions. b) Image for  $C_5^-$  ion.



Other field IDID characterisations by Dallanegra *et al.* (2014) and Feld *et al.* (2016) apply ToF-SIMS. Evidence of PIB-polyamide deposits was identified, by organo-nitrogen signals, PIB-characteristic hydrocarbon ions and succinimides (40, 59). By observing a low succinimide intensity, it can be suggested that the succinimide ring has been transformed in the IDID (59). Aromatic content was again found and linked to degradation (40). Other chemistries identified included inorganic components of sodium, copper and sulfur, polydimethylsiloxane (PDMS), fatty acids and quaternary ammonium compounds (40, 59). Feld *et al.* also characterised a fouled filter from an engine fuelled with biodiesel, identifying the notable biomolecules free sterols and sterol-glucosides. Analysis of biodiesel fuel from the region found more biomolecules, including sterols, steryl esters and fatty acids, suggesting that these compounds had trapped in the filters (59). Dallanegra *et al.* also applied dynamic SIMS depth profiling to an IDID to identify chemical variation with depth. This was limited to elemental secondary ions due to the hard Cs<sup>+</sup> analysis beam. Three “distinct regions” of the deposit were found: an outer organic film (carbon, nitrogen, oxygen and sodium), interfacing with a metal oxide layer (aluminium, zinc, iron, oxygen) before reaching the injector surface (iron) (40).

#### 1.3.3.2.2 Multivariate Analysis of ToF-SIMS Data

Manual interpretation of complex SIMS datasets for multiple samples, containing hundreds or thousands of ions, can be very time-consuming and important trends can be missed. Multivariate analysis (MVA) techniques are used in a multitude of applications to rapidly identify trends and relationships in complex datasets. They are very common tools in SIMS data interpretation for many types of samples (129, 130). Principal component analysis (PCA) is an MVA technique that reduces the dimensionality of data to identify the largest differences and correlations in the dataset. In SIMS data of multiple spectra, the data consists of a matrix of variables (the ions of different masses), with attributes (the intensity of the ion) for each observation (each sample's spectrum). PCA identifies the uncorrelated orthogonal axes of maximum variation across the observations to obtain principal components (PCs), such that PC 1 has the largest variance and therefore represents the axis of most

variation, followed by PC 2 and so on. Each PC's contribution to the variance between samples is quantified in terms of the percentage of variance that it accounts for. Therefore, the complex original dataset can be expressed and understood with a much smaller number of variables (the relevant PCs), thereby reducing the data dimensionality (131). Each original spectrum (sample) has a score for each PC, showing its relationship to other samples for that PC. Each PC has loading values for each ion, which show quantitatively which ions contribute and are correlated (positive loadings) or anticorrelated (negative loadings) in that PC (129).

An investigation by Barker *et al.* (2020) applied PCA to SIMS spectra of eight IDID samples (identified as Needle 1 to Needle 8) from around the world (North America, Europe and China) (128). PC 1 and 2 scores and loadings are shown in Figure 1.17 and separate the samples according to chemistries such as sodium, organosilicons, phosphates and sulfates. This work, while limited to very small ions due to the high fragmentation and low mass resolving power of ToF-SIMS, demonstrates an efficient method of interpretation of a large SIMS dataset of IDIDs. Here, the investigation aimed to find correlations in the geographic origin of IDID samples. Samples with the most similarities and differences can quickly be found and visualised, with the loadings pointing towards key inorganic and organic components.

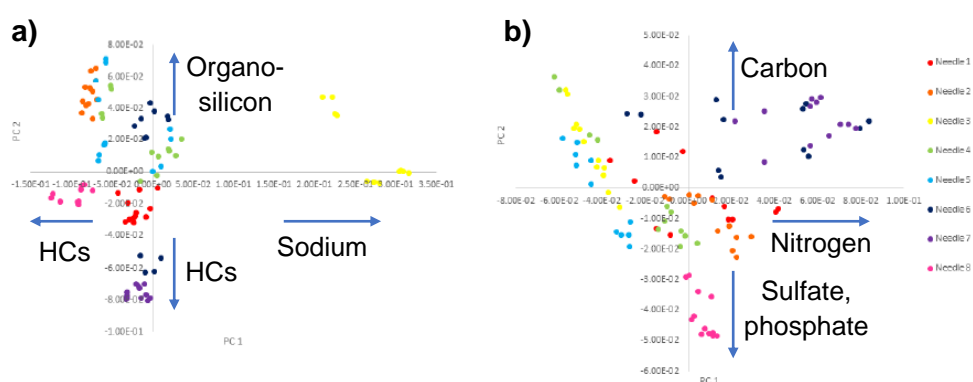


Figure 1.17: Results from PCA of static ToF-SIMS data from 8 injector needle IDIDs for showing PC 1 vs PC 2 scores for a) Positive polarity, b) Negative polarity. Adapted and annotated from Barker *et al.* (128).

### 1.3.3.2.3 ToF-SIMS Conclusion

ToF-SIMS has proven to be one of the most successful techniques for IDID characterisation, owing to its ability to access and analyse all types of deposit material (organic, inorganic and carbonaceous) in these complex samples. The spatial information gained from depth profiling was instrumental in the discovery of the layered nature of IDIDs; it follows that both surface and sub-surface characterisation of IDIDs is critical to understand their composition and formation processes in terms of how such layers develop. ToF-SIMS depth profiling is able to achieve this characterisation by preserving the sample's provenance during analysis. With MVA, it has been shown that interpretation of large diesel deposit datasets can be rapid and unambiguous. Previous investigations were limited by their harsher LMIG analysis beams and low mass resolution, resulting in extensive fragmentation and potentially ambiguous assignments. This limits the amount of chemical information that can be gained from this technique. Further, quantitative analysis is not possible with SIMS, so a quantitative technique such as XPS applied in support is recommended.

### 1.3.3.3 Matrix-Assisted Laser Desorption Ionisation Mass Spectrometry

The matrix effect, as outlined as a problem for SIMS, is the basis of matrix-assisted laser desorption ionisation mass spectrometry (MALDI-MS), in which a matrix is applied to the sample to enhance ionisation (124). MALDI uses a laser beam to irradiate the sample and lift-off molecules via a collective effect on the analyte and applied matrix, which absorbs the laser energy. In comparison to SIMS's single collisions, this is a softer ionisation method and preserves more molecular chemistry (132, 133). Sample preparation can be challenging for MALDI-MS as there is no single protocol; an appropriate matrix, solvent and method must be found and utilised depending upon the sample (134).

MALDI has had limited use for IDID analysis, however showed the ability to measure the MW distribution of aromatic solids from diesel, identifying much larger structures than pyrolysis GC-MS. The polyaromatics reached 1000 amu,

suggesting the largest molecules may contain up to fourteen condensed aromatic rings (48). Though MALDI imaging is possible for some samples, collecting spatial information is more challenging than with SIMS due to the more complex sample preparation and typically lower imaging resolution. Notably, depth profiling is not possible, limiting its utility for analysing sub-surface deposit chemistry.

#### 1.3.3.4 Orbitrap<sup>TM</sup>-Secondary Ion Mass Spectrometry

Orbitrap<sup>TM</sup>-secondary ion mass spectrometry (3D OrbiSIMS) is a recently developed SIMS technique, operating on the principles of ToF-SIMS but with the ability to send sputtered ions into an alternative high-resolution mass analyser, an Orbitrap<sup>TM</sup>. Orbitrap<sup>TM</sup> analysers electrostatically trap ions in orbit around a spindle and achieve a mass resolving power of 240,000 at  $m/z$  200, in comparison to typical ToF mass resolving power of 10,000 (135, 136). The technique was debuted in 2017 by Passarelli *et al.*, demonstrating its superior capabilities in mass resolving power and spatial resolution. Figure 1.18a shows this dramatic improvement in mass resolution, while Figure 1.18b shows the 3D capabilities of this technique. Larger chemical species can be identified, showing less fragmentation and with confirmation possible via tandem (MS/MS) mass spectrometry where an isolated ion can be further fragmented to aid in its assignment (135). Prior to the current work in this thesis, OrbiSIMS has not been applied to engine deposit analysis.

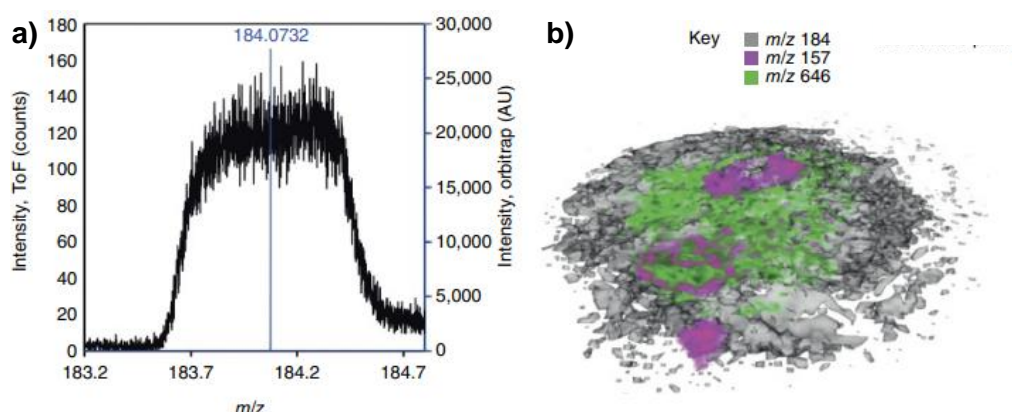


Figure 1.18: 3D OrbiSIMS example data. a) Mass spectra overlay using ToF analyser (black) and Orbitrap<sup>TM</sup> analyser (blue). b) 3D OrbiSIMS imaging of an animal cell. Adapted from Passarelli *et al.* (2017) (135).

### 1.3.4 Jet Fuel Thermal Oxidation Tester

Alongside analytical developments for determining the composition and structure of IDIDs, laboratory testing is key for developing understandings about IDID formation and how certain components affect deposition. The jet fuel thermal oxidation test (JFTOT) is an industry standard bench-test rig for determining the thermal oxidation stability of aviation fuel on a pass/fail basis based on its breakpoint (46, 137). In the test, aerated fuel flows over a resistively heated tube at a set temperature and the degree of deposit formation is measured (84, 113, 138). Resistance heating of the tube is achieved by passing a low voltage, high AC current through it (138). A diagram of the heater tube in its casing with fuel flowing between the heater tube and casing from the inlet to the outlet is shown in Figure 1.19a, where temperature variations in the fuel along the tube can be seen (139). A JFTOT heater tube temperature curve from a similar investigation is shown in Figure 1.19b, showing the peak temperature at a similar position (140). The degree of deposition is generally measured based on its optical light reflection using ellipsometry. The JFTOT tube is usually an aluminium and magnesium alloy to minimise catalytic effects, however steel is required for high temperatures (141).

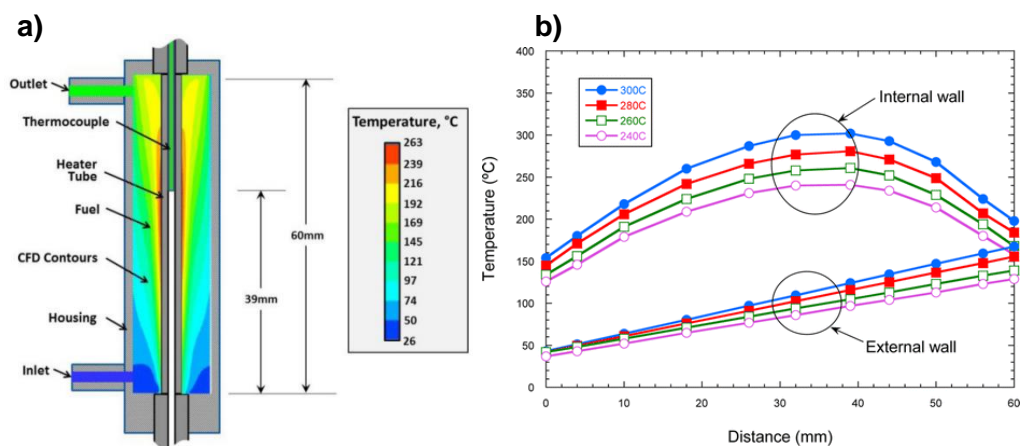


Figure 1.19: a) Internal and external temperature measurements for different positions along the JFTOT tube for different set temperature runs from Sander *et al.* (140). b) temperature profile of fuel in JFTOT calculated by CFD for a set-point of 260 °C from Lacey *et al.* (139).

Though intended for jet fuel, the JFTOT is capable of testing diesel fuel (a neighbouring fraction from crude oil), for which it is often called the diesel deposit formation test (DDFT) (142-144). As a simple laboratory bench test, its benefits are its low cost, quick run-time, and the control the operator has over the test. Assessing the deposit along the tube also allows the effect of the increasing temperature to be seen (113). However, it suffers limitations compared to engine testing. As the JFTOT is run for a short time (typically ~2.5 hours) and uses lower pressure (3.45 MPa vs. up to 300 MPa, commonly 250 MPa, in modern automotive diesel FIE), it necessitates higher temperature conditions than in an injector system (11, 145). Other differences between an engine and the JFTOT are the fuel residence time, heat flux, variation in fuelling and the cyclical nature of an injector (141).

There has been increasing interest in the JFTOT for IDID research, enabling the study of deposit formation from specific fuel/additive components in a controlled environment. These investigations make use of different fuels such as biodiesel and dopants, for example to explore the effect of sodium in different forms, or to study amide-type or carboxylate salt-type deposits (38, 84, 113, 139, 142-144, 146-148). Such JFTOT investigations have played a role in the knowledge of IDID compositions and formation mechanisms described in Section 1.2.

## 1.4 Scope and Aims of this Thesis

This thesis aims first to advance the methodological approaches to IDID analysis. MS analysis has been identified as the most effective technique for the characterisation of molecular species in IDIDs however so far has suffered from sample preparation and instrument capability issues. Their highly insoluble carbonaceous material is challenging for many conventional mass spectrometry techniques and therefore ToF-SIMS, which directly analyses samples via sputtering rather than solvent extraction, has become a very useful technique to ensure access of all deposit material. To overcome the current approach's shortcomings in terms of excessive fragmentation and low mass resolving power, OrbiSIMS analysis of IDIDs will be performed for the first

time to unambiguously identify the in-tact molecular species and elucidate the molecular compositions of these complex materials. The spatial information that can be gathered with SIMS in depth profiles and images will also be used to further understand the layering effects that have been observed in IDIDs. Considering SIMS's quantitative limitations, XPS will be applied in support. Though less novel in the field of IDID analysis, this complementary technique can be used to support the SIMS and develop a more comprehensive understanding of IDIDs.

The insights gathered from the improved methods can be used to understand the origins and formation of IDID chemistries, especially in terms of where gaps have been identified in the current literature. Aromatisation and carbonisation processes are thought to occur as organic fuel degrades within an injector and in the deposit material but this has not been proven. Testing has suggested that biodiesel and HVO can play a role in IDID formation but there are still many uncertainties with this relatively new and increasingly used renewable diesel. Even for the relatively well understood LMW PIBSI derived deposits, there are still unknowns around the specific chemical transformations that occur to form deposit and, further, how such deposit might degrade under the high temperature and pressure of the injector. The final chapter focuses on recreating IDID chemistries in the laboratory using the JFTOT fuelled with a range of different fuel and additive components. This investigation aims to validate the origin of components of field sample data and provide additional insights into how each component affects deposit formation.

## Chapter 2: Materials and Methods

### 2.1 Injector Samples

#### 2.1.1 Sourcing

Injector samples were sourced by Innospec mainly from field failures; they originated from engines that had failed due to operational issues related to injector deposit formation, both internally and externally. Often, to prevent biases and for commercial proprietary reasons, the sample information provided was minimal. One sample originated from an engine test (Needle 13/HT1). The injectors were disassembled at Innospec's site prior to receipt at the University of Nottingham.

#### 2.1.2 Table of Injector Samples

Table 2.1: IDID samples and marine injector deposit sample with thesis ID derived from the previous work by Angel-Smith (2017) (127, 128), ID supplied by Innospec and known geographical origins and information about the failure in service.

Thesis ID	Innospec ID	Origin	Known information
Needle 6	4999	New York	No start due to stuck needle
Needle 7	4998	New York	No start due to stuck needle
Needle 8	China 1	China	N/A
Needle 9	No5	Unknown	N/A
Needle 10	INJ9A	Unknown	N/A
Needle 11	1516	Colorado	From a highway truck, failed to start
Needle 12	N20A	Unknown	N/A
Needle 13	HT1	Engine test	B7 diesel with additive package
Needle 14	NC1	Unknown	N/A
Marine 1	H#1	Houston-related	Plunger from failed marine injector



## 2.2 Jet Fuel Thermal Oxidation Test

The Alcor Jet Fuel Thermal Oxidisation Tester 230 Mk. III (Petroleum Analyzer Company, L.P.) was used as a laboratory bench test to mimic IDID formation from specific fuels and dopants. For the purposes of this project, the main limitation of the JFTOT is the lower pressures of the fuel compared to those found within the injector system, as well as the aeration which does not occur in an injector. Compared to engine testing, its advantages are the lower cost, shorter running time, and the greater control over the test parameters.

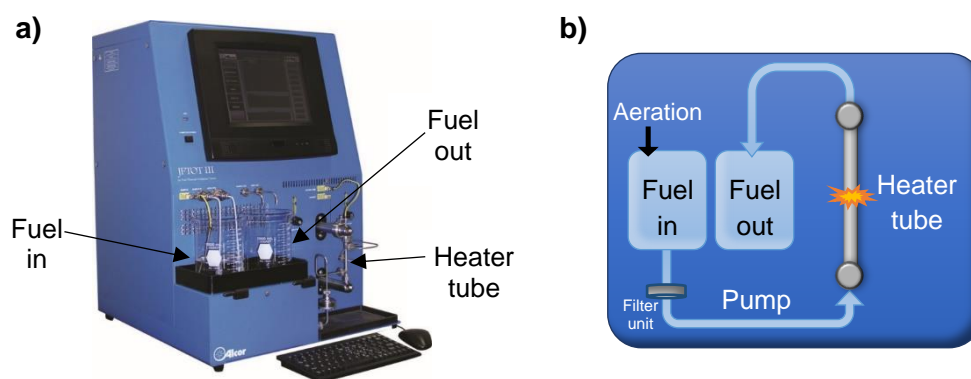


Figure 2.1: a) Image of Alcor JFTOT Mk II. b) Schematic of Alcor JFTOT Mk II functionality.

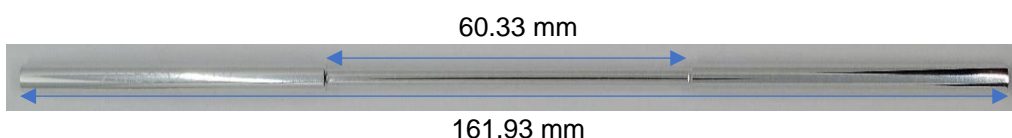


Figure 2.2: JFTOT heater tube with dimensions (149).

All JFTOT heater tube samples were generated at Innospec Manufacturing Park, Ellesmere Port (Innospec Ltd.) with fuel, additive and contaminant components of interest selected. Selection was based on components that are part of established injector deposit engine tests, are of interest due to being observed in the field IDID samples (Chapters 3-4) or are of interest due to reports of their potential to contribute to IDIDs (Chapter 1). The range of fuels, dopants, run times and heater tube materials can be seen in Section 2.2.3.

### 2.2.1 Experimental

As a diesel adaptation of the standard JFTOT test method (ASTM D3241), a volume (~500 mL) of diesel fuel was aerated to near saturation and pumped at 3.45 MPa through the JFTOT at a fixed rate of 3 mL min<sup>-1</sup> using no fuel recirculation (150). The fuel flowed through an initial filter unit containing a 4 µm filter paper cut from a new diesel fuel filter. Either an aluminium-magnesium alloy or steel standard JFTOT heater tube was used. The heater tube is heated through resistance heating. The standard set-point temperature used was 330 °C however some tests used alternative temperatures (Table 2.2). JFTOT 7 (Na + DDSA) used a much lower temperature than the other samples as this temperature has been recorded as suitable for the formation of sodium dodecenylsuccinate salts (143). JFTOT 2 (RME) and 3 (CME) used the highest temperature (360 °C) following tests that failed to form deposit at 330 °C, presumably due to a higher breakpoint of these biodiesels compared to RF-06. JFTOT 13 was an unused tube to use as a control sample. Ellipsometry was performed for aluminium-magnesium JFTOT tubes using a Deposit Rater DR10 (AD systems, France) to map the deposit thickness over the full surface of the JFTOT tube as in the ASTM D3241 'Standard Test Method for Thermal Oxidation Stability of Aviation Turbine Fuels' (150). Ellipsometry is not possible for steel JFTOT tubes. Following the test, the samples were cleaned with analytical grade hexane and acetone, oven-dried and cut to an appropriate size (<12 cm) for OrbiSIMS and XPS analysis.

### 2.2.2 Materials

The fuels used were RF-06 ULSD, HVO sourced from NESTE, rapeseed methyl ester (RME) biodiesel and coconut methyl ester (CME) biodiesel. The dopants were dodecenyl succinic acid (DDSA) with sodium naphthenate as a source of sodium, PIBSI (in mono form with a PIB chain of 260 MW and tetraethylenepentamine (TEPA) as the polyamine section), zinc (as zinc neodecanoate) and Halfords ISW/40 lubricating oil. The DDSA was synthesised in-house from the hydrolysis of dodecenyl succinic anhydride and dissolved in xylene. After each JFTOT experiment, the resulting fouled JFTOT

tubes were subjected to analysis with ellipsometry where possible and were then cut to an appropriate size (<12 cm) for OrbiSIMS and XPS analysis.

The JFTOT heater tube material is described in the standard method IP 323 as 6061-T6 aluminium, with an Mg:Si ratio  $\leq 1.9:1$  and Mg<sub>2</sub>Si percentage  $\leq 1.85\%$  and its dimensions were seen in Figure 2.2 (149). This is the standard JFTOT heater tube and was used for the majority of JFTOT experiments in this thesis, however some experiments used a steel JFTOT heater tube of the same dimensions, composed of EN 1.4401 316 stainless steel, a chromium (16-18 wt.%, nickel (10-14 wt.%) and molybdenum (2-3 wt.%) austenitic stainless steel developed to provide improved corrosion resistance than standard stainless alloy steel (304) in moderately corrosive environments (151).

### 2.2.3 JFTOT Samples

Table 2.2: JFTOT samples with fuel/dopant combination, temperature and run-time.

No.	Thesis ID	Fuel	Dopant	Temp. (°C)	Run time (hr)
1	JFTOT RF-06	RF-06	N/A	330	2.5
2	JFTOT RME	RME	N/A	360	2.5
3	JFTOT CME	CME	N/A	360	2.5
4	JFTOT HVO	HVO (filtered)	N/A	330	3
5	JFTOT B7	93% RF-06, 7% RME (B7)	N/A	330	2.5
6	JFTOT HVO50	50% RF-06, 50% HVO	N/A	330	2.5
7	JFTOT Na + DDSA	RF-06	Na naphthenate (1 ppm), DDSA (20 ppm)	180	2.5
8	JFTOT LMW PIBSI	RF-06	LMW PIBSI (500 ppm v/v)	330	2.5
9	JFTOT Lubricant	RF-06	Lubricant oil (50 ppm)	330	2.5
10	JFTOT Zinc <sup>1</sup>	RF-06	Zinc neodecanoate (1 ppm)	300	2.5
11	JFTOT 200 °C <sup>1</sup>	RF-06	N/A	200	5
12	JFTOT 250 °C <sup>1</sup>	RF-06	N/A	250	5
13	Clean	N/A	N/A	N/A	N/A

<sup>1</sup> – experiment used a steel JFTOT heater tube rather than the usual Al-Mg

### 2.2.4 JFTOT Heater Tube Analysis: General

Figure 2.3 shows the appearance of two typical post-treatment JFTOT tubes (JFTOT LMW PIBSI and JFTOT RME). The position of the thermocouple (where resistive heating occurs and thus the highest temperature position) is labelled and represents the region where large-scale deposition begins after high-temperature fuel breakdown.

Five positions (numbered 1 to 5) were analysed with OrbiSIMS for each JFTOT tube, with slightly different positions for each sample. Most samples have a deposit onset position near the centre where a thick deposit appears, which is set as position 3. This onset begins at different distances from the inlet

in different samples and therefore the positions selected vary based on where this thick deposit is. Position 1 was analysed within 1.5 cm of the inlet and position 5 was within 1.5cm of the outlet. Position 2 and 4 were then set approximately equidistant to positions 1 and 3 and positions 3 and 5, respectively. This ensures that the key position of interest, namely the thick deposit onset that occurs around position 3, is analysed for each sample and can be compared. This can be seen in Figure 2.3, where position 3 is further from the inlet in JFTOT RME than in JFTOT LMW PIBSI. XPS analysis was focused on position 3, with most samples also analysed around position 1-2 and 4-5.

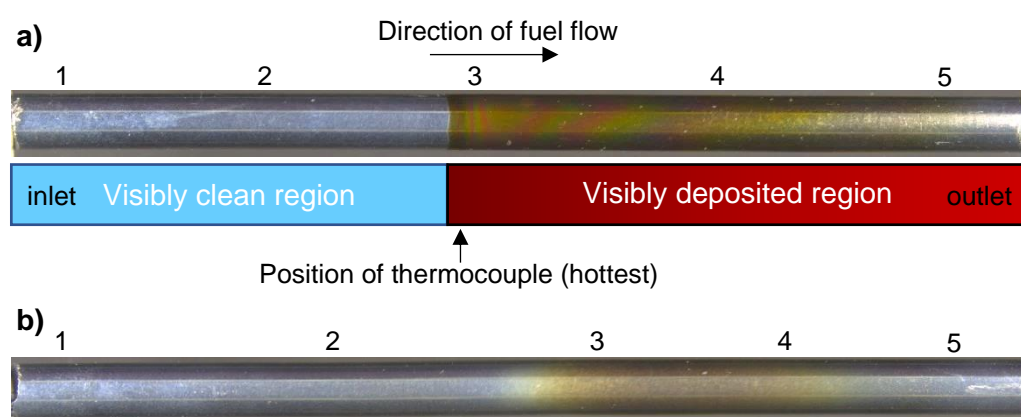


Figure 2.3: Photograph of post-treatment a) JFTOT LMW PIBSI and b) JFTOT RME with analysis positions identified.

## 2.3 Analytical Methods

### 2.3.1 SEM-EDS

SEM was used to produce images of samples to provide an idea of their appearance, morphology and the extent of deposition in terms of thickness and sample coverage.

Due to the possible presence of volatiles in the samples, an environmental SEM (E-SEM) was used so that a low vacuum (60 Pa) could be applied. Sample charging can be an issue with SEM due to build-up of current on sample surfaces. Coating with carbon, platinum or gold can aid charge dissipation to afford a higher quality image, however in the work in this thesis samples only required mounting on carbon adhesive discs to acquire

appropriate images. An X-ray cone was fitted to the detector to reduce electron scattering.

SEM micrographs were acquired for all samples using either a FEI Quanta 650 ESEM or FEI Quanta 600 ESEM instrument (ThermoFisher Scientific Inc.) equipped with an EDS detection system for elemental analysis. All sample analysis was performed in low vacuum (60 Pa) to prevent sample charging, with an incident energy of 10-20 kV. The accelerating voltage used was between 10-15 kV and the spot size was generally 5.0. EDS was primarily used to indicate possible elements present in the samples and as a supporting technique to inform OrbiSIMS and XPS analysis; quantification was avoided due to its known high variability, with XPS instead used for quantitative analysis.

### 2.3.2 XPS

XPS was used primarily for relative elemental quantification of samples. Quantification of carbon's bonding environments, though more challenging, was also used to compare samples by indicating the types of compounds present. XPS also serves to aid OrbiSIMS analysis by revealing the key elements to search and account for. The XPS data is highly complementary to SIMS data in providing the quantification that SIMS lacks as a semi-quantitative technique that is affected dramatically by sensitivity differences that are difficult to account for between different analytes and matrices (124). XPS lacks detailed molecular information, which is in turn afforded by OrbiSIMS. XPS can achieve very high elemental quantitative accuracy however perfecting this usually requires comparisons to reference materials; within the scope of this work, this is unachievable for such complex and unknown materials as diesel deposits (110). Nonetheless, XPS is considered to be the most accurate technique available for deposit analysis.

### 2.3.2.1 Experimental

#### 2.3.2.1.1 Sample preparation

No prior sample preparation was required in this work. Samples were secured to a standard Kratos sample bar (13cm × 1.5 cm) with non-conducting double-sided adhesive tape (Sellotape). Conductive carbon tape was avoided as it has been known to be a source of polysiloxane, sample contamination with which can transfer to SIMS instrumentation and compromise SIMS data. Further, sufficient charge compensation is achieved via the charge neutralizer electron source, making conductivity of the tape unnecessary. In the case of the sample Marine 1, which was too large and heavy for the sample bar, deposit material was scraped from the sample and placed on the tape. Pumping down in the instrument's airlock was generally carried out overnight before introduction to the sample stage for analysis.

#### 2.3.2.1.2 Acquisition of Spectra

Samples in this work were subjected to XPS analysis using the Kratos AXIS ULTRA DLD liquid phase photoelectron spectrometer (LiPPS) with the Kratos VISION II software. The instrument had received prior calibration using Cu, Ag, and Au samples; the resolution for the photoelectron detector was checked on the Ag 3d<sub>5/2</sub> peak FWHM of <0.55 eV at PE 20 in the hybrid slot mode. Instrument ultimate resolution is initially calibrated on the Ni Fermi edge (80%–20% ΔE) at a pass energy of 10 eV by using the 110 μm aperture and field-of-view 2 lens mode. The transmission function was calibrated using a clean gold sample for all lens modes and pass energies.

A monochromated Al Kα X-ray source (1486.6 eV) with a source power of 120 W was used and a charge neutralizer filament (1.9-2.0 A current, 3.3-3.6 V balance, 1.1-1.2 V bias) was operated to prevent surface charging. The analysis chamber pressure was < 5 × 10<sup>-9</sup> mbar. Small spot mode was used, with a 110 μm aperture and a measured sample area of approximately 200 × 200 μm<sup>2</sup>. Low-resolution survey spectra were recorded between a binding energy range 1400 or 1200 to -5 eV with pass energy 160 eV and step energy 0.5 or 1 eV. Survey spectra acquisition (sweep) times were 5-10 minutes. High resolution

scans for modelling chemical composition were also recorded using the relevant binding energy range for the respective element of interest, with pass energy 20 eV and step energy 0.1 eV and acquisition (sweep) times of 5-10 minutes. The data was converted to VAMAS format for processing.

#### **2.3.2.1.3 GCIB Etching for Depth Profiles**

XPS depth profiling was performed by etching samples using the equipped gas cluster ion beam (GCIB) of the Kratos Axis Ultra LiPPs instrument. The GCIB settings used a 20 keV Ar<sub>500-1000</sub><sup>+</sup> cluster beam and a rastered etch area of >0.75. The sample current during etching was generally 10-12 nA. Depth profiling was carried out with automated alternation between the acquirement of spectra and GCIS etching of a specified time. For many experiments in this work, the instrument had a GCIB issue that caused it to shut down; for experiments performed during this time, the etch was manually monitored and repeated when the shutdown occurred to achieve a desired etch time and these results therefore have inconsistent etch times throughout the profile.

#### **2.3.2.2 Data Processing and Analysis**

CasaXPS version 2.3.22 PR1.0 was used for data processing and analysis. The Kratos library of relative sensitivity factors (RSF) was used for all data. This accounts for the statistical likelihood of the emission of a photoelectron from a given orbital for each element for the Kratos LiPPs instrument, enabling quantification. Spectra were charge corrected to the surface C 1s peak, assumed to be adventitious carbon which was set to 285 eV, in all cases except JFTOT Zinc, which was charge corrected to the Fe 2p 3/2 peak of the Fe 2p doublet of a post-etched spectrum at 707.1 eV as the iron of its steel substrate gave a more reliable correction. The limitations of charge correction to adventitious carbon are recognised, however it serves as the standard charge correction method especially in the absence of an alternative reliable peak as is generally the case with deposits of unknown material. Where possible, repeat scans were summed within CasaXPS to improve the signal-to-noise ratio.



The practical guide on XPS quantification by Shard, A.G. (2020) (110) was used to guide fitting XPS data for elemental quantification. Resources were referred to including the reference pages of XPSFitting (Biesinger, M.C.) (152), ThermoScientific's XPS Knowledge Base (153), and any studies referenced where relevant. Peak selection for quantification prioritised the sharper peaks (1s, 2p, 3d) and lack of overlapping peaks.

Region and component peaks were fitted using a GL30 (70% Gaussian and 30% Lorentzian) line shape and generally a Tougaard background. Exceptions were doublet peaks showing a step which were generally fitted with a Shirley background, and smaller peaks where the baseline shows little or no rise were often fit with a Linear background (110, 119). These three background types are used in the vast majority of XPS studies (154). Where possible (when the background signal was not affected by other peaks), for Tougaard backgrounds the peak region selected included significant area either side of the peak to establish the most accurate background. The Tougaard background is considered a good approximation for most materials as it takes into account and corrects the inelastic scattering events which cause electrons to lose kinetic energy and produce the background (154, 155) and has been shown to give accurate results (110). The Shirley background is also considered a good approximation of the inelastic scattering of electrons but assumes that the change in the background is proportional to the peak intensity above the background while Tougaard is modelled on a physical basis (110). Component fitting of high-resolution spectra was performed only for surface data, due to the likely chemical damage that the  $\text{Ar}_{500}^+$  sputter beam would cause to the data. Statistical errors for both region peak fittings and component fittings were calculated based on a Monte Carlo simulation in CasaXPS. This represents a mathematical error of the peak itself though other sources of error exist in the instrument, quoted as around 1 at.%. Thus, peaks of below 1 at.% have very significant uncertainty in their values.

### 2.3.2.3 High-Resolution Spectra Component Fitting

Curve fitting of the C 1s peak was generally guided by Gengenbach *et al.*'s guide (2021) (119), with the binding energy ranges and full-width at half maximum (FWHM) of each component guided by XPS Fitting (156), ThermoScientific's XPS Knowledge Base (157) and Chastain and King's Handbook of XPS (1992) (158). The ranges from these references are summarised in Table 2.3, all based on spectra charge reference to adventitious carbon at 285 eV. Other studies involving high-resolution XPS of diesel deposits were also referred to for guiding curve fitting, including Dallanegra *et al.* (2014) (40), Venkataraman and Eser (2008) (48), Antonio *et al.* (2020) (101) and Spanu (2021) (159).

Table 2.3: Compiled references for binding energy and full-width-height-maxima expected for carbon's chemical states in XPS (156-158).

Chemical state	C 1s binding energy (FWHM) /eV		
	Handbook of XPS (1992)	XPSFitting	XPS Knowledge Base
Carbide	280.8-283.0	-	~283
Carbon (C-C)	284.2-285.0	-	
C-C, C-H (sp <sup>3</sup> )	-	285.0 (0.6-0.8) (oxidised polyethylene)	284.8
C=C (sp <sup>2</sup> )	-	~284.4 (oxidised polyethylene)	~284
C-N	285.2-288.4		
C-O (alcohol)	286.1-286.8	286.3-286.7 (0.6-1.2) (oxidised polyethylene)	~286
C-O (ether)	286.2-288.0		
C=O (ketone/aldehyde)	287.2-288.0	287.8-288.3 (0.6-1.2) (oxidised polyethylene)	~289
O-C=O (carboxyl)	288.0-289.2	289.0-289.5 (0.6-1.2) (oxidised polyethylene)	~288.5
CO <sub>3</sub> (carbonate)	289.0-291.5	288.7-289.9	288-290 (M-CO <sub>3</sub> )
$\pi$ - $\pi^*$ (aromatic shake-up)	-	290.9 (graphite)	Main C 1s peak + 6 eV (polyethylene terephthalate)

Overfitting, i.e. the introduction of more components than can be justified, was avoided and knowledge of the sample, such as the information acquired from the XPS wide scan and OrbiSIMS spectra, was used to guide the component modelling (119). Uncertainty for components was calculated using the Monte Carlo simulation in CasaXPS. The full width at half-maximum (FWHM) for were generally set equal for each component of the peak (119). An exception to this was the  $\pi$ - $\pi^*$  components, which represent an approximation of multiple satellite features. These “shake-up” features are generally more complex for more conjugated aromatic structures (119).

### 2.3.3 Orbitrap<sup>TM</sup>-Secondary Ion Mass Spectrometry

#### 2.3.3.1 Experimental

OrbiSIMS analysis was conducted using a Hybrid SIMS (IONTOF GmbH) instrument. All data was acquired using SurfaceLab 7.1 or 7.2 (IONTOF GmbH) according to the methodology outlined by Passarelli *et al.*, using Mode 4 for depth profiling and Mode 7 for imaging (135). Dynamic SIMS experiments were performed using a 20 keV Ar<sub>3000</sub><sup>+</sup> GCIB as the single beam except for one depth profile for the Needle 8’s 150-2250  $m/z$  mass range depth profile in negative polarity (Figure 4.2a) where Ar<sub>2300</sub><sup>+</sup> was used.

The primary beam was defocussed to 20  $\mu\text{m}$  with an injection time of 500 ms, a duty cycle of 4.4% (with slight variance to ensure consistent target current), and a target current of 0.23 nA, which was measured before analysis. The analysis area (field of view) was  $200 \times 200 \mu\text{m}^2$  with an interlaced border to prevent boundary effects, giving a crater size of around  $285 \times 285 \mu\text{m}^2$ . For charge compensation, a low-energy electron flood gun was applied (with 2.3A filament current and extraction bias of  $-20$ ), and the main chamber pressure was regulated with argon gas ( $9 \times 10^{-7}$  mbar) to facilitate dispersion of any charge that accumulates around the sample. The surface potential was adjusted on a sacrificial sample surface region to maximise the secondary ion yield. This optimises settings to negate the effect of sample charging during sputtering and operation of the flood gun, which can diminish the secondary ion signal.

Secondary ions were analysed using the Q Exactive HF Orbitrap<sup>TM</sup> (ThermoFisher Scientific, USA) mass analyzer (240,000 mass resolution at  $m/z$  200) which is operated via the Thermo Fisher software application programming interface (API). The Orbitrap<sup>TM</sup> was calibrated using silver cluster ions (up to  $^{107}\text{Ag}_8^{109}\text{Ag}^+$ , 1617.5735  $m/z$  in positive polarity and to  $^{107}\text{Ag}_8^{109}\text{Ag}^-$ , 1617.5746  $m/z$  in negative polarity) no more than 3 days before data acquisition. Generally, a mass range of 75-1125  $m/z$  was used for each measurement as this was found to maximise the utility of the data, though in some cases higher ranges were required. For 75-1125  $m/z$ , a cycle time of 200  $\mu\text{s}$  was used, while for 150-2250  $m/z$  and above, 400  $\mu\text{s}$  was used.

#### 2.3.3.1.1 Imaging

For imaging, the GCIB was rastered across the sample surface with low target current (18 pA), obtaining secondary ion data at each position (pixel). The duty cycle was 38.5% and the spot size was 2  $\mu\text{m}$ . The electron flood gun was applied for charge compensation (with 2.3A filament current and extraction bias of  $-20$ ). Two scans were acquired (900 s acquisition time per scan) over a sputter area of  $300 \times 300 \mu\text{m}$  with a resultant pixel size of 5  $\mu\text{m}$ .

#### 2.3.3.1.2 MS/MS

MS/MS spectra were acquired using the Hybrid SIMS which uses the higher-energy collisional dissociation (HCD) cell of the Q Exactive HF Orbitrap<sup>TM</sup> to fragment ions via collision. Acquisition was performed for around 50 s with an analysis area of  $200 \times 200 \mu\text{m}^2$  in random raster mode. Spectra under the normal conditions described in Section 2.3.3.1 were acquired to confirm presence of the target ion prior to MS/MS analysis. The mass windows and normalised collision energy values varied depending upon the scenario. Generally, a mass window of 0.9 amu was applied, though larger was used if possible (to around 4 amu) and smaller if required. A normalised collision energy (NCE) of around 35 eV was used as standard, though this varied from 10-250 eV depending upon the requirements for the ion in question; the optimal NCE is found with trial-and-error and use of a range of values is recommended to assess different degrees of ion fragmentation.

### 2.3.3.2 Data Processing and Analysis

OrbiSIMS data was processed and analysed in SurfaceLab 7.2.

#### 2.3.3.2.1 Treatment of Noise Artefacts

Four types of noise were present in OrbiSIMS spectra, these were:

1. An artefact in every spectrum at 301.06 amu.
2. “Fuzzy site” noise that is inherent to the analyser (160). These generally occur around the same  $m/z$  values with slight variation. Their depth profiles generally show constant signal throughout the acquisition. The mass ranges of these are shown in Table 2.4. Examples of this noise are shown in Figure 2.4.
3. “Partial ringing” occurring around high intensity peaks caused by saturation (160). Examples of these peaks surrounding a  $\text{PO}_3^-$  ion are shown in Figure 2.5a-b. Some peaks in Figure 2.5a resemble real peaks in a symmetrical pattern around the high intensity  $\text{PO}_3^-$  peak that has produced the partial ringing and their depth profiles also resemble that of the  $\text{PO}_3^-$  peak. Closest to the  $\text{PO}_3^-$  peak, they are more “fuzzy”. Figure 2.5b shows “fuzzy” ringing peaks at a further distance from the same peak.
4. A small peak at around 0.0010-0.0020 amu above a high intensity peak, also likely caused by saturation. Again, its depth profile resembles that of the high-intensity peak.

Table 2.4: Mass ranges of “fuzzy site” Orbitrap™ noise.

Lower mass range	Upper mass range
78.060	78.100
86.970	87.050
97.505	97.560
110.080	110.135
125.245	125.300
147.778	147.845
166.778	166.825
195.695	195.788
232.075	232.305
232.895	232.985
281.805	281.920
347.900	348.050
548.620	551.750
575.100	575.350
782.750	783.250

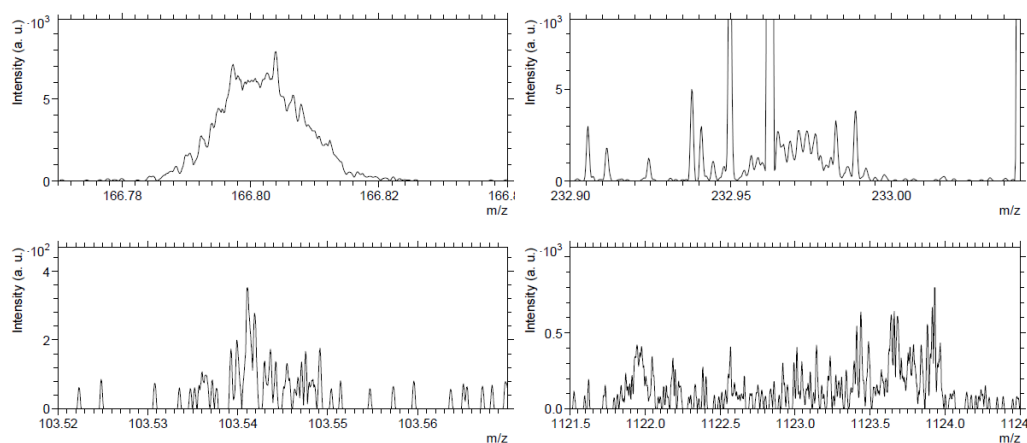


Figure 2.4: Examples of noise artefacts at typical fuzzy site regions in sample JFTOT 9.

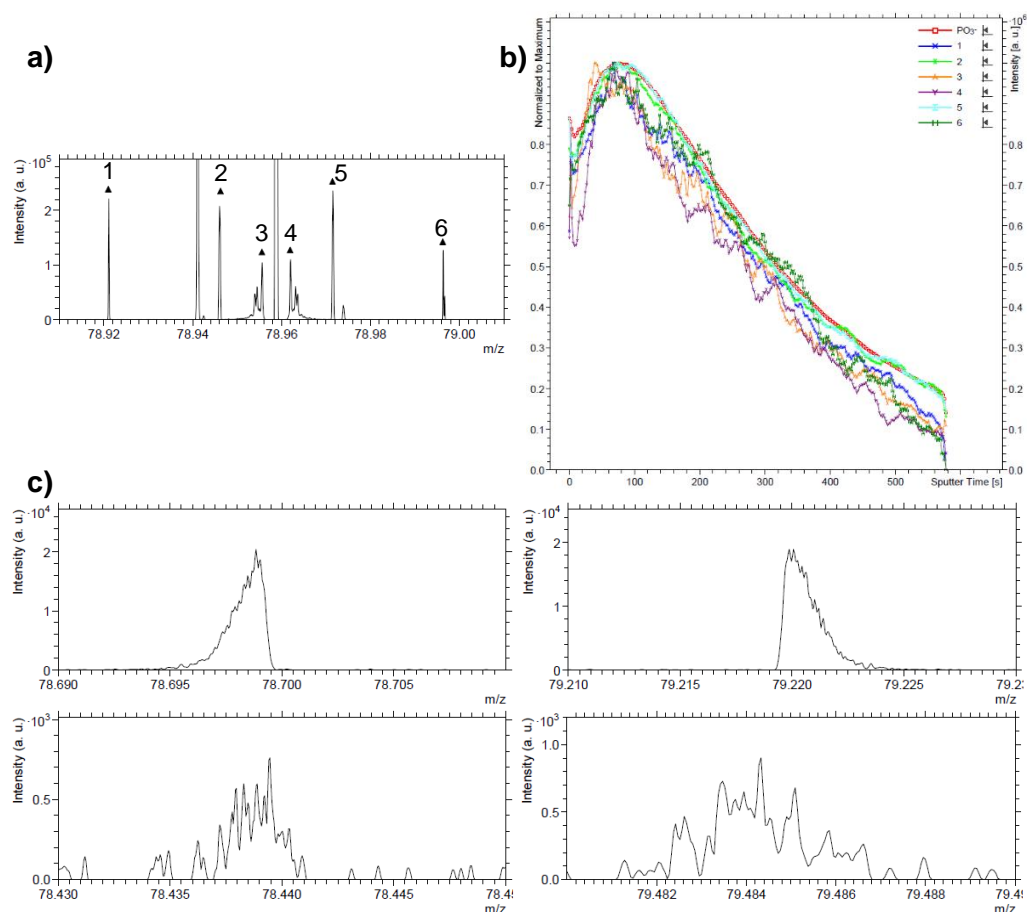


Figure 2.5: Partial ringing artefacts surrounding PO<sub>3</sub><sup>-</sup> peak in sample JFTOT 9, a) partial ringing that has the appearance of real peaks found neighbouring the saturating peak, b) depth profiles of partial ringing peaks and saturating PO<sub>3</sub><sup>-</sup> ion, c) partial ringing “fuzzy” peaks around PO<sub>3</sub><sup>-</sup>.

Removal of noise was necessary for processing of OrbiSIMS data in this thesis. In MVA, noise can interfere with the analysis and make results difficult to interpret. For batch formula calculation, formulae can be calculated for noise peaks that do not exist in the data. For both of these applications, filtering of “fuzzy site” noise was performed by removing peaks within the mass ranges shown in Table 2.4. For PCA, the filter in the ‘PCA Bundle’ was used for this (161). For batch formula calculation, a filter was made as part of an Excel macro to organise results. For NMF of depth profiles, manual removal was performed in SurfaceLab by inspecting the data in the regions of Table 2.4 to ensure no noise interference with the analysis. In data that exhibited partial ringing, the ringing artefacts were removed manually by assessing the highest intensity ions in the spectrum. Algorithms also exist to automatically identify

and discount noise artefacts based on their highly peak-dense nature however are beyond the scope of this work (160).

The partial ringing peaks that look like real peaks can be identified using the “Peak Difference” tool in SurfaceLab to measure the mass difference between them and the real high-intensity peak. If the peaks are symmetrical in both position and peak area, have much smaller peak area than the real central peak ( $<5 \times 10^{-4}$  relative intensity), and both have depth profiles that resemble the real central peak, they are likely ringing artefacts.

Low mass ions ( $<95 m/z$ ) have been observed in some spectra to split into a doublet peak which is interpreted by the peak search algorithm as two peaks. Both peaks are within the mass deviation threshold (4.5 ppm for  $<95 m/z$ ) for the peak’s correct assignment. Manual correction in SurfaceLab by assessing the low mass peak fittings was performed for PCA and for batch formula calculation.

#### 2.3.3.2.2 Ion Assignment

Formulae for OrbiSIMS ions were assigned using both the individual ion formula calculator in SurfaceLab and the batch formula calculator “compound\_finder” MATLAB script from Spanu (2021) that was later integrated into the SIMS-MFP program in Edney *et al.* (2022), where its use is described (162). Both calculators use user inputted constraints in terms of numbers of elements (which are also important for reducing computation time), but the compound\_finder script can calculate the possible formulae for a large number of ions simultaneously. The script uses an element list which can be extended freely by the user to accommodate any elements and isotopes that are required. This script also calculates the double bond equivalence (DBE) according to Equation 2 and was used to construct the fingerprint plots for the overviews of polyaromatic type ions (163, 164). This calculator has proven useful for researchers in a number of areas as a tool for assignment of a large number of unknown ions simultaneously and for rapid visualisation of data (162, 165). In all assignments in this thesis, an upper limit of 2.5 ppm was used



for masses  $>90\ m/z$  and 4.5 ppm for masses  $\leq 90\ m/z$ , a considerably lower threshold than previous ToF-SIMS analysis ( $\leq \sim 250$  ppm).

$$DBE = X - \frac{Y}{2} + \frac{Z}{2} + 1 \quad \text{Equation 2}$$

Where  $X = \text{no. C atoms}$   
 $Y = \text{no. H or halogen atoms}$   
 $Z = \text{no. N or P atoms}$   
 $N = \text{no. N atoms}$

The compound\_finder script's functionality was extended in the current work to facilitate searches for inorganic ions based on salt components identified in the sample. Inorganic salt species are composed of a metal cation (e.g.  $\text{Na}^+$ ) and an often molecular anion (e.g.  $\text{SO}_4^{2-}$ ). In OrbiSIMS data, inorganic ions' charges usually balance as expected to equal +1 in positive polarity or -1 in negative polarity. Thus, a simple sodium sulfate ion would appear in positive polarity as  $\text{Na}_3\text{SO}_4^+$  and in negative polarity as  $\text{NaSO}_4^-$ . To aid with such assignments, the compound\_finder script was operated using these molecular anion masses alongside element masses; for example, the output for the ion  $\text{Na}_3\text{SO}_4^+$  would produce a value of 3 in a column for  $\text{Na}^+$  and a value of 1 in a column for  $\text{SO}_4^{2-}$ . Next, the matrix output was pasted into Excel, the charges were inputted and using a macro the charges for each assignment were calculated. These could then be filtered in positive polarity for charges that total +1 and in -1 negative polarity. This allows for quicker assignments as unrealistic assignments with impossible charges can be immediately discarded.

### 2.3.3.2.3 Kendrick Mass Defect

Kendrick mass (KM) and Kendrick mass defect (KMD) were calculated according to Equation 3 and Equation 4, where the typical Kendrick base unit is  $\text{CH}_2$  (164). The SI molecular mass is defined relative to carbon, whereby an atomic mass unit (the Dalton, Da) is defined as one twelfth of the mass of carbon (as carbon's mass number is 12). Thus, formulae that differ by only multiples of carbon have the same decimal portion of their SI mass. For example,  $\text{C}_4\text{H}_{10}$  exact mass = 58.0783 and  $\text{C}_6\text{H}_{10}$  exact mass = 82.0783. When molecular masses are converted to KMs, they are defined by an alternative

base unit rather than carbon, most often CH<sub>2</sub> (SI mass = 14.0157 Da). This conversion means that the decimal portion of the KM will be the same for formulae that differ by multiples of CH<sub>2</sub>. For example, C<sub>4</sub>H<sub>10</sub> KM = 58.0134; C<sub>5</sub>H<sub>12</sub> KM = 72.0134. Thus these two species have the same KMD value (Equation 4) and when plotted as KMD vs. KM will appear on the same horizontal line. Alternative Kendrick base units to CH<sub>2</sub> can be used to see other units in the same line, which may be particularly useful if searching for polymers of known units.

$$KM = SI\ mass \times \frac{Kendrick\ base\ nominal\ SI\ mass}{Kendrick\ base\ SI\ mass} \quad \text{Equation 3}$$

$$KMD = nominal\ KM - KM \quad \text{Equation 4}$$

Where *nominal* refers to the mass rounded to a whole number.

### 2.3.3.3 Multivariate Analysis of OrbiSIMS Datasets

The concept of MVA was introduced and explained in Section 1.3.3.2.2. MVA is a very common technique used in conjunction with SIMS to rapidly and unambiguously identify differences and similarities between SIMS datasets (129). MVA is purely a mathematical function based on the data the user inputs. To ensure valid interpretations, the original data should also be referred to following MVA insights. Principal component analysis (PCA) is the most common form of MVA in the SIMS community and was described in Section 1.3.3.2.2.

#### 2.3.3.3.1 PCA of JFTOT Spectra in Chapter 5

PCA was performed on the OrbiSIMS data for five positions of each JFTOT samples in Chapter 5 in order to deconvolute the data and identify differences and similarities between the samples. PCA was carried out using the “PCA Bundle” for MATLAB by Hook, A.L. (University of Nottingham) (2021) (161) which uses the “PCA” function in MATLAB. In SurfaceLab, peak lists were created for each position of sample and unified via Mathematics in SurfaceLab (2.5 ppm catch mass radius, corresponding to the mass deviation threshold of the Orbitrap<sup>TM</sup>). A brand new, unused JFTOT tube (aluminium-magnesium)

was also analysed at three positions along the tube to create three reference lists of ions to remove from the unified peak lists via “Peaks not occurring in reference list” in Mathematics (3.5 ppm catch mass radius to ensure removal). This is intended to remove any highly generic and contaminant-related ions as well as JFTOT tube substrate ions that would be detrimental to PCA analysis by including random and uninformative features. As each JFTOT tube had been handled in the same fashion (equipment, container, sample preparation), there should be overlap of any surface contamination ions, most of which was removed via this method. The final unified list was exported for all datasets, then in Excel exact duplicates were removed and the list filtered such that only ions with a minimum normalised intensity of  $1 \times 10^{-5}$  in at least one sample were included.

Simultaneous MVA of organic and inorganic components can be problematic due to the often extremely high intensities of inorganic material which can dominate/skew results (130, 166). Therefore, a mass filtering approach developed by Trindade *et al.* (2018) for the simsMVA program was used to separate organics from inorganics. This works on the principle that the exact mass of an organic ion will generally be above the nominal mass while that of an inorganic ion will generally be below it. In other words, the decimal section of an organic ion’s mass is generally between 0-0.5000, while that of an inorganic ion is generally between 0.5001-0.9999. This mass filtering has previously been applied to ToF-SIMS data, where the smaller ions are less likely to break this trend (130, 166). In the OrbiSIMS work of this thesis, larger organic species can be measured and therefore a decimal mass threshold of 0.7 was used to ensure they would be included in the organic dataset. After mass filtering, PCA was successfully performed separately on the organics and inorganics, meaning four instances of PCA were run in total (positive polarity organics and inorganics, negative polarity organics and inorganics).

The results for each PCA were tested with and without square root means pre-processing applied. If square root means improved results by revealing more trends in the data via manual inspection of results, it was employed. The MATLAB “PCA” function automatically mean centres the data and uses the

singular value decomposition (SVD) algorithm (167). The PCA Bundle includes a set of mass ranges corresponding to Orbitrap<sup>TM</sup> “fuzzy site” noise peaks which can be excluded from the PCA. This filter was activated alongside custom additional ranges, giving an exclusion list of the noise ranges shown in Table 2.4. After identifying interesting trends in the PCA results, the original data was consulted to verify.

#### 2.3.3.3.2 NMF of IDID Depth Profiles in Chapter 4

MVA was performed on IDID depth profiles using each depth level of the profile as an observation (analogous to a sample position in the PCA described in Section 2.3.3.3.1). Therefore, the resulting scores describe the presence of correlated ions at each deposit depth level. This aids the identification of the differences between different depth levels and of trends and layering effects throughout the depth profile.

Non-negative matrix factorisation (NMF) is a similar MVA technique to PCA. In NMF results, endmembers (EMs) are outputted which are analogous to principal components in PCA. NMF’s main practical difference to PCA is that the matrices it produces are non-negative and so are more intuitive for relating to the original depth profile, the signals of which can also only be positive. In NMF, the non-negative data matrix,  $M$ , is factorised by approximation into two non-negative matrices,  $W$  and  $H$ , (Equation 5) by iteration (168). In this work, the multiplicative update algorithm was used which updates the values of  $W$  and  $H$  iteratively to find the best approximation. This algorithm was introduced by Lee and Seung (2000) and is one of several available in *simsMVA* from the MATLAB Statistics and Machine Learning toolbox.

$$M \approx WH \quad \text{Equation 5}$$

In ToF-SIMS data, Poisson (square root) scaling pre-processing is a standard practice to account for the distribution of noise and error in ToF-SIMS data, achieving error normalisation by dividing each value of the matrix by its square root (130, 169). This is not proven to apply to Orbitrap<sup>TM</sup> data so pre-processing was applied only when it improved the MVA results. In the NMF of

depth profiles, this improved the results by having the effect of compressing the dynamic range of the depth profile signals which mitigates the dominance of high intensity ions, allowing NMF to identify more trends.

NMF was performed using the MATLAB program simsMVA (Trindade, G.F., University of Nottingham/National Physical Laboratory, mvatools.com) (130, 166). For all datasets, square root mean pre-processing was applied, four EMs were achieved, and over 2000 iterations were performed which was found to be necessary to improve results.

Peak lists were created in SurfaceLab using the peak search feature. These lists were inspected to identify the lowest intensity that produced a coherent depth profile as opposed to sparsely scattered signals, and this intensity was used as the minimum for the respective samples. These minimum intensities and the size of the peak list generated (after removal of noise and partial ringing) are shown for each depth profile of each sample in Table 2.5. For each NMF in this chapter, the number of EMs was optimised which was found to be 4 for most samples. This is important to ensure the most information is found by NMF and to avoid multiple trends being captured in one EM where it is possible to split those trends. A high number of iterations were performed (>4000) which was found in some cases to produce better results.

Table 2.5: Peak search parameters for creating peak lists in SurfaceLab for NMF of negative and positive polarity OrbiSIMS depth profiles for Needles 6-8.

Sample	Polarity	Minimum peak area		Peak list population (peaks)
		Raw	Normalised	
Needle 6	Negative	1.75E+05	3.90E-06	1671
	Positive	1.00E+05	7.10E-06	648
Needle 8	Negative	2.50E+04	3.20E-06	672
	Positive	2.50E+05	3.60E-06	922
Needle 7	Negative	2.00E+05	6.60E-06	1301
	Positive	1.00E+05	4.90E-06	406

### 2.3.3.3.2.1 Comparative Method

In the current work, a novel method involving additional post-processing of data was used and named the Comparative Method. This was necessary to overcome the excessive overlap of high loading ions across multiple EMs which made interpretation difficult. The requirement for this is demonstrated in Chapter 4. The method involves filtering the ions in each EM's loadings plot to only include ions that have their largest loading in the respective EM. This was found to give a superior overview of each EM without convolution due to the overlap of chemistries.

To assess the results from NMF in more detail, a new parameter was then calculated and named the "relative loading". This is calculated for a given ion by normalising the original loading value from the NMF results to the total of the loadings for all EMs, as shown in Equation 6. The relative loading parameter allows for quantification of an ion's depth profile's signals distribution across the deposit thickness. These calculations were carried out using an Excel macro, which arranged the spreadsheet such that the data could be sorted and filtered.

$$Relative\ loading_x = \frac{Original\ loading_x}{\sum_{i=1}^N Original\ loading_i} \quad \text{Equation 6}$$

Where

$x = \text{endmember being calculated for}$

$N = \text{number of endmembers}$

For the loadings of an ion, the coefficient of variation (CV) was calculated according to Equation 7 which quantifies the level of distribution across the EMs. The highest CV means the ion is distributed 100% in one loading, while  $CV = 0$  means that the ion is equally distributed across all EMs. This parameter was useful to sort the ions by those that are the most or least distributed through the depth profile.

$$CV = \frac{\sigma}{\mu} \quad \text{Equation 7}$$

Where

$\sigma$  = standard deviation

$\mu$  = mean

#### 2.3.4 Atmospheric pressure matrix-assisted laser desorption/ionization high-resolution mass spectrometry (AP-MALDI-MS)

10 mg of the deposit was weighed after scraping it off the injector substrate using a scalpel. This was suspended in 1 ml of tetrahydrofuran (THF) and diluted further to create a 1 mg/ml concentration. A 0.5  $\mu$ L drop was spotted onto an ABI Opti-TOF 192-well target plate and on top of this spot (once dried for 10 minutes) a 1  $\mu$ L of tetracyanoquinodimethane (TCNQ) matrix was added, at a concentration of 5 mg/ml in THF. A Q Exactive Plus hybrid quadrupole-Orbitrap mass spectrometer (Thermo Scientific, San Jose, USA) was coupled to an AP-MALDI source (MassTech Inc., Columbia, MD). Target-ng software (MassTech) was used to control the XY stage motion and operation of the laser. The source utilized a diode-pumped solid-state Nd:YAG laser ( $\lambda = 355$  nm) operating at a 0.1–10 kHz repetition rate. Maximum laser pulse energy was 3  $\mu$ J at a 1 kHz repetition rate. A beam attenuator was used to adjust laser energy. The voltage applied between the MALDI plate and inlet capillary of mass spectrometer was 4 kV. The distance between the plate and the capillary was 3 mm. The inlet capillary was set to 400 °C. Each dried-droplet spot was scanned with a 50  $\mu$ m wide laser spot. Mass spectra were acquired in a positive-ion mode with mass resolution up to 180,000 at  $m/z$  200 and a mass range of  $m/z$  150–1500. Data was acquired and processed using Tune and Xcalibur software (Thermo Fisher Scientific, Waltham, MA). Batch ion assignment was performed for hydrocarbons with the compound\_finder script using a 6-ppm mass deviation threshold.

#### 2.3.5 Optical Profilometry for Measurement of GCIB Craters

A Zeta 20 3D Optical Profiler was used to measure surface GCIB craters from OrbiSIMS and XPS depth profiles. Zeta 3D software was used for acquisition and interpretation. Images were acquired generally using a 50 $\times$  optical lens,

though with the larger sputter craters from XPS, 20× was required. The sample is scanned over a specified vertical (Z) range at regular depth intervals for 800 steps, recording the lateral (XY) location and Z height of the pixels to produce a 3D true-colour image of the region of the sample surface. To aid the setting of the Z-height range, the ZDot™ focus-assist pattern was used which increases the visible contrast. 10 cross-sections were applied and arranged along the GCIB crater, then levelling of the deposit surface was performed on a region on one side of the crater and a region on the other side to enable measurement of the crater size. Two step sizes were measured for the 10 cross-sections: one from the bottom of the crater to the deposit surface on the first side, and another from the bottom of the crater to the deposit surface on the other side.

For OrbiSIMS GCIB craters, cross-sections were applied across the crater and deposit surface on both sides and levelling of the deposit surface on each side of the crater was performed. This means the step depth from the deposit surface (from either side of the crater) to the crater base would give the relative distance from the levelled deposit surface to the crater base. Note that GCIB craters from XPS depth profiles were too large in area to level both sides, therefore are much less reliable and are not used for estimating the deposit thickness. The step areas were created on relatively flat regions of the deposit surface and crater base, away from the boundary to avoid the crater wall and unusual sputtering effects that occur there (such as build-up of material on the deposit surface at the edge of the crater wall).

### 2.3.6 Optical Microscope

Optical micrographs of all samples were taken with a Leica M205 FA Stereo light microscope.

## 2.4 Graphs and Charts

Graphs and charts were made in GraphPad Prism 9.3.0.



## Chapter 3: OrbiSIMS and XPS Characterisation of Internal Diesel Injector Deposits

### 3.1 Introduction

ToF-SIMS has been a successful technique in the analysis of IDIDs, with the investigations discussed in Section 1.3.3.2 offering detailed chemical and spatial information (3, 39, 40, 47, 48, 59, 128). This chapter builds on this work by applying the recently developed technique of OrbiSIMS (discussed in Section 1.3.3.4) to a range of IDID samples. Owing to this technique's novel combination of soft ionisation and high mass resolving power via the  $\text{Ar}_{3000}^{+}$  GCIB and Orbitrap<sup>TM</sup> analyser respectively, more detailed chemistry of IDIDs than previous SIMS investigations is identified (3, 59). This allows identification of key molecular products of partial carbonisation for the first time that had previously been speculated to form within IDIDs. Other chemistries, including those from diesel additives and lubricant oil, are unambiguously identified with greater detail than previous investigations. XPS is used in support of OrbiSIMS to provide a quantitative context, which is crucial for quantitative validation of the semi-quantitative OrbiSIMS data.

After identifying these important IDID chemistries, the same techniques are then applied to a marine engine injector deposit sample. Key deposit components are identified and compared to IDID samples. Finally, MALDI-Orbitrap<sup>TM</sup> MS is applied to this sample as an alternative MS approach with gentler ionisation that causes less fragmentation of native deposit chemistries. This aims to validate the OrbiSIMS results by identifying the likely parent ions, however further work will be necessary to develop this method.

Some work in this chapter was published (Edney *et al.*, 2020) as an investigation comparing an IDID with a gasoline direct injection (GDI) deposit and a diesel filter, Edney *et al.* (170). Other data was featured in a conference paper (Lamb *et al.*, 2020) which compared Needle 6 and Needle 8 (78).

## 3.2 Results and Discussion

This chapter will serve as an introduction to the techniques used in the current work, a catalogue of key chemistries identified using OrbiSIMS and XPS, and a detailed characterisation of the IDIDs analysed herein. Comparisons between samples where relevant are also made alongside a discussion around their likely formation pathways.

### 3.2.1 Appearance and Morphology using Microscopy

Imaging of IDIDs is very common in previous IDID investigations using microscopy techniques: primarily using optical, scanning-electron, or transmission electron (where applicable) microscopy (Section 1.3.1). Developing a visualisation of the deposit morphology and its coverage on the sample is useful to understand the extent of IDID coverage and type of deposit present. Figure 3.1 shows optical images and scanning-electron images for Needles 6-8, all of which display a rough, grainy appearance consistent with IDIDs in previous studies (46, 86, 105, 128). Needle 8 (Figure 3.1c) appears to have the largest particle aggregates with pores in the deposit structure. Needles 6 and 7 both appear to have DLC coatings, which may have offered some

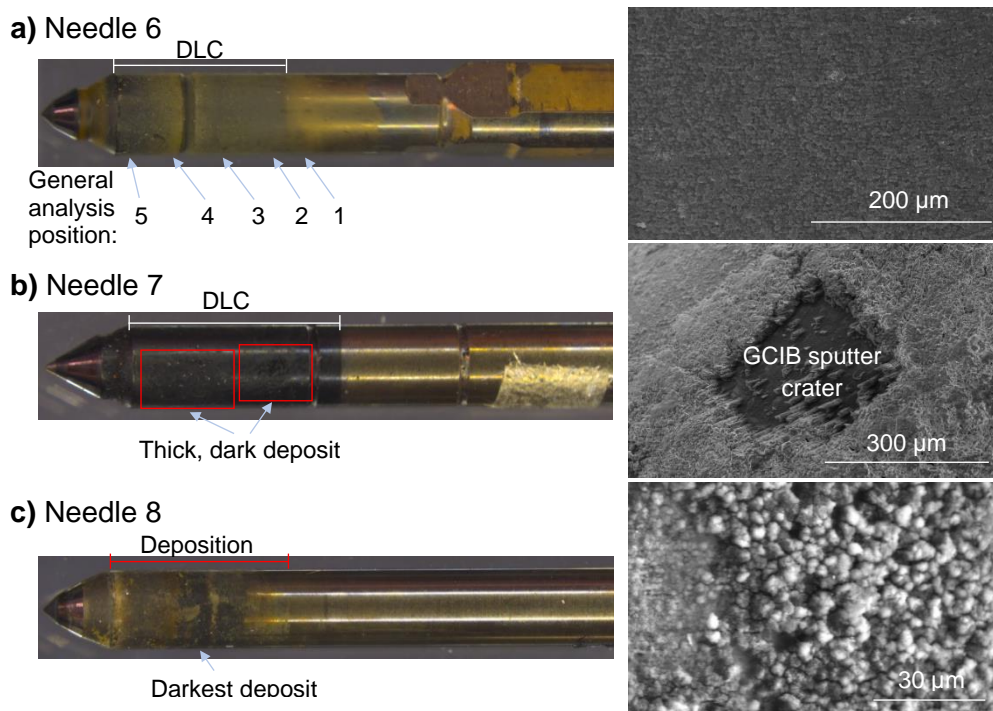


Figure 3.1: Optical microscope images (left) and SEM close-up images (right) for a) Needle 6 (with general OrbiSIMS analysis positions labelled), b) Needle 7 and c) Needle 8.

protection against IDID formation and adsorption. For Needle 7, a crater from OrbiSIMS depth profiling is visible, and demonstrates that the sputter beams used in later analyses are able to remove this grainy deposit material to reach the underlying substrate. Optical microscope and SEM Images of other samples that were collected can be found in Appendix 1.1.

### 3.2.2 Elemental Analysis using SEM-EDS

Regions of SEM micrographs can be probed for elemental content using EDS. Examples of EDS quantification are shown in Table 3.1 and Table 3.2 for Needle 6, where it can be seen that early on the needle shaft (position 1), before the DLC, iron is the dominant element measured whereas this becomes carbon where the DLC and deposit are located. Both positions have sodium, which is likely predominantly from deposition. EDS has been used extensively in previous studies (discussed in Section 1.3.2.1) and its quantitative accuracy is considered poor in many situations. Therefore XPS is favoured in the current work for elemental analysis, which has the additional benefit of being able to quantify chemical environments of the elements. EDS can nonetheless be useful for providing an overview of the elements present, as a crude analysis or to inform further investigations such as which elements to target in ion formula calculation when using OrbiSIMS analysis.

Table 3.1: Needle 6 EDS data from position 1, before the DLC.

	<b>Fe</b>	<b>O</b>	<b>Na</b>	<b>Cr</b>	<b>S</b>	<b>Ca</b>	<b>P</b>	<b>Mg</b>	<b>Al</b>	<b>Si</b>	<b>V</b>	<b>K</b>
<b>at.%</b>	39.3	28.6	18.3	2.0	3.0	1.5	1.7	1.7	1.5	1.4	0.7	0.4
<b>3<math>\sigma</math></b>	3.9	5.9	2.0	0.4	0.4	0.3	0.3	0.3	0.3	0.3	0.2	0.2

Table 3.2: Needle 6 EDS data from position 4, on the DLC and deposit.

	<b>C</b>	<b>O</b>	<b>Na</b>	<b>Al</b>	<b>S</b>	<b>Cl</b>	<b>Cr</b>	<b>Fe</b>
<b>at.%</b>	71.7	14.7	6.0	0.5	0.8	5.5	0.7	0.2
<b>3<math>\sigma</math></b>	19.4	6.5	1.4	0.2	0.2	1.0	0.3	0.2

### 3.2.3 Evidence of Carbonisation in IDIDs by OrbiSIMS and XPS

Carbonaceous IDIDs have been proposed to result from a progressive carbonisation process discussed in Section 1.2.2.3, whereby fuel (as well as additives and possible contaminants) degrades over time under high temperature and pressure (57). The mass spectrometry techniques used in previous analysis discussed in Section 1.3.3 had limited ability to analyse this type of deposit material. Carbonaceous material is inaccessible for GC-MS due to low solubility and volatility and is difficult to identify with ToF-SIMS due to fragmentation and low mass resolving power (3, 57). MALDI-MS analysis by Venkataraman and Eser (2008) has identified polyaromatic material in an EDID, discussed in Section 1.3.3.3 (48). In this section, the identities of IDID chemistry resulting from carbonisation are identified for the first time owing to the relatively soft ionisation and high mass resolving power of the  $\text{Ar}_{3000}^{+}$  GCIB and Orbitrap<sup>TM</sup> respectively, neither of which have been applied to IDIDs in the past. Prior ToF-SIMS analyses used  $\text{Bi}^{+}$  or  $\text{Bi}_3^{+}$  analysis beams and, where depth profiling was performed,  $\text{Cs}^{+}$  sputter beams, with ToF analysers of mass resolving power 15,000 compared to the Orbitrap<sup>TM</sup>'s 240,000 (3, 59, 135). In practice, this means larger species are present in the OrbiSIMS spectra and they can be assigned with a mass deviation threshold of typically  $\pm 2.5$  ppm while ToF-SIMS analysis is typically up to  $\pm 250$  ppm.

#### 3.2.3.1 Polyaromatic Compounds in OrbiSIMS and XPS

Evidence of carbonisation was found in the OrbiSIMS data in the form of ions with assignments consistent with polyaromatic and carbonaceous cluster ions, and in the C 1s XPS  $\pi$ - $\pi^{*}$  satellite component which represents  $\pi$ -bonding systems of polyaromatics, as well as chemistries such as alkenes and graphene (see Appendix Section 1.1.2.1 for full XPS results) (119, 171). 3D OrbiSIMS spectra in Figure 3.2a-b show the most PAH-affected sample (Needle 8 position 4) with a dense pattern of PAH ions as well as high intensities for calcium hydroxide salts while Needle 6 has much smaller PAHs, instead being dominated by sodium salts of chlorides and sulfates; inorganic salt IDID chemistries are discussed in Section 3.2.5. Figure 3.2c shows the spectra after filtering using the compound finder script (Spanu, 2021) (159) as described in

Section 2.3.3.2.2, where the pattern of PAHs in Needle 8 can be seen and the much more sparse PAHs with lower peak areas is seen for Needle 6. Inorganic salt deposit content, including of sodium and calcium, will be discussed in Section 3.2.5.1. As outlined in Section 2.3.3.2.2, these and all other ions in this thesis are assigned with a maximum mass deviation of 2.5 for masses  $>90$   $m/z$  and 4.5 for masses  $\leq 90$   $m/z$ . This mass deviation is greatly lower than the threshold for ToF-SIMS (up to around 200 ppm) and greatly reduces ambiguity in ion assignments, providing unprecedented accuracy in SIMS characterisation of IDIDs.

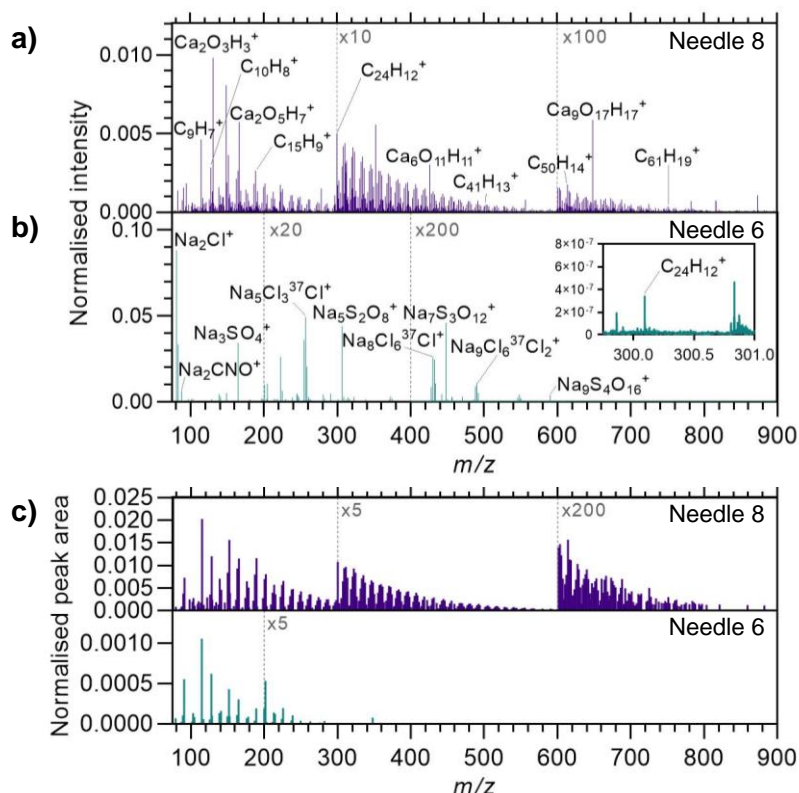


Figure 3.2: Normalised OrbiSIMS spectra for a) Needle 8 analysis position 4, and b) Needle 6 position 3. c) Spectra (normalised peak area) after filtering for hydrocarbon ions.

All IDID samples displayed ions consistent with polyaromatic compounds and carbonaceous cluster ( $\text{C}_x^+$ ) in their OrbiSIMS datasets. The polyaromatics appear to generally be in the form of radical cations ( $\text{M}^{\cdot+}$ ). These are identifiable with the high mass resolving power of OrbiSIMS without comparison to a standard sample as was required in Barker *et al.*'s ToF-SIMS investigation (3). As well as ions with true polyaromatic formulae such as coronene ( $\text{C}_{24}\text{H}_{12}^+$ ), hexabenzocoronene ( $\text{C}_{48}\text{H}_{16}^+$ ), and circumovalene

( $C_{66}H_{20}^+$ ), there are other more hydrogen deficient ions such as  $C_{30}H_8^+$  which have too low H:C ratios to represent pericondensed polyaromatics and must therefore have semi-fullerene character (172). These may represent more advanced carbonisation via loss of hydrogen. However, they may also be products of fragmentation from sputtering.

All samples also contain heteroatomic content, with N- and O-containing polyaromatic-type ions (N-PACs and O-PACs) as well as more H-deficient ions. N-PACs occur in the positive polarity data where many appear to be  $[M+H]^+$  ions. It is suggested that these are also products of carbonisation which has integrated nitrogen as previously theorised (3). Refined petrodiesel still contains nitrogen which can be destabilising compounds (173), though most is removed in the refining process (174). Many additives, such as PIBSI and 2-EHN, and contaminants, such as lubricant oil and its additives, contain N so are also potential sources. While the presence of nitrogen has been noted in IDIDs in many studies (40, 48), little elucidation of specific nitrogen species other than suspected LMW PIBSI-related succinimides and amides has been recorded (39, 87). Fragments of N-PACs from IDIDs have been suggested from ToF-SIMS IDID data ( $C_3N^-$ ), but the species themselves have not been unambiguously identified (3).

The sizes and intensities of polyaromatic-type ions vary between samples and point to key differences in deposit compositions. Figure 3.3a shows DBE (for hydrocarbons) and C:N ratios (for N-containing ions) expressed as a function of  $m/z$  for a range of needle IDID samples. The assignments were inspected manually, which were supported by consistent lower mass deviations for the assigned series. A minimum intensity threshold is used of  $1 \times 10^{-5}$  after normalising to the sum of ions of decimal mass  $<.5$ , acting as a total intensity that includes organic and PAH-type ions and ignores inorganic ions; thus, the ions are effectively normalised to the total intensity of organic/carbonaceous material. The largest hydrocarbon and N-containing ion from each sample is summarised in Table 3.3, showing Needles 6 and 12 with relatively small ions while Needles 7, 8, 13 and 9 extend to larger ions that indicate further progression of carbonisation. These largest PAHs are smaller than those

previously observed in the EDID by Venkataraman and Eser using MALDI, which reached 1000 amu (48). It is expected that greater carbonisation will occur in an external deposit due to the exposure to the flame, reaching much higher temperatures. This same trend was also observed in the comparison of Needle 6 with a GDI tip external injector deposit, which had much larger PAHs than the IDID. These results can be found in Appendix Figure A3 (170).

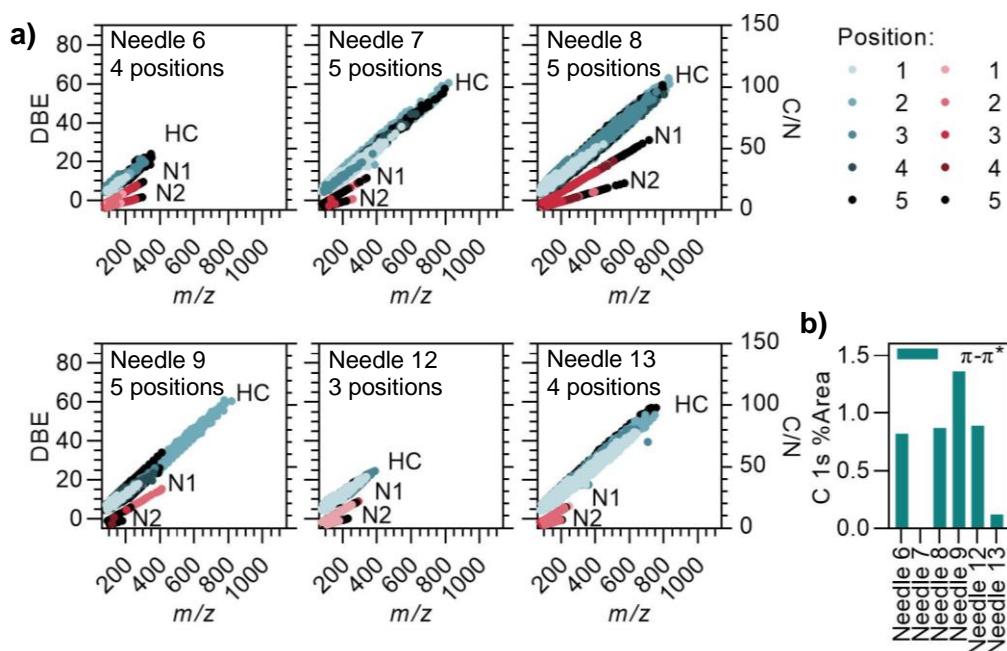


Figure 3.3: a) DBE v  $m/z$  and C/N v  $m/z$  plots for hydrocarbon and N1 and N2-containing ions in positive polarity for needle IDID samples. b) High-resolution C 1s XPS  $\pi-\pi^*$  component percentage area.

Table 3.3: Largest hydrocarbon and N-containing ( $N_1$  or  $N_2$ ) positive polarity polyaromatic-type ions. Minimum intensity  $1 \times 10^{-5}$  normalised to the total intensity for ions with decimal mass  $< .5$ .

Ion class		Needle ID					
		6	7	8	9	12	13
HC	ID	$C_{28}H_{14}^+$	$C_{67}H_{15}^+$	$C_{77}H_{17}^+$	$C_{67}H_{15}^+$	$C_{31}H_{15}^+$	$C_{62}H_{12}^+$
	$m/z$	350.1092	819.1181	941.1328	819.1177	387.1169	756.0938
1N/2N	ID	$C_{23}H_{11}N^+$	$C_{26}H_{13}N^+$	$C_{57}H_{17}N^+$	$C_{32}H_{12}N^+$	$C_{22}H_{12}N^+$	$C_{18}H_{16}N^+$
	$m/z$	301.0887	339.1044	715.1343	410.0966	290.0963	246.1276

Needle 8 has the largest PAH ions and the largest N-PAC ions compared to the other samples analysed which reach smaller masses (Table 3.3). Needle 13 is

notable for having the smallest N-PAC ions despite having relatively large PAHs. This could be due to this sample originating from an engine test, in which the fuel/additive mixture was likely “cleaner” than that for field samples, introducing less nitrogen to the system. This observation is supported by the XPS data, for which this sample had the lowest nitrogen content (0.5 at.%) except for Needle N20A which had undetectable levels. From high-resolution XPS curve fitting, the  $\pi$ - $\pi^*$  component seen in Figure 3.3b is in fact largest in Needle 9 (1.4%) which may indicate a larger concentration of polyaromatics in this sample despite its PAHs being slightly smaller in structure than Needle 8’s. Alternatively, this may represent other, non-aromatic species such as alkenes. The full XPS results, including high-resolution curve fittings, can be found in Appendix Section 1.1.2.

The polyaromatic MW distributions in Figure 3.3 establish Needle 8 as the most carbonised sample in terms of PAH/N-PAC sizes, indicating it has undergone the largest PAH extension reactions. Needle 8 also has the highest normalised intensities of PAH and N-PAC diagnostic secondary ions, illustrated in Figure 3.4 in a comparison with the two positions with the highest intensities of these ions from Needles 6-8 and 13. For each ion, Needle 8 has the largest intensity, suggesting it may have the highest concentration of these species, again supporting that this sample has undergone the most carbonisation. While it may be expected that the PAHs will grow along the needle due to proximity to the combustion chamber providing heat from the tip, this appears to not be the case here. Other factors such as backflow of fuel, presence of DCA or the force of high-pressure fuel removing deposit material from certain positions may play a role in where the maximum carbonisation occurs. Further work would be required to study the positions most vulnerable to IDIDs.



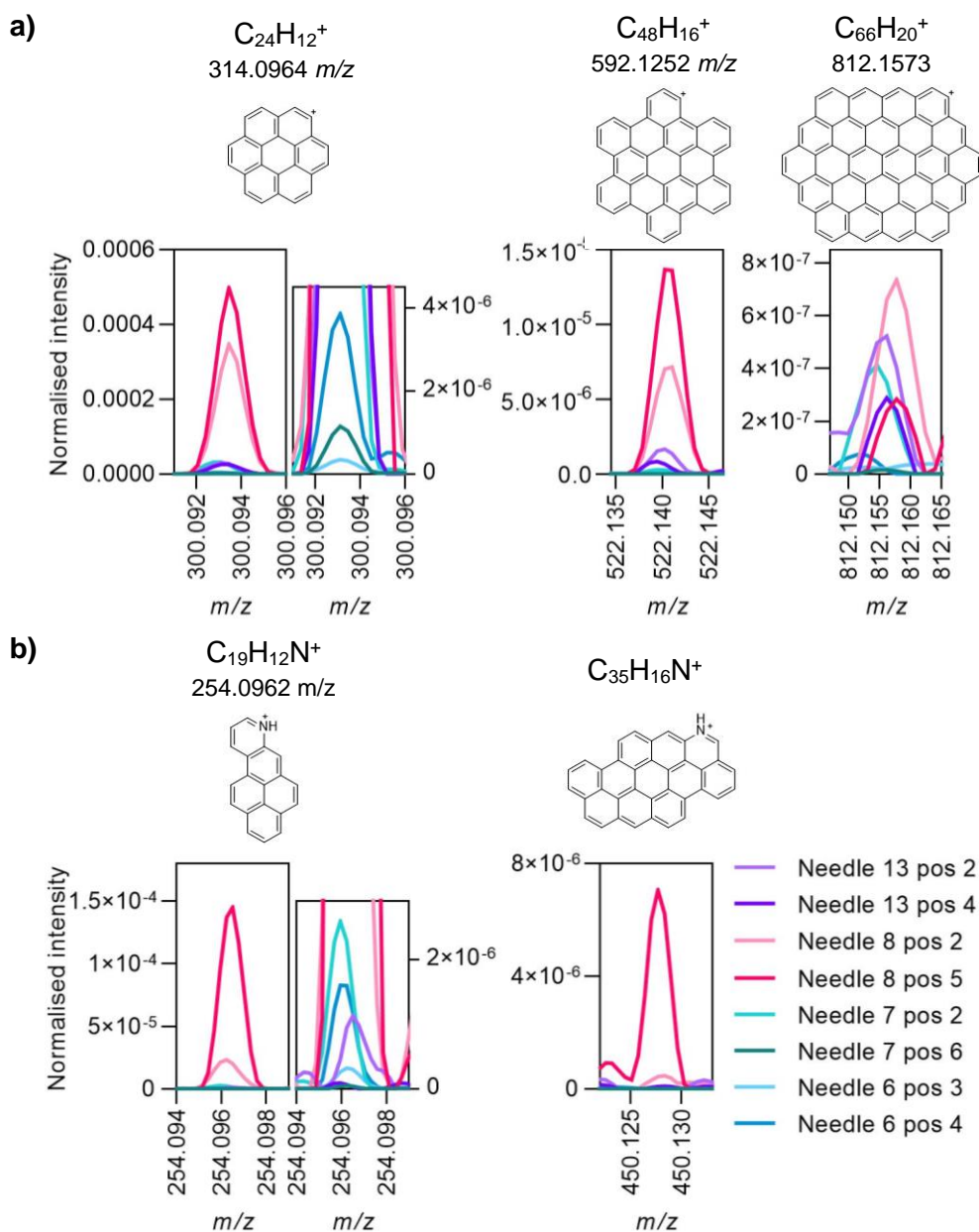


Figure 3.4: OrbiSIMS secondary ion overlaid normalised peaks for two positions of injector needle IDID samples. a) PAHs and b) N-PACs.

The negative polarity OrbiSIMS data contains oxygen-containing polyaromatic compounds (O-PACs), which may indicate integration of this element into carbonisation. Many of these ions appear to be of the form  $[M-H]^-$ . In comparison to nitrogen-containing species, a wider range of oxygen-containing compounds have been noted in IDIDs, such as carboxylates and esters (41, 175), however this is the first work to record O-PAC compounds. As with PAHs and N-PACs, Needle 8 has the largest mass O-PAC ions, shown in Figure 3.5. This suggests Needle 8 also experienced larger scale carbonisation

that involves oxygen than other samples. Needle 6's O-PAC distributions are comparable to Needle 7 despite having much smaller hydrocarbon and N-containing ions. Therefore, Needle 6's carbonisation processes likely involved more oxygen than Needle 7's. In terms of ion intensities, Needle 8 again shows by far the highest normalised intensities of these ions (Figure 3.5) while Needles 6 and 7 are comparable but Needle 7 consistently has slightly higher. Needle 8 has hence been shown by every OrbiSIMS measurement to possess the greatest degree of carbonisation in its deposit.

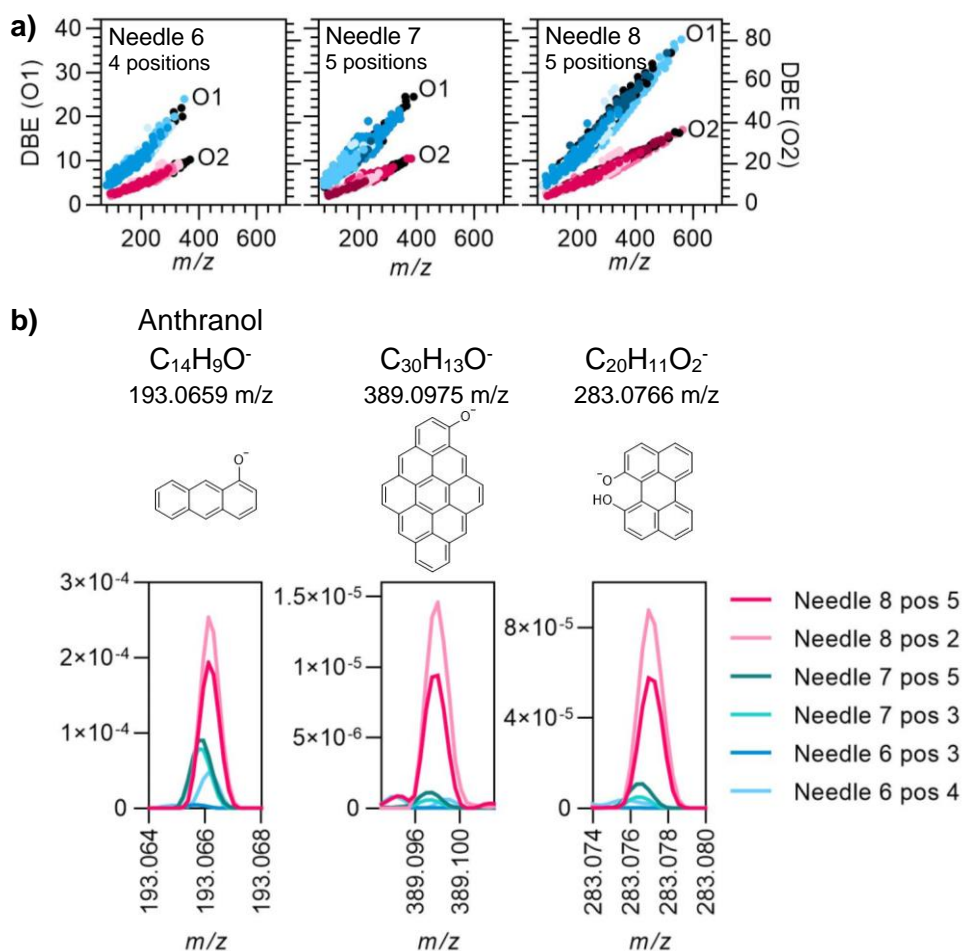


Figure 3.5: O-PAC-type ions OrbiSIMS data. a) O1 and O2-containing ions' DBE as a function of  $m/z$ . b) O1 and O2-containing polyaromatic ion normalised peaks for Needles 6-8.

### 3.2.3.1.1 Evidence of Carbonisation Mechanism from IDID OrbiSIMS Depth Profiling

One of the most useful attributes of SIMS is the spatial information that can be gained with depth profiling and imaging. ToF-SIMS depth profiling of IDIDs

to reveal their chemical variation with depth has found them to be “layered”, however previous work has been limited to only small fragment ions with little understanding of the molecular nature of the deposit layers, as discussed in Section 1.3.3.2.

Depth profiles of PAH-type, semi-fullerene and carbonaceous ions in Needle 8 (Figure 3.6) support the suggestion that carbonisation within IDIDs proceeds via formation of extended PAH systems. It is expected that the lower deposit material closer to the needle substrate, exposed later in the depth profile, is older deposit and will have progressed further along the carbonisation mechanism than higher material closer to the surface. As can be seen in Figure 3.6a, the larger PAHs are found later in the profile than smaller PAHs with a general trend of larger PAHs emerging at lower depths. At lower depth than the PAHs, there is a layer of carbonaceous material ( $C_{11}^+$  and  $C_{15}^+$ ), which likely represents ordered carbon deposit before the substrate ( $Fe_2O_6H_6^+$ ) is reached. Figure 3.6b shows depth profiles for the same small near-surface PAH (dibenzocoronene) as well as ions of the same C number but decreasing H number. As the depth profile progresses, the H/C ratio decreases, showing the progressive loss of hydrogen until reaching the  $C_x^+$  material. These results suggest carbonisation proceeds via aromatisation/PAH growth and loss of hydrogen towards ordered carbon, consistent with the possible mechanisms discussed in Section 1.2.2.3 which likely include HACA, Diels-Alder reactions, and/or methyl addition cyclisation (MAC) (56)

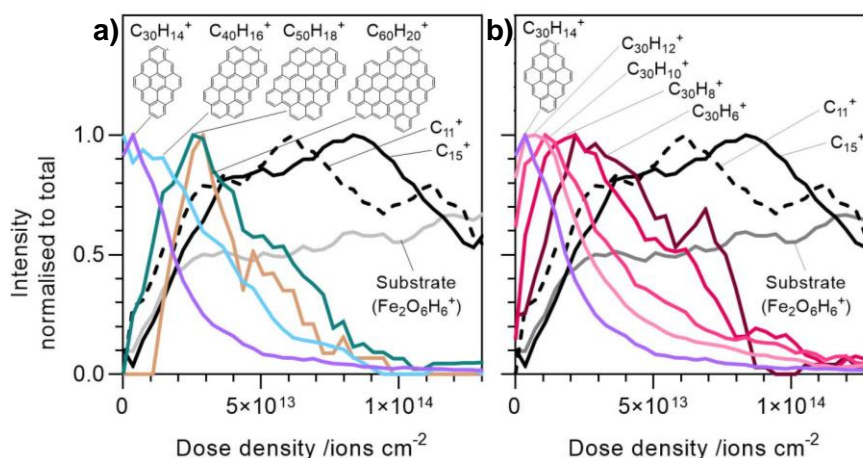


Figure 3.6: Needle 8 hydrocarbon OrbiSIMS ion depth profiles for a) a range of PAH sizes, and b) ions of the same C number with decreasing H number.

### 3.2.3.2 Polyaromatic Lateral Distributions from OrbiSIMS Imaging

Alongside depth profiling, SIMS can also provide lateral information via imaging by rastering the beam across the sample and recording data for each pixel. As discussed in Section 1.3.3.2, previous IDID research has used ToF-SIMS to provide such chemical mapping, however the species observed were only small fragments or elemental ions.

OrbiSIMS chemical images are shown in Figure 3.6 for Needle 8, the sample with the largest mass and highest intensity polyaromatic ions. The smaller PAH ( $C_{24}H_{12}^+$ , Figure 3.6a) and N-PAC ( $C_{19}H_{12}N^+$ , Figure 3.6d) ions, as well as the carbonaceous ( $C_{11}^+$ , Figure 3.6f) ion, show widespread coverage of the deposit, indicating that they are a ubiquitous deposit component rather than a localised contaminant. This is consistent with generic deposit material forming from the fuel and precipitating as it passes over the needle. Similarly, the inorganic salt ions for calcium hydroxide ( $Ca_2O_3H_3^+$ , Figure 3.6g) and calcium-zinc oxide ( $CaZnO^+$ , Figure 3.6h) are also widespread, indicating they too are a ubiquitous deposit component and therefore an extensive fuel contaminant. These ions have high intensities likely due to their pre-ionised nature. The lateral distribution for larger PAHs cannot be confidently deciphered due to their intensities being too low to achieve sufficient image contrast. These deposit components will be seen in more depth in Section 3.2.5 and Section 3.2.4.3.2 respectively. In contrast, the substrate ion ( $Fe_2O_6H_6^+$ , Figure 3.6i) is localised, likely due to its area of high intensity being a region where the substrate is more exposed, or where there has been a localised deposition of wear metals from the fuel.

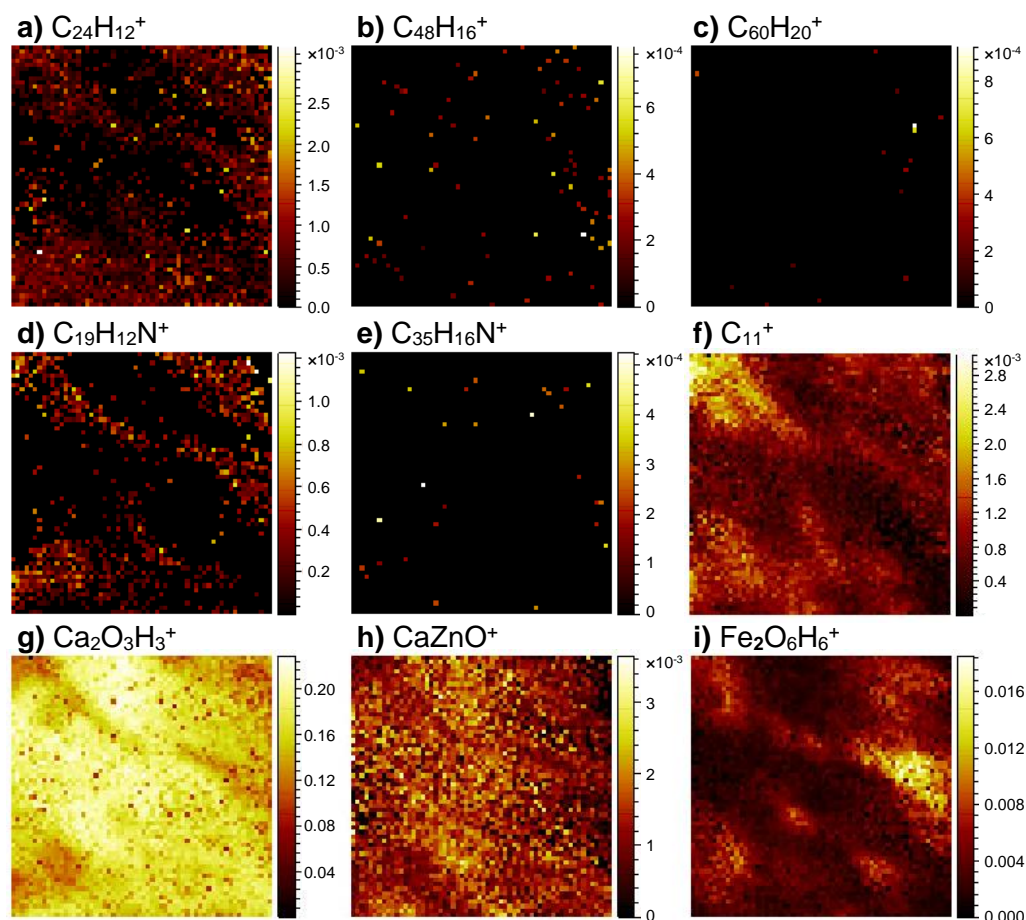


Figure 3.7: OrbiSIMS chemical images (two scans) for the IDID with the most intense and largest mass polyaromatics (Needle 8) at position 4, normalised to total ion image.

300×300  $\mu\text{m}$  images for inorganic salt, substrate, PAH, N-PAC and carbonaceous OrbiSIMS ions.

Thus, OrbiSIMS demonstrates widespread formation of carbonaceous material from the fuel proceeding via polyaromatic and semi-fullerene chemistries. A mechanism of PAH growth and hydrogen abstraction is shown through depth profiling, where older, lower depth deposit material is further along this process. The degree of carbonisation varies by sample, likely depending on a number of important factors that can drive carbonisation such as temperature and the nature of the needle substrate.

### 3.2.4 Evidence of Fuel and Lubricant Additive Chemistries in IDIDs by OrbiSIMS and XPS

Diesel additives and lubricant additives have been noted in a range of IDID studies, being detected in mass spectrometry studies including ToF-SIMS, as discussed in Section 1.3.3. Knowledge of the responsible additives and their

details and known mechanisms were discussed in Section 1.2.2.6 and lubricant oil in Section 1.2.2.4. OrbiSIMS ions were seen in all samples that appear to correspond to additive chemistries of both diesel fuel and engine lubricant oil (28, 80).

### 3.2.4.1 Polyisobutylene Succinimide by OrbiSIMS

The literature on PIBSI, a detergent DCA, was discussed in Section 1.2.2.6.1, describing its transformation to amide species which can precipitate to form deposits. However, identification of the specific amide species and PIB distributions of real-world IDIDs was not achieved. LMW PIBSI, associated with poorer quality DCA, is reported as the type of this additive that is responsible for promoting IDID formation due to the lower solubility of its shorter PIB chains.

#### 3.2.4.1.1 Succinimide ions

Small succinimide OrbiSIMS ions are in many samples and are suggested to represent the succinimide head group of PIBSI. The normalised spectra for some of these ions are shown for Needle 6, 7, 10 and 12 in Figure 3.8. The smaller mass ion ( $\text{C}_4\text{H}_2\text{NO}_2^-$ ) is the most intense and has its highest intensity in Needle 7. The succinimide with an 8-carbon alkyl chain containing one PIB unit ( $\text{C}_{12}\text{H}_{16}\text{NO}_2^-$ ) has a similar trend in intensity across the four samples as the smaller mass ion ( $\text{C}_4\text{H}_2\text{NO}_2^-$ ), indicating that it is related and likely represents part of a low MW PIBSI with its small alkyl chain. Needle 12 had larger PIBSI ions, shown for a similar ion in positive polarity with five PIB units ( $\text{C}_{31}\text{H}_{56}\text{NO}_2^+$ ), suggesting a presence of a higher MW PIBSI in this sample. Comparing Needle 6 with the GDI tip and diesel filter, the low mass succinimide ion ( $\text{C}_4\text{H}_2\text{NO}_2^-$ ) had a higher intensity in the IDID (170). This is consistent with most reports of PIBSI-type deposits being in the injector interior as discussed in Section 1.2.2.6.1.

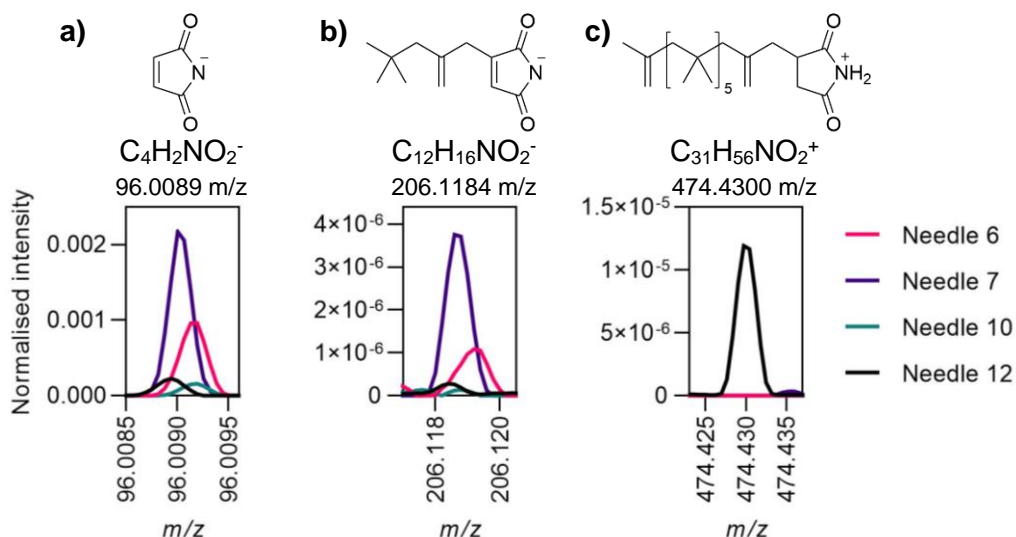


Figure 3.8: Succinimide OrbiSIMS ion normalised spectra for IDID samples, with varying sizes of alkyl groups. a) Succinimide head ion. b) Succinimide with 1 PIB unit ion. c) Derivative ion of succinimide with 6 PIB units.

In XPS elemental quantification, nitrogen is present in Needles 6, 7 and 10 (3.6 at.%, 6.7 at.% and 5.5 at.% respectively). No nitrogen was detected in Needle 12, likely due to the high MW PIB section being dominant, resulting in a nitrogen concentration below the XPS detection limit. No ions with formulae consistent with amides that would be expected to form from PIBSI's succinimides or amines were detected in Needles 6, 7 or 10, indicating that these samples had not undergone the characteristic transformations with acids described in Section 1.2.2.6.1. Needle 12 had more unique succinimide and amide chemistries that will be discussed in the next section.

#### 3.2.4.1.2 Very High MW PIBSI Species in Needle 12

Needle 12's OrbiSIMS positive polarity data showed much more complex PIBSI-type chemistry than Needles 6, 7 and 10, with several series of unique ions. To summarise the main homologous series of ions which differ by units of  $\text{CH}_2$ , a Kendrick Mass Defect (KMD) plot using base  $\text{CH}_2$  as described in Section 2.3.3.2.3 is shown in Figure 3.9 for N and O-containing ions calculated in Needle 12. In the KMD plot, these series appear in horizontal lines (176). The key series which reach the highest masses are labelled A-K and these are summarised in Table 3.4. Additional analysis was performed on this sample using a mass range of 400-6000  $m/z$  to identify the highest mass ion of each



series; the largest ions for each key series are shown in Table 3.4, finding that series J contains the largest structure (2936 amu,  $C_{201}^{13}C_2H_{403}N_2O_4^+$ ), which is suggested to have an alkyl chain containing 47 PIB units. LMW PIBSI have average MWs around 600-800 Da while a HMW PIBSI used in DCAs has around 3200 Da (84). Therefore, the mass of this PIBSI-derived species is proposed to be consistent with HMW PIBSI.

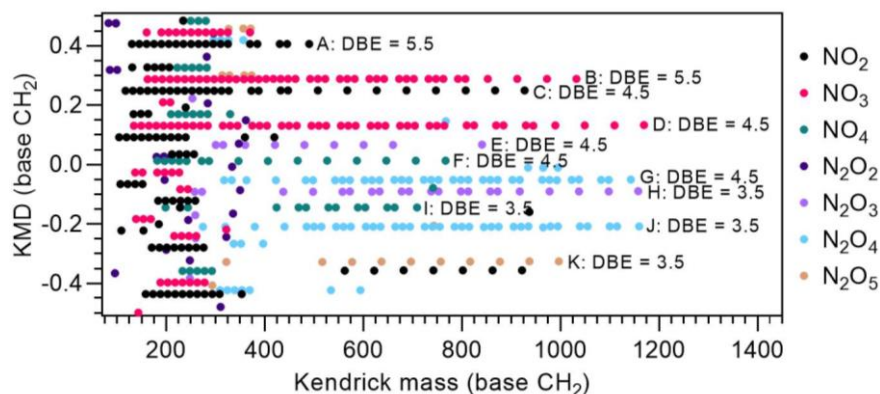


Figure 3.9: Kendrick mass defect (base  $CH_2$ ) for Needle 12 position 3 depth profile (75-1125  $m/z$  range) filtered for organic ions of minimum normalised intensity  $3.3E-6$ , N1-2, O2-5, DBE < 6.

Table 3.4: Homologous PIBSI-related ion series with highest intensity and mass ions from KMD.

ID	Class (DBE)	Highest intensity ion			Highest mass ion	
		$m/z$	Assignment	Peak area (norm)	$m/z$	Assignment
C	$NO_2$ (4.5)	110.0236	$C_5H_4NO_2^+$	$4.0 \times 10^{-2}$	1876.9971	$C_{130}^{13}CH_{256}NO_2^+$
A	$NO_2$ (5.5)	178.0859	$C_{10}H_{12}NO_2^+$	$8.9 \times 10^{-4}$	1131.1488	$C_{78}H_{148}NO_2^+$
D	$NO_3$ (4.5)	196.0965	$C_{10}H_{14}NO_3^+$	$3.3 \times 10^{-2}$	2552.7308	$C_{176}^{13}C_2H_{350}NO_3^+$
B	$NO_3$ (5.5)	236.1279	$C_{13}H_{18}NO_3^+$	$2.7 \times 10^{-3}$	1806.8841	$C_{124}^{13}CH_{242}NO_3^+$
I	$NO_4$ (3.5)	214.1071	$C_{10}H_{16}NO_4^+$	$2.5 \times 10^{-5}$	1223.2339	$C_{82}H_{160}NO_4^+$
F	$NO_4$ (4.5)	198.0757	$C_9H_{12}NO_4^+$	$3.8 \times 10^{-4}$	870.8260	$C_{57}H_{108}NO_4^+$
H	$N_2O_3$ (3.5)	241.1544	$C_{12}H_{21}N_2O_3^+$	$1.3 \times 10^{-3}$	2484.6620	$C_{171}^{13}CH_{341}N_2O_3^+$
E	$N_2O_3$ (4.5)	295.2014	$C_{16}H_{27}N_2O_3^+$	$7.6 \times 10^{-6}$	1585.6449	$C_{107}^{13}CH_{211}N_2O_3^+$
J	$N_2O_4$ (3.5)	635.5714	$C_{39}H_{75}N_2O_4^+$	$2.8 \times 10^{-3}$	2936.1529	$C_{201}^{13}C_2H_{403}N_2O_4^+$
G	$N_2O_4$ (4.5)	329.2275	$C_{18}H_{31}N_2O_4^+$	$1.3 \times 10^{-4}$	1980.0574	$C_{134}^{13}CH_{265}N_2O_4^+$
K	$N_2O_5$ (3.5)	651.5663	$C_{39}H_{75}N_2O_5^+$	$1.5 \times 10^{-5}$	1942.0102	$C_{130}^{13}CH_{259}N_2O_5^+$



While Needles 6, 7 and 10 showed no evidence of amide structures, many ion series in Needle 12 have formulae consistent with amides. Structures are suggested in Figure 3.10 for the highest mass ions for each of the eight series that reach the highest masses. Most of the suggested structures are amides that could form from hydrolytic ring-opening of the succinimide, including for the highest mass ion (Series J). Tandem MS (MS/MS) of  $C_{30}H_{54}NO_3^+$ , a high intensity ion from series B, supports its assignment based on likely fragmentation shown in Figure 3.11. MS/MS has never been performed on IDID samples in the past due to the limitations of older SIMS and mass spectrometry instrumentation; here, MS/MS was found to be crucial in many cases such as in assigning these large succinimide-type ions and helps elucidate the chemical structure of IDIDs. MS/MS of other ions is shown in Appendix 1.1.4.1, tentatively supporting their assignments. Alongside amides, there are also formulae consistent with unopened succinimides (C in Figure 3.10) which also reach much higher masses than in the other IDIDs.

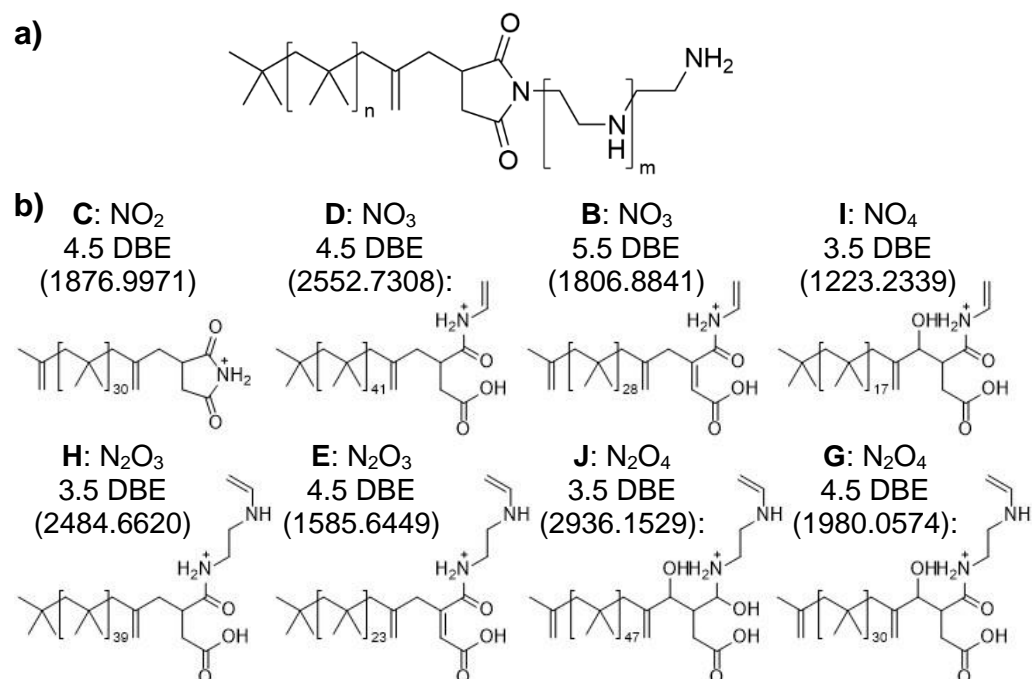


Figure 3.10: a) Structure of PIBSI. b) Suggested structures for the highest mass ions of key homologous ion series (C, D, B, I, H, E, J and G) from the KMD (base  $CH_2$ ) analysis.

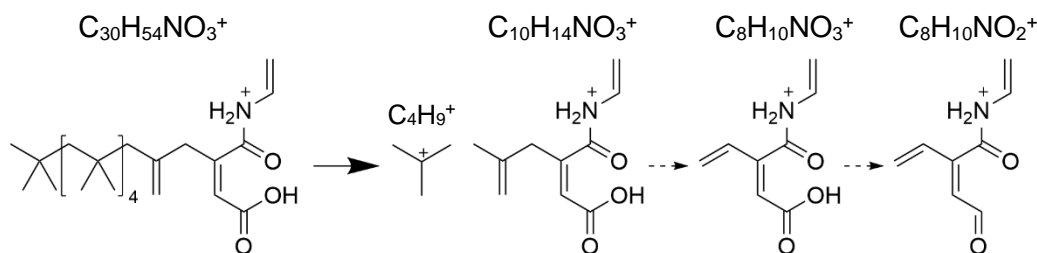


Figure 3.11: Fragmentation ions with suggested structures from an MS/MS experiment of a high intensity ion from series D ( $C_{29}H_{50}NO_3^+$ ).

FTIR has been a common technique to confirm amide and/or imide presence in such deposits but is limited to identification of only functional groups (41, 99). Previous ToF-SIMS analysis was able to identify the PIB chain's characteristic saturated alkyl ions and ions indicative of amides or succinimides, however analysis of a LMW PIBSI standard sample was required to validate results (39, 40). The chemical specificity of OrbiSIMS analysis, and the ability to identify the structure and the highest MW PIBSI species in the sample has not been seen in prior IDID analysis work. MS/MS is used to elucidate the chemical structures present, validating chemical assignments. The identification of a likely hydrolysed succinimide could explain how PIBSI succinimide ring-openings occur, a transformation that has been suggested in previous studies but with the process not explored (60). Knowledge of the masses of PIBSI can provide insight into its origin and how this deposit can be prevented. The understanding of the effect of the MW of PIBSI was discussed in Section 1.2.2.6.1. In Needle 12, the PIBSI species are clearly too high mass to be LMW PIBSI however they are also beyond the mass of DCA-associated PIBSIs. Thus, these species are suggested to originate from a lubricant detergent source rather than DCA and implicate PIBSIs of too high MW as well as those of too low MW in promoting IDID formation.

#### 3.2.4.2 DDSA and Carboxylates

DDSA is a dicarboxylic acid that is used as a corrosion inhibitor to protect fuel transportation pipelines (28). It has been implicated, alongside other carboxylic acids, as a commercial diesel component that is affected by sodium

contamination, forming sodium carboxylate type IDIDs as described in Section 1.2.2.4.1 (61).

Sodium DDS chemistry was most prominent in Needle 13, the deposit of which was white in appearance, consistent with soap-type deposits described in Section 1.2.2.4.1. Its OrbiSIMS spectra were dominated by Na-DDS and related ions, indicating extensive soap deposition. In the spectrum from position 3 (Figure 3.12a), the three most intense ions appear to all be Na-DDS related: sodium carbonate ( $\text{Na}_3\text{CO}_3^+$ ), a small sodium carboxylate ( $\text{C}_3\text{H}_3\text{O}_2\text{Na}_2^+$ ), and Na-DDS ( $\text{C}_{16}\text{H}_{26}\text{O}_4\text{Na}_3^+$ ). There are much higher mass ions present, which are clusters of Na-DDS featuring two DDS molecules ( $\text{C}_{32}\text{H}_{52}\text{O}_8\text{Na}_5^+$ ) or three ( $\text{C}_{48}\text{H}_{78}\text{O}_{12}\text{Na}_7^+$ ). Using MS/MS, the cluster fragments into the singular Na-DDS ion (Figure 3.12b, Appendix Table A5) which in turn fragments into the small sodium carboxylate ion which is prominent in the original spectrum shown in Figure 3.12a ( $\text{C}_3\text{H}_3\text{O}_2\text{Na}_2^+$ ). Additional MS/MS of DDSA using high collision energy (NCE = 150) did not produce sodium carbonate, so this ion is unlikely to be a SIMS fragment and instead may originate from the same sodium contamination or from decomposition of DDSA within the deposit.

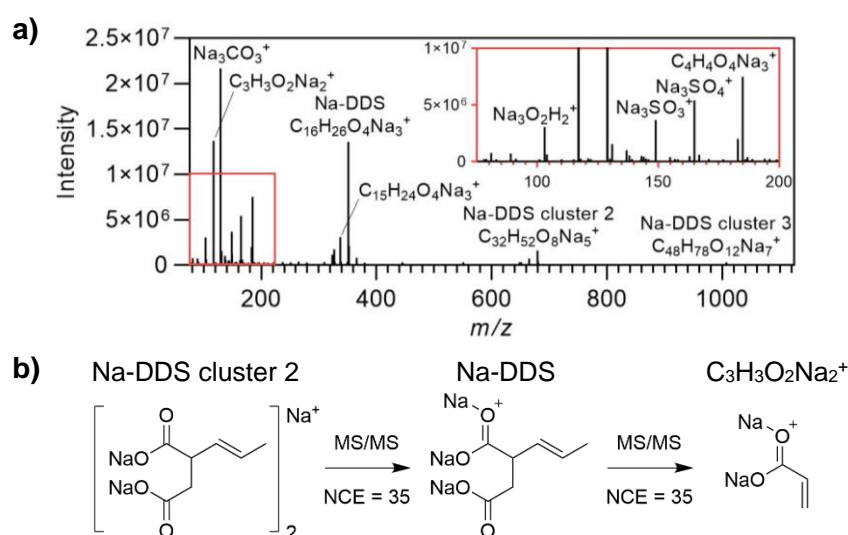


Figure 3.12: Sodium-DDS related OrbiSIMS data. a) OrbiSIMS spectrum from a central position of Needle 13, b) MS/MS fragmentation schematic for Na-DDS ions in Needle 14.

Needle 13 originated from an engine test fuelled with B7 (a common biodiesel blend level in commercial fuel) using a commercial additive package. It can be suggested that the biodiesel contributed sodium to the system, as it is known to be a source of sodium from the transesterification catalyst (as discussed in Section 1.2.2.5.1). This could cause soap formation with the DDSA corrosion inhibitor additive. The Na-DDS ion, alongside sodium carbonate, was also found with much lower intensity in the field samples Needles 6 and 7. Figure 3.13a shows normalised spectra for the Na-DDS ion ( $C_{16}H_{26}O_4Na_3^+$ ) and sodium carbonate ( $Na_3CO_3^+$ ) ion which Needle 13 dominates. Comparing the intensities, Needle 6 has a significantly lower intensity than Needle 7 for the Na-DDS ion, reflected in its C 1s XP spectra components (Figure 3.13b), in which it has the lowest carboxyl while Needle 13 has the highest, in line with its dominant Na-DDS ion. Needle 6 also has a smaller intensity for  $Na_3CO_3^+$ , however elemental quantification with XPS finds that it has a larger sodium concentration than Needle 7 therefore Needle 6 in fact has more sodium but likely in other forms than Na-DDS and sodium carbonate. According to the XPS data, Needle 13 has the largest sodium concentration as well as carboxyl concentration, thereby confirming this sample to have the most extensive sodium and sodium soap contamination and implicating biodiesel as a potential major factor in these types of deposits. Needles 9 and 11 also have high sodium concentration by XPS with Needle 9 in fact having a larger sodium concentration than Needles 6 and 7, indicative of the other sodium chemistries found in IDIDs.

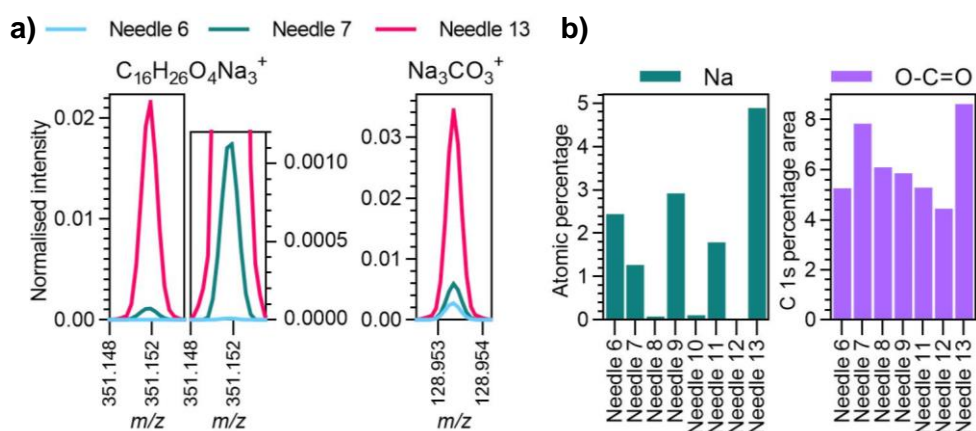


Figure 3.13: DDSA OrbiSIMS and XPS data. a) Normalised spectra for Na-DDS and Na carbonate OrbiSIMS ions. b) XPS data for sodium atomic concentration and high-resolution C 1s spectra carboxyl component percentage area.

Other sodium carboxylate species exist in Needles 6, 7 and 13. Both Needles 6 and 7 also contain HDSA ( $\text{C}_{20}\text{H}_{34}\text{O}_4\text{Na}_3^+$ ), used as another corrosion inhibitor, though with significantly reduced intensity. Needle 13 has other sodium carboxylate species, including palmitate ( $\text{C}_{16}\text{H}_{31}\text{O}_2\text{Na}_2^+$ ) and stearate ( $\text{C}_{18}\text{H}_{35}\text{O}_2\text{Na}_2^+$ ), also with lower intensity than Na-DDS (Table 3.5). These species have been suggested by Schwab *et al.* to also contribute to soap deposits (63). Needle 8, which showed very little sodium by XPS (<0.1 at.%) but significant calcium (0.9 at.%) (Appendix Figure A5a), lacks sodium carboxylates but contains calcium palmitate ( $\text{C}_{16}\text{H}_{31}\text{O}_2\text{Ca}^+$ ) and stearate ( $\text{C}_{18}\text{H}_{35}\text{O}_2\text{Ca}^+$ ). As discussed in Section 1.2.2.4.2, calcium can also form soaps which have been noted in IDIDs, though fewer studies have focused on calcium than sodium (38, 64). Free stearate ( $\text{C}_{18}\text{H}_{35}\text{O}_2^-$ ) and palmitate ( $\text{C}_{16}\text{H}_{31}\text{O}_2^-$ ) also appear in all samples' negative polarity data, with the highest intensities in the same samples showing the highest intensities of the positive polarity ions (Needle 8 and 13). These results show that both sodium and calcium can form problematic soaps, the speciation of which can be achieved with OrbiSIMS to identify all carboxylates.

Table 3.5: OrbiSIMS data for non-DDS carboxylate secondary ions.

Assignment	m/z	Needle 13	Needle 6	Needle 7	Needle 8
$\text{C}_{16}\text{H}_{31}\text{O}_2\text{Na}_2^+$	301.2112	$6.3 \times 10^{-4}$	N/A	N/A	N/A
$\text{C}_{18}\text{H}_{35}\text{O}_2\text{Na}_2^+$	329.2424	$6.8 \times 10^{-4}$	N/A	$9.7 \times 10^{-5}$	N/A
$\text{C}_{15}\text{H}_{25}\text{O}_2\text{Na}_2^+$	283.1642	$1.2 \times 10^{-3}$	N/A	N/A	N/A
$\text{C}_{16}\text{H}_{31}\text{O}_2\text{Ca}^+$	295.1941	$2.7 \times 10^{-5}$	N/A	N/A	$4.0 \times 10^{-5}$
$\text{C}_{18}\text{H}_{35}\text{O}_2\text{Ca}^+$	323.2255	$6.5 \times 10^{-5}$	N/A	N/A	$1.5 \times 10^{-4}$
$\text{C}_{16}\text{H}_{31}\text{O}_2^-$	255.2337	$2.2 \times 10^{-3}$	$1.6 \times 10^{-5}$	$2.4 \times 10^{-4}$	$3.9 \times 10^{-3}$
$\text{C}_{18}\text{H}_{35}\text{O}_2^-$	283.265	$2.7 \times 10^{-3}$	$3.8 \times 10^{-5}$	$7.6 \times 10^{-4}$	$5.3 \times 10^{-3}$

The characterisation of sodium DDS type deposits by OrbiSIMS shows the paradigm shift of OrbiSIMS compared to ToF-SIMS. Previous work applied ToF-SIMS to Needles 6, 7 and 8 but no carboxylate chemistry was identified (128). Other techniques (primarily FTIR) have proved useful in identifying sodium carboxylate deposits based on identifying the functional group,

however not with the certainty and specificity seen with OrbiSIMS, where the exact deposited species present can be probed.

### 3.2.4.3 Lubricant Additive Chemistries in IDIDs

Lubricant oil is applied to engine parts to ensure good engine operation and consists of a base oil with lubricant additives (80, 177). There are multiple components of lubricant oils that it is suspected can contribute to IDID formation if contamination of FIE occurs, as discussed in Section 1.2.2.4.4.

#### 3.2.4.3.1 Alkylbenzene Sulfonates in IDIDs by OrbiSIMS

Alkylbenzene sulfonates (ABS) are detergent additives used in lubricant oils to solubilise deposit precursors and are identified as present in all IDID samples by OrbiSIMS with intensities shown for multiple positions of Needles 6-9 in Figure 3.14a. This type of chemistry was confirmed with MS/MS (Appendix Figure A4). Similar chemistry has been identified in previous ToF-SIMS analysis of lubricant oil on steel surfaces and of an IDID (59, 178). The GDI tip's OrbiSIMS data also possessed ABS ions, exhibiting much larger mass ABS structures (to  $C_{74}H_{141}SO_3^-$ ) than the IDIDs, beyond the mass of the native compound added to lubricant oils ( $C_{18}H_{29}SO_3^-$ ). This was attributed again to the higher temperature experienced by the external injector deposit, which could drive combinations with saturated hydrocarbons in the fuel to extend the alkyl chain via free-radical mechanisms (179). Such reactions would be promoted by high temperature and hence less likely to occur in the milder conditions within the diesel injector of Needle 6, where the identified species is that of the native additive itself ( $C_{18}H_{29}SO_3^-$ ) (80, 170).

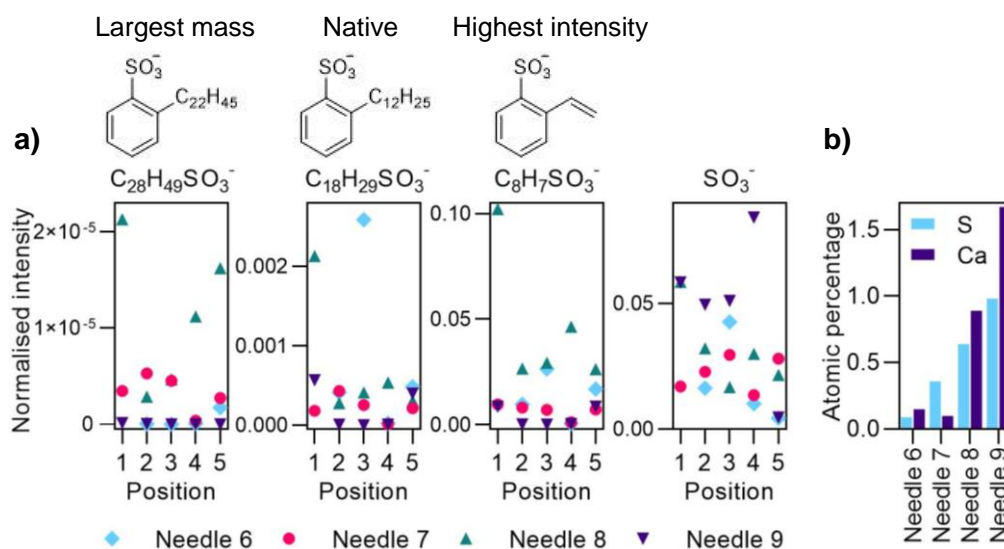


Figure 3.14: ABS data for Needles 6-9. a) ABS OrbiSIMS secondary ions normalised intensities for multiple positions (note Needle 6 only has four positions, labelled 2-5), b) S and Ca XPS atomic concentrations

Figure 3.14a shows the normalised intensities in Needles 6-9 for the largest mass ABS observed ( $C_{28}H_{49}SO_3^-$ ) which likely forms within the injector system, the native species ion ( $C_{18}H_{29}SO_3^-$ ), the most intense ABS ion ( $C_8H_7SO_3^-$ ), and the sulfite ion ( $SO_3^-$ ). All samples have significant ABS intensities and are therefore likely contaminated with lubricant oil, with Needle 8 likely being the most as it shows the highest normalised intensities for most ABS ions. Needle 8 also generally has the highest intensities of the largest species, with Needle 7 comparable at some positions, indicating that Needles 8 and 7 have experienced the most combination of ABS with alkanes in radical mechanisms and hence likely reached higher temperatures (170).

XPS atomic quantification for sulfur and for calcium for Needles 6-9 (Figure 3.14b) shows that all samples have detectable levels of both elements, supporting the presence of lubricant oil. In lubricant oil, calcium generally accompanies the ABS additives in over-based detergent particles (65, 80, 180). Other sulfur-containing chemistry is part of all of these samples (discussed more in Section 3.2.5), therefore the small concentrations of sulfur show that ABS compounds can only be a small component of the deposits. Their high intensity in OrbiSIMS is likely a result of high sensitivity due to being a pre-ionised molecule; pre-ionisation is a known very efficient mechanism of ion

generation in SIMS (121). Needle 9 has the highest sulfur and calcium concentrations despite lower ABS intensities, indicating it has comparatively more of other sulfur-containing compounds.

### 3.2.4.3.2 Zinc Chemistry in IDIDs by OrbiSIMS and XPS

Zinc is known to contribute to IDID formation and is present in lubricant oil in the additive zinc dialkyldithenophosphate (ZDDP), discussed in Sections 1.2.2.4.3 and 1.2.2.4.4 respectively. Using both OrbiSIMS and XPS, evidence of zinc was found only in Needle 8 in which it had a low concentration of 0.5 at.%. A summary of zinc ions are shown in Table 3.6 for Needle 8 positions 1-5. These are salts with a range of anions (hydroxide, sulfate, sulfide, cyanide, chloride), likely indicating a range of accompanying contaminants; the prevalence of sulfur alongside this zinc further supports a lubricant oil source. Though there is little trend along the needle in these salts, it is notable that position 1 generally has the lowest or near the lowest intensity for all zinc ions. This demonstrates that zinc is part of the deposit rather than the needle substrate. Alongside the ABS and calcium, this strongly evidences a pervasive lubricant oil contamination that likely resulted in the formation of this IDID.

Table 3.6: Zinc-containing OrbiSIMS secondary ions (all deviations <2.5 ppm) for multiple positions of Needle 8.

Assignment	Mass	1	2	3	4	5
$\text{ZnO}_3\text{H}_3^-$	114.9382	2.25E-05	3.51E-05	2.06E-04	3.91E-04	7.78E-05
$\text{ZnSO}_5\text{H}^-$	176.8844	3.20E-05	2.87E-04	6.07E-05	7.60E-05	3.11E-04
$\text{ZnSOH}^-$	112.9048	1.55E-05	5.82E-06	1.33E-05	1.00E-05	N/A
$\text{ZnSCN}^-$	121.9050	1.20E-05	2.40E-05	3.05E-05	1.28E-04	5.72E-05
$\text{ZnSO}_4\text{Cl}^-$	194.8507	N/A	3.82E-05	4.91E-05	N/A	N/A
$\text{ZnCl}_3^-$	168.8357	N/A	N/A	1.09E-03	N/A	N/A

### 3.2.5 Inorganic Salt Chemistries in IDIDs by OrbiSIMS and XPS

A wide range of inorganic salt chemistries are found in all IDID samples analysed in this work; calcium and sodium salts were seen in the wide spectra of Needle 8 and Needle 6 respectively in Figure 3.2. Previous studies have identified many types of inorganic IDID and their components, discussed



throughout Section 1.2.2, using techniques discussed in Section 1.3. ToF-SIMS provided the most sensitive measurements of inorganic content, including small molecular species, while XPS has been used for their quantification (40, 47, 128). Here, the application of OrbiSIMS with XPS support allows further developments in inorganic IDID analysis, identifying key unambiguous inorganic chemistries with greater detail and quantitative accuracy than ToF-SIMS could afford.

#### 3.2.5.1 Sodium and Calcium Inorganic Salts

Of the known inorganic IDID components, sodium and calcium have received the most attention in the literature. In the inorganic OrbiSIMS ions in the IDID data of the current work, sodium and calcium's salts were the most intense. A range of these ions' normalised intensities are shown in Figure 3.15a. Needles 6, 7, 9, and 14 are characterised by high intensities of sodium-containing ions; all contain high intensities of sodium sulfate ions which may originate from fuel contamination from refinery processes (65). Of these samples, all that XPS spectra collected show the presence of sulfur (Figure 3.15b). Needle 6 has very intense sodium chlorides, validated by XPS which shows sodium and chlorine concentrations of 1.5 at.% and 0.6 at.% at the deposit surface and 15.8 at.% and 6.7 at.% after 10 minutes of etching with an  $\text{Ar}_{500}^{+}$  GCIB. This significant sodium chloride contamination likely originates from a seawater contamination such as from barge transportation (65). The range of other sodium salts, including cyanide, cyanate, hydroxide, carbonate and sulfide, evidences the wide range of chemistries present in the system during IDID formation. They may have diverse sources, including storage tank bottoms, refinery polishing and biodiesel, as discussed in Section 1.2.2.4.

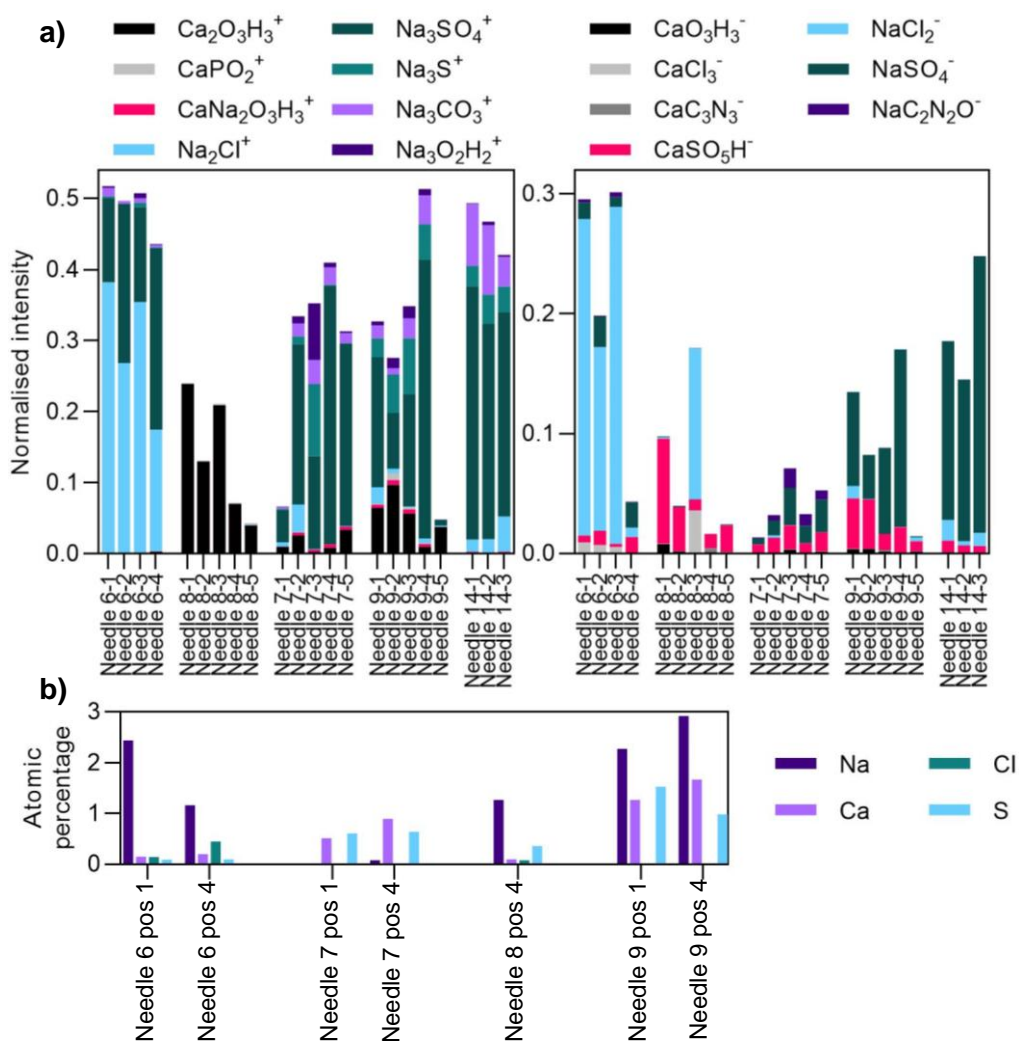


Figure 3.15: Inorganic salt material in IDID samples at multiple positions from low on the needle shaft (position 1) to the end of the needle, of Needles 6, 8, 7, 9, 14. a) Positive polarity data. b) Negative polarity data.

According to the XPS data, Needles 8 and 9 both contain high concentrations of calcium (Figure 3.15b), as noted in Section 3.2.4.3.1. Needle 9's sodium concentration is greater than its calcium, giving it a large deposition of both elements. The dominant calcium ions in Needle 8 are in the form of hydroxide, phosphate ( $\text{PO}_2^-$ ) and sulfate with smaller amounts of chloride and cyanide. These chemistries are again consistent with the lubricant components, though XPS finds phosphorus to be below the detection limit and therefore in very small concentrations. As with sodium inorganic salts, Figure 3.15a reveals a range of other anions in the calcium salts of Needles 6-9, including chloride and cyanide.

### 3.2.6 Characterisation of Marine Injector Deposit Sample

Following the establishment of the OrbiSIMS and XPS method for detailed chemistries of IDIDs, application of the method was extended to a marine injector deposit sample associated with an event referred to in the media as “the Houston problem”, which was a series of severe marine engine failures occurring in vessels that were fuelled using bunker oil from the Houston area (181). The operational issues that led to these failures included injector failure due to deposits as well as larger scale sludge formation, blocked filters and seized engine pumps and affected large vessels, for example a 13,000-ton cargo ship. These severe issues continued for a reported 9 weeks in 2018, with 2% of fuel delivered to Houston reported to be contaminated (181). As the consequences of marine engine failure for such large commercial vessels are so severe, endangering the ship’s crew as well as nearby ships and incurring significant financial damages, understanding of the deposit composition is of high importance. Analysis of an internal injector part (a plunger) is shown in this section using the same methods as the IDID samples, as well as a MALDI-MS approach, the first application of these techniques to a marine deposit.

#### 3.2.6.1 Appearance and Morphology by SEM

The marine sample analysed in this work was a plunger, an internal piece of a fuel injector. The movement of a plunger up and down controls the introduction of fuel into the injector and the pressurisation and injection of atomised fuel through the injector nozzle (182). This deposit has a dark and dense appearance with green-coloured speckling. In contrast to IDIDs, it has a smoother appearance rather than a grainy porous texture (Figure 3.16d).

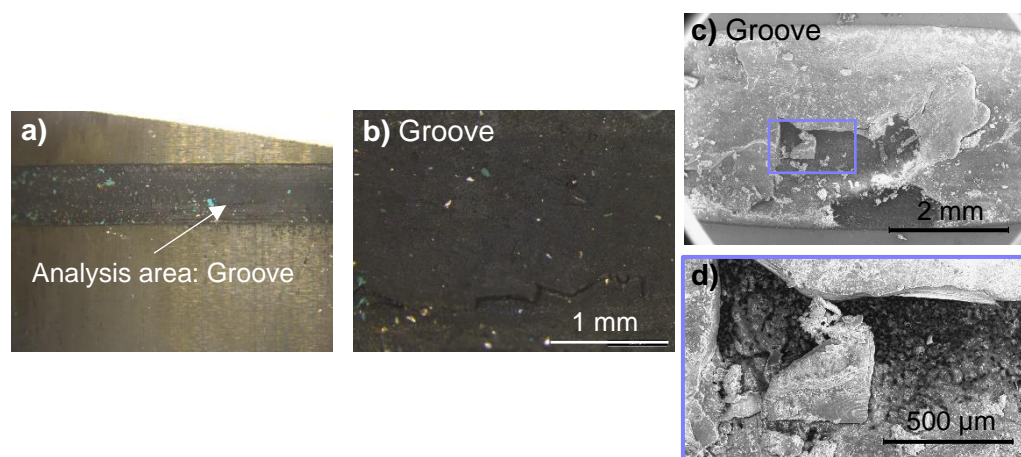


Figure 3.16: Optical microscope images of marine injector plunger sample (Marine 1). a) View of metal surface and heavily deposited groove (7.8× zoom) with general analysis position marked. b) Zoomed in (51.1×) view of groove position. c) SEM image (36× zoom) of groove. d) SEM image (154× zoom) of groove.

### 3.2.6.2 Phenols and Salicylates from OrbiSIMS

Forensic analysis of the fuels responsible for the Houston-related engine failures found a unique presence of phenolic compounds that were suspected to have played a role in the issues (183). Both OrbiSIMS and XPS showed evidence of this chemistry, to a greater extent than IDID samples, with salicylates also apparent. As shown in Figure 3.17a, the phenolate ion ( $\text{C}_6\text{H}_5\text{O}^-$ ) has much greater intensity in the Marine 1 sample which is likely a fragment of larger phenolic structures. In the reported fuels forensic analysis, the specific compound 4-cumylphenol was identified with the highest concentration in the and was thought to be the primary contaminant responsible. This has many industrial uses including in the manufacture of epoxy resins and as an emulsifier in pesticides (183). In the OrbiSIMS data, an ion consistent with 4-cumylphenol ( $\text{C}_{15}\text{H}_{15}\text{O}^-$ ) was found, however with very low intensity which was equal to Needle 12's (Figure 3.17a). This species could not be confirmed by MS/MS due to its low intensity, however, being much less intense than other phenolate ions it is suggested that it only represents a small concentration and hence likely played less of a role than other investigations indicated. High resolution C 1s XP spectra curve fitting showed a higher C-O component, which could include phenols, in Marine 1 than in any IDID sample (Figure 3.17b), indicating a larger quantity of this type of bonding and therefore likely a larger concentration of the phenol structures.

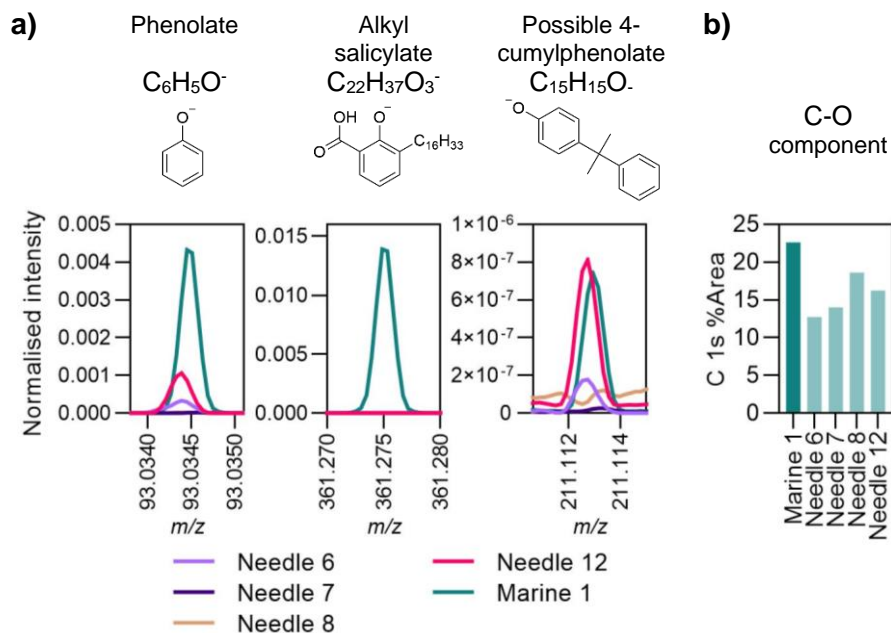


Figure 3.17: a) Phenolate and salicylate OrbiSIMS normalised peaks in Marine 1 and IDID samples. b) High-resolution XPS C 1s C-O components for the same samples.

Alkyl salicylates (Figure 3.17a), used as lubricant oil detergent additives with calcium similarly to ABS compounds, had very high intensity in Marine 1, likely indicating a significant lubricant oil contamination (80). Investigation of a high intensity, high mass series of ions using MS/MS found fragmentation relationships between them and the salicylates. This is shown for the most intense of the series (assigned  $C_{49}H_{87}O_6^-$ ) in Table 3.7, which fragments via a large oxygen-containing neutral loss into the salicylate species, as well as the alkylphenol via further loss of  $CO_2$ . MS/MS with a higher normalised collision energy (NCE = 60) also produced a small alkylphenol ( $C_8H_7O^-$ ), indicating fragmentation of these very high mass ions as a source of the small phenolate ions in the spectrum. MS/MS also reveals that the larger alkylphenol ( $C_{22}H_{37}O^-$ ) fragments into the smaller phenolates such as  $C_6H_5O^-$  and  $C_8H_7O^-$  (Appendix Section 1.1.6.1). Alongside the O6 series were some O7 ions; although they had exhibited inadequate ion intensity for successful MS/MS, their suggested formulae were related to the O6 series by a loss of  $H_2$  and gain of O, suggesting a possible oxidation of the O6 series.

Table 3.7: MS/MS results for high mass O6 series ion. NCE = 40.

Mass	Assignment	DBE	Intensity	Neutral loss
<b>771.6511</b>	<b>C<sub>49</sub>H<sub>87</sub>O<sub>6</sub><sup>-</sup></b>	<b>6.5</b>	<b>N/A</b>	<b>Parent</b>
361.2748	C <sub>23</sub> H <sub>37</sub> O <sub>3</sub> <sup>-</sup>	5.5	4.70E4	C <sub>26</sub> H <sub>50</sub> O <sub>3</sub>
317.2849	C <sub>22</sub> H <sub>37</sub> O <sup>-</sup>	4.5	3.72E4	C <sub>27</sub> H <sub>50</sub> O <sub>5</sub>
119.0502 (NCE 60)	C <sub>8</sub> H <sub>7</sub> O <sup>-</sup>	4.5	8.53E3	C <sub>41</sub> H <sub>80</sub> O <sub>5</sub>

The salicylate, O6 and O7 series are shown in Table 3.8. The relationships between the ions can be seen, where the salicylates are the most numerous and reach the highest intensities. The most intense salicylates are matched in the O6 series with the same intensity pattern, as well as in the few O7 ions. This data strongly suggests that these ions are related, however from this data the structures of the O6 and O7 series are unknown; the large neutral losses in their MS/MS analysis are difficult to assign and further work would be required to elucidate them.

Table 3.8: Salicylate, O6 and O7 homologous series of OrbiSIMS ions, with colourmap for each series' intensities.

Salicylates		O6 series		O7 series	
C <sub>x</sub> H <sub>2x-9</sub> O <sub>3</sub> <sup>-</sup> (O3, DBE 5.5)		C <sub>x</sub> H <sub>2x-9</sub> O <sub>3</sub> <sup>-</sup> + C <sub>26</sub> H <sub>50</sub> O <sub>3</sub> <sup>-</sup> (O6, DBE 6.5)		C <sub>x</sub> H <sub>2x-9</sub> O <sub>3</sub> <sup>-</sup> + C <sub>26</sub> H <sub>48</sub> O <sub>4</sub> <sup>-</sup> (O7, DBE 7.5)	
Assignment	Area	Assignment	Area	Assignment	Area
C <sub>13</sub> H <sub>17</sub> O <sub>3</sub> <sup>-</sup>	1.60E-05	C <sub>39</sub> H <sub>67</sub> O <sub>6</sub> <sup>-</sup>	1.00E-06	C <sub>39</sub> H <sub>65</sub> O <sub>7</sub> <sup>-</sup>	N/A
C <sub>19</sub> H <sub>29</sub> O <sub>3</sub> <sup>-</sup>	7.10E-05	C <sub>45</sub> H <sub>79</sub> O <sub>6</sub> <sup>-</sup>	1.50E-06	C <sub>45</sub> H <sub>77</sub> O <sub>7</sub> <sup>-</sup>	N/A
C <sub>21</sub> H <sub>33</sub> O <sub>3</sub> <sup>-</sup>	3.20E-02	C <sub>47</sub> H <sub>83</sub> O <sub>6</sub> <sup>-</sup>	1.40E-03	C <sub>47</sub> H <sub>81</sub> O <sub>7</sub> <sup>-</sup>	1.07E-04
C <sub>22</sub> H <sub>35</sub> O <sub>3</sub> <sup>-</sup>	2.00E-05	C <sub>48</sub> H <sub>85</sub> O <sub>6</sub> <sup>-</sup>	3.10E-05	C <sub>48</sub> H <sub>83</sub> O <sub>7</sub> <sup>-</sup>	1.36E-06
C <sub>23</sub> H <sub>37</sub> O <sub>3</sub> <sup>-</sup>	6.00E-02	C <sub>49</sub> H <sub>87</sub> O <sub>6</sub> <sup>-</sup>	2.70E-03	C <sub>49</sub> H <sub>85</sub> O <sub>7</sub> <sup>-</sup>	2.97E-04
C <sub>25</sub> H <sub>41</sub> O <sub>3</sub> <sup>-</sup>	4.10E-02	C <sub>51</sub> H <sub>91</sub> O <sub>6</sub> <sup>-</sup>	2.20E-03	C <sub>51</sub> H <sub>89</sub> O <sub>7</sub> <sup>-</sup>	1.46E-04
C <sub>27</sub> H <sub>45</sub> O <sub>3</sub> <sup>-</sup>	3.50E-04	C <sub>53</sub> H <sub>95</sub> O <sub>6</sub> <sup>-</sup>	3.60E-04	C <sub>53</sub> H <sub>93</sub> O <sub>7</sub> <sup>-</sup>	N/A
C <sub>32</sub> H <sub>55</sub> O <sub>3</sub> <sup>-</sup>	3.90E-06	C <sub>58</sub> H <sub>105</sub> O <sub>6</sub> <sup>-</sup>	N/A	C <sub>58</sub> H <sub>103</sub> O <sub>7</sub> <sup>-</sup>	N/A
C <sub>37</sub> H <sub>65</sub> O <sub>3</sub> <sup>-</sup>	1.50E-03	C <sub>63</sub> H <sub>115</sub> O <sub>6</sub> <sup>-</sup>	1.70E-06	C <sub>63</sub> H <sub>113</sub> O <sub>7</sub> <sup>-</sup>	N/A
C <sub>39</sub> H <sub>69</sub> O <sub>3</sub> <sup>-</sup>	2.20E-03	C <sub>65</sub> H <sub>119</sub> O <sub>6</sub> <sup>-</sup>	2.60E-06	C <sub>65</sub> H <sub>117</sub> O <sub>7</sub> <sup>-</sup>	N/A
C <sub>41</sub> H <sub>73</sub> O <sub>3</sub> <sup>-</sup>	1.40E-03	C <sub>67</sub> H <sub>123</sub> O <sub>6</sub> <sup>-</sup>	1.90E-06	C <sub>67</sub> H <sub>121</sub> O <sub>7</sub> <sup>-</sup>	N/A
C <sub>43</sub> H <sub>77</sub> O <sub>3</sub> <sup>-</sup>	3.70E-04	C <sub>69</sub> H <sub>129</sub> O <sub>6</sub> <sup>-</sup>	N/A	C <sub>69</sub> H <sub>127</sub> O <sub>7</sub> <sup>-</sup>	N/A
C <sub>49</sub> H <sub>89</sub> O <sub>3</sub> <sup>-</sup>	1.20E-06	C <sub>75</sub> H <sub>131</sub> O <sub>6</sub> <sup>-</sup>	>1125 <i>m/z</i>	C <sub>75</sub> H <sub>129</sub> O <sub>7</sub> <sup>-</sup>	>1125 <i>m/z</i>

### 3.2.6.3 Organophosphates

Organophosphate species were also identified in the Marine 1 sample. The largest ( $\text{C}_{28}\text{H}_{42}\text{PO}_4^-$ , Figure 3.18a left) likely originates from tris(2,4-di-tert-butylphenyl)phosphite ( $\text{C}_{42}\text{H}_{63}\text{PO}_3$ ), an antioxidant additive used in plastics to stabilise them against degradation (184). Oxidation of this additive to the phosphate seen in Marine 1 is known, and has been found to be abundant in particulate matter in urban air environments (185). MS/MS supported this assignment of this ion (Figure 3.18a), as well as a similar ion seen in positive polarity (Figure 3.18b). This chemistry was not expected based on the early reports of the Houston fuel forensics findings. Other organophosphate species exist in Marine 1, including the ion in Figure 3.18c which interestingly features the predominant alkylphenol seen earlier. This suggests a complex relationship between these organophosphates, phenols, and the large O6/O7 ion series, which would require further work to fully understand. It is possible that phenols have undergone reactions with phosphates and other species to form these chemistries within the fuel or deposit.

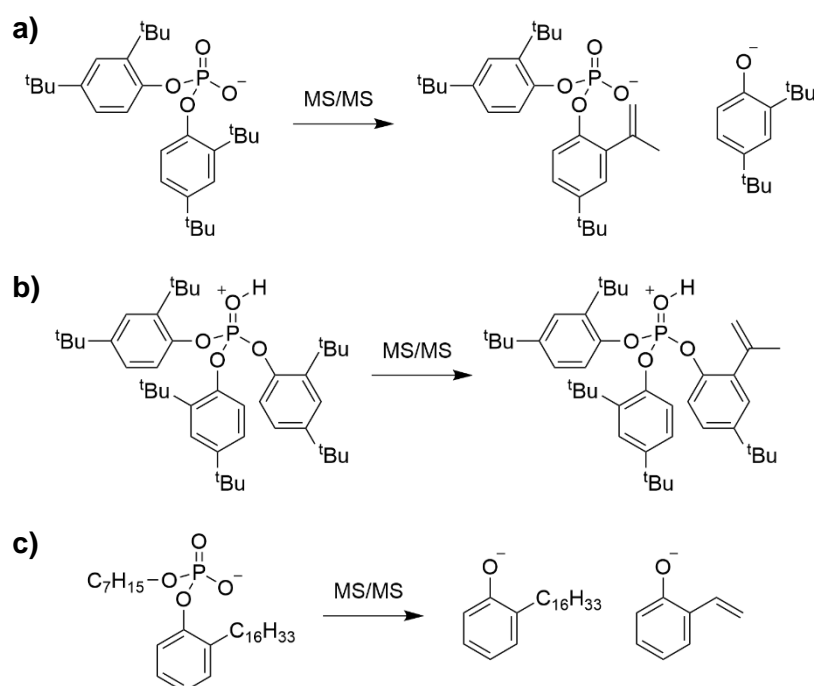


Figure 3.18: Organophosphate OrbiSIMS ions in sample Marine 1. MS/MS analysis of a)  $\text{C}_{28}\text{H}_{42}\text{PO}_4^-$ , b)  $\text{C}_{42}\text{H}_{64}\text{PO}_4^+$  and c)  $\text{C}_{29}\text{H}_{52}\text{PO}_4^-$ .

#### 3.2.6.4 AP-MALDI-Orbitrap<sup>TM</sup> Validation of PAH Distribution from OrbiSIMS

Two limitations of SIMS were discussed in Section 1.3.3.2: its semi-quantitative nature and the fragmentation which occurs during high energy sputtering. The semi-quantitative nature of SIMS has been mitigated with complementary XPS analysis, providing quantitative data to contextualise and validate the OrbiSIMS results. To minimise the impact of fragmentation on data interpretation, AP-MALDI-MS will now be explored as a method for acquiring MS data with minimal fragmentation to help identify the likely parent ions from the OrbiSIMS data. MALDI-MS has had minimal use in IDID analysis in previous studies, but as discussed in Section 1.3.3.3 is an effective MS technique that benefits from relatively easy ionisation that induces less fragmentation. Applied by Venkataraman *et al.* (2014) to an EDID from an engine test, it was able to analyse the distribution of PAHs in the deposit (48).

Here, initial AP-MALDI-Orbitrap<sup>TM</sup> analysis was performed on the Marine 1 sample to identify PAH compounds via this alternative ionisation source. The matrix used here was tetracyanoquinodimethane (TCNQ), a strong electron acceptor that has been demonstrated capable of the analysis of large insoluble polyaromatic compounds (186). From formula calculation and comparison with OrbiSIMS of DBE as a function of  $m/z$  (Figure 3.19a), hydrocarbon structures of similar mass are identified via AP-MALDI-MS. These ions reach  $C_{58}H_{26}^+$  with 19% laser power and  $C_{63}H_{36}^+$  with 6.2%. The largest AP-MALDI ions are comparable in size to those of OrbiSIMS ( $C_{59}H_{21}^+$ ), validating that both techniques identify similar size hydrocarbon structures. This suggests that the sputtering process in OrbiSIMS did not significantly alter the chemistry of the polyaromatic deposit. The OrbiSIMS ions are much more numerous than in AP-MALDI, which suggests there is indeed significant fragmentation occurring in the sputtering processes in SIMS as would be anticipated.

The ions from AP-MALDI are generally more hydrogen-saturated, suggesting a possible fragmentation via loss of hydrogen in OrbiSIMS. However, MALDI may have failed to access deposit material that is analysed by SIMS; MALDI requires optimisation of matrix, solvent and laser power to ensure the



compounds of interest are ablated and ionised for analysis. It is possible that PAH deposit material was insufficiently ionised in this work to analyse similar ions to those of OrbiSIMS. Figure 3.19b shows that the higher laser power experiment appears to detect more hydrogen-deficient material, while the lower laser power detects larger masses, possibly due to increased fragmentation with the higher energy laser. Future work to fine-tune the technique would be required to build on this work to understand the processes occurring under SIMS sputtering.

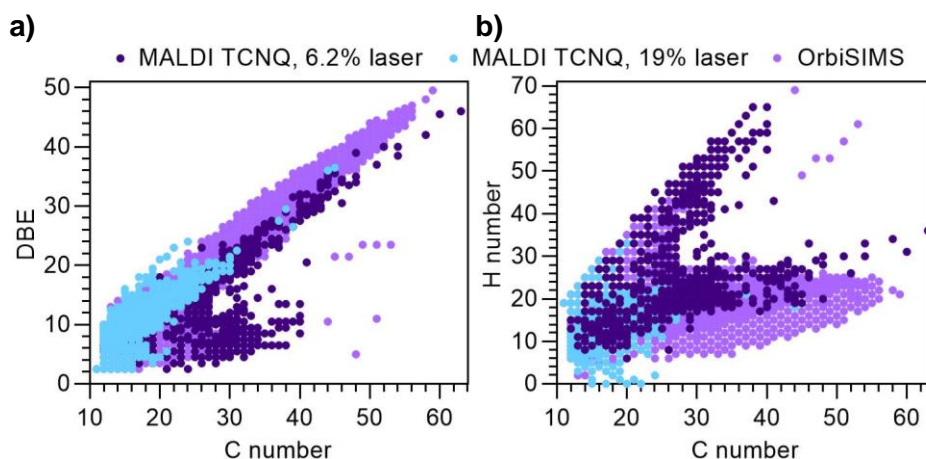


Figure 3.19: Hydrocarbon distributions in Marine 1 from AP-MALDI (using TCNQ matrix with laser power of 6.2% or 19%) and OrbiSIMS (using  $\text{Ar}_{3000}^+$  GCIB). a) DBE as a function of carbon number. b) Hydrogen number as a function of carbon number.

MALDI may also offer a technique to probe other high-mass parent species, such as the O6 and O7 series seen in the OrbiSIMS data in Section 3.2.6.2, however in this work these ions did not appear in the AP-MALDI spectra. Therefore, further work would also be required to achieve these aims.

### 3.3 Conclusions

In this chapter, a range of injector needle IDID samples mainly from real-world injector failures have been extensively characterised with the recently developed technique of OrbiSIMS, first introduced in 2017. Quantitative support using XPS analysis was also of key importance throughout. By SEM, the IDIDs have appearances typical of those in the literature, with a grainy texture covering the needle shaft particularly towards the tip end. Chemistries observed are consistent with known IDID types from previous analysis of

IDIDs, but the improved mass resolving power of the Orbitrap<sup>TM</sup> analyser over previous ToF-SIMS investigations enables improved chemical speciation and unambiguous characterisation.

Polyaromatic compounds and other hydrogen-deficient chemistries indicative of carbonaceous deposit material are important chemistries that can now be analysed with OrbiSIMS. Previous techniques struggled with sample preparation to access such material for analysis. ToF-SIMS was able to access these compounds via sputtering however extensive fragmentation and poor mass resolving power limited the ability to identify specific molecular deposit chemistry. With OrbiSIMS, the Ar<sub>3000</sub><sup>+</sup> GCIB ion source is soft enough to limit fragmentation and the mass resolving power of the Orbitrap<sup>TM</sup> is sufficient to characterise these materials. With formula calculation using the MATLAB script by Spanu (2021) (159), these ions can be rapidly identified and visualised to reveal the distribution of compounds present in the samples, indicating the degree of carbonisation that has occurred during deposit formation on each sample.

Spatial information gained from OrbiSIMS was crucial in understanding IDID carbonisation. Depth profiling has supported the carbonisation process by identifying lower deposit layers closer to the substrate as having increased intensity for ions expected to be products of carbonisation, via such reactions as HACA, Diels-Alder and MCA. Lateral information is also important; analysis of different positions finds the more carbonised deposit generally towards the needle tip, where fuel has travelled longer and reached higher temperatures and therefore undergone more extensive carbonisation. Additionally, chemical imaging shows widespread polyaromatic coverage rather than localised deposition. Some IDIDs indicate greater carbonisation than others, a significant result in demonstrating that carbonisation processes occur to significantly variable degrees when comparing IDID samples based on polyaromatic compound size, OrbiSIMS ion intensity and XPS  $\pi$ - $\pi^*$  component area. These IDID compositional results inform the nature of these deposits which can be related to mechanisms, the understanding of which can be utilised by industry for developing mitigation strategies.

Other chemistries identified include succinimides, of which Needle 12 had very large structures high MW PIBSI-derived species. Application of OrbiSIMS to PIBSI-type deposits enables identification of the largest species present, indicative of the type of PIBSI that has affected the system which here are larger than those used in DCAs. While other techniques such as FTIR have been able to indicate the type of functional groups present in such deposits to indicate amide or imide groups, OrbiSIMS offers the ability to identify the specific products of reactions that PIBSI has undergone. Here, the results suggest hydrolytic succinimide ring-opening reactions have occurred. For deposits formed from sodium carboxylates, particularly involving DDSA, OrbiSIMS here indicates accompanying sodium carbonate which may form from Na-DDS deposition.

Chemistries associated with lubricants are found with OrbiSIMS, notably of alkylbenzene sulfonates and zinc species. XPS analysis was significant here to show that most samples contain very little or no detectable sulfur and hence ABS ions likely represent a minor contaminant. Zinc content was also quantified with XPS, alongside other lubricant-associated elements (calcium and sulfur). A wide range of inorganic salts were also seen in many samples, likely indicative of many sources of contamination. Again, as these species are pre-ionised they appear with very high intensity in OrbiSIMS, therefore XPS analysis was crucial to reveal their concentrations. In all cases, carbon was the dominant element by XPS, despite some samples' OrbiSIMS spectra being dominated by inorganic salts.

To expand the methods into a new area, a marine deposit sample was analysed and key chemistries were identified, some consistent with forensic fuel analysis and some providing new insights into the deposit. To validate OrbiSIMS data, MALDI-MS was applied to this sample with the aim of identifying the native parent peaks. Initial results show this could be a promising complementary technique, identifying PAH ions of similar sizes to those of OrbiSIMS. As MALDI relies on a solvent/matrix combination complementary to the material being analysed, further work is required in this area to develop the method and accomplish the aim of confirming the native parent species.

## Chapter 4: Towards a Comprehensive Characterisation of Chemical Variation with Depth of IDIDs

### 4.1 Introduction

This chapter is a sample-based investigation aiming to understand the depth variation of three IDID samples that showed complex layering effects in extended depth profiling experiments. The IDID profiles herein are large, often containing over 1000 ions with dose densities of  $>2 \times 10^{17}$  ions  $\text{cm}^{-2}$  over a sputter time of up to >55 hours. Manual interpretation comparing two of the samples was first performed, in which the high mass resolving power of the OrbiSIMS affords exceptionally detailed IDID chemical information compared to previous investigations (39, 47). Coupled with elemental quantification throughout the deposit depth with XPS depth profiling, quantitative validation is achieved to complement the semi-quantitative OrbiSIMS data.

NMF was then utilised as a data deconvolution tool to simplify each deposit depth profile into a model of four pseudo-layers based on key trends, enabling more efficient, detailed and reliable interpretations. These pseudo-layers are described, with further depth behaviour nuance explored with a new comparative method for the interpretation of endmember loadings which will be described herein. Corresponding regions of the XPS depth profiles are used to support the interpretation of each pseudo-layer. This builds on previous investigations which used ToF-SIMS (3, 40, 59, 128, 187) to characterise engine deposits, particularly a ToF-SIMS depth profiling study discussed in Section 1.3.3.2 that described an IDID as four layers/pseudo-layers primarily based on elemental and small inorganic ion chemistries (47). This method also builds on Chapter 3 to probe the depth location of the identified chemistries.

The manual analysis in this chapter was published as a conference paper and subsequently in the associated journal, Lamb *et al.* (2020) (78).

## 4.2 Results and Discussion

The results presented in this chapter first compare two IDID needle samples that showed significant differences in their chemistries in Chapter 3 and had complex and long depth profiles. OrbiSIMS and XPS depth profiling is used to characterise and compare these deposits (Section 4.2.2). This involves a time-consuming inspection of spectra and depth profiles by the analyst which are prone to ambiguities and analyst bias. To improve data interpretation, NMF is then used with a description of the current method and interpretation of the same two needle samples alongside an additional needle that also exhibited a complex depth profile (Section 4.2.3).

### 4.2.1 Estimating deposit thickness from profilometry of OrbiSIMS depth profiling GCIB craters

In the analysis of each sample in this chapter, three craters were etched (from positive polarity and negative polarity OrbiSIMS depth profiles and the XPS depth profile), reaching needle substrate chemistry in each case. The crater step size from the deposit surface to the base of the crater can therefore be measured using optical profilometry to estimate the deposit thickness. Due to these deposits being topographical and likely variable in thickness, this measurement applies only approximately and at the respective analysis positions, however can provide insight into the depth of each sample's deposit. The XPS crater was too large to image both sides so levelling is only applied on one side, only one step is measured and its results are hence less reliable and shown as an example for only Needle 6.

Based on the measurements for the craters for Needles 6, 7 and 8 shown in Figure 4.1 (Table 4.1), the samples differ significantly in thickness, from 0.2-10  $\mu\text{m}$ . Needle 8 has the thinnest deposit (0.22-0.34  $\mu\text{m}$ ) and Needle 7 the thickest (2.29-9.39  $\mu\text{m}$ ) with Needle 6 in between (1.40-1.92  $\mu\text{m}$ ). However, particularly for Needle 8 where the standard deviation represents 75-91% of the step height, there is considerable uncertainty, highlighting the difficulty in measuring the deposit due to topography.

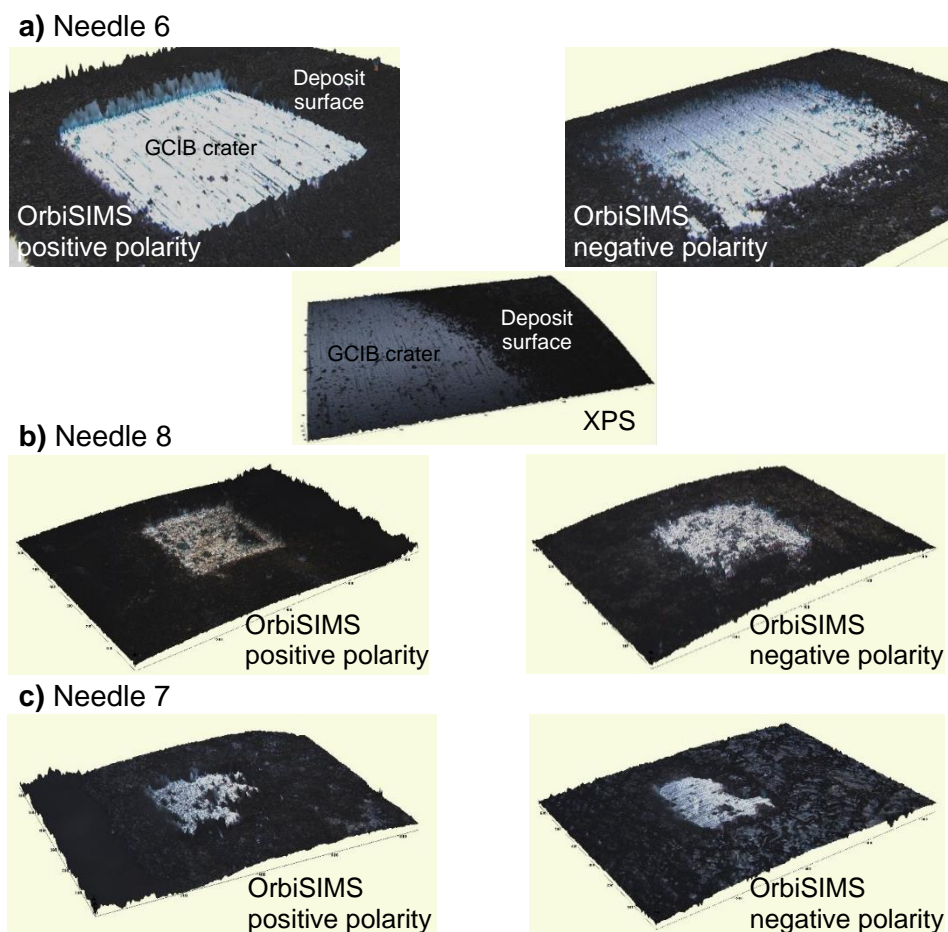


Figure 4.1: Profilometry 3D images of craters from OrbiSIMS positive and negative polarity depth profiles. a) Needle 6, b) Needle 8 and c) Needle 7.

Table 4.1: Profilometry step height data for Needles 6-8 OrbiSIMS and XPS depth profiling craters using average of ten cross sections across each crater.

Sample	Crater	Data	Side 1 ( $\mu\text{m}$ )	Side 2 ( $\mu\text{m}$ )	1+ 2 average ( $\mu\text{m}$ )
Needle 6	a) OrbiSIMS positive	Average	1.96	1.88	1.92
		St. dev	0.13	0.19	0.23
	b) OrbiSIMS negative	Average	1.26	1.54	1.40
		St. dev	0.15	0.18	0.22
	c) XPS	Average	3.24	N/A	N/A
Needle 8	a) OrbiSIMS positive	Average	0.24	0.21	0.22
		St. dev	0.15	0.13	0.20
	a) OrbiSIMS negative	Average	0.32	0.35	0.34
		St. dev	0.21	0.14	0.25
Needle 7	b) OrbiSIMS negative	Average	1.73	3.30	2.52
		St. dev	0.42	1.22	1.29
	a) OrbiSIMS positive	Average	11.02	7.75	9.39
		St. dev	2.02	1.52	2.53

#### 4.2.2 Manual Depth Profile Interpretation of Needle 6 and 8 to Probe Chemical Variation with Depth

In this section, the OrbiSIMS depth profiles of two samples that were shown to differ significantly in composition in previous work using ToF-SIMS PCA are manually assessed to identify and compare key chemistries and their variation with depth. This data is supported by XPS to provide quantitative context and validation to the semi-quantitative OrbiSIMS data. This work is the first application of XPS depth profiling to IDIDs and is highly complementary to the OrbiSIMS depth profiles (78).

##### 4.2.2.1 Needle 8 OrbiSIMS Depth Profile for Detailed Chemical Information as a Function of Depth

Both Needle 8's negative (Figure 4.2a) and positive (Figure 4.2b) polarity depth profiles for selected key ions in Needle 8 show agreement in layering effects. Carbonaceous material ( $C_{14}H^-$ ,  $C_{17}^-$ ) is the most intense chemistry throughout the negative polarity depth profile, which loses intensity sharply near the surface and then more steadily throughout the profile. This same shape is seen for many ions and appears to represent the bulk carbonaceous, hydrocarbon and inorganic salt deposit material, including the hydrocarbon ion ( $C_{17}H_5^-$ ), N-containing ions ( $C_{13}N^-$  and  $C_{14}NH_4^-$ ) and salt material (e.g.  $Ca_2O_5H_5^-$ ,  $Ca_3O_7H_7^-$ ,  $Ca_2C_3N_3O_2H_2^-$ ). In positive polarity, the calcium salts ( $Ca_2O_4H_5^+$ ,  $CaPO_2^+$ ,  $Ca_2O_2H_2CNO^+$ ) follow this same trend and are the highest intensity type of material throughout. Nuances exist between the negative polarity ions, with the more H-rich nitrogenous ion ( $C_{14}NH_4^-$ ) and the calcium sulfate-cyanide ( $CaSO_4CN^-$ ) showing a steeper decline near the surface suggesting these chemistries are more prevalent in the upper deposit. In both polarities, needle substrate metal-containing ions ( $WO_3^-$ ,  $MoO_4^-$ ;  $Fe_2O_6H_6^+$ ,  $MoO_3H_2^+$ ) gradually rise towards the end of the profile, evidencing exposure of the needle.

Another trend in both polarities for Needle 6 is that of ions with significant intensity only towards the surface ( $<2 \times 10^{16}$  ions  $\text{cm}^{-2}$  dose density). In negative polarity this comprises only ABS fragments ( $\text{C}_8\text{H}_7\text{SO}_3^-$ ,  $\text{C}_{17}\text{H}_{27}\text{SO}_3^-$ ) and oxygenates ( $\text{C}_{16}\text{H}_{31}\text{O}_2^-$ ,  $\text{C}_{12}\text{H}_7\text{O}^-$ ) while in positive mode there are carbon fragments ( $\text{C}_{11}^+$ ,  $\text{C}_{15}^+$ ), hydrocarbons ( $\text{C}_9\text{H}_7^+$ ,  $\text{C}_{24}\text{H}_{12}^+$ ), oxygenates ( $\text{C}_{12}\text{H}_9\text{O}^+$ ) and nitrogenous ions ( $\text{C}_9\text{H}_8\text{N}^+$ ,  $\text{C}_{10}\text{H}_7\text{N}_2^+$ ). For each of these classes of ion, the larger, more complex fragments decrease earlier than the simpler fragments, possibly implying a breakdown of complex chemistries over time resident in the deposit. The oxygenates in negative mode (including palmitate,  $\text{C}_{16}\text{H}_{31}\text{O}_2^-$ , and stearate,  $\text{C}_{18}\text{H}_{35}\text{O}_2^-$ , as well as PDMS in positive mode ( $\text{Si}_2\text{O}_2\text{C}_4\text{H}_{13}^+$ ), show the most precipitous declines, falling to noise by  $5 \times 10^{15}$  ions  $\text{cm}^{-2}$  dose density. This suggests these materials arise from either deposition on a pre-formed deposit or sample surface contamination. PDMS and palmitic acid have been seen together in previous ToF-SIMS analysis of a needle shaft IDID (59).

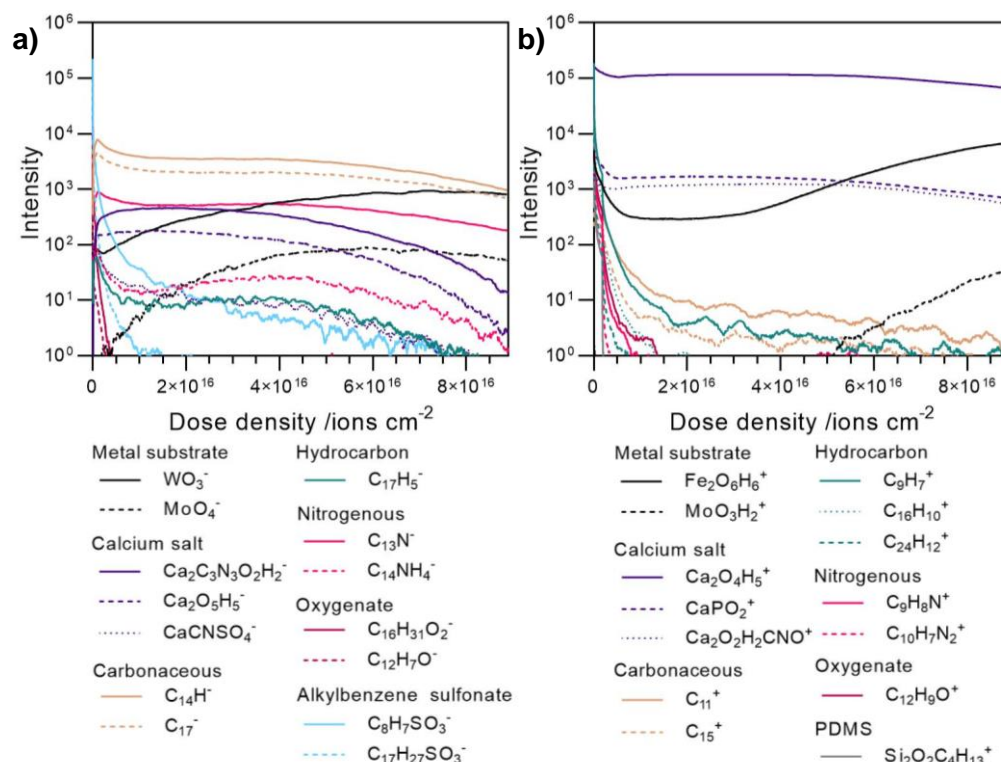


Figure 4.2: Depth profiles of selected key ions for Needle 8 a) negative polarity, and b) positive polarity. Published in Lamb *et al.* (2020) (78).



#### 4.2.2.2 Needle 6 OrbiSIMS Depth Profile for Detailed Chemical Information as a Function of Depth

Needle 6's positive (Figure 4.3a) and negative (Figure 4.3b) polarity depth profiles show trends that mostly agree with one another and have more dramatic layering effects than Needle 8's. Both polarities highlight the large intensity of inorganic salt material, with an initial steep rise near the surface to a salt-dominated sub-surface layer (peaking at around  $5 \times 10^{15}$  ions  $\text{cm}^{-2}$ ), followed by a decline with a temporary plateau at an interface with a carbonaceous layer at around  $1.5 \times 10^{16}$  ions  $\text{cm}^{-2}$ . This includes sodium salts of chloride, cyanate, sulfate, hydroxide and carbonate ( $\text{NaCl}_2^-$ ,  $\text{NaCNOCI}^-$ ,  $\text{Na}_3\text{S}_2\text{O}_8^-$ ,  $\text{Na}_2\text{SO}_4\text{OH}^-$ ;  $\text{Na}_2\text{Cl}^+$ ,  $\text{Na}_3\text{SO}_4^+$ ,  $\text{Na}_3\text{O}_2\text{H}_2^+$  and  $\text{Na}_3\text{CO}_3^+$ ), calcium salts of chloride, sulfates and hydroxides ( $\text{CaCl}_3^-$ ,  $\text{CaSO}_3\text{OH}^-$ ), and potassium salts which are found mixed with sodium ( $\text{KNaCl}^+$ ).

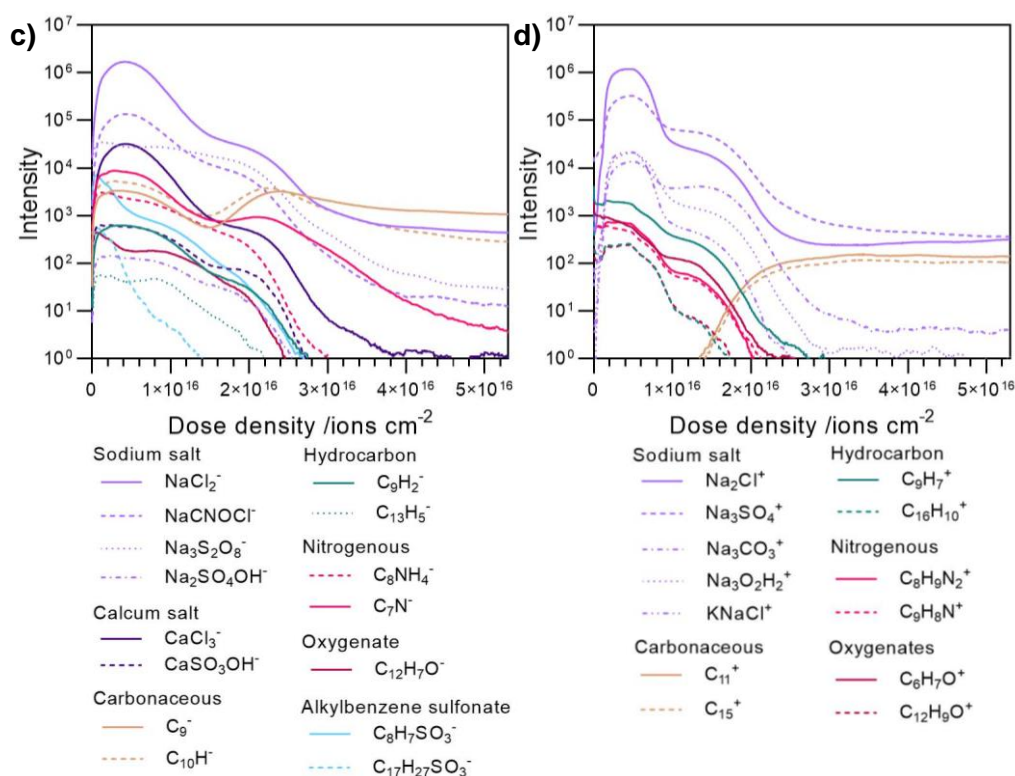


Figure 4.3: Depth profiles of selected key ions for Needle 6 a) negative polarity, b) positive polarity. Published in Lamb *et al.* (2020) (78).

Dominance of carbonaceous ions in the deepest layer is seen for both polarities ( $\text{C}_9^-$ ,  $\text{C}_{10}\text{H}^-$ ;  $\text{C}_{11}^+$ ,  $\text{C}_{15}^+$ ) and is maintained to the end of each profile, however in negative polarity these ions are also present in the sub-surface layer alongside the inorganic salts. This behaviour relates to etching having reached a sputter-

resistant layer of likely DLC or hardened carbonaceous deposit material. The positive polarity carbonaceous ions generally relate only to this layer, with some exceptions ( $C_{16}^+$  and  $C_{21-23}^+$ ) which are also present towards the surface. Most negative carbonaceous ions are from both this and the upper deposit material, excluding  $C_xH^-$  where  $x = 7, 9, 11$ , and  $\geq 23$  which are not present in the lower layer and hence represent only upper deposit material. Interestingly,  $C_7N^-$  is part of the upper deposit but extends significantly into the carbonaceous layer, showing that the lower carbonaceous layer has some nitrogen content. Some inorganic ions ( $NaCl_2^-$ ,  $Na_2Cl^+$  and  $Na_3SO_4^+$ ) remain among the most intense ions in the lower carbonaceous layer though this is most likely due to their higher SIMS sensitivity.

Much of the deposit chemistry in both positive and negative polarity follows a common trend of a slow decline that accelerates at around  $1.4 \times 10^{16}$  ions  $cm^{-2}$ . As with Needle 8, for more complex or larger ions this shape generally has a steeper drop in intensity that begins sooner in the profile. This occurs for hydrocarbon ( $C_9H_2^-$ ,  $C_{13}H_5^-$ ,  $C_9H_7^+$ ,  $C_{16}H_{10}^+$ ), oxygenate ( $C_{12}H_7O^-$ ,  $C_8H_7O^+$ ,  $C_{12}H_9O^+$ ), nitrogenous ( $C_8NH_4^-$ ,  $C_8H_9N_2^+$ ,  $C_9H_8N^+$ ) and ABS ( $C_8H_7SO_3^-$ ,  $C_{17}H_{27}SO_3^-$ ) ions. Again, this may suggest a breakdown of the more complex material over time in the deposit. For hydrocarbon and nitrogenous material, the more hydrogenated ions are closer to the surface which again suggests lower layers possess a lower H/C ratio.

#### 4.2.2.3 Needle 8 XPS Depth Profile for Atomic Concentration as a Function of Depth

For Needle 8's XPS depth profile, an established method for the removal of metal-related oxygen, shown by Smith *et al.* (2002) on a diesel piston deposit, was used (82). A good peak fitting could be achieved for its O 1s spectra throughout the profile using two components, seen in Figure 4.4a-b. One component is consistent with metal oxides (ranging from 529.7-530.0 eV) and can be seen growing from 1.9% to 15.4% through the profile in Figure 4.4c, therefore is thought to represent the substrate metal oxides exposed during etching (188). The other component at 531.7-532.5 eV is thought to represent

“other” deposit-associated oxygen including organic and salts such as calcium hydroxides and sulfates (189, 190). To exclude substrate and characterise solely deposit material, the metal oxide component, alongside the substrate elements identified in the XPS profile which increased in concentration as etching progressed (Fe, Cr, Mo; at.% data can be found in Appendix Table A10) were removed.

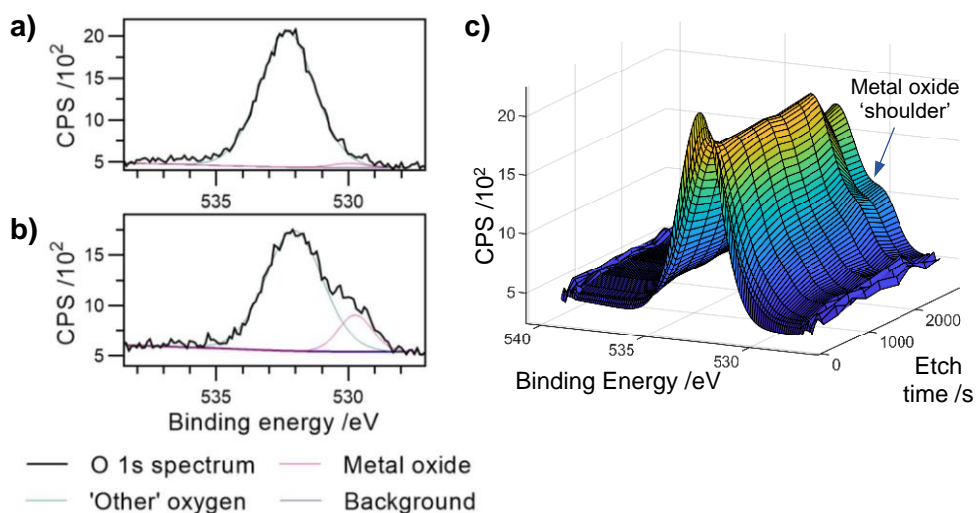


Figure 4.4: O 1s XPS depth profile for Needle 8. a) O 1s spectrum at surface. b) O 1s spectrum at 2725s etch time. c) 3D graph of O 1s spectra vs. etch time, showing growth of metal oxide shoulder.

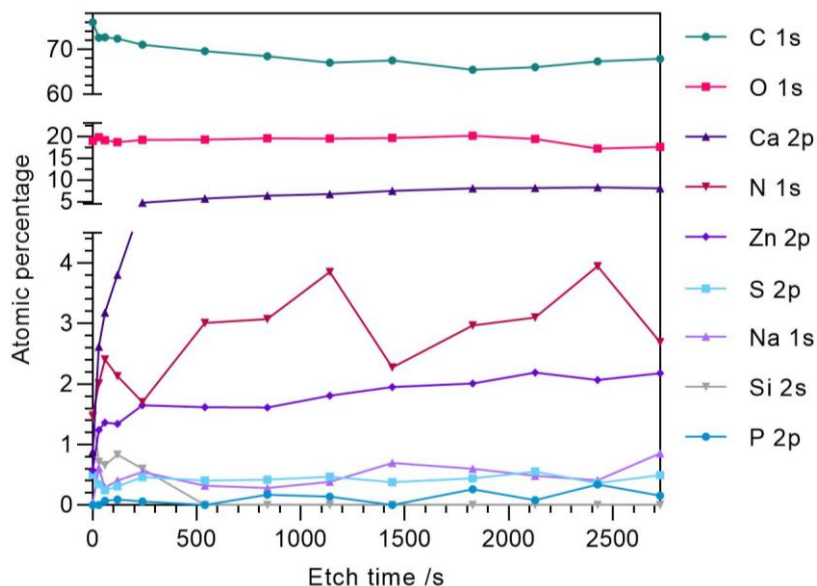


Figure 4.5: XPS depth profile of Needle 8 excluding substrate elements and substrate oxygen. Published in Lamb *et al.* (2020) (78).

After removing substrate chemistry, the profile (Figure 4.5) shows relatively stable concentrations of carbon which fell from 76 at.% to 68 at.% and oxygen which rose from 19 at.% to 20 at.% at 1825 s before falling to 17 at.%. This partially correlates with the OrbiSIMS data, which showed a decrease in carbon, hydrocarbons and oxygenates. While these elements remain relatively constant, there is a steady rise in calcium from 0.8 at.% to 8 at.% at 1825 s, along with small increases in zinc and nitrogen. In OrbiSIMS, calcium decreased throughout the profile, a discrepancy which may be a matrix effect in SIMS, or may be due to the different analysis positions in the sample having different structures.

This XPS data implies a changing form of the carbon and oxygen in the deposit with increasing depth as the OrbiSIMS data indicated that much of the calcium material is in oxygen and nitrogen containing forms (sulfate, hydroxide, cyanide and cyanate), seen in the ions of Figure 4.2, Figure 4.3 and in Section 3.2.5.1. Therefore, the oxygen and nitrogen at lower layers is present in these salts while in higher layers, where calcium is less concentrated, it must exist in other (likely organic) forms. This further agrees with the OrbiSIMS data for nitrogen and oxygen-containing organic material which decreases with etch time from a maximum intensity at the surface. As carbon remains the most prevalent element throughout, this implies that organic or amorphous carbon with fewer oxygen/nitrogen-containing functional groups forms the lower layers, suggesting graphitisation of the organic material. Again, the OrbiSIMS data supports this as the more complex hydrocarbon/organic ions lost intensity with etching time, while the carbon fragments extended deeper, reaching the metal interface.

#### **4.2.2.4 Needle 6 XPS Depth Profile for Atomic Concentration as a Function of Depth**

No substrate metals were present in XPS analysis of Needle 6 despite a longer etch time and the dark coloured metal needle being visible in the crater. Needle 6 showed more dramatic changes in concentration during the profile than Needle 8, with carbon falling from 76 at.% at the surface to 52 at.% at 860s,

then rising throughout the rest of the profile towards the lower carbon layer. If this is a DLC substrate, then its data is convoluted with the deposit's carbon data. XPS validates the sub-surface presence of the sodium inorganic salts; many of the key salt-associated elements' (Na, Cl, S) intensities rise while carbon's decreases, reaching their peak at 860s where sodium is 16 at.% and chlorine 6.5 at.%. Sulfur reaches its peak of 1.0 at.% after the next etch at 1130s. These elements then decline throughout the rest of the profile while carbon's abundance is restored. Oxygen and nitrogen are the other elements present in the OrbiSIMS inorganic salt ions (sodium chlorides, cyanides, cyanates, sulfates, hydroxides and carbonates) and also decrease from 860 s onwards, however unlike other salt components they have high concentrations at the surface (16 at.% and 5 at.% respectively). Their high surface concentration most likely results from the presence of N- and/or O-containing organic material as seen in the OrbiSIMS profiles with larger intensities towards the surface.

A much smaller amount of silicon is seen on Needle 6 than on Needle 8, with only 0.2 at.% on the surface and falling to 0 at.% after the first (30s) etch. This indicates less surface contamination or antifoam deposition on Needle 6. PDMS was not seen in Needle 6's OrbiSIMS spectrum despite SIMS being the more sensitive technique, hence silicon's presence in the XPS data is likely due to differences in composition across the surface. As in Needle 8, the XPS and OrbiSIMS results support an organic content with more functional groups at the surface, with more oxygenates and nitrogenous material. However, in Needle 6 this layer is above a salt layer, beneath which there is likely another carbonaceous layer and finally the etch-resistant carbon layer.

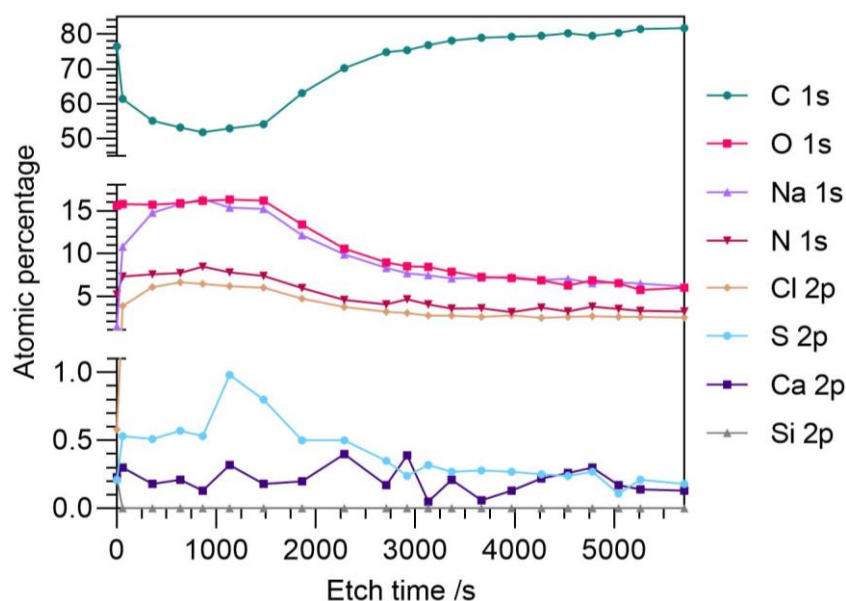


Figure 4.6: XPS depth profile of Needle 6 showing all detected elements. Published in Lamb *et al.* (2020) (78).

### 4.2.3 Multivariate Analysis to Understand IDID Layering Effects

To achieve more thorough and efficient depth profile interpretation, NMF was performed using each depth level (i.e. the signal at each recorded sputter time) of the depth profile as an observation and the ions as variables, as described in Section 2.3.3.3.2. This is the first application of NMF for the interpretation of IDID SIMS datasets. For each sample analysed herein, NMF with four endmembers produced optimal results (maximising endmembers without repeating chemistries or convoluting endmembers). Thus, the depth profiles of each sample can be understood in terms of four “pseudo-layers”. For all trends identified herein, the original data was consulted to confirm the finding.

#### 4.2.3.1 NMF Method Development for Needle 6 Negative Polarity

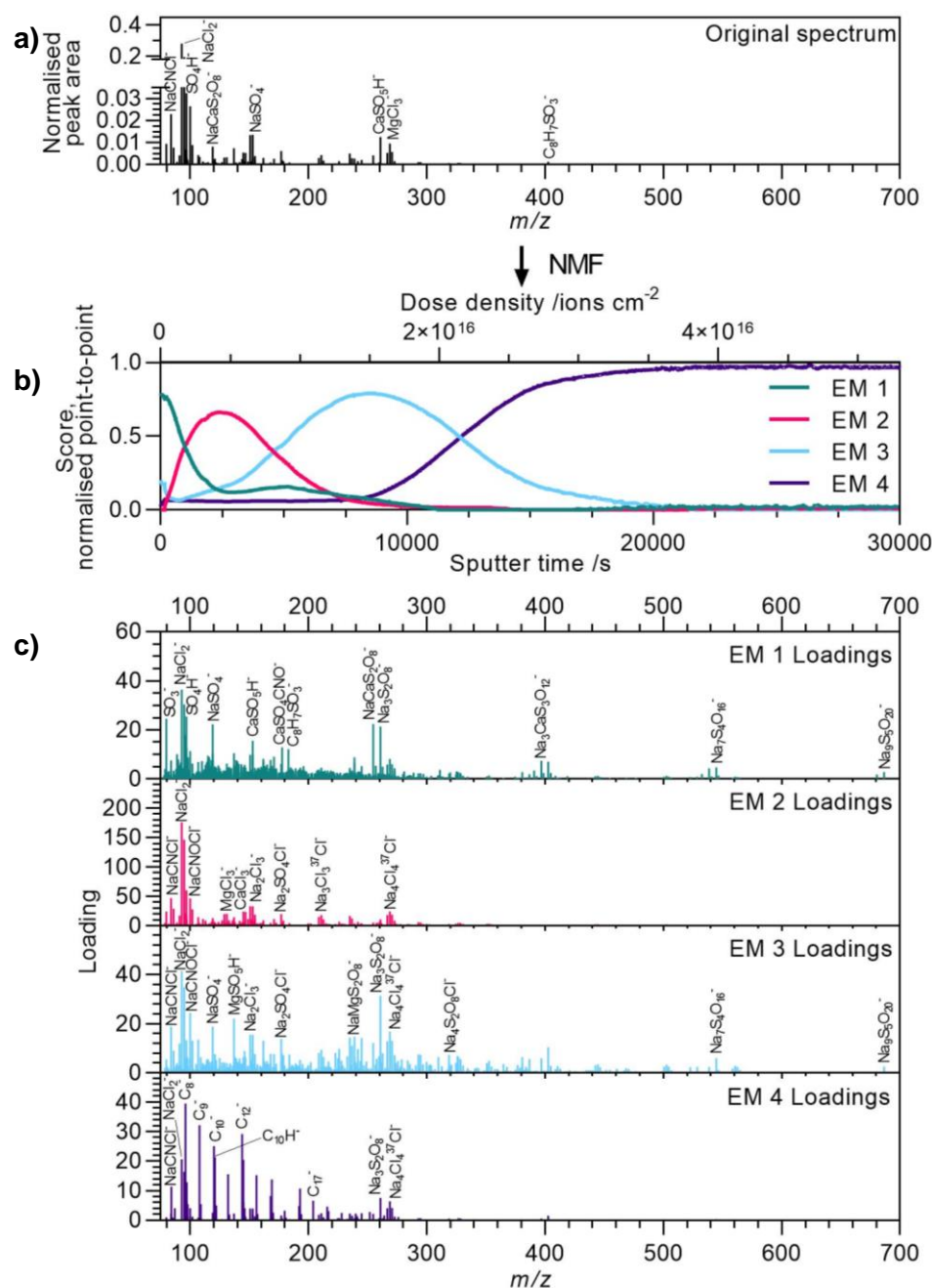
##### OrbiSIMS Depth Profile

NMF of Needle 6’s negative polarity depth profile will be discussed in detail to establish the current method and interpret its results, with this method then applied to the positive polarity profile and other samples in Section 4.2.3.2. Overviews for each profile can be found in Appendix Section 2.8.

**4.2.3.1.1.1 Interpretation of Original Loadings from NMF**

The spectrum from this depth profile is seen in Figure 4.7a, the NMF scores in Figure 4.7b and NMF loadings in Figure 4.7c. In these NMF results, the scores for each EM quantify the presence of their associated loadings at the respective depth levels. The loading value for each ion quantifies the ion's contribution to that EM. Therefore, an ion with a high loading for an EM is present primarily over the range of depth levels where that EM has high scores.

Through interpretation of the NMF results using the ions' original loadings, chemical information about the sample can be interpreted in terms of the four endmembers. However, this is hindered by the dominance of high intensity ions which have very high loadings in multiple endmembers, including those that do not describe their depth profile behaviour. Such high intensity ions can be a common issue in SIMS (78, 170) due to differences in the relative sensitivity of different types of chemistry (121, 126). This produces a convolution of endmembers, particularly for EMs 1-3, whereby these ions have high loadings across multiple endmembers and therefore they appear to be shared by these endmembers.



Interpretation of the highest loading ions (the highest 20 for each EM can be found in Appendix Table A19) finds EM 1 has considerable sulfur content as sodium, calcium and magnesium sulfates ( $\text{NaCaS}_2\text{O}_8^-$ , EM 1 normalised-to-maximum loading = 0.62;  $\text{MgSO}_5\text{H}^-$ , 0.29) and ABS ions ( $\text{C}_8\text{H}_7\text{SO}_3^-$ , EM 1 = 0.33). EM 1 is also characterised by organics, with a high loading for a nitrogenous ion ( $\text{C}_7\text{H}_3\text{N}_2^-$ , EM 1 = 0.26). Sodium chlorides are high in EM 1



( $\text{NaCl}_2^-$ , 1.00), but chloride salts appear more numerous in EM 2, with sodium, magnesium and calcium represented in EM 2 ( $\text{NaCl}_2^-$ , EM 1 = 1.00;  $\text{MgCl}_3^-$ , EM 1 = 0.12;  $\text{CaCl}_3^-$ , EM 1 = 0.14). Some chloride salts in EM 2 also contain cyanide and cyanate ( $\text{NaCNOCl}^-$ , EM 1 = 0.27) as well as sulfate ( $\text{Na}_2\text{SO}_4\text{Cl}^-$ , EM 1 = 0.12). EM 3 has the highest sulfate/sulfite character, with sodium and magnesium salts appearing here ( $\text{Na}_3\text{S}_2\text{O}_8^-$ , EM 1 = 0.76;  $\text{MgSO}_5\text{H}^-$ , EM 1 = 0.54). EM 4 is clearly a carbonaceous layer, primarily composed of pure carbon ions ( $\text{C}_8^-$ , EM 1 = 1.00), with some  $\text{C}_x\text{H}^-$  ions with generally slightly lower loadings ( $\text{C}_{10}\text{H}^-$ , EM 1 = 0.54). Salts of chlorides and sulfates also maintain a signal in this region and appear with high loadings ( $\text{NaCl}_2^-$ , EM 1 = 0.52;  $\text{NaS}_2\text{O}_8^-$ , EM 1 = 0.19).

In this NMF, mixing of endmembers occurs to such an extent that  $\text{NaCl}_2^-$ , the most intense ion by more than an order of magnitude, has a normalised-to-maximum loading of 1.00 for EMs 1-3, with also a high loading in EM 4 (0.52). To understand an endmember, its loadings must often be compared to other endmembers to determine if ions have significant, or greater, character in another endmember. Endmembers can be compared using an endmember combination method in simsMVA which was tested using EMs 1 and 2 of Needle 6's negative polarity depth profile NMF and can be found in Appendix Section 2.4. Some deconvolution of two endmembers could be achieved, though primarily ions of the highest intensity are still dominant in each endmember and further issues would occur if using this method to understand all endmembers especially for bulk endmembers. Therefore, a new method was developed which would allow efficient comparison of endmember loadings in order to understand the NMF results.

#### 4.2.3.1.1.2 Method Development: Comparative Method

This section will describe the development of the new method (given the name "Comparative Method") for NMF interpretation. This method is described in Section 2.3.3.3.2.1 and its application to the negative polarity profile of Needle 6 will be discussed in detail in this section to demonstrate how in-depth analysis can be achieved.

Since interpretation of NMF was hindered by convolution of endmembers, the ions were filtered in each endmember's loadings to show only ions that have their highest loading in the respective endmember (shown in Figure 4.9). The resulting loadings for each endmember therefore only include ions that are most associated with that endmember's score curve, removing those that are more prevalent elsewhere in the depth profile. This provides a clearer overview of which ions are characteristic of which pseudo-layer.

Secondly, as a supplementary tool for representing an ion's distribution across the four endmembers, a new loadings normalisation parameter was calculated and given the name 'relative loading'. This is calculated by normalising the loadings of the respective ion to the sum of that ion's loadings in all endmembers. Thus, the ion's loadings distribution is quantified. In this work, this is expressed as a percentage with the unit %EM. Hence, an ion's depth behaviour can be understood in terms of the distribution of its loadings across the endmembers in relation to their score curves. For example, an ion scoring 100% in EM 1 is found only at that region, while another ion with 50% EM 1 and EM 2 is split across those regions. A visualisation of this normalisation can be seen in Figure 4.8. Examples of depth profiles for a range of %EM loadings for each endmember can be found in Appendix Figure A12, where the higher the %EM for an ion, the more characteristic that ion is of the pseudo-layer represented by that endmember. It should be noted that an ion that does not fit strongly into one endmember (e.g. having 25%EM in each endmember) can also reveal valuable information, in this case that the ion is significant at the depth region of each endmember and is therefore significant throughout the profile. This is a novel post-processing parameter for NMF analysis that has not been reported in literature examples.

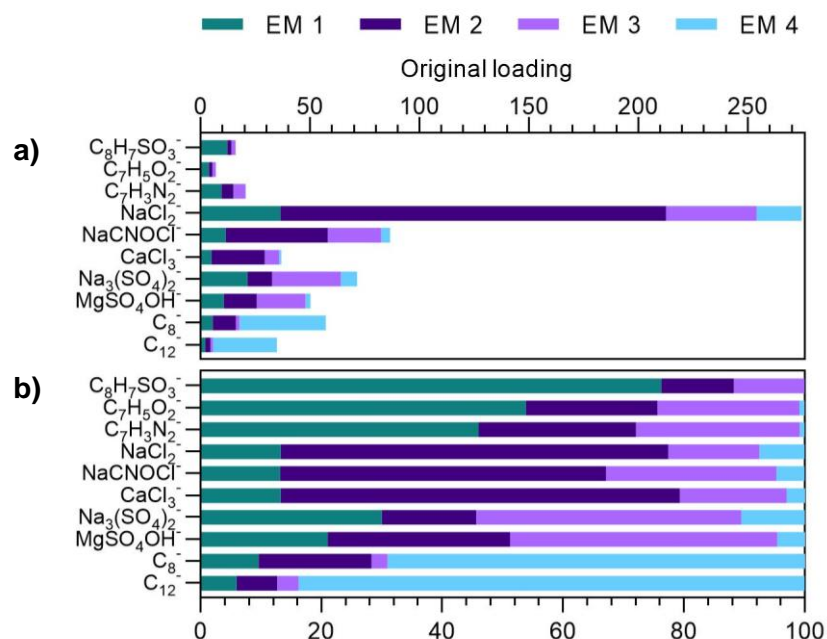


Figure 4.8: Example ions' loadings for Needle 6 in negative polarity. a) Original loadings from simMVA NMF results. b) Relative loadings after normalisation in Equation 6.

Further details of the comparative method can be found in Appendix Section 2.6.

#### 4.2.3.1.1.3 Negative polarity OrbiSIMS NMF results overview using Comparative Method

The filtered loadings for Needle 6's negative polarity depth profile NMF are shown in Figure 4.9. The data for key high loading ions for each endmember is shown in Table 4.2 with additional ions at the bottom that are highly distributed across several endmembers.

This method reveals further character about the layers than the original loadings method, which will be described here. EM 1 has high sulfur content in the form of calcium and sodium (mostly mixed together) sulfates that are also high in EM 3 ( $Na_3CaS_3O_{12}^-$ : 50 %EM1, 40 %EM3). Alkylbenzene sulfonates and other organics are also dominant in EM 1 (61-76 %EM1). EM 2 has a large presence of chlorides of both sodium and calcium and sodium cyanide/cyanate, which also have presence in EMs 1 and 3 ( $NaCl_2^-$ : 64 %EM2, 13 %EM1, 15 %EM3;  $CaCl_3^-$ : 66 %EM2, 13 %EM1, 18 %EM3). In EM 3, sulfates of

sodium and magnesium are strong ( $\text{Na}_3\text{S}_2\text{O}_8^-$ : 44 %EM3;  $\text{MgSO}_5\text{H}^-$ : 44 %EM3), with many mixed with other anions including chlorides, cyanides and cyanates (e.g.  $\text{MgSO}_4\text{CNO}^-$ ,  $\text{Na}_3\text{SO}_4\text{ClCN}^-$ ).

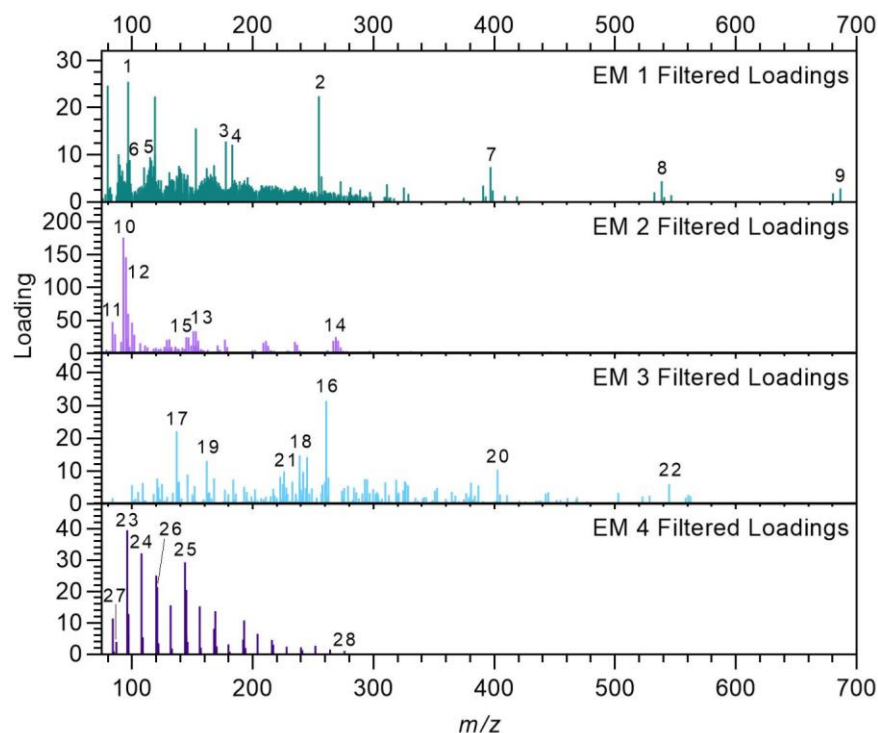


Figure 4.9: Loadings plots for each endmember after filtering to remove ions that have a higher loading in another endmember.

EM 4 is clearly carbonaceous, but here it can be seen that the  $\text{C}_{10}\text{H}^-$  and  $\text{C}_6\text{NH}^-$  ions have more presence in EMs 1-3 than  $\text{C}_x^-$  ions (56 and 40 %EM4 vs. 69-84 %EM4 respectively), likely indicating a lower hydrogen and nitrogen content in the lower material while the upper deposit has more of this content. This is further supported by the  $\text{C}_{13}\text{H}_3^-$  ion which is highly distributed across all endmembers; with its higher H:C ratio it exists more in the upper deposit compared to  $\text{C}_{10}\text{H}^-$  and  $\text{C}_{13}\text{H}^-$ , which in turn are more distributed than purely carbon ions (e.g.  $\text{C}_8^-$  and  $\text{C}_{12}^-$ ). Another highly distributed ion,  $\text{CaMg}(\text{SO}_4)_2\text{OH}^-$ , being a mixed ion of calcium (found more in EM 1) and magnesium (found more in EM 3) sulfate and hydroxide, is split between EMs 1 and 3, with some presence in EM 2. This method will be used to assess the data in-depth for both polarities of Needles 6-8's depth profiles, with detailed discussion in Section 4.2.3.2 and a summary in Figure 4.10 alongside the XPS depth profile data.

Table 4.2: Needle 6 negative polarity depth profile NMF results for key ions with ID numbers from Figure 4.9, loadings and relative loadings, separated by which endmember their loading is highest for. Additional ions shown at the bottom which are highly distributed across multiple endmembers. Heat map applied to each column: for original loadings green = maximum value and red = minimum, for relative loadings green = 100 and red = 0.

I D	m/z	ID	Peak area (norm)	Original loading				Relative loading (%EM)			
				1	2	3	4	1	2	3	4
1	96.9599	SO <sub>4</sub> H <sup>-</sup>	6.8×10 <sup>-3</sup>	25.5	18.6	4.1	1.2	51.6	37.6	8.3	2.4
2	254.8566	NaCaS <sub>2</sub> O <sub>8</sub> <sup>-</sup>	2.8×10 <sup>-1</sup>	22.5	5.9	12.3	2.2	52.5	13.7	28.7	5.1
3	177.9128	CaSO <sub>4</sub> CNO <sup>-</sup>	1.9×10 <sup>-3</sup>	12.9	5.6	7.8	0.6	47.9	20.8	28.9	2.4
4	183.0119	C <sub>8</sub> H <sub>7</sub> SO <sub>3</sub> <sup>-</sup>	6.2×10 <sup>-4</sup>	12.2	1.9	1.9	0.0	76.3	12.0	11.7	0.0
5	119.0501	C <sub>8</sub> H <sub>7</sub> O <sup>-</sup>	5.3×10 <sup>-4</sup>	10.2	2.3	2.3	0.1	68.5	15.6	15.5	0.4
6	98.0246	C <sub>4</sub> H <sub>4</sub> NO <sub>2</sub> <sup>-</sup>	5.4×10 <sup>-4</sup>	8.9	2.9	2.6	0.3	60.5	19.5	18.0	2.0
7	396.7878	Na <sub>3</sub> CaS <sub>3</sub> O <sub>12</sub> <sup>-</sup>	5.6×10 <sup>-4</sup>	7.4	1.1	6.0	0.6	49.5	7.3	39.6	3.7
8	538.7193	Na <sub>5</sub> CaS <sub>4</sub> O <sub>16</sub> <sup>-</sup>	1.1×10 <sup>-4</sup>	4.4	0.0	2.5	0.1	62.7	0.0	35.3	2.0
9	686.6673	Na <sub>9</sub> S <sub>5</sub> O <sub>20</sub> <sup>-</sup>	7.5×10 <sup>-5</sup>	2.9	0.0	2.6	0.1	51.5	0.0	46.8	1.7
10	92.9278	NaCl <sub>2</sub> <sup>-</sup>	2.8×10 <sup>-1</sup>	36.4	176.2	41.4	20.6	13.3	64.2	15.1	7.5
11	83.962	NaCNCl <sup>-</sup>	2.3×10 <sup>-2</sup>	7.6	47.5	18.9	2.3	9.9	62.3	24.7	3.0
12	99.957	NaCNOCl <sup>-</sup>	2.6×10 <sup>-2</sup>	11.4	46.7	24.4	4.1	13.2	54.0	28.2	4.7
13	150.8865	Na <sub>2</sub> Cl <sub>3</sub> <sup>-</sup>	1.3×10 <sup>-2</sup>	9.9	33.5	15.6	4.0	15.7	53.3	24.7	6.4
14	268.8013	Na <sub>4</sub> Cl <sub>4</sub> <sup>37</sup> Cl <sup>-</sup>	9.5×10 <sup>-3</sup>	8.2	24.8	16.9	6.4	14.6	44.1	30.0	11.3
15	144.8696	CaCl <sub>3</sub> <sup>-</sup>	5.5×10 <sup>-3</sup>	4.9	24.4	6.5	1.1	13.3	66.1	17.7	3.0
16	260.8736	Na <sub>3</sub> S <sub>2</sub> O <sub>8</sub> <sup>-</sup>	1.2×10 <sup>-2</sup>	21.5	11.2	31.4	7.5	30.0	15.6	43.9	10.5
17	136.9399	MgSO <sub>5</sub> H <sup>-</sup>	7.4×10 <sup>-3</sup>	10.5	15.1	22.2	2.3	21.0	30.2	44.3	4.5
18	238.879	NaMgS <sub>2</sub> O <sub>8</sub> <sup>-</sup>	2.8×10 <sup>-3</sup>	8.9	6.1	14.8	1.0	28.9	19.9	48.1	3.1
19	161.9352	MgSO <sub>4</sub> CNO <sup>-</sup>	3.0×10 <sup>-3</sup>	8.2	9.7	13.1	0.3	26.2	31.0	42.0	0.8
20	402.8045	Na <sub>5</sub> S <sub>3</sub> O <sub>12</sub> <sup>-</sup>	1.2×10 <sup>-3</sup>	7.0	1.7	10.5	1.6	33.7	8.3	50.5	7.5
21	225.8934	Na <sub>3</sub> SO <sub>4</sub> CICN <sup>-</sup>	1.4×10 <sup>-3</sup>	2.0	7.2	9.9	0.7	9.9	36.4	50.1	3.6
22	544.7363	Na <sub>7</sub> S <sub>4</sub> O <sub>16</sub> <sup>-</sup>	3.7×10 <sup>-4</sup>	4.8	0.7	6.0	0.4	40.7	5.7	50.5	3.1
23	96.0003	C <sub>8</sub> <sup>-</sup>	6.2×10 <sup>-3</sup>	5.5	10.7	1.5	39.5	9.6	18.7	2.7	69.1
24	108.0005	C <sub>9</sub> <sup>-</sup>	3.4×10 <sup>-3</sup>	3.1	5.0	1.0	32.2	7.5	12.1	2.5	77.9
25	144.0004	C <sub>12</sub> <sup>-</sup>	2.6×10 <sup>-3</sup>	2.1	2.3	1.2	29.3	6.0	6.7	3.5	83.8
26	121.0083	C <sub>10</sub> H <sup>-</sup>	2.7×10 <sup>-3</sup>	5.2	6.0	5.8	21.4	13.5	15.8	15.0	55.7
27	87.0112	C <sub>6</sub> NH <sup>-</sup>	2.2×10 <sup>-4</sup>	1.9	2.5	1.8	4.0	19.0	24.0	17.4	39.6
28	276.0005	C <sub>23</sub> <sup>-</sup>	5.0×10 <sup>-6</sup>	0.1	0.1	0.2	1.1	8.4	3.6	11.9	76.0
	157.0082	C <sub>13</sub> H <sup>-</sup>	5.5×10 <sup>-5</sup>	1.3	1.2	1.1	1.5	24.7	24.2	22.4	28.7
	159.0239	C <sub>13</sub> H <sub>3</sub> <sup>-</sup>	5.8×10 <sup>-6</sup>	0.4	0.5	0.4	0.2	28.6	31.2	28.0	12.2
	272.8546	CaMg(SO <sub>4</sub> ) <sub>2</sub> OH <sup>-</sup>	4.9×10 <sup>-6</sup>	0.4	0.3	0.5	0.2	30.7	22.0	36.3	11.0
	90.9711	CaO <sub>3</sub> H <sub>3</sub> <sup>-</sup>	6.0×10 <sup>-6</sup>	0.7	0.3	0.4	0.3	40.7	18.7	25.0	15.6
	149.0395	C <sub>12</sub> H <sub>5</sub> <sup>-</sup>	6.4×10 <sup>-6</sup>	0.5	0.5	0.5	0.1	29.6	28.8	33.8	7.8

#### 4.2.3.2 Characterisation of IDID Pseudo-layers from OrbiSIMS-NMF and XPS of Needles 6-8

The comparative method was applied to all depth profiles in this work (negative and positive polarity for Needles 6-8). Overviews of the high loading ions for Needle 6 positive polarity and Needles 7 and 8 can be found in Appendix Section 2.8 while detailed summaries and conclusions for each sample are shown and discussed in this section.

In each sample, the score curves separate the profile into four relatively distinct pseudo-layers. There are transitional stages between them where their chemistries overlap, therefore the pseudo-layers likely do not relate to real distinct deposit layers but represent trends in deposit chemical variation with depth. The OrbiSIMS NMF scores (Figure 4.10a-b, d-e, g-h) generally show agreement between each polarity, with interfaces at sputter times/primary ion doses shown in Table 4.3. In Needles 6 and 8, EM 1 is relatively surface exclusive, particularly for Needle 8 where it is removed after only 300-400 seconds of sputtering. In Needle 6, the dose density at the interfaces in each respective polarity's profiles was similar and indicates a heterogeneous deposit of similar thickness at both polarities' positions. The other samples show more variation, particularly Needle 7, where the positive polarity profile required a much longer etch time to reach the suspected DLC substrate, indicating a thicker deposit and therefore likely a more heterogeneous deposit coverage in this sample.

Table 4.3: OrbiSIMS depth profile NMF score interfaces for Needle 6, Needle 8 and Needle 7 in both polarities.

		<b>Etch time /s (primary ion dose density /ions cm<sup>-2</sup>) to reach EM X – Y interface</b>		
<b>Sample</b>	<b>Polarity</b>	<b>EM 1 – 2</b>	<b>EM 2 – 3</b>	<b>EM 3 – 4</b>
Needle 6	Negative	1000 (1.78×10 <sup>15</sup> )	4600 (8.19×10 <sup>15</sup> )	12200 (2.17×10 <sup>16</sup> )
	Positive	1300 (2.31×10 <sup>15</sup> )	3200 (5.70×10 <sup>15</sup> )	10900 (1.94×10 <sup>16</sup> )
Needle 8	Negative	310 (5.52×10 <sup>14</sup> )	5960 (1.06×10 <sup>16</sup> )	24700 (4.40×10 <sup>16</sup> )
	Positive	370 (6.59×10 <sup>14</sup> )	27900 (4.97×10 <sup>16</sup> )	46300 (8.24×10 <sup>16</sup> )
Needle 7	Negative	4100 (7.30×10 <sup>15</sup> )	16100 (2.87×10 <sup>16</sup> )	31800 (5.66×10 <sup>16</sup> )
	Positive	10500 (1.88×10 <sup>16</sup> )	71500 (1.28×10 <sup>17</sup> )	147000 (2.62×10 <sup>17</sup> )

For Needle 7, changes in surface potential were made due to loss of signal (described in Section 2.3.3.1) at two points (16100s, 2.87×10<sup>16</sup> ions cm<sup>-2</sup> and 31800s, 5.66×10<sup>16</sup> ions cm<sup>-2</sup>, marked with dotted lines in Figure 4.10g), which became two of the endmember interfaces.

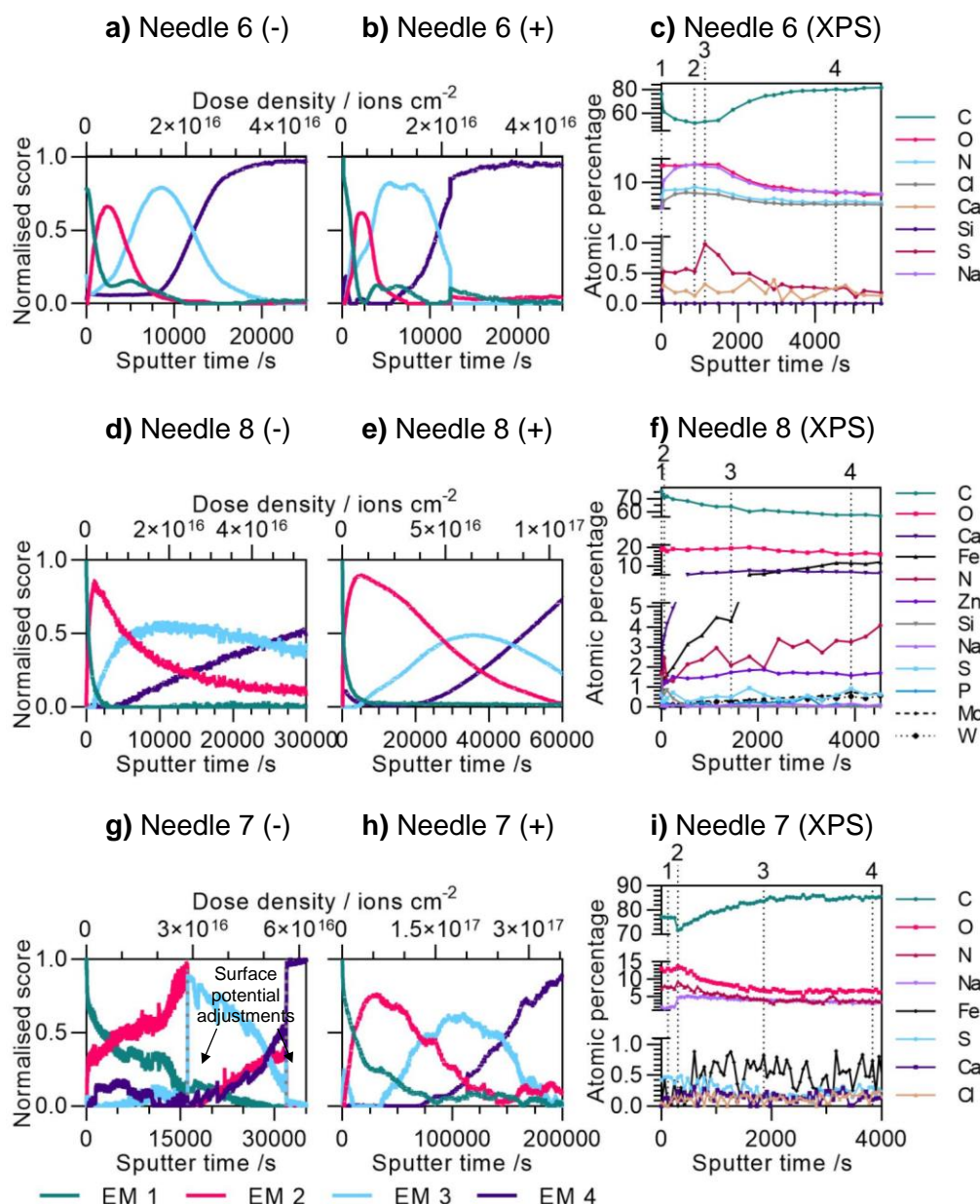


Figure 4.10: OrbiSIMS depth profile NMF scores for negative and positive polarity and XPS atomic percentage depth profiles for Needles 6-8.

Atomic percentage depth profiles from XPS are used to support the OrbiSIMS results with quantitative data (Figure 4.10c, f, i) which also show depth variations for all samples. Regions characteristic of each endmember were identified (labelled 1-4 for each sample in Figure 4.10c, f, i) and the quantification from these positions is used to contextualise each EM's OrbiSIMS data.



An overview of the key chemistries (OrbiSIMS ions and XPS elements)

characterising each pseudo-layer of each sample is shown in Figure 4.11.

These summaries are based on in-depth tables of each sample's results which can be found in Appendix Section 2.8 and which interpret the ions' depth behaviours based on their distributions across the endmembers.

	EM 1	EM 2	EM 3	EM 4
a) Needle 6	OrbiSIMS	OrbiSIMS	OrbiSIMS	OrbiSIMS
	ABS, small polyaromatics, Na-carboxylates, succinimides. Sulfate inorganics (Ca, Na, Fe).	Chloride, cyanide, cyanate inorganics (mainly Na, some K, Ca, Mg). Carbonaceous with some H, S, P.	Sulfate, carbonate inorganics (mainly Na, some K, Ca, Mg, Cu, Fe);	Carbonaceous: likely DLC substrate combined with deposit material.
XPS	C: 68.4 at.% O: 16.0 at.% Na: 6.1 at.% Cl: 2.3 at.% N: 6.6 at.% S: 0.4 at.%	C: 52.8 at.% ▼ O: 16.1 at.% Na: 16.0 at.% ▲▲ Cl: 6.6 at.% ▲▲ N: 8.0 at.% ▲ S: 0.5 at.%	C: 53.5 at.% O: 16.5 at.% Na: 15.3 at.% ▼ Cl: 6.1 at.% ▼ N: 7.6 at.% ▼ S: 0.8 at.% ▲	C: 80.2 at.% ▲▲ O: 6.4 at.% ▼▼ Na: 6.8 at.% ▼▼ Cl: 2.7 at.% ▼▼ N: 3.4 at.% ▼▼ S: 0.2 at.% ▼▼
1.92 µm				
b) Needle 8	OrbiSIMS	OrbiSIMS	OrbiSIMS	OrbiSIMS
	ABS, larger polyaromatics, carboxylates, PDMS, sulfate salts (Ca, Mg, Na, Zn).	Carbonaceous, Ca inorganics (hydroxide, cyanide, cyanate, sulfate, PO <sub>2</sub> ), Ca-Zn oxide.	Ca-Fe hydroxides (and PO <sub>2</sub> ), Zn oxides and hydroxides, S- and P-containing carbonaceous.	Fe, Cr, Mo, V, W, Mn, oxides and hydroxides (steel needle substrate).
XPS	C: 74.1 at.% O: 19.4 at.% N: 1.7 at.% Ca: 1.7 at.% Zn: 0.8 at.% Fe: 0.9 at.% S: 0.3 at.%	C: 70.0 at.% ▼ O: 18.8 at.% ▼ N: 2.1 at.% ▲ Ca: 5.6 at.% ▲▲ Zn: 1.5 at.% ▲ Fe: 3.8 at.% ▲▲ S: 0.4 at.%	C: 63.4 at.% ▼ O: 19.6 at.% N: 2.1 at.% Ca: 6.6 at.% ▲ Zn: 1.8 at.% ▲ Fe: 4.4 at.% ▲ S: 0.4 at.%	C: 58.1 at.% ▼ O: 16.7 at.% ▼ N: 3.1 at.% ▲ Ca: 6.9 at.% ▲ Zn: 1.4 at.% ▼ Fe: 11.6 at.% ▲▲ S: 0.4 at.%
0.22 µm				
c) Needle 7	OrbiSIMS	OrbiSIMS	OrbiSIMS	OrbiSIMS
	ABS, small polyaromatics, Na-DDS, Na-HDS, Na-carboxylates, succinimides, fatty amines.	Mainly Na, some Ca inorganics (mostly sulfates, carbonate, some cyanide, cyanate).	More diverse Na and Ca inorganics; N-, S- and P-containing carbonaceous; N-organic.	Carbonaceous: likely DLC substrate combined with deposit material.
XPS	C: 76.4 at.% Na: 1.5 at.% O: 14.0 at.% N: 7.6 at.% S: 0.4 at.%	C: 72.2 at.% ▼ Na: 4.0 at.% ▲▲ O: 13.4 at.% ▼ N: 9.1 at.% ▲ S: 0.6 at.% ▲	C: 83.5 at.% ▲▲ Na: 3.9 at.% O: 7.6 at.% ▼▼ N: 3.8 at.% ▼▼ S: 0.2 at.% ▼	C: 84.1 at.% ▲ Na: 3.3 at.% ▼ O: 7.4 at.% N: 3.9 at.% S: 0.3 at.%
5.95 µm				

Figure 4.11: Summary of OrbiSIMS-NMF (from both polarities) and XPS key results for Needles 6-8 depth profiles, with deposit thickness estimate from profilometry of OrbiSIMS depth profile average crater depth. XPS element concentrations are marked with ▲ where there is an increase from the previous pseudo-layer and ▼ where there is a decrease (with 2 arrows marking a more significant increase/decrease and no arrow where no significant change occurs).



#### 4.2.3.2.1 Discussion of Pseudo-layers

##### 4.2.3.2.1.1 Organic Surface Pseudo-layer: EM 1

The surface pseudo-layers represented by EM 1 across Needles 6-8 share similarities, with all representing a high organic content with many chemistries in common, some of which can be related to additives of fuel and lubricant oil. A largely organic surface is supported by XPS, with all samples having a higher carbon content in the region corresponding to EM 1 than that of EM 2-3 (Needle 6: 68.4 at.%, Needle 8: 74.1 at.%, Needle 7: 76.4 at.%). The organics show many functional groups containing heteroatoms, with XPS also showing high oxygen content, as well as significant presence of nitrogen and a trace of sulfur which indicates that ABS are in very low concentration.

Needles 6-8 all share ABS, polyaromatics and carboxylate content in EM 1. Some of these are in different forms: Needle 8 reaches higher masses for polyaromatic and ABS ( $\text{C}_{29}\text{H}_{51}\text{SO}_3^-$ ) ions than Needles 6 and 7 and likely indicate a harsher injector environment in Needle 8 as was noted in Sections 3.2.3.1 and 3.2.4.3.1, respectively. The carboxylates in Needle 8 are carboxylate anions such as stearate ( $\text{C}_{18}\text{H}_{35}\text{O}_2^-$ ) while Needles 6 and 7 both have sodium carboxylates and succinates from the DDS-Na that was noted in Section 3.2.4.2.

Needles 6 and 7 have ions consistent with succinimides ( $\text{C}_4\text{H}_2\text{NO}_2^-$ ,  $\text{C}_6\text{H}_6\text{NO}_2^+$ ,  $\text{C}_7\text{H}_8\text{NO}_2^-$ ) which are absent in Needle 8 and likely originate from LMW PIBSI as seen in Section 3.2.4.1. XPS finds a higher nitrogen concentration in the region of EM 1 for Needle 6 (6.6 at.%) and Needle 7 (7.6 at.%) compared to Needle 8 (1.7 at.%), suggesting this nitrogen content may have come from LMW PIBSI. Needle 7 also uniquely contains fatty amines in EM 1 ( $\text{C}_{26}\text{H}_{56}\text{N}^+$ ,  $\text{C}_{14}\text{H}_{32}\text{N}^+$ ) which may, alongside the ABS ions, indicate lubricant oil contamination, in which such amines are used as friction modifier additives (80, 191, 192).

The high organic content of the surface pseudo-layer may be due to a stronger adherence of such material to initial salt deposit layers than to the needle

substrate. It may also suggest a deposit formation mechanism whereby more complex organics graphitise over time, losing functional groups and hydrogen content to form lower carbonaceous material as well as potentially the cyanide, cyanate and carbonate anions seen in inorganic salts of lower layers. Therefore, the newer chemistry deposited at the surface would be less degraded. Some surface material is also likely from surface contamination such as from the container, skin or other materials. For analysis of organic deposit components, OrbiSIMS represents a significant development in IDID analysis over the ToF-SIMS work discussed in Section 1.3.3.2. Previous ToF-SIMS depth profiling concluded with a deposit layers model only in terms of inorganic components and inorganics dominated other previous ToF-SIMS investigations of deposit surfaces (38, 39, 47, 128).

#### **4.2.3.2.1.2 Carbonaceous Ions Located in EMs 2-4**

Carbonaceous ions have higher %EM values in EMs 2-4 than the organics which have been shown to dominate EM 1 all samples. This supports a carbonisation process over time as described in Section 1.2.2.3 and indicated in 3.2.3.1.1. Convolution of deposit and DLC substrate carbonaceous ions occurs in Needles 6 and 7, which will be discussed in Section 4.2.3.2.1.4.

In Needles 6 and 8, carbonaceous ions with small numbers of hydrogen or heteroatoms such as the series of  $C_xH_{1-3}^-$ ,  $C_xN^-$  and  $C_xS^-$  are most prevalent in EM 2, underneath the mostly organic EM 1. As these ions contain hydrogen and heteroatoms they are likely deposit-related rather than DLC. Needle 7 instead shows more hydrogen-saturated nitrogenous ions in EM 2 such as  $C_5H_7N_2^+$  (42 %EM2) and  $C_8H_4N^-$  (43 %EM2), supported by an increase in nitrogen in XPS from 7.6 at.% at EM 1 to 9.1 at.% at the region corresponding to EM 2. Some of these persist into EM 3, however carbonaceous ions containing small numbers of hydrogen or heteroatoms predominate in EM 3 while XPS shows a decrease in nitrogen to 3.8 at.% and increase in carbon to 82.2 at.%, indicating that highly carbonaceous material is being exposed, with much of this therefore likely being DLC with smaller amounts of deposit.

**4.2.3.2.1.3 Sodium and Calcium Content in Middle Pseudo-layers: EM 2-3**

In EMs 2 and 3, the inorganic content in each sample increases in comparison to EM 1. In Needles 6 and 7, this takes the form of sodium salts while Needle 8 is mostly calcium. This is shown in XPS however with a smaller increase than the very high intensities in SIMS suggest, where Needle 6 and Needle 7 increase in sodium towards their peak at EM 2 of 16.0 at.% and 4.0 at.% respectively while Needle 8 increases in calcium to 6.6 at.% by EM 3. Throughout their XPS depth profiles, Needles 6 and 7 have only a trace of calcium and Needle 8 only a trace of sodium ( $\leq 0.8$  at.%).

Needle 6 in its sub-surface OrbiSIMS data (EM 2) is dominated by sodium chlorides, as well as cyanides and cyanates, supported by its increasing chlorine (from 2.3 to 6.6 at.%) and nitrogen concentration (from 6.6 to 8.0 at.%) in XPS. There are smaller calcium, potassium and magnesium ions, however XPS finds that both potassium and magnesium are below detectable levels. Example ions in EM 2 include  $\text{Na}_2\text{Cl}^+$  (70 %EM2),  $\text{KNaCl}^+$  (76 %EM2),  $\text{NaCNCl}^-$  (62 %EM2), and  $\text{MgCl}_3^-$  (78 %EM2). While OrbiSIMS suggests this layer to contain significantly more chlorides than other layers, XPS shows the increase is in fact subtle, with a ratio of Cl:Na of 0.41 (compared to 0.36, 0.40 and 0.39 for EMs 1, 3 and 4 respectively). This is important evidence that depth variations in IDIDs are more subtle than previous investigations in the literature which have them as “layered”, implying discreet chemical layering (39, 40, 47). This shows the importance of XPS depth profiling for quantitative validation of OrbiSIMS data, detail that has not been achieved previously using other techniques; before this work, quantification was only achieved for the surface using XPS (40, 48).

In Needle 6, EM 3 remains high in sodium but with an increase in sulfate/sulfite and carbonate salts. XPS validates this, with an increase of sulfur from 0.4 at.% to its peak of 0.8 at.%. As with EM 2, OrbiSIMS also shows small intensities of potassium and magnesium which remain undetectable in XPS. Examples of ions among the highest %EM2 values are  $\text{Na}_3\text{SO}_4^+$  (43 %EM3),  $\text{KNa}_2\text{SO}_4^+$  (47 %EM3),  $\text{Na}_3\text{CO}_3^+$  (67 %EM3), and  $\text{KNa}_2\text{CO}_3^+$  (82 %EM3). As EM 3 is the pseudo-layer above the substrate, these

chemistries may represent the original nascent deposit and therefore may be the components that caused initial deposit formation. Thus, it is suggested that sodium contamination with a source of sulfates and carbonate was the cause of this IDID and injector failure.

In Needle 7, EM 2 appears to comprise sodium salts of mostly sulfur-containing anions, with smaller amounts of other anions (cyanate, cyanide and hydroxide), for example in  $\text{Na}_3\text{S}_2\text{O}_8^-$  (47 %EM2) and  $\text{NaC}_2\text{N}_2\text{O}_2^-$  (46 %EM2). This pseudo-layer containing higher sulfur content is supported by XPS as it reaches its peak of 0.6 at.%, however this remains a trace concentration. Ions more prevalent in EM 3 show a wider diversity, including carbide, amide and phosphate, with the cations also including calcium, magnesium, copper and iron, though these metals are at concentrations undetectable by XPS. EM 3 contains sodium carbides ( $\text{Na}_2\text{C}_{3,5,7}^+$ ) which are exclusive to the sub surface (with 0 %EM1), indicating they represent a combination of sodium inorganic content with the lower carbonaceous deposit chemistry. This may indicate an integration of sodium into carbonaceous deposit material.

Calcium salts are the dominant inorganics in Needle 8, with calcium reaching 6.6 at.% in the XPS depth profile region corresponding to EM 3. EM 2 shows the most diversity of salts, identifying mainly hydroxides, sulfates, phosphate, cyanides and cyanates. Towards EMs 3 and 4 these salts appear to integrate with the substrate, which will be discussed in Section 4.2.3.2.1.4. Needle 8's EM 3 and EM 4 also contain zinc, in EM 3 as sulfides with cyanide, cyanate and oxide ( $\text{ZnSCN}^-$ : 43 %EM3;  $\text{ZnSO}^-$ : 49 %EM3) and in EM 4 as oxides and hydroxides with some sulfide ( $\text{ZnO}_2^-$ ,  $\text{ZnSOH}^-$ ,  $\text{ZnO}_3\text{H}_3^-$ ; 47-53 %EM4). Positive polarity shows its presence with calcium in EM 2 as the intense ion  $\text{CaZnO}^+$ . Zinc does not appear to be part of the substrate as XPS shows a decrease in zinc concentration towards EM 4 from its peak at EM 3 (1.8 at.%). Zinc and calcium's relatively high content together in the sub-surface deposit indicates that lubricant oil contamination was likely responsible for the initial generation of this deposit. Additionally, EM 4 contains small phosphorus- and sulfur-containing anions ( $\text{PO}_3^-$  and  $\text{PSO}_2^-$ ), which may originate from the ZDDP additive in lubricant oil which likely contributes the zinc (80).

The range of cation and anion components of the inorganic salts in these samples include most inorganic chemistries identified in previous studies (Section 1.2.2.4.1) (2, 19, 61, 65). Thus, this work builds on these examples with OrbiSIMS identifying the inorganic salts with high sensitivity, specificity and with spatial information from depth profiling. Previous studies discussing sodium IDIDs generally focus on sodium carboxylate soaps as discussed in Section 1.2.2.4.1, however XPS of Needles 6-8 demonstrates the large quantity of inorganic sodium salts alongside carboxylates.

#### 4.2.3.2.1.4 Substrate Pseudo-layers: EM 4

Each depth profile indicated that the needle substrate was reached. In the case of Needles 6 and 7, their substrates appeared to be a sputter resistant DLC layer indicated by the high intensity of  $C_x^{+/-}$  carbonaceous ions that emerge in EM 4. This is supported by XPS, with a high carbon content in the region corresponding to EM 4. In both samples, H-containing carbonaceous ions are also significant in EM 4, though with smaller %EM4 values than  $C_x^{+/-}$  ions; this is suggested to indicate presence of deposit material that has less hydrogen in the deeper, older deposit, as with the depth profile shown in Figure 3.2.3.1.1.

Both Needles 6 and 7 also have some heteroatom-containing carbonaceous ions in EM 4, however again with generally lower %EM4 values than  $C_x^{+/-}$  ions. Examples for Needle 6 include  $C_{6-13}NH_{0-1}^-$  (to 40 %EM4) and for Needle 7 include  $C_{12}S^-$  (66 %EM4) and  $C_8O^-$  (94 %EM4). This is suggested to be carbonaceous heteroatom-containing deposit material accompanying the DLC substrate, likely resulting from integration of heteroatoms into deposit carbonisation processes as indicated in Section 3.2.3.1. The decrease in oxygen, nitrogen and sulfur towards EM 4 shown by XPS indicates that such material is a minor component in EM 4. Further work would be needed to distinguish DLC from carbonaceous deposit and the impact DLC has on deposit formation.

Needle 8's depth profile progressively reaches a steel needle substrate. Steel-associated elements (mainly Fe and Cr) first emerge in EM 2 as part of

hydroxide ions mixed with calcium where the number of Fe or Cr is 1 and the number of Ca is  $\geq 2$  ( $\text{Ca}_{\geq 2}\text{FeO}_x\text{H}_y^{+/-}$ ,  $\text{Ca}_{\geq 2}\text{CrO}_x\text{H}_y^{+/-}$ ). EM 3 contains similar ions with increased substrate element content (Ca 1-5 with Fe/Cr 1-2), indicating an integration of calcium with substrate in the deep deposit material close to the needle substrate. The progression with depth from calcium hydroxide to substrate hydroxide/oxide is observed as ions of higher Ca:M ratio generally have higher %EM2 and %EM3 while those of higher M:Ca ratio have a higher %EM4. For example,  $\text{Ca}_5\text{FeO}_{10}\text{H}_{12}^+$  (29 %EM2, 56 %EM3, 12 %EM4) with its higher calcium is more distributed towards EM 3 (and EM 2) than  $\text{CaFeO}_3^+$  (19 %EM2, 43 %EM3, 30 %EM4) which has a larger relative loading in EM 4. As EM 3 is the last pseudo-layer before the substrate, this suggests calcium may have combined with oxidised substrate material in the early stages of deposit formation. At EM 4, steel alloy metal (Fe, Cr, Mo, W, V, Mn) oxides and hydroxides dominate such as  $\text{FeO}_2^-$  (47 %EM4) and  $\text{Fe}_2\text{O}_5\text{H}_4^+$  (83 %EM4), indicating the final transition to substrate. Some calcium remains but in calcium-substrate metal hydroxide ions with a calcium number of 1 and substrate metal  $\geq 1$  with generally smaller %EM4 values than those without calcium (e.g.  $\text{CaCrO}_3^+$ : 68 %EM4). In a prior study, an oxidised metal layer was reported on the surface of a fouled needle beneath the deposit, seen using dynamic elemental ToF-SIMS in Section 1.3.3.2 (40, 47). However, this is the first work to reveal integration with deposit material (here, primarily calcium inorganic salts).

#### 4.2.3.2.1.5 Summary of Pseudo-layers for Needles 6-8

A schematic summarising the key chemistries of each deposit pseudo-layer is shown in Figure 4.12, with approximations for the thickness of each pseudo-layer assuming constant sputter rate throughout the depth profiles. Though sputter rates likely vary throughout the profile due to the changing deposit composition with depth, XPS quantification suggests that each deposit consists of a primarily carbon-containing matrix, making this assumption more reasonable despite the dominance of inorganic ions in certain pseudo-layers' OrbiSIMS datasets. The thickness of each pseudo-layer is estimated based on

the sputter time between EM interfaces; a summary of this data can be seen in Appendix Table A30.

Some similarities between the corresponding endmembers are present across the samples. EM 1, suggested to be the thinnest pseudo-layer with high organic content in each sample, has ABS compounds common to all samples and succinimides and sodium dicarboxylates found in Needles 6 and 7. EMs 2 and 3 generally show increased inorganic salt content that differs between samples, with Needles 6 and 7 being more sodium-based and Needle 8 containing more calcium. This contrasts with the initial ToF-SIMS IDID depth profiling investigation which suggested an inorganic IDID surface “coating” (Section 1.3.3.2) (47). In this NMF analysis, inorganics are found closer to the substrate and hence may be more fundamental to each deposit, playing a more crucial role in deposit initiation. Figure 4.12 shows the key data for each sample’s lower deposit layers as discussed through Section 4.2.3, including the sodium sulfate and carbonate of EM 3 in Needle 6, the lubricant oil-associated calcium, zinc, sulfur and phosphorus of EM 3 in Needle 8 and the more diverse inorganics of EM 3 in Needle 7. Towards EM 4, all samples reach their needle substrate, with Needles 6 and 7 showing a DLC nature while Needle 8 has a steel needle substrate. There is also evidence of a progression of carbonisation in all samples, with carbonaceous ions generally found in lower pseudo-layers than the organic material.

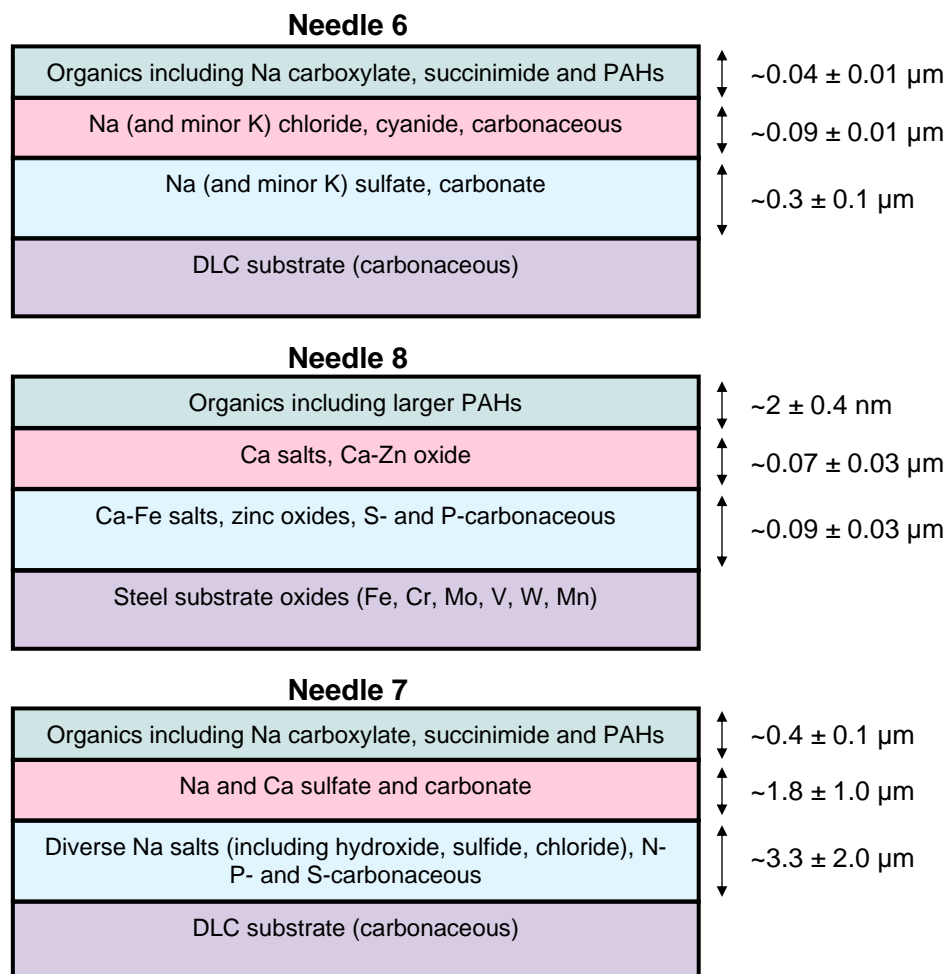


Figure 4.12: Schematic summarising key chemistries from Figure 4.11, with estimates for the thickness of each layer averaged from profilometry measurements (Table 4.1) for positive and negative depth profiles with error from the standard deviation, assuming constant sputter rates throughout each depth profile.

### 4.3 Conclusions

This chapter has demonstrated the capability of OrbiSIMS coupled with XPS depth profiling to provide much greater chemical detail than prior IDID investigations, particularly owing to OrbiSIMS's improved mass resolving power enabling unambiguous chemical assignments (78). This enabled a detailed characterisation of two IDIDs identified in prior work as differing significantly in composition. The crucial importance of IDID depth profiling is demonstrated, for both OrbiSIMS and XPS, as significant variation is seen throughout each profile where surface data alone would be misleading.



Manual interpretation of OrbiSIMS depth profiles suffers limitations from working with large amounts of data with spatial information. To overcome this, an NMF-based approach with a novel “Comparative” post-processing method was then applied to aid interpretation by simplifying three IDIDs’ OrbiSIMS depth profiles into macroscale models of four pseudo-layers. This post-processing consisted of filtering endmembers for their main chemistries and calculation of a new parameter (“relative loading”) to quantify an ion’s distribution throughout these layers, enabling probing of the nuances of their depth behaviour. Again, the findings from this investigation are validated by XPS to ensure reliable quantitative interpretation that cannot be achieved with SIMS, a semi-quantitative technique, alone. Compared to previous examples of IDID characterisation by ToF-SIMS and/or other techniques (40, 47, 59, 78, 128, 170, 193), this depth profile NMF method coupled with the improved mass resolution of OrbiSIMS has enabled larger scale, more accurate and more detailed findings that can be linked to real fuel and additive chemistries. Importantly the lower pseudo-layers identify chemistries that were likely responsible for the initial nascent deposit formation that could have triggered further build-up of the chemistries in higher pseudo-layers. Hence, components likely responsible for the deposit, such as sodium sulfates and carbonates in Needle 6 and lubricant oil additive components in Needle 8, are identified.

Each sample possesses a surface pseudo-layer of high organic content, underpinned by a range of inorganic salts, carbonaceous material and some persisting organic structures before reaching the needle substrate material. Some chemistries are consistent across all samples, though with some variation; all samples have ABS and polyaromatics towards the surfaces, however Needle 8 has evidence of larger masses of these compounds. Needle 6 and Needle 7, both originating from the Eastern USA are affected by sodium dicarboxylate salts and succinimides that may come from DDSA corrosion inhibitor additives and low quality LMW PIBSI additives (possibly from lubricant oil), respectively. Both these samples are highly affected by sodium, which increased concentration in the sub-surface and both share high intensity sulfur-containing anions (often sulfates) and carbonate in these salts, as well as a range of other chemistries, notably chloride in Needle 6 which is minimal in

Needle 7. These samples also share similar substrates, appearing to represent DLC coatings placed by the FIE manufacturer; one motivation for such coatings is deposit prevention, the failure of which is notable here (88). In contrast, Needle 8 from China has a steel substrate which is progressively reached via ions of mixed calcium-steel element ions, suggesting a pervasive calcium deposit content that integrated with substrate metals. Lower pseudo-layers here also contain hallmarks of lubricant oil, being phosphorus-, sulfur-, zinc- and calcium-containing chemistries.

Importantly for method development of deposit depth profiling with NMF interpretation, NMF of Needle 7's negative depth profile shows that comprehensive characterisation using this method is possible even when surface potential changes have been required mid-depth profile to mitigate a diminished secondary ion signal. This is likely to occur for many IDID samples due to the difference in conductivity between different types of deposit material (carbonaceous and inorganic salts) as well as the steel needle and DLC substrates that are uncovered during etching.

## **Chapter 5: Simulating Diesel Deposit Formation Using the Jet Fuel Thermal Oxidation Test for Chemical and Mechanistic Insights into IDID Composition**

### **5.1 Introduction**

This chapter will use the jet fuel thermal oxidation test (JFTOT), a laboratory bench test that is considered a good rudimentary simulation of an internal diesel injector environment (38, 139, 143), as a model to mimic real-world IDID formation utilising key fuel and additive components of interest to deposit formation. Prior IDID-related JFTOT research was discussed in Section 1.3.4 and the experimental rig and procedure used in this investigation, including samples produced that will be analysed in this chapter, can be found in Section 2.2. Here, the effects of different fuels and additives identified in previous work as either contributing to or present in IDIDs are investigated in the JFTOT system. These components were discussed throughout Section 1.2.2 and in the prior results chapters and include biodiesel, lubricant oil and sodium with DDSA. Thus, this work builds on previous work in this area using the improved mass resolving power of the Hybrid SIMS (IONTOF GmbH) and quantification from XPS to acquire new detail and information about IDID formation relating to key components of interest in a model system.

Five positions of each JFTOT tube were analysed with OrbiSIMS depth profiles, generally profiling through all deposit material to reach the aluminium or steel JFTOT tube substrate. This is the first application of OrbiSIMS and XPS to JFTOT samples or any laboratory simulation of an IDID. PCA was used to guide interpretation of OrbiSIMS data, ensuring efficient and accurate data interpretation that identifies key chemistries of interest and which samples are affected by them, therefore indicating which key fuel/additive components contribute these deposit chemistries. Replication of chemistries seen in real

world injector systems is achieved, with new insight into how they may form and from which components of interest.

Table 5.1: Motivation for the investigation of each JFTOT sample in this chapter.

<b>JFTOT ID</b>	<b>Motivation for investigation</b>
JFTOT RF-06	Study deposits produced by reference diesel (RF-06) alone.
JFTOT RME	Biofuels (RME, CME, HVO) have been implicated in previous studies as promoting deposit formation, as discussed in Section 1.2.2.5. Compounds of possible biological origin were also seen in Chapters 3 and 4, such as carboxylic acids and sodium salts. Study deposit produced from biofuels and if biomolecules are seen.
JFTOT CME	
JFTOT HVO	
JFTOT B7	Study deposits produced by a realistic biodiesel blend (7% RME).
JFTOT HVO50	Study deposits produced by a blend of reference diesel and HVO (HVO blending is possible to higher concentrations than biodiesel).
JFTOT Na + DDSA	Sodium contamination is well known to form soaps with carboxylic acids, commonly DDSA (Section 1.2.2.4.1). Study whether other acids are involved and the soap deposit's fate when heated.
JFTOT LMW PIBSI	LMW PIBSI is also well known to promote deposits (Section 1.2.2.6.1) and succinimides were observed in Chapters 3 and 4. Validate succinimide origin and study the deposit's fate when heated.
JFTOT Lubricant	Lubricant oil contamination can promote deposition particularly due to zinc (Section 1.2.2.4.4) which was seen in Chapters 3 and 4, alongside other likely lubricant oil components such as calcium and ABS. Validate lubricant origin for these chemistries and study any other chemistry contributed by lubricant.
JFTOT Zinc	Zinc is known to promote deposition (Section 1.2.2.4.3). Study by what mechanism this occurs and whether zinc neodecanoate integrates into deposit.
JFTOT 200 °C	Assess optimum temperature to perform JFTOT at as a test for simulation of carbonaceous/polyaromatic IDID formation.
JFTOT 250 °C	
Clean	Analyse with OrbiSIMS to produce dataset of substrate and contaminant ions for removal from PCA, to reduce contamination's convolution of data.

## 5.2 Results and Discussion

The results presented here will describe key types of deposit chemistry identified using PCA of JFTOT samples 1-10 (Section 2.2.3, Table 2.2) with OrbiSIMS data from positions 1-5. All PCA findings were validated by manual inspection of the original ion intensity data. Chemistries and their distributions were calculated using ion formula calculation using the `compound_finder` script. Elemental quantification from XPS provides validation and additional insights. PCA was performed separately on organics and inorganics using mass filtering pre-processing to prevent convolution and skew of data (method described in Section 2.3.3.3.1). Meaningful interpretations of this data are described with discussions of variation across samples, variation within depth profiles and relevance to real world IDID samples. Lastly, results from additional JFTOT samples using lower temperatures will be discussed to optimise the JFTOT as a system for the simulation of IDIDs. This is the first known application of OrbiSIMS and XPS to JFTOT deposit samples.

### 5.2.1 Hydrocarbon and Carbonaceous Deposit Chemistries in JFTOTs and an IDID using OrbiSIMS and XPS

A range of hydrocarbons, many with formulae matching PAH-type compounds, and carbonaceous ions were prevalent in all JFTOT samples except for JFTOT Na + DDSA and JFTOT CME. This section will discuss the JFTOT deposit hydrocarbon and carbonaceous results as identified by PCA, with investigation of further details and findings from OrbiSIMS depth profiling.

#### 5.2.1.1 Interpretation of Hydrocarbon and Carbonaceous JFTOT Deposit OrbiSIMS PCA with XPS Quantification

The JFTOT samples are separated by PCA according to their OrbiSIMS intensities of these ions (PC 1 in positive polarity, <0.7 mass filtered as described in Section 2.3.3.3.1, Figure 5.1a), finding JFTOT Na + DDSA with low PAH intensities which can be attributed to the nature of its deposit, being formed at a lower temperature (180 °C) and from a combination of sodium and DDSA which are known to form sodium carboxylates (discussed more in

Section 5.2.4) (2). The OrbiSIMS PCA scores in the negative direction relate to the intensities of PAHs, while the positive direction relates to DDSA-related material with PC 1 accounting for 50.3% of the variation between samples (Figure 5.1a). Samples with moderate PAH/carbonaceous content in OrbiSIMS are those expected to be chemically diverse due to the presence of heteroatoms and/or salts, for example from additives in lubricating oil (JFTOT Lubricant) and impurities in biodiesels (JFTOT RME). Being from a highly hydrocarbon fuel source with no dopant (i.e. no source of extra heteroatoms or inorganics), JFTOT RF-06 has amongst the highest PC 1 scores and hence highest hydrocarbon/carbonaceous intensities, though there are some samples with higher intensities, likely due to them containing PAH-type deposit-promoting components such as HVO in the case of JFTOT HVO50 and zinc or the steel JFTOT tube used in the case of JFTOT Zinc. The presence of PAHs and carbonaceous ions in the IDIDs of Section 3.2.3 were suggested to indicate a heat/pressure-driven carbonisation process of organic fuel which is supported here by their low intensities in the lower temperature JFTOT Na + DDSA however the suggested PAH-promoting components here could not be suggested from IDID data.

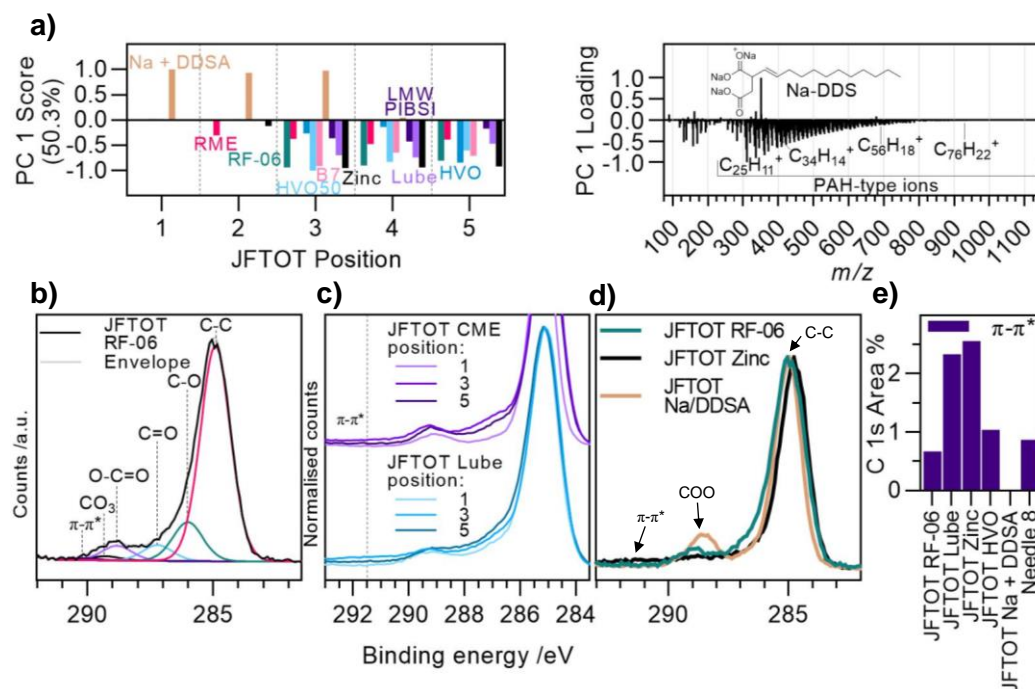


Figure 5.1: Hydrocarbon data for JFTOT samples and Needle 8. a) OrbiSIMS principal component 1 (mass filtered <0.7) in positive polarity scores and loadings. b) C 1s XP spectrum components model example for JFTOT RF-06. c) Overlay of C 1s XP spectra from positions 1, 3 and 5 for JFTOT CME and JFTOT Lubricant. d) Overlay of C 1s XP spectra for position 3 of JFTOT RF-06, JFTOT Zinc and JFTOT Na + DDSA. e) C 1s  $\pi$ - $\pi^*$  percentage area for key JFTOT and IDID samples.

In terms of lateral positions of the JFTOT tubes, PAH-type and carbonaceous OrbiSIMS ions are generally most intense at position 3 (the highest temperature position) after being very low at positions 1-2, then maintain high intensities through to position 5. This is seen in the PC 1 scores (Figure 5.1a), which are generally most negative at position 3, as well as in XPS quantification, based on high resolution C 1s component models like that for RF-06 shown in Figure 5.1b, where the spectra for JFTOT CME and JFTOT Lubricant (Figure 5.1c) show the largest  $\pi$ - $\pi^*$  contribution and hence aromatic content at position 3. The full JFTOT XPS data can be found in Appendix Section 0.

The scores for PC 1 also suggest HVO fuel is very stable, resisting deposition until position 5, evidenced by the lack of PAH/carbonaceous material until this point; it has less negative PC 1 scores than other samples at positions 3 and 4 though amongst the highest at position 5, where the fuel appears to break. This

is in line with the visible appearance of this sample, appearing clean until the final position where a deposit is present (Appendix 3.1). This result is interesting considering JFTOT HVO50 has the largest PAH/carbonaceous intensities at position 3 (seen in its large negative PC 1 score in Figure 5.1a), suggesting HVO can promote deposits in this blended system while these have somehow been mitigated with HVO alone, perhaps due to solubility differences or interactions between components of each fuel.

JFTOT Zinc, which used a steel JFTOT tube rather than aluminium and magnesium, has very high PAH/carbonaceous content shown by its PC 1 scores at positions 3-5 (Figure 5.1a). The high-resolution C 1s XP spectra from position 3 indicate this to be quantitatively true for polyaromatics and hence supports this sample being highly carbonised, having large  $\pi$ - $\pi^*$  satellite features and hence more aromatic content than RF-06 while JFTOT Na + DDSA lacks these features, instead having a strong acid component (seen in the overlaid spectra in Figure 5.1d). JFTOT Zinc, when charge referenced to the Fe 2p peak (707.1 eV) has a C-C component binding energy of 284.7 eV, consistent with increased  $sp^2$  content like that of polyaromatic or graphitic material (194). Indeed, JFTOT Zinc has the largest  $\pi$ - $\pi^*$  components of all samples (2.6%, Figure 5.1e), much larger than the field IDID that showed the largest polyaromatic structures (Needle 8 with 0.9%, as discussed in Section 3.2.3.1) which has a comparable  $\pi$ - $\pi^*$  component to JFTOT RF-06 (0.7%). This suggests that JFTOT RF-06 is a closer simulation of the real-world IDID than JFTOT Zinc based on polyaromatic concentration. HVO, which as discussed has little visible deposit until position 5, has significant polyaromatics at position 5, with a larger  $\pi$ - $\pi^*$  component (1.0%) than JFTOT RF-06 has at position 3.

Another PC (PC 6 in positive polarity, <0.7 mass filtered, representing 1.9% of variance) suggested that for many samples (JFTOT RF-06, RME, B7, and Zinc), later positions have progressed further along the deposition mechanism, resulting in a more carbonised material with a lower H:C ratio. The results for PC 6 are shown in Figure 5.2, separating the carbonaceous ( $C_x^+$ ) and low H:C ratio (e.g.  $C_{13}H_2^+$ ) hydrocarbon ions likely of semi-fullerene nature associated



with advanced carbonisation in the positive direction from those of higher H:C ratios, which have H numbers closer to PAH formulae, in the negative direction. JFTOT RF-06, RME, B7, and Zinc have larger positive scores (Figure 5.2) at later positions, indicating the advancement in carbonisation. An exception to this is the JFTOTs containing HVO (JFTOT HVO and HVO50) which show the opposite, suggesting lesser carbonisation at these positions, possibly due to higher stability as suggested by the very late break point for visible deposition seen for JFTOT HVO. Other exceptions to this are the JFTOTs that contain little PAH material (Na + DDSA, CME), JFTOT LMW PIBSI due to its uniquely nitrogenous chemistry (discussed in Section 5.2.2), as well as JFTOT Lubricant which is near neutral at all positions.

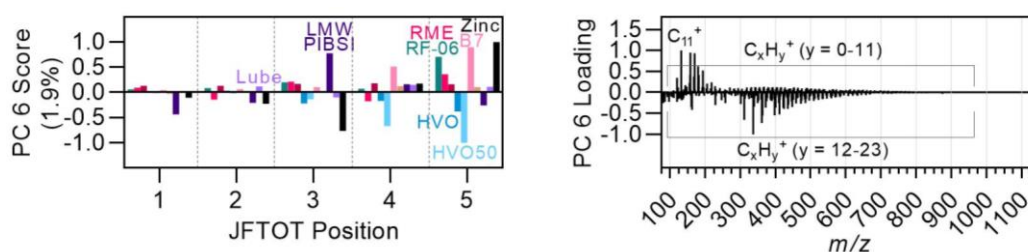


Figure 5.2: JFTOT OrbiSIMS principal component 6 (positive polarity, mass filtered <0.7), separating higher H-number hydrocarbons (negative loadings) from lower (positive).

The results from this section find large PAHs that are consistent across both real-world IDIDs and JFTOT deposits as a model system, confirmed with more chemical detail than any prior IDID/bench test investigation. Through PCA, a time-efficient and unambiguous approach, the samples can be characterised by their content of this material which indicates the level of carbonisation occurring at each position of each sample. Previous work applying ToF-SIMS to JFTOT deposits was unable to identify this sort of chemistry due to the lower mass resolving power with high fragmentation of chemistries occurring with use of an LMIG. PCA of that data found only small hydrocarbons (to  $C_7H_{11}^+$ ), small clusters of carbon (to  $C_8H^+$ ), small ions indicative of chemistries such as  $CNO^-$  and  $PO_3^-$  and elements ( $Na^+$ ,  $Ca^+$ ,  $K^+$ ). OrbiSIMS using a GCIB analysis beam is a crucial development to enable such characterisation of these extensively carbonised materials.

### 5.2.1.2 Comparisons of Polyaromatic Hydrocarbon 3D OrbiSIMS Ion Intensities and Distributions in JFTOTs and an IDID

The normalised intensities for a range of different mass positive polarity ions that have high loadings in PC 1 are shown in Figure 5.3a for JFTOTs that showed significant PAH content. JFTOT HVO, despite its unique deposit distribution, by position 5 has similar intensities of PAHs to the other samples, confirming that it develops a similar carbonaceous deposit. It has the highest intensity for the smaller ion  $C_{25}H_{11}^+$ , but for the larger ions JFTOT Zinc generally has the highest intensity, consistent with the PCA and XPS quantification that showed extensive carbonisation on this sample. For the largest ion shown ( $C_{80}H_{22}^+$ , circumcircumphyrene), its intensity is highest for JFTOT HVO50. This was the sample with the highest PC 1 score, and hence suggests that the blending of HVO with the RF-06 fuel has promoted larger and more extensive PAH formation, despite JFTOT HVO appearing to be the most stable fuel until position 5.

The same ions are shown in Figure 5.3b for Needle 8, which has much lower normalised intensities due to its strong inorganic and other organic content as was seen throughout Chapter 3. This IDID also has smaller PAHs than the JFTOT samples suggesting less carbonisation in the IDID, with a higher proportion of the smallest PAH relative to the larger ones and no peak present for  $C_{80}H_{22}^+$ . DBE vs.  $m/z$  fingerprint plots, calculated using the `compound_finder` script are shown in Figure 5.3c for JFTOT positions 1-5 and multiple positions along the IDID, for which temperature is expected to be higher at later positions (towards position 5) owing to the closer proximity to the combustion process and further distance from the cooling system. These plots use a minimum intensity threshold ( $>1 \times 10^{-5}$ ) normalised to the sum of ions of decimal mass  $<0.5$ , acting as a total intensity that includes all PAH-type ions and ignores inorganic ions. They show the wider distribution of these ions in JFTOT RF-06 than in the IDID and the much larger PAHs of JFTOT Zinc.

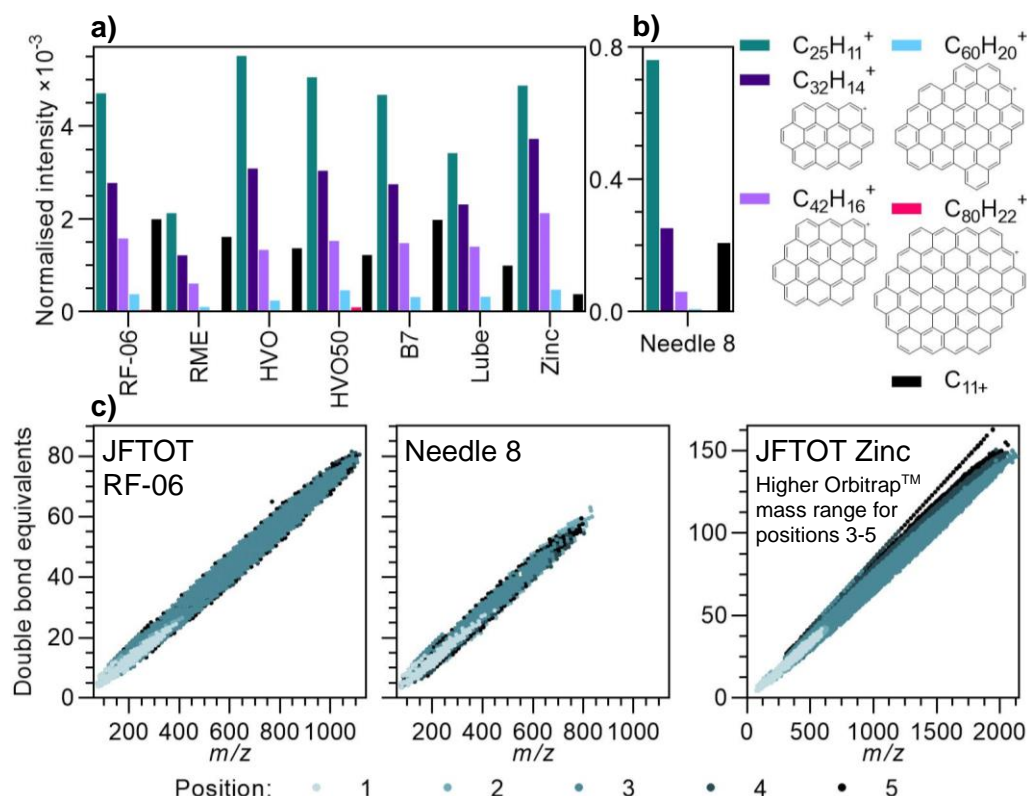


Figure 5.3: PAH/carbonaceous data from key JFTOT samples. a) Normalised secondary ion intensities of key PAH ions with high loadings for samples that had high scores in PC 1 (positive polarity,  $<0.7$  mass filter), all data from position 3 except HVO which is position 5, b) normalised intensities of those ions for Needle 8, c) DBE vs.  $m/z$  plots with intensity  $>1 \times 10^{-5}$  normalised to total of ions with decimal masses  $<0.5$  for each position of JFTOT RF-06, Needle 8, and JFTOT Zinc (using a higher cycle time and mass range).

Zinc, including in the form of the zinc neodecanoate salt used here, is known to promote deposits however its mechanism is unknown (Section 1.2.2.4.3).

These JFTOT results suggest it may strongly promote carbonaceous deposit formation, however this test used a steel tube while others used aluminium-magnesium, the former substrate potentially having catalytic activity beyond the scope of this work. Many species, including some metals, are known to catalyse aromatization from small hydrocarbons including methane (195, 196), the steel JFTOT tube is considered catalytic and a role of the substrate in diesel deposit formation has been indicated by Antonio *et al.*'s laboratory testing of diesel (101). Such substrate catalysis would be of note, as the field IDID sample of the highest PAH content (Needle 8) lacks a DLC, so the metal substrate may promote PAH formation while those with suspected DLCs generally appear to have less PAH content and smaller PAH ions.

### 5.2.1.3 Evidence of Carbonisation Mechanism from JFTOT RF-06

#### Hydrocarbon and Carbonaceous OrbiSIMS Depth Profiles

The depth profiles of hydrocarbon and carbonaceous ions in JFTOT RF-06's highly deposited positions (3 and 4) suggest a progression of carbonisation with increasing depth. The deeper material will be older and closer to the heated substrate so it is expected to be at a later stage of the formation process. Figure 5.4 shows depth profiles at position 3 of JFTOT RF-06, where ions thought to be associated with later stages of carbonisation are found deeper in the profile. Two trends evidence this, larger structures (Figure 5.4a, blue) and hydrocarbons of decreasing H:C ratio down to carbonaceous ions ( $C_x^+$ ) (Figure 5.4b) exist deeper than smaller structures and higher H:C ions. This mirrors the lateral trend from PC 6 in Figure 5.2, where H:C ratio generally decreased at later positions of the tube, suggesting the same progression of carbonisation occurs both laterally and with deposit depth. Figure 5.4c shows H number expressed as a function of C number at positions 3 and 4 of JFTOT RF-06 from the compound\_finder script with a colourmap applied for the time at which each ion reaches its maximum intensity. The larger distribution of hydrocarbons, extending to larger masses, can be seen in position 4 (where the largest ion is  $C_{89}H_{25}^+$   $m/z$  compared to  $C_{84}H_{22}^+$  at position 3) as well as the consistent trend for larger, less hydrogen-rich hydrocarbons existing deeper in the deposit. The progression of PAH growth and carbonisation likely progresses by a multitude of reaction pathways which were discussed in Section 1.2.2.3, likely involving similar reactions to those of the IDIDs in Section 3.2.3.1.1 such as HACA, Diels-Alder and MAC, leading to growth of semi-graphitic materials.

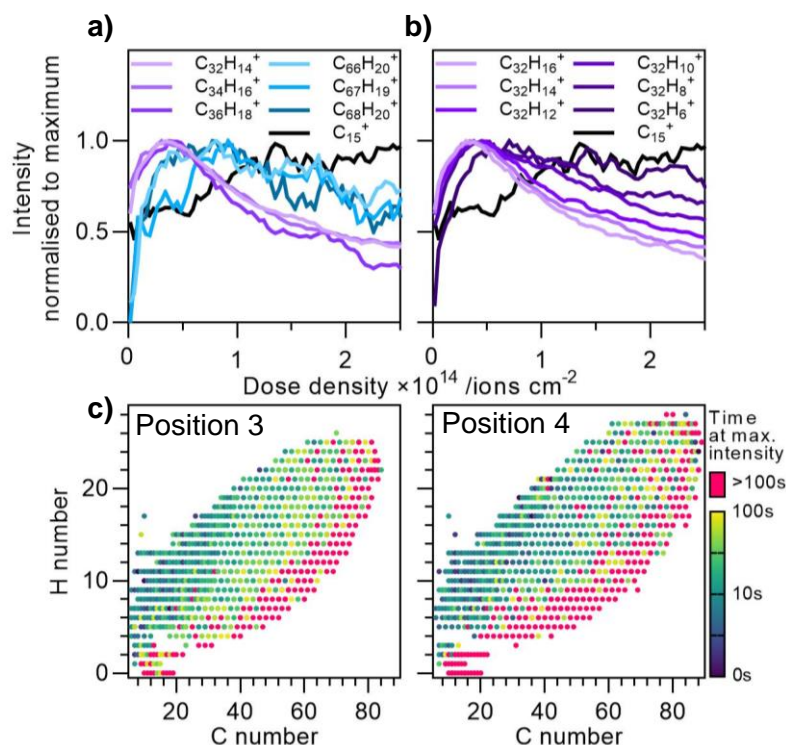


Figure 5.4: OrbiSIMS depth profile data for hydrocarbon secondary ions in JFTOT RF-06. Depth profiles of PAHs of a) increasing size and b) decreasing H/C ratio. c) H number as a function of C number for all hydrocarbons ( $>2.5\text{E-}5$  normalised intensity) at positions 3 and 4 with colourmap for sputter time at which each ion reaches its maximum intensity.

### 5.2.2 Nitrogen-Containing Deposit Chemistries in JFTOTs and IDIDs using OrbiSIMS and XPS

Nitrogenous organic and N-carbonaceous material ( $\text{C}_x\text{N}_y^{+/-}$ ) was present in nearly all JFTOT samples. This is unsurprising based on the presence of nitrogen species in the IDID samples in Section 3.2.3.1 which were attributed to the integration of nitrogen into deposit carbonisation, however the variation between the different JFTOTs herein provide new insights into possible origins of this chemistry. Ions are identified representing parts of the LMW PIBSI molecules, and other nitrogenous chemistries correlate with the JFTOT LMW PIBSI sample. There are literature examples of JFTOT tests involving amide polymer-forming compounds which formed deposits at  $<200^\circ\text{C}$  however there is no known characterisation of such deposits (142). The LMW PIBSI JFTOT experiment was performed as this lower quality form of PIBSI is indicated in the literature to increase deposit formation, as described in Section 1.2.2.6.1,

and evidence of succinimides and PIBSI species were seen in the IDIDs analysed in Section 3.2.4.1.

#### **5.2.2.1 Interpretation of Nitrogen-Containing JFTOT Deposit OrbiSIMS PCA with XPS Quantification and Comparison to IDIDs**

Nitrogen-containing organic/carbonaceous material was revealed through two PCs that separate nitrogenous content from other chemistries, one in positive polarity (Figure 5.5a, PC 4), including organic chemistries such as nitrogen-containing polyaromatic (N-PAC) type ions of one or multiple nitrogen atoms, and one in negative polarity (Figure 5.5b, PC 1) finding primarily N-carbonaceous ( $C_xN_{1-3}^-$ ) material. A high intensity N-PAC type ion ( $C_{24}H_{10}N^+$ ) in JFTOT LMW PIBSI was assessed with MS/MS, supporting its assignment through fragmentation via loss of carbon and hydrogen atoms (Table 5.2) with a lower collision energy showing less fragmentation than higher (Appendix Table A38). Full MS/MS results can be found in Appendix 3.5.1. As the inclusion of LMW PIBSI in this JFTOT results in much greater intensities of N-PAC ions than other JFTOT samples as analysed by OrbiSIMS, this additive's nitrogen content can be suggested to integrate into the aromatisation and carbonisation processes which form the deposit, supporting the mechanism of nitrogen integration suggested in Section 3.2.3.1 and providing this additive as a possible source of nitrogen. While some nitrogen is present in diesel fuel, most is removed in refining and the dominance of JFTOT LMW PIBSI in these PCs suggests that the main source of nitrogen-containing chemistry in diesel deposits is additive rather than fuel, in this case from the LMW PIBSI additive (173). This is significant in understanding the mechanism of nitrogenous deposit formation as the origin of nitrogen in IDIDs has only been speculated in previous work (78). The suggested carbonisation of LMW PIBSI here to form N-PACs and N-carbonaceous ions may be related to LMW PIBSI specifically or such carbonisation may result from many sources of nitrogen in the fuel.

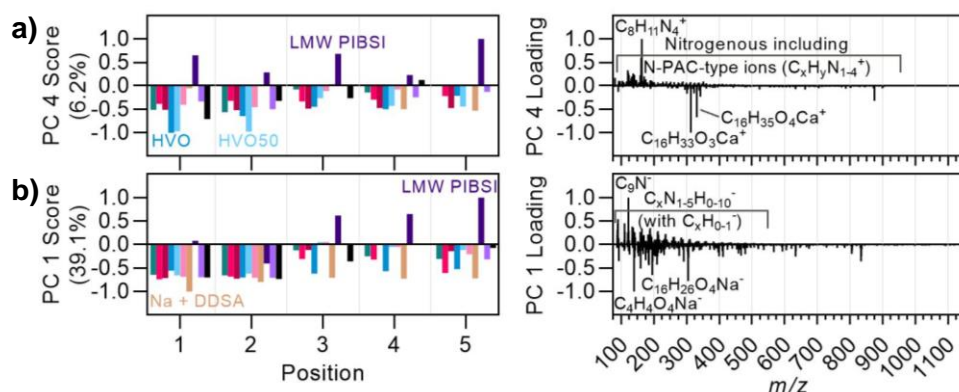


Figure 5.5: Principal components describing nitrogenous ions, a) PC 4 positive polarity with <0.7 mass filtering, b) PC 1 negative polarity with <0.7 mass filtering.

Table 5.2: MS/MS results for N-PAC type ion  $C_{24}H_{10}N^+$  (NCE = 70 and width = 0.9).

Mass	Assignment	DBE	Intensity	Neutral loss
312.0808	$C_{24}H_{10}N^+$	20.5	5.27E5	Parent
310.0649	$C_{24}H_8N^+$	21.5	4.86E4	$H_2$ (1)
286.0649	$C_{22}H_8N^+$	19.5	8.22E3	$C_2H_2$ (1)

LMW PIBSI and nitrogen-containing chemistry were observed in the OrbiSIMS data of JFTOT LMW PIBSI and JFTOT Lubricant as well as the field IDIDs discussed in Section 3.2.4.1. Lubricant oil contains additives with succinimide chemistry and has been suggested as an injector system contaminant, contributing lower quality, generally low mass, PIBSI species known to promote deposit formation (170). This was discussed in Section 1.2.2.6.1, however the PIBSIs of lubricant oil origin have not been investigated before. In JFTOT LMW PIBSI, ions appearing to be derived from LMW PIBSI's polyamine chain were evident as very intense N3 and N4 ions, revealed by PC 4's highest positive loadings (Figure 5.5a). The specific type of PIBSI (which can describe a range of chemical structures) added was polyisobutylene 260 mono tetraethylenepentamine, i.e. the PIB polymeric structures had an average MW of 260, while the amine structure had four units of ethylamine. Like ethylamine units, these small, nitrogen-rich ions generally have a C/N ratio of 2 ( $C_8H_{11}N_4^+$ ,  $C_8H_9N_4^+$ ,  $C_6H_6N_3^+$ ,  $C_6H_8N_3^+$ ,  $C_7H_{10}N_3^+$ ), though much higher DBE values, suggesting they originate from this section of the PIBSI structure and have been dehydrogenated either when heated in the JFTOT or by SIMS fragmentation.

Ions consistent with succinimides ( $\text{C}_4\text{H}_2\text{NO}_2^-$ ,  $\text{C}_6\text{H}_6\text{NO}_2^+$ ) were also found, likely originating from PIBSI's central succinimide structure as hypothesised in earlier work (39, 170). The needle IDIDs originate from a more diverse system involving different fuels, additives and contaminants so it is possible that these ions could have different origins, however the JFTOT data gives confidence that these ions have high succinimide specificity, as they are only seen for JFTOT LMW PIBSI and Lubricant, which both contain succinimides. Other high intensity ions indicative of LMW PIBSI were identified in JFTOT LMW PIBSI ( $\text{C}_6\text{H}_{10}\text{N}_3\text{O}^+$ ,  $\text{C}_8\text{H}_{11}\text{N}_4^+$ ) and were present in the field IDIDs that had succinimide ions while the field IDID with absent or very low intensity succinimide ions (Needle 8) lacks these ions (ion intensities can be found in Appendix Table A40), suggesting they are significant markers of LMW PIBSI in both JFTOT and injector deposits.

For samples affected by succinimide ions (JFTOT LMW PIBSI, JFTOT Lubricant, Needle 6 and Needle 10), succinimides (Figure 5.6a, left) have higher intensity in Needles 6 and 10, indicating that the field samples may have experienced higher succinimide concentrations than JFTOT LMW PIBSI. JFTOT RF-06 has no succinimide peaks, as expected since no succinimide source was included. JFTOT Lubricant position 1 has the lowest intensity of succinimides, which is also expected as succinimides will be a minor component of the lubricant oil. Succinimide declines in intensity from position 1 towards 3, seen in the lateral normalised intensity plots for JFTOT LMW PIBSI (Figure 5.6c), suggesting thermal decomposition of this chemistry occurs. This is quantitatively supported by the C 1s high-resolution XP spectrum of position 1 which required an additional component attributed to an amide/imide type bond (binding energy 288.04 eV, 1.2 % Area, Appendix Table A46) to achieve a good fit, while this component was not required for positions 3 or 5. In contrast, the larger N-PAC ion ( $\text{C}_{40}\text{H}_{14}\text{N}^+$ ) and N-carbonaceous ion ( $\text{C}_9\text{N}^-$ ) increase from position 1 to position 3 (Figure 5.6d), suggesting that they are the products of the succinimide's thermal decomposition.



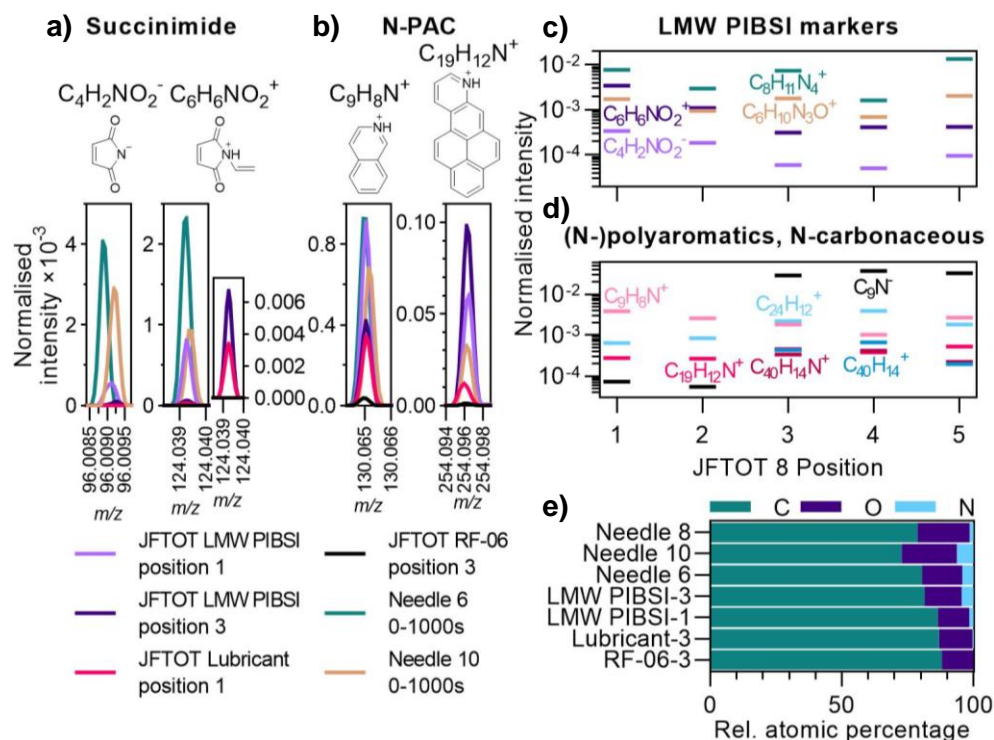


Figure 5.6: Key OrbiSIMS and XPS data for LMW PIBSI and nitrogenous chemistries in JFTOTs and IDIDs. Normalised OrbiSIMS secondary ion peaks for a) Succinimides and b) N-PACs. Normalised secondary ion intensities along JFTOT LMW PIBSI positions 1-5 for c) LMW PIBSI marker ions and d) N-PAC and N-carbonaceous ions. e) XPS relative atomic concentrations of C, O and N.

Relative atomic quantification using XPS (Figure 5.6e) showed agreement with OrbiSIMS results regarding nitrogen content, and provides additional quantitative context. RF-06 showed no nitrogen, while nitrogen's concentration increases along JFTOT LMW PIBSI from position 1 (1.6 relative at.%) to position 3 (4.5 relative at.%). Therefore, XPS suggests that as carbonisation proceeds towards position 3, it integrates a disproportionately large amount of nitrogen and increases its atomic concentration in the deposit. LMW PIBSI is therefore likely contributing to and partaking in this N-carbonaceous deposit's formation, a phenomenon not seen in previous investigations. JFTOT Lubricant (position 3), as implied by its modest intensities of nitrogenous OrbiSIMS ions, has a smaller concentration of nitrogen (0.5 relative at. %), slightly lower than at position 1 (0.7 at. %) and considerably lower than JFTOT LMW PIBSI. Some of this nitrogen likely is also from other nitrogen-containing components of lubricant oil such as diphenylamine or Mannich bases (80).

The field IDIDs with evidence of significant succinimides (Needle 6 and Needle 10) have comparable nitrogen content (4.3 and 6.3 at.% respectively) to JFTOT LMW PIBSI position 3 and have more oxygen which may come from O-containing additives in real world systems. Needle 8 is a field IDID that showed little to no evidence of succinimide in its OrbiSIMS data (Appendix Table A40) but has significant nitrogen concentration by XPS, though lower than Needles 6 and 10. Its moderate nitrogen content differentiates it from JFTOT RF-06 which had undetectable levels, likely as Needle 8 has incorporated nitrogen from non-PIBSI sources such as other additives like 2-EHN which is linked to lowering of fuel stability (discussed in Section 1.2.2.6.2).

#### **5.2.2.2 Hydrocarbon and Nitrogenous OrbiSIMS MW distributions in Key JFTOTs and IDIDs**

So far, PCs of nitrogenous material have shown the significance of N-PAC type ions. Their distributions are visualised in Figure 5.7 for all positions of each sample for hydrocarbon, N1- and N2-ions. Each plot uses the same minimum intensity threshold as the HC plots in Section 5.2.1.2 (after normalisation to the total intensity for masses with decimal <0.5). The progression of PAH growth is seen along the JFTOT tubes with rising temperature as was observed in Figure 5.3, and the same is also generally observed here for N-PAC material in affected samples. JFTOT LMW PIBSI's distributions have smaller PAHs and larger N-PACs than JFTOT RF-06, indicating that the additional nitrogen introduced from the LMW PIBSI contributes to the formation of more and larger N-containing carbonised structures in the form of N-PAC type ions with both one and multiple N atoms. The additional nitrogen in JFTOT LMW PIBSI is likely integrated into similar carbonisation processes such that the N-PACs outcompete the PAHs, leading to the larger N-PACs and smaller PAHs. This likely proceeds via a multitude of reaction pathways similar to the carbonisation of other organic materials occurring during pyrolysis (197).

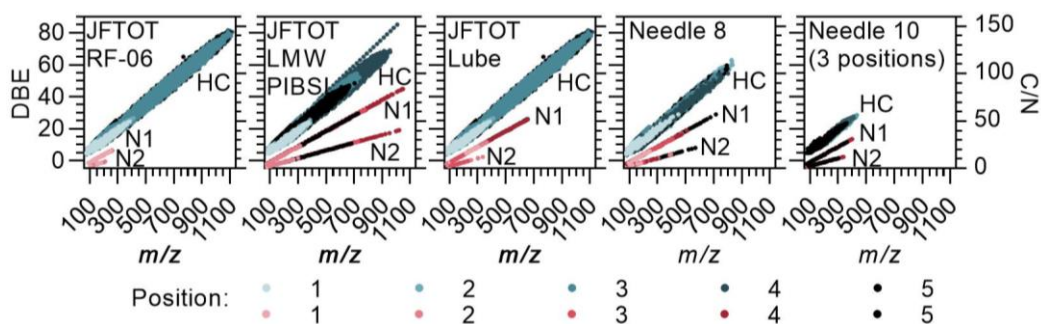


Figure 5.7: DBE or C/N as a function of  $m/z$  for hydrocarbon and N-containing secondary ions at five positions of JFTOT and IDID samples. Calculated using the Formula\_calculator script ( $1 \times 10^{-5}$  minimum intensity normalised to sum of ions with decimal mass  $< .5$ ).

JFTOT Lubricant, with its lower nitrogen concentration, shows N-PACs which are smaller than JFTOT LMW PIBSI but significantly larger than JFTOT RF-06 (Figure 5.7). With these components having low concentrations in lubricant oil, the fuel-lubricant mixture used for JFTOT Lubricant likely has a lower nitrogen concentration than that of fuel-LMW PIBSI used for JFTOT LMW PIBSI, hence nitrogen is involved less in the carbonisation process and results in lower intensity N-PAC ions containing fewer nitrogen atoms. The field IDIDs (Needles 8 and 10 in Figure 5.7) also show significant incorporation of nitrogen into their carbonaceous deposit as they both have larger N-containing ions than JFTOT RF-06, despite Needle 10 having the smallest hydrocarbons (up to 399  $m/z$ ). This indicates an integration of nitrogen likely from their additive sources. For Needle 10, this includes the succinimide chemistry seen earlier likely from LMW PIBSI, while Needle 8 lacked this and hence likely had other sources of nitrogen.

### 5.2.2.3 Mechanistic Evidence from OrbiSIMS Depth Profiles in JFTOT LMW PIBSI and IDIDs

Positive polarity depth profiles for key nitrogen-containing and PAH/carbonaceous ions are displayed in Figure 5.8 for positions 2 and 3 of JFTOT LMW PIBSI and two field IDIDs that exhibited succinimide ions. The progression of the deposit can be seen from position 2 (Figure 5.8a) to position 3 (Figure 5.8b) of JFTOT LMW PIBSI where position 2 lacks evidence of advanced carbonisation (larger PAH ions:  $C_{40}H_{14}^+$ ; N-PAC ions:  $C_{40}H_{14}N^+$ ; (N-)carbonaceous ions:  $C_9NH^+$ ,  $C_{11}^+$ ) and comprises only a thin homogenous

“film” on the surface with no depth effects observed. At position 3, the deposit has developed into a complex layered system that suggests a process of decomposition, where the deeper (hence older) deposit contains the products of carbonisation, similar to the mechanism suggested earlier for JFTOT RF-06 (Figure 5.4) except with increased nitrogen content.

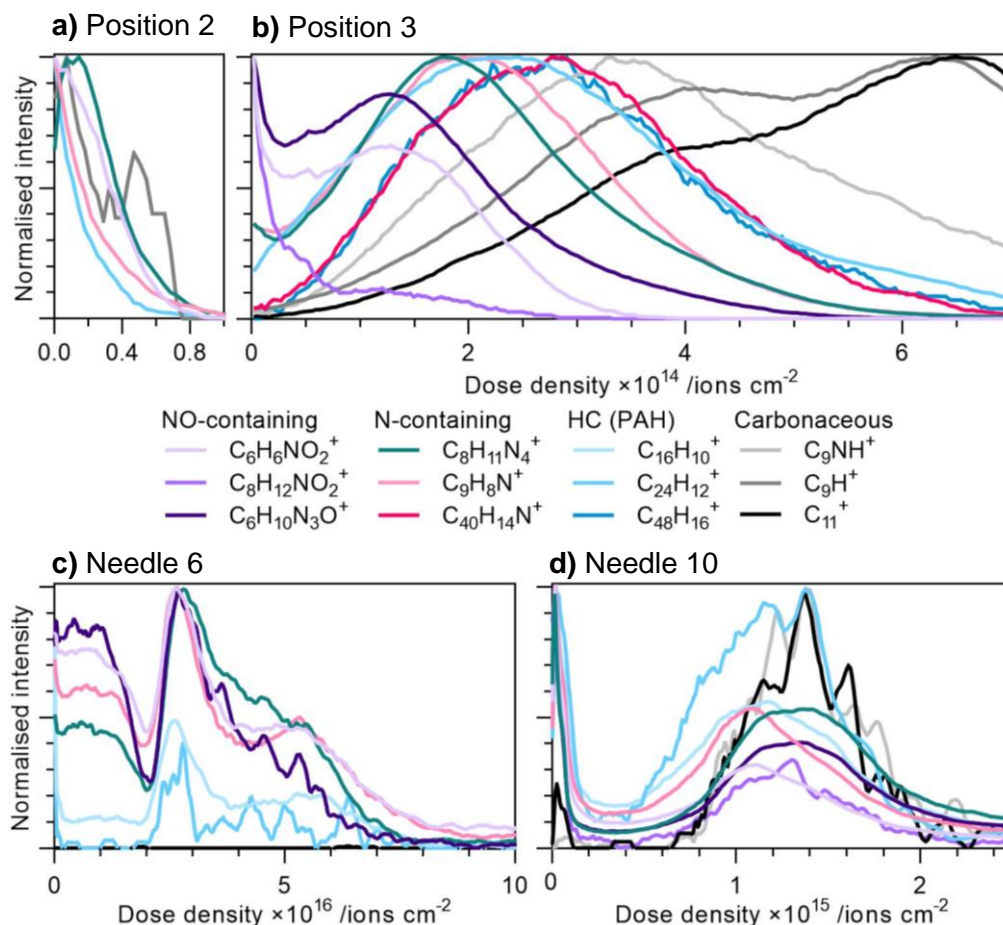


Figure 5.8: OrbiSIMS depth profiles showing nitrogen-containing secondary ions for JFTOT LMW PIBSI a) position 2, b) position 3. c) Needle 6 and d) Needle 10.

The surface and upper deposit has high intensities of the in-tact succinimide structures ( $\text{C}_6\text{H}_6\text{NO}_2^+$  and  $\text{C}_8\text{H}_{12}\text{NO}_2^+$ ) as well as other ions representing LMW PIBSI ( $\text{C}_6\text{H}_{10}\text{N}_3\text{O}^+$ ). Their decreasing intensity in the sub-surface suggests succinimides deposit and decompose when heated. Beyond these ions, secondary ions indicative of the initial stages of carbonisation (small PAHs and N-PACs,  $\text{C}_{24}\text{H}_{12}^+$  and  $\text{C}_9\text{H}_8\text{N}^+$ ) emerge, as well as the  $\text{C}_8\text{H}_{11}\text{N}_4^+$  ion thought to originate from the polyamine, suggesting that it forms during early

carbonisation processes or is a SIMS fragment of such chemistry. At further depth, larger PAHs and N-PACs ( $C_{48}H_{16}^+$ ,  $C_{40}H_{14}N^+$ ) increase in intensity, evidencing more advanced carbonisation, which then give way to the N-carbonaceous ion  $C_9NH^+$  and finally the carbonaceous ions, first  $C_9H^+$  and lastly the purely carbon ion  $C_{11}^+$ , representing the latter stages of carbonisation. Corresponding negative polarity OrbiSIMS depth profiles can be found in Appendix Figure A31, which also show succinimides at the surface and carbon structures increasing in mass with lower H:C ratios as depth increases.

Pyrolytic decomposition of succinimide vapour was reported by Choudhary, G. *et al.* (1968) to proceed towards ethylcyanide, ethylene, HCN, CO and  $H_2O$  (198). Sharma *et al.* (2006) observed production of succinimides from amino acids during pyrolysis, which subsequently progressed to PAHs and N-PACs at high temperature, with significant concentrations of two and three-membered rings produced at 870 °C (199). It was suggested that the amino acid formed polyaromatics via Choudhary's decomposition products following succinimide formation. While the temperature of JFTOT LMW PIBSI was much lower (330 °C), as well as that of the internal FIE (200-300 °C) (12), similar decomposition mechanisms can be proposed, potentially catalysed by fuel components/LMW PIBSI, the products of the breakdown of fuel/LMW PIBSI, the heater tube substrate, or the air in the system. This mechanism is shown in Figure 5.9, consisting of the decomposition of LMW PIBSI to small compounds which could integrate with the hydrocarbons of diesel during their carbonisation to form PAHs and N-PACs which subsequently grow towards N-carbonaceous deposit material.

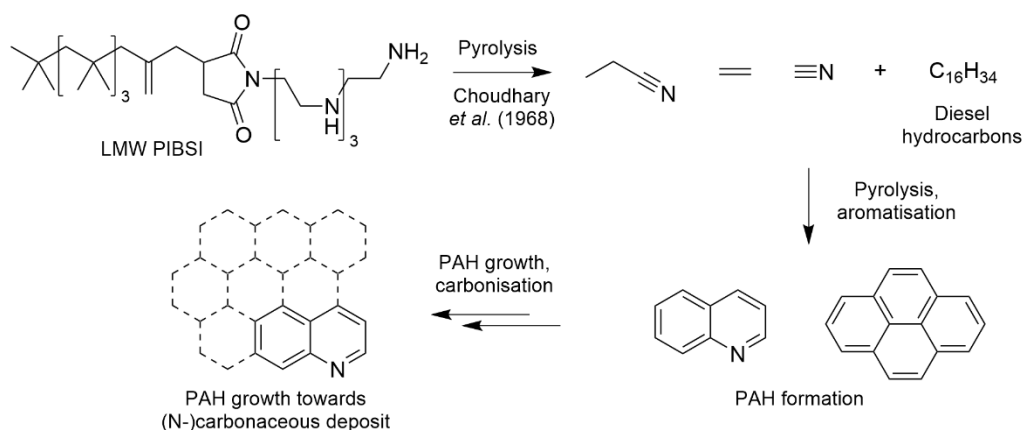


Figure 5.9: Suggested mechanism of N-carbonaceous JFTOT deposit formation from diesel and LMW PIBSI (typical PIB length shown), based on Choudhary's succinimide pyrolytic decomposition and proposed integration of nitrogenous products into diesel carbonisation via N-PACs based on evidence from OrbiSIMS depth profiling (198).

The depth profiles of the field IDID samples do not clearly evidence mechanistic insights. Both samples display upper organic layers which the succinimide ions and N-PAC/PAH ions are part of. Both samples appear less affected by polyaromatic deposits, so are likely in an earlier stage of carbonisation compared to the higher temperature JFTOT deposits. The lack of nuance in the depth profiles may result from matrix effects due to the more complex IDID material or may indicate more homogeneity than the JFTOT deposit (126).

As discussed in Section 1.2.2.6.1, PIBSI's mechanism of deposition is understood to often proceed via a transformation to an amide of either a secondary amine or, via a ring-opening, the succinimide (39). The relationship of this mechanism to the presence of acids of different types has been explored in previous studies and was found to be key to this type of IDID. In JFTOT LMW PIBSI, in the absence of an acid, no amide formation was detected via OrbiSIMS, with the succinimides present instead and the PIBSI contributing its nitrogen to the carbonised deposit material. Such detailed evidence of nitrogen-integrating carbonisation has not been seen before in previous studies (Section 1.2.2.3), while OrbiSIMS with its ability to probe the sub-surface with high mass accuracy enables such characterisation in this work.

### 5.2.3 Sulfur and Phosphorus-Containing Deposit Chemistries in JFTOTs and IDIDs using OrbiSIMS and XPS

Sulfur and/or phosphorus were present in several JFTOTs and IDIDs as both inorganic salt ions and S- or P-containing carbonaceous ions, the latter suggesting an integration of these elements into the carbonisation process analogous to that seen for nitrogen (Section 5.2.2).

#### 5.2.3.1 Interpretation of Sulfur and Phosphorus in JFTOT Deposit OrbiSIMS PCA with XPS Quantification and Comparison to IDIDs

Several PCs from the JFTOT PCA in both polarities (Figure 5.10) identified S- and P-containing ions, with the samples with the highest intensities being those of solely biodiesel (JFTOT RME and CME), while JFTOT Lubricant and B7 have smaller intensities. As sulfur and phosphorus are removed from petrodiesel during refining, the absence in JFTOT RF-06 is expected, while biodiesel, including from coconut, can contain phosphorus that has been suggested to be linked to diesel engine deposits and lubricant oil additives contain S and P (Section 1.2.2.5.1 and Section 1.2.2.4.4).

##### 5.2.3.1.1 Sulfur and Phosphorus-containing Carbonaceous Chemistry

Previous reports of biodiesels promoting deposit formation, as discussed in Section 1.2.2.5.1, along with possible chemistries of biodiesel origin in Chapters 3 and 4 such as carboxylic acids and sodium salts motivated their inclusion in this study. JFTOT RME and JFTOT CME showed the highest intensities of S- and P-carbonaceous ions as identified by PC 4 (>0.7 mass filtering, Figure 5.10a) which contained ions including  $C_{4-12}S^-$ ,  $C_{6-12}SH^-$ ,  $C_{4-8}S_2^-$ ,  $C_{5-9}P^-$  and  $C_{5-7}PS^-$ , chemistry which has not been observed in diesel deposits before. JFTOT RME appears to have high content of both P- and S-carbonaceous material with by far the largest  $C_5P^-$  OrbiSIMS ion intensity and the most S and P content in XPS (1.9 and 1.3 at.% respectively). JFTOT CME has the largest  $C_6S^-$  OrbiSIMS intensity and relatively low  $C_5P^-$ , with XPS showing moderate S (1.0 at.%) and below detectable levels of P. Hence, relative to CME, RME appears to have integrated more P while CME has



integrated more S. Much of their S and P is also likely in non-carbonaceous inorganic forms, such as those in this PC's loadings as sulfate/sulfite and phosphate salts ( $\text{NaMgS}_2\text{O}_8^-$ ,  $\text{NaMgS}_2\text{O}_7^-$ ,  $\text{NaCaS}_2\text{O}_8^-$ ,  $\text{MgP}_2\text{O}_7\text{H}^-$ ,  $\text{NaSO}_4^-$ ).

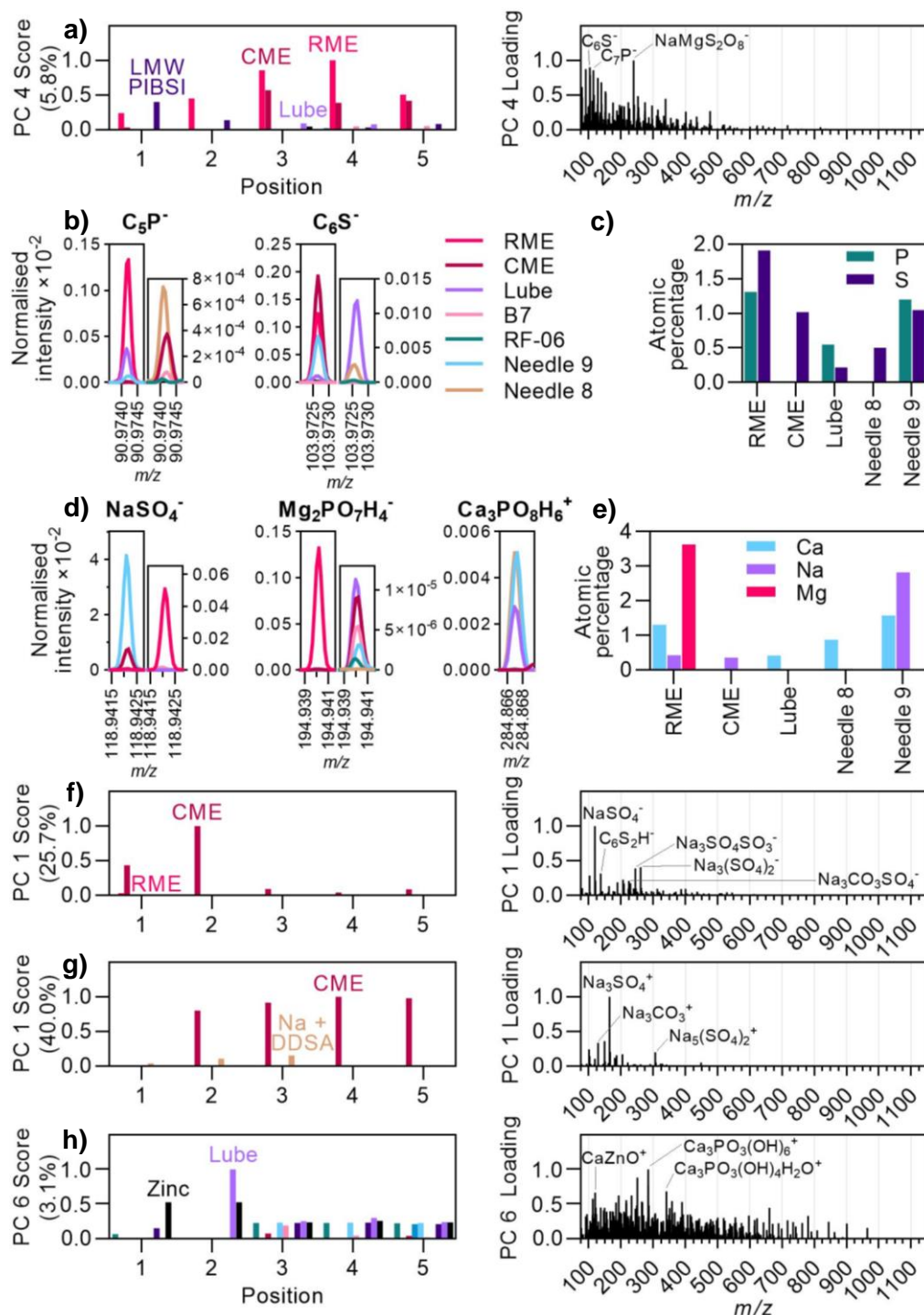


Figure 5.10: OrbiSIMS and XPS data for phosphorus and sulfur-containing ions. a) OrbiSIMS PC 4 (negative polarity, >0.7 mass filter) positive direction results. b) P- and S-carbonaceous secondary ion spectra. c) P and S atomic concentrations from XPS. d) Sulfate and phosphate-containing inorganic secondary ion spectra, e) Ca, Na and Mg atomic concentrations from XPS, and positive direction PCA results for f) PC 1 (negative polarity, >0.7 mass filter), g) PC 1 (positive polarity, >0.7 mass filter), and h) PC 6 (positive polarity, >0.7 mass filter).



JFTOTs Lubricant and B7 have smaller intensities of S- and P-carbonaceous ions at the positions of high deposition (3 to 5), shown by their smaller scores in PC 4 (Figure 5.10a); lubricant oil likely contains relatively little S and P compared to biodiesel, being only part of some of its additives, while it is expected that B7 will contribute the same chemistries as RME to a lesser degree. While ABS additives in lubricant oil were hypothesised to contribute sulfur to IDIDs in Section 3.2.4.3.1, in the JFTOT samples this chemistry is seen in most samples with no trend identifiable, suggesting they originate from a common sample surface contamination. This data can be seen in Appendix Section 3.10. XPS data of JFTOT Lubricant (Figure 5.10c) confirms it has less P (0.6 at.%) and S (0.2 at.%) than JFTOTs CME and RME. JFTOT LMW PIBSI also has a significant PC 4 score at positions 1-2, however this is due to a presence of inorganic ( $\text{NaMgS}_2\text{O}_8^-$ ) species likely from a minor sample contamination, while S- and P-carbonaceous ions are absent. The real-world IDID of Needle 9 is affected by this chemistry, with XPS concentrations of S and P (1.1 and 1.2 at.%, Figure 5.10c) comparable to JFTOT RME and significant  $\text{C}_5\text{P}^-$  and  $\text{C}_6\text{S}^-$  peaks (Figure 5.10b), hence biodiesel and/or lubricant oil are possible origins of this field deposit chemistry.

#### 5.2.3.1.2 Sulfur and Phosphorus-containing Salt Chemistry

Inorganic sulfate or phosphate OrbiSIMS salt ions of sodium, magnesium and calcium were identified by multiple PCs with mass filtering  $>0.7$ . Sodium sulfates (in PC 1 of negative and positive polarity, Figure 5.10f-g) were intense across all positions of JFTOT CME, with lower intensity in JFTOT RME ( $\text{NaSO}_4^-$  peak in Figure 5.10d). This correlation with biodiesel JFTOT samples suggests it originates from the catalyst used in transesterification for biodiesel production (19). JFTOT B7 has minimal peaks for the S- and P-containing ions found in JFTOT CME and RME ( $\text{C}_5\text{P}^-$ ,  $\text{C}_6\text{S}^-$ ,  $\text{NaSO}_4^-$ ), indicating these components are less problematic for deposits when used in real-world blending proportions. However, the presence of these species may still cause issues which appear to also affect the field samples which show the same associated ions, as with Needles 8 and 9 in Figure 5.10b-e.

Calcium phosphates are prominent in JFTOT Lubricant at position 2 (PC 6, Figure 5.10h). Lubricant is a known source of calcium (65), however biodiesel can also contain calcium originating from the washing and drying during its purification (200). XPS (Figure 5.10e) shows that JFTOT RME contains more calcium than JFTOT Lubricant, likely in other (non-phosphate) forms.

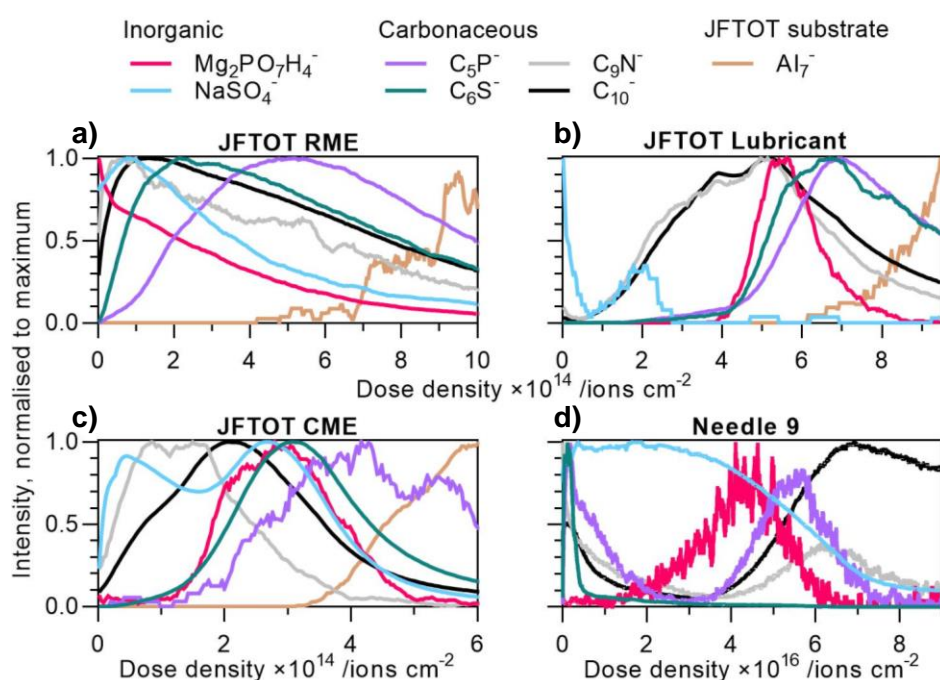
Ions of both these types ( $\text{NaSO}_4^-$  and  $\text{Ca}_3\text{PO}_8\text{H}_6^+$ , Figure 5.10d) were more intense in field IDIDs than the JFTOT deposits (Needles 8 and 9 in Figure 5.10d). XPS (Figure 5.10e) shows that Needle 9 has the highest Na (2.8 at.%) and Ca (1.6 at.%) content of all samples, however Needle 8 has only moderate calcium content (0.9 at.%) with no detectable sodium. This observation links real world deposits of calcium phosphate in both field samples' salts to lubricant oil and deposits of sodium sulfate in Needle 9 to biodiesel and indicates more contamination in these real-world samples than in the JFTOTs.

Magnesium is significant only in JFTOT RME, shown by magnesium phosphate ( $\text{Mg}_2\text{PO}_7\text{H}_4^-$ , Figure 5.10d) being strong only in JFTOT RME and this being the only sample showing magnesium at position 3 in the XPS data (3.6 at.%), where it has the largest atomic concentration of all the salt metals (Figure 5.10b). Like calcium, magnesium is used in washing and drying of biodiesel, with concerns of potential soap formation from either metal (200). It is also a component of the JFTOT tube substrate, however the absence of aluminium (the major substrate metal) shows the substrate was not being measured here.

### 5.2.3.2 Mechanistic Evidence from OrbiSIMS Depth Variations in JFTOTs and IDIDs

Depth profiles of Needle 9 and JFTOTs RME, Lubricant and CME support a mechanism of carbonisation over time that integrates sulfur and phosphorus from inorganic sources (Figure 5.11a-d). In each sample,  $\text{C}_5\text{P}^-$  and  $\text{C}_6\text{S}^-$  are found nearest the substrate, with the former slightly deeper. This suggests that this material is more fundamental to the deposit formation mechanism than purely carbonaceous deposit material, as these ions exist deeper than  $\text{C}_{10}^-$  and

hence their precursors must be involved in the initial stages of deposit formation. For Needle 9,  $C_{10}^-$  is the deepest ion (closest to the substrate) but likely represents a DLC substrate rather than the lowest deposit layer; above the DLC,  $C_5P^-$  is found and suggested to be the deepest deposit chemistry. The  $Mg_2PO_7H_4^-$  ion is closer to the surface than the P-carbonaceous ions, indicating that decomposition of this salt during carbonisation may contribute the phosphorus chemistry. Indeed, this ion is found above  $C_5P^-$  in all samples and its occurrence towards the surface in JFTOT RME confirms that it is not part of the JFTOT substrate.



e)

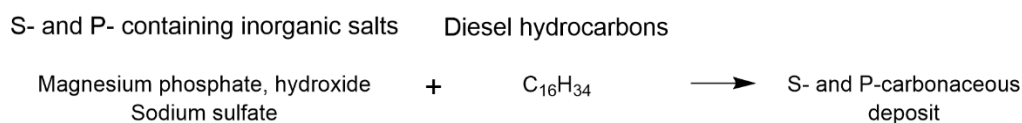


Figure 5.11: Depth profiles of key S- and P-containing OrbiSIMS secondary ions at central positions of a) JFTOT RME, b) JFTOT Lubricant, c) JFTOT CME and d) Needle 9. e) Schematic summary of S- and P-carbonaceous deposit formation.

All samples show a presence of  $NaSO_4^-$  through their depth profiles except for JFTOT Lubricant, in which it is more surface localised. Sodium is not a typical component of lubricant oil (80) and this sample had a relatively small  $NaSO_4^-$  peak (Figure 5.11d). In Needle 9, this ion covers the full range of upper deposit

material, with the needle likely having been exposed to this chemistry from biodiesel or another source consistently during its lifetime. Other S- and P-containing compounds as well as those discussed in this section are likely also involved in contributing the elements to carbonaceous deposit.

This is the first work to suggest P- and S-containing carbonaceous IDIDs can originate from inorganic salt precursors and to link them to biodiesel/lubricant sources and specific chemistries therein. Identification of these compounds is important as this deposit chemistry's origin has not been previously established and points to likely harmful compounds in biodiesel and lubricants. Prior work has generally been limited to elemental analysis and small inorganic salts of S and P (2, 40, 128), though P-containing compounds in biodiesel have been linked to deposit formation (92).

#### **5.2.4 DDSA and Sodium Carboxylate Deposit Chemistry in JFTOTs and IDIDs using OrbiSIMS and XPS**

Sodium contamination in diesel systems is known to form soap type deposits with carboxylic acids in commercial diesel fuel, discussed in Section 1.2.2.4.1. DDSA is a dicarboxylic corrosion inhibitor additive that has been seen in this type of deposit in previous studies including in Section 3.2.4.2, but other acids, whether from additives or contaminants, can form similar insoluble soaps (41). Sodium-DDS soaps were observed in multiple IDID samples in Section 3.2.4.2 in samples showing high sodium content. JFTOT Na + DDSA, doped with DDSA and a sodium source (sodium naphthenate), was run at a lower temperature of 180 °C, reported as capable of producing Na-DDS soap deposits, while others used 300-360 °C (Section 2.2.3, Table 2.2) (139, 143).

##### **5.2.4.1 Interpretation of DDS-Na in JFTOT OrbiSIMS PCA with XPS Quantification and Comparison to IDIDs**

The deposit of JFTOT Na + DDSA was confirmed to contain Na-DDS by its presence as sodium-adducted ( $[M + Na]^+$ ) OrbiSIMS ions ( $C_{16}H_{26}O_4Na_3^+$ ). It was expected that DDSA with sodium would be an origin of this chemistry as noted in Section 3.2.4.2 and previously described in the literature in Section

1.2.2.4.1. It was shown in Section 5.2.1 that, among the JFTOT samples, DDS-Na chemistry is anti-correlated with PAH and carbonaceous type ions in PCA (Figure 5.1a) and is unique to JFTOT Na + DDSA. This was expected as lower temperature drives less extensive aromatisation/carbonisation and is proven quantitatively in the C 1s XP spectra in Figure 5.1d, where JFTOT Na + DDSA shows more carboxylate than other samples and has a lack of a  $\pi$ - $\pi^*$  contribution, proving the absence of aromatics. Being able to form at lower temperatures, these soaps deposit at positions 1-3, shown by the high PC 1 scores (Figure 5.1a). This contrasts with carbonaceous-type deposit that forms at high temperatures, typically occurring in other samples at positions 3-5. Deposition of the sodium carboxylate at position 1 shows that only low temperatures are required. This has been observed by Trobaugh *et al.* and here is demonstrated in the JFTOT model system mimicking an injector environment (2). Other ions in JFTOT Na + DDSA include those consisting of a cluster of two Na-DDS units ( $\text{C}_{32}\text{H}_{52}\text{O}_8\text{Na}_5^+$ ), and many smaller carboxylate salts ( $\text{C}_5\text{H}_6\text{O}_2\text{Na}_2^+$ ,  $\text{C}_8\text{H}_8\text{O}_4\text{Na}_3^+$ ), similar to the field samples in Section 3.2.4.2.

Inorganic salts of sodium have high intensities in JFTOT Na + DDSA, with sodium carbonate ( $\text{Na}_3\text{CO}_3^+$ ), sodium (with some calcium) hydroxides and oxides ( $\text{Na}_3\text{O}_2\text{H}_2^+$ ,  $\text{Na}_2\text{CaO}_3\text{H}_3^+$ ,  $\text{Na}_2\text{O}_2^+$ ) and sodium-aluminium and sodium-magnesium hydroxides likely from combining with substrate elements ( $\text{Na}_4\text{Al}_6\text{O}_6\text{H}_6^+$ ,  $\text{Na}_3\text{MgO}_4\text{H}_4^+$ ). Previous studies have found similar sodium salts as components of inorganic IDIDs (2, 78, 170) and may therefore originate from sodium contamination's interactions with carboxylic acids. They have high intensity at position 1 but increase towards position 3 before a significant decline at positions 4 and 5. This is seen in PC 2's scores ( $>0.7$  mass filtered) in Figure 5.12, the loadings of which contain these inorganic ions and small carboxylate salts ( $\text{C}_4\text{H}_4\text{O}_4\text{Na}_3^+$ ,  $\text{C}_4\text{H}_2\text{O}_4\text{Na}_3^+$ ). The rise in intensity from position 1 to position 3 suggests a breakdown of Na-DDS into inorganic salts, driven by the increasing temperature along the tube.  $\text{Na}_3\text{CO}_3^+$  is unlikely to be a SIMS fragment of sodium carboxylate ions, as it was absent from high collision energy MS/MS analysis of the Na-DDS ion in Section 3.2.4.2.

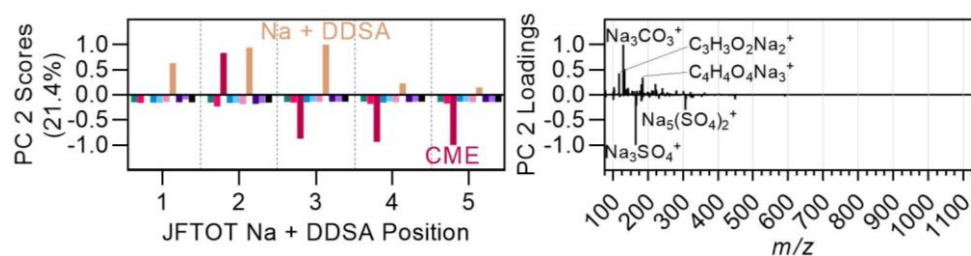


Figure 5.12: OrbiSIMS positive polarity PC 2 scores (>0.7 mass filtered) and loadings, identifying sodium inorganic salts in JFTOT Na + DDSA and JFTOT CME.

The normalised ion intensities for some key species are shown for each JFTOT Na + DDSA position in Figure 5.13a-b, confirming that the in-tact fully deprotonated  $\text{Na}_2\text{-DDS}$  and partially protonated  $\text{NaH-DDS}$  ions maintain their intensity from position 1-3 while the inorganic suspected breakdown products (sodium succinate, sodium carbonate, sodium hydroxide) rise towards PC 3. The decline in intensity of all the sodium ions after position 3 suggests that most of the sodium has been deposited by position 3, leaving a low sodium content in the fuel towards positions 4-5. This is supported by the XPS data (Figure 5.13c), which shows positions 1 and 3 with comparable high concentrations of sodium (5.2 and 5.0 at.% respectively), which falls to 0.7 at.% at position 5. The IDID surfaces have lower sodium concentrations than JFTOT Na + DDSA (1.7 and 1.4 at.% in Needles 6 and 7 respectively), however these samples' bulk data (from 0-1850s of the depth profile) reach 14.1 at.% in Needle 6 and 4.4 at.% in Needle 7. Thus, the IDIDs likely contain more sodium than the JFTOT sample and therefore experienced a very significant sodium contamination during their lifetime.

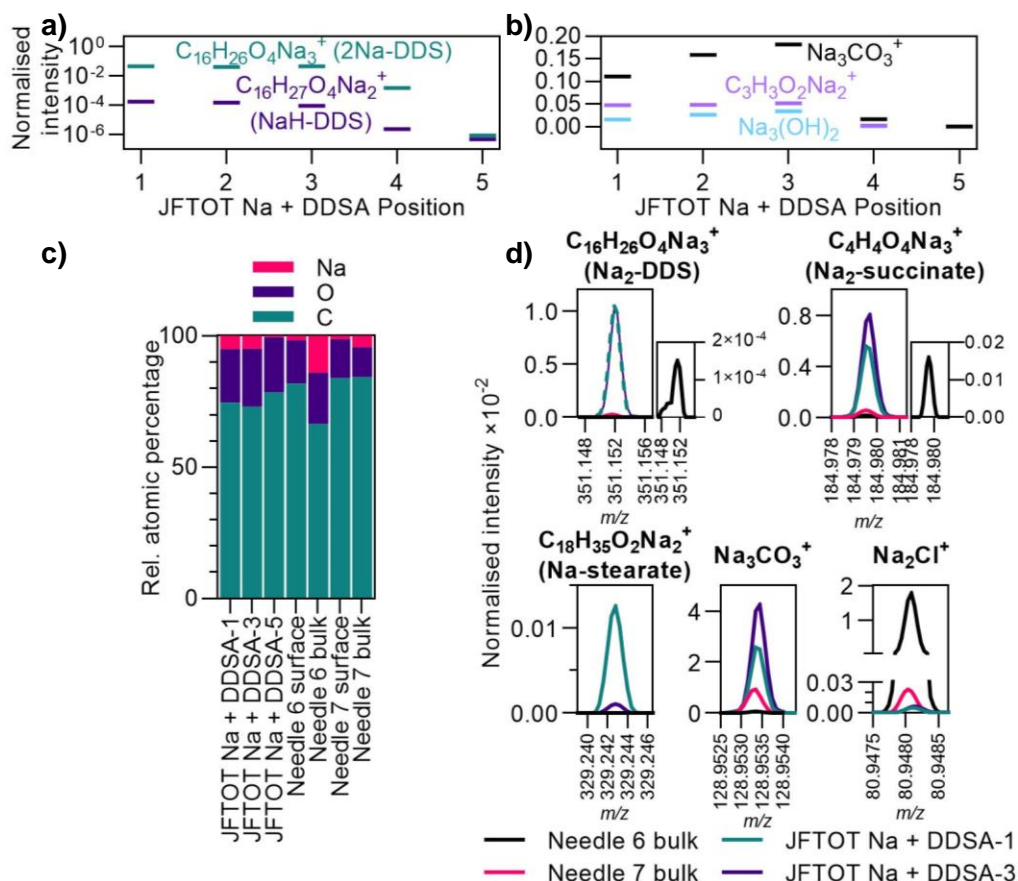


Figure 5.13: DDSA-related OrbiSIMS and XPS results. 3D OrbiSIMS normalised intensities along JFTOT Na + DDSA of a) sodium DDS and b) sodium inorganic secondary ions. c) C, O and Na relative atomic concentrations from XPS for JFTOT Na + DDSA (surface) and two IDIDs (surface and bulk from 0-1850s region of depth profiles). d) Normalised OrbiSIMS peak comparisons for key secondary ions.

The OrbiSIMS and XPS data indicate that JFTOT Na + DDSA has more sodium carboxylate than the field samples (Needles 6 and 7). The normalised intensity of Na<sub>2</sub>-DDS in JFTOT Na + DDSA is much higher than in Needles 6 and 7, with Needle 6 registering the smallest peak (Figure 5.13d). Other sodium carboxylate species exist in JFTOT Na + DDSA with smaller intensities, which may also play a role in deposit formation. Sodium stearate ( $C_{18}H_{35}O_2Na_2^+$ ) is absent from Needles 6 and 7 but significant mainly at JFTOT position 1 (Figure 5.13d). This is a common carboxylic acid occurring naturally which can be present in diesel, originating from additives, contamination or biodiesel oxidation (28, 201). Another sodium carboxylate ( $C_{15}H_{25}O_2Na_2^+$ ), likely from the sodium naphthenate included in this JFTOT run, was also present in JFTOT Na + DDSA with a higher intensity than the

IDIDs, see Appendix Table A42 for intensities (202). The OrbiSIMS data for Needles 6 and 7 contains more diverse sodium inorganic ions than JFTOT Na + DDSA, for example having higher normalized intensities of  $\text{Na}_2\text{Cl}^+$  and  $\text{Na}_3\text{SO}_4^+$  (Figure 5.13d). This is expected since real world injector systems will have experienced a wider range of chemistries from fuels, additives and contaminants. Normalised intensities are summarized in Appendix Table A42.

In quantitative high-resolution C 1s XP spectra (Figure 5.14e), JFTOT Na + DDSA has more of its carbon in the form of carboxyl chemistry, representing 11.6% of peak area compared to 7.8% in Needle 7 and 5.3% in Needle 6 (Figure 5.14b). XPS suggests that Needle 6 has undergone the most carboxyl to carbonate breakdown while Needle 7 has the least, as Needle 6 has the largest carbonate presence (2.5%) and Needle 7 (1.0%) the least (Figure 5.14b), with the same being true of the ratio of carbonate to carboxyl components (0.47 for Needle 6 and 0.12 for Needle 7) (Figure 5.14c). The carboxyl component being larger than carbonate in all samples is expected since high temperature is likely required for conversion to carbonate. The varying extent of carbonate formation may result from many factors including the age of the deposit in the system and the conditions it was subjected to in terms of temperature, pressure and chemical environment. These results suggest that such conditions vary, with IDIDs showing both more (Needle 6) and less (Needle 7) conversion than in the JFTOT.

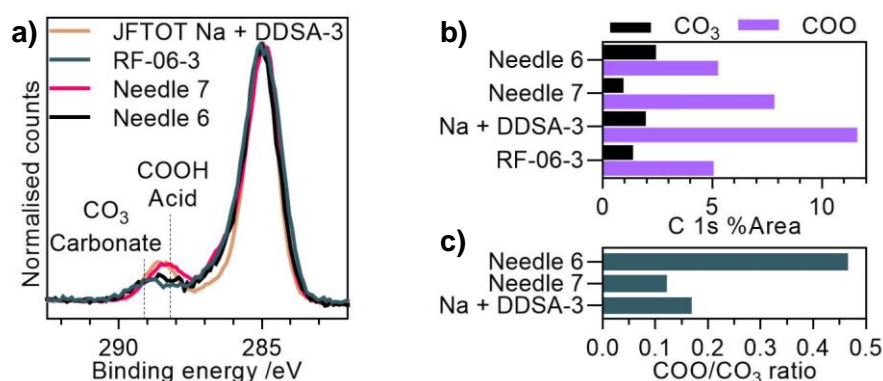


Figure 5.14: DDSA-related high-resolution C 1s XPS data for JFTOT Na + DDSA position 3, JFTOT RF-06 position 3, Needle 6 and Needle 7. a) C 1s spectra overlay. b) Quantification of carboxyl and carbonate components. c) Ratios of carboxyl:carbonate components.



#### 5.2.4.2 Mechanistic Insight from JFTOT and IDID OrbiSIMS Depth Profiles

Depth profiles at positions 1 and 3 of JFTOT Na + DDSA for the established key ions (Figure 5.15a-b) support the thermal decomposition of carboxylates to carbonates, with the same trends seen in the field IDID samples (Figure 5.15c-d). Species found lower in the profile at position 3 and in Needles 6 and 7 are consistent with those that were more prevalent at hotter positions of the tube. Both positions require a similar dose density to reach the substrate ion ( $Al^{7+}$ ), confirming that significant deposition occurs at low temperature as well as at high.

The depth profile for the position 1 (Figure 5.15a), at which point it has been established that the in-tact Na-DDS is more prevalent, shows fewer layering effects than position 3, where decomposition products are more prevalent (Figure 5.15b). Position 1 has a possible surface film of NaH-DDS and Na-stearate above a composite layer of  $Na_2$ -DDS, Na-naphthenate, carboxylate fragments and sodium inorganic salts. A similar surface film appears at position 3, however below this the Na-DDS and Na-naphthenate species appear slightly earlier in the profile than the smaller Na-carboxylates, below which emerge the small inorganics (sodium carbonate and hydroxide as well as other anions such as sulfates). This indicates that the small sodium inorganics ( $Na_3CO_3^+$  and  $Na_3(OH)_2^+$ ) are the final decomposition products which are formed via the small sodium carboxylates. It also suggests that the process integrates other contaminants such as sulfate to form the other sodium salts in this lower layer. The field IDID (Needles 6 and 7) depth profiles (Figure 5.15c-d) show similar trends; the only carboxylate is  $Na_2$ -DDS which is primarily found towards the surface, with the smaller carboxylate fragments more intense in the sub-surface before sodium inorganic salts dominate at lower depths. These sub-surface salt pseudo-layers were identified and extensively characterised for Needles 6 and 7 using NMF in Section 4.2.3.2. Here, the JFTOT model suggests sodium contamination-driven Na-DDS deposition and decomposition, integrating other inorganic components, may be the origin of these IDIDs.

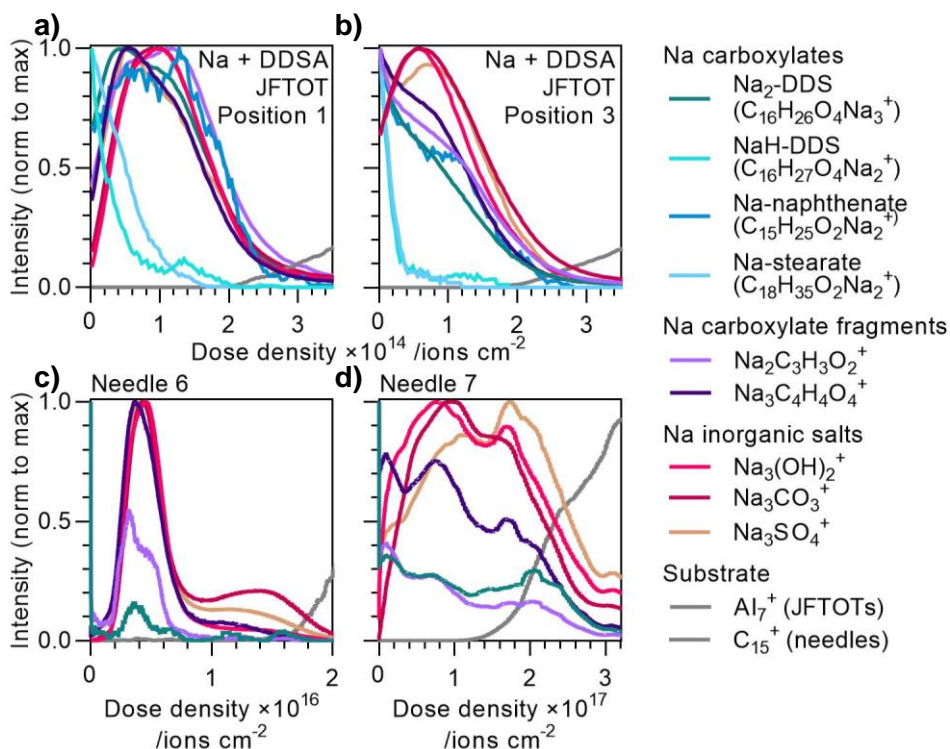
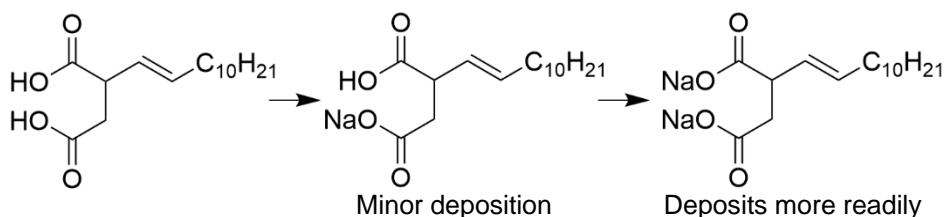


Figure 5.15: Depth profiles of Na-DDS and key related ions for a) JFTOT Na + DDSA position 1, b) JFTOT Na + DDSA position 3, c) Needle 6 and d) Needle 7.

A schematic for the suggested mechanism of formation and decomposition of DDSA based on the depth profiles from Figure 5.15 is shown in Figure 5.16. This is the first research to indicate a sodium carboxylate source for sodium carbonate in diesel deposits. Similarly, zinc carbonates have been suggested to form from zinc carboxylates in IDIDs within the injector tip nozzle holes, based on a study finding their prevalent location within the nozzle relative to zinc carboxylates' location (76). There is a literature precedence for decomposition of sodium succinate into sodium carbonate based on a thermogravimetric study, however the oxidation step to sodium carbonate required high temperatures of 415-535 °C compared to this JFTOT's 180 °C and an internal injector of likely significantly below 300 °C (12, 203). The TGA environment is unpressurised and uses an inert atmosphere, while the JFTOT is moderately pressurised (3.45 MPa), aerated and contains other components, as well as the substrate which may act catalytically. A diesel

injector is at much higher pressure (up to 270 MPa) which could further promote Na-DDS breakdown (204).

**a) Acid-base reaction to form insoluble soap**



**b) Minor decomposition of deposit**

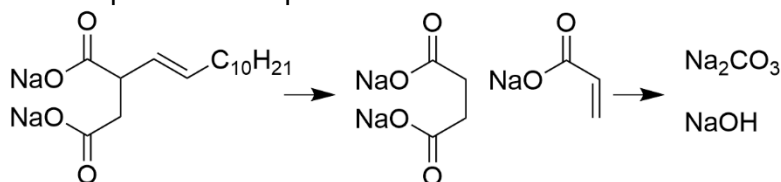


Figure 5.16: Mechanism of a) deposition and b) subsequent thermal decomposition suggested by OrbiSIMS depth profiles of JFTOT Na + DDSA.

### 5.2.5 Carboxylates and Triglycerides from Biofuels in JFTOT Deposits using OrbiSIMS

As mentioned in Section 5.2.3.1.1, biodiesel and HVO were included in this study in part due to the detection of possible chemistry of biological origin in Chapters 3 and 4, such as carboxylic acids. In this JFTOT study, similar chemistries were found correlating with biofuel samples. Calcium carboxylates were prevalent at early positions of JFTOTs containing HVO which may indicate a carboxylate soap formation resulting from leftover carboxylic acids if the hydrogenation process shown in 1.1.4 is incomplete and calcium contamination which can originate from the plant oil (205). This is evidenced by OrbiSIMS ions of calcium stearate ( $C_{18}H_{35}O_2Ca^+$ ) and calcium palmitate hydrates ( $C_{16}H_{31}O_2Ca.H_2O^+$  and  $C_{16}H_{31}O_2Ca.(H_2O)_2^+$ ) present at position 1 of JFTOT HVO and positions 1 and 2 of JFTOT HVO50. These were detected by PCA (PC 5, positive polarity, <0.7 mass filtering), seen in Figure 5.17a-b. Calcium stearate also has a significant peak in JFTOT Lubricant, likely due to lubricant oil's calcium content and carboxylic acid additives (80). Calcium is detected in JFTOT HVO and JFTOT HVO50 by XPS, however is also present in similar concentrations in other JFTOT samples (Figure 5.17c) which have small or absent calcium carboxylate OrbiSIMS ions so is likely present in other

forms. Calcium is at its highest concentration at position 1, but for many samples remains present at position 3, including in JFTOT Lubricant. Some of this calcium may originate from sample surface contamination, but as calcium carboxylates are exclusive to JFTOTs with HVO and lubricant, the calcium in these components appears to have formed soaps that are likely to be problematic for injector systems.

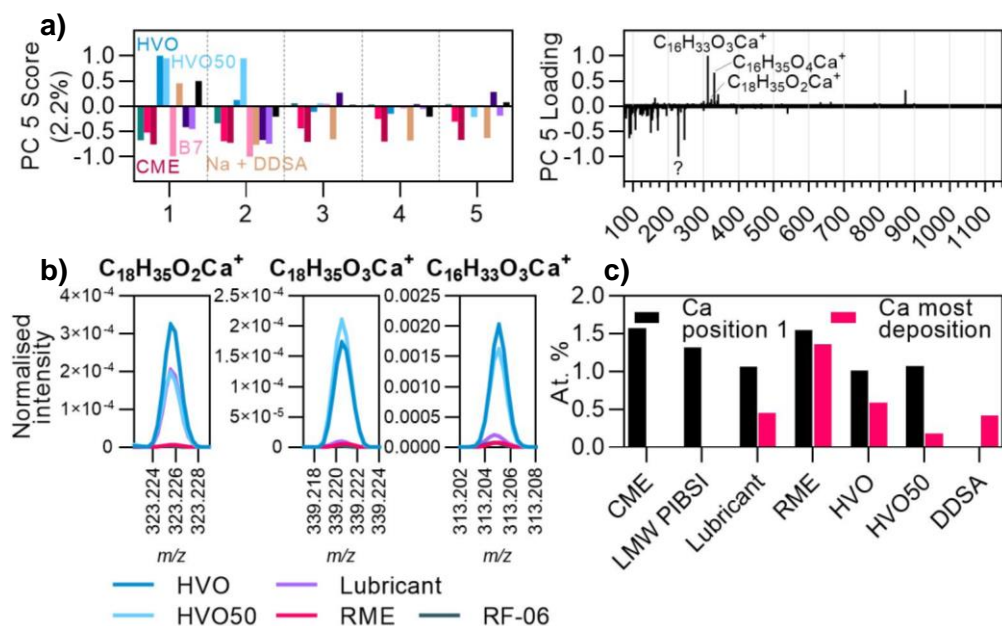


Figure 5.17: JFTOT calcium carboxylate data. a) Scores and loadings for PC 5 (positive polarity, <0.7 mass filtering). b) Normalised peaks of secondary ions of interest found by PC 5. c) Calcium atomic percentage from XPS quantification for position 1 and the position of most deposition (position 3 for all samples except HVO, position 5).

Sodium-adducted triglycerides (TAGs) were found only in JFTOT CME, alongside free fatty acids and sodium-adducted fatty acids, with intensity distributions that roughly correspond to the fatty acid profile of coconut oil. Hence, these ions are linked to the coconut feedstock and strongly indicate that the TAGs and acids of the coconut oil have contaminated the system and deposited. Trilaurin was confirmed in this sample via MS/MS (Table 5.3), showing fragmentation into structures close to dilaurin after loss of laurate or sodium laurate. Figure 5.18 shows the relative intensity distributions of the acids from these ion types (for TAGs, constituent acid intensity distribution was derived from TAG intensities according to their constituent acids) compared to a literature range for coconut oil, where the dominant acids are

the same as those of the oil. For each ion type, lauric acid (12:0) is dominant, followed by myristic (14:0), capric (10:0) and palmitic (16:0) which are in comparable proportions to the oil range. Triglycerides can remain in biodiesel from unreacted feedstock which could cause issues for injector systems (89). The acids may be present in the fuel/deposit or may generally be SIMS fragments of the triglycerides.

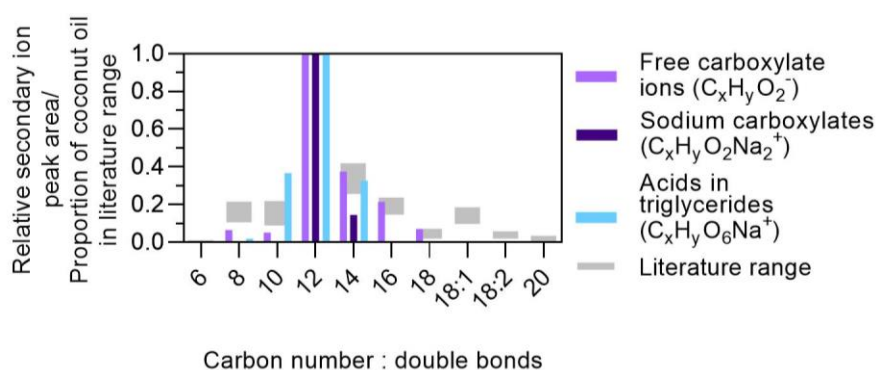


Figure 5.18: Distribution of carboxylics in JFTOT CME (position 3) as free carboxylate, Na-carboxylate, and TAG secondary ions, compared to the Caballero *et al.*'s reported range for coconut oil's acids distribution normalised to lauric acid (12:0) (206).

Table 5.3: MS/MS results for sodium adducted trilaurin ion in JFTOT CME position 3.

Mass	ID	Assignment	DBE	Intensity	Neutral loss
661.5375	Trilaurin	C <sub>39</sub> H <sub>74</sub> O <sub>6</sub> Na <sup>+</sup>	2.5	1.62E4	Parent
461.3597	Dilaurin	C <sub>27</sub> H <sub>50</sub> O <sub>4</sub> Na <sup>+</sup>	2.5	2.81E3	C <sub>12</sub> H <sub>24</sub> O <sub>2</sub>
439.3780	Dilaurin	C <sub>27</sub> H <sub>51</sub> O <sub>4</sub> <sup>+</sup>	2.5	3.22E3	C <sub>12</sub> H <sub>23</sub> O <sub>2</sub> Na

Free carboxylate ions were seen in other samples' negative polarity data, though the two most common (palmitate and stearate) were likely generally from sample surface contamination and not originating from the fuel (Appendix Section 0). There were other ions of possible biological origin that are common in plant oils (sterols and tocopherols), summarised in Appendix 3.8. This demonstrates the ability to probe, with high sensitivity, the presence of such compounds in a lab-produced deposit using OrbiSIMS and highlights that biodiesel can contribute unique chemistries to JFTOTs and IDIDs.

The data in this section has demonstrated that carboxylic acids and sodium/calcium carboxylates, triglycerides, and possibly other biomolecules

are present in diesel deposits. This supports the hypothesis that such compounds can play a role in diesel deposition and has potential implications for the tendency of biofuels to form deposits and could suggest that better treatment of biodiesel/HVO is necessary to ensure prevention of IDIDs. OrbiSIMS offers advantages for identification of such compounds over previous ToF-SIMS work with its superior mass resolving power and MS/MS capability (38, 59). Further work would be required to confirm the assignments in JFTOT RME using MS/MS and to investigate the effects of the species herein on fuel stability and deposit formation.

#### **5.2.6 Heavy Metals in JFTOT and IDID Deposits by OrbiSIMS and XPS: Zinc and Molybdenum**

OrbiSIMS ions containing zinc were present in JFTOT Zinc and JFTOT Lubricant while molybdenum appeared in JFTOT Lubricant. The zinc JFTOT experiment was performed as zinc was observed, most dramatically in Needle 8, in Section 3.2.4.3.2 which was attributed to lubricant oil contamination. Here, the presence of zinc in both JFTOT Zinc and JFTOT Lubricant supports this hypothesis, and indicates that zinc contamination in diesel, both as a neodecanoate salt and as ZDDP in lubricant oil, likely plays a role in diesel deposit formation. The use of ZDDP and other lubricant oil additives was discussed in Section 1.2.2.4.4. JFTOT Zinc possessed a set of zinc sulfate and phosphate-containing OrbiSIMS ions, as well as hydroxide (as was present in Needle 8 in Section 3.2.4.3.2), which were found in PC 2 (>0.7 mass filtering), shown in Figure 5.19a. These ions all had their highest intensity in JFTOT Zinc, with Needle 8 and JFTOT Lubricant generally having moderate intensities; this could suggest a higher prevalence, however is more likely a matrix effect as only Needle 8 registered zinc in its XPS spectrum (0.5 at.%) and is therefore the most affected by zinc. The only ion of potential zinc carboxylate origin found is  $\text{ZnC}_2\text{O}_2\text{H}^-$ , which is also most intense in JFTOT Zinc and may suggest a deposition of zinc neodecanoate as a soap; soap formation is one of the modes of deposition suggested to result from zinc contamination by Ikemoto *et al.* and by Ullmann *et al.* (60, 76).

In the positive polarity data,  $\text{CaZnO}^+$  (identified by PC6, >0.7 mass filtered earlier in Figure 5.10h) was present in both JFTOT Zinc and JFTOT Lubricant, appearing to represent a combination of zinc with calcium contamination. PCA (Figure 5.10h) identified positions 1-2 of JFTOT Zinc as having moderate intensities, and JFTOT Lubricant position 2 having the highest intensity. This result is expected as lubricant oil contains both zinc and calcium, and its deposition in the low temperature region suggests it could readily occur in an injector system. Needle 8 has a higher normalised intensity of this ion (Figure 5.19b), further supporting the theory of lubricant oil contamination of this sample, alongside the detectable zinc and significant concentration of calcium in its XPS data (Figure 5.10e). It can be proposed that Needle 8 had likely experienced a very significant zinc contamination from lubricant oil, greater than supplied by the dopant concentrations used in the JFTOT (50 ppm lubricant oil or 1 ppm zinc neodecanoate).

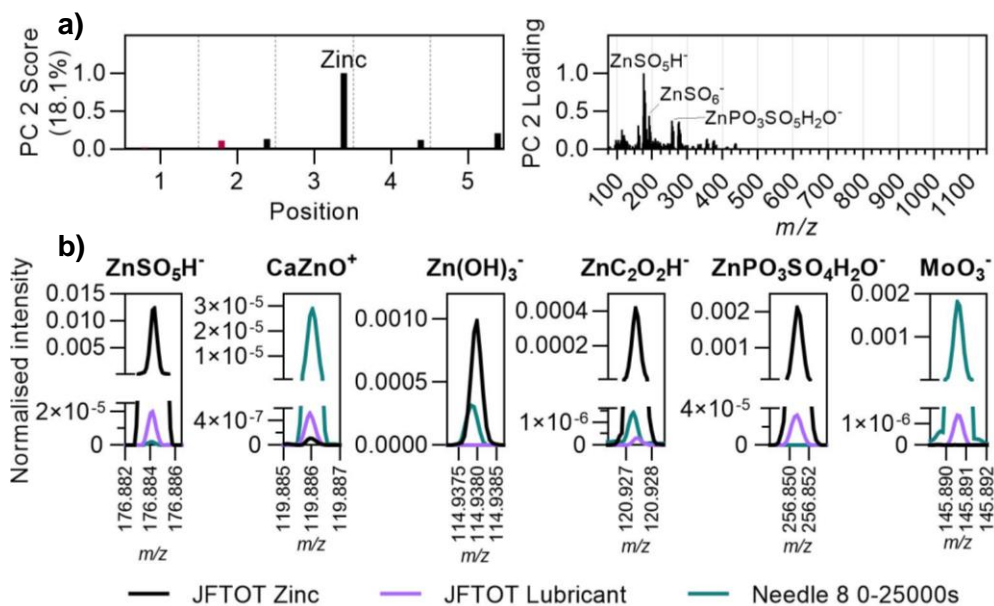


Figure 5.19: Zinc and Molybdenum OrbiSIMS data for relevant JFTOTs and for Needle 8 from 0-25,000 seconds etch time, a) PC 2 (>.7 mass filtering, negative polarity) results and b) normalised peaks of key ions comparing affected samples.

### 5.2.7 Optimising JFTOT Temperature for Simulation of IDID

#### Formation by OrbiSIMS and XPS Analysis

The JFTOT samples so far appear to be more carbonised than the real world IDIDs based on the higher mass polyaromatic ions (both PAHs and N-PACs) in OrbiSIMS which suggest formation of larger carbonised structures.

Therefore the conditions were too harsh to replicate IDIDs, with the high temperature thought to be responsible since the set-point temperatures of 300-360 °C are higher than that of fuel flowing over the needle in real injector systems which could theoretically reach 240 °C during pressure release (12, 139). To investigate more accurate JFTOT simulation of real-world IDID formation, JFTOT experiments were performed using RF-06 at lower temperatures (200 °C, 250 °C) and their hydrocarbon OrbiSIMS and XPS C 1s  $\pi$ - $\pi^*$  data is examined here. Previous investigations by Berndt and Shümann *et al.* (143, 146) have considered the region of the tube <180 °C relevant for IDID simulation as it is close to an injector's temperature, however this does not account for the injector using a higher pressure (144, 146). A temperature of 260 °C has been reported as a typical JFTOT temperature (139). With these lower temperatures, a longer run-time of 5 hours was necessary to produce sufficient deposit coverage.

Multiple positions of JFTOT 200 °C, JFTOT 250 °C and Needle 8 were analysed, shown in Figure 5.20. Note that the thermocouple was placed in a position closer to the inlet than previous samples to produce more deposit coverage on the tube. Across the tubes, the deposit distribution was different for the two samples. Visually, deposit formation appears closer to the inlet on JFTOT 250 °C, as expected due to the higher temperature of the tube, and proceeds to form its darkest appearing deposit near the centre (position 5); JFTOT 200 °C develops colour closer to the outlet, becoming darkest near the end (position 8). This has been observed previously by Lacey *et al.*, with higher temperature forming a deposit earlier on the tube (139). It should be noted that to ensure positions of interest (where colour changes occur) were analysed, the analysis positions for JFTOTs 200 °C and 250 °C are slightly different to one another.



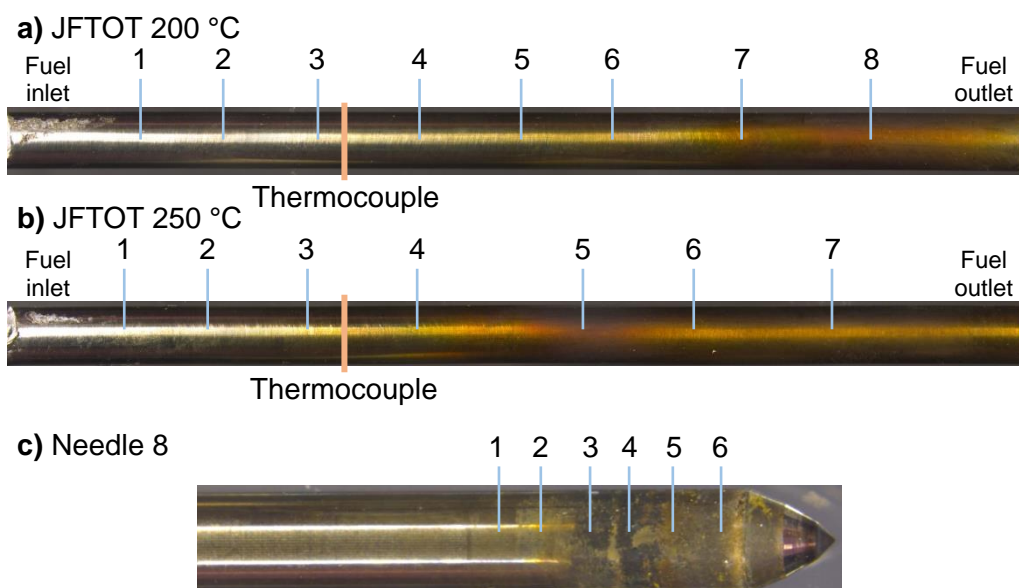


Figure 5.20: Images of a) JFTOT 200 °C, b) JFTOT 250 °C and c) Needle 8 with analysis positions labelled. Position of thermocouple (position of heating) is marked for JFTOT samples.

The OrbiSIMS and XPS results from JFTOT 200 °C, JFTOT 250 °C and Needle 8 indicate that a set temperature of 200 °C achieves carbonisation that is most comparable to Needle 8, particularly at positions 3-5 of this JFTOT tube which are near the heat source. OrbiSIMS PAH fingerprints of DBE as a function of  $m/z$  (Figure 5.21a) show this similarity, where the largest PAHs at JFTOT 200 °C positions 3, 4 and 5 ( $C_{53}H_{17}^+$ ,  $C_{59}H_{19}^+$  and  $C_{76}H_{18}^+$  respectively) are closest to the largest of Needle 8 ( $C_{72}H_{18}^+$ ). JFTOT 250 °C's deposit becomes significantly more carbonised than Needle 8 by only position 4, immediately after the thermocouple. At position 4, the PAH ions (highest mass  $C_{91}H_{21}^+$ ) are significantly larger than those in Needle 8 ( $C_{72}H_{18}^+$   $m/z$ ). Considering this more extensive carbonisation occurs next to the thermocouple, this temperature can be considered too high for IDID simulation.

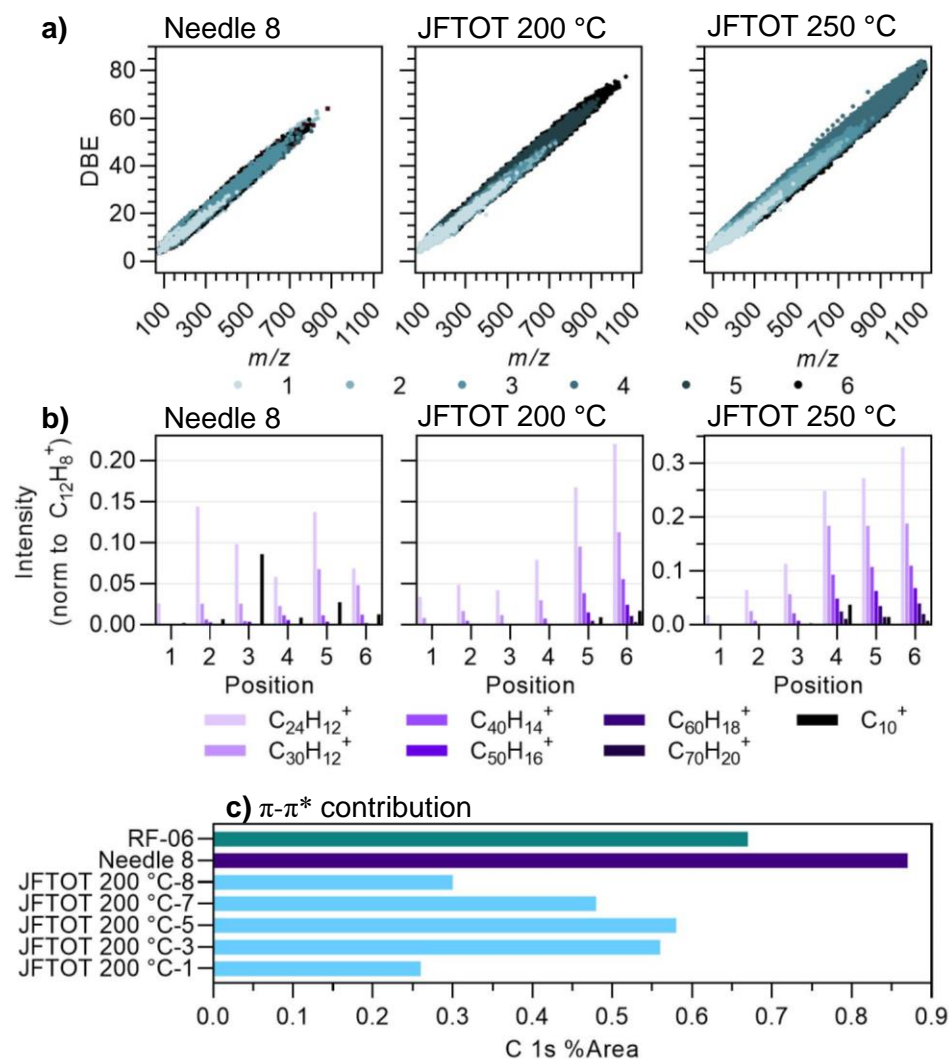


Figure 5.21: PAH data for Needle 8 and JFTOT 200 °C and JFTOT 250 °C. a) Hydrocarbon distributions of DBE as a function of  $m/z$ , b) PAH intensities normalised to  $C_{12}H_8^+$ . c) C 1s XPS  $\pi$ - $\pi^*$  component percentage area contributions.

At position 5 and above of JFTOT 200 °C, the polyaromatic ions are larger than in Needle 8, becoming comparable to the largest ions of JFTOT RF-06 seen earlier (Figure 5.3) which used a temperature of 300 °C. This supports the steel JFTOT tube having a catalytic effect as theorised in Section 5.2.1, with lower temperatures here producing comparable PAH ions to the higher temperature aluminium-magnesium tube.

The growth of PAH structures can be seen from the intensities of larger PAHs relative to a smaller PAH. Figure 5.21b shows a range of PAH intensities normalised to  $C_{12}H_8^+$  (acenaphthylene) of JFTOT 200 °C, where the

progression of growth of the larger PAHs can be seen along the JFTOT tubes. In contrast, a consistent progression is not observed for Needle 8, where many positions closer to the outlet have smaller relative intensities than those closer to the inlet. This is likely due to the injector being a more complex system, in which backflow can occur and other factors such as DCAs and high pressure exist. These normalised intensities (Table 5.4, full data in Appendix Table A50) also support the idea that positions 3-5 of JFTOT 200 °C are the optimum simulation of Needle 8's deposit, as they generally have values within the range of positions 2-5 of Needle 8. Interestingly, position 3 of Needle 8 has a much larger peak for  $C_{10}^+$  than other positions of this sample as well as the two JFTOTs. This is a position on a thick black ring of deposit on the needle (Figure 5.21c) and possibly suggests an alternative type of carbonised deposit at this position.

Table 5.4: PAH secondary ion intensities in JFTOT 200 °C, JFTOT 250 °C and Needle 8 normalised to intensity of  $C_{12}H_8^+$ , then normalised to the largest intensity position for each respective ion in either JFTOT 200 °C or Needle 8, with heat map applied to relevant sample positions. Heat map applied to all table where red = 0 and green = 1, with the exception of JFTOT 250 °C position 4 which is excluded due to its much larger values.

Sample, position		Intensities normalised to C <sub>12</sub> H <sub>8</sub> <sup>+</sup> , then normalised to largest intensity position for each ion in JFTOT 200 °C or Needle 8						
		C <sub>24</sub> H <sub>12</sub> <sup>+</sup>	C <sub>30</sub> H <sub>12</sub> <sup>+</sup>	C <sub>40</sub> H <sub>16</sub> <sup>+</sup>	C <sub>50</sub> H <sub>18</sub> <sup>+</sup>	C <sub>60</sub> H <sub>16</sub> <sup>+</sup>	C <sub>70</sub> H <sub>16</sub> <sup>+</sup>	C <sub>10</sub> <sup>+</sup>
JFTOT 250 °C	1	0.11	0.03	0.00	0.00	0.00	0.00	0.00
	2	0.38	0.26	0.19	0.10	0.00	0.00	0.00
	3	0.68	0.59	0.55	0.50	0.41	0.00	0.03
	4	1.48	1.92	2.41	3.19	5.22	9.17	0.43
JFTOT 200 °C	1	0.20	0.09	0.03	0.00	0.00	0.00	0.00
	2	0.29	0.17	0.13	0.09	0.00	0.00	0.00
	3	0.25	0.12	0.03	0.00	0.00	0.00	0.00
	4	0.47	0.31	0.20	0.10	0.00	0.00	0.02
	5	1.00	1.00	1.00	1.00	1.00	1.00	0.11
Needle 8	1	0.15	0.00	0.00	0.00	0.00	0.00	0.03
	2	0.86	0.27	0.16	0.19	0.22	0.19	0.08
	3	0.59	0.27	0.11	0.25	0.00	0.00	1.00
	4	0.35	0.24	0.30	0.38	0.00	0.00	0.10
	5	0.82	0.71	0.30	0.24	0.00	0.00	0.32
	6	0.41	0.50	0.32	0.15	0.20	0.00	0.15

The polyaromatic deposit at positions 3-5 of JFTOT 200 °C was also found to be quantifiably comparable to Needle 8, further validating these parameters as an effective simulation temperature. High-resolution C 1s XP spectra of JFTOT 200 °C show the growth of the  $\pi$ - $\pi^*$  component (Figure 5.21c) from position 1 to 5 before declining. It is therefore proposed that though the later position has larger PAHs, they are smaller in concentration. At position 3 and 5, the  $\pi$ - $\pi^*$  components as a share of the C 1s peak (0.56% and 0.58% respectively) are smaller but comparable to Needle 8 (0.87 %) and only slightly smaller than JFTOT RF-06's central position (0.67%).

### 5.2.7.1 Lateral PAH Distribution in JFTOTs using OrbiSIMS

The lateral distributions of the PAHs on the surface of JFTOT 200 °C were investigated using GCIB-Orbitrap<sup>TM</sup> imaging (Figure 5.22), showing a relatively ubiquitous and heterogeneous surface presence, indicating a widespread formation of such material from the fuel. This resembles the distributions of these ion types that were shown for Needle 8 in Section 3.2.3.2, supporting the finding that the JFTOT is an effective simulation of carbonaceous IDID formation. This widespread distribution is seen for PAHs, N-PACs and the carbonaceous ion, with each having a lack of features in their images. In contrast, the calcium hydroxide ion is localised on the right side of the image, likely originating from surface contamination of the sample as it was present also on the clean, unused JFTOT tube.

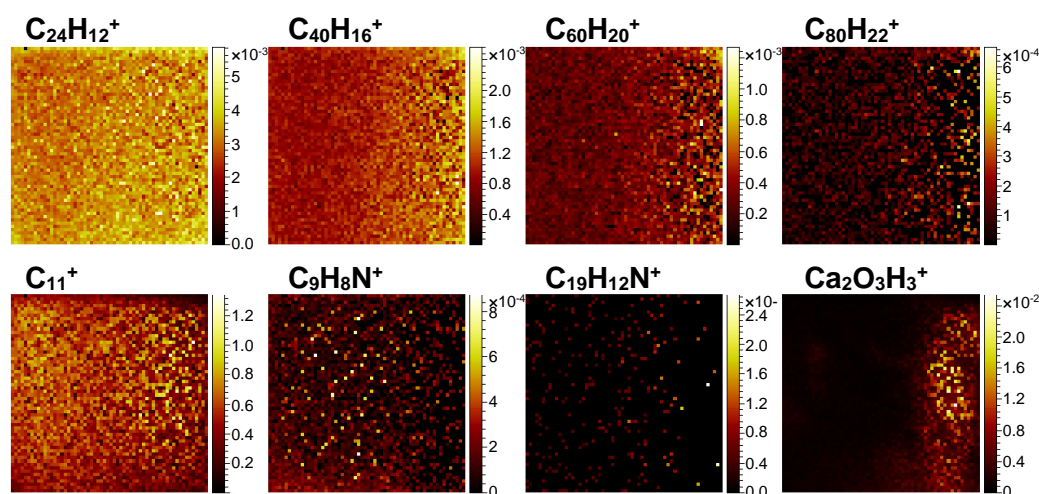


Figure 5.22: GCIB-Orbitrap<sup>TM</sup> 300×300 μm images of PAH ions, a carbonaceous ion, N-PAC ions and a calcium hydroxide ion at position 8 of JFTOT 200 °C (the position of highest deposition). All normalised to the total ion image.

### 5.3 Conclusions

This chapter has discussed an investigation of the effects of a broad range of fuels and additive components in the JFTOT and implications for real world IDIDs. With OrbiSIMS, the unprecedented combination of SIMS with high resolution mass spectrometry enables identification of molecular species *in-situ*. Multivariate analysis identifies important deposit chemistries that correlate with each component, with greater detail and certainty than has been achieved in previous investigations using other techniques such as ToF-SIMS and GC-MS. Surface XPS scans quantitatively probed the atomic content of the main deposits of interest to validate and build on the semi-quantitative OrbiSIMS data interpretations. With comparisons to field samples, the same chemistries have been shown to affect real systems and evidence the ways in which each component can contribute to the IDID phenomena. Depth profiling was again a key technique to probe potential mechanisms, as well as analysis of multiple positions along a sample to determine the changes in deposit composition along the tube's temperature profile, which peaks at the central thermocouple position. Mechanistic evidence was afforded for the polyaromatic material which was widespread in most samples as PAHs, N-PACs and O-PACs, as well as carbonaceous material including N-, P- and S- carbonaceous ions. It was found that larger PAH ions and those with lower H:C ratios exist deeper in the deposit material, evidencing a progression of carbonisation closer to the heated JFTOT tube. The *formula\_calculator* script has been employed to create fingerprints of polyaromatic ions, which can be used to visually compare the composition of and degree of carbonisation at each position of each sample. The JFTOT doped with zinc, which used a steel JFTOT tube, was found to possess extremely large PAH ions using this method.

A unique sample was produced at lower temperature from the addition of DDSA and sodium, which produced a sodium carboxylate deposit like those well-documented in the literature for real-world samples. A key finding here was evidence of a minor decomposition of this deposit into sodium carbonate, which has not been established in previous studies. With sodium carbonates

prevalent in field IDIDs, this is one possible source of such deposit chemistry. Other unique chemistries contributed by certain components were nitrogen from LMW PIBSI which formed extensive N-PACs, S- and P-containing chemistries from biodiesels and lubricant oil which integrated into carbonised material, biomolecules including triglycerides from biodiesels, and zinc contributed by zinc neodecanoate or lubricant oil.

A persistent issue with many JFTOT deposits herein was the extent of carbonisation observed, finding polyaromatic material of much greater mass than in IDIDs. This was suspected to be linked to the high temperatures used ( $\geq 300$  °C), so additional JFTOT deposit samples formed using lower temperatures were analysed, finding polyaromatic molecular weight distributions that matched more closely with a highly PAH-affected field sample. Based on this finding, it is recommended that further JFTOT investigations intending to mimic IDID formation use a temperature of 200 °C to produce a more comparable material. Imaging of this sample also showed a relatively even distribution of the polyaromatic ions, which has also been observed in a field IDID. This investigation also found that the steel JFTOT tube promotes carbonisation of the fuel compared to the aluminium-magnesium JFTOT tube; with the importance of this substrate, the steel tube is recommended to mimic more closely a real steel injector needle. These findings relate to the limitations of the JFTOT as discussed in Section 1.3.4; the higher temperature was thought to be required due to the lower pressure of the JFTOT compared to the injector and low run-time of the JFTOT, as well as the material of the JFTOT tube differing from that of a real injector system. The results here indicate the conditions that can reduce this limitation by better replicating the environment that forms carbonaceous deposits within diesel FIE. However, being a rudimentary model system, the JFTOT suffers from significant intrinsic limitations in replicating this environment compared to engine testing using real diesel engines and FIE.

Though no repeats were included for PCA to ensure a statistically robust model, this data can serve to inform future analysis of IDIDs, indicating the potential origins of certain chemistries and their mechanisms of formation. The

success of the techniques also lays a foundation for further work, where other components can be probed or the same fuels and additives used in different proportions, with different temperatures or other test parameters and with more in-depth analysis. Incorporation of MALDI-MS could confirm which ions are the native parent species and which are fragments thereof. Future work could involve repeats to ensure the PCA model can be predictive of which chemistries are associated with each fuel/additive/contaminant.

## Chapter 6: Conclusions and Future Work

### 6.1 Research summary

Throughout the work in this thesis, the novel application of OrbiSIMS to IDIDs has shown new chemical detail compared to prior investigations involving ToF-SIMS and other techniques. Chapter 3 provides an overview of this, with samples from real-world injector failures analysed using an OrbiSIMS and complementary XPS approach, where the XPS data proved invaluable for quantitative contextualisation and validation of the OrbiSIMS results. This indicated carbonisation processes occur in IDID formation, as well as interactions of additives such as poor quality (low and high mass) PIBSI, and deposits from contamination such as zinc and inorganic salts of sodium and calcium. Chapter 4 introduces a novel post-processing method for the interpretation of NMF results and provides extensive detail for three IDID samples, suggesting how these deposits may have formed. Chapter 5 extends the analytical methods to samples generated in the laboratory using the JFTOT. A PCA approach for a range of JFTOT samples identified their differences and similarities which highlighted chemistries shared by real-world samples, including polyaromatics from carbonisation, inorganic salts and sodium succinate salts. Thus, the origin of these chemistries is indicated by the components that were used to produce the relevant JFTOT.

### 6.2 Conclusions

Throughout the OrbiSIMS data of IDIDs and JFTOT deposits, polyaromatic ions are commonly seen and suggest the occurrence of a process of carbonisation that likely begins with fuel components and progresses towards a soot-like carbonaceous deposit under the heat and pressure in the injector or JFTOT heater section. This process is supported by depth profiles, showing larger polyaromatic structures in the lower deposit, and by the JFTOT samples which show similar larger structures towards the hotter and later positions (towards the fuel outlet). Ions of nitrogen- or oxygen-containing polyaromatic



structures are also prevalent and are suggested to result from the incorporation of nitrogen- and oxygen-containing compounds from the fuel mixture into the carbonisation process. This is supported by their prevalence in the JFTOT sample that was doped with LMW PIBSI, a nitrogen-containing additive. Succinimide ions, thought to represent this compound's central structure were seen above the N-PAC ions in the depth profiles, supporting that they decompose to form N-PAC chemistry. Evidence of LMW PIBSI was also seen in the IDID samples with succinimide ions, however one IDID sample contained extremely high mass structures similar to PIBSI which are thought to represent similarly low-quality PIBSIs with masses too large to originate from DCAs. MS/MS analysis of these ions suggested hydrolytic ring-opening of the succinimide may have occurred, which has not been seen before.

Alkylbenzene sulfonate (ABS) chemistry was observed on many field IDIDs and thought to originate from lubricant oil contamination of the injector system. Other evidence of lubricant oil was seen in the form of calcium and zinc salts, particularly on Needle 8, the only sample that registered zinc in its XP spectra. OrbiSIMS data showed ABS presence on all JFTOT samples, where it was only expected on JFTOT Lubricant, therefore ABS may in fact originate from surface contamination rather than, or as well as, lubricant oil. However, JFTOTs Lubricant, RME and CME all showed an integration of sulphur and phosphorus into carbonaceous deposit material, indicating that these components do contribute sulphur as well as phosphorus; each of these components are known to contain both elements, therefore a similar process to that involving nitrogen for LMW PIBSI is suggested to occur with sulfur and phosphorus. JFTOT Lubricant as well as JFTOT Zinc show zinc presence, confirming lubricant oil as a zinc deposit source and that zinc neadecanoate as included in the DW10b IDID engine test forms a zinc-containing deposit. JFTOT Zinc was seen with extremely larger polyaromatic ions in OrbiSIMS and a large  $\pi$ - $\pi^*$  component by XPS, however it is suggested that the steel tube used in this experiment promotes deposit carbonisation by catalysis, therefore it is unknown if zinc itself also promotes carbonisation.

Sodium carboxylates, an IDID issue known for a long time, are seen in IDIDs and in JFTOT Na + DDSA, most predominantly by OrbiSIMS as sodium dicarboxylates (specifically succinates). Na-DDS was observed in multiple IDIDs and JFTOT Na + DDSA, while Na-HDS was also seen in some IDIDs; other carboxylate salts were also seen in JFTOT Na + DDSA, primarily Na-stearate and Na-palmitate, which may originate from the naphthenate, however they have much lower intensity than Na-DDS and are therefore likely less prevalent in the deposit. Depth profiles of JFTOT Na + DDSA revealed sodium carbonate situated closer to the substrate than the carboxylates, indicating its production from a mechanism of thermal decomposition of the carboxylates that exist closer to the surface; comparison to the IDID samples found the same structure with sodium carboxylates above carbonate. Other sodium inorganics such as sulfates occur in the lower layer in all samples, indicating sodium contamination may form the carboxylate salts alongside inorganic components, which may occur primarily from deposit decomposition and are widespread in the OrbiSIMS data of IDIDs in Chapter 3 and 4.

The in-depth statistical analysis of three IDID depth profiles in Chapter 4 observed many of the chemistries previously discussed, though many inorganic salt components were most prominent. This analysis involved a novel “comparative” post-processing method described in Section 4.2.3.1 which facilitates deconvolution of the NMF results. In Needles 6 and 8, a needle substrate of primarily carbon was seen which indicates a DLC needle coating, while Needle 7 had a steel substrate of typical steel alloying elements in ions of oxide and hydroxide form. The results of this study suggest Needle 6 formed via sodium sulfate- and carbonate-contributing components. This may be biodiesel which is formed using sodium catalysts and may contain sulfur as seen in the JFTOT results. Sodium carboxylates were seen in the upper deposit which, as discussed above for the JFTOT, may be the source of the deeper sodium carbonate. Needle 8 shows extensive lubricant oil evidence which appears more apparent in the deeper pseudo-layers; zinc, calcium, sulfates and phosphates are increasingly evident towards the substrate, and the substrate appears to have integrated with some of these chemistries, with OrbiSIMS showing ions of mixed calcium and steel alloy element hydroxides/oxides,

many also containing phosphates. Needle 7, like Needle 6, showed extensive sodium contamination, however with greater diversity, including carbides, amides and phosphates, indicating a wide range of inorganic contamination and possible integration of carbonaceous material with sodium to form salts, which may suggest these different deposit types are more related than previously thought.

While the temperature of the internal injector environment is thought to be around 200-300 °C, the JFTOT has typically been run at 300 °C to accelerate the deposit formation process and allow the test to be conducted in a short period of time and under its lower pressure than in diesel FIE (12). Here, additional experiments at 250 °C and 200 °C for five hours indicated that a temperature of 200 °C simulates IDID formation most accurately in terms of carbonisation to produce similar mass polyaromatic species. Therefore, JFTOT experimental conditions of 200 °C for five hours are recommended for further IDID simulation investigations.

## **6.3 Future Work**

### **6.3.1 Use of Novel SIMS and XPS Methods**

This work has introduced new methods to the field of IDID characterisation, namely the application of GCIB depth profiling, OrbiSIMS and combining XPS with depth profiling. Based on the successful characterisations using these methods, it can be recommended to be adopted where available for characterisation of IDIDs where detail is required or where other techniques fail to provide the information of interest. XPS to support OrbiSIMS can be recommended routinely to prevent focus on minor components during OrbiSIMS interpretation, particularly for samples containing inorganic salts. The NMF ‘comparative’ method in this work could also be applied to other systems for detailed characterisation of layered (whether distinctly or with significant transitional stages as is the case here) materials.

### 6.3.2 Validation of GCIB Depth Profiling

While the  $\text{Ar}_{3000}^+$  beam is known to be highly effective for preserving the underlying sample material beneath the sputtered top layer and there is corroboration between the results of OrbiSIMS  $\text{Ar}_{3000}^+$  depth profiling and XPS  $\text{Ar}_{500}^+$  depth profiling, an alternative method of probing chemical variation with depth could provide further validation of these methods, ensuring no misinterpretation of data due to sample damage or differential sputter rates of different deposit components. For example, a technique that has previously been applied was etching with a focused ion beam (FIB) at an angle to create a ramp that exposes the cross-sectional full thickness of the deposit (127, 128). Subsequent OrbiSIMS imaging of the cross-section should show the same layering effects and pseudo-layering compositions as observed through depth profiling. This would potentially require less analysis time, provide validation of the depth profiling methodology and allow for the distribution of chemistries in the lateral plane to be seen, adding an extra dimension. However, care must be taken with FIB methodology to avoid damaging the material to be imaged; this can be mitigated if necessary by using a GCIB to remove any damaged material from the surface of the cross-section.

### 6.3.3 Expansion of JFTOT IDID Simulation Investigation

The OrbiSIMS and XPS methods of Chapter 5's JFTOT investigation prove to be successful in identifying a greater range of chemistries, with more detail and discoveries, than previous JFTOT investigations. While the investigation was large-scale, featuring numerous samples produced using four fuels and four dopants with a range of combinations and temperatures, there are other components and parameters that could be explored with the method. Examples include the effect of 2-EHN, calcium contamination and the effect of different degrees of fuel aeration on the deposit composition. Based on the range of temperatures used in the current work, it is recommended to perform future JFTOT tests at 200 °C for 5 hours. Though PCA in this investigation included many JFTOT sample datasets, it can only be considered indicative due to the lack of repeats of the same region for each sample and the resulting lack of confidence intervals for PC scores. Producing a robust statistical model that is

predictive and can probe subtle differences between the different fuel/dopant deposit datasets could be the focus of further investigations. This would be recommended to involve repeat analysis runs of the JFTOT analysis positions and repeats of JFTOT experiments using the same fuel to ensure that findings are repeatable and consistent, providing more robust statistical predictions. Due to the continuously changing environment across the lateral positions of the JFTOT heater tube, repeats of OrbiSIMS spectra should be acquired using stage rotation to ensure the same lateral position is measured for each acquisition. Then, utilising the feature selection tools of the PCA Bundle could enable identification of the key ions responsible for the differences and similarities between the samples, simplifying the data significantly (161). However, given the JFTOT's limitations in simulating the internal injector environment, future investigations based on findings from the current work would be more effective using engine testing if available.

A more complete JFTOT/engine testing deposit characterisation method could also be employed, for example a full characterisation of the fuel prior to analysis might enable further insights into the impact of specific compounds or how they form the deposit. This could be of particular value for biodiesel which may contain a wider range of compounds of biological origin that could produce the unique ions observed in the biodiesel JFTOT's deposit. As another expansion to the method to investigate how deposit layering might arise, the fuel could be changed or dopant introduced during the JFTOT/engine test run, to observe if this forms a new layer on top of the other similarly to in real-world deposits.

#### **6.3.4 Determination of IDID Formation Mechanisms**

Mechanisms of deposit formation have been suggested throughout this thesis based on OrbiSIMS data, from both IDIDs and JFTOT deposits, primarily using the spatial information acquired, building on those described in the literature. While the JFTOT offered a controlled environment where deposit formation could be related to individual components, the limitations of the JFTOT in mimicking the internal FIE environment potentially results in

different mechanisms to those occurring in real FIE IDIDs. Therefore, engine testing should be pursued to provide validation for these mechanisms. Another important consideration in a subsequent larger-scale investigation would be an analysis of the fuels used in any JFTOT or engine tests so the “reagents” of the deposit-forming reactions are known and mechanisms can therefore be understood more reliably. Further, a modified, simpler version of diesel could be used, for example consisting of only one alkane species, to limit the investigation’s variables and better understand what reactions such species undergo based on the chemistries in the resultant deposit and their location in terms of deposit depth. JFTOT/engine test work could also use carbon-13 labelling of components of interest to observe which chemistries of certain components contribute to the deposit and the transformations they undergo in deposit formation. Laboratory investigations of the reactions of certain fuel/additive/contaminant components could also feature to validate proposed reaction mechanisms, however the engine/injector environment is difficult to recreate and therefore this should likely be limited to investigating the fundamental qualities and interactions of certain compounds.

### **6.3.5 Expansion of AP-MALDI-MS Methodology**

The initial test performed in Section 3.2.6.4 involving AP-MALDI-MS of the marine injector deposit demonstrates promise that the technique can be used to validate the OrbiSIMS data by identifying the likely parent species with reduced fragmentation. This could be expanded to IDID analysis in any situation where there is uncertainty about which ions represent the native, intact parent compounds. In this work, this would particularly apply to the polyaromatic ions which show complex patterns in OrbiSIMS. MALDI experiments would be recommended for the IDIDs seen in Section 3.2.3 and particularly for the very high mass PAHs seen in JFTOT Zinc in Section 5.2.1. Further optimisation of MALDI appears to be required based on the variability of results for different parameters, therefore this is recommended initially for PAH-type ions and subsequently for any other chemistries of interest to ensure that intended material is accessed and analysed.

### 6.3.6 Automation of Orbitrap<sup>TM</sup> Noise Treatment

Noise treatment was performed in this work manually by the analyst inspecting the spectra in SurfaceLab. The development of an automated method to achieve this is recommended to reduce the time required for processing of OrbiSIMS data. Mitchell *et al.*'s algorithm for identifying "fuzzy site" noise in mass spectra could be a basis for this (160).

### 6.3.7 Future Analytical Workflow Recommendations

For future investigations building on the insights into IDID and diesel deposit chemistry generated throughout this thesis, large scale OrbiSIMS investigations with the PCA approach can be recommended for understanding the influence of any range of factors of interest, whether using FIE samples or simulations such as the JFTOT. Ideally such investigations should include several repeats to improve statistical validity, and potentially feature selection (in the PCA Bundle) to simplify the results by identifying the most important ions responsible for differences between different samples' datasets.

Incorporation of real-world IDID samples alongside JFTOT or engine testing samples would also be of value to indicate the fuel/additive/contaminant components that are likely present in and responsible for each IDID with a statistical basis rather than the more qualitative comparison between IDIDs and JFTOT deposits used in Chapter 5. XPS should always be advised where OrbiSIMS identifies elemental differences between samples and potentially advised where differences are identified that could be explained with curve-fitting of the C 1s peak or others, though these fittings are often difficult due to the chemical heterogeneity of these deposits and thus the range of chemistries that would produce many components of these peaks. If further corroboration between OrbiSIMS and AP-MALDI-MS data is demonstrated for a range of types of deposit chemistry, it is suggested that AP-MALDI-MS can be applied in certain cases in support of OrbiSIMS, however it should likely be recruited when validation of the parent species of OrbiSIMS ions is required.

## References

1. Dingle P, Lai M-C. Diesel common rail and advanced fuel injection systems: SAE; 2005.
2. Trobaugh C, Burbrink C, Zha Y, Whitacre S, Corsi C, Blizzard N. Internal Diesel Injector Deposits: Theory and Investigations into Organic and Inorganic Based Deposits. *SAE Int J Fuels Lubr.* 2013;6(3):772-84.
3. Barker J, Snape C, Scurr D. Information on the Aromatic Structure of Internal Diesel Injector Deposits From Time of Flight Secondary Ion Mass Spectrometry (ToF-SIMS). *SAE Technical Paper* 2014-01-13872014.
4. Stępień Z. Types of internal Diesel injector deposits and counteracting their formation. *Combustion Engines.* 2015;54.
5. Reif K. Fundamentals of automotive and engine technology. Springer: Bosch professional automotive information. 2014.
6. Mollenhauer K, Tschöke H, Johnson KG. Handbook of diesel engines: Springer Berlin; 2010.
7. Richards P. Automotive Fuels Reference Book. 3rd Edition R-297 ed: SAE International; 2014.
8. Winterbone D, Turan A. Advanced thermodynamics for engineers: Butterworth-Heinemann; 2015.
9. Kalghatgi G. Fuel/engine interactions: SAE international; 2013.
10. Strotos G, Koukouvini P, Theodorakakos A, Gavaises M, Bergeles G. Transient heating effects in high pressure Diesel injector nozzles. *International Journal of Heat and Fluid Flow.* 2015;51:257-67.
11. Moon S, Tsujimura T, Gao Y, Park S, Wang J, Kurimoto N, et al. Biodiesel effects on transient needle motion and near-exit flow characteristics of a high-pressure diesel injector. *Int J Engine Res.* 2014;15(4):504-18.
12. Königsson F, Stalhammar P, Angstrom H-E. Controlling the injector tip temperature in a diesel dual fuel engine. *SAE Technical Paper*; 2012. Report No.: 0148-7191.
13. Crua C, Heikal MR. Time-resolved fuel injector flow characterisation based on 3D laser Doppler vibrometry. *Measurement Science and Technology.* 2014;25(12):125301.
14. Wexler P, Anderson BD, Gad SC, Hakkinen PB, Kamrin M, De Peyster A, et al. Encyclopedia of toxicology: Academic Press; 2005.
15. de Souza CV, Correa SM. Polycyclic aromatic hydrocarbons in diesel emission, diesel fuel and lubricant oil. *Fuel.* 2016;185:925-31.
16. Puricelli S, Cardellini G, Casadei S, Faedo D, Van den Oever A, Grosso M. A review on biofuels for light-duty vehicles in Europe. *Renewable and Sustainable Energy Reviews.* 2021;137:110398.
17. Union E. Directive (EU) 2018/2001 of the European Parliament and of the Council of 11 December 2018 on the promotion of the use of energy from renewable sources Official Journal of the European Union; 2018.
18. Brutschin E, Fleig A. Geopolitically induced investments in biofuels. *Energy Economics.* 2018;74:721-32.



19. Fukuda H, Kondo A, Noda H. Biodiesel fuel production by transesterification of oils. *Journal of bioscience and bioengineering*. 2001;92(5):405-16.
20. Hoekman SK, Broch A, Robbins C, Cenicerros E, Natarajan M. Review of biodiesel composition, properties, and specifications. *Renewable and sustainable energy reviews*. 2012;16(1):143-69.
21. Ramos MJ, Fernández CM, Casas A, Rodríguez L, Pérez Á. Influence of fatty acid composition of raw materials on biodiesel properties. *Bioresource technology*. 2009;100(1):261-8.
22. Atadashi I, Aroua MK, Aziz AA. High quality biodiesel and its diesel engine application: a review. *Renewable and sustainable energy reviews*. 2010;14(7):1999-2008.
23. Flach B, Lieberz S, Bolla S. *Biofuels Annual*. United States Department of Agriculture; 2020.
24. Erkkilä K, Nylund N-O, Hulkkonen T, Tilli A, Mikkonen S, Saikkonen P, et al. Emission performance of paraffinic HVO diesel fuel in heavy duty vehicles. *SAE Technical Paper Series* 2011.
25. Huber GW, O'Connor P, Corma A. Processing biomass in conventional oil refineries: Production of high quality diesel by hydrotreating vegetable oils in heavy vacuum oil mixtures. *Applied Catalysis a-General*. 2007;329:120-9.
26. Aatola H, Larimi M, Sarjovaara T, Mikkonen S. Hydrotreated Vegetable Oil (HVO) as a Renewable Diesel Fuel: Trade-off between NO<sub>x</sub>, Particulate Emission, and Fuel Consumption of a Heavy Duty Engine. *SAE International Journal of Engines*. 2009;1(1):1251-62.
27. Ribeiro NM, Pinto AC, Quintella CM, da Rocha GO, Teixeira LS, Guarieiro LL, et al. The role of additives for diesel and diesel blended (ethanol or biodiesel) fuels: a review. *Energy & fuels*. 2007;21(4):2433-45.
28. *Fuel Additives: Uses and Benefits*. 2013.
29. Topham G. The death of diesel: can struggling industry woo back consumers? *The Guardian*. 2018.
30. Leggett T. Air pollution: Are diesel cars always the biggest health hazard? *BBC News*. 2018.
31. Leggett T. Electric vehicle sales outpace diesel again. 2021.
32. Association EAM. Fuel types of new passenger cars in the EU: European Automobile Manufacturers' Association; 2021 [
33. Association EAM. *Vehicles In Use Europe 2022*. 2022.
34. Carey N, Steitz C. EU proposes effective ban for new fossil-fuel cars from 2035. *Reuters*. 2021.
35. Union E. Regulation (EC) No 715/2007 of the European Parliament and of the Council of 20 June 2007 on type approval of motor vehicles with respect to emissions from light passenger and commercial vehicles (Euro 5 and Euro 6) and on access to vehicle repair and maintenance information. *Official Journal of the European Union: European Union*; 2007.
36. Posada Sanchez F, Bandivadekar A, German J. *Estimated Cost of Emission Reduction Technologies for Light-Duty Vehicles*. 2012.

37. Barker J, Richards P, Goodwin M, Wooler J. Influence of high injection pressure on diesel fuel stability: A study of resultant deposits. *SAE Int J Fuels Lubr.* 2009;2(1):877-84.
38. Barker J, Reid J, Smith SA, Snape C, Scurr D, Langley G, et al. The Application of New Approaches to the Analysis of Deposits from the Jet Fuel Thermal Oxidation Tester (JFTOT). *SAE Int J Fuels Lubr.* 2017;10(3):741-55.
39. Barker J, Reid J, Snape C, Scurr D, Meredith W. Spectroscopic Studies of Internal Injector Deposits (IDID) Resulting from the Use of Non-Commercial Low Molecular Weight Polyisobutylenesuccinimide (PIBSI). *SAE Int J Fuels Lubr.* 2014;7(3):762-70.
40. Dallanegra R, Caprotti R. Chemical Composition of Ashless Polymeric Internal Diesel Injector Deposits. *SAE Technical Paper* 2014-01-27282014.
41. de Goede S, Barbour R, Velaers A, Sword B, Burton D, Mokheseng K. The Effect of Near-Zero Aromatic Fuels on Internal Diesel Injector Deposit Test Methods. *SAE Int J Fuels Lubr.* 2017;10(1):163-83.
42. Fang HL, McCormick RL. Spectroscopic Study of Biodiesel Degradation Pathways. *SAE Technical Paper* 2006.
43. Assessment and Standards Division OoTaAQ. Heavy-Duty Engine and Vehicle Standards and Highway Diesel Fuel Sulfur Control Requirements: Response to Comments. 2000.
44. Cook S, Richards P. Possible influence of high injection pressure on diesel fuel stability: a review and preliminary study. *SAE Technical Paper*; 2009. Report No.: 0148-7191.
45. Barker J, Richards P, Snape C, Meredith W. Diesel Injector Deposits - An Issue That Has Evolved with Engine Technology. *SAE Technical Paper*: SAE; 2011.
46. Barker J, Reid J, Piggott M, Fay MW, Davies A, Parmenter C, et al. The Characterisation of Diesel Internal Injector Deposits by Focused Ion-Beam Scanning Electron Microscopy (FIB-SEM), Transmission Electron Microscopy (TEM), Atomic Force Microscopy and Raman Spectroscopy. *SAE Technical Paper Series*: SAE Technical Paper; 2015.
47. Barker J, Snape C, Scurr D. A Novel Technique for Investigating the Characteristics and History of Deposits Formed Within High Pressure Fuel Injection Equipment. *SAE Int J Fuels Lubr.* 2012;5(3):1155-64.
48. Venkataraman R, Eser S. Characterization of deposits formed on diesel injectors in field test and from thermal oxidative degradation of n-hexadecane in a laboratory reactor. *Chem Cent J.* 2008;3.
49. Lewis I. Chemistry of carbonization. *Carbon.* 1982;20(6):519-29.
50. Michelsen HA, Colket MB, Bengtsson PE, D'Anna A, Desgroux P, Haynes BS, et al. A Review of Terminology Used to Describe Soot Formation and Evolution under Combustion and Pyrolytic Conditions. *Acs Nano.* 2020;14(10):12470-90.
51. Frenklach M. Reaction mechanism of soot formation in flames. *Physical Chemistry Chemical Physics.* 2002;4(11):2028-37.
52. Frenklach M, Mebel AM. On the mechanism of soot nucleation. *Physical Chemistry Chemical Physics.* 2020;22(9):5314-31.

53. Richter H, Howard JB. Formation of polycyclic aromatic hydrocarbons and their growth to soot - a review of chemical reaction pathways. *Progress in Energy and Combustion Science*. 2000;26(4-6):565-608.
54. Chu TC, Buras ZJ, Smith MC, Uwagwu AB, Green WH. From benzene to naphthalene: direct measurement of reactions and intermediates of phenyl radicals and acetylene. *Physical Chemistry Chemical Physics*. 2019;21(40):22248-58.
55. Shukla M, Susa A, Miyoshi A, Koshi M. Role of phenyl radicals in the growth of polycyclic aromatic hydrocarbons. *Journal of Physical Chemistry A*. 2008;112(11):2362-9.
56. Reizer E, Viskolcz B, Fiser B. Formation and growth mechanisms of polycyclic aromatic hydrocarbons: A mini-review. *Chemosphere*. 2021:132793.
57. Barker J, Richards P, Snape C, Meredith W. A novel technique for investigating the nature and origins of deposits formed in high pressure fuel injection equipment. *SAE Int J Fuels Lubr*. 2010;2(2):38-44.
58. Quigley R, Barbour R, Fahey E, Arters DC, Wetzel W, Ray J. A Study of the Internal Diesel Injector Deposit Phenomenon 2011.
59. Feld H, Oberender N. Characterization of Damaging Biodiesel Deposits and Biodiesel Samples by Infrared Spectroscopy (ATR-FTIR) and Mass Spectrometry (TOF-SIMS). *SAE Int J Fuels Lubr*. 2016;9(3):717-24.
60. Ullmann J, Geduldig M, Stutzenberger H, Caprotti R, Balfour G. Investigation into the formation and prevention of internal diesel injector deposits. SAE Technical Paper 2008-01-0926: SAE Technical Paper; 2008.
61. Reid J, Cook S, Barker J. Internal Injector Deposits From Sodium Sources. *SAE Int J Fuels Lubr*. 2014;7(2):436-44.
62. Arondel M, Rodeschini H, Lopes M, Dequenne B. Fuel Additives for Reduction of Internal Diesel Injectors Deposits (IDID, "lacquering"): A Critical and Priority Route. SAE Technical Paper Series 2012.
63. Schwab SD, Bennett JJ, Dell SJ, Galante-Fox JM, Kulinowski AM, Miller KT. Internal Injector Deposits in High-Pressure Common Rail Diesel Engines. *SAE Int J Fuels Lubr*. 2010;3(2):865-78.
64. Lacey P, Gail S, Kientz JM, Milovanovic N, Gris C. Internal fuel injector deposits. *SAE Int J Fuels Lubr*. 2012;5(1):132-45.
65. Barker J, Cook S, Richards P. Sodium Contamination of Diesel Fuel, its Interaction with Fuel Additives and the Resultant Effects on Filter Plugging and Injector Fouling. *SAE Int J Fuels Lubr*. 2013;6(3):826-38.
66. Smith A, Williams R. Linking the Physical Manifestation and Performance Effects of Injector Nozzle Deposits in Modern Diesel Engines. *SAE Int J Fuels Lubr*. 2015;8(2):344-57.
67. Csontos B, Fiorenza RM, Pach M, Hittig H, Bernemyr H, Christiansen Erlandsson A, editors. Factors Influencing the Formation of Soft Particles in Biodiesel. SAE technical paper series; 2020: SAE International.
68. Birgel A, Ladommatos N, Aleiferis P, Milovanovic N, Lacey P, Richards P. Investigations on deposit formation in the holes of diesel injector nozzles. *SAE Int J Fuels Lubr*. 2012;5(1):123-31.
69. Arpaia A, Catania AE, d'Ambrosio S, Ferrari A, Luisi SP, Spessa E, editors. Injector Coking Effects on Engine Performance and Emissions. Internal Combustion Engine Division Fall Technical Conference; 2009.

70. Stepien Z, Krasodonski W. Effect of trace zinc amounts introduced in various chemical structures in diesel fuel on coke deposits of fuel injectors of a CI engine. *Int J Engine Res.* 2020;21(5):755-65.
71. Barbour RH, Quigley R, Panesar A. Investigations into Fuel Additive Induced Power Gain in the CEC F-98-08 DW10B Injector Fouling Engine Test. SAE Technical Paper Series 2014.
72. Hawthorne M, Roos JW, Openshaw MJ. Use of fuel additives to maintain modern Diesel engine performance with severe test conditions. SAE Technical Paper; 2008. Report No.: 0148-7191.
73. Barker J, Langley GJ, Richards P. Insights into Deposit Formation in High Pressure Diesel Fuel Injection Equipment. SAE 2010 Powertrains Fuels & Lubricants Meeting: SAE; 2010.
74. Tang J, Pischinger S, Lamping M, Körfer T, Tatur M, Tomazic D. Coking phenomena in nozzle orifices of DI-diesel engines. *SAE Int J Fuels Lubr.* 2009;2(1):259-72.
75. Barbour R, Arters D, Dietz J, Macduff M, Panesar A, Quigley R. Diesel Detergent Additive Responses in Modern, High-Speed, Direct-Injection, Light-Duty Engines. SAE Technical Paper; 2007. Report No.: 0148-7191.
76. Ikemoto M, Omae K, Nakai K, Ueda R, Kakehashi N, Sunami K. Injection nozzle coking mechanism in common-rail diesel engine. *SAE Int J Fuels Lubr.* 2012;5(1):78-87.
77. Stehouwer DM, Fang HL, Wooton D, Martin H. Interaction Between Fuel Additive and Oil Contaminant:(I) Field Experiences. SAE Technical Paper; 2003. Report No.: 0148-7191.
78. Lamb JS, Barker J, Wilmot E, Scurr DJ, Snape CE, Smith EF, et al. Internal Diesel Injector Deposit Chemical Speciation and Quantification Using 3D OrbiSIMS and XPS Depth Profiling. *SAE International Journal of Advances and Current Practices in Mobility.* 2020;3(2020-01-2098):349-64.
79. Diaby M, Sablier M, Le Negrate A, El Fassi M, Bocquet J. Understanding carbonaceous deposit formation resulting from engine oil degradation. *Carbon.* 2009;47(2):355-66.
80. Lubricant Additives: Use and Benefits. 2016.
81. Birgel A, Ladommatos N, Aleiferis P, Zülch S, Milovanovic N, Lafon V, et al. Deposit formation in the holes of diesel injector nozzles: A critical review. SAE Technical Paper Series: SAE Technical Paper; 2008.
82. Smith GC, Hopwood AB, Titchener KJ. Microcharacterization of heavy-duty diesel engine piston deposits. *Surface and Interface Analysis.* 2002;33(3):259-68.
83. Chen B, Jie F, Li X, Song C, He T, Wang J. Experimental investigation of effect of biodiesel fatty acid methyl ester on performance of engine oil dispersant additive. *Int J Engine Res.* 2021;22(9):2779-85.
84. Reid J, Barker J. Understanding Polyisobutylene Succinimides (PIBSI) and Internal Diesel Injector Deposits. SAE Technical Paper 2013-01-2682: SAE; 2013.
85. Johnson DW, Hils JE. Phosphate esters, thiophosphate esters and metal thiophosphates as lubricant additives. *Lubricants.* 2013;1(4):132-48.

86. Hoang AT, Le AT. A review on deposit formation in the injector of diesel engines running on biodiesel. *Energy Sources, Part A*. 2019;41(5):584-99.
87. Lacey P, Gail S, Kientz JM, Benoist G, Downes P, Daveau C. Fuel Quality and Diesel Injector Deposits. *SAE Int J Fuels Lubr*. 2012;5(3):1187-98.
88. Omori T, Tanaka A, Yamada K, Bunne S. Biodiesel deposit formation mechanism and improvement of Fuel Injection Equipment (FIE). SAE Technical Paper 2011-01-1935: SAE; 2011.
89. Fernando S, Karra P, Hernandez R, Jha SK. Effect of incompletely converted soybean oil on biodiesel quality. *Energy*. 2007;32(5):844-51.
90. Ashraf I, Li C, Wang T, Li R, Chen B. Phosphorus removal from oil and aqueous phases with a multifunctional adsorbent. *Analytical Methods*. 2020;12(4):466-70.
91. Zezza TRC, de Souza Castilho M, Stradiotto NR. Determination of phosphorus in biodiesel using 1: 12 phosphomolybdic modified electrode by cyclic voltammetry. *Fuel*. 2012;95:15-8.
92. Kratzeisen M, Muller J. Influence of phosphorus content of coconut oil on deposit and performance of plant oil pressure stoves. *Renewable Energy*. 2010;35(11):2585-9.
93. STAnik W, Jakóbiec J, MAzAnek A. Engine tests for coking and contamination of modern multi-injection injectors of high-pressure fuel supplies compression-ignition engine. *Eksplatacja i Niezawodność*. 2018;20(1).
94. Lapuerta M, Villajos M, Agudelo JR, Boehman AL. Key properties and blending strategies of hydrotreated vegetable oil as biofuel for diesel engines. *Fuel Processing Technology*. 2011;92(12):2406-11.
95. Alves Fortunato M, Lenglet F, Ben Amara A, Starck L. Are Internal Diesel Injector Deposits (IDID) Mainly Linked to Biofuel Chemical Composition or/and Engine Operation Condition? SAE Technical Paper 2019-01-00612019.
96. Hilbers TJ, Sprakel LM, van den Enk LB, Zaalberg B, van den Berg H, van der Ham LG. Green diesel from hydrotreated vegetable oil process design study. *Chemical Engineering & Technology*. 2015;38(4):651-7.
97. Ruffell JE, Farmer TJ, Macquarrie DJ, Stark MS. The Autoxidation of Alkenyl Succinimides-Mimics for Polyisobutenyl Succinimide Dispersants. *Industrial & Engineering Chemistry Research*. 2019;58(42):19649-60.
98. Galante-Fox J, Bennett J. Diesel injector internal deposits in High Pressure Common Rail diesel engines. *Fuel Systems for IC Engines* 2012. p. 157-66.
99. Stępień Z, Wojtasik M. Effect of PIBSI Chemical Structures of Various Molecular Masses on the IDID Formation in Engine-Dynamometer Testing. *Journal of Energy Engineering*. 2020;146(3).
100. Bornemann H, Scheidt F, Sander W. Thermal decomposition of 2-ethylhexyl nitrate (2-EHN). *International Journal of Chemical Kinetics*. 2002;34(1):34-8.
101. Antonio EN, Wicking C, Filip S, Ryan MP, Heutz S. Role of Iron Speciation in Oxidation and Deposition at the Hexadecane-Iron Interface. *Acs Applied Materials & Interfaces*. 2020;12(16):19140-52.

102. Treutler CPO. Industrial use of plasma-deposited coatings for components of automotive fuel injection systems. *Surface & Coatings Technology*. 2005;200(5-6):1969-75.
103. Goldstein JI, Newbury DE, Michael JR, Ritchie NW, Scott JHJ, Joy DC. *Scanning electron microscopy and X-ray microanalysis*: Springer; 2017.
104. Reimer L. *Transmission electron microscopy: physics of image formation and microanalysis*: Springer; 2013.
105. Cardenas Almendra MD, Lucio Esperilla O, Martin Manzanero F, Murillo Duarte Y, Quintero Toscano LC, Wolff G. Internal Diesel Injector Deposits: Sodium Carboxylates of C12 Succinic Acids and C16 and C18 Fatty Acids. *SAE Technical Paper 2012-01-1689*2012.
106. Rounthwaite NJ, Williams R, McGivern C, Jiang J, Giulliani F, Britton B. A Chemical and Morphological Study of Diesel Injector Nozzle Deposits - Insights into their Formation and Growth Mechanisms. *SAE Int J Fuels Lubr*. 2017;10(1):106-14.
107. Gujrati A, Khanal SR, Pastewka L, Jacobs TD. Combining TEM, AFM, and profilometry for quantitative topography characterization across all scales. *ACS applied materials & interfaces*. 2018;10(34):29169-78.
108. Barker J, Reid J, Smith SA, Snape C, Scurr D, Piggott M, et al. Internal Injector Deposits (IDID). 11th International Colloquium: Fuels - Conventional and Future Energy for Automobiles; Stuttgart/Ostfildern: Technische Akademie Esslingen; 2017.
109. Vickerman JC, Gilmore IS. *Surface analysis: the principal techniques*: John Wiley & Sons; 2011.
110. Shard AG. Practical guides for x-ray photoelectron spectroscopy: Quantitative XPS. *Journal of Vacuum Science & Technology A*. 2020;38(4).
111. Jenkins R. *Quantitative X-ray spectrometry*: CRC Press; 1995.
112. Carlisle HW, Frew RW, Mills JR, Aradi AA, Avery NL. The effect of fuel composition and additive content on injector deposits and performance of an air-assisted direct injection spark ignition (DISI) research engine. *SAE Transactions*. 2001:1549-65.
113. Barker J, Reid J. Injector and Fuel System Deposits. 10th International Colloquium: Fuels - Conventional and Future Energy for Automobiles; Stuttgart/Ostfildern: Technische Akademie Esslingen; 2015.
114. Smith E, Dent G. *Modern Raman spectroscopy: a practical approach*: John Wiley & Sons; 2019.
115. Meredith W, Snape CE, Love GD. Development and Use of Catalytic Hydropyrolysis (HyPy) as an Analytical Tool for Organic Geochemical Applications. In: Grice K, editor. *Principles and Practice of Analytical Techniques in Geosciences*. RSC Detection Science Series. 42015. p. 171-208.
116. Bull I. *Gas Chromatography Mass Spectrometry (GC/MS)*: University of Bristol; 2008 [Available from: <http://www.bris.ac.uk/nerclsmsf/techniques/gcms.html>].
117. Tanaka A, Yamada K, Omori T, Bunne S, Hosokawa K. Inner Diesel Injector Deposit Formation Mechanism. *SAE Int J Fuels Lubr*. 2013;6(3):755-61.

118. Fearn S. An introduction to time-of-flight secondary ion mass spectrometry (ToF-SIMS) and its application to materials science: Morgan & Claypool Publishers San Rafael, CA, USA; 2015.
119. Gengenbach TR, Major GH, Linford MR, Easton CD. Practical guides for x-ray photoelectron spectroscopy (XPS): Interpreting the carbon 1s spectrum. *Journal of Vacuum Science & Technology A*. 2021;39(1).
120. Gnaser H, Ichiki K, Matsuo J. Strongly reduced fragmentation and soft emission processes in sputtered ion formation from amino acid films under large Ar-n(+) ( $n \leq 2200$ ) cluster ion bombardment. *Rapid Communications in Mass Spectrometry*. 2012;26(1):1-8.
121. Pachuta SJ, Cooks R. Mechanisms in molecular SIMS. *Chemical Reviews*. 1987;87(3):647-69.
122. Winograd N. The magic of cluster SIMS. ACS Publications; 2005.
123. Bich C, Havelund R, Moellers R, Touboul D, Kollmer F, Niehuis E, et al. Argon Cluster Ion Source Evaluation on Lipid Standards and Rat Brain Tissue Samples. *Analytical Chemistry*. 2013;85(16):7745-52.
124. Fletcher JS, Vickerman JC. Secondary Ion Mass Spectrometry: Characterizing Complex Samples in Two and Three Dimensions. *Analytical Chemistry*. 2013;85(2):610-39.
125. Matsuo J, Ninomiya S, Nakata Y, Honda Y, Ichiki K, Seki T, et al. What size of cluster is most appropriate for SIMS? *Applied Surface Science*. 2008;255(4):1235-8.
126. Vickerman JC, Briggs D. ToF-SIMS: materials analysis by mass spectrometry: im publications; 2013.
127. Angel-Smith S. Characterisation of diesel injector deposits using advanced analytical techniques: Univeristy of Nottingham; 2018.
128. Barker J, Reid J, Wilmot E, Mulqueen S, Smith SA, Scurr D, et al. Investigations of Diesel Injector Deposits Characterization and Testing. *SAE Technical Papers*. 2020.
129. Graham DJ, Castner DG. Multivariate Analysis of ToF-SIMS Data from Multicomponent Systems: The Why, When, and How. *Biointerphases*. 2012;7(1-4).
130. Trindade GF, Abel ML, Watts JF. simsMVA: A tool for multivariate analysis of ToF-SIMS datasets. *Chemometrics and Intelligent Laboratory Systems*. 2018;182:180-7.
131. Afifi A, May S, Clark VA. Computer-aided multivariate analysis: CRC Press; 2003.
132. Garrison BJ, Delcorte A, Krantzman KD. Molecule liftoff from surfaces. *Accounts of Chemical Research*. 2000;33(2):69-77.
133. El-Aneed A, Cohen A, Banoub J. Mass spectrometry, review of the basics: electrospray, MALDI, and commonly used mass analyzers. *Applied Spectroscopy Reviews*. 2009;44(3):210-30.
134. Hillenkamp F, Peter-Katalinic J. MALDI MS: a practical guide to instrumentation, methods and applications: John Wiley & Sons; 2013.
135. Passarelli MK, Pirkel A, Moellers R, Grinfeld D, Kollmer F, Havelund R, et al. The 3D OrbiSIMS-label-free metabolic imaging with subcellular lateral resolution and high mass-resolving power. *Nat Methods*. 2017;14(12):1175-83.
136. Xian F, Hendrickson CL, Marshall AG. High resolution mass spectrometry. *Analytical chemistry*. 2012;84(2):708-19.

137. Datschefschi G, Farthing T. Evaluation of JFTOT Tube Deposits by Carbon Burnoff. SAE Transactions. 1985:1014-9.
138. Bert J, Painter LJ. JFTOT—A New Fuel Thermal Stability Test (A Summary of Coordinating Research Council Activity). SAE Transactions. 1973:1351-62.
139. Lacey P, Gail S, Grinstead D, Daveau C, Caprotti R, Dallanegra R, et al. Use of a Laboratory Scale Test to Study Internal Diesel Injector Deposits. SAE Technical Paper Series 2016.
140. Sander ZH, West ZJ, Ervin JS, Zabarnick S. Experimental and Modeling Studies of Heat Transfer, Fluid Dynamics, and Autoxidation Chemistry in the Jet Fuel Thermal Oxidation Tester (JFTOT). Energy & Fuels. 2015;29(11):7036-47.
141. Strauss KH. Thermal Stability Specification Testing of Jet Fuel—A Critical Review. SAE transactions. 1988:444-52.
142. Buchholz B, Berndt S, Schümann U, Cepelak S. Application and validation of a lab-test method for classification of diesel fuels according to their tendency for deposit formation in injection systems as a function of temperature. Forschungsvereinigung Verbrennungskraftmaschinen; 2020.
143. Berndt S, Schümann U, Sadlowski T, Buchholz B. Development of a laboratory test for the deposit forming tendency of diesel fuels. ATZoffhighway worldwide. 2018;11(1):50-5.
144. Schümann U, Berndt S, Wicht R, Buchholz B. Avoiding Internal Injector Deposits by Using Biodiesel. ATZheavy duty worldwide. 2021;14(1):44-9.
145. Vera-Tudela W, Haefeli R, Barro C, Schneider B, Boulouchos K. An experimental study of a very high-pressure diesel injector (up to 5000 bar) by means of optical diagnostics. Fuel. 2020;275:117933.
146. Schümann U, Berndt S, Cepelak S, Buchholz B. Deposit Forming Tendency of Diesel Fuels in Injectors. ATZheavy duty worldwide. 2020;13(2):56-61.
147. Zabarnick S, West ZJ, Shafer LM, Mueller SS, Striebich RC, Wrzesinski PJ. Studies of the Role of Heteroatomic Species in Jet Fuel Thermal Stability: Model Fuel Mixtures and Real Fuels. Energy & Fuels. 2019;33(9):8557-65.
148. Schümann U, Buchholz B. Deposit Formation and Prevention of Deposit Formation Biodiesel (EN 14214). University of Rostock 2018.
149. Institute TE. Jet fuel thermal oxidation tube rating training guidelines (IP 323). 2000.
150. International A. Standard Test Method for Thermal Oxidation Stability of Aviation Turbine Fuels (ASTM D3241).
151. Specification Sheet: Alloy 316/316L. In: Company SS, editor. 2014.
152. Biesinger MC. XPS Reference Pages XPSFitting: XPSFitting; [Available from: [www.XPSFitting.com](http://www.XPSFitting.com)].
153. ThermoScientific. XPS Knowledge Base: ThermoScientific; [Available from: <https://www.jp.xpssimplified.com/periodictable.php>].
154. Engelhard MH, Baer DR, Herrera-Gomez A, Sherwood PMA. Introductory guide to backgrounds in XPS spectra and their impact on determining peak intensities. Journal of Vacuum Science & Technology A. 2020;38(6).



155. Tougaard S, Braun W, Holubkrappe E, Saalfeld H. TEST OF ALGORITHM FOR BACKGROUND CORRECTION IN XPS UNDER VARIATION OF XPS PEAK ENERGY. *Surface and Interface Analysis*. 1988;13(4):225-7.
156. Biesinger MC. Carbon XPSFitting: XPSFitting; [Available from: <http://www.xpsfitting.com/search/label/carbon>.
157. ThermoScientific. Carbon: ThermoScientific; [Available from: <https://www.jp.xpssimplified.com/elements/carbon.php>.
158. Chastain J, King Jr RC. Handbook of X-ray photoelectron spectroscopy. Perkin-Elmer Corporation. 1992;40:221.
159. Spanu M. Advanced Characterisation of Deposits in Diesel Fuel Filters. 2021.
160. Mitchell JM, Flight RM, Wang QJ, Higashi RM, Fan TWM, Lane AN, et al. New methods to identify high peak density artifacts in Fourier transform mass spectra and to mitigate their effects on high-throughput metabolomic data analysis. *Metabolomics*. 2018;14(10).
161. Hook AL, Hogwood J, Gray E, Mulloy B, Merry CL. High sensitivity analysis of nanogram quantities of glycosaminoglycans using ToF-SIMS. *Communications Chemistry*. 2021;4(1):1-8.
162. Edney MK, Kotowska AM, Spanu M, Trindade GF, Wilmot E, Reid J, et al. Molecular formula prediction for chemical filtering of 3D OrbiSIMS Datasets. *Analytical Chemistry*. 2022.
163. Koch BP, Dittmar T. From mass to structure: an aromaticity index for high-resolution mass data of natural organic matter. *Rapid Communications in Mass Spectrometry*. 2006;20(5):926-32.
164. Marshall AG, Rodgers RP. Petroleomics: Chemistry of the underworld. *Proceedings of the National Academy of Sciences of the United States of America*. 2008;105(47):18090-5.
165. Starr NJ, Khan MH, Edney MK, Trindade GF, Kern S, Pirkel A, et al. Elucidating the molecular landscape of the stratum corneum. *Proceedings of the National Academy of Sciences*. 2022;119(12).
166. Trindade GF. The Development of Multivariate Analysis Methodologies for Complex ToF-SIMS Datasets: Applications to Material Sciences: University of Surrey; 2018.
167. MathWorks. Principal component analysis of raw data MathWorks: MathWorks; [
168. Gillis N, Glineur F. Accelerated multiplicative updates and hierarchical ALS algorithms for nonnegative matrix factorization. *Neural computation*. 2012;24(4):1085-105.
169. Keenan MR, Kotula PG. Accounting for Poisson noise in the multivariate analysis of ToF-SIMS spectrum images. *Surface and Interface Analysis: An International Journal devoted to the development and application of techniques for the analysis of surfaces, interfaces and thin films*. 2004;36(3):203-12.
170. Edney MK, Lamb JS, Spanu M, Smith EF, Steer E, Wilmot E, et al. Spatially Resolved Molecular Compositions of Insoluble Multilayer Deposits Responsible for Increased Pollution from Internal Combustion Engines. *Acs Applied Materials & Interfaces*. 2020;12(45):51026-35.
171. Al-Gaashani R, Najjar A, Zakaria Y, Mansour S, Atieh M. XPS and structural studies of high quality graphene oxide and reduced graphene

- oxide prepared by different chemical oxidation methods. *Ceramics International*. 2019;45(11):14439-48.
172. Andrews H, Boersma C, Werner M, Livingston J, Allamandola L, Tielens A. PAH emission at the bright locations of PDRs: The grandPAH hypothesis. *The Astrophysical Journal*. 2015;807(1):99.
173. da Cunha A, Sa A, Mello SC, Vasquez-Castro YE, Luna AS, Aucelio RQ. Determination of nitrogen-containing polycyclic aromatic compounds in diesel and gas oil by reverse-phase high performance liquid chromatography using introduction of sample as detergentless microemulsion. *Fuel*. 2016;176:119-29.
174. Prado GH, Rao Y, de Klerk A. Nitrogen removal from oil: a review. *Energy & Fuels*. 2017;31(1):14-36.
175. Pach M, Hittig H, Cronhjort A, Bernemyr H. Characterization of Internal Diesel Injector Deposits from Heavy-Duty Vehicles. SAE Technical Paper; 2021. Report No.: 0148-7191.
176. Hughey CA, Hendrickson CL, Rodgers RP, Marshall AG, Qian KN. Kendrick mass defect spectrum: A compact visual analysis for ultrahigh-resolution broadband mass spectra. *Analytical Chemistry*. 2001;73(19):4676-81.
177. Hasannuddin A, Wira J, Sarah S, Aqma WWS, Hadi AA, Hirofumi N, et al. Performance, emissions and lubricant oil analysis of diesel engine running on emulsion fuel. *Energy conversion and management*. 2016;117:548-57.
178. Murase A, Mori H, Ohmori T. TOF-SIMS analysis of friction surfaces of hard coatings tested in engine oil. *Applied Surface Science*. 2008;255(4):1494-7.
179. Boot MD, Tian M, Hensen EJM, Sarathy SM. Impact of fuel molecular structure on auto-ignition behavior Design rules for future high performance gasolines. *Progress in Energy and Combustion Science*. 2017;60:1-25.
180. Bearchell C, Heyes D, Moreton D, Taylor S. Overbased detergent particles: Experimental and molecular modelling studies. *Physical Chemistry Chemical Physics*. 2001;3(21):4774-83.
181. Pskowski RP. Bad Bunker: Fuel Contamination Claims, IMO 2020, and the Houston Problem. *Tulane Maritime Law Journal*. 2019;44(1):217-50.
182. Taylor DA. *Introduction to marine engineering*; Elsevier; 1996.
183. Bee S. Houston Marine Fuel Contamination: Veritas Petroleum Services Announce Exclusive Findings. *Ship and Bunker*. 2018.
184. Wolf R, Kaul BL. *Plastics, additives*. Ullmann's Encyclopedia of Industrial Chemistry. 2000.
185. Shi J, Xu C, Xiang L, Chen J, Cai Z. Tris (2, 4-di-tert-butylphenyl) phosphate: An unexpected abundant toxic pollutant found in PM<sub>2.5</sub>. *Environmental Science & Technology*. 2020;54(17):10570-6.
186. Przybilla L, Brand J-D, Yoshimura K, Räder HJ, Müllen K. MALDI-TOF mass spectrometry of insoluble giant polycyclic aromatic hydrocarbons by a new method of sample preparation. *Analytical Chemistry*. 2000;72(19):4591-7.
187. Spanu M, Barker J, Pinch D, Reid J, Innospec EP, Scurr D, et al. Detailed characterisation of diesel fuel filter deposits by ToF-SIMS and other analytical methods. *Technische Akademie Esslingen*; Esslingen2019.

188. Dupin J-C, Gonbeau D, Vinatier P, Levasseur A. Systematic XPS studies of metal oxides, hydroxides and peroxides. *Physical Chemistry Chemical Physics*. 2000;2(6):1319-24.
189. Zähr J, Oswald S, Türpe M, Ullrich H, Füssel U. Characterisation of oxide and hydroxide layers on technical aluminum materials using XPS. *Vacuum*. 2012;86(9):1216-9.
190. Oxygen XPS Simplified: Thermo Scientific; [
191. Nouryon. Fuels and lubricants [Available from: <https://www.nouryon.com/markets/fuels-and-lubricants/>].
192. Murase A, Mori H, Ohmori T. TOF-SIMS Analysis of Engine Oil Additives Adsorbed onto Friction Surfaces. 2011.
193. Edney MK, Barker J, Reid J, Scurr DJ, Snape CE. Recent Advances in the Analysis of GDI and Diesel Fuel Injector Deposits. *Fuel*. 2020;272.
194. Blyth R, Buqa H, Netzer F, Ramsey M, Besenhard J, Golob P, et al. XPS studies of graphite electrode materials for lithium ion batteries. *Applied Surface Science*. 2000;167(1-2):99-106.
195. Spivey JJ, Hutchings G. Catalytic aromatization of methane. *Chemical Society Reviews*. 2014;43(3):792-803.
196. Tian M, Liu BS, Hammonds M, Wang N, Sarre PJ, Cheung ASC. Catalytic conversion of acetylene to polycyclic aromatic hydrocarbons over particles of pyroxene and alumina. *Philosophical Transactions of the Royal Society a-Mathematical Physical and Engineering Sciences*. 2013;371(1994).
197. Liya EY, Hildemann LM, Niksa S. Characteristics of nitrogen-containing aromatic compounds in coal tars during secondary pyrolysis. *Fuel*. 1999;78(3):377-85.
198. Choudhary G, Cameron A, Back R. Photolysis and pyrolysis of succinimide vapor. *The Journal of Physical Chemistry*. 1968;72(7):2289-92.
199. Sharma RK, Chan WG, Hajaligol MR. Product compositions from pyrolysis of some aliphatic  $\alpha$ -amino acids. *Journal of Analytical and Applied pyrolysis*. 2006;75(2):69-81.
200. de Jesus A, Zmozinski AV, Barbara JA, Vale MG, Silva MM. Determination of calcium and magnesium in biodiesel by flame atomic absorption spectrometry using microemulsions as sample preparation. *Energy & fuels*. 2010;24(3):2109-12.
201. de Carvalho AL, Cardoso EA, da Rocha GO, Teixeira LS, Pepe IM, Grosjean DM. Carboxylic acid emissions from soybean biodiesel oxidation in the EN14112 (Rancimat) stability test. *Fuel*. 2016;173:29-36.
202. Brient JA, Wessner PJ, Doyle MN. Naphthenic acids. *Kirk-Othmer Encyclopedia of Chemical Technology*. 2000.
203. Caires FJ, Lima L, Carvalho C, Ionashiro M. Thermal behaviour of succinic acid, sodium succinate and its compounds with some bivalent transition metal ions. *Thermochimica acta*. 2010;500(1-2):6-12.
204. Zhao J, Grekhov L, Ma X, Denisov A. Specific features of diesel fuel supply under ultra-high pressure. *Applied Thermal Engineering*. 2020;179:115699.

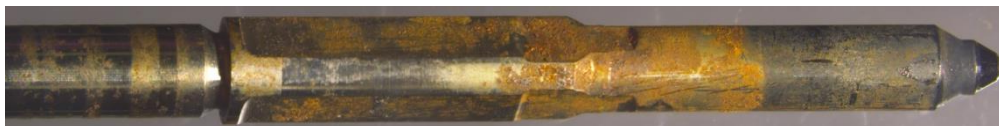
205. Lorenzi G, Baptista P, Venezia B, Silva C, Santarelli M. Use of waste vegetable oil for hydrotreated vegetable oil production with high-temperature electrolysis as hydrogen source. *Fuel*. 2020;278:117991.
206. Caballero B, Trugo LC, Finglas PM. *Encyclopedia of food sciences and nutrition*: Academic; 2003.
207. Monson. Corrosion inhibitor [Available from: <https://monsonco.com/product-application/corrosion-inhibitor/>].
208. Mokhtar R, Shtewi F, Al-Zawik A, Karsheman S. The Determination of Ultra-trace Amounts of N, N-Diethylhydroxylamine Residues in Water Used for High-Pressure, High-Temperature Steam Turbines. *Jordan Journal of Chemistry (JJC)*. 2008;3(3):305-19.
209. Przybylski R, Lee YC, Kim IH. Oxidative stability of Canola oils extracted with supercritical carbon dioxide. *Food Science and Technology-Lebensmittel-Wissenschaft & Technologie*. 1998;31(7-8):687-93.
210. Matthaus B, Özcan MM, Al Juhaimi F. Some rape/canola seed oils: Fatty acid composition and tocopherols. *Zeitschrift für Naturforschung C*. 2016;71(3-4):73-7.

## Appendix

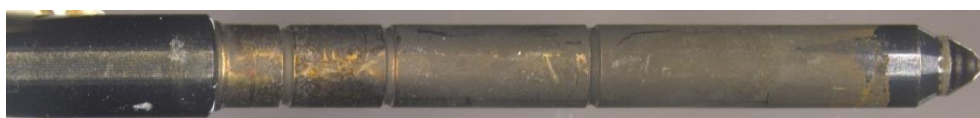
### 1. Supporting Information for Chapter 3: OrbiSIMS and XPS of IDIDs

#### 1.1. Sample Images

a) Needle 14



b) Needle 9



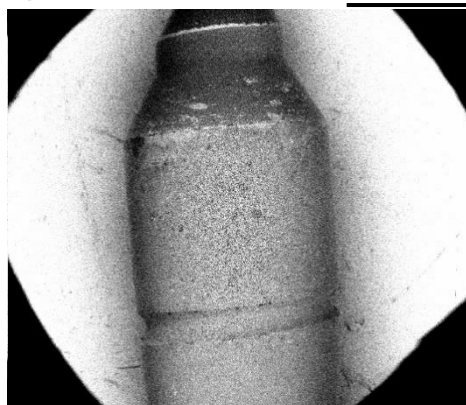
c) Needle 12



Figure A1: Optical microscope images of IDID needle samples.

a) Needle 6 backscatter

1mm



b) Needle 8 backscatter

2mm



Figure A2: SEM backscatter images of Needle 6 and Needle 8, top of needle shaft position.

## 1.1.1. IDID and External GDI Injector Deposit Comparisons

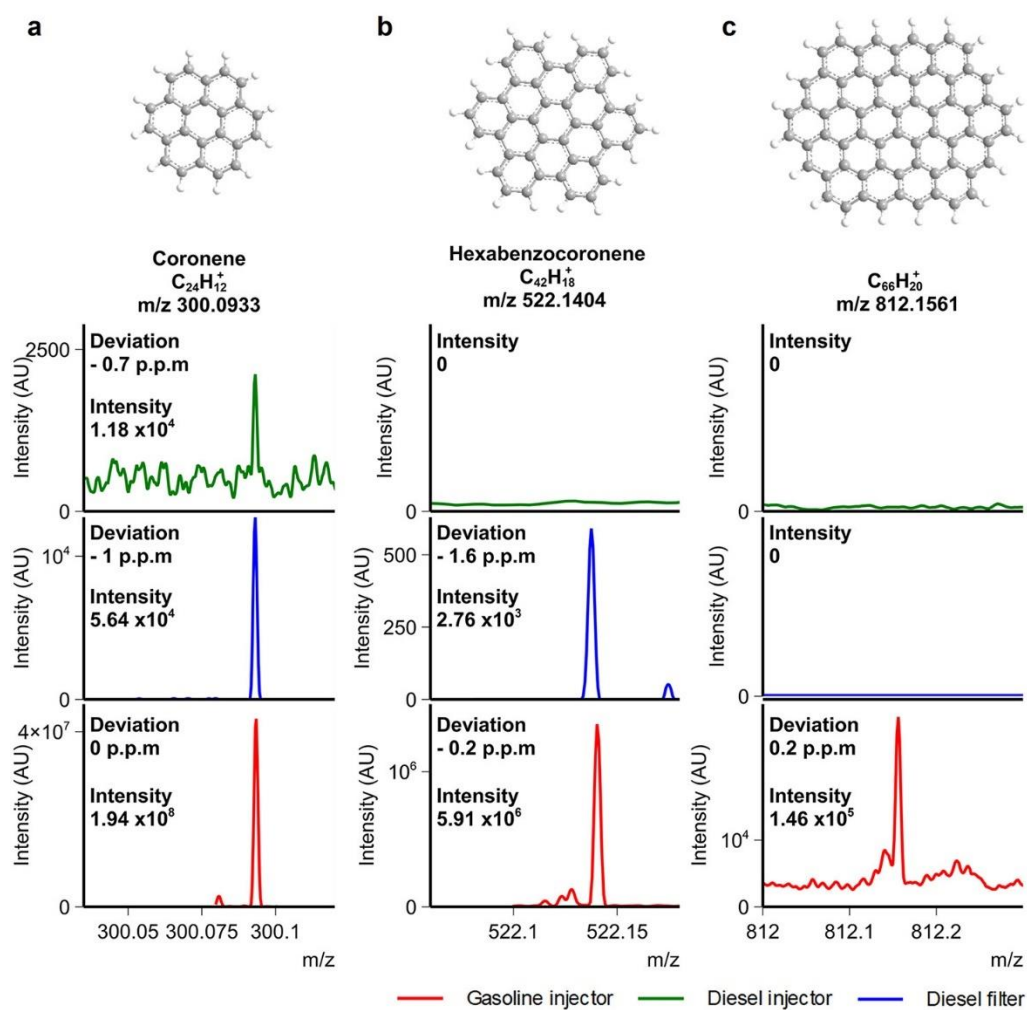


Figure A3: Molecular PAHs identified in the insoluble deposits. 3D structures for the three PAHs studied (above) and spectra of the PAH in each sample (below). a)  $C_{24}H_{12}^+$  (coronene), b)  $C_{42}H_{18}^+$  (hexabenzocoronene), and c)  $C_{66}H_{20}^+$ . Published in Edney *et al.* (2020) (170).

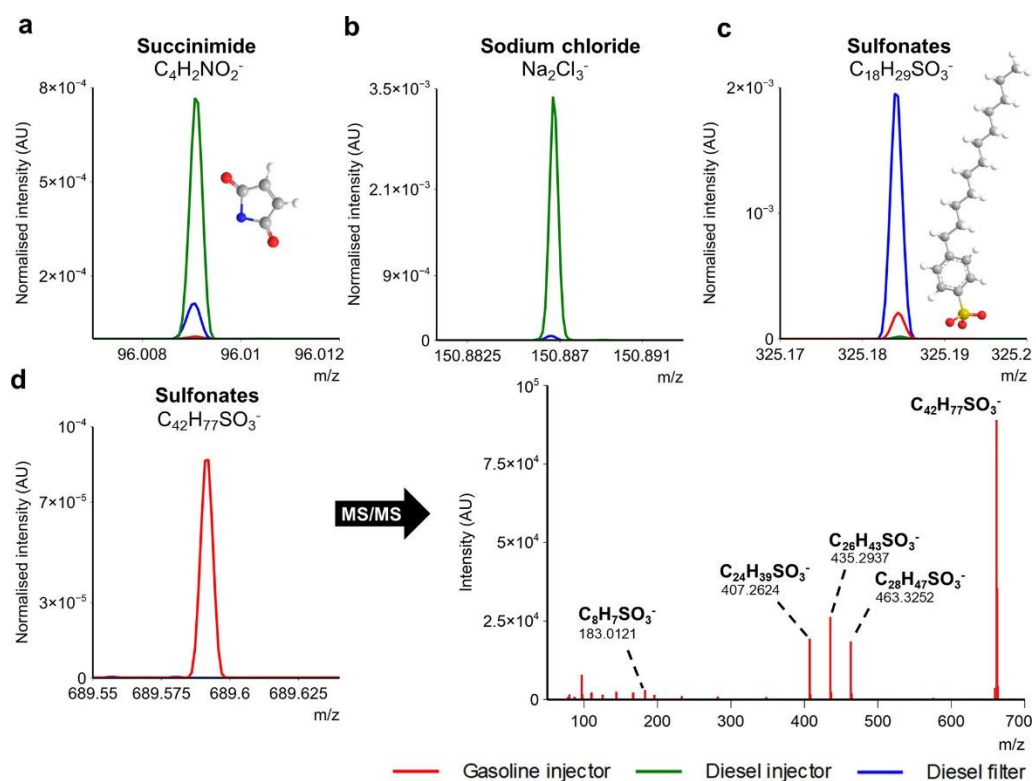


Figure A4: Normalized spectral comparison and MS/MS analysis of insoluble deposits. Comparison of ion intensities for representative ions for (a) succinimides ( $C_4H_2NO_2^-$ ), (b) sodium chloride ( $Na_2Cl_3^-$ ), and (c) parent sulfonate ion ( $C_{18}H_{29}SO_3^-$ ). (d) Spectra of a higher mass sulfonate ion ( $C_{42}H_{77}SO_3^-$ ), unique to the gasoline deposit, and its subsequent fragmentation pattern from a higher energy collisional dissociation MS/MS experiment. Published in Edney *et al.* (2020) (170).



### 1.1.2. Quantification of Deposits with XPS

XPS was used for accurate quantification and provides initial insight into the elements present in each sample. It should be noted that XPS cannot measure hydrogen so the at.% values are relative for the elements that are measured.

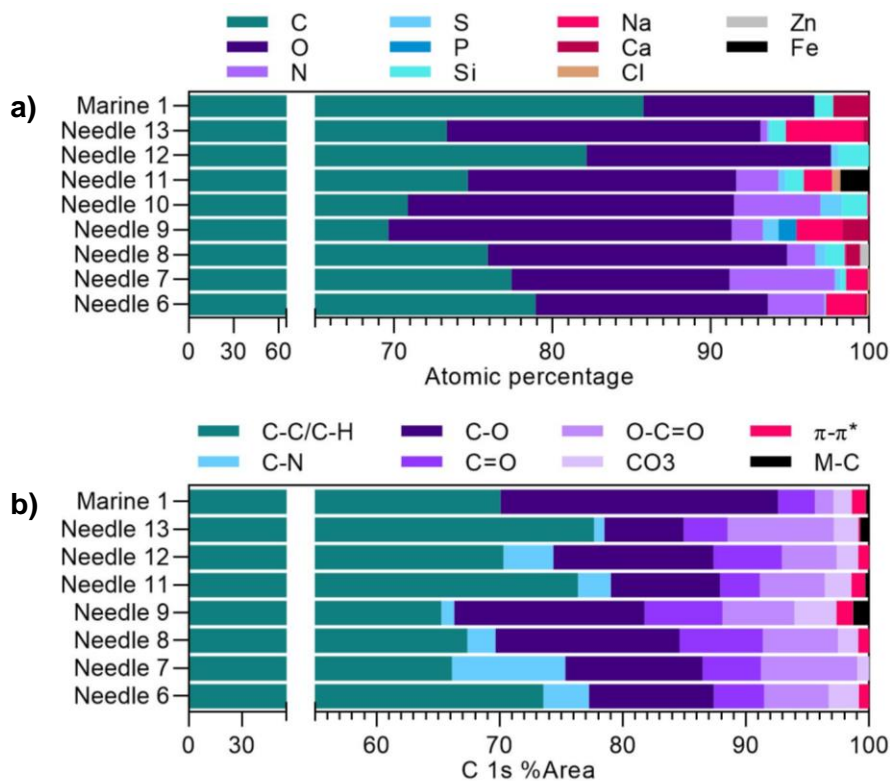


Figure A5: XPS data for field samples. a) Elemental atomic percentage data. b) C 1s components percentage area data.



Table A1: XPS wide scan relative atomic concentration data (atomic percentage).

<b>Sample</b>	<b>C 1s</b>	<b>O 1s</b>	<b>N 1s</b>	<b>S 2p</b>	<b>P 2p</b>	<b>Si 2p</b>	<b>Na 1s</b>	<b>Ca 2p</b>	<b>Cl 2p</b>	<b>Zn 2p</b>	<b>Fe 2p</b>
<b>Needle 6</b>	78.93	14.68	3.57	0.09	0.00	0.00	2.44	0.15	0.14	0.00	0.00
<b>Needle 7</b>	77.41	13.77	6.67	0.36	0.00	0.35	1.27	0.10	0.08	0.00	0.00
<b>Needle 8</b>	75.92	18.92	1.78	0.64	0.00	1.22	0.08	0.89	0.00	0.54	0.00
<b>Needle 9</b>	69.62	21.71	1.97	0.98	1.13	0.00	2.92	1.67	0.00	0.00	0.00
<b>Needle 10</b>	70.85	20.63	5.46	1.36	0.00	1.60	0.11	0.00	0.00	0.00	0.00
<b>Needle 11</b>	74.67	16.94	2.68	0.46	0.00	1.13	1.79	0.00	0.52	0.00	1.83
<b>Needle 12</b>	82.14	15.47	0.00	0.48	0.00	1.91	0.00	0.00	0.00	0.00	0.00
<b>Needle 13</b>	73.32	19.83	0.42	0.19	0.00	0.98	4.89	0.36	0.00	0.00	0.00
<b>Marine 1</b>	85.76	10.79	0.00	0.00	0.00	1.19	0.00	2.27	0.00	0.00	0.00

Table A2: XPS wide scan Monte Carlo standard deviation errors (atomic percentage) for Table A1.

<b>Sample</b>	<b>C 1s</b>	<b>O 1s</b>	<b>N 1s</b>	<b>S 2p</b>	<b>P 2p</b>	<b>Si 2p</b>	<b>Na 1s</b>	<b>Ca 2p</b>	<b>Cl 2p</b>	<b>Zn 2p</b>	<b>Fe 2p</b>
<b>Needle 6</b>	0.95	0.57	0.86	0.05	0.00	0.00	0.38	0.21	0.09	0.00	0.00
<b>Needle 7</b>	0.15	0.12	0.09	0.03	0.00	0.04	0.05	0.03	0.02	0.00	0.00
<b>Needle 8</b>	0.52	0.32	0.44	0.12	0.00	0.18	0.04	0.25	0.00	0.09	0.00
<b>Needle 9</b>	1.08	0.64	1.17	0.26	0.37	0.00	0.31	0.29	0.00	0.00	0.00
<b>Needle 10</b>	1.03	0.66	0.90	0.22	0.00	0.54	0.39	0.00	0.00	0.00	0.00
<b>Needle 11</b>	1.01	0.57	0.81	0.17	0.00	0.51	0.26	0.00	0.17	0.00	0.47
<b>Needle 12</b>	2.74	1.43	2.75	0.43	0.00	0.57	0.00	0.74	0.00	0.00	0.00
<b>Needle 13</b>	0.20	0.12	0.16	0.04	0.00	0.10	0.10	0.00	0.00	0.00	0.00
<b>Marine 1</b>	0.57	0.51	0.00	0.00	0.00	0.23	0.00	0.23	0.00	0.00	0.00

Table A3: XPS C 1s high-resolution component percentage area.

Sample	M-C	C-C	C-N	C-O	C=O	O-C=O	CO <sub>3</sub>	$\pi$ - $\pi^*$
Needle 6	0.00	73.56	3.68	10.16	4.07	5.26	2.45	0.82
Needle 7	0.00	66.13	9.20	11.15	4.73	7.84	0.96	0.00
Needle 8	0.00	67.38	2.29	14.94	6.77	6.10	1.66	0.87
Needle 9	1.25	65.27	1.03	15.49	6.31	5.86	3.39	1.36
Needle 11	0.32	76.37	2.65	8.89	3.23	5.28	2.17	1.10
Needle 12	0.00	70.30	4.07	12.99	5.59	4.44	1.73	0.89
Needle 13	0.72	77.68	0.83	6.43	3.57	8.63	2.02	0.12
Marine 1	0.24	70.07	0.00	22.55	3.00	1.51	1.47	1.16

Table A4: XPS C 1s high-resolution component Monte Carlo standard deviation errors.

Sample	M-C	C-C	C-N	C-O	C=O	O-C=O	CO <sub>3</sub>	$\pi$ - $\pi^*$
Needle 6	0.00	3.12	3.67	1.97	1.51	1.68	2.26	0.48
Needle 7	0.00	2.16	1.90	2.35	1.97	2.13	0.57	0.00
Needle 8	0.00	2.11	1.24	1.18	0.68	1.12	0.97	1.02
Needle 9	0.98	10.57	0.42	6.02	1.20	1.79	1.61	1.36
Needle 11	0.57	2.12	2.45	1.44	1.39	1.48	0.68	0.60
Needle 12	0.00	3.95	2.16	3.19	1.55	1.55	1.72	1.04
Needle 13	0.12	0.77	0.65	0.52	0.15	0.25	0.25	0.08
Marine 1	0.22	0.68	0.00	0.33	0.20	0.22	0.37	0.38

### 1.1.2.1. XPS C 1s Curve Fittings

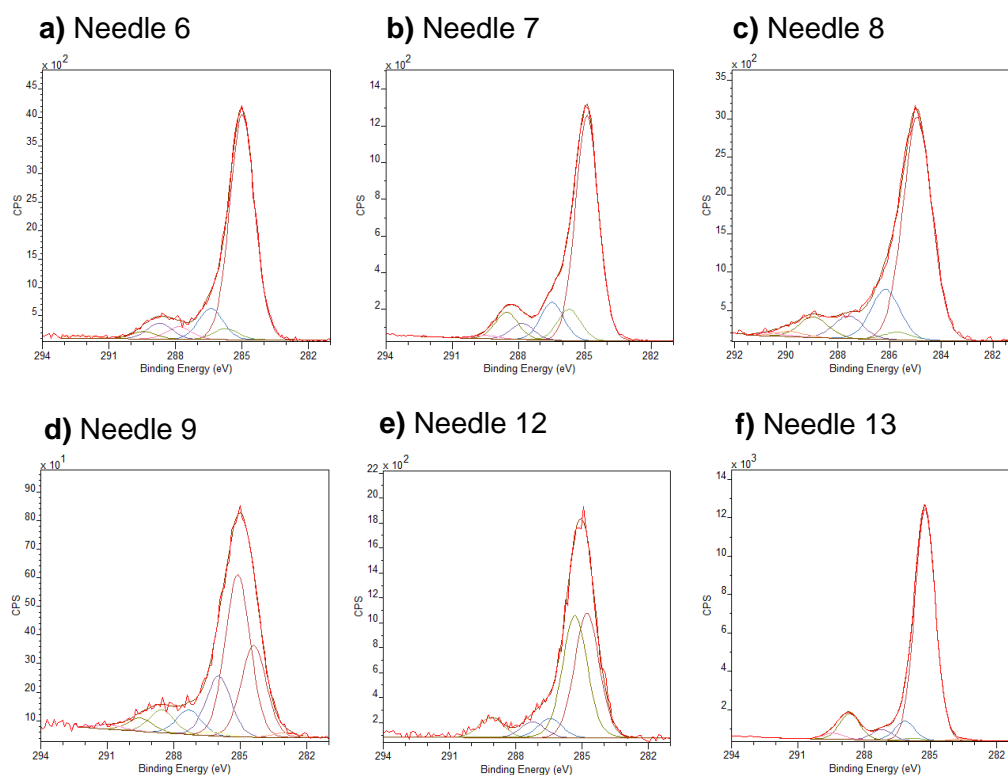


Figure A6: High-resolution C 1s XP spectra for IDID needle samples.

### 1.1.3. OrbiSIMS DDSA-related Chemistry

#### 1.1.3.1. MS/MS of DDSA-related Ions

Table A5: DDSA MS/MS. Parameters for A: 1.5 width, 50 normalised collision energy; B: 1.5 w, 30 NCE; C: 0.9 w, 35 NCE; D: 0.9 w, 70 NCE; E: 0.9 w, 35 NCE. In the DBE calculations, Na is treated as equal to H as it directly substitutes the acids' protons.

Run	Mass	ID	Assignment	DBE	Intensity	Neutral loss
<b>A</b>	<b>1007.4767</b>	<b>A</b>	<b>C<sub>48</sub>H<sub>78</sub>O<sub>12</sub>Na<sub>7</sub><sup>+</sup></b>	<b>6.5</b>	<b>N/A</b>	<b>Parent</b>
	351.1517	1	C <sub>16</sub> H <sub>26</sub> O <sub>4</sub> Na <sub>3</sub> <sup>+</sup>	2.5	1.85E4	C <sub>32</sub> H <sub>52</sub> O <sub>8</sub> Na <sub>4</sub> <sup>+</sup>
	116.9922	2	C <sub>3</sub> H <sub>3</sub> O <sub>2</sub> Na <sub>2</sub> <sup>+</sup>	1.5	1.52E4	C <sub>45</sub> H <sub>75</sub> O <sub>10</sub> Na <sub>5</sub> <sup>+</sup>
<b>B</b>	<b>1007.4767</b>	<b>A</b>	<b>C<sub>48</sub>H<sub>78</sub>O<sub>12</sub>Na<sub>7</sub><sup>+</sup></b>	<b>6.5</b>	<b>3.27E4</b>	<b>Parent</b>
	679.3140	3	C <sub>32</sub> H <sub>52</sub> O <sub>8</sub> Na <sub>5</sub> <sup>+</sup>	4.5	3.32E3	C <sub>16</sub> H <sub>26</sub> O <sub>4</sub> Na <sub>2</sub> <sup>+</sup>
	351.1517	1	C <sub>16</sub> H <sub>26</sub> O <sub>4</sub> Na <sub>3</sub> <sup>+</sup>	2.5	1.57E4	C <sub>32</sub> H <sub>52</sub> O <sub>8</sub> Na <sub>4</sub> <sup>+</sup>
<b>C</b>	<b>679.3140</b>	<b>3</b>	<b>C<sub>32</sub>H<sub>52</sub>O<sub>8</sub>Na<sub>5</sub><sup>+</sup></b>	<b>4.5</b>	<b>2.57E4</b>	<b>Parent</b>
	445.1546	4	C <sub>19</sub> H <sub>29</sub> O <sub>6</sub> Na <sub>4</sub> <sup>+</sup>	3.5	8.00E3	C <sub>13</sub> H <sub>23</sub> O <sub>2</sub> Na <sup>+</sup>
	351.1517	1	C <sub>16</sub> H <sub>26</sub> O <sub>4</sub> Na <sub>3</sub> <sup>+</sup>	2.5	9.98E4	C <sub>16</sub> H <sub>26</sub> O <sub>4</sub> Na <sub>2</sub> <sup>+</sup>
<b>D</b>	<b>679.3140</b>	<b>3</b>	<b>C<sub>32</sub>H<sub>52</sub>O<sub>8</sub>Na<sub>5</sub><sup>+</sup></b>	<b>4.5</b>	<b>2.57E4</b>	<b>Parent</b>
	116.9922	2	C <sub>3</sub> H <sub>3</sub> O <sub>2</sub> Na <sub>2</sub> <sup>+</sup>	1.5	3.94E4	C <sub>29</sub> H <sub>49</sub> O <sub>6</sub> Na <sub>3</sub> <sup>+</sup>
<b>E</b>	<b>351.1517</b>	<b>1</b>	<b>C<sub>16</sub>H<sub>26</sub>O<sub>4</sub>Na<sub>3</sub><sup>+</sup></b>	<b>2.5</b>	<b>2.17E5</b>	<b>Parent</b>
	116.9922	2	C <sub>3</sub> H <sub>3</sub> O <sub>2</sub> Na <sub>2</sub> <sup>+</sup>	1.5	1.55E5	C <sub>13</sub> H <sub>23</sub> O <sub>2</sub> Na <sup>+</sup>

Table A5 presents MS/MS results for Na-DDS related ions on Needle 13. It is noted that the DDSA ions in MS/MS fragmentation do not form Na<sub>3</sub>CO<sub>3</sub><sup>+</sup>, hence collision-induced formation of carbonate is unlikely. Similar energetic collisions from GCIB sputtering should therefore not be expected to form Na<sub>3</sub>CO<sub>3</sub><sup>+</sup>, supporting the appearance of this ion being from thermal degradation rather than SIMS fragmentation/rearrangement.

### 1.1.4. Needle 12 High Mass PIBSI-derived Ions

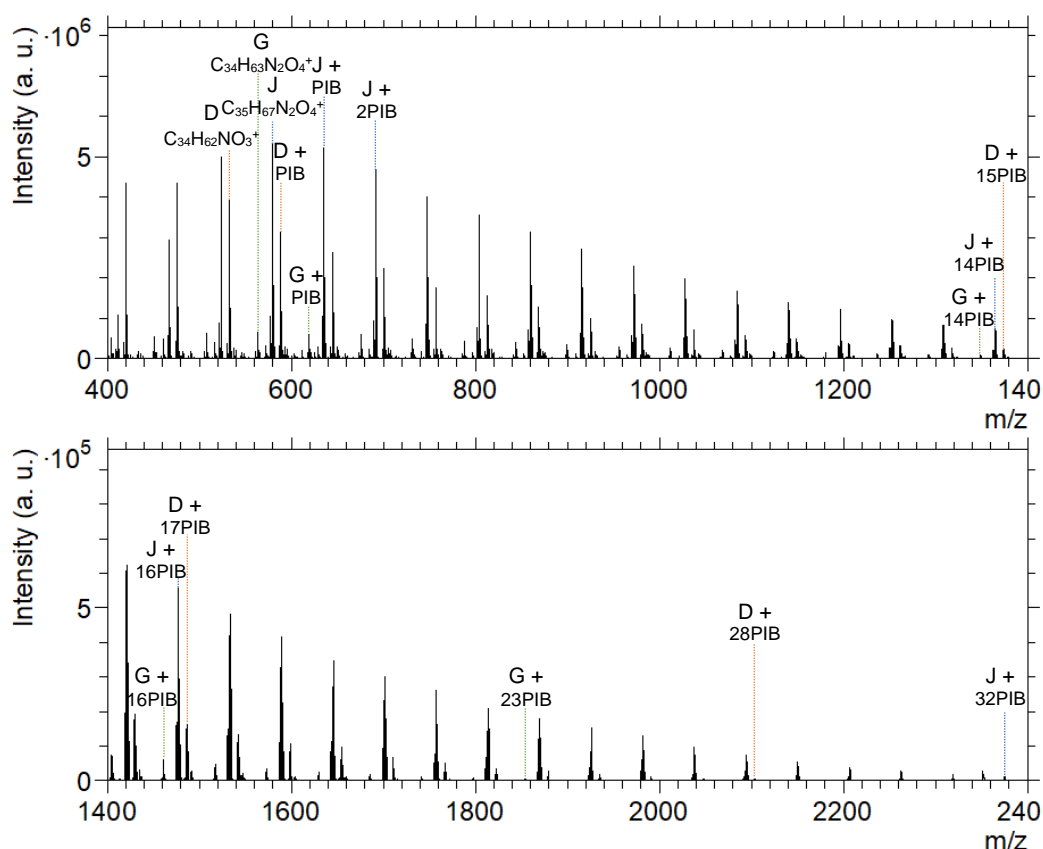
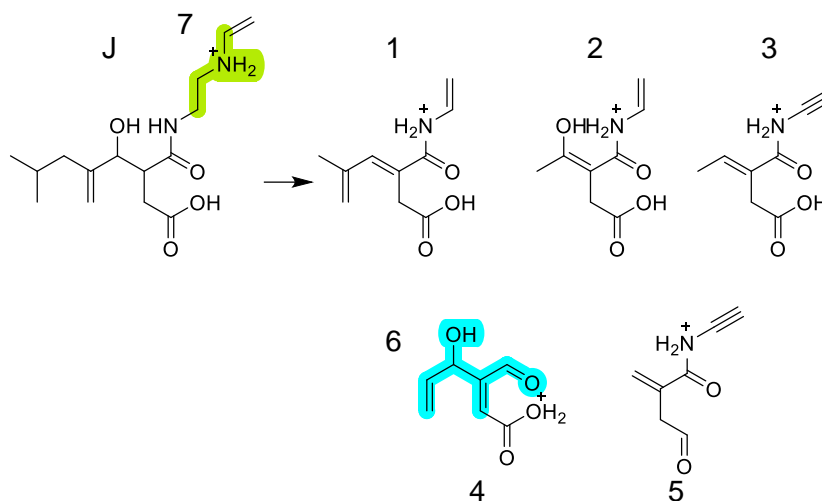


Figure A7: Needle 12 position 3 spectrum (showing 400-2400  $m/z$ ) with main ion series labelled (D, G and J series from Figure 3.9 and Table 3.4).

#### 1.1.4.1. MS/MS Analysis of High Mass PIBSI-derived Ions

Table A6: Needle 12 MS/MS results from a high intensity ion from Series J ( $N_2O_4$ , 3.5 DBE) from Section 3.2.4.1.2.

NCE	Mass	ID	Assignment	DBE	Intensity	Neutral loss
35	299.1963	J	$C_{15}H_{27}N_2O_4^+$	3.5	2.44E5	Parent
	196.0966	1	$C_{10}H_{14}NO_3^+$	4.5	4.00E6	$C_5H_{13}NO$
	186.0758	2	$C_8H_{12}NO_4^+$	3.5	2.58E4	$C_7H_{15}N$
	168.0652	3	$C_8H_{10}NO_3^+$	4.5	4.82E5	$C_7H_{17}NO$
	157.0494	4	$C_7H_9O_4^+$	3.5	4.65E3	$C_8H_{18}N$
	138.0548	5	$C_7H_8NO_2^+$	4.5	2.15E5	$C_8H_{19}NO_2$
	111.0440	6	$C_6H_7O_2^+$	3.5	1.28E4	$C_9H_{20}N_2O_2$
	58.0655	7	$C_3H_8N^+$	0.5	4.71E4	$C_{12}H_{19}NO_4$

Figure A8: Suggested structures of ions from MS/MS of  $C_{15}H_{27}N_2O_4^+$  in Table A6.Table A7: MS/MS results from an ion from Series D ( $NO_3$ , 4.5 DBE) from Section 3.2.4.1.2.

NCE	Mass	ID	Assignment	DBE	Intensity	Neutral loss
<b>50</b>	<b>532.4721</b>	<b>D</b>	<b><math>C_{34}H_{62}NO_3^+</math></b>	<b>4.5</b>	<b>3.47E5</b>	<b>Parent</b>
	196.0966	1	$C_{10}H_{14}NO_3^+$	4.5	6.54E4	$C_{24}H_{48}$
	138.0548	2	$C_7H_8NO_2^+$	4.5	1.75E4	$C_{27}H_{54}O$
	57.0703	3	$C_4H_9^+$	0.5	7.76E3	$C_{30}H_{58}NO_3$

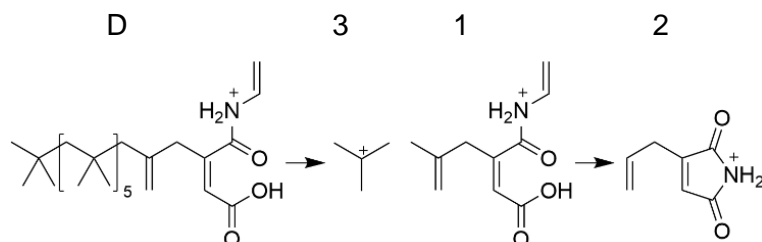


Figure A9: Suggested structures of ions from MS/MS in Table A7.

### 1.1.5. Molybdenum-containing Ions in OrbiSIMS

As well as zinc, lubricant oils contain molybdenum in the friction modifier additive molybdenum dithiocarbamate (MoDTC) (80). Though molybdenum was below the detection limits of XPS in Needle 8, its OrbiSIMS data showed molybdenum oxides and hydroxides (Table A8). As with ABS ions, similar ions were found in a study performing ToF-SIMS analysis of lubricant oil on a steel surface (178). However, in contrast to the zinc ions, position 1 has amongst the highest intensities for molybdenum, decreasing towards position 5 suggesting that this is substrate-related rather than deposit material.

Table A8: Molybdenum-containing OrbiSIMS secondary ions (all deviations <2.5 ppm) for multiple positions of Needle 8.

Assignment	Mass	Needle 8 analysis position				
		1	2	3	4	5
MoO <sub>3</sub> <sup>-</sup>	145.8909	1.88E-03	1.51E-03	6.55E-04	5.26E-03	4.36E-03
MoO <sub>4</sub> H <sup>-</sup>	162.8937	3.59E-04	1.56E-04	1.33E-04	9.98E-04	9.59E-04
MoO <sub>5</sub> <sup>-</sup>	177.8808	1.73E-04	7.86E-05	2.47E-05	4.15E-04	3.09E-04

### 1.1.6. Marine 1 OrbiSIMS Analysis

#### 1.1.6.1. Salicylate and Alkylphenol MS/MS

Table A9: MS/MS of 361.27 (width = 1.9, NCE = 60) and 317.29 *m/z* (width = 1.9, NCE = 60).

Mass	ID	Assignment	DBE	Intensity	Neutral loss
<b>361.2752</b>	<b>2</b>	<b>C<sub>23</sub>H<sub>37</sub>O<sub>3</sub><sup>-</sup></b>	<b>5.5</b>	<b>N/A</b>	<b>Parent</b>
317.2850	3	C <sub>22</sub> H <sub>37</sub> O <sup>-</sup>	4.5	1.31E4	CO <sub>2</sub>
133.0660	5	C <sub>9</sub> H <sub>9</sub> O <sup>-</sup>	5.5	1.24E3	C <sub>14</sub> H <sub>28</sub> O <sub>2</sub>
119.0502	6	C <sub>8</sub> H <sub>7</sub> O <sup>-</sup>	4.5	7.41E4	C <sub>15</sub> H <sub>30</sub> O <sub>2</sub>
<b>317.2849</b>	<b>3</b>	<b>C<sub>22</sub>H<sub>37</sub>O<sup>-</sup></b>	<b>4.5</b>	<b>1.99E5</b>	<b>Parent</b>
161.0972	7	C <sub>11</sub> H <sub>13</sub> O <sup>-</sup>	5.5	1.35E3	C <sub>11</sub> H <sub>24</sub>
147.0814	8	C <sub>10</sub> H <sub>11</sub> O <sup>-</sup>	5.5	1.94E3	C <sub>12</sub> H <sub>26</sub>
133.0658	5	C <sub>9</sub> H <sub>9</sub> O <sup>-</sup>	5.5	7.39E4	C <sub>13</sub> H <sub>28</sub>
121.0658	10	C <sub>8</sub> H <sub>9</sub> O <sup>-</sup>	4.5	5.34E3	C <sub>14</sub> H <sub>28</sub>
120.0536	6a	C <sub>7</sub> <sup>13</sup> CH <sub>7</sub> O <sup>-</sup>	4.5	2.80E4	C <sub>14</sub> H <sub>30</sub>
119.0502	6	C <sub>8</sub> H <sub>7</sub> O <sup>-</sup>	4.5	1.44E6	C <sub>14</sub> H <sub>30</sub>
106.0424	11	C <sub>7</sub> H <sub>6</sub> O <sup>-</sup>	5.0	2.30E3	C <sub>15</sub> H <sub>31</sub>
93.0344	12	C <sub>6</sub> H <sub>5</sub> O <sup>-</sup>	4.5	2.70E3	C <sub>16</sub> H <sub>32</sub>



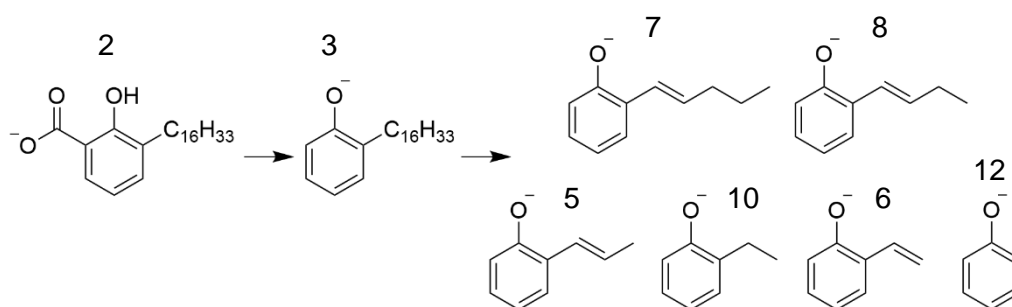


Figure A10: Suggested structures of phenolate OrbiSIMS ions in the MS/MS data from Table A10.

## 2. Supporting Information for Chapter 4: Characterisation of Chemical Variation with Depth of IDIDs

### 2.1. XPS Atomic Concentration Depth Profile Raw Data

#### 2.1.1. Needle 8

For the O 1s component fit to remove metal oxide, the full width at half maximum (FWHM) of the “other” oxygen component was constrained to 2-2.6 and the metal oxide (M-O) component was constrained to 1-1.5 with a position -2.32 eV relative to “other”/deposit oxygen.

Table A10: Needle 8 XPS depth profile including substrate at.% data.

Etch time /s	C 1s	O 1s	Fe 2p	Ca 2p	P 2p	S 2p	Na 1s	Si 2s	Mo 3d	N 1s	Zn 2p
0	75.87	18.78	0.00	0.89	0.00	0.64	0.08	1.49	0.00	1.70	0.54
30	72.39	19.59	1.17	3.20	0.00	0.27	0.08	0.72	0.11	1.23	1.25
60	71.37	18.75	1.43	3.50	0.09	0.32	0.07	0.64	0.20	2.44	1.18
120	71.90	17.97	1.63	4.14	0.16	0.45	0.07	0.85	0.16	1.29	1.25
240	69.61	19.05	1.99	4.91	0.10	0.72	0.10	0.43	0.16	1.30	1.52
540	68.23	18.62	3.15	5.57	0.10	0.25	0.06	0.00	0.23	2.14	1.44
840	65.79	19.16	3.58	6.46	0.22	0.44	0.06	0.00	0.29	2.37	1.46
1140	63.99	19.16	4.48	6.64	0.06	0.54	0.07	0.00	0.30	2.96	1.56
1440	64.09	19.44	4.30	7.02	0.14	0.49	0.12	0.00	0.32	2.09	1.73
1825	60.34	19.93	5.71	7.68	0.26	0.95	0.10	0.00	0.37	2.52	1.84
2125	61.51	19.32	6.15	7.62	0.21	0.61	0.08	0.00	0.41	1.95	1.87
2425	60.52	18.10	7.27	7.55	0.26	0.41	0.12	0.00	0.44	3.39	1.67
2725	59.78	17.87	8.31	7.77	0.23	0.33	0.15	0.00	0.49	3.01	1.73
3025	59.50	17.19	9.18	7.06	0.52	0.57	0.10	0.00	0.51	3.29	1.68
3325	58.40	18.09	10.41	7.24	0.05	0.37	0.07	0.00	0.56	2.72	1.72
3625	57.78	16.44	11.86	7.10	0.17	0.60	0.07	0.00	0.55	3.32	1.67
3925	57.69	16.34	11.54	7.09	0.10	0.93	0.19	0.00	0.75	3.25	1.58
4225	58.02	17.06	11.36	6.57	0.05	0.61	0.07	0.00	0.64	3.52	1.66
4525	57.05	16.30	12.28	6.46	0.13	0.64	0.12	0.00	0.68	4.07	1.70

Table A11: Needle 8 XPS depth profile including substrate Monte Carlo standard deviation errors for at.% data.

Etch time /s	C 1s	O 1s	Fe 2p	Ca 2p	P 2p	S 2p	Na 1s	Si 2s	Mo 3d	N 1s	Zn 2p
0	0.52	0.27	0.00	0.26	0.00	0.12	0.04	0.20	0.00	0.47	0.12
30	0.68	0.32	0.24	0.17	0.00	0.15	0.05	0.19	0.04	0.75	0.13
60	0.68	0.31	0.25	0.21	0.06	0.15	0.03	0.21	0.04	0.73	0.12
120	0.74	0.33	0.24	0.18	0.07	0.17	0.02	0.19	0.03	0.83	0.10
240	0.76	0.38	0.24	0.19	0.09	0.17	0.03	0.20	0.03	0.87	0.12
540	0.72	0.37	0.29	0.19	0.14	0.23	0.03	0.00	0.03	0.80	0.12
840	0.74	0.37	0.28	0.19	0.13	0.25	0.02	0.00	0.04	0.85	0.12
1140	0.67	0.38	0.34	0.18	0.13	0.22	0.02	0.00	0.04	0.70	0.13
1440	0.58	0.37	0.33	0.22	0.12	0.21	0.03	0.00	0.04	0.45	0.13
1825	0.54	0.34	0.36	0.24	0.11	0.21	0.03	0.00	0.04	0.42	0.13

2125	0.58	0.38	0.34	0.19	0.13	0.26	0.03	0.00	0.04	0.40	0.17
2425	0.60	0.39	0.39	0.21	0.14	0.24	0.04	0.00	0.04	0.45	0.16
2725	0.60	0.39	0.34	0.22	0.13	0.26	0.03	0.00	0.04	0.46	0.14
3025	0.64	0.39	0.39	0.20	0.13	0.24	0.04	0.00	0.05	0.51	0.17
3325	0.64	0.42	0.36	0.21	0.14	0.29	0.03	0.00	0.04	0.52	0.16
3625	0.63	0.38	0.39	0.21	0.14	0.27	0.04	0.00	0.04	0.54	0.15
3925	0.65	0.36	0.43	0.22	0.14	0.35	0.04	0.00	0.04	0.54	0.17
4225	0.65	0.41	0.42	0.23	0.09	0.26	0.04	0.00	0.04	0.54	0.17
4525	0.64	0.39	0.42	0.23	0.15	0.25	0.04	0.00	0.04	0.51	0.17

Table A12: Needle 8 XPS depth profile excluding substrate at.% data.

Etch time /s	C 1s	O 1s	Fe 2p	Ca 2p	P 2p	S 2p	Na 1s	Si 2s	Mo 3d	N 1s	Zn 2p
0	76.03	18.98	0.88	1.47	0.58	0.00	0.50	0.04	1.52	76.03	18.98
30	72.65	19.80	2.62	2.01	1.24	0.00	0.35	0.61	0.71	72.65	19.80
60	72.67	19.12	3.18	2.40	1.36	0.07	0.25	0.29	0.66	72.67	19.12
120	72.43	18.65	3.80	2.13	1.34	0.09	0.31	0.41	0.83	72.43	18.65
240	71.04	19.18	4.77	1.70	1.65	0.06	0.46	0.55	0.60	71.04	19.18
540	69.67	19.27	5.70	3.01	1.62	0.00	0.41	0.32	0.00	69.67	19.27
840	68.48	19.56	6.40	3.07	1.61	0.17	0.42	0.28	0.00	68.48	19.56
1140	67.09	19.53	6.73	3.85	1.81	0.14	0.47	0.38	0.00	67.09	19.53
1440	67.55	19.67	7.49	2.27	1.95	0.00	0.38	0.70	0.00	67.55	19.67
1825	65.51	20.15	8.05	2.96	2.01	0.26	0.44	0.60	0.00	65.51	20.15
2125	66.08	19.40	8.12	3.10	2.19	0.08	0.55	0.48	0.00	66.08	19.40
2425	67.37	17.19	8.31	3.95	2.07	0.34	0.36	0.41	0.00	67.37	17.19
2725	67.96	17.60	8.07	2.69	2.18	0.16	0.49	0.85	0.00	67.96	17.60

Table A13: Needle 8 XPS depth profile excluding substrate standard deviation errors for at.% data.

Etch time /s	C 1s	O 1s	Fe 2p	Ca 2p	P 2p	S 2p	Na 1s	Si 2s	Mo 3d	N 1s	Zn 2p
0	0.33	0.22	0.10	0.22	0.12	0.00	0.09	0.03	0.17	0.33	0.22
30	0.40	0.26	0.10	0.27	0.12	0.00	0.09	0.12	0.14	0.40	0.26
60	0.46	0.28	0.12	0.37	0.11	0.04	0.07	0.11	0.15	0.46	0.28
120	0.42	0.27	0.14	0.27	0.08	0.05	0.09	0.12	0.20	0.42	0.27
240	0.44	0.28	0.14	0.29	0.11	0.03	0.11	0.13	0.14	0.44	0.28
540	0.47	0.28	0.15	0.41	0.10	0.00	0.11	0.08	0.00	0.47	0.28
840	0.52	0.28	0.14	0.53	0.10	0.11	0.13	0.10	0.00	0.52	0.28
1140	0.50	0.31	0.14	0.48	0.09	0.08	0.14	0.10	0.00	0.50	0.31
1440	0.48	0.29	0.16	0.38	0.11	0.00	0.15	0.16	0.00	0.48	0.29
1825	0.50	0.28	0.16	0.47	0.11	0.09	0.16	0.11	0.00	0.50	0.28
2125	0.53	0.31	0.18	0.48	0.13	0.06	0.17	0.16	0.00	0.53	0.31
2425	0.56	0.31	0.18	0.49	0.13	0.14	0.15	0.14	0.00	0.56	0.31
2725	0.55	0.29	0.20	0.44	0.13	0.11	0.16	0.15	0.00	0.55	0.29

## 2.1.2. Needle 6

Table A14: Needle 6 XPS depth profile at.% data.

Etch time /s	C 1s	O 1s	Na 1s	N 1s	Cl 2p	S 2p	Ca 2p	Si 2p
0	76.45	15.58	1.48	5.25	0.58	0.21	0.23	0.22
60	61.38	15.79	10.79	7.34	3.87	0.53	0.30	0
360	55.15	15.70	14.77	7.59	6.11	0.51	0.18	0
640	53.19	15.87	15.76	7.73	6.67	0.57	0.21	0
860	51.82	16.16	16.39	8.50	6.47	0.53	0.13	0
1100	52.99	16.30	15.37	7.83	6.22	0.98	0.32	0
1500	54.17	16.20	15.21	7.41	6.03	0.80	0.18	0
1900	63.04	13.40	12.14	5.97	4.74	0.50	0.20	0
2300	70.24	10.58	9.89	4.61	3.78	0.50	0.40	0
2700	74.85	8.97	8.35	4.09	3.21	0.35	0.17	0
2900	75.41	8.52	7.71	4.66	3.07	0.24	0.39	0
3100	76.87	8.43	7.49	4.07	2.78	0.32	0.05	0
3400	78.18	7.89	7.09	3.59	2.76	0.27	0.21	0
3700	78.98	7.29	7.16	3.62	2.62	0.28	0.06	0
4000	79.23	7.12	7.29	3.16	2.81	0.27	0.13	0
4300	79.57	6.87	6.90	3.70	2.49	0.25	0.22	0
4500	80.31	6.28	7.05	3.24	2.62	0.24	0.26	0
4800	79.53	6.88	6.53	3.80	2.69	0.27	0.30	0
5000	80.34	6.54	6.67	3.56	2.60	0.11	0.17	0
5300	81.45	5.75	6.50	3.32	2.63	0.21	0.14	0
5700	81.69	6.03	6.18	3.24	2.55	0.18	0.13	0

Table A15: Needle 6 XPS depth profile standard deviation errors for at.% data.

Etch time /s	C 1s	O 1s	Na 1s	N 1s	Cl 2p	S 2p	Ca 2p	Si 2p
0	0.44	0.32	0.11	0.34	0.07	0.04	0.13	0.07
60	0.22	0.17	0.10	0.19	0.05	0.06	0.06	0.00
360	0.49	0.43	0.21	0.40	0.12	0.09	0.09	0.00
640	0.48	0.41	0.23	0.34	0.14	0.07	0.10	0.00
860	0.51	0.42	0.23	0.46	0.13	0.09	0.08	0.00
1100	0.49	0.37	0.22	0.40	0.12	0.12	0.09	0.00
1500	0.52	0.40	0.23	0.42	0.13	0.10	0.06	0.00
1900	0.45	0.34	0.18	0.35	0.10	0.09	0.11	0.00
2300	0.43	0.31	0.16	0.36	0.10	0.09	0.12	0.00
2700	0.45	0.34	0.15	0.34	0.09	0.07	0.09	0.00
2900	0.45	0.30	0.14	0.38	0.08	0.06	0.11	0.00
3100	0.42	0.33	0.14	0.30	0.08	0.05	0.08	0.00
3400	0.21	0.16	0.07	0.16	0.04	0.03	0.05	0.00
3700	0.41	0.31	0.15	0.30	0.08	0.06	0.07	0.00
4000	0.39	0.28	0.14	0.30	0.08	0.05	0.08	0.00
4300	0.41	0.32	0.13	0.29	0.07	0.06	0.10	0.00
4500	0.41	0.34	0.12	0.26	0.08	0.06	0.10	0.00
4800	0.43	0.30	0.13	0.34	0.08	0.06	0.09	0.00
5000	0.43	0.32	0.13	0.33	0.07	0.05	0.08	0.00
5300	0.35	0.26	0.12	0.23	0.07	0.05	0.09	0.00
5700	0.21	0.14	0.06	0.17	0.04	0.03	0.04	0.00

## 2.1.3. Needle 7

Table A16: Needle 7 XPS depth profile at.% data

Etch time /s	C 1s	O 1s	Na 1s	N 1s	Cl 2p	S 2p	Ca 2p	Si 2p
0	77.13	13.05	7.40	1.94	0.00	0.42	0.00	0.06
300	71.63	13.73	9.34	4.51	0.00	0.46	0.24	0.08
600	75.94	11.24	6.43	4.84	0.88	0.32	0.31	0.03
900	79.40	9.26	5.75	4.40	0.54	0.43	0.12	0.10
1200	81.11	8.49	4.99	4.11	0.81	0.31	0.17	0.00
1500	82.95	7.20	4.60	4.11	0.43	0.38	0.14	0.18
1800	83.77	6.83	4.36	4.02	0.62	0.09	0.13	0.18
2100	83.95	7.03	3.92	3.85	0.80	0.16	0.18	0.11
2400	85.26	6.17	4.17	3.69	0.30	0.18	0.14	0.08
2700	85.20	7.00	3.52	3.41	0.46	0.12	0.21	0.07
3000	84.23	6.99	4.05	3.75	0.49	0.19	0.24	0.05
3300	84.76	6.61	3.88	3.40	0.57	0.33	0.29	0.16
3600	85.14	6.63	3.59	3.32	0.69	0.35	0.10	0.18
3900	85.08	7.07	3.94	3.22	0.20	0.14	0.12	0.22
4200	84.49	6.95	4.20	3.14	0.41	0.41	0.14	0.26
4500	85.28	6.45	4.38	2.98	0.35	0.33	0.02	0.22
4800	85.74	6.73	3.35	2.96	0.58	0.36	0.10	0.18
5100	85.58	6.93	3.43	3.15	0.25	0.38	0.08	0.19
5400	86.12	6.60	3.43	2.78	0.47	0.36	0.10	0.13
5700	86.50	5.79	3.39	3.02	0.61	0.40	0.00	0.30
6000	86.06	6.82	3.63	2.73	0.34	0.25	0.05	0.12
6300	85.76	6.80	3.90	2.89	0.26	0.11	0.04	0.24

Table A17: Needle 7 XPS depth profile standard deviation errors for at.% data.

Etch time /s	C 1s	O 1s	Na 1s	N 1s	Cl 2p	S 2p	Ca 2p	Si 2p
0	0.35	0.17	0.21	0.09	0.12	0.04	0.04	0.04
300	0.62	0.36	0.42	0.19	0.27	0.08	0.09	0.07
600	0.62	0.30	0.45	0.21	0.19	0.11	0.09	0.07
900	0.62	0.31	0.45	0.18	0.20	0.11	0.09	0.07
1200	0.63	0.34	0.46	0.18	0.20	0.10	0.07	0.06
1500	0.65	0.32	0.48	0.19	0.21	0.11	0.07	0.06
1800	0.60	0.29	0.41	0.16	0.20	0.06	0.08	0.06
2100	0.57	0.39	0.38	0.13	0.16	0.05	0.07	0.05
2400	0.62	0.43	0.40	0.15	0.16	0.05	0.08	0.06
2700	0.67	0.37	0.52	0.14	0.15	0.06	0.08	0.05
3000	0.68	0.39	0.51	0.14	0.14	0.07	0.08	0.06
3300	0.60	0.35	0.46	0.17	0.18	0.07	0.08	0.06
3600	0.57	0.32	0.43	0.16	0.18	0.08	0.08	0.06
3900	0.59	0.32	0.45	0.17	0.19	0.07	0.07	0.06
4200	0.61	0.35	0.48	0.16	0.18	0.08	0.07	0.06
4500	0.58	0.33	0.43	0.15	0.18	0.08	0.07	0.06
4800	0.54	0.35	0.34	0.12	0.18	0.06	0.07	0.06
5100	0.56	0.38	0.35	0.14	0.19	0.07	0.08	0.06
5400	0.56	0.35	0.37	0.16	0.21	0.07	0.08	0.06
5700	0.57	0.34	0.40	0.15	0.20	0.07	0.07	0.06
6000	0.54	0.35	0.34	0.12	0.21	0.06	0.09	0.06
6300	0.57	0.33	0.41	0.12	0.20	0.03	0.08	0.06

## 2.2. Profilometry of Craters

Table A18: Profilometry step height data for Needles 6-8 OrbiSIMS and XPS depth profiling craters using average of ten cross sections across each crater.

Sample	Crater	Data	Side 1 (μm)	Side 2 (μm)	Average (μm)
Needle 6	a) OrbiSIMS positive	Min	1.71	1.62	
		Max	2.12	2.22	
		Average	1.96	1.88	1.92
		St. dev	0.13	0.19	0.23
	b) OrbiSIMS negative	Min	1.04	1.22	
		Max	1.52	1.8	
		Average	1.26	1.54	1.4
		St. dev	0.15	0.18	0.22
	Average (pos & neg)	Average			1.66
		St dev			0.32
	c) XPS	Min	2.19	N/A	
		Max	4.65	N/A	
		Average	3.24	N/A	N/A
		St. dev	0.66	N/A	N/A
Needle 8	a) OrbiSIMS positive	Min	0.06	0	
		Max	0.46	0.47	
		Average	0.24	0.21	0.22
		St. dev	0.15	0.13	0.2
	b) OrbiSIMS negative	Min	0.02	0.11	
		Max	0.7	0.57	
		Average	0.32	0.35	0.34
		St. dev	0.21	0.14	0.25
	Average (pos & neg)				0.28
					0.32
Needle 7	a) OrbiSIMS positive	Min	2.55	1.01	
		Max	1.06	5.31	
		Average	1.73	3.30	2.52
		St. dev	0.42	1.22	1.29
	b) OrbiSIMS negative	Min	14.83	5.56	
		Max	8.48	10.84	
		Average	11.02	7.75	9.39
		St. dev	2.02	1.52	2.53
	Average (pos & neg)				5.95
					2.84

### 2.3. Needle 6 negative polarity Original Loadings Tables

Table A19: Ions listed by top 20 loadings in EM 1, EM 2, EM 3 and EM 4 with normalised-to-total peak area, endmember loadings (raw and normalised to maximum) and heat mapping applied. Additional ions included for some EMs at the bottom to illustrate other chemistries. Heat map applied to each column: green = maximum value and red = minimum, for normalised loadings green = 1.00 and red = 0.

<i>m/z</i>	Assignment	Peak area (norm)	Raw and normalised-to-maximum loadings /a.u.							
			EM 1		EM 2		EM 3		EM 4	
92.9278	NaCl <sub>2</sub> <sup>-</sup>	2.8E-01	36.4	1.00	176.2	1.00	41.4	1.00	20.6	0.52
94.9249	NaCl <sup>37</sup> Cl <sup>-</sup>	1.9E-01	30.4	0.84	146.2	0.83	34.8	0.84	16.4	0.42
96.9599	SO <sub>4</sub> H <sup>-</sup>	6.8E-03	25.5	0.70	18.6	0.11	4.1	0.10	1.2	0.03
79.9570	SO <sub>3</sub> <sup>-</sup>	9.4E-03	24.7	0.68	24.6	0.14	5.6	0.13	1.0	0.02
254.8566	NaCaS <sub>2</sub> O <sub>8</sub> <sup>-</sup>	4.1E-03	22.5	0.62	5.9	0.03	12.3	0.30	2.2	0.06
118.9419	NaSO <sub>4</sub> <sup>-</sup>	8.2E-03	22.4	0.61	13.6	0.08	18.9	0.46	2.6	0.07
260.8736	Na <sub>3</sub> S <sub>2</sub> O <sub>8</sub> <sup>-</sup>	1.2E-02	21.5	0.59	11.2	0.06	31.4	0.76	7.5	0.19
95.9521	SO <sub>4</sub> <sup>-</sup>	6.8E-03	17.9	0.49	21.8	0.12	6.4	0.15	1.1	0.03
152.9174	CaSO <sub>5</sub> H <sup>-</sup>	2.7E-03	15.6	0.43	6.7	0.04	9.7	0.23	1.9	0.05
177.9128	CaSO <sub>4</sub> CNO <sup>-</sup>	1.8E-03	12.9	0.35	5.6	0.03	7.8	0.19	0.6	0.02
96.9219	Na <sup>37</sup> Cl <sub>2</sub> <sup>-</sup>	3.2E-02	12.6	0.35	60.4	0.34	13.4	0.32	2.9	0.07
183.0119	C <sub>8</sub> H <sub>7</sub> SO <sub>3</sub> <sup>-</sup>	6.2E-04	12.2	0.33	1.9	0.01	1.9	0.05	0.0	0.00
99.957	NaCNOCl <sup>-</sup>	2.6E-02	11.4	0.31	46.7	0.27	24.4	0.59	4.1	0.10
136.9399	MgSO <sub>5</sub> H <sup>-</sup>	7.4E-03	10.5	0.29	15.1	0.09	22.2	0.54	2.3	0.06
119.0501	C <sub>8</sub> H <sub>7</sub> O <sup>-</sup>	5.3E-04	10.2	0.28	2.3	0.01	2.3	0.06	0.1	0.00
89.0143	C <sub>5</sub> N <sub>2</sub> H <sup>-</sup>	1.2E-03	10.1	0.28	6.2	0.04	4.1	0.10	0.3	0.01
152.8836	Na <sub>2</sub> Cl <sub>2</sub> <sup>37</sup> Cl <sup>-</sup>	1.3E-02	9.9	0.27	33.6	0.19	15.5	0.38	4.0	0.10
150.8865	Na <sub>2</sub> Cl <sub>3</sub> <sup>-</sup>	1.3E-02	9.9	0.27	33.5	0.19	15.6	0.38	4.0	0.10
115.0301	C <sub>7</sub> H <sub>3</sub> N <sub>2</sub> <sup>-</sup>	1.1E-03	9.5	0.26	5.4	0.03	5.6	0.14	0.2	0.00
170.8836	CaClSO <sub>4</sub> <sup>-</sup>	2.7E-03	9.0	0.25	12.0	0.07	7.7	0.19	0.7	0.02
396.7878	Na <sub>3</sub> CaS <sub>3</sub> O <sub>12</sub> <sup>-</sup>	5.6E-04	7.4	1.1	1.1	0.6	6.0	0.01	0.6	0.01
544.7363	Na <sub>7</sub> S <sub>4</sub> O <sub>16</sub> <sup>-</sup>	3.7E-04	4.8	0.7	0.7	0.4	6.0	0.00	0.4	0.01
686.6673	Na <sub>9</sub> S <sub>5</sub> O <sub>20</sub> <sup>-</sup>	7.5E-05	2.9	0.0	0.0	0.1	2.6	0.00	0.1	0.00

<i>m/z</i>	Assignment	Peak area /a.u.	Raw and normalised-to-maximum loadings /a.u.							
			EM 1		EM 2		EM 3		EM 4	
92.9278	NaCl <sub>2</sub> <sup>-</sup>	2.8E-01	36.4	1.00	176.2	1.00	41.4	1.00	20.6	0.52
94.9249	NaCl <sup>37</sup> Cl <sup>-</sup>	1.9E-01	30.4	0.84	146.2	0.83	34.8	0.84	16.4	0.42
96.9219	Na <sup>37</sup> Cl <sub>2</sub> <sup>-</sup>	3.2E-02	12.6	0.35	60.4	0.34	13.4	0.32	2.9	0.07
83.9620	NaCNCl <sup>-</sup>	2.3E-02	7.6	0.21	47.5	0.27	18.9	0.46	2.3	0.06
99.9570	NaCNOCl <sup>-</sup>	2.6E-02	11.4	0.31	46.7	0.27	24.4	0.59	4.1	0.10
152.8836	Na <sub>2</sub> Cl <sub>2</sub> <sup>37</sup> Cl <sup>-</sup>	1.3E-02	9.9	0.27	33.6	0.19	15.5	0.38	4.0	0.10
150.8865	Na <sub>2</sub> Cl <sub>3</sub> <sup>-</sup>	1.3E-02	9.9	0.27	33.5	0.19	15.6	0.38	4.0	0.10
85.9590	NaCN <sup>37</sup> Cl <sup>-</sup>	7.7E-03	3.4	0.09	29.1	0.17	9.1	0.22	0.7	0.02
101.9541	NaCNO <sup>37</sup> Cl <sup>-</sup>	8.9E-03	6.2	0.17	28.2	0.16	13.2	0.32	1.2	0.03
268.8013	Na <sub>4</sub> Cl <sub>4</sub> <sup>37</sup> Cl <sup>-</sup>	9.5E-03	8.2	0.22	24.8	0.14	16.9	0.41	6.4	0.16
79.957	SO <sub>3</sub> <sup>-</sup>	9.4E-03	24.7	0.68	24.6	0.14	5.6	0.13	1.0	0.02
144.8696	CaCl <sub>3</sub> <sup>-</sup>	5.5E-03	4.9	0.13	24.4	0.14	6.5	0.16	1.1	0.03
146.8666	CaCl <sub>2</sub> <sup>37</sup> Cl <sup>-</sup>	5.4E-03	4.8	0.13	24.2	0.14	6.5	0.16	1.1	0.03
95.9521	SO <sub>4</sub> <sup>-</sup>	6.8E-03	17.9	0.49	21.8	0.12	6.4	0.15	1.1	0.03
130.8891	MgCl <sub>2</sub> <sup>37</sup> Cl <sup>-</sup>	3.4E-03	0.9	0.02	21.0	0.12	4.0	0.10	0.2	0.00
176.9006	Na <sub>2</sub> SO <sub>4</sub> Cl <sup>-</sup>	6.1E-03	6.1	0.17	20.6	0.12	13.9	0.34	1.7	0.04
128.8921	MgCl <sub>3</sub> <sup>-</sup>	3.2E-03	1.2	0.03	20.3	0.12	4.3	0.10	0.1	0.00
270.7985	Na <sub>4</sub> Cl <sub>3</sub> <sup>37</sup> Cl <sub>2</sub> <sup>-</sup>	5.7E-03	6.0	0.16	19.3	0.11	13.2	0.32	4.2	0.11
154.8806	Na <sub>2</sub> Cl <sup>37</sup> Cl <sub>2</sub> <sup>-</sup>	4.0E-03	4.5	0.12	19.2	0.11	7.7	0.19	1.3	0.03
210.8423	Na <sub>3</sub> Cl <sub>3</sub> <sup>37</sup> Cl <sup>-</sup>	4.3E-03	4.6	0.13	18.8	0.11	9.4	0.23	2.4	0.06

<i>m/z</i>	Assignment	Peak area /a.u.	Raw and normalised-to-maximum loadings /a.u.							
			EM 1		EM 2		EM 3		EM 4	
92.9278	NaCl <sub>2</sub> <sup>-</sup>	2.8E-01	36.4	1.00	176.2	1.00	41.4	1.00	20.6	0.52
94.9249	NaCl <sup>37</sup> Cl <sup>-</sup>	1.9E-01	30.4	0.84	146.2	0.83	34.8	0.84	16.4	0.42
260.8736	Na <sub>3</sub> S <sub>2</sub> O <sub>8</sub> <sup>-</sup>	1.2E-02	21.5	0.59	11.2	0.06	31.4	0.76	7.5	0.19
99.9570	NaCNOCl <sup>-</sup>	2.6E-02	11.4	0.31	46.7	0.27	24.4	0.59	4.1	0.10
136.9399	MgSO <sub>5</sub> H <sup>-</sup>	7.4E-03	10.5	0.29	15.1	0.09	22.2	0.54	2.3	0.06
118.9419	NaSO <sub>4</sub> <sup>-</sup>	8.2E-03	22.4	0.61	13.6	0.08	18.9	0.46	2.6	0.07
83.9620	NaCNCl <sup>-</sup>	2.3E-02	7.6	0.21	47.5	0.27	18.9	0.46	2.3	0.06
268.8013	Na <sub>4</sub> Cl <sub>4</sub> <sup>37</sup> Cl <sup>-</sup>	9.5E-03	8.2	0.22	24.8	0.14	16.9	0.41	6.4	0.16
150.8865	Na <sub>2</sub> Cl <sub>3</sub> <sup>-</sup>	1.3E-02	9.9	0.27	33.5	0.19	15.6	0.38	4.0	0.10
152.8836	Na <sub>2</sub> Cl <sub>2</sub> <sup>37</sup> Cl <sup>-</sup>	1.3E-02	9.9	0.27	33.6	0.19	15.5	0.38	4.0	0.10
238.879	NaMgS <sub>2</sub> O <sub>8</sub> <sup>-</sup>	2.8E-03	8.9	0.24	6.1	0.03	14.8	0.36	1.0	0.02
234.8593	Na <sub>3</sub> SO <sub>4</sub> Cl <sub>2</sub> <sup>-</sup>	5.0E-03	4.6	0.13	17.3	0.10	14.4	0.35	2.2	0.06
244.8784	Na <sub>3</sub> S <sub>2</sub> O <sub>7</sub> <sup>-</sup>	2.1E-03	5.2	0.14	4.5	0.03	14.3	0.34	2.3	0.06
176.9006	Na <sub>2</sub> SO <sub>4</sub> Cl <sup>-</sup>	6.1E-03	6.1	0.17	20.6	0.12	13.9	0.34	1.7	0.04
106.9862	NaC <sub>2</sub> N <sub>2</sub> O <sub>2</sub> <sup>-</sup>	4.3E-03	6.9	0.19	15.3	0.09	13.5	0.33	0.9	0.02
96.9219	Na <sup>37</sup> Cl <sub>2</sub> <sup>-</sup>	3.2E-02	12.6	0.35	60.4	0.34	13.4	0.32	2.9	0.07
101.9541	NaCNO <sup>37</sup> Cl <sup>-</sup>	8.9E-03	6.2	0.17	28.2	0.16	13.2	0.32	1.2	0.03
270.7985	Na <sub>4</sub> Cl <sub>3</sub> <sup>37</sup> Cl <sub>2</sub> <sup>-</sup>	5.7E-03	6.0	0.16	19.3	0.11	13.2	0.32	4.2	0.11
161.9352	MgSO <sub>4</sub> CNO <sup>-</sup>	3.0E-03	8.2	0.22	9.7	0.05	13.1	0.32	0.3	0.01
266.8041	Na <sub>4</sub> Cl <sub>5</sub> <sup>-</sup>	5.4E-03	5.9	0.16	18.6	0.11	12.9	0.31	4.0	0.10
318.8317	Na <sub>4</sub> S <sub>2</sub> O <sub>8</sub> Cl <sup>-</sup>	6.1E-04	2.2	0.06	3.2	0.02	7.4	0.18	0.6	0.02

<i>m/z</i>	Assignment	Peak area /a.u.	Raw and normalised-to-maximum loadings /a.u.							
			EM 1		EM 2		EM 3		EM 4	
96.0003	C <sub>8</sub> <sup>-</sup>	6.2E-03	5.5	0.15	10.7	0.06	1.5	0.04	39.5	1.00
108.0005	C <sub>9</sub> <sup>-</sup>	3.4E-03	3.1	0.09	5.0	0.03	1.0	0.02	32.2	0.81
144.0004	C <sub>12</sub> <sup>-</sup>	2.6E-03	2.1	0.06	2.3	0.01	1.2	0.03	29.3	0.74
120.0004	C <sub>10</sub> <sup>-</sup>	2.0E-03	2.5	0.07	3.4	0.02	1.3	0.03	25.1	0.63
121.0083	C <sub>10</sub> H <sup>-</sup>	2.7E-03	5.2	0.14	6.0	0.03	5.8	0.14	21.4	0.54
92.9278	NaCl <sub>2</sub> <sup>-</sup>	2.8E-01	36.4	1.00	176.2	1.00	41.4	1.00	20.6	0.52
145.0082	C <sub>12</sub> H <sup>-</sup>	1.7E-03	2.6	0.07	2.5	0.01	3.7	0.09	20.5	0.52
94.9249	NaCl <sup>37</sup> Cl <sup>-</sup>	1.9E-01	30.4	0.84	146.2	0.83	34.8	0.84	16.4	0.42
132.0004	C <sub>11</sub> <sup>-</sup>	7.8E-04	1.4	0.04	2.0	0.01	0.6	0.02	15.6	0.40
156.0004	C <sub>13</sub> <sup>-</sup>	6.4E-04	0.7	0.02	1.0	0.01	0.0	0.00	15.3	0.39
169.0083	C <sub>14</sub> H <sup>-</sup>	6.7E-04	1.1	0.03	0.8	0.00	2.0	0.05	13.8	0.35
97.0082	C <sub>8</sub> H <sup>-</sup>	3.1E-03	7.6	0.21	11.1	0.06	6.8	0.16	12.9	0.33
84.0002	C <sub>7</sub> <sup>-</sup>	6.3E-04	1.9	0.05	4.1	0.02	0.6	0.01	11.4	0.29
193.0083	C <sub>16</sub> H <sup>-</sup>	3.6E-04	0.4	0.01	0.0	0.00	1.1	0.03	10.8	0.27
168.0004	C <sub>14</sub> <sup>-</sup>	1.9E-04	0.3	0.01	0.0	0.00	0.5	0.01	8.2	0.21
260.8736	Na <sub>3</sub> S <sub>2</sub> O <sub>8</sub> <sup>-</sup>	1.2E-02	21.5	0.59	11.2	0.06	31.4	0.76	7.5	0.19
204.0004	C <sub>17</sub> <sup>-</sup>	1.4E-04	0.7	0.02	0.3	0.00	0.8	0.02	6.6	0.17
97.0037	C <sub>7</sub> <sup>13</sup> C <sup>-</sup>	1.6E-04	0.8	0.02	1.7	0.01	0.2	0.00	6.6	0.17
268.8013	Na <sub>4</sub> Cl <sub>4</sub> <sup>37</sup> Cl <sup>-</sup>	9.5E-03	8.2	0.22	24.8	0.14	16.9	0.41	6.4	0.16
145.0038	C <sub>11</sub> <sup>13</sup> C <sup>-</sup>	1.2E-04	0.8	0.02	0.4	0.00	0.3	0.01	6.3	0.16

## 2.4. Endmember Combination Method

Figure A11 shows plots for a) EM 1's original loadings, c) EM 2's original loadings followed by b) EM 1's loadings after subtraction of EM 2 and d) EM 2's loadings after subtraction of EM 1. Additional understandings of these two



endmembers can be drawn from this data. Being representative of the uppermost and second uppermost layers respectively, it is logical that EM 1 and EM 2 will contain some mixing; the real profile shapes of the ions do not follow the precise shape of the endmember scores, and ions that fall in-between will be present in both endmembers' loadings. Hence, many high intensity ions will have high loadings in both endmembers.

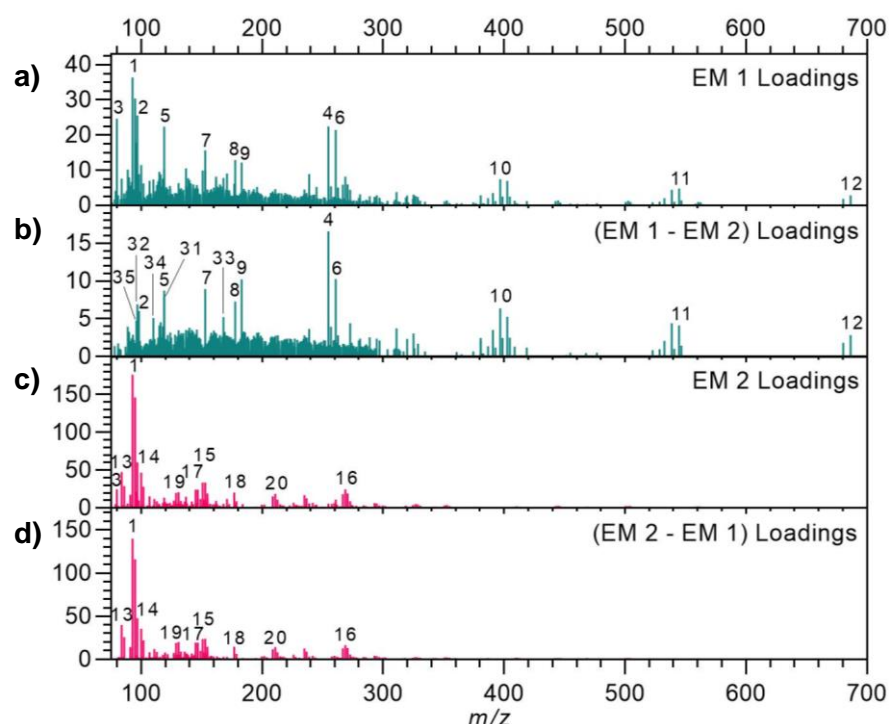


Figure A11: Combination of endmembers 1 and 2, showing the original loadings for each above the subtracted loadings.

The combination removes sodium chloride ions from EM 1, while EM 2 appears almost unchanged. EM 1 contains some dense peaks until almost 300  $m/z$  which have loadings generally around 5 which are now slightly more apparent. These ions are generally organic and are indeed characteristic of EM 1 and the uppermost deposit layer. In the highest 20 loading ions for EM 1 shown in Table A20, organic ions are now more numerous.

Table A20: EM 1 and 2 highest 20 loadings after combination of EM 1 and EM 2. Heat map applied to peak area and loading columns: green = maximum value and red = minimum.

EM 1					EM 2				
ID	m/z	Assignment	Peak area (norm)	EM 1 – EM 2 loading	ID	m/z	Assignment	Peak area (norm)	EM 2 – EM 1 loading
4	254.8566	NaCaS <sub>2</sub> O <sub>8</sub> <sup>-</sup>	4.1E-03	16.6	1	92.9278	NaCl <sub>2</sub> <sup>-</sup>	2.8E-01	139.8
6	260.8736	Na <sub>3</sub> S <sub>2</sub> O <sub>8</sub> <sup>-</sup>	1.2E-02	10.3		94.9249	NaCl <sup>37</sup> Cl <sup>-</sup>	1.9E-01	115.7
9	183.0119	C <sub>8</sub> H <sub>7</sub> SO <sub>3</sub> <sup>-</sup>	6.2E-04	10.2		96.9219	Na <sup>37</sup> Cl <sub>2</sub> <sup>-</sup>	3.2E-02	47.8
7	152.9174	CaSO <sub>5</sub> H <sup>-</sup>	2.7E-03	8.9	13	83.9620	NaCNCl <sup>-</sup>	2.3E-02	39.9
5	118.9419	NaSO <sub>4</sub> <sup>-</sup>	8.2E-03	8.8	14	99.9570	NaCNOCl <sup>-</sup>	2.6E-02	35.3
31	119.0501	C <sub>8</sub> H <sub>7</sub> O <sup>-</sup>	5.3E-04	7.9		85.9590	NaCN <sup>37</sup> Cl <sup>-</sup>	7.7E-03	25.7
8	177.9128	CaSO <sub>4</sub> CNO <sup>-</sup>	1.8E-03	7.3		152.8836	Na <sub>2</sub> Cl <sub>2</sub> <sup>37</sup> Cl <sup>-</sup>	1.3E-02	23.8
2	96.9599	SO <sub>4</sub> H <sup>-</sup>	6.8E-03	6.9	15	150.8865	Na <sub>2</sub> Cl <sub>3</sub> <sup>-</sup>	1.3E-02	23.7
10	396.7878	Na <sub>3</sub> CaS <sub>3</sub> O <sub>12</sub> <sup>-</sup>	5.6E-04	6.4		101.9541	NaCNO <sup>37</sup> Cl <sup>-</sup>	8.9E-03	21.9
32	98.0246	C <sub>4</sub> H <sub>4</sub> NO <sub>2</sub> <sup>-</sup>	5.4E-04	6.0	19	130.8891	MgCl <sub>2</sub> <sup>37</sup> Cl <sup>-</sup>	3.4E-03	20.1
23	402.8045	Na <sub>5</sub> S <sub>3</sub> O <sub>12</sub> <sup>-</sup>	1.2E-03	5.3	17	144.8696	CaCl <sub>3</sub> <sup>-</sup>	5.5E-03	19.5
33	167.9046	CaSO <sub>6</sub> <sup>-</sup>	5.1E-04	5.2		146.8666	CaCl <sub>2</sub> <sup>37</sup> Cl <sup>-</sup>	5.4E-03	19.4
34	110.0247	C <sub>5</sub> H <sub>4</sub> NO <sub>2</sub> <sup>-</sup>	3.8E-04	5.1	19	128.8921	MgCl <sub>3</sub> <sup>-</sup>	3.2E-03	19.1
35	96.0089	C <sub>4</sub> H <sub>2</sub> NO <sub>2</sub> <sup>-</sup>	6.0E-04	4.7	16	268.8013	Na <sub>4</sub> Cl <sub>4</sub> <sup>37</sup> Cl <sup>-</sup>	9.5E-03	16.6
	116.0253	C <sub>6</sub> H <sub>2</sub> N <sub>3</sub> <sup>-</sup>	8.0E-04	4.6		154.8806	Na <sub>2</sub> Cl <sup>37</sup> Cl <sub>2</sub> <sup>-</sup>	4.0E-03	14.7
	538.7193	Na <sub>5</sub> CaS <sub>4</sub> O <sub>16</sub> <sup>-</sup>	1.1E-04	4.4	20	176.9006	Na <sub>2</sub> SO <sub>4</sub> Cl <sup>-</sup>	6.1E-03	14.5
	272.8674	NaCaS <sub>2</sub> O <sub>9</sub> H <sub>2</sub> <sup>-</sup>	1.2E-04	4.4		90.9912	NaCNOCN <sup>-</sup>	4.2E-03	14.3
	119.0249	C <sub>6</sub> H <sub>3</sub> N <sub>2</sub> O <sup>-</sup>	5.7E-04	4.2		210.8423	Na <sub>3</sub> Cl <sub>3</sub> <sup>37</sup> Cl <sup>-</sup>	4.3E-03	14.2
11	544.7363	Na <sub>7</sub> S <sub>4</sub> O <sub>16</sub> <sup>-</sup>	3.7E-04	4.1		270.7985	Na <sub>4</sub> Cl <sub>3</sub> <sup>37</sup> Cl <sub>2</sub> <sup>-</sup>	5.7E-03	13.3
	115.0301	C <sub>7</sub> H <sub>3</sub> N <sub>2</sub> <sup>-</sup>	1.1E-03	4.1	1	234.8593	Na <sub>3</sub> SO <sub>4</sub> Cl <sub>2</sub> <sup>-</sup>	5.0E-03	12.8

Attempting deconvolution of a bulk endmember rather than a surface or substrate layer via endmember combination would be more challenging as such an endmember is likely mixed with, at minimum, the layer above it and the layer below it while combination can only process two endmembers. Another issue would occur if an ion was present in the layers represented by non-neighbouring endmembers; in the above example this could be an ion prevalent in both EM 1 and EM 3, whereby combining EM 1 and EM 2 as shown here would not account for this ion's prevalence elsewhere. Another complication arises for ions that are near-evenly distributed across the two endmembers being combined, as those ions will be erased in the subtraction and their information lost.

## 2.5. Relative loadings depth profile examples

In the example depth profiles for ions of a range of %EM values for EMs 1-4 of Needle 6's negative polarity NMF (Figure A12), ions with a higher %EMX are more characteristic of the score curve of EM X. Ions with a lower %EMX value have less character of that endmember and more of another, with presence of their intensity signal seen elsewhere in the depth profile, in the region of other EMs that they will also have a significant %EM value in.

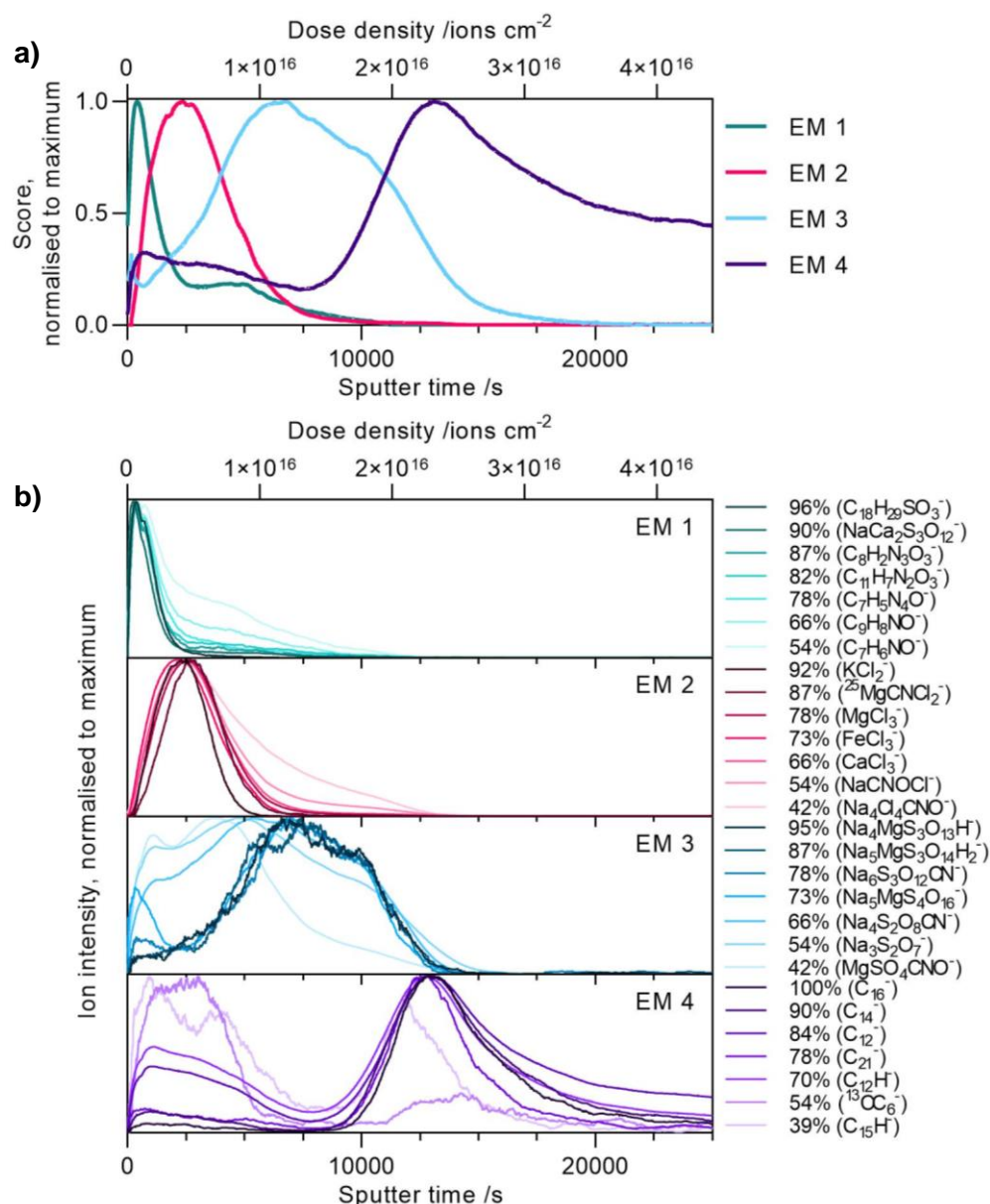


Figure A12: Examples of Needle 6 negative polarity OrbiSIMS ion depth profiles showing that a higher %EM value corresponds to more character of the respective EM's score curve. a) Score curves from NMF, normalised to maximum. b) Examples of ions with a %EM loading for each endmember.

## 2.6. Comparative Method Details

The relative loadings normalisation was applied to original loadings rather than to normalised-to-maximum loadings. This is due to the issue of the highly intense ions that are amongst the highest loadings for multiple endmembers resulting in highly distributed relative loadings which do not accurately capture the ions' intensity distributions. An extreme example of this can be seen in Appendix Table A19 where  $\text{NaCl}_2^-$  is the most intense ion across EMs 1 to 3, which would give it equal relative loadings for these endmembers if the loadings are first normalised to the maximum while the ion in reality most closely resembles EM 2.

There are two caveats to the interpretation of relative loadings. The first is the effect of the ion's intensity. While intensity has a direct effect on the original loading value, intensity also has an indirect effect on the relative loading, as a more intense ion will appear earlier in the profile and maintain a signal for longer than an ion of an identical trend but smaller intensity. Hence, there is a tendency for higher intensity ions to have a lower %EM loading for the EM that best describes them since their signal in other endmembers' regions will be larger. Comparisons between specific ions based on %EM values should therefore be made with care; significant differences that are consistent across multiple ions of the same type indicates trends in the data. The second caveat is that the application of this method would likely be less useful for systems with more complex endmember score curves (resulting from more complex depth profile shapes), while here the endmember scores describe somewhat distinct pseudo-layers where the original depth profile curves consist of an ion simply rising and subsequently falling in intensity.

## 2.7. %EM frequency distributions

### 2.7.1. Example: Needle 6 negative polarity

The distribution of %EM loadings are shown for each endmember of Needle 6's negative polarity depth profile NMF in Figure A13 as a visual overview of the data, where the frequency of ions from 0-100 %EM is shown as a histogram in 1 %EM windows. This shows that each endmember's most frequent score is 0% which is expected as these ions will be represented by the

other endmembers. EM 4 has a concentration of ions below 15 %EM and a small number of high (70-80) %EM ions, hence a small number of ions show this endmember's shape strongly. EM 1 shows many ions distributed around 60% and EMs 2 and 3 show a large number below 30 %EM with the remaining ions distributed from 30-90 %EM. This gives information on how distinct these pseudo-layers are in this depth profile and is assessed in the next section using a more compact visualisation alongside the other depth profiles.

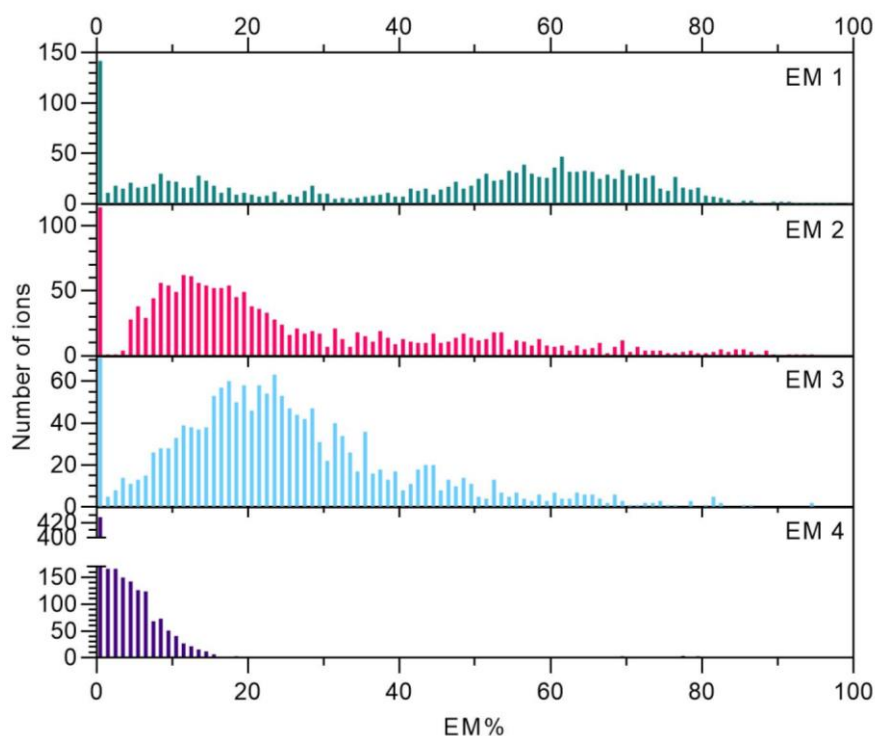


Figure A13: Histograms showing the distribution of %EM loadings for each endmember in NMF of Needle 6 (negative polarity).

#### 2.7.1.1. Needles 6-8 analysis and comparison

The distributions of %EM loadings are shown as a cumulative frequency plot in Figure A14, where the percentage of ions scoring below an %EM value is shown for that %EM value for each endmember (dashed lines). For Needle 6, EM 4 has relatively very few ions associated with it, with >80% of ions in both polarities having <10 %EM4. The other Needle 6 EMs are more distributed, though EM 1 has a larger number of ions with higher %EM1 values, with over 35% of ions having >60 %EM1 while the other EMs have <15% of ions with >60 %EM. In Needle 7, where EM 4 represents a similar DLC layer to EM 4 in Needle 6, it is also the EM with the fewest ions associated with it. For

most profiles, EM 1 has the most ions associated with it, particularly for Needle 8's positive polarity profile where 14.5% of ions have 100 %EM1, hence the surface has the largest number of ions.

A summary of this data can be seen in Table A21, showing the percentage of ions in each depth profile with ions having <30, <35, <40, <45 and <50 %EM in all EMs. In all cases, around 70-80% of ions have >50 %EM in an EM, except for Needle 7 positive polarity where this is only 55%, indicating less distinct layering effects in this depth profile.. This means that in all profiles, the majority of ions have loadings distributed mostly in one EM.

Table A21: Number and percentage of ions with all EM 1-4 loadings below the %EM values specified in NMF of Needles 6-8.

	Ions below X %EM (left), as percentage of all ions (right)											
Sample	Needle 6				Needle 8				Needle 7			
%EM	Negative		Positive		Negative		Positive		Negative		Positive	
30	3	0.2	0	0	6	0.9	4	0.4	1	0.1	5	1.2
35	18	1.1	3	0.5	31	4.6	11	1.2	16	1.2	34	8.4
40	75	4.5	26	4.0	74	11.0	50	5.4	61	4.7	82	20.2
45	189	11.3	87	13.4	148	22.0	98	10.6	157	12.1	134	33.0
50	375	22.4	146	22.5	211	31.4	209	22.7	286	22.0	184	45.0
Total	1671		648		672		922		1301		406	

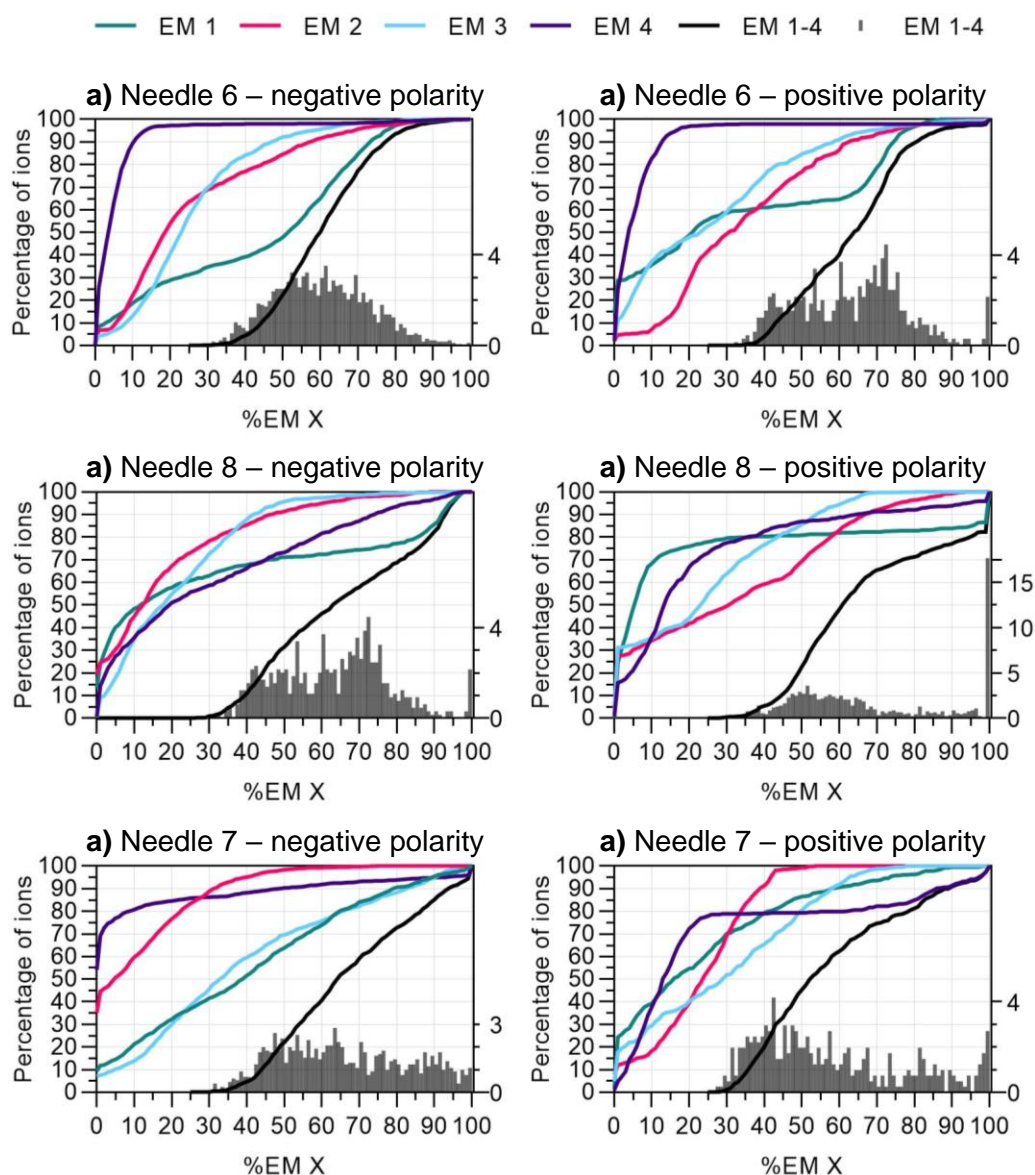


Figure A14: Cumulative frequency plots of percentage of ions below X %EM values for individual endmembers (dashed lines) and across all endmembers (solid line). On right y-axis, the frequency distribution as a percentage of ions is also shown across all endmembers as a histogram for 1 %EM windows (bars).

## 2.8. NMF Results Overviews for Needles 6-8 using Comparative Method

This Appendix section covers the interpretation of NMF results from Needles 6's positive polarity depth profile and Needles 7 and 8's negative and positive polarity depth profiles in the same manner as that for Needle 6's negative polarity profile in Section 4.2.3.1.1.3. Here, an overview of the high loading ions is presented to characterise each EM of each profile based on the high intensity ions that are most prominent in the NMF results. Also presented here are tabulated summaries of the ions found in each EM of each sample which are referred to in the detailed descriptions of each sample in Section 4.2.3.2.

### 2.8.1. Overview of Needle 6 OrbiSIMS NMF using the Comparative Method

#### 2.8.1.1. Positive polarity OrbiSIMS NMF results overview

In positive polarity, the NMF endmember score curves for Needle 6 (Figure A15b) resemble those of the negative polarity seen from their comparable interfaces (Figure A15a). The chemical information from these EMs' loadings also strongly corresponds with that found in the negative polarity data (Figure 4.10, Table 4.2).

The upper pseudo-layer consists of primarily organic ions including small PAHs and oxygen and/or nitrogen-containing species ( $C_{16}H_{10}^+$ : 69 %EM1;  $C_6H_6NO_2^+$ : 74 %EM1). The sub-surface pseudo-layer shows the same rise in chloride salts of primarily sodium ( $Na_2Cl^+$ : 70 %EM2), though here potassium chlorides are also evident ( $KNaCl^+$ : 76 %EM2). The third pseudo-layer shows sulfate salts of primarily sodium ( $Na_3SO_4^+$ : 43 %EM2) but also with potassium presence ( $KNa_2SO_4^+$ : 50 %EM3), as well as sodium carbonate ( $Na_3CO_3^+$ : 67 %EM3). Some sulfates of this pseudo-layer are mixed with other anions such as chloride ( $Na_4SO_4Cl^+$ : 49.4 %EM3). The lowest pseudo-layer is carbonaceous, composed of  $C_x^+$  and  $C_xH^+$  ions, which here are near-exclusive to this layer ( $C_{11}$ : 100 %EM4;  $C_9H^+$ : 93.3 %EM4), while some of the  $C_x^-$  anions seen above were highly distributed through the upper layers of deposit material in the negative polarity profile.



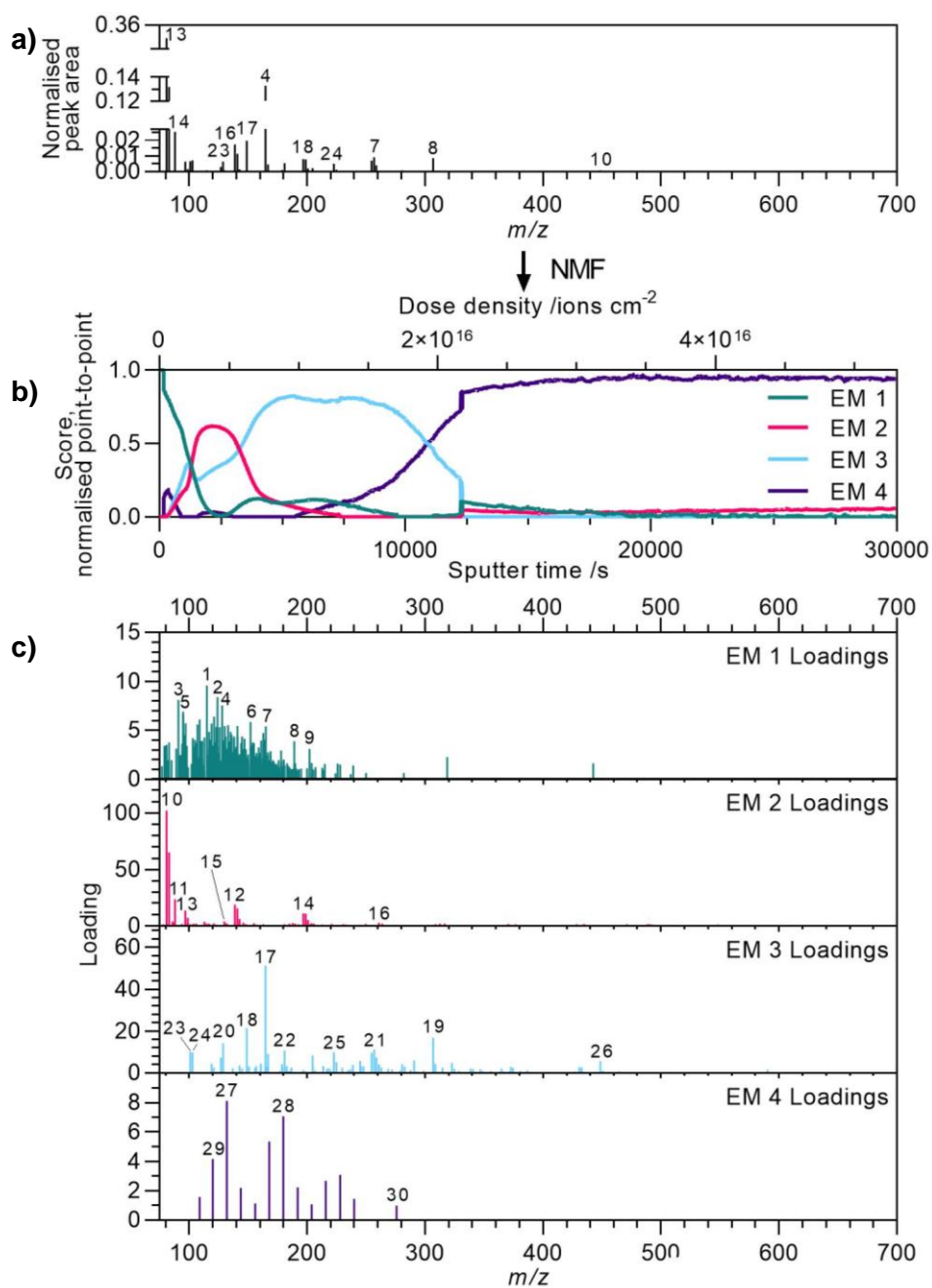


Figure A15: NMF results for Needle 6 negative polarity depth profile. a) OrbiSIMS spectrum over the full depth profile range. b) Endmember scores (normalised point-to-point). c) Loadings for all endmembers after filtering to remove ions that have a higher loading in another endmember.

Table A22: Needle 6 negative polarity NMF results for key ions with ions assigned numbers from Figure A15, loadings and relative loadings, separated by which endmember their loading is highest for. Additional ions shown at the bottom which are highly distributed across multiple endmembers. Heat map applied to each column: for original loadings green = maximum value and red = minimum, for relative loadings green = 100 and red = 0.

Ion	m/z	ID	Peak area (norm)	Original loading (EM)				Relative loading (%EM)			
				1	2	3	4	1	2	3	4
1	115.0542	C <sub>9</sub> H <sub>7</sub> <sup>+</sup>	9.5E-04	9.6	1.6	2.8	0.2	67.7	11.5	19.6	1.1
2	124.0392	C <sub>6</sub> H <sub>6</sub> NO <sub>2</sub> <sup>+</sup>	5.4E-04	8.4	1.4	1.6	0.0	73.8	12.1	14.0	0.0
3	91.0544	C <sub>7</sub> H <sub>7</sub> <sup>+</sup>	5.0E-04	8.1	1.0	1.6	0.2	73.8	9.3	14.8	2.2
4	128.0619	C <sub>10</sub> H <sub>8</sub> <sup>+</sup>	5.6E-04	7.6	1.5	1.9	0.0	68.7	13.6	17.4	0.3
5	95.0492	C <sub>6</sub> H <sub>7</sub> O <sup>+</sup>	3.6E-04	5.9	1.5	1.5	0.0	73.6	10.5	14.0	1.9
6	152.0618	C <sub>12</sub> H <sub>8</sub> <sup>+</sup>	3.9E-04	6.9	1.0	1.3	0.2	66.1	17.1	16.7	0.0
7	165.0696	C <sub>13</sub> H <sub>9</sub> <sup>+</sup>	2.7E-04	5.4	1.2	1.1	0.0	69.8	16.0	14.2	0.0
8	189.0696	C <sub>15</sub> H <sub>9</sub> <sup>+</sup>	1.8E-04	3.9	1.3	0.7	0.0	66.0	22.1	11.9	0.0
9	202.0775	C <sub>16</sub> H <sub>10</sub> <sup>+</sup>	9.7E-05	3.1	1.0	0.4	0.0	68.5	23.1	8.4	0.0
10	80.9481	Na <sub>2</sub> Cl <sup>+</sup>	3.5E-01	5.0	102.4	32.0	7.6	3.4	69.7	21.8	5.2
11	87.9772	Na <sub>2</sub> CNO <sup>+</sup>	2.5E-02	3.9	23.8	12.5	0.0	9.8	59.1	31.1	0.0
12	138.9063	Na <sub>3</sub> Cl <sub>2</sub> <sup>+</sup>	1.7E-02	4.4	19.0	10.9	1.2	12.5	53.5	30.7	3.4
13	96.9219	KNaCl <sup>+</sup>	6.4E-03	0.0	13.8	4.4	0.0	0.0	76.0	24.0	0.0
14	196.8649	Na <sub>4</sub> Cl <sub>3</sub> <sup>+</sup>	8.0E-03	4.4	11.1	9.0	0.9	17.3	43.6	35.4	3.6
15	129.9406	Na <sub>3</sub> CNCl <sup>+</sup>	8.8E-04	0.7	4.1	2.5	0.0	10.1	55.9	34.0	0.0
16	260.8147	Na <sub>5</sub> Cl <sup>37</sup> Cl <sub>3</sub> <sup>+</sup>	6.7E-04	1.6	2.8	2.7	0.0	22.2	39.8	38.0	0.0
17	164.9203	Na <sub>3</sub> SO <sub>4</sub> <sup>+</sup>	1.3E-01	25.9	27.8	51.2	15.4	21.6	23.1	42.5	12.8
18	148.9254	Na <sub>3</sub> SO <sub>3</sub> <sup>+</sup>	2.0E-02	5.1	10.3	21.4	3.6	12.6	25.6	53.0	8.8
19	306.8516	Na <sub>5</sub> S <sub>2</sub> O <sub>8</sub> <sup>+</sup>	8.5E-03	9.5	1.5	16.9	2.8	31.0	4.9	54.9	9.2
20	128.9534	Na <sub>3</sub> CO <sub>3</sub> <sup>+</sup>	6.3E-03	0.7	3.8	14.2	2.5	3.1	18.0	67.2	11.8
22	256.8206	Na <sub>5</sub> Cl <sub>3</sub> <sup>37</sup> Cl <sup>+</sup>	9.2E-03	6.5	10.0	11.2	1.9	21.9	33.7	37.9	6.4
23	180.8942	KNa <sub>2</sub> SO <sub>4</sub> <sup>+</sup>	5.4E-03	6.2	5.1	10.8	0.6	27.4	22.5	47.4	2.7
24	100.9409	Na <sub>3</sub> S <sup>+</sup>	6.7E-03	0.0	9.0	10.1	0.3	0.0	46.2	52.1	1.7
25	102.9743	Na <sub>3</sub> O <sub>2</sub> H <sub>2</sub> <sup>+</sup>	7.1E-03	1.6	9.7	9.8	0.2	7.4	45.4	46.1	1.1
26	222.879	Na <sub>4</sub> SO <sub>4</sub> Cl <sup>+</sup>	5.0E-03	3.4	6.1	9.8	0.5	17.1	30.8	49.4	2.7
27	448.7828	Na <sub>7</sub> S <sub>3</sub> O <sub>12</sub> <sup>+</sup>	9.0E-04	3.8	0.0	5.7	0.4	38.1	0.0	58.3	3.6
28	131.9993	C <sub>11</sub> <sup>+</sup>	4.9E-04	0.0	0.0	0.0	8.1	0.0	0.0	0.0	100
29	179.9992	C <sub>15</sub> <sup>+</sup>	3.6E-04	0.0	0.0	0.0	7.1	0.0	0.0	0.0	100
30	109.0073	C <sub>9</sub> H <sup>+</sup>	1.8E-05	0.0	0.1	0.0	1.6	0.0	6.7	0.0	93.3

### 2.8.1.2. Comparison to atomic concentration depth profile from XPS

Needle 6's XPS profile was seen in Chapter 4 (Figure 4.6) and shows consistency with the NMF endmembers, with a surface layer (0-60s etching) high in carbon, oxygen and nitrogen matching the organic/carbonaceous ions seen in EM 1, with relatively high oxygen and nitrogen accounting for the heteroatom presence in these organic chemistries. Below this (350-850s) exists a layer of increased sodium and chlorine content corresponding to EM 2 where such salts dominated. Upon further etching (1150-1500s), there is a rise in sulfur while oxygen remains high, matching the sulfate content in EM 3, before finally there is a rise in carbon (occurring from 1500s and nearing a plateau at 3300s) matching the carbonaceous content of EM 4. Tables of this XPS data,

with standard deviations, can be found for Needles 6-8 in Appendix Section 2.1.

### **2.8.1.3. Summary of Deposit Characterisation by OrbiSIMS NMF and XPS**

Table A23 presents a summary of the findings from the above NMF analysis of Needle 6's negative and positive polarity depth profiles using the comparative method, alongside the XPS depth profile data for regions that appear to represent each EM.

Table A23: Needle 6 summary of OrbiSIMS and XPS data for pseudo-layers identified by NMF endmembers with example ions and relative loadings.

EM/pseudo-layer (etch time range /s)		1	2	3	4	Split
Technique						
OrbiSIMS						
	Negative Polarity	<ul style="list-style-type: none"> <li>Organics (to 325 <math>m/z</math>): <ul style="list-style-type: none"> <li>Sulfonates: <math>C_8H_7SO_3^-</math> to <math>C_{18}H_{29}SO_3^-</math> (76-96 %EM1)</li> <li>Other organics &lt; 320 <math>m/z</math> ranging from 36-91 %EM1: nitrogenous (<math>C_xH_yN_{1-4}^-</math>), oxygenate (<math>C_xH_yO_{1-2}^-</math>) and NO-containing (<math>C_xH_yN_{1-4}O_{1-3}^-</math>) where <math>x \leq 23</math>, <math>y = 3-11</math>, hydrocarbons to <math>C_{15}H_5^-</math>.</li> <li>Sodium succinate: (<math>C_4H_4O_4Na^-</math>: 46 %EM1)</li> <li>Includes H-deficient (<math>H &lt; 3</math>) N- and/or O-containing ions e.g. <math>C_{11-13}N^-</math> (26-42 %EM1), <math>C_{4-7}NO_3^-</math> (59-77 %EM1)</li> </ul> </li> <li>Sulfate salts: <ul style="list-style-type: none"> <li>Sodium (generally larger in EM 3, &lt;52 %EM1), iron and mixed sodium-calcium, sodium-potassium and sodium-magnesium (up to ~90 %EM), many of which are split with EM 3.</li> </ul> </li> <li>Copper cyanide, cyanate, chloride (<math>CuCNOC^-</math>: 60 %EM1, <math>CuC_2N_2^-</math>: 48 %EM1) with presence in EM 2</li> <li>Iron oxide/hydroxide (<math>FeO_3H_2^-</math>: 71 %EM1, <math>FeO_3^-</math>: 54 %EM1)</li> </ul>	<ul style="list-style-type: none"> <li>Salts generally containing chlorides and cyanides/cyanates, many existing mixed (sodium-magnesium, sodium-calcium). 50-95 %EM2: <ul style="list-style-type: none"> <li>Sodium chlorides, cyanides, cyanates and mixed chloride-sulfite, chloride-carbonate, chloride-hydroxide (<math>NaCl^-</math>, <math>NaCNCl^-</math>, <math>Na_3SO_4Cl_2^-</math>, <math>Na_2Cl_2OH^-</math>)</li> <li>Magnesium chlorides, cyanides, cyanates, hydroxides, chloride-sulfite, chloride-sulfate (<math>MgCl_3^-</math>, <math>MgSO_4Cl^-</math>, <math>MgCl_2OH^-</math>, <math>MgCl_2CN^-</math>)</li> <li>Potassium chloride (<math>KCl_2^-</math>)</li> <li>Calcium chlorides, cyanides, cyanates, chloride-sulfate, chloride-hydroxides (<math>CaCl_3^-</math>, <math>CaSO_4Cl^-</math>, <math>CaCl_2CNO^-</math>, <math>CaCl_2OH^-</math>)</li> <li>Iron chlorides, cyanides, cyanates (<math>FeCl_3^-</math>, <math>FeCNCl_2^-</math>)</li> <li>Copper chlorides, chloride-cyanides (<math>CuCNCl^-</math>, <math>CuCl_2^-</math>); <math>\leq 61</math> %EM2 split with EM 1</li> <li><math>C_{4,6-8}S^-</math> (40-66 %EM2 split with EM 3, <math>C_4SH^-</math> (48 %EM2), <math>C_{3,5}SN^-</math> (56-59 %EM2),</li> </ul> </li> </ul>	<ul style="list-style-type: none"> <li>Salts generally containing sulfur (sulfate, sulfite, thiosulfate), many exist mixed (sodium-magnesium, sodium-calcium). 50-95 %EM3: <ul style="list-style-type: none"> <li>Sodium sulfates, sulfites, carbonate, sulfate-cyanides, thiosulfate-hydroxide, sulfate-cyanate/cyanide-chloride (<math>Na_3S_2O_8^-</math>, <math>Na_3S_2O_7^-</math>, <math>Na_3SO_4CNOCl^-</math>, <math>NaCO_3SO_4^-</math>). ~40-60 %EM3 with presence in EMs 1 and 2.</li> <li>Mixed sodium-magnesium and sodium-calcium sulfates, sulfites (<math>NaMgS_2O_8^-</math>, <math>NaCaS_2O_7^-</math>) also mixed with hydroxides, cyanates (<math>NaMgSO_4OHCNO^-</math>, <math>NaCaSO_4OHCNO^-</math>). 48-80 %EM2 with presence in EMs 1 and 2.</li> <li>Magnesium sulfates, cyanide, cyanate, mixed sulfate-cyanide, sulfate-hydroxide, hydroxide-cyanide/cyanate (<math>MgSO_5H^-</math>, <math>MgSO_4CNO^-</math>, <math>Mg_2SO_4(OH)_2CNO^-</math>). 37-76 %EM3 with presence in EMs 1 and 2.</li> </ul> </li> </ul>	<ul style="list-style-type: none"> <li>Carbonaceous: <ul style="list-style-type: none"> <li><math>C_{7-23}^-</math>, 63-100 %EM4;</li> </ul> </li> <li><math>C_xH^-</math> (<math>x = 7-9, 11, 13, 15</math> are highly distributed across EMs 1-4; <math>x = 10</math> has 55 %EM4; <math>x = 12, 14, 16, 18, 20</math> have 69-90 %EM4)</li> </ul>	<ul style="list-style-type: none"> <li>Many small hydrocarbons (e.g. <math>C_{13}H_3^-</math>: 29 %EM1, 31 %EM2, 28 %EM3, 12 %EM4)</li> <li><math>C_{7-11}N^-</math> (e.g. <math>C_{11}N^-</math>: 26 %EM1, 25 %EM2, 25 %EM3, 24 %EM4)</li> <li>Salts of Ca and Mg, many with mixed cations, distributed EMs 1-3 (e.g. <math>CaMgS_2O_9H^-</math>: 31 %EM1, 22 %EM2, 36 %EM3; <math>CaO_3H_3^-</math>: 41 %EM1, 19 %EM2, 25 %EM3)</li> </ul>

			C <sub>6,8</sub> OH <sup>+</sup> (38 %EM2 split with EM 1 and 3)			
	<b>Positive Polarity</b>	<ul style="list-style-type: none"> <li>Organics <math>\leq 250</math> <i>m/z</i> (46-84 %EM1): <ul style="list-style-type: none"> <li>Nitrogenous (C<sub>x</sub>H<sub>y</sub>N<sub>1-4</sub><sup>+</sup> including PAHs e.g. C<sub>15</sub>H<sub>10</sub>N<sup>+</sup>) <math>&lt; 215</math> <i>m/z</i></li> <li>Oxygenate (C<sub>x</sub>H<sub>y</sub>O<sup>+</sup>) <math>&lt; 170</math> <i>m/z</i></li> <li>NO-containing (C<sub>x</sub>H<sub>y</sub>N<sub>1-4</sub>O<sub>1-3</sub><sup>+</sup>),</li> <li>Hydrocarbon <math>\leq 250</math> <i>m/z</i> (PAHs to C<sub>20</sub>H<sub>10</sub><sup>+</sup>)</li> <li>Sodium-carboxylate: C<sub>3</sub>H<sub>3</sub>O<sub>2</sub>Na<sub>2</sub><sup>+</sup> (49 %EM1), succinate in EMs 1-3 (C<sub>4</sub>H<sub>4</sub>O<sub>4</sub>Na<sub>3</sub><sup>+</sup>: 34 %EM1, 35 %EM2, 32 %EM3)</li> </ul> </li> <li>Presence of sodium, potassium and calcium inorganic salts with greater prevalence elsewhere (<math>&lt; 49</math> %EM1): <ul style="list-style-type: none"> <li>Sodium (and mixed sodium-potassium) sulfate, with <math>&lt; 43</math> %EM1 (K<sub>2</sub>NaSO<sub>4</sub><sup>+</sup>, Na<sub>7</sub>S<sub>3</sub>O<sub>12</sub><sup>+</sup>)</li> <li>Calcium salts <math>\leq 30</math> %EM1 (Ca<sub>2</sub>O<sub>4</sub>H<sub>5</sub><sup>+</sup>).</li> </ul> </li> </ul>	<ul style="list-style-type: none"> <li>Salts generally of chlorides, cyanides, cyanates, many existing mixed (35-90 %EM2) <ul style="list-style-type: none"> <li>Sodium chlorides, cyanates, chloride-hydroxide, oxide, carbide (Na<sub>2</sub>Cl<sup>+</sup>, Na<sub>2</sub>CNO<sup>+</sup>, Na<sub>3</sub>O<sub>2</sub><sup>+</sup>, Na<sub>2</sub>C<sub>3,5,7</sub><sup>+</sup>) (35-86 %EM2)</li> <li>Sodium-potassium chloride, cyanide, cyanate, hydroxide, sulfide (KNaCl<sup>+</sup>, KNaCN<sup>+</sup>, KNaOH<sup>+</sup>, KNaS<sup>+</sup>): 49-90 %EM2</li> <li>Calcium and sodium-calcium hydroxide (Ca<sub>2</sub>O<sub>3</sub>H<sub>3</sub><sup>+</sup>, NaCaO<sub>2</sub>H<sub>2</sub><sup>+</sup>; 47-81 %EM2%), sodium-calcium chloride (Na<sub>4</sub>CaCl<sub>5</sub><sup>+</sup>; 61-81 %EM2) and sulfate-hydroxide (Na<sub>2</sub>CaSO<sub>4</sub>OH<sup>+</sup>; 56 %EM2)</li> <li>Potassium (K<sub>2</sub>Cl<sup>+</sup>, K<sub>2</sub>CN<sup>+</sup>, K<sub>2</sub>CNO<sup>+</sup>), 70-90 %EM2</li> </ul> </li> <li>Magnesium-sodium salts: chloride and hydroxide (Na<sub>2</sub>MgClO<sub>2</sub>H<sub>2</sub><sup>+</sup>, 63 %EM2).</li> </ul>	<ul style="list-style-type: none"> <li>Salts generally containing sulfur, with additional presence in EMs 1-2. <ul style="list-style-type: none"> <li>Sodium sulfates and sulfites (Na<sub>3</sub>SO<sub>4</sub><sup>+</sup>, Na<sub>3</sub>SO<sub>3</sub><sup>+</sup>, 43-91 %EM3 with presence in EM 2), carbonate (Na<sub>3</sub>CO<sub>3</sub><sup>+</sup>, 67 %EM3), sulfide (Na<sub>3</sub>S<sup>+</sup>, 52 %EM3 split with EM 2), hydroxide (Na<sub>4</sub>O<sub>3</sub>H<sub>3</sub><sup>+</sup>, 46-72 %EM3), phosphate-hydroxide (Na<sub>4</sub>PO<sub>5</sub>H<sub>2</sub>, 48-55 %EM3 split with EM 2), sulfate-chloride (Na<sub>4</sub>SO<sub>4</sub>Cl<sup>+</sup>, 49 %EM3 split with EMs 1-2), thiosulfate-hydroxide (Na<sub>5</sub>S<sub>2</sub>O<sub>3</sub>(OH)<sub>2</sub><sup>+</sup>, 100 %EM3).</li> <li>Mixed sodium-potassium sulfates (KNa<sub>2</sub>SO<sub>4</sub><sup>+</sup>, 47-71 %EM3), carbonate (KNa<sub>2</sub>CO<sub>3</sub><sup>+</sup>, 82 %EM3); sodium-magnesium hydroxide (Na<sub>3</sub>MgO<sub>4</sub>H<sub>4</sub><sup>+</sup>, 60-85 %EM3), sulfate-hydroxide (Na<sub>4</sub>MgSO<sub>7</sub>H<sub>3</sub><sup>+</sup>, 100 %EM3); sodium-calcium hydroxide (Na<sub>2</sub>CaO<sub>3</sub>H<sub>3</sub><sup>+</sup>, 58-59 %EM3), sulfate-hydroxide (Na<sub>3</sub>CaSO<sub>6</sub>H<sub>2</sub><sup>+</sup>, 56-99 %EM3).</li> <li>Calcium hydroxide (Ca<sub>4</sub>O<sub>8</sub>H<sub>9</sub><sup>+</sup>, 46 %EM3 with presence in EMs 1-2).</li> </ul> </li> </ul>	<ul style="list-style-type: none"> <li>Carbonaceous (C<sub>10-23</sub><sup>+</sup>, 90-100 %EM4)</li> <li>C<sub>8</sub>H<sub>2</sub><sup>+</sup> prevalent (30 %EM4 with <math>&gt; 30</math> %EM1 and %EM2) – ion relates to lower carbonaceous layer and upper deposit material</li> </ul>	<ul style="list-style-type: none"> <li>Fe, Mo, V-oxides and hydroxides (e.g. Fe<sub>2</sub>O<sub>4</sub>H<sub>5</sub><sup>+</sup>, MoO<sub>2</sub><sup>+</sup>, VO<sub>2</sub><sup>+</sup>) and mixed Cr-Fe (e.g. CrFe<sub>2</sub>O<sub>8</sub>H<sub>6</sub><sup>+</sup>), 65-100 %EM4</li> <li>M (substrate) Ca hydroxides/oxides (CaFe<sub>1-3</sub>O<sub>x</sub>H<sub>y</sub><sup>+</sup>, 30-49 %EM4; CaCrO<sub>x</sub>H<sub>y</sub><sup>+</sup> where <math>b \geq 0</math>, 60-68 %EM4; CaAlO<sub>6</sub>H<sub>8</sub><sup>+</sup>, 38 %EM4)</li> </ul>
	<b>Time /s</b>	0-60s*	640 + 860s	1130-1480s	4530-5700s	

<b>XPS relative at.% (left) and relative ratio to carbon (right)</b>	<b>C</b>	68.4	1.000	52.8	1.000	53.5	1.000	80.2	1.000	
	<b>O</b>	16.0	0.097	16.1	0.306	16.5	0.308	6.4	0.080	
	<b>N</b>	6.6	0.234	8.0	0.152	7.6	0.142	3.4	0.042	
	<b>Na</b>	6.1	0.089	16.0	0.308	15.3	0.286	6.8	0.085	
	<b>Ca</b>	0.3	0.034	0.1	0.002	0.2	0.004	0.2	0.002	
	<b>Cl</b>	2.3	0.005	6.6	0.125	6.1	0.114	2.7	0.034	
	<b>S</b>	0.4	0.001	0.5	0.011	0.8	0.015	0.2	0.002	
	<b>Si</b>	0.1	0.004	0	0	0	0.000	0	0	

\* = averaged rather than summed within CasaXPS (spectra too dissimilar to successfully sum)

### 2.8.2. Overview of Needle 8 OrbiSIMS NMF using the Comparative Method

Needle 8's depth profiles appear to show less distinct layering than Needle 6's, with more subtle layering effects and depth trends. NMF results are presented here using the same comparative method to find meaningful data and again construct a model of four pseudo-layers.

#### 2.8.2.1. Negative polarity OrbiSIMS NMF results overview

In the highest loading ions of Needle 8's negative polarity OrbiSIMS depth profile NMF, (Figure A16c, Table A24), it can be seen in the upper deposit material (EMs 1-2) that there is an organic surface pseudo-layer (EM 1) over a second carbonaceous pseudo-layer (EM 2). Among the organics are ABS ions ( $\text{C}_8\text{H}_7\text{SO}_3^-$ : 67 %EM1;  $\text{C}_{18}\text{H}_{29}\text{SO}_3^-$ : 98 %EM1) and related ions ( $\text{SO}_3^-$ : 31 %EM1 and  $\text{C}_8\text{H}_7\text{O}^-$ : 58 %EM1). This layer also has a silicon ion,  $\text{Si}_2\text{O}_6\text{H}_3^-$  (69 %EM1). EM 2, dominated by carbonaceous ions, also has some heteroatom content ( $\text{C}_7\text{N}^-$ : 44 %EM2;  $\text{C}_6\text{S}^-$ : 36 %EM2;  $\text{C}_5\text{P}^-$ : 25 %EM2). However, S- and P-containing carbonaceous ions are most characteristic of EM 3 ( $\text{C}_6\text{S}^-$ : 58 %EM3;  $\text{C}_5\text{P}^-$ : 75 %EM3), as well as some H-containing carbonaceous ions which are less characteristic of EM 3 ( $\text{C}_9\text{H}^-$ : 39 %EM3,  $\text{C}_9\text{H}_2^-$ : 39 %EM3). EM 3 also contains salt ions of calcium cyanide, cyanate-hydroxide and copper cyanide). Finally, EM 4 contains mostly oxides and hydroxides of needle substrate alloy metals with some calcium content. The phosphate anion is also largest in EM 4 ( $\text{PO}_3^-$ : 42 %EM4).

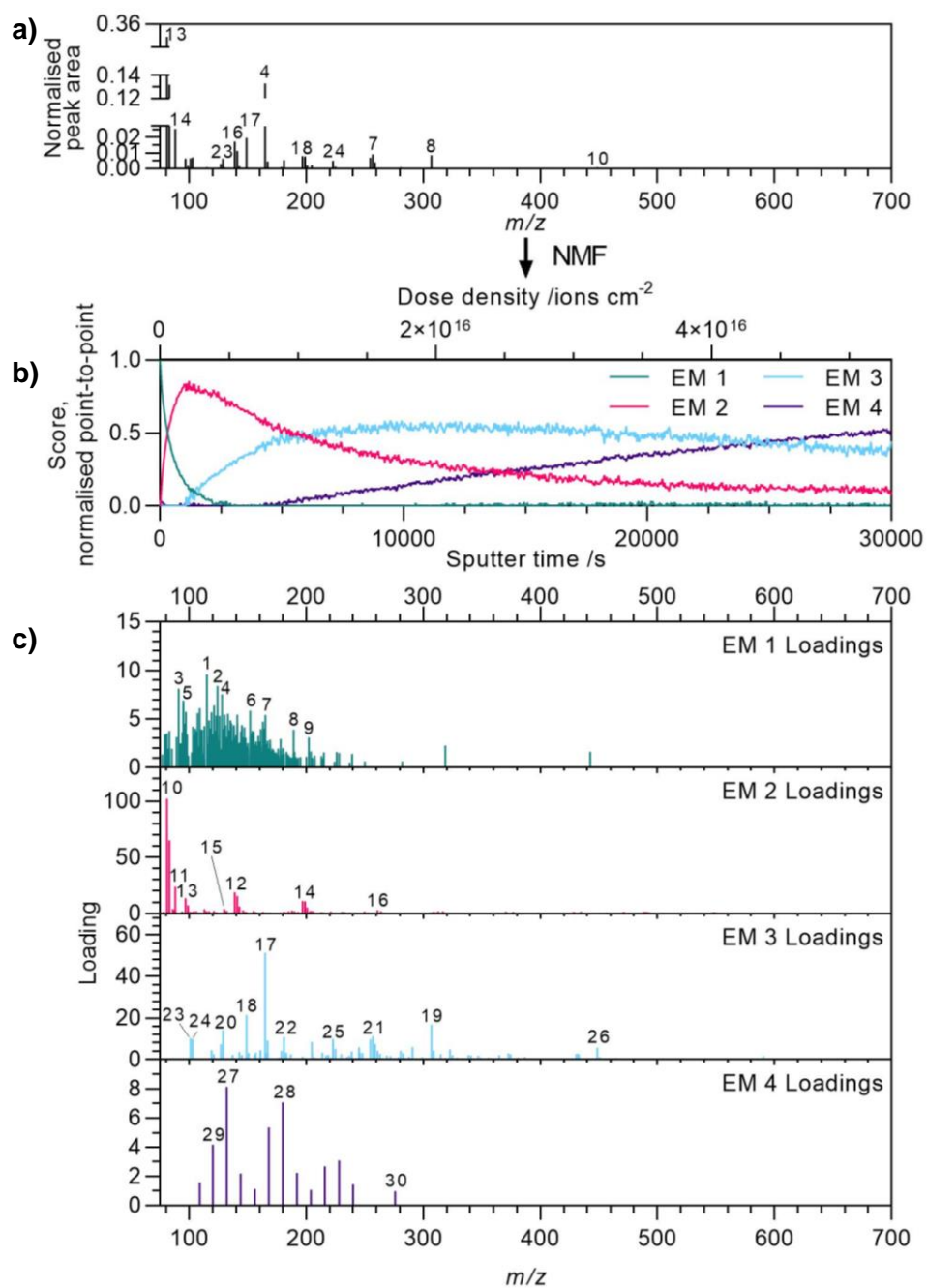


Figure A16: NMF results for Needle 8 negative polarity. a) OrbiSIMS spectrum over the full depth profile range. b) Endmember scores (normalised point-to-point). c) Loadings for all endmembers after filtering to remove ions that have a higher loading in another endmember.



Table A24: Needle 8 negative polarity NMF results for key ions with ions assigned numbers from Figure A16, loadings and relative loadings, separated by which endmember their loading is highest for. Additional ions shown at the bottom which are highly distributed across multiple endmembers. Heat map applied to each column: green = maximum value and red = minimum, for normalised loadings green = 1.00 and red = 0.

Ion	m/z	ID	Peak area (norm)	Original loading				Relative loading (%EM)			
				1	2	3	4	1	2	3	4
1	183.0121	C <sub>8</sub> H <sub>7</sub> SO <sub>3</sub> <sup>-</sup>	1.8E-03	16.9	8.5	0.0	0.0	66.5	33.5	0.0	0.0
2	79.957	SO <sub>3</sub> <sup>-</sup>	6.2E-03	14.2	13.2	8.2	10.7	30.6	28.5	17.8	23.1
3	119.0502	C <sub>8</sub> H <sub>7</sub> O <sup>-</sup>	1.4E-03	13.6	9.8	0.0	0.0	58.2	41.8	0.0	0.0
4	197.0278	C <sub>9</sub> H <sub>9</sub> SO <sub>3</sub> <sup>-</sup>	1.9E-04	6.5	0.8	0.0	0.0	88.6	11.4	0.0	0.0
5	154.9473	Si <sub>2</sub> O <sub>6</sub> H <sub>3</sub> <sup>-</sup>	2.2E-04	5.9	2.7	0.0	0.0	68.9	31.1	0.0	0.0
6	311.1687	C <sub>17</sub> H <sub>27</sub> SO <sub>3</sub> <sup>-</sup>	1.5E-04	5.9	0.0	0.1	0.0	97.8	0.0	2.2	0.0
7	325.1842	C <sub>18</sub> H <sub>29</sub> SO <sub>3</sub> <sup>-</sup>	1.1E-04	5.2	0.0	0.1	0.0	97.6	0.0	2.4	0.0
8	96.96	SO <sub>4</sub> H <sup>-</sup>	1.7E-04	5.0	2.1	0.0	0.9	62.4	26.4	0.0	11.1
9	96.0004	C <sub>8</sub> <sup>-</sup>	8.1E-02	1.0	59.4	52.5	27.4	0.7	42.3	37.4	19.5
10	97.0082	C <sub>8</sub> H <sup>-</sup>	2.5E-02	2.6	31.1	28.2	15.4	3.3	40.2	36.5	19.9
11	144.0004	C <sub>12</sub> <sup>-</sup>	1.9E-02	0.5	30.7	23.2	12.5	0.8	45.9	34.7	18.7
12	98.0035	C <sub>7</sub> N <sup>-</sup>	4.1E-03	0.8	13.9	11.7	5.0	2.6	44.4	37.2	15.9
13	204.0005	C <sub>17</sub> <sup>-</sup>	8.7E-04	0.2	9.5	4.1	1.6	1.3	61.8	26.5	10.5
14	252.0006	C <sub>21</sub> <sup>-</sup>	9.4E-05	0.0	4.3	0.0	0.8	0.0	84.8	0.0	15.2
15	276.0005	C <sub>23</sub> <sup>-</sup>	1.5E-05	0.1	1.3	0.0	0.2	5.7	82.6	0.0	11.6
16	109.0083	C <sub>9</sub> H <sup>-</sup>	2.8E-03	1.2	10.0	10.3	4.6	4.5	38.4	39.4	17.7
17	99.9716	CaCNO <sub>2</sub> H <sub>2</sub> <sup>-</sup>	6.0E-04	0.6	2.8	6.1	2.0	5.3	24.3	52.9	17.5
18	114.9362	CuC <sub>2</sub> N <sub>2</sub> <sup>-</sup>	3.0E-04	0.0	0.6	3.4	3.1	0.0	7.9	47.9	44.2
19	173.9397	Ca <sub>2</sub> CNO <sub>4</sub> H <sub>4</sub> <sup>-</sup>	1.5E-04	0.1	1.1	3.3	0.9	1.1	21.3	60.7	16.8
20	117.9723	CaC <sub>3</sub> N <sub>3</sub> <sup>-</sup>	8.8E-05	0.0	0.3	3.0	0.5	0.0	7.0	80.9	12.1
21	103.9726	C <sub>6</sub> S <sup>-</sup>	8.3E-05	0.0	1.5	2.4	0.3	0.0	35.8	57.8	6.5
22	110.0162	C <sub>9</sub> H <sub>2</sub> <sup>-</sup>	1.1E-04	0.6	1.9	2.2	0.9	10.9	34.2	39.1	15.7
23	90.9741	C <sub>5</sub> P <sup>-</sup>	2.9E-05	0.0	0.5	1.6	0.0	0.0	25.2	74.8	0.0
24	78.9587	PO <sub>3</sub> <sup>-</sup>	1.1E-01	5.4	30.8	49.1	62.5	3.7	20.9	33.2	42.3
25	103.9202	FeO <sub>3</sub> <sup>-</sup>	2.4E-02	0.5	12.2	21.4	30.5	0.8	18.8	33.2	47.2
26	145.8906	MoO <sub>3</sub> <sup>-</sup>	1.3E-02	1.3	7.2	12.5	25.7	2.9	15.4	26.7	55.0
27	231.9362	WO <sub>3</sub> <sup>-</sup>	1.4E-02	1.6	7.9	14.5	25.0	3.3	16.0	29.6	51.0
28	152.9175	CaSO <sub>3</sub> H <sup>-</sup>	2.0E-02	5.1	16.9	20.9	23.1	7.8	25.6	31.7	35.0
29	116.9398	VO <sub>4</sub> H <sub>2</sub> <sup>-</sup>	1.1E-02	0.0	5.6	13.9	22.2	0.0	13.4	33.4	53.2
30	99.9257	CrO <sub>3</sub> <sup>-</sup>	9.9E-03	0.0	5.5	13.1	20.8	0.0	14.0	33.3	52.7
31	304.8965	CaWO <sub>5</sub> H <sup>-</sup>	3.0E-03	0.5	0.6	4.6	14.4	2.6	3.1	23.0	71.3

### 2.8.2.2. Positive polarity OrbiSIMS NMF results overview

The overview of filtered loadings for NMF of Needle 8's positive polarity OrbiSIMS depth profile (Figure A17c, Table A25) shows some agreement with the negative EM data though some (particularly EM 2 and 3) show differences or additional information. The surface is again largely organic, with PAHs (to C<sub>27</sub>H<sub>13</sub><sup>+</sup>: 100 %EM1) and another silicon-containing ion (Si<sub>2</sub>C<sub>3</sub>H<sub>13</sub>O<sub>4</sub><sup>+</sup>: 100 %EM1) likely representing PDMS. While carbonaceous ions were characteristic of EM 2 in negative, here EM 2 is dominated by calcium hydroxide salt ions to large masses (Ca<sub>9</sub>O<sub>17</sub>H<sub>17</sub><sup>+</sup>: 54 %EM2), indicating upper deposit sub-surface salt content. Some of these ions include phosphate

( $\text{Ca}_2\text{PO}_8\text{H}_8^+$ : 50 %EM2) and iron, notably with a large Ca:Fe ratio (5:1) and larger EM% values for EMs 3-4 than salts of solely calcium ( $\text{Ca}_5\text{FeO}_{12}\text{H}_{12}^+$ : 39 %EM2, 34 %EM3 and 26 %EM4). EM 3 contains calcium-iron hydroxides (e.g.  $\text{Ca}_3\text{FeO}_8\text{H}_8^+$ : 36 %EM2, 37 %EM3, 25 %EM4), with lower Ca:Fe ratios (2-3:1) which are significantly distributed across EMs 2-4. Finally, at the lowest pseudo-layer the needle substrate is confidently reached as substrate metal hydroxides appear and dominate (e.g.  $\text{Fe}_2\text{O}_6\text{H}_6^+$ : 74 %EM4;  $\text{CrFeO}_7\text{H}_4^+$ : 94 %EM4), with some Ca-Fe hydroxide also present with Ca:Fe ratios of 1:1 and lower EM%4 values ( $\text{CaFeO}_6\text{H}_8^+$ : 38 %EM4).

### 2.8.2.3. Comparison to atomic concentration depth profile from XPS

An XPS depth profile for Needle 8 was seen in the manual analysis (Figure 4.5) which had substrate chemistry removed. In this NMF, the substrate has been identified as part of the trends in calcium and substrate metal content. The XPS depth profile including substrate can be found in Figure 4.10f. There are twelve elements, considerably more than the eight in Needle 6 due to the steel elements (Fe, Mo and W) as well as zinc and phosphorus presence. The depth profile shows a rise in iron throughout, preceded by a rise in calcium which plateaus at around 500s; this agrees particularly with the salt content of EMs 2-4 in the positive polarity OrbiSIMS profile, which showed a sub-surface EM 2 presence of calcium salts (mainly with hydroxide), transitioning through Ca-Fe hydroxides of decreasing Ca:Fe ratios and finally reaching mainly substrate metal hydroxides in EM 4. Carbon content is highest at the surface, aligning with the organic EM 1 in both polarities. While carbon decreases sub-surface, as noted in Section 4.2.2.3, the rise of calcium which is associated with mainly oxygen-containing anions in OrbiSIMS suggests less oxygen is part of functional groups in this region, which could explain the carbonaceous character of EM 2 in negative polarity.

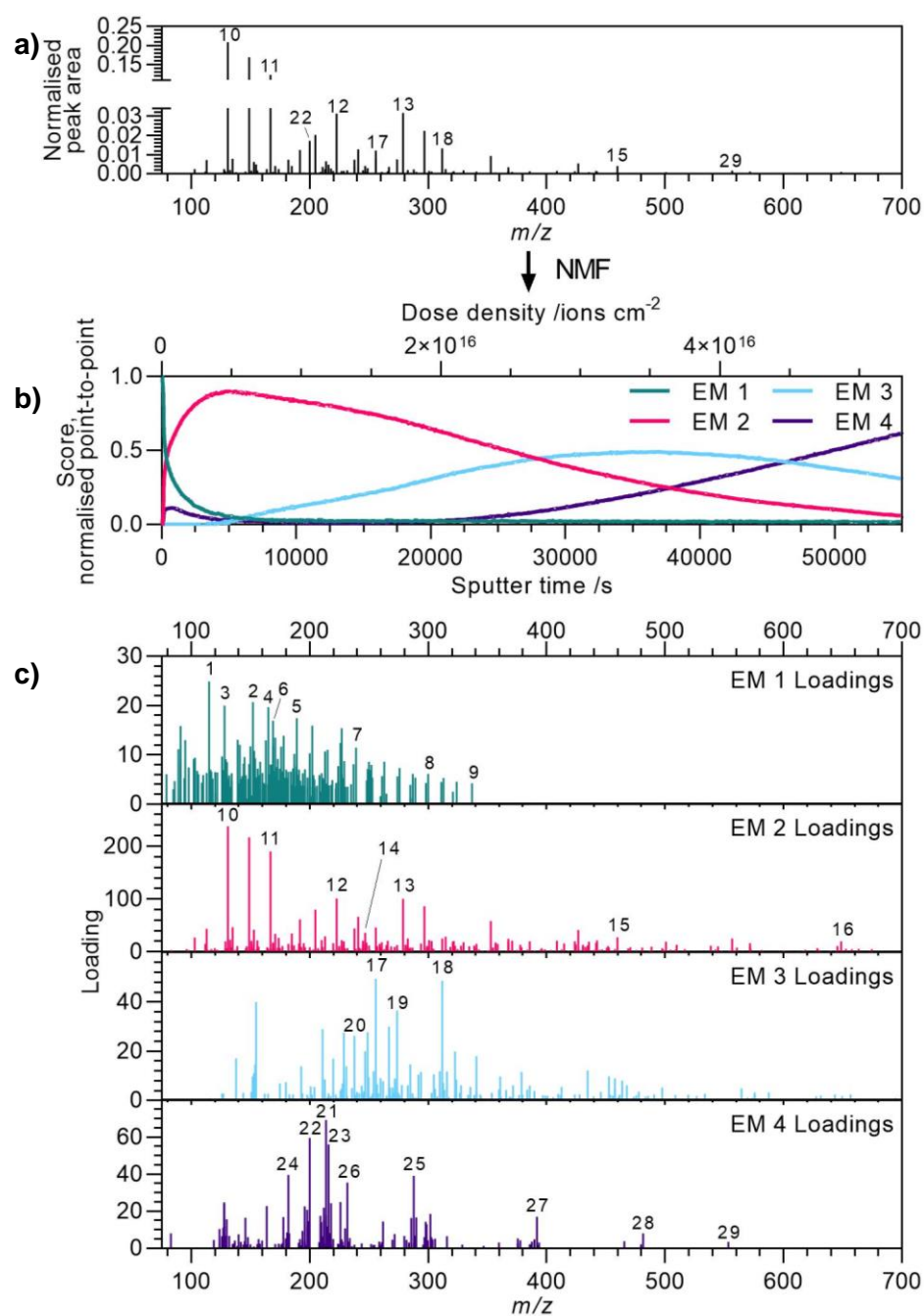


Figure A17: NMF of Needle 8 (positive polarity) a) spectrum, b) scores and c) loadings for all endmembers after filtering to remove ions that have a higher loading in another endmember.

Table A25: Needle 8 positive polarity NMF examples: measured  $m/z$ , assignment, peak area (normalised to total) original endmember loadings (EM X), relative loadings (%EM X) for ions from Figure A17. Heat map applied to each column: green = maximum value and red = minimum, for normalised loadings green = 1.00 and red = 0.

Ion	$m/z$	ID	Peak area (norm)	Original loading				Relative loading (%EM)			
				1	2	3	4	1	2	3	4
1	115.0542	C <sub>9</sub> H <sub>7</sub> <sup>+</sup>	1.1E-04	24.9	0.0	0.0	0.0	100	0.0	0.0	0.0
2	152.0619	C <sub>12</sub> H <sub>8</sub> <sup>+</sup>	8.2E-05	20.7	0.0	0.0	0.0	100	0.0	0.0	0.0
3	128.0620	C <sub>10</sub> H <sub>8</sub> <sup>+</sup>	7.0E-05	20.0	0.0	0.0	0.0	100	0.0	0.0	0.0
4	165.0697	C <sub>13</sub> H <sub>9</sub> <sup>+</sup>	6.6E-05	19.6	0.0	0.0	0.0	100	0.0	0.0	0.0
5	189.0697	C <sub>15</sub> H <sub>9</sub> <sup>+</sup>	5.4E-05	17.4	0.0	0.0	0.0	100	0.0	0.0	0.0
6	169.0345	Si <sub>2</sub> C <sub>3</sub> H <sub>13</sub> O <sub>4</sub> <sup>+</sup>	2.0E-05	16.9	0.0	0.0	0.0	100	0.0	0.0	0.0
7	239.0855	C <sub>19</sub> H <sub>11</sub> <sup>+</sup>	2.1E-05	11.5	0.0	0.0	0.0	100	0.0	0.0	0.0
8	300.0933	C <sub>24</sub> H <sub>12</sub> <sup>+</sup>	7.3E-06	6.1	0.0	0.0	0.0	100	0.0	0.0	0.0
9	337.1011	C <sub>27</sub> H <sub>13</sub> <sup>+</sup>	4.2E-06	4.3	0.0	0.0	0.0	100	0.0	0.0	0.0
10	130.9327	Ca <sub>2</sub> O <sub>3</sub> H <sub>3</sub> <sup>+</sup>	2.1E-01	33.7	237.4	131.5	127.2	6.4	44.8	24.8	24.0
11	166.9537	Ca <sub>2</sub> O <sub>3</sub> H <sub>7</sub> <sup>+</sup>	1.2E-01	24.5	190.0	93.3	96.0	6.1	47.1	23.1	23.8
12	222.9114	Ca <sub>3</sub> O <sub>6</sub> H <sub>7</sub> <sup>+</sup>	3.1E-02	14.2	101.0	44.5	40.5	7.1	50.5	22.2	20.2
13	278.8689	Ca <sub>4</sub> O <sub>7</sub> H <sub>7</sub> <sup>+</sup>	3.2E-02	10.9	100.5	47.5	39.0	5.5	50.8	24.0	19.7
14	246.9201	Ca <sub>2</sub> PO <sub>8</sub> H <sub>8</sub> <sup>+</sup>	4.1E-03	6.0	35.7	16.0	14.3	8.3	49.6	22.2	19.9
15	459.7799	Ca <sub>5</sub> FeO <sub>12</sub> H <sub>12</sub> <sup>+</sup>	4.1E-03	1.2	27.8	24.2	18.2	1.7	38.9	33.9	25.5
16	648.7088	Ca <sub>9</sub> O <sub>17</sub> H <sub>17</sub> <sup>+</sup>	1.1E-03	1.9	19.7	7.9	6.8	5.2	54.2	21.9	18.7
17	255.8864	Ca <sub>2</sub> FeO <sub>7</sub> H <sub>8</sub> <sup>+</sup>	1.2E-02	2.6	39.5	49.4	34.8	2.0	31.3	39.1	27.6
18	311.8438	Ca <sub>3</sub> FeO <sub>8</sub> H <sub>8</sub> <sup>+</sup>	1.3E-02	2.5	46.4	48.6	33.0	1.9	35.6	37.2	25.3
19	273.8969	Ca <sub>2</sub> FeO <sub>8</sub> H <sub>10</sub> <sup>+</sup>	7.6E-03	2.0	32.5	36.6	28.6	2.0	32.6	36.7	28.7
20	237.8758	Ca <sub>2</sub> FeO <sub>6</sub> H <sub>6</sub> <sup>+</sup>	3.7E-03	1.5	21.5	26.2	19.8	2.2	31.1	38.0	28.7
21	213.8856	Fe <sub>2</sub> O <sub>6</sub> H <sub>6</sub> <sup>+</sup>	6.7E-03	4.6	9.0	11.0	69.4	4.9	9.6	11.7	73.9
22	199.9288	CaFeO <sub>6</sub> H <sub>8</sub> <sup>+</sup>	1.7E-02	6.3	37.4	53.8	59.8	4.0	23.8	34.2	38.0
23	215.9013	Fe <sub>2</sub> O <sub>6</sub> H <sub>8</sub> <sup>+</sup>	4.7E-03	4.4	13.9	6.9	56.2	5.4	17.1	8.4	69.1
24	181.9182	CaFeO <sub>5</sub> H <sub>6</sub> <sup>+</sup>	7.5E-03	4.2	23.6	35.5	39.7	4.1	22.9	34.5	38.5
25	287.8310	Fe <sub>3</sub> O <sub>7</sub> H <sub>8</sub> <sup>+</sup>	2.4E-03	4.3	9.8	5.3	39.2	7.3	16.7	9.1	66.9
26	225.8861	CrFeO <sub>7</sub> H <sub>6</sub> <sup>+</sup>	6.9E-04	0.0	0.0	1.5	24.9	0.0	0.0	5.8	94.2
27	391.7506	Fe <sub>4</sub> O <sub>10</sub> H <sub>8</sub> <sup>+</sup>	3.4E-04	2.3	3.0	0.0	17.0	10.5	13.3	0.0	76.2
28	481.6909	Fe <sub>5</sub> O <sub>12</sub> H <sub>10</sub> <sup>+</sup>	6.7E-05	1.1	0.5	0.0	8.0	11.7	5.2	0.0	83.0
29	553.6207	Fe <sub>6</sub> O <sub>13</sub> H <sub>10</sub> <sup>+</sup>	1.2E-05	0.4	0.3	0.0	3.4	9.9	7.4	0.0	82.7

#### 2.8.2.4. Summary of Deposit Characterisation by OrbiSIMS and XPS

Table A26 presents a summary of the findings from the above NMF analysis of Needle 8's negative and positive polarity depth profiles using the comparative method, alongside the XPS depth profile data for regions that appear to represent each EM.

Table A26: Needle 8 summary of OrbiSIMS and XPS data for pseudo-layers identified by NMF endmembers with example ions and relative loadings.

EM/pseudo-layer		1	2	3	4	Split
Technique						
OrbiSIMS	Negative Polarity	<ul style="list-style-type: none"> <li>Organics &lt; 480 <i>m/z</i>: <ul style="list-style-type: none"> <li>ABS: C<sub>6</sub>H<sub>5</sub>SO<sub>3</sub><sup>-</sup> to C<sub>29</sub>H<sub>51</sub>SO<sub>3</sub><sup>-</sup> (67-98 %EM1) and SO<sub>3</sub>H<sup>-</sup> (92 %EM1)</li> <li>Nitrogenous (C<sub>6</sub>H<sub>4</sub>N<sup>-</sup> to C<sub>14</sub>H<sub>4</sub>N<sup>-</sup>), 32-51 %EM1</li> <li>Oxygenates: O-PAC type (C<sub>6</sub>H<sub>3</sub>O<sup>-</sup> to C<sub>16</sub>H<sub>9</sub>O<sup>-</sup>, 58-95 %EM1; C<sub>5</sub>H<sub>3</sub>O<sub>2</sub><sup>-</sup> to C<sub>15</sub>H<sub>7</sub>O<sub>2</sub><sup>-</sup>, 79-96 %EM1), carboxylates (C<sub>16</sub>H<sub>31</sub>O<sub>2</sub><sup>-</sup>, C<sub>18</sub>H<sub>35</sub>O<sub>2</sub><sup>-</sup>, 81-86 %EM1)</li> <li>NO-containing (C<sub>7</sub>H<sub>4</sub>NO<sup>-</sup> to C<sub>13</sub>H<sub>6</sub>NO<sup>-</sup>, C<sub>10</sub>H<sub>4</sub>NO<sub>2</sub><sup>-</sup>)</li> <li>Hydrocarbon: C<sub>7</sub>H<sub>5</sub><sup>-</sup> to C<sub>17</sub>H<sub>5</sub><sup>-</sup>, 34-78 %EM1</li> </ul> </li> <li>Carbonaceous-hydroxide (C<sub>8</sub>OH<sup>-</sup>, 37 %EM1)</li> <li>Silicon-containing (Si<sub>2</sub>O<sub>6</sub>H<sub>3</sub><sup>-</sup>, Si<sub>2</sub>CH<sub>5</sub>O<sub>5</sub><sup>-</sup>) 47-98 %EM1</li> <li>Sulfates (SO<sub>3</sub><sup>-</sup>, 31 %EM1; SO<sub>4</sub>H<sup>-</sup>, 62 %EM1; SO<sub>3</sub>H<sup>-</sup>, 92 %EM1)</li> <li>Ca, Mg, Na and Zn sulfates (CaSO<sub>4</sub>CN<sup>-</sup>, CaSO<sub>4</sub>CNO<sup>-</sup>, Ca<sub>2</sub>SO<sub>6</sub>H<sub>3</sub><sup>-</sup>, MgSO<sub>5</sub>H<sup>-</sup>, NaMgS<sub>3</sub>O<sub>12</sub><sup>-</sup>, ZnSO<sub>5</sub>H<sup>-</sup>) where Ca has mixed anions with cyanide, cyanate and hydroxide 45-78 %EM1</li> </ul>	<ul style="list-style-type: none"> <li>Carbonaceous ions, generally split with EM 3 with some having a presence in EM 1 <ul style="list-style-type: none"> <li>C<sub>x</sub><sup>-</sup> x = 7-27, 42-88 %EM2 with significant EM 3 (&lt;37%), generally higher %EM2 for higher C number</li> <li>C<sub>x</sub>H<sup>-</sup> x = 7-20 38-78 EM2% with significant EM 3, generally higher %EM2 for higher C number</li> <li>C<sub>11-21</sub>H<sub>2</sub><sup>-</sup>, 41-66 %EM2</li> <li>N-carbonaceous: C<sub>6-14</sub>N<sup>-</sup>, C<sub>8-12</sub>NH<sup>-</sup>, C<sub>5-7</sub>N<sub>2</sub><sup>-</sup>, 43-68 %EM2 with significant EM 3</li> <li>Other carbonaceous types: C<sub>5</sub>SN<sup>-</sup>, C<sub>5</sub>NO<sup>-</sup>, both widely distributed (43-45 %EM2 with strong EM 1 and 3 respectively)</li> </ul> </li> <li>Salts <ul style="list-style-type: none"> <li>Copper cyanide-cyanate, CuC<sub>2</sub>N<sub>2</sub>O<sup>-</sup> (38 %EM2 split with EM 3)</li> <li>Calcium cyanate with hydroxide (CaC<sub>2</sub>N<sub>2</sub>O<sub>3</sub>H<sup>-</sup>, CaC<sub>3</sub>N<sub>3</sub>O<sub>2</sub><sup>-</sup>, CaCNO<sub>3</sub>H<sub>2</sub><sup>-</sup>; 36-49 %EM2)</li> </ul> </li> </ul>	<ul style="list-style-type: none"> <li>Salts <ul style="list-style-type: none"> <li>Calcium cyanide, cyanate, cyanide-hydroxide (CaC<sub>3</sub>N<sub>3</sub><sup>-</sup>, 81 %EM3; CaC<sub>3</sub>N<sub>3</sub>O<sup>-</sup>, 72 %EM3; Ca<sub>2</sub>C<sub>2</sub>N<sub>2</sub>O<sub>3</sub>H<sub>3</sub><sup>-</sup>, 56 %EM3)</li> <li>Copper cyanide, sulfide-cyanide (CuC<sub>2</sub>N<sub>2</sub><sup>-</sup>, 48 %EM3; CuSCN<sup>-</sup>, 41 %EM3) split with EM 4</li> <li>Iron hydroxide-cyanide</li> <li>Zinc hydroxide and oxide (Zn<sup>66</sup>ZnO<sub>5</sub>H<sub>5</sub><sup>-</sup>, ZnO<sub>3</sub>H<sub>2</sub><sup>-</sup>, ZnO<sub>2</sub>H<sup>-</sup>, ZnO<sub>2</sub><sup>-</sup>; 34-47 %EM3), zinc sulfide-cyanide/cyanate/oxide (ZnSCN<sup>-</sup>, 43 %EM3; ZnSCNO<sup>-</sup>, 45 %EM3; ZnSO<sup>-</sup>, 49 %EM3) with presence in EM 4</li> <li>Bromide and iodide (Br<sup>-</sup>, 48 %EM3; I<sup>-</sup>, 51 %EM3)</li> </ul> </li> <li>S- and P-carbonaceous <ul style="list-style-type: none"> <li>C<sub>4-8</sub>S<sup>-</sup> and C<sub>4-8</sub>SH<sup>-</sup> with 49-64 %EM3, 44-47 %EM3 respectively, split with EM 2 (29-45 %EM2)</li> <li>C<sub>5-9</sub>P<sup>-</sup>, 64-87 %EM3 (13-36 %EM2)</li> </ul> </li> </ul>	<ul style="list-style-type: none"> <li>Zinc hydroxides (ZnO<sub>2</sub>H<sup>-</sup> to Zn<sub>2</sub>O<sub>5</sub>H<sub>5</sub><sup>-</sup>, 42-52 %EM4), oxide (ZnO<sub>2</sub><sup>-</sup>, 53 %EM4) and sulfide-hydroxide (ZnSOH<sup>-</sup>, 44 %EM3)</li> <li>Calcium sulfate (CaSO<sub>5</sub>H<sup>-</sup>, 35 %EM4; CaSO<sub>6</sub><sup>-</sup>, 33 %EM4; CaSO<sub>4</sub>H<sup>-</sup>, 37 %EM4; distributed EMs 2-4) and hydroxide (CaO<sub>3</sub>H<sub>3</sub><sup>-</sup> to Ca<sub>3</sub>O<sub>7</sub>H<sub>7</sub><sup>-</sup>, 52-68 %EM4). Ca sulfates have presence across all EMs</li> <li>M-Ca hydroxides CaWO<sub>5</sub>H<sup>-</sup> (71 %EM4), CaWO<sub>6</sub><sup>-</sup> (87 %EM4), CaFeO<sub>6</sub>H<sub>5</sub><sup>-</sup> (74 %EM4), CaMoO<sub>6</sub><sup>-</sup> (97 %EM4), CaCrO<sub>5</sub>H<sup>-</sup> (75 %EM4)</li> <li>Metal (iron, molybdenum, tungsten, vanadium, manganese, chromium) hydroxides, some mixed (e.g. FeMoO<sub>6</sub>H<sub>2</sub><sup>-</sup>, FeWO<sub>6</sub>H<sub>2</sub><sup>-</sup>, MoO<sub>4</sub><sup>-</sup>, MoO<sub>5</sub><sup>-</sup>VO<sub>3</sub><sup>-</sup>, Fe<sub>2</sub>O<sub>6</sub>H<sub>4</sub><sup>-</sup>, FeO<sub>3</sub>H<sub>3</sub><sup>-</sup>, MnO<sub>3</sub><sup>-</sup>, WO<sub>5</sub><sup>-</sup>, CrFeO<sub>7</sub>H<sub>7</sub><sup>-</sup>, FeO<sub>4</sub><sup>-</sup>, CrO<sub>4</sub>H<sup>-</sup> (53-100 %EM4)</li> <li>Small P anions: PO<sub>3</sub><sup>-</sup> (42 %EM4), PSO<sub>2</sub><sup>-</sup></li> </ul>	<ul style="list-style-type: none"> <li>C<sub>6</sub>OH<sup>-</sup>: 29 %EM1, 33 %EM2, 20 %EM3, 18 %EM4</li> <li>Many small hydrocarbons (e.g. C<sub>10</sub>H<sub>3</sub><sup>-</sup>: 24 %EM1, 27 %EM2, 22 %EM3, 26 %EM4)</li> <li>SiO<sub>3</sub><sup>-</sup> - mainly EMs 2-4: 14 %EM1, 30 %EM2, 29 %EM3, 28 %EM4</li> <li>Some calcium sulfate salts (e.g. CaSO<sub>5</sub><sup>-</sup>: 24 %EM1, 26 %EM2, 20 %EM3, 31 %EM4)</li> <li>Sulfite, SO<sub>3</sub><sup>-</sup>: 31 %EM1, 29 %EM2, 18 %EM3, 23 %EM4</li> </ul>

XPS relative atomic percentage (left) and								(45 %EM4) – both highly distributed.			
	Positive Polarity	<ul style="list-style-type: none"><li>Organic &lt; 340 <i>m/z</i>:<ul style="list-style-type: none"><li>PAH-type ions (up to C<sub>27</sub>H<sub>13</sub><sup>+</sup>, &gt;94 %EM1)</li><li>Nitrogenous: 1N, N-PAC type ions (to C<sub>17</sub>H<sub>14</sub>N<sup>+</sup>), 75-100 %EM1; 2N ion (C<sub>10</sub>H<sub>7</sub>N<sub>2</sub><sup>+</sup>, 100 %EM1)</li><li>Oxygenate (1O, O-PAC type ions, to C<sub>16</sub>H<sub>11</sub>O<sup>+</sup>)</li></ul></li><li>PDMS (Si<sub>2</sub>C<sub>3</sub>H<sub>13</sub>O<sub>4</sub><sup>+</sup>, 100 EM1%)</li><li>Carbonaceous (C<sub>x</sub><sup>+</sup> where x = 10-15, 52-61 %EM1; C<sub>x</sub>H<sup>+</sup> where x = 7, 9, 11, 13, 64-67 %EM1; C<sub>x</sub>H<sub>2</sub> where x = 7-14, 81-86 %EM1)</li><li>Presence of some iron hydroxide and iron-calcium hydroxide ions, ≤51 EM1% (FeO<sub>2</sub>H<sub>3</sub><sup>+</sup>, Fe<sub>4</sub>O<sub>10</sub>H<sub>9</sub><sup>+</sup>)</li><li>Sodium salts of sulfate, cyanide-sulfate (Na<sub>3</sub>SO<sub>4</sub><sup>+</sup>, Na<sub>4</sub>SO<sub>4</sub>CN<sup>+</sup>)</li><li>Calcium-magnesium hydroxide (CaMgO<sub>5</sub>H<sub>7</sub><sup>+</sup>)</li></ul>		<ul style="list-style-type: none"><li>Calcium hydroxide and hydroxide-mixed ions (to 700 <i>m/z</i>) including hydroxide-sulfate/sulfite/sulfide (Ca<sub>2</sub>SOH<sup>+</sup> to Ca<sub>10</sub>SO<sub>16</sub>H<sub>15</sub><sup>+</sup>, 64-94 %EM2), hydroxide-cyanide/cyanate (Ca<sub>2</sub>O<sub>2</sub>H<sub>2</sub>CNO<sup>+</sup> to Ca<sub>10</sub>O<sub>17</sub>H<sub>16</sub>CN<sup>+</sup>, 47-93 %EM2), hydroxide-PO<sub>2</sub><sup>-</sup> (CaPO<sub>2</sub><sup>+</sup> to Ca<sub>10</sub>PO<sub>19</sub>H<sub>14</sub><sup>+</sup>, 42-88 %EM2), hydroxide-chloride (Ca<sub>2</sub>ClO<sub>2</sub>H<sub>2</sub><sup>+</sup>, Ca<sub>3</sub>ClO<sub>6</sub>H<sub>8</sub><sup>+</sup>, 63-72%).</li><li>Some presence of calcium-substrate metal (M) hydroxides with nCa ≥ 2 and nFe/nCr = 1 with moderate and below (≤48) %EM2 generally split with EM 3 with presence in EM 4. E.g. Ca<sub>8</sub>FeO<sub>16</sub>H<sub>14</sub><sup>+</sup> (43%), Ca<sub>3</sub>FeO<sub>9</sub>H<sub>10</sub><sup>+</sup> (37%).</li><li>Some Na-Ca hydroxide (NaCa<sub>2</sub>O<sub>4</sub>H<sub>4</sub><sup>+</sup>, NaCa<sub>2</sub>O<sub>5</sub>H<sub>6</sub><sup>+</sup>, 51-56 %EM1)</li><li>Ca-Zn oxide (CaZnO<sup>+</sup>, 56 %EM2)</li></ul>		<ul style="list-style-type: none"><li>Ca-M ions (Ca<sub>x</sub>Fe<sub>y</sub>O<sub>a</sub>H<sub>b</sub><sup>+</sup> x = 2-5, y = 1-2; Ca<sub>x</sub>CrO<sub>a</sub>H<sub>b</sub><sup>+</sup> x = 2-5; CaMoO<sub>x</sub>H<sub>y</sub><sup>+</sup>, Ca<sub>2</sub>WO<sub>x</sub>H<sub>y</sub>) with ~30-70 %EM3. Higher Ca:M ratio ions generally have higher %EM3 (as well as higher %EM2), with lower ratios having higher %EM4. Some of these ions have significant (≤ 36) %EM1. E.g. Ca<sub>5</sub>FeO<sub>10</sub>H<sub>12</sub><sup>+</sup> (56%), Ca<sub>2</sub>FeO<sub>8</sub>H<sub>9</sub><sup>+</sup> (46 %EM3), CaFeO<sub>3</sub><sup>+</sup> (43%).</li><li>Ca-Zn hydroxide (CaZnO<sub>2</sub>H<sub>2</sub><sup>+</sup>, 52 %EM3 split with 48 %EM4)</li></ul>		<ul style="list-style-type: none"><li>Fe, Mo, V-oxides and hydroxides (e.g. Fe<sub>2</sub>O<sub>4</sub>H<sub>5</sub><sup>+</sup>, MoO<sub>2</sub><sup>+</sup>, VO<sub>2</sub><sup>+</sup>) and mixed Cr-Fe (e.g. CrFe<sub>2</sub>O<sub>8</sub>H<sub>6</sub><sup>+</sup>), 65-100 %EM4</li><li>M (substrate) Ca hydroxides/oxides (CaFe<sub>1-3</sub>O<sub>x</sub>H<sub>y</sub><sup>+</sup>, 30-49 %EM4; CaCrO<sub>x</sub>H<sub>y</sub><sup>+</sup>, 60-68 %EM4; CaAlO<sub>6</sub>H<sub>8</sub><sup>+</sup>, 38 %EM4)</li></ul>		<ul style="list-style-type: none"><li>Ca-Fe hydroxide-hydrates (e.g. CaFeO<sub>6</sub>H<sub>9</sub><sup>+</sup>: 29 %EM1, 22 %EM2, 22 %EM3, 27 %EM4; CaFeO<sub>5</sub>H<sub>7</sub><sup>+</sup>: 20 %EM1, 24 %EM2, 27 %EM3, 28 %EM4)</li></ul>	
		Time /s	0-30		540-840		1400-2100		3900-4500		
		C	73.7	1	67.5	1	62.9	1	57.4	1	
		O	19.4	0.26	18.8	0.28	19.6	0.31	16.7	0.29	
N	1.7	0.02	2.1	0.03	2.1	0.03	3.1	0.05			

<b>relative ratio to carbon (right)</b>	<b>Ca</b>	1.6	0.02	6.1	0.09	6.9	0.11	6.8	0.12	
	<b>Na</b>	0.4	0.01	0.1	0.00	0.6	0.01	0.8	0.01	
	<b>Zn</b>	0.9	0.01	1.5	0.02	1.8	0.03	1.7	0.03	
	<b>S</b>	0.3	0	0.4	0.01	0.4	0.01	0.4	0.01	
	<b>P</b>	0	0	0.1	0.00	0	0	0.1	0	
	<b>Fe</b>	0.9	0.01	3.1	0.05	5.1	0.08	11.8	0.21	
	<b>Mo</b>	0.1	0	0.3	0.00	0.3	0	0.7	0.01	
	<b>W</b>	0	0	0.2	0.00	0.3	0	0.6	0.01	
	<b>Si</b>	1.1	0.01	0	0.00	0	0	0	0	

### **2.8.3. Overview of Needle 7 OrbiSIMS NMF using the Comparative Method**

#### **2.8.3.1. Negative polarity OrbiSIMS NMF results overview**

This sample's negative polarity depth profile required adjustment of the surface potential (described in Section 2.3.3.1) during analysis due to loss of signal. This is thought to be due to variations in deposit material causing changes in conductivity as the deposit is removed by etching. Point-to-point normalisation of each ion's depth profile to the total signal was hence applied to mitigate fluctuations in total signal. The changes in surface potential were made at two points (16,100s,  $2.87 \times 10^{16}$  ions  $\text{cm}^{-2}$  and 31,800s,  $5.66 \times 10^{16}$  ions  $\text{cm}^{-2}$ , marked with dotted lines in Figure A18a), which represent two of the endmember interfaces. In the overview of key, high-loading ions shown in Table A27, many ions have a relatively wide distribution across the endmembers, resulting in their highest %EM values being only moderate (~50 %EM) compared to other depth profiles analysed in this work. This is likely partially due to the normalisation applied here as described. The distributions can nonetheless be interpreted to indicate where each ion is concentrated in the depth profile.



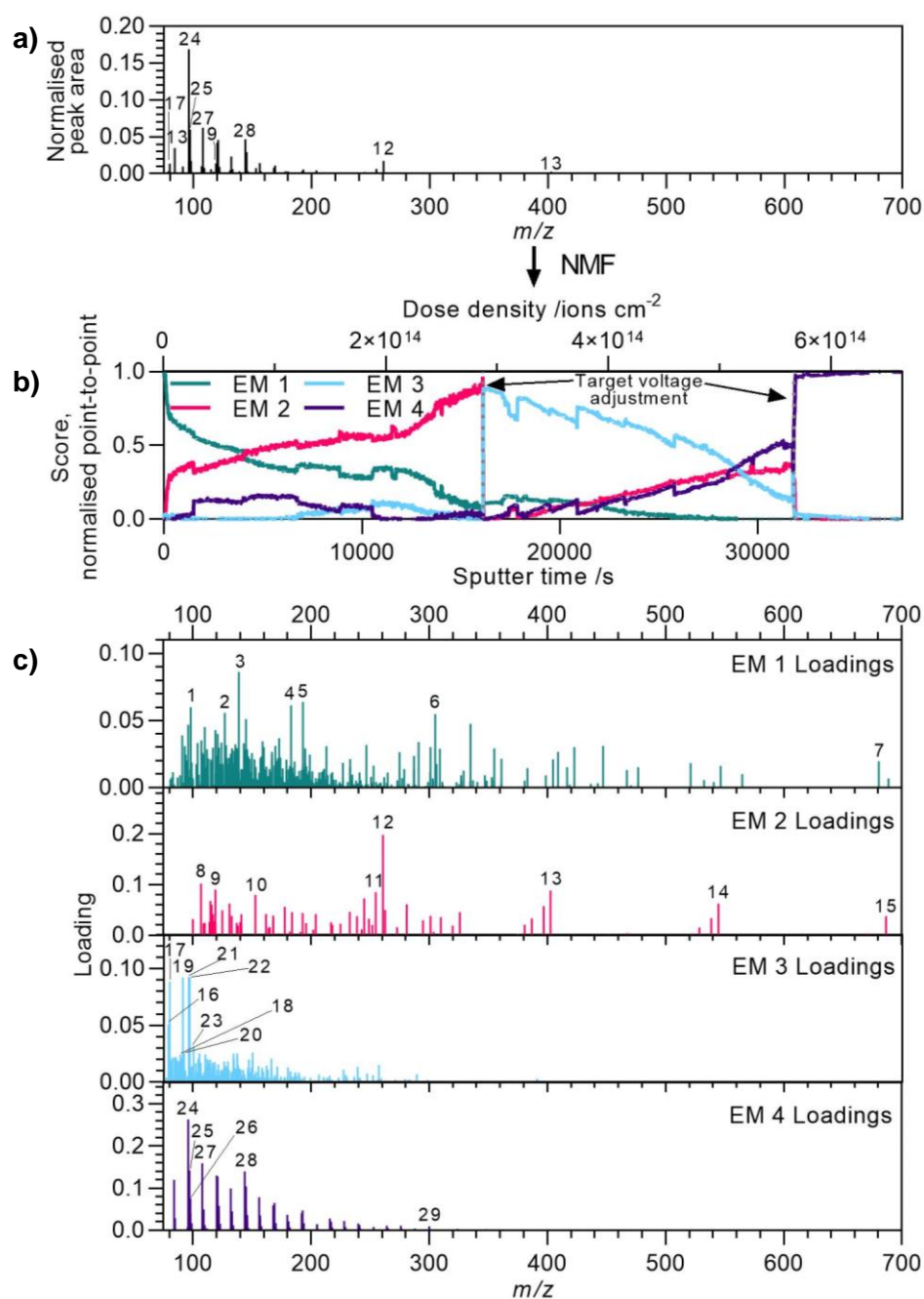


Figure A18: NMF of Needle 7 (negative polarity) a) spectrum, b) scores and c) loadings for all endmembers after filtering to remove ions that have a higher loading in another endmember.

Table A27: Needle 7 depth profile NMF results for key ions with ID numbers from Figure A18, loadings and relative loadings, separated by which endmember their loading is highest for. Additional ions shown at the bottom which are highly distributed across multiple endmembers. Heat map applied to each column: green = maximum value and red = minimum, for normalised loadings green = 1.00 and red = 0.

Ion	<i>m/z</i>	Assignment	Peak area (norm.)	Original loading				Relative loading (%EM)			
				1	2	3	4	1	2	3	4
1	98.0246	C <sub>4</sub> H <sub>4</sub> NO <sub>2</sub> <sup>-</sup>	2.2E-03	0.1	0.0	0.0	0.0	43.2	35.3	18.5	3.0
2	127.0764	C <sub>7</sub> H <sub>11</sub> O <sub>2</sub> <sup>-</sup>	7.2E-04	0.1	0.0	0.0	0.0	61.0	27.7	10.7	0.7
3	139.0012	C <sub>4</sub> H <sub>4</sub> O <sub>4</sub> Na <sup>-</sup>	3.3E-03	0.1	0.1	0.0	0.0	47.7	32.8	15.9	3.6
4	193.0481	C <sub>8</sub> H <sub>10</sub> O <sub>4</sub> Na <sup>-</sup>	9.9E-04	0.1	0.0	0.0	0.0	58.2	34.6	6.7	0.5
5	183.012	C <sub>8</sub> H <sub>7</sub> SO <sub>3</sub> <sup>-</sup>	1.3E-03	0.1	0.0	0.0	0.0	53.2	28.8	13.8	4.2
6	305.1733	C <sub>16</sub> H <sub>26</sub> O <sub>4</sub> Na <sup>-</sup>	6.9E-04	0.1	0.0	0.0	0.0	58.5	36.8	4.8	0.0
7	680.6499	Na <sub>7</sub> CaS <sub>5</sub> O <sub>20</sub> <sup>-</sup>	1.0E-04	0.0	0.0	0.0	0.0	61.7	35.8	2.5	0.0
8	106.9863	NaC <sub>2</sub> N <sub>2</sub> O <sub>2</sub> <sup>-</sup>	1.0E-02	0.0	0.1	0.1	0.0	8.9	46.1	37.6	7.4
9	118.942	NaSO <sub>4</sub> <sup>-</sup>	1.4E-02	0.1	0.1	0.1	0.0	20.8	32.7	30.8	15.7
10	152.9176	CaSO <sub>5</sub> H <sup>-</sup>	7.8E-03	0.1	0.1	0.1	0.0	25.1	35.9	27.3	11.7
11	254.8564	NaCaS <sub>2</sub> O <sub>8</sub> <sup>-</sup>	6.5E-03	0.0	0.1	0.1	0.0	23.4	41.0	25.0	10.6
11	244.8783	Na <sub>3</sub> S <sub>2</sub> O <sub>7</sub> <sup>-</sup>	2.5E-03	0.0	0.1	0.0	0.0	20.2	52.8	20.7	6.2
12	260.8733	Na <sub>3</sub> S <sub>2</sub> O <sub>8</sub> <sup>-</sup>	1.8E-02	0.1	0.2	0.1	0.0	29.3	48.9	16.8	5.0
13	402.8044	Na <sub>5</sub> S <sub>3</sub> O <sub>12</sub> <sup>-</sup>	2.6E-03	0.1	0.1	0.0	0.0	31.7	54.4	11.4	2.4
14	544.7357	Na <sub>7</sub> S <sub>4</sub> O <sub>16</sub> <sup>-</sup>	1.2E-03	0.0	0.1	0.0	0.0	34.3	55.0	10.2	0.5
15	686.6669	Na <sub>9</sub> S <sub>5</sub> O <sub>20</sub> <sup>-</sup>	4.8E-04	0.0	0.0	0.0	0.0	41.4	51.1	7.5	0.0
16	78.9588	PO <sub>3</sub> <sup>-</sup>	3.2E-03	0.0	0.0	0.1	0.0	31.1	7.3	47.3	14.3
17	79.9571	SO <sub>3</sub> <sup>-</sup>	1.4E-02	0.0	0.0	0.1	0.0	16.6	14.1	45.1	24.2
18	89.0143	C <sub>5</sub> N <sub>2</sub> H <sup>-</sup>	7.6E-04	0.0	0.0	0.0	0.0	7.2	29.3	53.7	9.8
19	90.9912	NaCNOCN <sup>-</sup>	9.8E-03	0.0	0.1	0.1	0.0	0.6	40.2	50.9	8.2
20	92.0253	C <sub>4</sub> H <sub>2</sub> N <sub>3</sub> <sup>-</sup>	8.9E-04	0.0	0.0	0.0	0.0	17.2	30.9	45.0	7.0
21	95.9522	SO <sub>4</sub> <sup>-</sup>	1.6E-02	0.0	0.0	0.1	0.1	6.9	17.5	46.0	29.6
22	96.96	SO <sub>4</sub> H <sup>-</sup>	1.3E-02	0.0	0.0	0.1	0.0	15.4	18.8	45.1	20.6
23	99.9571	NaCNOCl <sup>-</sup>	1.0E-03	0.0	0.0	0.0	0.0	0.0	17.1	68.6	14.3
24	96.0004	C <sub>8</sub> <sup>-</sup>	1.7E-01	0.0	0.1	0.1	0.3	6.2	23.6	20.8	49.5
25	97.0082	C <sub>8</sub> H <sup>-</sup>	6.0E-02	0.0	0.1	0.1	0.1	10.4	27.7	26.0	35.9
26	98.0035	C <sub>7</sub> N <sup>-</sup>	1.7E-02	0.0	0.1	0.1	0.1	0.0	29.2	33.8	37.0
27	108.0005	C <sub>9</sub> <sup>-</sup>	6.3E-02	0.0	0.1	0.1	0.2	6.8	27.0	20.2	46.0
28	144.0005	C <sub>12</sub> <sup>-</sup>	4.7E-02	0.0	0.1	0.1	0.1	6.3	29.2	18.9	45.7
29	300.0004	C <sub>25</sub> <sup>-</sup>	2.1E-04	0.0	0.0	0.0	0.0	15.2	13.4	15.3	56.1

From the high-loading ions (Figure A18c, Table A27), the deposit can be understood in terms of a surface layer composed largely of organic material, including Na-DDS ions and fragments thereof (C<sub>x</sub>H<sub>y</sub>O<sub>4</sub>Na<sup>-</sup>: 48-59 %EM1), likely succinimide ions (C<sub>4</sub>H<sub>4</sub>NO<sub>2</sub><sup>-</sup>: 43 %EM1) and alkylbenzene sulfonates (C<sub>8</sub>H<sub>7</sub>SO<sub>3</sub><sup>-</sup>: 53 %EM1), as well as an inorganic sodium-calcium sulfate (62 %EM1). The second endmember is inorganic salt material of mainly sodium sulfates (NaSO<sub>4</sub><sup>-</sup>: 33 %EM2), with some calcium sulfate (CaSO<sub>5</sub>H<sup>-</sup>: 36 %EM2) and sodium cyanate (Na(CNO)<sub>2</sub><sup>-</sup>: 46 %EM2). Beneath this lies a pseudo-layer of increased small anions (SO<sub>4</sub><sup>-</sup>: 46 %EM3; PO<sub>3</sub><sup>-</sup>: 47 %EM3) as well as a continuation of sodium inorganic salts but containing cyanate alongside cyanide (NaCNOCN<sup>-</sup>: 51 %EM3) and chloride (NaCNOCl<sup>-</sup>:

69 %EM3). Also in this pseudo-layer are nitrogenous ions with low H:C ratios ( $C_5N_2H^-$ : 54 %EM3;  $C_4H_2N_3^-$ : 45 %EM3). This leads to EM 4 which contains carbonaceous ions indicative of a DLC, though the presence of  $C_7N^-$  (37 %EM4) suggests this to be partially an extension of further carbonisation of the nitrogenous material seen in EM 3, where similar ions of higher nitrogen number and small H numbers were present. This is supported by this ion's smaller %EM4, alongside the H-containing  $C_8H^-$  (36 %EM4), in this EM than  $C_x^-$  ions (46-56 %EM4). In the profilometry images (Figure 4.1), the substrate of the needle can be seen at the bottom of each crater, therefore the lack of metals and abundance of carbon strongly indicate a DLC substrate was reached in this bottom layer.

### 2.8.3.2. Positive polarity OrbiSIMS NMF results overview

For ions of high loadings in Needle 7's positive polarity depth profile NMF (Figure A19c, Table A28), there is an upper pseudo-layer of organic material, including sodium adducts of Na-DDS ( $C_{16}H_{26}O_4Na_3^+$ : 46 %EM1), Na-HDS ( $C_{20}H_{34}O_4Na_3^+$ : 71 %EM1) and their fragments (e.g.  $Na_3C_4H_4O_4^+$ : 45 %EM1), whether from SIMS or degradation of DDSA in the deposit, and a saturated alkyl ammonium ( $C_{26}H_{56}N^+$ : 68 %EM1). Inorganics are also in EM 1, with the two most surface exclusive ions are calcium hydroxides ( $Ca_3O_6H_7^+$ ,  $Ca_4O_7H_7^+$ ) at 86 %EM1. Sodium is widespread and its inorganic salts dominate EM 2 and EM 3. EM 2 is less populated but has a prevalence of sulfur-containing sodium salts (sulfate,  $Na_5S_2O_8^+$ : 29 %EM2 and sulfide,  $Na_3S_2^+$ : 51 %EM2), including high mass ions ( $Na_7S_3O_{12}^+$ : 44 %EM2), which also have significant presence in EM 3. The next EM is characterised by sodium salts of greater diversity, including cyanate ( $Na_2CNO^+$ : 41 EM%3), sulfide ( $Na_3S^+$ : 48 EM%3), hydroxide ( $Na_3O_2H_2^+$ : 52 EM%3), carbide ( $Na_2C_5^+$ : 62 EM%3), carbonate ( $Na_3CO_3^+$ : 37 %EM3), sulfite ( $Na_3SO_3^+$ : 36 %EM3) and sulfate ( $Na_3SO_4^+$ : 32 %EM3). The ions that dominate EM 4 are carbonaceous with minimal hydrogen content, generally  $C_x^+$  ions (90-100 %EM1) with a decreasing %EM4 with higher H numbers ( $C_9H^+$ : 85 %EM4, 15 %EM2;  $C_8H_2^+$ : 81 %EM4, 18 %EM2). This indicates that, like Needle 6, higher H/C ratios have more presence in the upper deposit (EM 2). Like with the negative

polarity data, this is indicative of the lower DLC material, however may also involve lower carbonaceous material of aged carbonised deposit.

#### **2.8.3.3. Comparison to atomic concentration depth profile from XPS**

Needle 7's XPS depth profile confirms the high sodium content (though lower than Needle 6) which increases in the sub-surface, as well as quantitatively validating the surface presence of organic compounds of higher carbon, oxygen, nitrogen and sulfur content which will include the sodium carboxylate, succinimide and ABS chemistries. Finally, the profile confirms the increasing carbon concentration at lower depth, indicative of a DLC substrate as well possible carbonaceous deposit bottom material. The profile was shown until the elements reach their plateau (4000s) in Figure 4.10i. Note that fluorine was also detected in the spectra throughout all scans with increasing intensity; the instrument was thought to be contaminated with fluorine, which is supported by no evidence of fluorine being found in the OrbiSIMS data, so it was omitted from the data presented here.

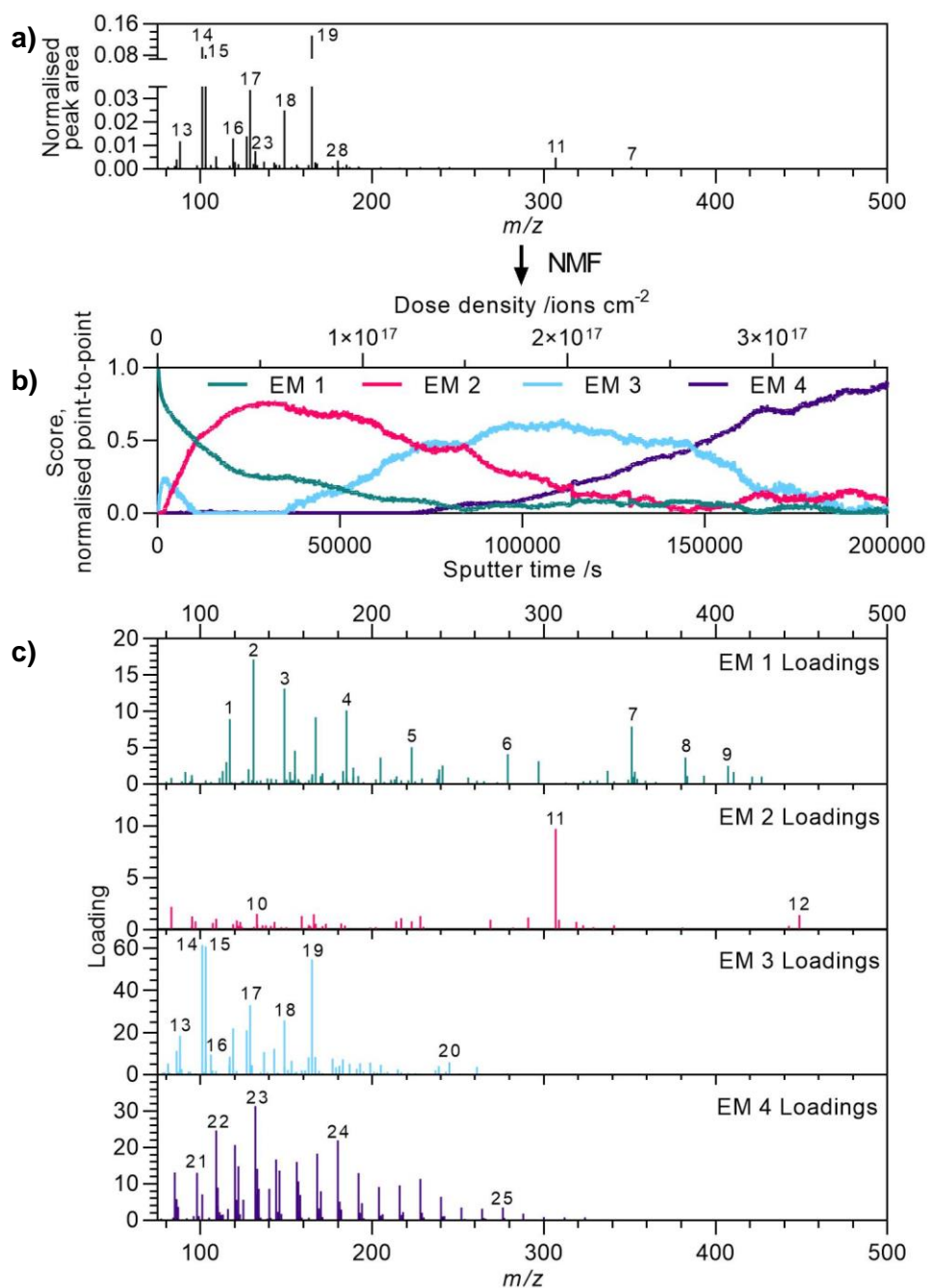


Figure A19: NMF of Needle 7 (positive polarity) a) spectrum, b) scores and c) loadings for all endmembers after filtering to remove ions that have a higher loading in another endmember.

Table A28: Needle 7 positive polarity depth profile NMF results for key ions with ID numbers from Figure A19, loadings and relative loadings, separated by which endmember their loading is highest for. Additional ions shown at the bottom which are highly distributed across multiple endmembers. Heat map applied to each column: green = maximum value and red = minimum, for normalised loadings green = 1.00 and red = 0.

Ion	m/z	ID	Peak area (norm.)	Original loading				Relative loading (%EM)			
				1	2	3	4	1	2	3	4
1	116.9922	Na <sub>2</sub> C <sub>3</sub> H <sub>3</sub> O <sub>2</sub> <sup>+</sup>	8.7E-04	9.0	2.4	3.9	1.3	54.2	14.2	23.6	8.0
2	130.9328	Ca <sub>2</sub> O <sub>3</sub> H <sub>3</sub> <sup>+</sup>	2.3E-03	17.2	2.9	5.9	2.6	60.2	10.0	20.7	9.0
3	148.9433	Ca <sub>2</sub> O <sub>4</sub> H <sub>5</sub> <sup>+</sup>	1.1E-03	13.2	1.4	3.9	1.3	66.5	7.3	19.7	6.5
4	184.9797	Na <sub>3</sub> C <sub>4</sub> H <sub>4</sub> O <sub>4</sub> <sup>+</sup>	1.9E-03	10.1	3.8	7.0	1.5	45.1	17.0	31.2	6.8
5	222.9114	Ca <sub>3</sub> O <sub>6</sub> H <sub>7</sub> <sup>+</sup>	9.6E-05	5.1	0.0	0.8	0.0	85.7	0.0	14.3	0.0
6	278.8691	Ca <sub>4</sub> O <sub>7</sub> H <sub>7</sub> <sup>+</sup>	6.3E-05	4.1	0.0	0.7	0.0	86.1	0.0	13.9	0.0
7	351.1518	C <sub>16</sub> H <sub>26</sub> O <sub>4</sub> Na <sub>3</sub> <sup>+</sup>	9.8E-04	8.0	3.5	3.7	2.1	46.0	20.1	21.6	12.3
8	382.4405	C <sub>26</sub> H <sub>56</sub> N <sup>+</sup>	8.5E-05	3.7	0.8	0.9	0.1	67.5	14.1	16.4	2.0
9	407.2145	C <sub>20</sub> H <sub>34</sub> O <sub>4</sub> Na <sub>3</sub> <sup>+</sup>	3.5E-05	2.5	0.5	0.4	0.1	71.1	13.9	11.2	3.8
10	132.9128	Na <sub>3</sub> S <sub>2</sub> <sup>+</sup>	7.6E-05	0.0	1.5	1.5	0.0	0.0	51.0	49.0	0.0
11	306.8515	Na <sub>5</sub> S <sub>2</sub> O <sub>8</sub> <sup>+</sup>	5.0E-03	7.7	9.7	9.7	6.2	23.1	29.2	29.1	18.6
12	448.7829	Na <sub>7</sub> S <sub>3</sub> O <sub>12</sub> <sup>+</sup>	5.6E-05	0.7	1.4	0.7	0.4	21.5	44.0	22.7	11.9
13	87.9771	Na <sub>2</sub> CNO <sup>+</sup>	1.2E-02	5.9	12.8	18.4	7.8	13.2	28.5	41.0	17.4
14	100.9408	Na <sub>3</sub> S <sup>+</sup>	1.0E-01	3.7	38.2	61.6	25.7	2.9	29.5	47.7	19.9
15	102.9742	Na <sub>3</sub> O <sub>2</sub> H <sub>2</sub> <sup>+</sup>	8.0E-02	10.6	27.2	60.8	17.9	9.1	23.3	52.2	15.3
16	105.9789	Na <sub>2</sub> C <sub>5</sub> <sup>+</sup>	1.8E-03	0.0	4.5	9.6	1.2	0.0	29.6	62.3	8.1
17	128.9534	Na <sub>3</sub> CO <sub>3</sub> <sup>+</sup>	3.4E-02	23.9	16.6	32.9	15.0	27.1	18.8	37.2	16.9
18	148.9254	Na <sub>3</sub> SO <sub>3</sub> <sup>+</sup>	2.5E-02	12.9	18.8	25.7	14.8	17.9	26.0	35.6	20.4
19	164.9203	Na <sub>3</sub> SO <sub>4</sub> <sup>+</sup>	1.3E-01	38.8	43.4	54.8	35.6	22.5	25.1	31.7	20.6
20	244.9054	Na <sub>5</sub> SO <sub>4</sub> O <sub>2</sub> H <sub>2</sub> <sup>+</sup>	8.5E-04	1.5	3.5	5.9	0.9	12.5	29.9	50.0	7.6
21	98.0151	C <sub>8</sub> H <sub>2</sub> <sup>+</sup>	1.6E-03	0.1	2.9	0.0	13.1	0.6	18.0	0.0	81.4
22	109.0072	C <sub>9</sub> H <sup>+</sup>	5.5E-03	0.0	4.3	0.0	24.7	0.0	14.9	0.0	85.1
23	131.9993	C <sub>11</sub> <sup>+</sup>	7.7E-03	0.0	3.6	0.0	31.4	0.0	10.3	0.0	89.7
24	179.9993	C <sub>15</sub> <sup>+</sup>	3.7E-03	0.0	2.1	0.0	22.0	0.0	8.6	0.0	91.4
25	275.9993	C <sub>23</sub> <sup>+</sup>	8.0E-05	0.0	0.0	0.0	3.5	0.0	0.0	0.3	99.7

#### 2.8.3.4. Summary and Discussion of Deposit Characterisation by OrbiSIMS and XPS

Table A29 presents a summary of the findings from the above NMF analysis of Needle 7's negative and positive polarity depth profiles using the comparative method, alongside the XPS depth profile data for regions that appear to represent each EM.

Table A29: Needle 7 summary of OrbiSIMS and XPS data for pseudo-layers identified by NMF endmembers with example ions and relative loadings.

EM/pseudo-layer (etch time range /s)		1	2	3	4	Split
Technique						
OrbiSIMS	Negative Polarity	<ul style="list-style-type: none"> <li>Organics <ul style="list-style-type: none"> <li>ABS (<math>C_8H_7SO_3^-</math> to <math>C_{18}H_{29}SO_3^-</math>, 53-96 %EM1 with presence in EM 2 particularly for larger ions)</li> <li>Hydrocarbon <math>C_{7-19}H_{3-9}^-</math> with 45-78 %EM1 and many (generally of lower H number) split with EM 3. E.g. <math>C_{14}H_{11}</math> (78 %EM1), <math>C_{12}H_3^-</math> (28 %EM1).</li> <li>Na-DDS (<math>C_{16}H_{26}O_4Na^-</math>, 58 %EM1), fragments (<math>C_{15}H_{24}O_4Na^-</math>, 87 %EM1; <math>C_4H_4O_4Na^-</math>, 48 %EM1; <math>C_8H_{10}O_4Na^-</math>, 58 %EM1) and clusters (<math>C_{20}H_{30}O_8Na_3^-</math>, 100 %EM1; <math>C_{24}H_{36}O_8Na_3^-</math>, 99 %EM1), Na-HDS (<math>C_{20}H_{34}O_4Na^-</math>, 99 %EM1)</li> <li>Wide range of nitrogenous (and NO-containing) to 312 <math>m/z</math> likely from LMW PIBSI, aromatics and N-PAC (ions of <math>C_xH_yN^-</math>, <math>N_2^-</math>, <math>N_3^-</math>, <math>N_4^-</math>, <math>NO^-</math>, <math>NO_2^-</math>, <math>NO_3^-</math>, <math>N_2O^-</math>, <math>N_2O_2^-</math>, <math>N_2O_3^-</math>, <math>N_3O_2^-</math>, <math>N_4O^-</math>) up to 98 %EM1. E.g. <math>C_4H_4NO_2^-</math> (43 %EM1), <math>C_7H_4NO^-</math> (36 %EM1), <math>C_{24}H_{10}N^-</math> (50 %EM1), <math>C_8H_6N^-</math> (39 %EM1), <math>C_{16}H_8N_2^-</math> (47 %EM1), <math>C_6H_3N_2O_2^-</math> (45 %EM1), <math>C_{11}H_5N_2O_3^-</math> (58 %EM1)</li> <li>Aromatic/PAH-type oxygenates to 264 <math>m/z</math> (<math>C_5H_7O^-</math> to <math>C_{16}H_{11}O^-</math>, 37-95 %EM1; <math>C_4H_5O_2^-</math> to <math>C_{15}H_8O_2^-</math>, 42-97 %EM1; <math>C_4H_2O_3^-</math> to <math>C_9H_5O_3^-</math>, 62-87 %EM1)</li> <li>Pentadecanoate (<math>C_{15}H_{27}O_2^-</math>, 50 %EM1)</li> </ul> </li> </ul>	<ul style="list-style-type: none"> <li>Salts <ul style="list-style-type: none"> <li>Sodium and calcium (many of mixed cations and anions) sulfates (<math>Na_3S_2O_8^-</math>, 49 %EM2; <math>NaCaS_2O_8^-</math>, 41 %EM2; <math>CaSO_5H^-</math> 36 %EM2), cyanides/cyanates (<math>NaC_2N_2O_2^-</math> 46 %EM1; <math>CaSO_4CNO^-</math>, 44 %EM2; <math>CaSO_4CN^-</math>, 43 %EM2),</li> <li>Sodium carbonate-sulfate (<math>Na_3SO_4CO_3^-</math>, 43 %EM2),</li> </ul> </li> <li>Some organics, particularly nitrogenous, persist here to 165 <math>m/z</math> (e.g. <math>C_{13}H_7N_2^-</math>, 35 %EM2; <math>C_6H_3N_2O^-</math>, 38 %EM2) present in this EM, split generally across EMs 1-3.</li> <li><math>C_{17}^-</math> and <math>C_{21}^-</math> carbonaceous ions (37, 34 %EM2) split with EM 4.</li> </ul>	<ul style="list-style-type: none"> <li>Carbonaceous ions, mostly with heteroatoms <ul style="list-style-type: none"> <li><math>C_{5-8}OH^-</math> (54-85 %EM3), <math>C_{6-10}N^-</math> (45-60 %EM3 split with EM 4), <math>C_{5-9}N_2^-</math> (67-76 %EM3 with presence in EM 4), <math>C_{4-6}N_3^-</math> (73-94 %EM3), <math>C_{4-12}S^-</math> (34-78 %EM3), <math>C_4S_2^-</math> (97 %EM3), <math>C_{3-7}SN^-</math> (78-98 %EM2)</li> <li><math>C_{6-16}NH^-</math> (40-68 %EM3, present in EM 4), <math>C_{7-19}H_2^-</math> (31-37 %EM3, present in EM 4).</li> </ul> </li> <li>Organics to 283 <math>m/z</math>, generally also strong in EM 1 with presence in EM 2 <ul style="list-style-type: none"> <li>Hydrocarbon and N and/or O-containing generally with low H (<math>\leq 7</math>) numbers, generally present across EM 1-3). Those of the lowest H (<math>\leq 3</math>) numbers have higher %EM3. E.g. <math>C_{19}H_7N_2^-</math> (38 %EM3), <math>C_5H_9O_2^-</math> (51 %EM3), <math>C_7H_5N_4^-</math> (60 %EM3), <math>C_8H_5N_4O^-</math> (45 %EM3)</li> <li>DDSA (<math>C_{16}H_{27}O_4^-</math>, 76 %EM3 with presence in EM 1)</li> </ul> </li> <li>Variety of inorganic salt ions mostly containing sodium, as well as calcium, magnesium, copper and iron: <ul style="list-style-type: none"> <li>Sulfates (<math>Na_5S_3O_{11}^-</math>, 49 %EM3; <math>Ca_2S_2O_8OH^-</math>, 42 %EM3; <math>MgSO_5H^-</math>, 63 %EM3; <math>FeSO_4CNO^-</math>, 81 %EM3), generally also strong in EM 1.</li> </ul> </li> </ul>	<ul style="list-style-type: none"> <li>Carbonaceous: <math>C_{7-29}^-</math> (37-97 %EM4), <math>C_{7-18}^-</math> (37-90 %EM4), <math>C_{8-24}^-</math> (36-94 %EM4), generally with presence in EMs 2-3 and some in EM 1</li> <li>Heteroatom-containing carbonaceous: <math>C_{12}S^-</math> (66 %EM4 with presence in EM 3), <math>C_8O^-</math> (94 %EM 4).</li> </ul>	<ul style="list-style-type: none"> <li>HCs with low H number (e.g. <math>C_9H_2^-</math>: 21 %EM1, 30 %EM2, 30 %EM3, 19 %EM4; <math>C_{15}H_2^-</math>: 26 %EM1, 20 %EM2, 31 %EM3, 24 %EM4).</li> </ul>

		<ul style="list-style-type: none"> <li>Salts <ul style="list-style-type: none"> <li>Sodium (some with calcium, magnesium or potassium) sulfates (<math>\text{Na}_{11}\text{S}_6\text{O}_{24}^-</math>, 59 %EM1; <math>\text{Na}_7\text{CaS}_5\text{O}_{20}^-</math>, 62 %EM1; <math>\text{Na}_3\text{MgS}_3\text{O}_{12}^-</math>, 51 %EM1; <math>\text{KNa}_4\text{S}_3\text{O}_{12}^-</math>, 64 %EM1) with cyanide (<math>\text{NaSO}_4\text{CN}^-</math>, 71 %EM1), cyanate (<math>\text{Na}_2\text{SO}_4\text{CNO}^-</math>, 64 %EM1), hydroxide (<math>\text{Na}_2\text{SO}_4\text{OH}^-</math>, 51 %EM1) with presence in EMs 2 and 3.</li> <li>Calcium hydroxide (<math>\text{Ca}_2\text{O}_5\text{H}_5^-</math>, 78 %EM1), cyanate (<math>\text{CaC}_3\text{N}_3\text{O}_3^-</math>, 65 %EM1), sulfate-hydroxide (<math>\text{CaSO}_7\text{H}_3^-</math>, 53 %EM1), with mixed anions (<math>\text{Ca}_2\text{CNO}_4\text{H}_4^-</math>, 43 %EM1). Strong presence in EM 3.</li> </ul> </li> <li>Others: copper cyanide and cyanate (<math>\text{CuC}_3\text{N}_3^-</math>, 59 %EM1; <math>\text{CuC}_2\text{N}_2\text{O}^-</math>, 57 %EM1) split with EM 3, iron oxide (<math>\text{FeO}_3^-</math>, 49 %EM1 with significant loadings in EMs 2-3), magnesium cyanate-hydroxide (<math>\text{MgCNO}_3\text{H}_2^-</math>, 42 %EM1 split with EM 3).</li> </ul>		<ul style="list-style-type: none"> <li>Chlorides (<math>\text{NaCl}_2^-</math>, 96 %EM3; <math>\text{CaSO}_4\text{Cl}^-</math>, 87 %EM3; <math>\text{CaClO}_2\text{H}_2^-</math>, 54 %EM3 split with EM 1; <math>\text{CuCNOCl}^-</math>, 89 %EM3)</li> <li>Cyanide/cyanate (<math>\text{NaC}_2\text{N}_2\text{O}^-</math>, 51 %EM3; <math>\text{CaCNO}_3\text{H}_2^-</math>, 65 %EM3; <math>\text{MgSO}_4\text{CNO}^-</math>, 81 %EM1; <math>\text{FeO}_2\text{H}_2\text{CN}^-</math>, 62 %EM3; <math>\text{CuCNOH}^-</math>, 43 %EM3 with strong presence in EM 1) and azanide (<math>\text{Na}_3\text{NH}_2\text{CNO}^+</math>, 43 %EM3)</li> <li>Iron hydroxide (<math>\text{FeO}_2\text{H}_2^-</math>, 46 %EM3 split with EM 1), chromium oxide (<math>\text{CrO}_3^-</math>, 63 %EM3 with strong presence in EM 1).</li> </ul>		
	Positive Polarity	<ul style="list-style-type: none"> <li>Organics &lt; 340 m/z: <ul style="list-style-type: none"> <li>Hydrocarbons, some of PAH-type, to very low mass (up to <math>\text{C}_{16}\text{H}_{10}^+</math>, 57-73 %EM1)</li> <li>Nitrogenous: PAH-type (1N, to <math>\text{C}_9\text{H}_8\text{N}^+</math>, 34-44 %EM1; 2N to <math>\text{C}_6\text{H}_9\text{N}_2^+</math>, 37-75 %EM1; 3N to <math>\text{C}_6\text{H}_{10}\text{N}_3^+</math>, 30-41 %EM1) often with presence in EMs 2-4, saturated ammoniums (<math>\text{C}_{14}\text{H}_{32}\text{N}^+</math>, 80 %EM1; <math>\text{C}_{26}\text{H}_{56}\text{N}^+</math>, 67 %EM1)</li> <li>DDS-Na (<math>\text{C}_{16}\text{H}_{26}\text{O}_4\text{Na}_3^+</math>, 46 %EM1) and fragments (<math>\text{C}_{15}\text{H}_{24}\text{O}_4\text{Na}_3^+</math>, 47 %EM1; <math>\text{Na}_3\text{C}_4\text{H}_4\text{O}_4^+</math>, 45 %EM1;</li> </ul> </li> </ul>	<ul style="list-style-type: none"> <li>Larger sodium sulfate ions (to <math>\text{Na}_7\text{S}_3\text{O}_{12}^+</math>, 44 %EM2 with presence in EMs 1 and 3), sodium carbonate-chloride (<math>\text{Na}_3\text{CO}_3\text{Cl}^+</math>, 43 %EM2)</li> <li>Nitrogenous organics persist into this layer (N1-4; up to 42 %EM2), with a succinimide ion (<math>\text{C}_6\text{H}_6\text{NO}_2^+</math>, 37 %EM2) and small sodium</li> </ul>	<ul style="list-style-type: none"> <li>Variety of inorganic salt ions of sodium, calcium, magnesium, with sodium the dominant metal <ul style="list-style-type: none"> <li>Hydroxides are prevalent for the various metals: sodium (<math>\text{Na}_4\text{O}_3\text{H}_3^+</math>, 60 %EM3), sodium-calcium (<math>\text{Na}_3\text{Ca}_2\text{O}_6\text{H}_6^+</math>, 68 %EM3), sodium-potassium (<math>\text{KNa}_2\text{O}_2\text{H}_2^+</math>, 77 %EM3) and sodium magnesium (<math>\text{Na}_3\text{MgO}_4\text{H}_4^+</math>, 62 %EM3)</li> <li>Sodium salts of sulfide (<math>\text{Na}_3\text{S}^+</math>, 48 %EM3), bisulfide (<math>\text{Na}_2\text{SH}^+</math>, 61 %EM3), chloride (<math>\text{Na}_2\text{Cl}^+</math>,</li> </ul> </li> </ul>	<ul style="list-style-type: none"> <li><math>\text{C}_{7-27}^+</math> (74-100 %EM4), generally larger for larger ions.</li> <li><math>\text{C}_{5-9}\text{OH}^+</math> (73-100 %EM4), <math>\text{C}_8\text{O}^+</math> (98 %EM4), <math>\text{C}_{7,9}\text{O}_2^+</math> (100 %EM4)</li> <li><math>\text{C}_{7-17}\text{H}^+</math> (80-94 %EM4),</li> </ul>	



		$\text{Na}_2\text{C}_3\text{H}_3\text{O}_2^+$ , 54 %EM1), Na-HDS ( $\text{C}_{20}\text{H}_{34}\text{O}_4\text{Na}_3^+$ , 71 %EM1) <ul style="list-style-type: none"> <li>Some inorganic salts <ul style="list-style-type: none"> <li>Calcium and sodium-calcium hydroxides (<math>\text{Ca}_2\text{O}_3\text{H}_3^+</math> to <math>\text{Ca}_6\text{H}_{11}\text{O}_{11}^+</math>, 60-83 %EM1; <math>\text{NaCaO}_2\text{H}_2^+</math> to <math>\text{Na}_2\text{Ca}_2\text{O}_6\text{H}_7^+</math>, 38-46 %EM1)</li> <li>Na bisulfide (<math>\text{Na}_2\text{SH}^+</math>, 74 %EM1)</li> <li>Sodium-potassium cyanate (<math>\text{KNaCNO}^+</math>, 48 %EM1)</li> <li>Small presence of sodium carbonate (27 %EM1), strongest in EM 3.</li> </ul> </li> </ul>		$\text{Na}_3\text{C}_3\text{H}_2\text{O}_3^+$ , 3 %EM2) <ul style="list-style-type: none"> <li>Some larger carbonaceous ions become significant in this EM (<math>\text{C}_{18-20}^-</math>, 33 %EM2).</li> </ul>		41 %EM3), sulfate ( $\text{Na}_3\text{SO}_4^+$ , 32 %EM3), sulfite ( $\text{Na}_3\text{SO}_3^+$ , 36 %EM3), carbonate ( $\text{Na}_3\text{CO}_3^+$ , 37 %EM3) and carbides ( $\text{NaC}_{3-7}^+$ , 62-68 %EM3; $\text{NaC}_{5-7}\text{H}^+$ , 74-78 %EM3). Generally with presence in EM 2, with smaller %EM1 and %EM4. <ul style="list-style-type: none"> <li>Sulfur-containing anions also prevalent alongside hydroxide in calcium: sulfides (<math>\text{Na}_3\text{CaSO}_3\text{H}_4^+</math>, 62 %EM3) and sulfates (<math>\text{Na}_3\text{CaSO}_6\text{H}_2^+</math>, 31 %EM3 with strong presence in EMs 1-2)</li> <li>Additional potassium-sodium salts with variety of anions: Cyanide (<math>\text{KNaCN}^+</math>, 67 %EM3), cyanate (<math>\text{KNaCNO}^+</math>, 65 %EM3), sulfide (<math>\text{KNa}_2\text{S}^+</math>, 57 %EM3), sulfate (<math>\text{KNaSO}_4^+</math>, 35 %EM3 split with EMs 1-2), and chloride (<math>\text{KNaCl}^+</math>, 49 %EM3).</li> </ul>		$\text{C}_{7-22}\text{H}_{2-3}^+$ (51-87 %EM4).		
<b>XPS relative atomic conc. (left) and relative ratio to carbon (right)</b>	<b>Time /s</b>	0-240		300-360		1860-2040		3840-4020		
	<b>C</b>	76.1	1	72.2	1	84.2	1	84.8	1	
	<b>O</b>	13.9	0.183	13.4	0.186	6.9	0.082	6.7	0.079	
	<b>N</b>	7.6	0.100	9.1	0.126	4.1	0.049	4	0.047	
	<b>Na</b>	1.8	0.024	4.0	0.055	3.8	0.045	3.3	0.039	
	<b>Ca</b>	0.2	0.003	0.3	0.004	0.1	0.001	0.2	0.002	
	<b>S</b>	0.4	0.005	0.6	0.008	0.2	0.002	0.3	0.004	
	<b>Cl</b>	0.0	0.000	0.0	0.000	0.1	0.001	0.2	0.002	
	<b>Fe</b>	0.0	0.000	0.4	0.006	0.6	0.007	0.6	0.007	

#### 2.8.4. Endmember Thickness Estimation from Depth Profile Crater Depth Measurements

Table A30: Summary of etch time ranges for each endmember of positive and negative polarity depth profiles of Needles 6-8, with EM interface depths and EM thicknesses estimated based on profilometry crater depth measurements (Table A18), and averaged for both polarities for each endmember.

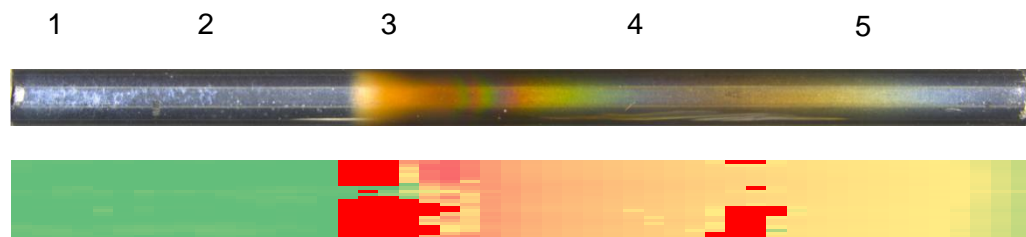
	Positive polarity				Negative polarity				Average	
	Etch time start /s	Etch time end /s	Interface depth / $\mu\text{m}$	EM thickness / $\mu\text{m}$	Etch time start /s	Etch time end /s	Interface depth / $\mu\text{m}$	EM thickness / $\mu\text{m}$	EM thickness / $\mu\text{m}$	Standard deviation / $\mu\text{m}$
<b>Needle 6</b>										
<b>EM 1</b>	0	1000	0.03	0.03	0	1300	0.05	0.05	0.04	0.01
<b>EM 2</b>	1000	4600	0.12	0.10	1300	3200	0.13	0.08	0.09	0.01
<b>EM 3</b>	4600	12200	0.32	0.23	3200	10900	0.45	0.37	0.30	0.07
<b>EM 4</b>	12200	52909	1.40	1.17	10900	46956	1.92	1.55	1.36	0.19
<b>Needle 8</b>										
<b>EM 1</b>	0	370	0.001	0.001	0	310	0.002	0.002	0.002	0.0004
<b>EM 2</b>	370	27900	0.09	0.09	310	5960	0.04	0.04	0.07	0.03
<b>EM 3</b>	27900	46300	0.16	0.06	5960	24700	0.17	0.13	0.10	0.03
<b>EM 4</b>	46300	64976	0.22	0.16	24700	49544	0.34	0.21	0.18	0.03
<b>Needle 7</b>										
<b>EM 1</b>	0	10500	0.49	0.49	0	4100	0.28	0.28	0.38	0.11
<b>EM 2</b>	10500	71500	3.35	2.86	4100	16100	1.09	0.81	1.83	1.02
<b>EM 3</b>	71500	147000	6.89	4.03	16100	31800	2.15	1.34	2.68	1.35
<b>EM 4</b>	147000	200313	9.39	5.36	31800	37330	2.52	1.18	3.27	2.09

### 3. Supporting Information for Chapter 5: JFTOT

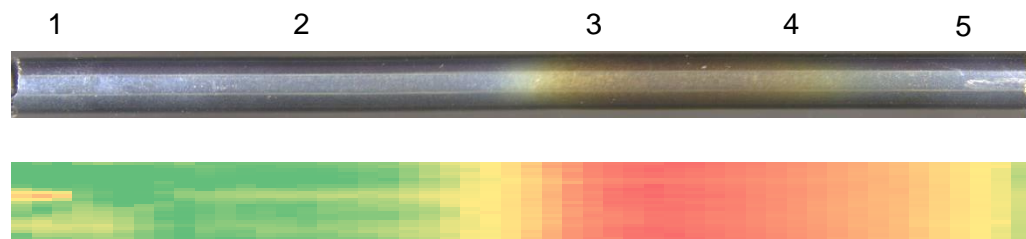
#### 3.1. JFTOT Sample Images and Ellipsometry Profiles

In the ellipsometry heat maps presented in this section, many recorded values exceed the limit of the instrument and record a null value. These are marked here as the darkest red shaded cells. Ellipsometry is not possible for a steel JFTOT tube, and for some samples ellipsometry was not recorded.

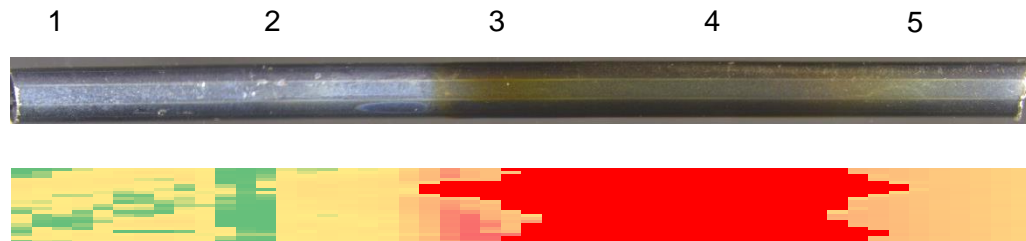
JFTOT RF-06



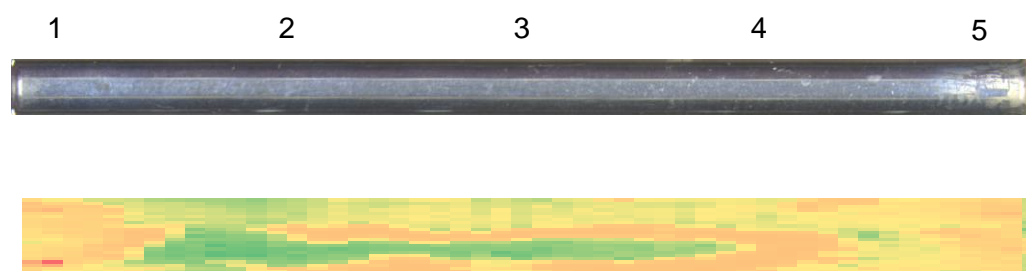
JFTOT RME



JFTOT CME



JFTOT HVO



JFTOT HVO50

1 2 3 4 5



JFTOT B7

1 2 3 4 5



JFTOT Na naphthenate + DDSA

1 2 3 4 5



JFTOT LMW PIBSI

1 2 3 4 5



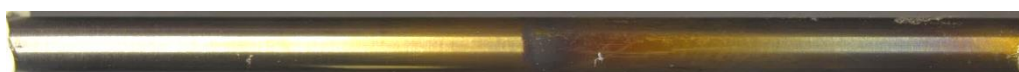
JFTOT Lubricant

1 2 3 4 5



JFTOT Zinc (steel tube)

1 2 3 4 5



JFTOT 200 °C (steel tube) (thermocouple at early position)



JFTOT 250 °C (steel tube) (thermocouple at early position)



Figure A20: Photographs and ellipsometry maps of the JFTOT samples.

Most JFTOT samples appear clean until around the position of the thermocouple (position 3) where dark deposition begins. JFTOT Na + DDSA is an exception, which forms a whiter deposit immediately (position 1), then develops a weaker brown coloured deposit at position 3. Another exception is JFTOT HVO, which appears almost clean until position 5 where it has a white-light brown deposit. For JFTOTs of different temperatures, JFTOT 300 °C is similar to other samples, developing the dark deposit at the central position. JFTOT 200 °C and 250 °C had the thermocouple at an earlier position than the other JFTOTs, so they develop their dark colour later.

Ellipsometry's measurements depend upon the absorption of light by the sample, which is considered effective for jet fuel deposits as jet fuel is thought to break down solely by oxidation, producing the same type of deposit so the measurements are directly comparable. With the use of diesel, IDIDs are known to form through more complex mechanisms involving fuel and additives, and hence the deposit formation can vary in its characteristics, mostly importantly here it varies in colour (139). Ellipsometry is hence considered a low priority technique here.

### 3.1.1. Deposit appearance ratings

Table A31: Visual JFTOT deposit rating system used in the current work, adapted and expanded from Reid *et al.* (61).






Rating	0	1	2	3	4
Appearance	Clean	White staining/speckling	White/light deposit	Brown deposit	Black deposit
Example					

Table A32: JFTOT tube visual deposit ratings based on the rating system adapted from Reid *et al.* (61) in Table A31.

JFTOT		Position				
		1	2	3	4	5
1	RF-06	0	0	3	3	2
2	RME	0	0	3	3	2
3	CME	0	0	3	3	2
4	HVO	0	0	0	1	2
5	HVO50	0	0	3	3	3
6	B7	0	0	3	3	2
7	Na + DDSA	1	2	3	2	2
8	PIBSI	0	0	3	3	3
9	Lube	0	0	3	3	3
10	Zinc	0	0	4	3	3
11	200 °C	0	0	2	3	3
12	250 °C	0	2	3	3	3

### 3.2. Profilometry of OrbiSIMS GCIB Craters

Profilometry was performed on three diverse JFTOT samples' OrbiSIMS craters: JFTOT RME, JFTOT LMW PIBSI, JFTOT Zinc. Step heights were measured for each at position 3 (the position found with OrbiSIMS to have the most deposition). JFTOT RME was found to be too topographical to measure the step, indicating its deposit was too thin for this approach. The data for JFTOT LMW PIBSI and JFTOT Zinc is presented in Table A33. The craters are of comparable thickness to those of IDIDs seen in Section 4.2.1, though the IDIDs were highly varied, including deposits both thicker and thinner than those of the JFTOTs

here. JFTOT Zinc's deposit at the central, thickest position is likely significantly thicker than JFTOT LMW PIBSI's, though the step size for each cross-section is highly variable, giving a large SD and indicating considerable topography. By position 4, JFTOT Zinc's crater is much shallower, with an average step size under a fifth of that of position 3. Therefore, the position where the heating is focused (position 3) produces much more deposit than other positions of the JFTOT tube.

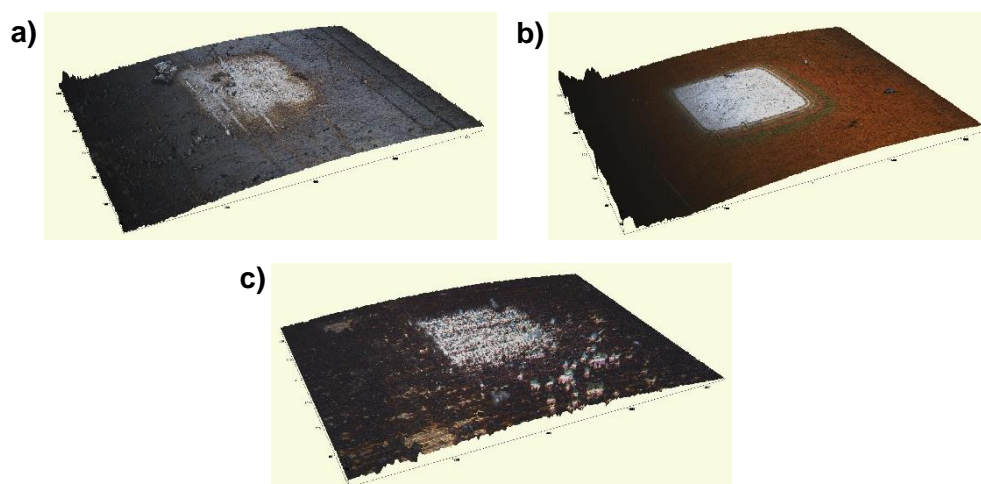


Figure A21: Profilometry of OrbiSIMS craters at position 3 of a) JFTOT RME, b) JFTOT LMW PIBSI, and c) JFTOT Zinc.

Table A33: JFTOT profilometry crater step size data.

JFTOT Sample-position		Side 1 ( $\mu\text{m}$ )	Side 2 ( $\mu\text{m}$ )	1 + 2 average ( $\mu\text{m}$ )
LMW PIBSI-3	Min	1.03	0.42	
	Max	0.48	0.96	
	Average	0.82	0.79	0.81
	St. dev	0.14	0.15	0.20
Zinc-3	Min	1.42	0.41	
	Max	0.05	2.67	
	Average	1.07	1.70	1.39
	St. dev	0.39	0.58	0.70
Zinc-4	Min	0.37	0.08	
	Max	0.08	0.41	
	Average	0.19	0.23	0.21
	St. dev	0.11	0.10	0.15



## 3.3. SEM-EDS

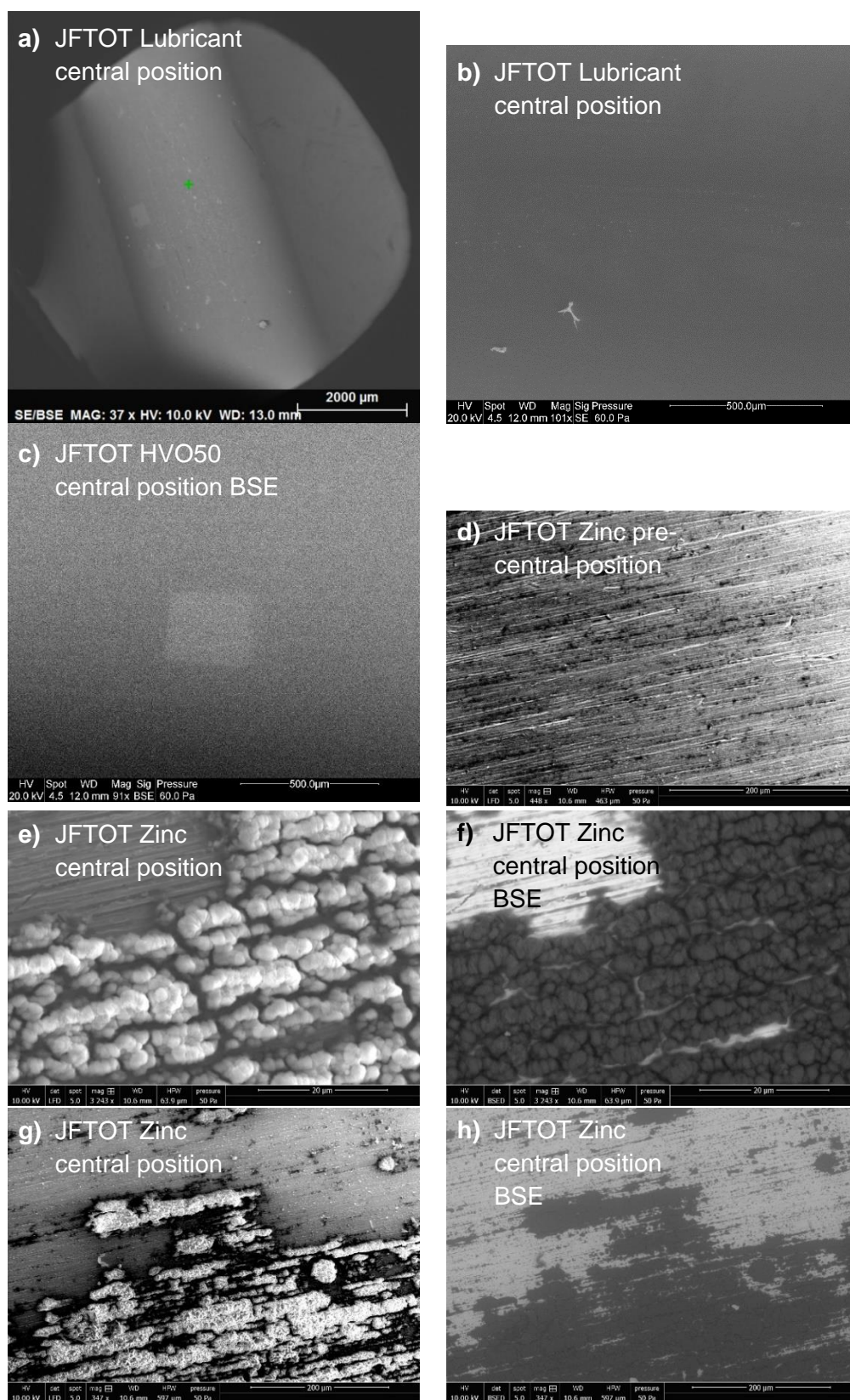


Figure A22: SEM images for JFTOT Lubricant, JFTOT HVO50 and JFTOT Zinc. All images are secondary electron images except where labelled BSE (backscatter).



SEM had limited utility for JFTOT samples due to the thin nature of the deposit. This meant there were very few surface features to view and meant that EDS detected primarily substrate atoms. Only JFTOT Zinc, with evidence of the thickest/most developed carbonaceous deposit (visibly darkest in colour, largest PAH distributions (Section 5.2.1.2) indicating widespread deposit formation, and thickest deposit by profilometry), had a topographical sample with features visible in SEM (Figure A22d-h), finding a central-position deposit with a granular appearance, as well as a “streaky” appearance in other areas. This resembles the appearance of published SEM micrographs of IDID samples as seen in Section 1.3.1.1 and the IDIDs analysed in Chapter 3 (Figure 3.1).

EDS also had very limited utility in this work due to the thin deposits, generally only detecting substrate elements with small amounts deposit elements. XPS was found to be better for elemental analysis, as well as providing extra chemical information that effectively characterises JFTOT deposits alongside OrbiSIMS data. Again, it was most effective for JFTOT Zinc, where maps could show the distribution of elements of interest, which were widely distributed (Figure A23).

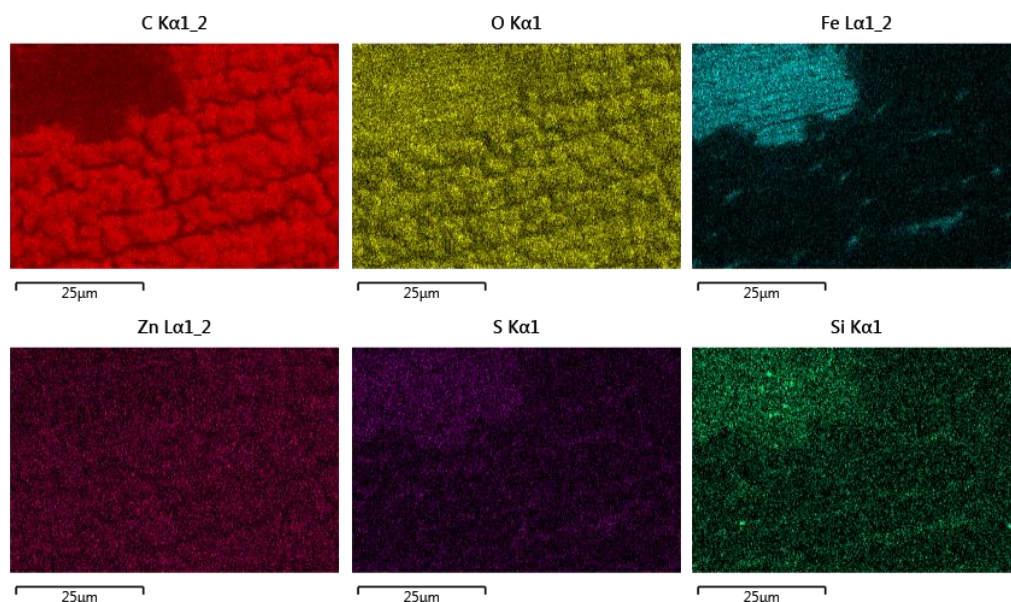


Figure A23: SEM-EDS image maps for JFTOT Zinc central position showing elements of interest.

### 3.4. PCA of JFTOT Samples

Here, all PCA results for PCs 1-6 are presented with tables of the key highest scoring ions for each PC. Some of these figures are part of the main text but are also included here as a complete record of the PCA results.

#### 3.4.1. PCA Exclusions

When PCA was performed on all data, some results showed little correlation between samples/positions and could be assigned as either unexpected chemistries or could not be assigned despite attempts using ion calculation as described in Section 2.3.3.2.2 with elements informed by XPS. In depth profiles, these ions were generally surface and near-surface exclusive. Some examples of this are shown in Figure A24, where in JFTOT Na + DDSA position 3, these chemistries are found above the deposit material. Identified contaminants were of:

- Positive polarity:
  - Saturated ammonium ions (e.g.  $\text{C}_{28}\text{H}_{60}\text{N}^+$ ,  $\text{C}_{26}\text{H}_{56}\text{N}^+$ )
  - Unknown series of high mass ions (including 873.6534, 901.6846)
- Negative polarity:
  - Silicon-containing/PDMS (e.g.  $\text{SiCH}_3\text{O}_3^-$ )
  - Alkylbenzene sulfonate (ABS) (e.g.  $\text{C}_{10}\text{H}_9\text{SO}_3^-$ )

Note that these are not necessarily all contaminant species on the samples; these were ions identified as very likely of surface contaminant origin and were significant enough in intensity to convolute PCA such that their removal was required to achieve good results. All of these ions affected the organic PCA (<.7 mass filtering).

JFTOT Zinc used a steel JFTOT tube while others, including the clean JFTOT tube used to remove contaminants and substrate ions from the peak list, were aluminium-magnesium. Hence, metal oxide/hydroxide ions from the steel persisted and convoluted PCA, so were removed manually. Examples in positive polarity include  $\text{Fe}_2\text{O}_6\text{H}_8^+$ ,  $\text{CaFeO}_6\text{H}_8^+$  and  $\text{CrFeO}_7\text{H}_6^+$ , and in negative polarity include  $\text{FeO}_3^-$ ,  $\text{CrO}_3^-$  and  $\text{MoO}_3^-$ . Depth profiles of these ions are shown in Figure A25 for position 2 of JFTOT Zinc, showing that they appear after

markers of organic/carbonaceous material ( $C_9H_7^+$  and  $C_9H_7^-$ ) and are strong towards the end of the profiles.

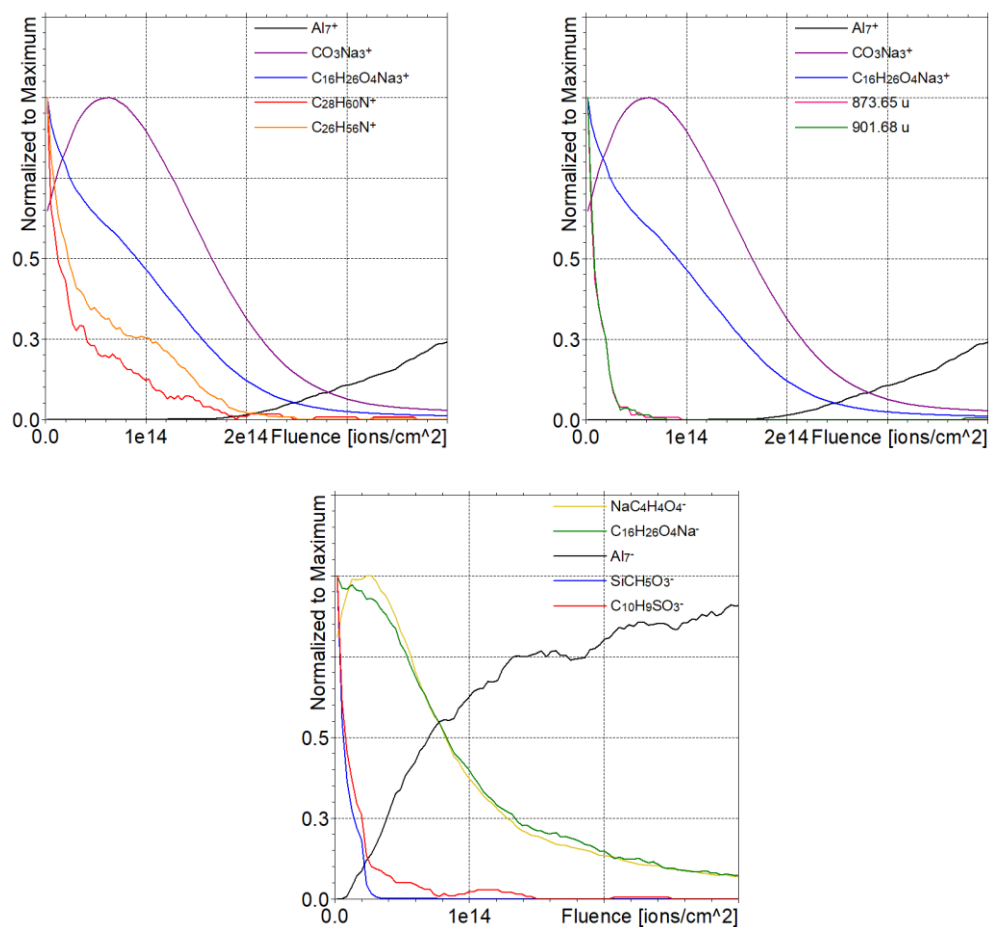


Figure A24: Depth profiles of example contaminants identified in PCA, for JFTOT Na + DDSA position 3.

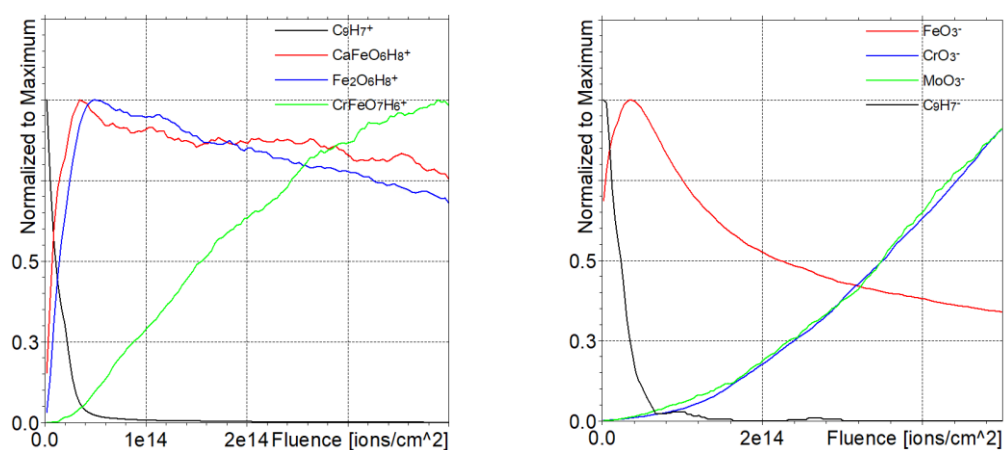


Figure A25: Depth profiles of example JFTOT Zinc steel substrate ions identified in PCA, for JFTOT Zinc position 2.

## 3.4.2. Positive polarity &lt;0.7 Mass Filtered PCA Results

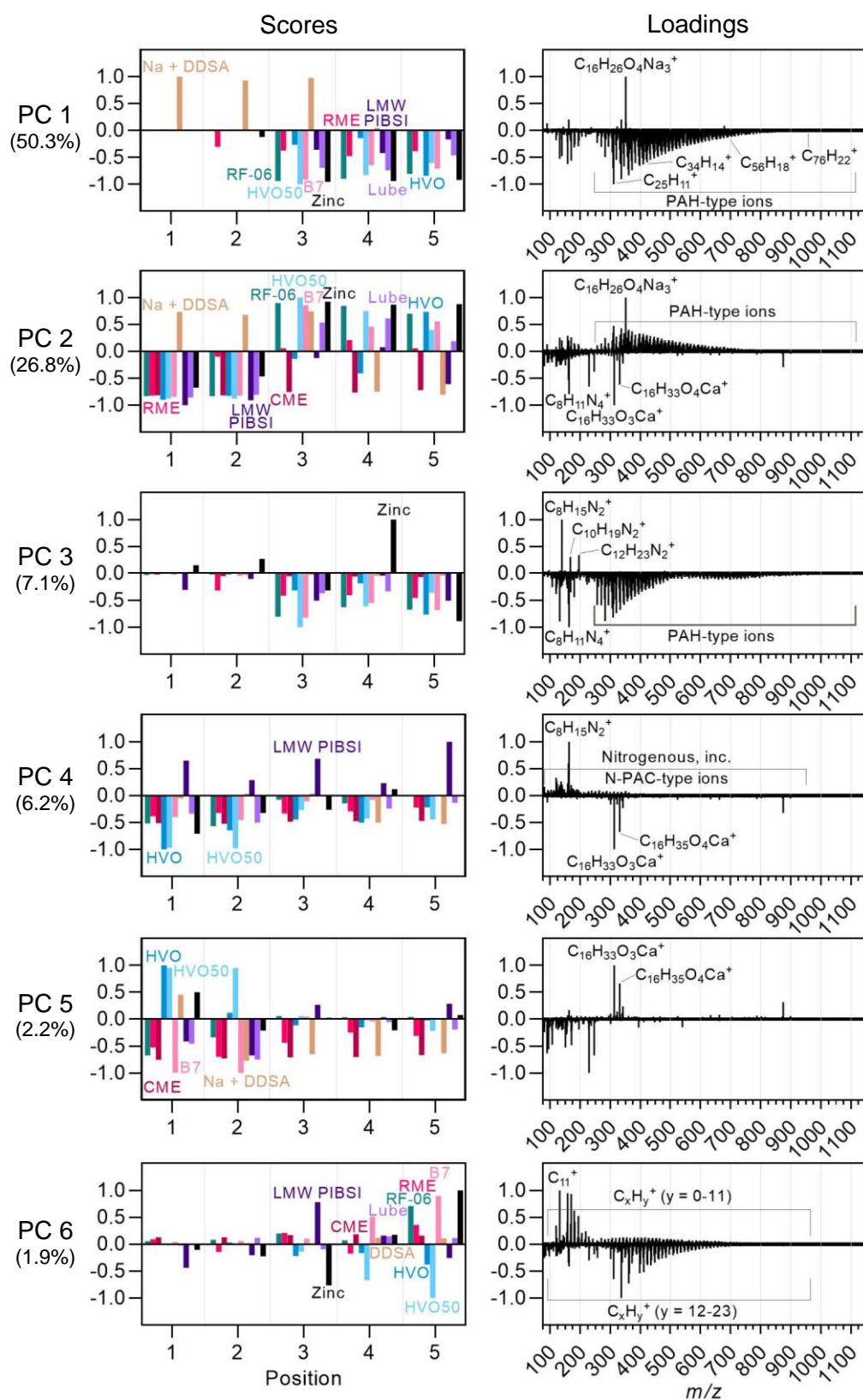


Figure A26: PCA results, scores and loadings normalised in both directions (positive polarity, &lt;0.7 mass filtering).

Table A34: PCA loadings (normalised to maximum) (positive polarity, <0.7 mass filtering). Column “#” is the rank of the ion in the loadings.

PC 1 Positive loadings (normalised to max)				PC 1 Negative loadings (normalised to max)			
#	m/z	Loading	Assignment	#	m/z	Loading	Assignment
1	351.1518	1.000	C <sub>16</sub> H <sub>26</sub> O <sub>4</sub> Na <sub>3</sub> <sup>+</sup>	1	311.0853	-0.097	C <sub>25</sub> H <sub>11</sub> <sup>+</sup>
2	337.1368	0.207	C <sub>15</sub> H <sub>24</sub> O <sub>4</sub> Na <sub>3</sub> <sup>+</sup>	2	337.1009	-0.088	C <sub>27</sub> H <sub>13</sub> <sup>+</sup>
3	162.149	0.206	C <sub>8</sub> H <sub>20</sub> NO <sub>2</sub> <sup>+</sup>	3	361.1009	-0.081	C <sub>29</sub> H <sub>13</sub> <sup>+</sup>
5	90.0913	0.136	C <sub>4</sub> H <sub>12</sub> NO <sup>+</sup>	8	398.1087	-0.064	C <sub>32</sub> H <sub>14</sub> <sup>+</sup>
5	372.0931	0.551	C <sub>14</sub> H <sub>22</sub> O <sub>4</sub> Na <sub>3</sub> <sup>+</sup>	11	158.0149	-0.060	C <sub>13</sub> H <sub>2</sub> <sup>+</sup>
6	144.0158	0.074	C <sub>5</sub> H <sub>6</sub> O <sub>2</sub> Na <sub>2</sub> <sup>+</sup>	22	131.9993	-0.051	C <sub>11</sub> <sup>+</sup>
7	237.0090	0.064	C <sub>8</sub> H <sub>8</sub> O <sub>4</sub> Na <sub>3</sub> <sup>+</sup>	45	507.1166	-0.037	C <sub>41</sub> H <sub>15</sub> <sup>+</sup>

Alongside Na-DDS, PC 1 has high loadings for formulae matching *N*-Butyldiethanolamine (C<sub>8</sub>H<sub>20</sub>NO<sub>2</sub><sup>+</sup>) and diethylhydroxylamine (C<sub>4</sub>H<sub>12</sub>NO<sup>+</sup>), two other commercially available corrosion inhibitors which were not intentionally added to the fuel in this JFTOT run though appear to have been present (207, 208).

PC 2 Positive loadings (normalised to max)				PC 2 Negative loadings (normalised to max)			
#	m/z	Loading	Assignment	#	m/z	Loading	Assignment
1	351.1518	1.000	C <sub>16</sub> H <sub>26</sub> O <sub>4</sub> Na <sub>3</sub> <sup>+</sup>	1	313.2049	-0.192	C <sub>16</sub> H <sub>33</sub> O <sub>3</sub> Ca <sup>+</sup>
2	311.0853	0.477	C <sub>25</sub> H <sub>11</sub> <sup>+</sup>	2	163.0976	-0.153	C <sub>8</sub> H <sub>11</sub> N <sub>4</sub> <sup>+</sup>
3	337.1009	0.429	C <sub>27</sub> H <sub>13</sub> <sup>+</sup>	3	229.0015	-0.126	<sup>13</sup> CC <sub>18</sub> <sup>+</sup>
4	361.1009	0.403	C <sub>29</sub> H <sub>13</sub> <sup>+</sup>	4	331.2155	-0.119	C <sub>16</sub> H <sub>35</sub> O <sub>4</sub> Ca <sup>+</sup>
9	398.1087	0.333	C <sub>32</sub> H <sub>14</sub> <sup>+</sup>	5	161.0819	-0.102	C <sub>8</sub> H <sub>9</sub> N <sub>4</sub> <sup>+</sup>
16	158.0149	0.290	C <sub>13</sub> H <sub>2</sub> <sup>+</sup>				
25	131.9993	0.257	C <sub>11</sub> <sup>+</sup>				

PC 3 Positive loadings (normalised to max)				PC 3 Negative loadings (normalised to max)			
#	m/z	Loading	Assignment	#	m/z	Loading	Assignment
1	139.1228	1.000	C <sub>8</sub> H <sub>15</sub> N <sub>2</sub> <sup>+</sup>	1	163.0976	-0.052	C <sub>8</sub> H <sub>11</sub> N <sub>4</sub> <sup>+</sup>
2	195.1854	0.342	C <sub>12</sub> H <sub>23</sub> N <sub>2</sub> <sup>+</sup>	2	131.9993	-0.046	C <sub>11</sub> <sup>+</sup>
3	167.154	0.306	C <sub>10</sub> H <sub>19</sub> N <sub>2</sub> <sup>+</sup>	3	283.054	-0.046	C <sub>23</sub> H <sub>7</sub> <sup>+</sup>
4	193.1697	0.075	C <sub>12</sub> H <sub>21</sub> N <sub>2</sub> <sup>+</sup>	4	309.0696	-0.043	C <sub>25</sub> H <sub>9</sub> <sup>+</sup>
5	140.1261	0.062	<sup>13</sup> CC <sub>7</sub> H <sub>15</sub> N <sub>2</sub> <sup>+</sup>	5	320.0619	-0.038	C <sub>26</sub> H <sub>8</sub> <sup>+</sup>
6	96.0683	0.059	C <sub>5</sub> H <sub>8</sub> N <sub>2</sub> <sup>+</sup>				

PC 3 found nitrogen-containing ions present at JFTOT Zinc position 4. Their origin is unknown but, being localised at position 4, could be surface contamination.

PC 4 Positive loadings (normalised to max)				PC 4 Negative loadings (normalised to max)			
#	<i>m/z</i>	Loading	Assignment	#	<i>m/z</i>	Loading	Assignment
1	163.0976	1.000	C <sub>8</sub> H <sub>11</sub> N <sub>4</sub> <sup>+</sup>	1	313.2049	-0.227	C <sub>16</sub> H <sub>33</sub> O <sub>3</sub> Ca <sup>+</sup>
2	161.0819	0.595	C <sub>8</sub> H <sub>9</sub> N <sub>4</sub> <sup>+</sup>	2	331.2155	-0.152	C <sub>16</sub> H <sub>35</sub> O <sub>4</sub> Ca <sup>+</sup>
3	120.0555	0.331	C <sub>6</sub> H <sub>6</sub> N <sub>3</sub> <sup>+</sup>	6	323.2275	-0.038	C <sub>18</sub> H <sub>35</sub> O <sub>2</sub> Ca <sup>+</sup>
6	140.0493	0.229	C <sub>10</sub> H <sub>6</sub> N <sup>+</sup>	7	120.0555	-0.030	SiC <sub>3</sub> H <sub>11</sub> O <sup>+</sup>
12	140.0817	0.192	C <sub>6</sub> H <sub>10</sub> N <sub>3</sub> O <sup>+</sup>	8	122.0712	-0.024	C <sub>18</sub> H <sub>35</sub> O <sub>3</sub> Ca <sup>+</sup>
17	124.0392	0.136	C <sub>6</sub> H <sub>6</sub> NO <sub>2</sub> <sup>+</sup>	9	136.0868	-0.019	C <sub>16</sub> H <sub>31</sub> O <sub>2</sub> Ca <sup>+</sup>
40	264.0806	0.097	C <sub>20</sub> H <sub>10</sub> N <sup>+</sup>				

The structure of C<sub>6</sub>H<sub>10</sub>N<sub>3</sub>O<sup>+</sup> is unidentified, however its N<sub>3</sub>O motif suggests it includes oxygen from the succinimide as well as several nitrogen atoms from the TEPA component.

PC 5 Positive loadings (normalised to max)				PC 5 Negative loadings (normalised to max)			
#	<i>m/z</i>	Loading	Assignment	#	<i>m/z</i>	Loading	Assignment
1	351.1518	1.000	C <sub>16</sub> H <sub>33</sub> O <sub>3</sub> Ca <sup>+</sup>	1	229.0015	-0.121	<sup>13</sup> CC <sub>18</sub> <sup>+</sup>
2	139.1228	0.662	C <sub>16</sub> H <sub>35</sub> O <sub>4</sub> Ca <sup>+</sup>	2	247.012	-0.081	?
5	163.0976	0.168	C <sub>8</sub> H <sub>11</sub> N <sub>4</sub> <sup>+</sup>	3	90.0913	-0.077	C <sub>4</sub> H <sub>12</sub> NO <sup>+</sup>
6	323.2275	0.146	C <sub>18</sub> H <sub>35</sub> O <sub>2</sub> Ca <sup>+</sup>	4	95.0160	-0.068	?
7	339.2207	0.114	C <sub>18</sub> H <sub>35</sub> O <sub>3</sub> Ca <sup>+</sup>	5	151.0239	-0.064	Si <sub>2</sub> C <sub>3</sub> H <sub>11</sub> O <sub>3</sub> <sup>+</sup>

PC 6 Positive loadings (normalised to max)				PC 6 Negative loadings (normalised to max)			
#	<i>m/z</i>	Loading	Assignment	#	<i>m/z</i>	Loading	Assignment
1	131.9993	1.000	C <sub>11</sub> <sup>+</sup>	1	337.1009	-0.664	C <sub>27</sub> H <sub>13</sub> <sup>+</sup>
2	158.0149	0.947	C <sub>13</sub> H <sub>2</sub> <sup>+</sup>	2	361.1009	-0.485	C <sub>29</sub> H <sub>13</sub> <sup>+</sup>
3	170.0148	0.933	C <sub>14</sub> H <sub>2</sub> <sup>+</sup>	5	398.1087	-0.361	C <sub>32</sub> H <sub>14</sub> <sup>+</sup>
4	179.9992	0.624	C <sub>15</sub> <sup>+</sup>	6	411.1165	-0.346	C <sub>33</sub> H <sub>15</sub> <sup>+</sup>
15	227.9993	0.145	C <sub>19</sub> <sup>+</sup>	7	163.0976	-0.276	C <sub>8</sub> H <sub>11</sub> N <sub>4</sub> <sup>+</sup>
16	368.0618	0.130	C <sub>30</sub> H <sub>8</sub> <sup>+</sup>	11	422.1087	-0.242	C <sub>34</sub> H <sub>14</sub> <sup>+</sup>
				13	161.0819	-0.230	C <sub>8</sub> H <sub>9</sub> N <sub>4</sub> <sup>+</sup>

## 3.4.3. Negative polarity &lt;0.7 Mass Filtered PCA Results

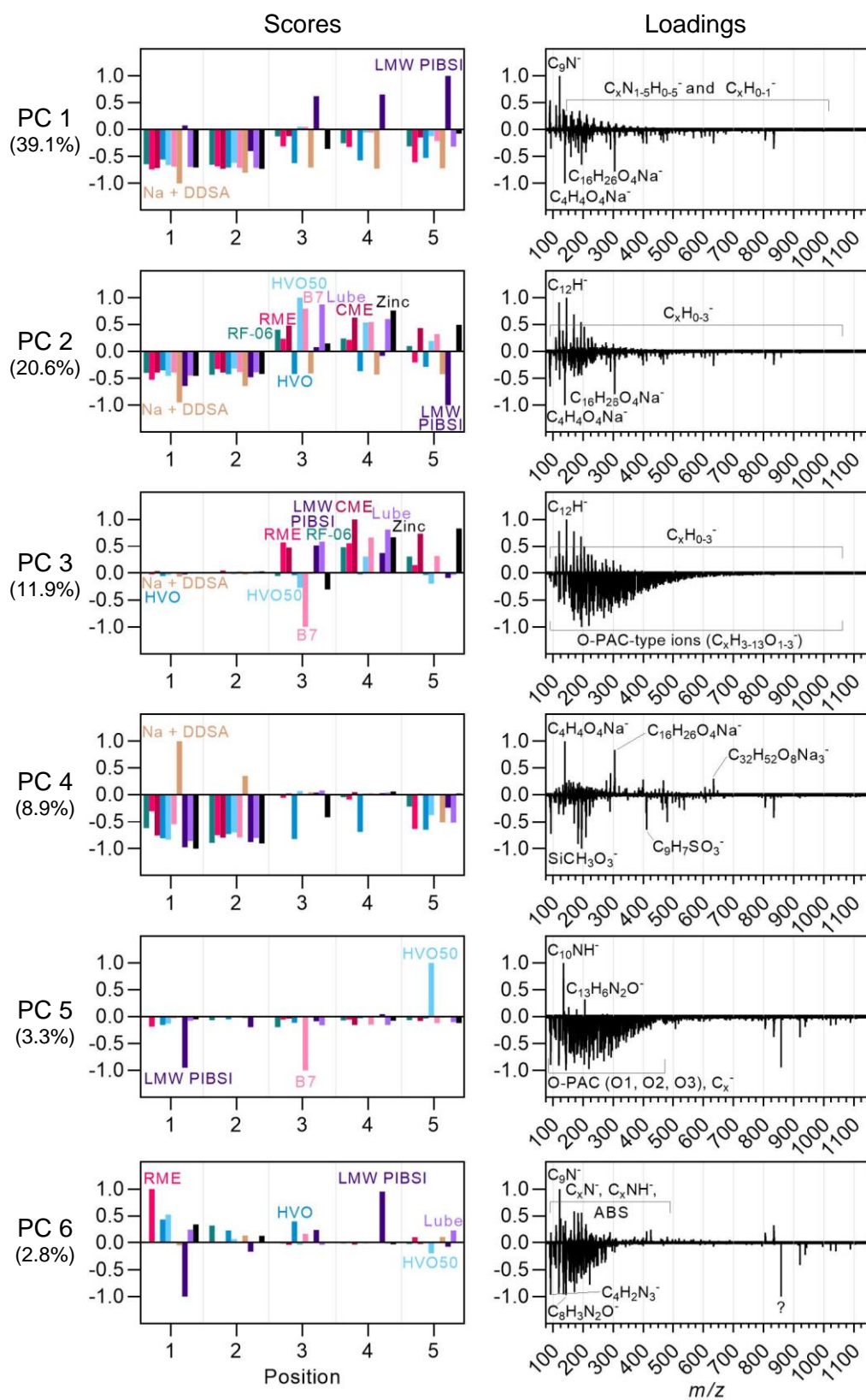


Figure A27: PCA results, scores and loadings normalised in both directions (negative polarity, &lt;0.7 mass filtering).



Table A35: PCA loadings (normalised to maximum) (negative polarity, <0.7 mass filtering).

PC 1 Positive loadings (normalised to max)				PC 1 Negative loadings (normalised to max)			
#	m/z	Loading	Assignment	#	m/z	Loading	Assignment
1	122.0036	1.000	C <sub>9</sub> N <sup>-</sup>	1	139.0014	-0.095	C <sub>4</sub> H <sub>4</sub> O <sub>4</sub> Na <sup>-</sup>
2	90.0092	0.544	C <sub>4</sub> N <sub>3</sub> <sup>-</sup>	2	305.1742	-0.074	C <sub>16</sub> H <sub>26</sub> O <sub>4</sub> Na <sup>-</sup>
3	110.0037	0.454	C <sub>8</sub> N <sup>-</sup>	3	195.0123	-0.062	C <sub>9</sub> H <sub>7</sub> SO <sub>3</sub> <sup>-</sup>
4	89.0144	0.448	C <sub>5</sub> N <sub>2</sub> H <sup>-</sup>	4	159.024	-0.048	C <sub>13</sub> H <sub>3</sub> <sup>-</sup>
22	145.0083	0.272	C <sub>12</sub> H <sup>-</sup>	5	187.0189	-0.043	C <sub>14</sub> H <sub>3</sub> O <sup>-</sup>
26	141.0210	0.256	C <sub>7</sub> HN <sub>4</sub> <sup>-</sup>				

PC 2 Positive loadings (normalised to max)				PC 2 Negative loadings (normalised to max)			
#	m/z	Loading	Assignment	#	m/z	Loading	Assignment
1	145.0083	1.000	C <sub>12</sub> H <sup>-</sup>	1	139.0014	-0.272	C <sub>4</sub> H <sub>4</sub> O <sub>4</sub> Na <sup>-</sup>
2	120.0006	0.914	C <sub>10</sub> <sup>-</sup>	2	305.1742	-0.216	C <sub>16</sub> H <sub>26</sub> O <sub>4</sub> Na <sup>-</sup>
3	169.0084	0.690	C <sub>14</sub> H <sup>-</sup>	3	90.0092	-0.178	C <sub>4</sub> N <sub>3</sub> <sup>-</sup>
17	228.0006	0.252	C <sub>19</sub> <sup>-</sup>	4	122.0036	-0.143	C <sub>9</sub> N <sup>-</sup>
44	195.0452	0.116	C <sub>13</sub> H <sub>7</sub> O <sub>2</sub> <sup>-</sup>	7	183.0115	-0.122	C <sub>8</sub> H <sub>7</sub> SO <sub>3</sub> <sup>-</sup>

PC 3 Positive loadings (normalised to max)				PC 3 Negative loadings (normalised to max)			
#	m/z	Loading	Assignment	#	m/z	Loading	Assignment
1	145.0083	1.000	C <sub>12</sub> H <sup>-</sup>	1	195.0452	-0.692	C <sub>13</sub> H <sub>7</sub> O <sub>2</sub> <sup>-</sup>
2	120.0006	0.784	C <sub>10</sub> <sup>-</sup>	2	219.0452	-0.676	C <sub>15</sub> H <sub>7</sub> O <sub>2</sub> <sup>-</sup>
3	169.0084	0.778	C <sub>14</sub> H <sup>-</sup>	4	191.0503	-0.600	C <sub>14</sub> H <sub>7</sub> O <sup>-</sup>
4	193.0084	0.682	C <sub>16</sub> H <sup>-</sup>	6	235.0402	-0.547	C <sub>15</sub> H <sub>7</sub> O <sub>3</sub> <sup>-</sup>
12	228.0006	0.343	C <sub>19</sub> <sup>-</sup>	31	343.0766	-0.420	C <sub>25</sub> H <sub>11</sub> O <sub>2</sub> <sup>-</sup>
27	122.0036	0.254	C <sub>9</sub> N <sup>-</sup>	34	137.0397	-0.402	C <sub>11</sub> H <sub>5</sub> <sup>-</sup>

PC 3 in the positive direction describes carbonaceous material (generally C<sub>x</sub>H<sub>0-3</sub><sup>-</sup> ions with some C<sub>x</sub>N<sup>-</sup>) and shows that most samples have high intensities of these ions at positions 3-5, where their deposits are visibly concentrated. In the negative direction are O-PAHs, with results described in Section 3.6.

PC 4 Positive loadings (normalised to max)				PC 4 Negative loadings (normalised to max)			
#	m/z	Loading	Assignment	#	m/z	Loading	Assignment
1	163.0976	1.000	C <sub>4</sub> H <sub>4</sub> O <sub>4</sub> Na <sup>-</sup>	1	195.0123	-0.073	C <sub>9</sub> H <sub>7</sub> SO <sub>3</sub> <sup>-</sup>
2	161.0819	0.595	C <sub>16</sub> H <sub>26</sub> O <sub>4</sub> Na <sup>-</sup>	2	183.0115	-0.066	C <sub>8</sub> H <sub>7</sub> SO <sub>3</sub> <sup>-</sup>
3	120.0555	0.331	C <sub>15</sub> H <sub>24</sub> O <sub>4</sub> Na <sup>-</sup>	6	209.0279	-0.058	C <sub>10</sub> H <sub>9</sub> SO <sub>3</sub> <sup>-</sup>
6	140.0493	0.229	C <sub>15</sub> <sup>13</sup> CH <sub>26</sub> O <sub>4</sub> Na <sup>-</sup>	7	93.0013	-0.053	SiCH <sub>5</sub> O <sub>3</sub> <sup>-</sup>
12	140.0817	0.192	C <sub>32</sub> H <sub>52</sub> O <sub>8</sub> Na <sub>3</sub> <sup>-</sup>	8			

PC 5 Positive loadings (normalised to max)				PC 5 Negative loadings (normalised to max)			
#	m/z	Loading	Assignment	#	m/z	Loading	Assignment
1	135.0120	1.000	C <sub>10</sub> NH <sup>-</sup>	1	143.0247	-0.048	C <sub>8</sub> H <sub>3</sub> N <sub>2</sub> O <sup>-</sup>
2	206.0497	0.323	C <sub>13</sub> H <sub>6</sub> N <sub>2</sub> O <sup>-</sup>	2	219.0452	-0.047	C <sub>15</sub> H <sub>7</sub> O <sub>2</sub> <sup>-</sup>
3	152.0389	0.191	C <sub>10</sub> H <sub>4</sub> N <sub>2</sub> <sup>-</sup>	3	858.6956	-0.046	?
4	178.0186	0.138	C <sub>11</sub> H <sub>2</sub> N <sub>2</sub> O <sup>-</sup>	4	119.0252	-0.044	C <sub>6</sub> H <sub>3</sub> N <sub>2</sub> O <sup>-</sup>
				5	92.0251	-0.043	C <sub>4</sub> H <sub>2</sub> N <sub>3</sub> <sup>-</sup>



PC 6 Positive loadings (normalised to max)				PC 6 Negative loadings (normalised to max)			
#	<i>m/z</i>	Loading	Assignment	#	<i>m/z</i>	Loading	Assignment
1	122.0036	1.000	C <sub>9</sub> N <sup>-</sup>	1	858.6956	-0.583	?
2	170.0044	0.585	C <sub>13</sub> N <sup>-</sup>	2	143.0247	-0.565	C <sub>8</sub> H <sub>3</sub> N <sub>2</sub> O <sup>-</sup>
3	195.0123	0.559	C <sub>9</sub> H <sub>7</sub> SO <sub>3</sub> <sup>-</sup>	3	92.0251	-0.562	C <sub>4</sub> H <sub>2</sub> N <sub>3</sub> <sup>-</sup>
4	183.0115	0.557	C <sub>8</sub> H <sub>7</sub> SO <sub>3</sub> <sup>-</sup>	4	135.012	-0.558	C <sub>10</sub> NH <sup>-</sup>
				5	119.0252	-0.548	C <sub>6</sub> H <sub>3</sub> N <sub>2</sub> O <sup>-</sup>

## 3.4.4. Positive polarity &gt;0.7 Mass Filtered PCA Results

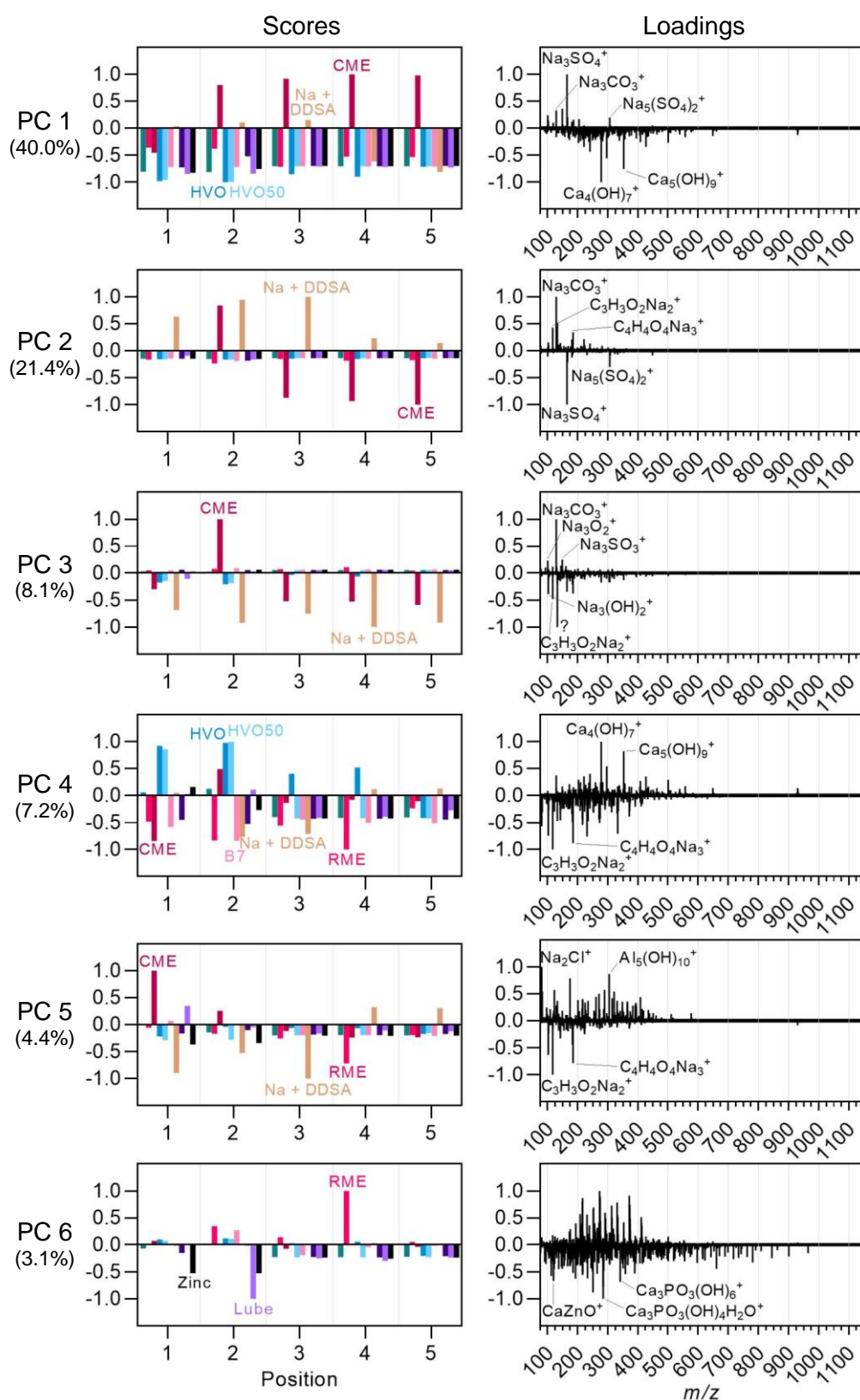


Figure A28: PCA results, scores and loadings normalised in both directions (positive polarity, &gt;0.7 mass filtering).

Table A36: PCA loadings (normalised to maximum) (positive polarity, &gt;0.7 mass filtering).

PC 1 Positive loadings (normalised to max)				PC 1 Negative loadings (normalised to max)			
#	m/z	Loading	Assignment	#	m/z	Loading	Assignment
1	164.9202	1.000	Na <sub>3</sub> SO <sub>4</sub> <sup>+</sup>	1	278.8688	-0.048	Ca <sub>4</sub> O <sub>7</sub> H <sub>7</sub> <sup>+</sup>
2	148.9253	0.364	Na <sub>3</sub> SO <sub>3</sub> <sup>+</sup>	2	352.8367	-0.036	Ca <sub>5</sub> O <sub>9</sub> H <sub>9</sub> <sup>+</sup>
3	128.953	0.335	Na <sub>3</sub> CO <sub>3</sub> <sup>+</sup>	3	296.8794	-0.027	Ca <sub>4</sub> O <sub>8</sub> H <sub>9</sub> <sup>+</sup>
4	100.9408	0.242	Na <sub>3</sub> S <sup>+</sup>	4	240.9219	-0.021	Ca <sub>3</sub> O <sub>7</sub> H <sub>9</sub> <sup>+</sup>
6	145.0083	0.272	Na <sub>5</sub> S <sub>2</sub> O <sub>8</sub> <sup>+</sup>				
7	141.0210	0.256	Na <sub>4</sub> PO <sub>5</sub> H <sub>2</sub> <sup>+</sup>				
11	180.8942	0.122	KNa <sub>2</sub> SO <sub>4</sub> <sup>+</sup>				

PC 2 Positive loadings (normalised to max)				PC 2 Negative loadings (normalised to max)			
#	m/z	Loading	Assignment	#	m/z	Loading	Assignment
1	128.953	1.000	Na <sub>3</sub> CO <sub>3</sub> <sup>+</sup>	1	164.9202	-0.387	Na <sub>3</sub> SO <sub>4</sub> <sup>+</sup>
2	132.9049	0.519	?	2	306.8503	-0.118	Na <sub>5</sub> S <sub>2</sub> O <sub>8</sub> <sup>+</sup>
3	116.9918	0.428	C <sub>3</sub> H <sub>3</sub> O <sub>2</sub> Na <sub>2</sub> <sup>+</sup>	3	166.9159	-0.085	Na <sub>3</sub> <sup>34</sup> SO <sub>4</sub> <sup>+</sup>
4	184.9807	0.344	Na <sub>3</sub> C <sub>4</sub> H <sub>4</sub> O <sub>4</sub> <sup>+</sup>	4	180.8942	-0.050	KNa <sub>2</sub> SO <sub>4</sub> <sup>+</sup>
5	220.9577	0.217	Na <sub>4</sub> AlO <sub>5</sub> H <sub>6</sub> <sup>+</sup>	5	166.9178	-0.044	Na <sub>3</sub> <sup>34</sup> SO <sub>4</sub> <sup>+</sup>
6	180.9631	0.210	Na <sub>3</sub> AlO <sub>5</sub> H <sub>5</sub> <sup>+</sup>	6	100.9408	-0.041	Na <sub>3</sub> S <sup>+</sup>

PC 3 Positive loadings (normalised to max)				PC 3 Negative loadings (normalised to max)			
#	m/z	Loading	Assignment	#	m/z	Loading	Assignment
1	128.953	1.000	Na <sub>3</sub> CO <sub>3</sub> <sup>+</sup>	1	132.9049	-0.988	?
2	148.9253	0.252	Na <sub>3</sub> SO <sub>3</sub> <sup>+</sup>	2	116.9918	-0.475	Na <sub>2</sub> C <sub>3</sub> H <sub>3</sub> O <sub>2</sub> <sup>+</sup>
3	100.9591	0.231	Na <sub>3</sub> O <sub>2</sub> <sup>+</sup>	3	102.9744	-0.385	Na <sub>3</sub> O <sub>2</sub> H <sub>2</sub> <sup>+</sup>
4	144.9272	0.141	Na <sub>2</sub> ClO <sub>4</sub> <sup>+</sup>	4	184.9807	-0.376	Na <sub>3</sub> C <sub>4</sub> H <sub>4</sub> O <sub>4</sub> <sup>+</sup>
5	160.9643	0.130	Na <sub>3</sub> MgO <sub>4</sub> H <sub>4</sub> <sup>+</sup>	5	164.9202	-0.340	Na <sub>3</sub> SO <sub>4</sub> <sup>+</sup>

PC 4 Positive loadings (normalised to max)				PC 4 Negative loadings (normalised to max)			
#	m/z	Loading	Assignment	#	m/z	Loading	Assignment
1	278.8688	1.000	Ca <sub>4</sub> O <sub>7</sub> H <sub>7</sub> <sup>+</sup>	1	116.9918	-0.187	C <sub>3</sub> H <sub>3</sub> O <sub>2</sub> Na <sub>2</sub> <sup>+</sup>
2	352.8367	0.823	Ca <sub>5</sub> O <sub>9</sub> H <sub>9</sub> <sup>+</sup>	2	184.9807	-0.165	Na <sub>3</sub> C <sub>4</sub> H <sub>4</sub> O <sub>4</sub> <sup>+</sup>
3	296.8794	0.540	Ca <sub>4</sub> O <sub>8</sub> H <sub>9</sub> <sup>+</sup>	4	102.9744	-0.139	Na <sub>3</sub> O <sub>2</sub> H <sub>2</sub> <sup>+</sup>
4	240.9219	0.403	Ca <sub>3</sub> O <sub>7</sub> H <sub>9</sub> <sup>+</sup>	6	80.9478	-0.106	Na <sub>2</sub> Cl <sup>+</sup>
5	128.953	0.372	Na <sub>3</sub> CO <sub>3</sub> <sup>+</sup>	9	182.9638	-0.091	C <sub>4</sub> H <sub>2</sub> O <sub>4</sub> Na <sub>3</sub> <sup>+</sup>

PC 5 Positive loadings (normalised to max)				PC 5 Negative loadings (normalised to max)			
#	m/z	Loading	Assignment	#	m/z	Loading	Assignment
1	80.9478	1.000	Na <sub>2</sub> Cl <sup>+</sup>	1	116.9918	-0.639	Na <sub>2</sub> C <sub>3</sub> H <sub>3</sub> O <sub>2</sub> <sup>+</sup>
2	304.9336	0.867	Al <sub>5</sub> O <sub>10</sub> H <sub>10</sub> <sup>+</sup>	2	184.9807	-0.503	Na <sub>3</sub> C <sub>4</sub> H <sub>4</sub> O <sub>4</sub> <sup>+</sup>
3	174.9285	0.786	Al <sub>4</sub> O <sub>4</sub> H <sub>3</sub> <sup>+</sup>	3	102.9744	-0.405	Na <sub>3</sub> O <sub>2</sub> H <sub>2</sub> <sup>+</sup>
4	122.9814	0.573	Al <sub>2</sub> O <sub>4</sub> H <sub>5</sub> <sup>+</sup>	4	182.9638	-0.285	Na <sub>3</sub> C <sub>4</sub> H <sub>2</sub> O <sub>4</sub> <sup>+</sup>
				5	142.9659	-0.211	Na <sub>4</sub> O <sub>3</sub> H <sub>3</sub> <sup>+</sup>

PC 6 Positive loadings (normalised to max)				PC 6 Negative loadings (normalised to max)			
#	m/z	Loading	Assignment	#	m/z	Loading	Assignment
1	272.9557	1.000	?	1	284.8683	-0.292	Ca <sub>3</sub> PO <sub>8</sub> H <sub>6</sub> <sup>+</sup>
2	370.9261	0.912	?	2	250.9127	-0.259	?
3	273.9576	0.907	?	3	284.8698	-0.228	?
4	274.9528	0.871	?	4	340.8264	-0.199	Ca <sub>4</sub> PO <sub>9</sub> H <sub>6</sub> <sup>+</sup>
5	216.9630	0.867	?	5	119.886	-0.195	CaZnO <sup>+</sup>

## 3.4.5. Negative polarity &gt;0.7 Mass Filtered PCA Results

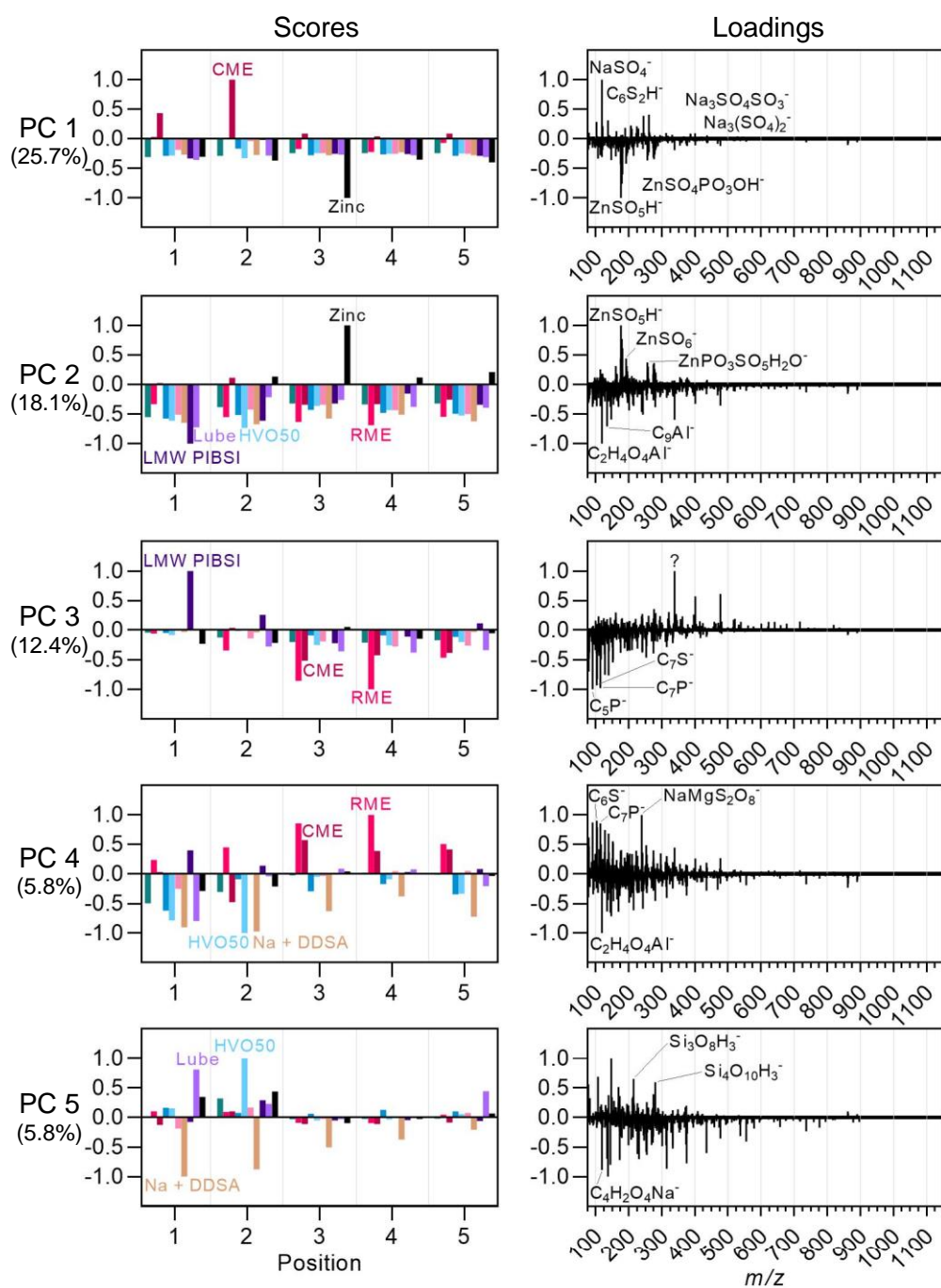


Figure A29: PCA results, scores and loadings normalised in both directions (negative polarity, >0.7 mass filtering).

Table A37: PCA loadings (normalised to maximum) (negative polarity, &gt;0.7 mass filtering).

PC 1 Positive loadings (normalised to max)				PC 1 Negative loadings (normalised to max)			
#	m/z	Loading	Assignment	#	m/z	Loading	Assignment
1	118.9421	1.000	NaSO <sub>4</sub> <sup>-</sup>	1	164.9202	-0.081	ZnSO <sub>5</sub> H <sup>-</sup>
2	260.8733	0.407	Na <sub>3</sub> S <sub>2</sub> O <sub>8</sub> <sup>-</sup>	4	306.8503	-0.035	ZnSO <sub>5</sub> <sup>-</sup>
3	244.8798	0.391	Na <sub>3</sub> S <sub>2</sub> O <sub>7</sub> <sup>-</sup>	5	166.9159	-0.034	ZnSO <sub>6</sub> <sup>-</sup>
4	136.9524	0.315	C <sub>6</sub> HS <sub>2</sub> <sup>-</sup>	6	256.8503	-0.029	ZnPSO <sub>8</sub> H <sub>2</sub> <sup>-</sup>
5	102.9473	0.285	NaSO <sub>3</sub> <sup>-</sup>	10	274.8188	-0.026	Zn <sub>2</sub> SO <sub>7</sub> H <sub>3</sub> <sup>-</sup>
8	224.9063	0.210	Na <sub>3</sub> CO <sub>3</sub> SO <sub>4</sub> <sup>-</sup>				

PC 2 Positive loadings (normalised to max)				PC 2 Negative loadings (normalised to max)			
#	m/z	Loading	Assignment	#	m/z	Loading	Assignment
1	164.9202	1.000	ZnSO <sub>5</sub> H <sup>-</sup>	1	118.993	-0.091	C <sub>2</sub> H <sub>4</sub> O <sub>4</sub> Al <sup>-</sup>
4	306.8503	0.438	ZnSO <sub>5</sub> <sup>-</sup>	2	134.9876	-0.065	C <sub>9</sub> Al <sup>-</sup>
5	166.9159	0.438	ZnSO <sub>6</sub> <sup>-</sup>	3	338.8991	-0.054	?
6	256.8503	0.376	ZnPSO <sub>8</sub> H <sub>2</sub> <sup>-</sup>	6	238.8792	-0.042	NaMgS <sub>2</sub> O <sub>8</sub> <sup>-</sup>
8	274.8188	0.337	Zn <sub>2</sub> SO <sub>7</sub> H <sub>3</sub> <sup>-</sup>	9	90.9742	-0.035	C <sub>5</sub> P <sup>-</sup>
15	114.9380	0.257	ZnO <sub>3</sub> H <sub>3</sub> <sup>-</sup>				

PC 3 Positive loadings (normalised to max)				PC 3 Negative loadings (normalised to max)			
#	m/z	Loading	Assignment	#	m/z	Loading	Assignment
1	338.8991	1.000	?	1	90.9742	-0.147	C <sub>5</sub> P <sup>-</sup>
2	476.8681	0.614	?	2	114.9743	-0.144	C <sub>7</sub> P <sup>-</sup>
3	400.8754	0.574	?	3	103.9726	-0.137	C <sub>6</sub> S <sup>-</sup>
4	276.9327	0.356	?	4	104.9805	-0.123	C <sub>6</sub> SH <sup>-</sup>
5	320.8884	0.306	?	8	78.941	-0.103	PSO <sup>-</sup>
6	160.9593	0.297	NaAl <sub>2</sub> O <sub>5</sub> H <sub>4</sub> <sup>-</sup>				

PC 3's positive loadings were unidentified and likely are a contaminant present in the LMW PIBSI, hence the predominant deposition at position 1 of the this sample.

PC 4 Positive loadings (normalised to max)				PC 4 Negative loadings (normalised to max)			
#	m/z	Loading	Assignment	#	m/z	Loading	Assignment
1	238.8792	1.000	NaMgS <sub>2</sub> O <sub>8</sub> <sup>-</sup>	1	118.993	-0.768	C <sub>2</sub> H <sub>4</sub> O <sub>4</sub> Al <sup>-</sup>
2	103.9726	0.900	C <sub>6</sub> S <sup>-</sup>	2	146.9612	-0.548	?
3	90.9742	0.873	C <sub>5</sub> P <sup>-</sup>	3	144.982	-0.503	?
4	114.9743	0.856	C <sub>7</sub> P <sup>-</sup>	4	168.9487	-0.489	?
5	104.9805	0.790	C <sub>6</sub> SH <sup>-</sup>	5	134.9876	-0.487	?
9	180.9631	0.615	PSO <sup>-</sup>				

PC 5 Positive loadings (normalised to max)				PC 5 Negative loadings (normalised to max)			
#	m/z	Loading	Assignment	#	m/z	Loading	Assignment
1	146.9612	1.000	?	1	136.9852	-0.716	?
2	106.9120	0.686	?	2	118.993	-0.636	C <sub>2</sub> H <sub>4</sub> O <sub>4</sub> Al <sup>-</sup>
3	214.9143	0.651	Si <sub>3</sub> O <sub>8</sub> H <sub>3</sub> <sup>-</sup>	3	314.9231	-0.618	?
7	274.8813	0.393	Si <sub>4</sub> O <sub>10</sub> H <sub>3</sub> <sup>-</sup>				
8	138.9525	0.379	Si <sub>2</sub> O <sub>5</sub> H <sub>3</sub> <sup>-</sup>				

### 3.5. LMW PIBSI and Nitrogenous supplementary information

#### 3.5.1. N-PAC MS/MS

Table A38: MS/MS results for N-PAC type ion  $C_{24}H_{10}N^+$  using NCE = 135 and width = 0.9.

Mass	Assignment	DBE	Intensity	Neutral loss
312.0808	$C_{24}H_{10}N^+$	20.5	N/A	Parent
310.0649	$C_{24}H_8N^+$	21.5	4.22E5	H <sub>2</sub> (1)
308.0494	$C_{24}H_6N^+$	22.5	2.77E5	H <sub>4</sub> (1)
286.0649	$C_{22}H_8N^+$	19.5	8.22E3	C <sub>2</sub> H <sub>2</sub> (1)
284.0494	$C_{22}H_6N^+$	20.5	1.31E5	C <sub>2</sub> H <sub>4</sub> (1)
282.0337	$C_{22}H_4N^+$	21.5	6.31E3	C <sub>2</sub> H <sub>6</sub> (1)

This MS/MS experiment, using a higher collision energy, showed more fragmentation than the lower collision energy experiment seen in Table 5.2.

Table A39: N-PAC ( $C_{24}H_{10}N^+$ ) MS/MS results (270 NCE, 0.9 width). Some intermediate mass ions are excluded.

Mass	Assignment	DBE	Intensity	Neutral loss
312.0808	$C_{24}H_{10}N^+$	20.5	N/A	Parent 1
312.0887	$C_{24}^{13}CH_{11}^+$	20.5	N/A	Parent 2
306.0418	$C_{24}^{13}CH_5^+$	23.5	2.37E3	H <sub>6</sub> (2)
304.0262	$C_{24}^{13}CH_3^+$	24.5	2.42E4	H <sub>8</sub> (2)
281.0384	$C_{23}H_5^+$	21.5	3.63E3	CH <sub>5</sub> N (1) C <sup>13</sup> CH <sub>6</sub> (2)
280.0261	$C_{22}C^{13}H_3^+$	22.5	1.38E4	C <sub>2</sub> H <sub>6</sub> (2)
279.0228	$C_{23}H_3^+$	22.5	4.83E4	CH <sub>7</sub> N (1) C <sup>13</sup> CH <sub>8</sub> (2)
...	...	...	...	...
179.9992	$C_{15}^+$	16	1.96E5	C <sub>9</sub> H <sub>10</sub> N (1) C <sub>9</sub> <sup>13</sup> CH <sub>11</sub> (2)
158.0149	$C_{13}H_2^+$	13	1.21E5	C <sub>11</sub> H <sub>8</sub> N (1) C <sub>11</sub> <sup>13</sup> CH <sub>9</sub> (2)
131.9993	$C_{11}^+$	12	2.17E5	C <sub>13</sub> H <sub>10</sub> N (1) C <sub>13</sub> <sup>13</sup> CH <sub>9</sub> (2)
110.0151	$C_9H_2^+$	9	2.33E5	C <sub>15</sub> H <sub>8</sub> N (1) C <sub>15</sub> <sup>13</sup> CH <sub>9</sub> (2)
86.0153	$C_7H_2^+$	7	1.88E5	C <sub>15</sub> H <sub>5</sub> N (1) C <sub>14</sub> <sup>13</sup> CH <sub>9</sub> (2)
85.0074	$C_7H^+$	7.5	9.76E4	C <sub>17</sub> H <sub>9</sub> N (1) C <sub>17</sub> <sup>13</sup> CH <sub>10</sub> (2)
63.0233	$C_5H_3^+$	4.5	1.05E5	C <sub>19</sub> H <sub>7</sub> N (1) C <sub>19</sub> <sup>13</sup> CH <sub>8</sub> (2)
61.0076	$C_5H^+$	5.5	5.13E4	C <sub>11</sub> H <sub>9</sub> N (1) C <sub>19</sub> <sup>13</sup> CH <sub>10</sub> (2)

In these MS/MS results, two parent ions were analysed due to proximity in the spectrum. As this spectrum was dense, containing PAHs and N-PACs, this was unavoidable when using necessary widths ( $0.9\ m/z$ ) to collect enough material for successful MS/MS. Nonetheless, fragment ions containing nitrogen with a loss of carbon and hydrogen were seen which confirms the assignment of the N-PAC.

### 3.5.2. LMW PIBSI-Associated OrbiSIMS Ions

Table A40: Succinimide and LMW PIBSI markers normalised intensities in samples of interest.

Ion	Position	Needle 8	Needle 6	Needle 10	LMW PIBSI	Lubricant
$C_6H_6NO_2^+$	1	N/A	2.37E-04	1.94E-03	3.43E-03	1.73E-04
	2	N/A	1.27E-04	7.28E-03	1.09E-03	7.69E-06
	3	N/A	5.41E-04	8.24E-04	3.14E-04	N/A
	4	3.70E-05	3.46E-03		4.15E-04	1.93E-06
	5	1.20E-04			5.29E-04	1.31E-05
$C_6H_8NO_2^+$	1	N/A	6.84E-05	1.09E-03	1.71E-03	1.15E-04
	2	N/A	2.19E-05	2.91E-03	2.36E-03	2.63E-06
	3	N/A	1.99E-04	6.51E-04	3.10E-04	N/A
	4	N/A	1.17E-03		2.19E-04	1.07E-06
	5	N/A			3.80E-04	8.01E-06
$C_8H_{12}NO_2^+$	1	N/A	N/A	1.67E-05	2.25E-04	1.61E-05
	2	N/A	N/A	6.88E-05	4.37E-04	N/A
	3	N/A	1.19E-06	1.41E-05	2.00E-05	N/A
	4	N/A	1.56E-05		1.60E-05	N/A
	5	N/A			4.15E-05	N/A
$C_6H_{10}N_3O^+$	1	N/A	1.05E-04	1.54E-03	1.74E-03	8.89E-05
	2	N/A	1.46E-05	3.38E-03	7.90E-04	1.07E-06
	3	N/A	6.38E-05	9.59E-04	1.78E-03	2.63E-06
	4	N/A	1.12E-03		6.96E-04	8.79E-07
	5	N/A			2.03E-03	5.03E-06
$C_8H_{11}N_4^+$	1	N/A	1.79E-04	1.95E-03	7.72E-03	4.68E-05
	2	N/A	4.70E-05	2.83E-03	2.95E-03	N/A
	3	N/A	2.22E-04	1.07E-03	7.31E-03	N/A
	4	N/A	1.81E-03		1.62E-03	N/A
	5	N/A			1.35E-02	N/A
$C_8H_9N_4^+$	1	N/A	1.25E-04	2.17E-03	5.39E-03	5.13E-05
	2	N/A	2.89E-05	2.61E-03	2.73E-03	N/A
	3	N/A	1.70E-04	1.07E-03	3.72E-03	8.29E-06
	4	N/A	1.58E-03		1.17E-03	1.67E-06
	5	N/A			7.64E-03	9.99E-06

### 3.5.3. N-PAC depth profiles

Like the trends for PAH ions in Section 5.2.1.3, N-PACs of N1-N3 in JFTOT LMW PIBSI position 3 show the same trend of larger PAHs (Figure A30a-c, pink) being deeper in the profile than smaller (green). Also like PAHs, N-PACs of lower H number are also found deeper (Figure A30d).

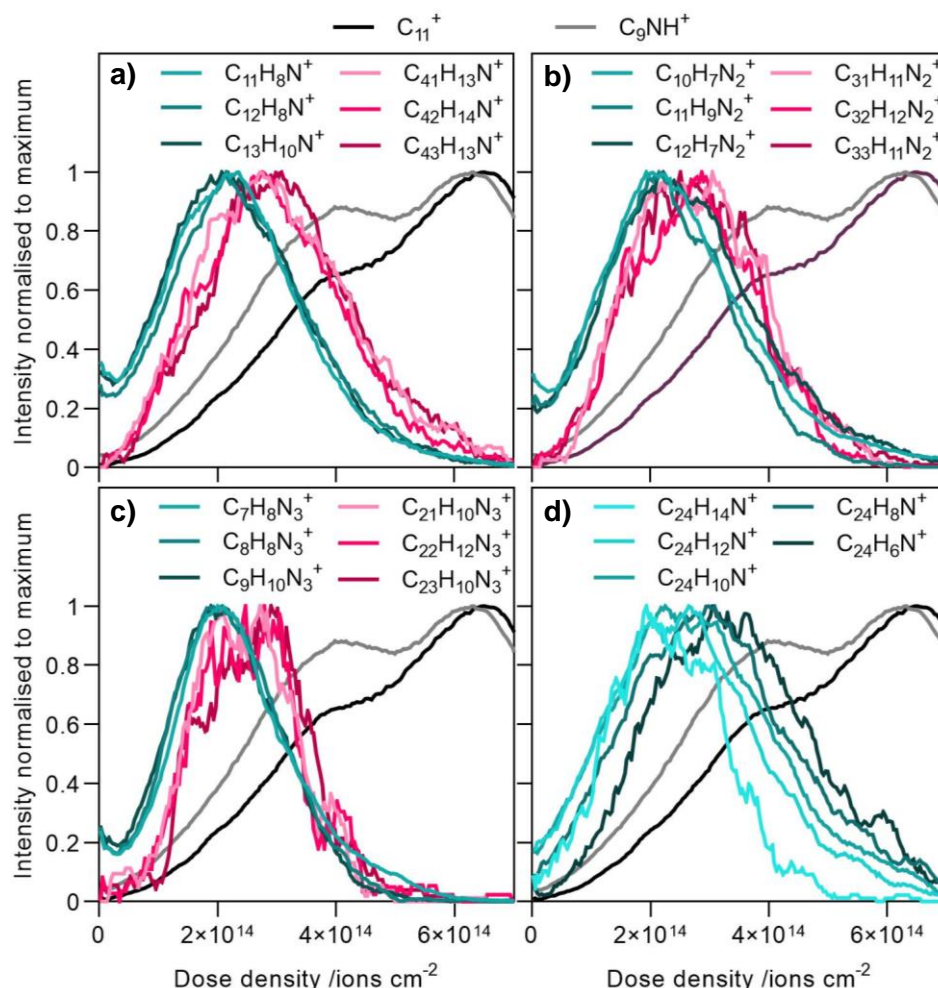


Figure A30: JFTOT LMW PIBSI position 3 depth profiles for N-PAC ions of a range of smaller (green) and larger (pink) masses for a) N1-, b) N2- and c) N3-ions, as well as for d) a range of H/C ratios (darker = decreasing) for N1-PAC ions of the same C number.

Negative polarity depth profiles for position 2 and 3 of JFTOT LMW PIBSI show similar trends to the positive polarity (Figure 5.8), with succinimide ions at the surface, followed by sub-surface hydrocarbon and N-containing ions, for which those of lower H number are found deeper in the profile. The lowest ions are carbonaceous ions, indicating the most carbonised deposit material next to the JFTOT substrate.



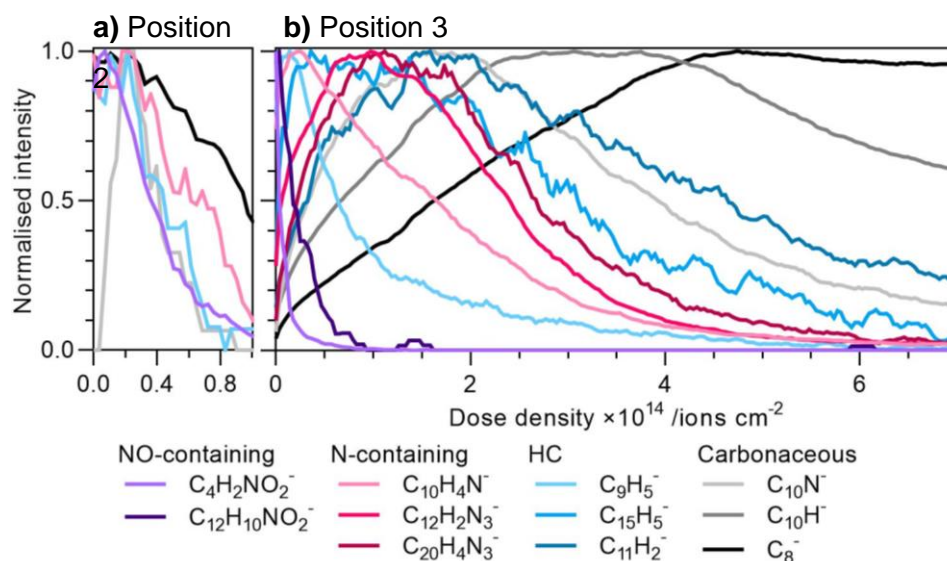


Figure A31: JFTOT 8 (LMW PIBSI) negative polarity depth profiles for PIBSI-related ions and hydrocarbon/carbonaceous ions for a) Position 2 and b) Position 3 (central).

### 3.6. Oxygen-containing polyaromatics

The negative polarity PCA revealed the presence of oxy-polyaromatic compounds (O-PACs), with PC 3 (<.7 mass filter, negative polarity) separating this chemistry from carbonaceous ( $\text{C}_x\text{H}_{0-3}^-$ ) ions (Figure A32a). This is a notable incorporation of another heteroatom into the carbonised deposit material analogously to the N-PACs and S- and P-containing carbonaceous ions discussed this far. It could be suggested that oxygen-containing deposit components could contribute to this type of deposit, however only position 3 of JFTOT B7, JFTOT Zinc and JFTOT HVO50 have significant scores correlating with this PC. If components of the B7 and HVO50 (RME biodiesel and HVO) experiments are contributing oxygen, they would contribute more so in JFTOT RME and JFTOT HVO, which have more of those same components. As this is not the case in the PCA results or the normalised peaks shown in Figure A32b, no discernible correlation can be found and further work would be required to investigate this type of chemistry.

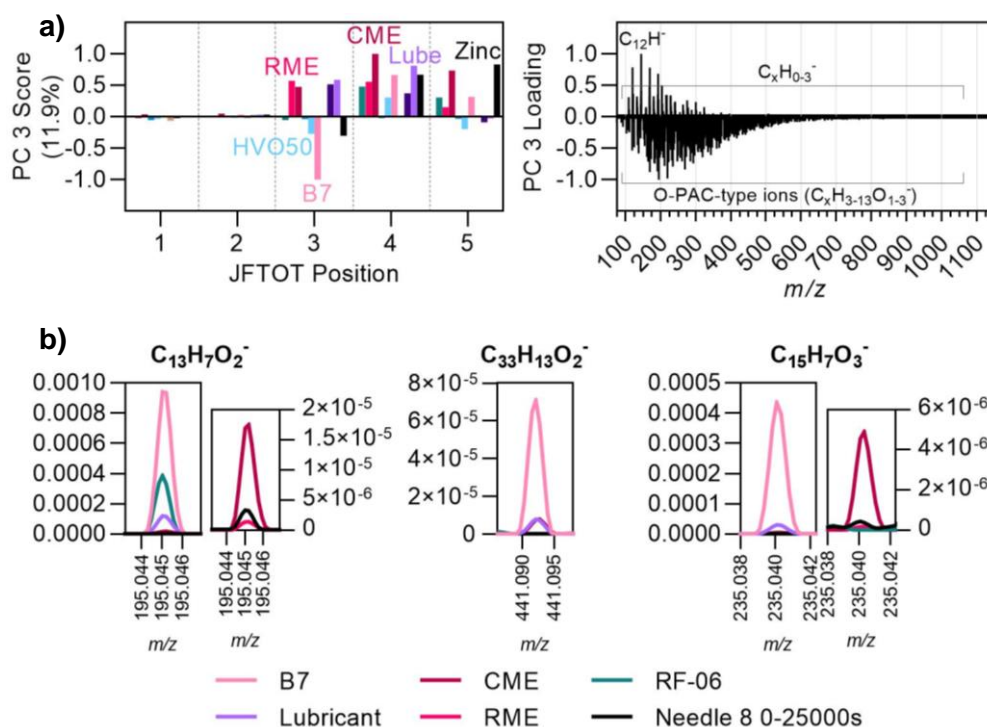


Figure A32: OrbiSIMS results for O-PAC ions, a) PC 3 results (<0.7 mass filter, negative polarity) and b) Normalised peaks for key O-PAC ions in JFTOT and IDID samples of interest.

### 3.7. S- and P-containing chemistries

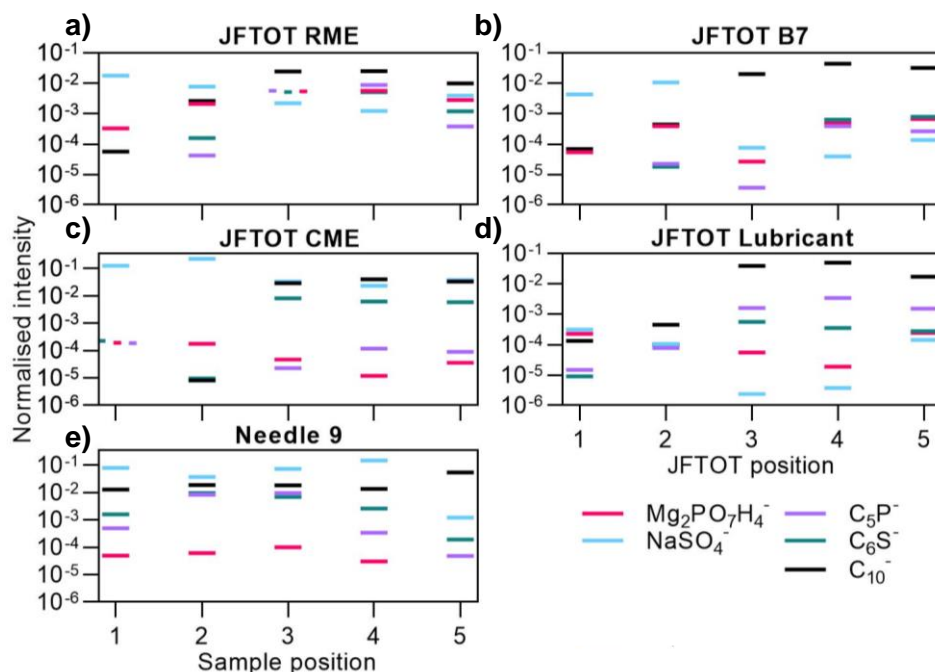


Figure A33: Normalised intensities of key ions at each position of JFTOTs RME, B7, CME, Lubricant, Needle 9.

The intensity distribution of S- and P-containing ions along the JFTOT tube supports that these elements are integrated into the carbonised deposit material prevalent at positions 3-5 of the JFTOT (Figure A33a). S- and P-carbonaceous ions ( $C_5P^-$  and  $C_6S^-$ ), alongside the carbonaceous ion  $C_{10}^-$ , have low normalised intensities at positions 1-2, with dramatic intensity increases at position 3 which vary by sample; JFTOT B7 was established as having much lower intensity peaks for  $C_5P^-$  and  $C_6S^-$  at position 3 (Figure 5.10b), but here it is seen that these become higher at positions 4 and 5 though remain significantly lower than JFTOT RME. The high intensity of  $C_6S^-$  relative to  $C_5P^-$  can be seen in JFTOT CME across positions 3 to 5, in line with the lack of phosphorus seen in its data XPS (Figure 5.10c). In Needle 9, these ions drop at position 5 which was a visibly less deposited area at the end of the needle shaft, possibly due to the high-pressure flow preventing build-up of deposit here as has been reported possible due to cavitation (81). Position 1 also has low intensity of  $C_5P^-$  and  $C_6S^-$  however it has the highest for  $C_{10}^-$ ; this position is before the presence of visible deposit and this carbonaceous ion is thought to be indicative of a DLC substrate on the needle. In contrast to carbonaceous ions, the salt ion  $NaSO_4^-$  is highest at early positions of each JFTOT (except Lubricant which has less of this salt), perhaps due to a lower temperature of deposition of salt material, while carbonaceous deposit is prevalent at positions 3-5 where the tube is hottest. Magnesium phosphate ( $Mg_2PO_7H_4^-$ ) salts appear to form at higher temperature positions; these salts primarily affect JFTOT RME, with the highest intensity at positions 3 and 4.

### 3.8. Biological Compounds in JFTOT RME

Table A41: Possible sterols and tocopherols in JFTOT RME sample from position 1.

Mass	Putative assignment [M+H] <sup>+</sup>	Suggested compound	Normalised intensity
395.3309	C <sub>28</sub> H <sub>43</sub> O <sup>+</sup>	Dehydroergosterol	1.90E-05
397.3465	C <sub>28</sub> H <sub>45</sub> O <sup>+</sup>	Ergocalciferol	6.18E-04
399.3623	C <sub>28</sub> H <sub>47</sub> O <sup>+</sup>	Brassicasterol	4.64E-06
409.3465	C <sub>29</sub> H <sub>45</sub> O <sup>+</sup>	Conicasterol B	1.01E-05
411.3638	C <sub>29</sub> H <sub>47</sub> O <sup>+</sup>	Elaesterol	8.83E-04
415.3587	C <sub>28</sub> H <sub>47</sub> O <sub>2</sub> <sup>-</sup>	γ-Tocopherol	5.92E-06
429.3742	C <sub>29</sub> H <sub>49</sub> O <sub>2</sub> <sup>-</sup>	α-Tocopherol	2.59E-06

In JFTOT RME, there are several ions with putative assignments that match biomolecules. These were present at position 1 and can be expected to break down at later positions when heated. Table A41 summarises ions identified as possible sterols and tocopherols. Of the three sterols reported as common in rapeseed oil (β-sitosterol, campesterol and brassicasterol), only a formula matching brassicasterol (C<sub>28</sub>H<sub>47</sub>O<sup>+</sup>) was found, which had the lowest intensity. For tocopherols, small peaks were present that could be assigned as γ-tocopherol (C<sub>28</sub>H<sub>47</sub>O<sub>2</sub><sup>-</sup>) and α-tocopherol (C<sub>29</sub>H<sub>49</sub>O<sub>2</sub><sup>-</sup>), the main tocopherols present in rapeseed oil (209, 210). The absence of these ions from JFTOT B7 suggests that blends used in the real world may not be affected by deposition of such compounds, whether simply due to their lower concentrations or a solubility or other effect. Further work would be required to confirm these compounds' assignments using MS/MS and explore their effects on fuel stability and deposit formation. This work demonstrates the ability to probe, with high sensitivity, the presence of such compounds in a lab-produced deposit using OrbiSIMS and highlights that biodiesel can contribute unique chemistries to JFTOTs and IDIDs.

### 3.9. JFTOT Na Naphthenate + DDSA OrbiSIMS Ions

Table A42: DDSA and related sodium-containing OrbiSIMS ion data for affected JFTOT and IDID needle samples.

Sample	JFTOT Na + DDSA					N7 <sup>1</sup>	N6 <sup>2</sup>
Position	1	2	3	4	5	Central	Central
Ion assignment	OrbiSIMS peak area normalised to total peak area (top), normalised to DDS-Na peak area (bottom)						
C <sub>16</sub> H <sub>26</sub> O <sub>4</sub> Na <sub>3</sub> <sup>+</sup>	0.0446	0.0107	0.0433	1.49E-3	N/A	9.83E-4	1.47E-6
	1	1	1	1	N/A	1	1
C <sub>16</sub> H <sub>27</sub> O <sub>4</sub> Na <sub>2</sub> <sup>+</sup>	1.73E-4	3.93E-5	8.83E-5	N/A	N/A	N/A	N/A
	3.88E-3	3.67E-3	2.04E-3	N/A	N/A	N/A	N/A
C <sub>4</sub> H <sub>4</sub> O <sub>4</sub> Na <sub>3</sub> <sup>+</sup>	0.0239	8.60E-3	0.0348	9.13E-4	N/A	1.92E-3	3.47E-4
	0.537	0.804	0.804	0.611	N/A	1.96	237
C <sub>3</sub> H <sub>3</sub> O <sub>2</sub> Na <sub>2</sub> <sup>+</sup>	0.0473	0.0128	0.0516	2.22E-3	N/A	8.66E-4	1.04E-5
	1.06	1.19	1.19	1.49	N/A	0.882	7.07
Na <sub>3</sub> CO <sub>3</sub> <sup>+</sup>	0.111	0.0422	0.182	0.0158	6.62E-5	0.0337	6.35E-3
	2.49	3.94	4.21	10.6	N/A	34.3	4330
Na <sub>3</sub> O <sub>2</sub> H <sub>2</sub> <sup>+</sup>	1.56E-2	0.0262	0.0341	6.63E-4	N/A	0.0805	7.12E-3
	0.349	0.650	0.787	0.444	N/A	82.0	4850
Na <sub>2</sub> C <sub>5</sub> <sup>+</sup>	1.91E-4	1.30E-4	6.17E-4	N/A	N/A	0.00183	1.40E-4
	4.27E-3	0.0121	0.0143	N/A	N/A	1.86	95.6
Na <sub>3</sub> C <sub>2</sub> O <sub>4</sub> <sup>+</sup>	1.34E-3	2.02E-3	2.26E-3	2.29E-5	N/A	1.20E-5	4.68E-4
	0.0301	0.0501	0.0523	0.0154	N/A	0.0122	319
C <sub>15</sub> H <sub>25</sub> O <sub>2</sub> Na <sub>2</sub> <sup>+</sup>	5.23E-4	4.33E-4	5.56E-4	4.17E-5	N/A	2.74E-6	N/A
	0.0117	0.0405	0.0128	0.0280	N/A	0.00279	N/A
C <sub>16</sub> H <sub>31</sub> O <sub>2</sub> Na <sub>2</sub> <sup>+</sup>	4.41E-4	N/A	3.06E-5	4.17E-5	N/A	N/A	N/A
	0.0099	N/A	0.0007	0.0280	N/A	N/A	N/A
C <sub>18</sub> H <sub>35</sub> O <sub>2</sub> Na <sub>2</sub> <sup>+</sup>	5.66E-4	N/A	4.55E-5	3.47E-5	N/A	N/A	N/A
	0.0127	N/A	0.0011	0.0233	N/A	N/A	N/A
Na <sub>2</sub> Cl <sup>+</sup>	3.11E-4	4.20E-4	4.02E-4	1.71E-4	1.10E-5	1.11E-3	0.355
	6.97E-3	0.0104	9.29E-3	0.115	N/A	1.13	374
Na <sub>3</sub> SO <sub>4</sub> <sup>+</sup>	6.08E-3	0.0128	0.0228	3.97E-3	0.00394	0.131	0.133
	0.136	0.319	0.527	2.66	N/A	133	140
Na <sub>2</sub> CNO <sup>+</sup>	7.98E-6	8.27E-6	6.93E-6	1.29E-5	N/A	0.0120	0.0253
	1.79E-4	2.05E-4	1.60E-4	8.63E-3	N/A	12.2	26.7

### 3.10. Notable JFTOT Contaminants

Certain ions of interest identified in IDID samples were present in JFTOTs but did not show the expected trends. Alkylbenzene sulfonates were linked to lubricant oil, however the intensities shown in Figure A34a show a distribution of a key marker ( $\text{C}_8\text{H}_7\text{SO}_3^-$ ) across all samples with no identifiable trend and presence on the clean, new JFTOT tube. This shows that ABS compounds are common contaminants to these samples, likely from the handling environment as they find use as detergents in many applications as well as in lubricant oil. Sulfate ( $\text{SO}_3^-$ ) is also distributed somewhat randomly (Figure A34b). It is strongest in JFTOT CME which is consistent with this sample having large intensities of sodium sulfates (Section 5.2.3), however it is present in all samples at nearly every position. A correlation of ABS and sulfate ions with JFTOT Lubricant was expected due to the presence of these chemistries in lubricant oil. Here, a surface contamination origin of these chemistries is indicated, though cannot conclude this as their sole origin; in field IDID samples, particularly where present in deposit bulk, a lubricant oil origin remains possible. ABS compounds are common as cleaning agents and are hence present in indoor environments, shown to be present in a mass spectrometry study of floor dust from an office, where the ABS compounds had alkyl groups of  $\text{C}_{10}$ - $\text{C}_{13}$ . Notably, the largest ABS ion found in JFTOT ions also had a  $\text{C}_{13}$  alkyl group ( $\text{C}_{19}\text{H}_{31}\text{SO}_3^-$ ), suggesting that these compounds in the environment could contaminate the samples.

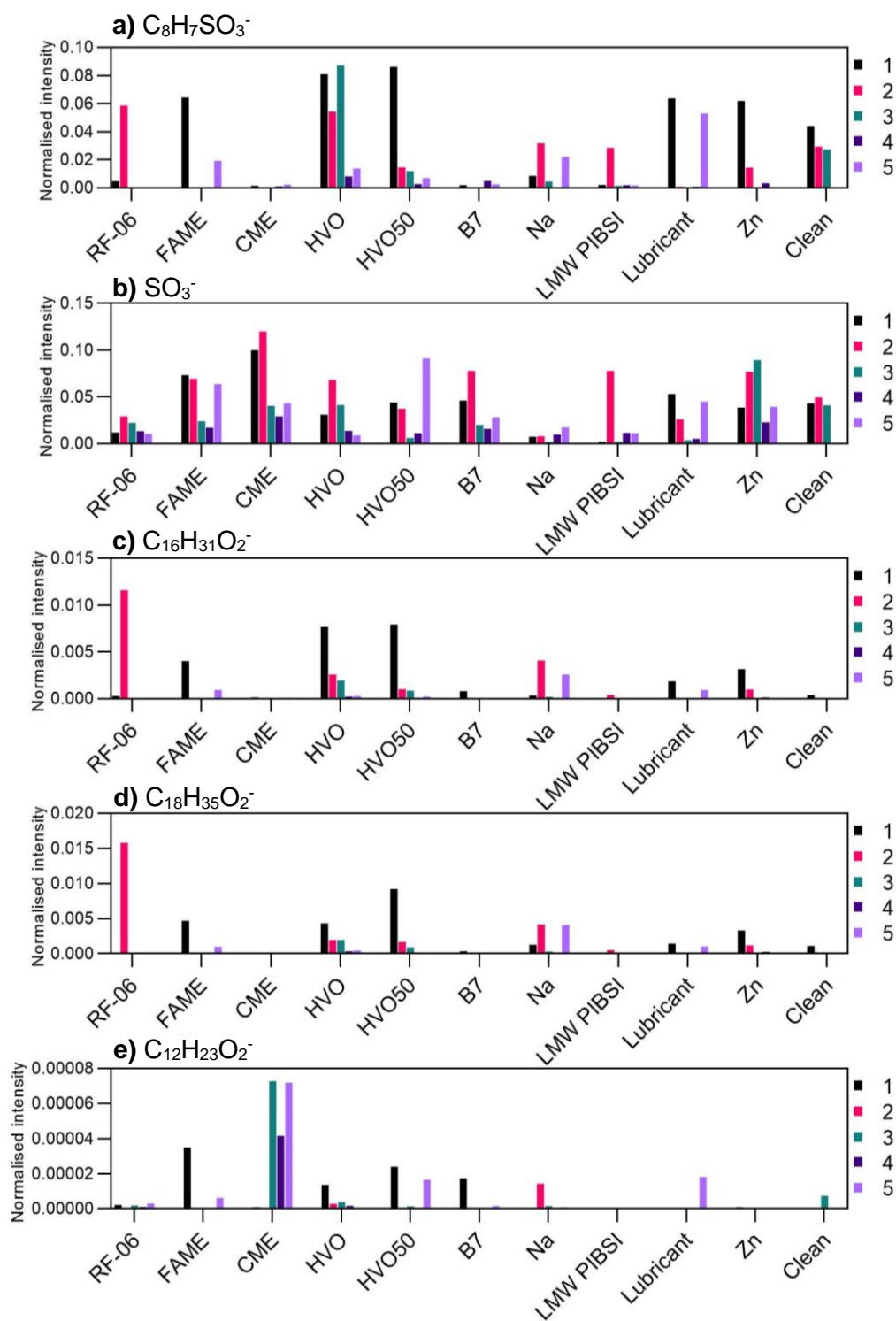


Figure A34: Normalised intensity charts at each position of each JFTOT sample for a)  $C_8H_7SO_3^-$  (ABS), b)  $SO_3^-$  (sulfate), c)  $C_{16}H_{31}O_2^-$  (palmitate), d)  $C_{18}H_{35}O_2^-$  (stearate), e)  $C_{12}H_{23}O_2^-$  (laurate).

The two fatty carboxylates seen in many samples (palmitate  $C_{16}H_{31}O_2^-$  and stearate  $C_{18}H_{35}O_2^-$ , Figure A34c-d) were expected to correlate with bio-fuels however are again present in every sample, with the highest normalised intensity

appearing in JFTOT RF-06 position 2, strongly suggesting a surface contaminant origin independent of the fuels/additive mixture as there is no rationale for solely RF-06 to have a more abundant source of fatty acids than any other sample. These two ions can be contrasted with laurate ( $\text{C}_{12}\text{H}_{23}\text{O}_2^-$ ) in Figure A34e which strongly evidences a fuel origin from CME, as the sample JFTOT CME has much stronger signals for this ion while having much less palmitate and stearate than the other samples (Figure A34c-d). This is discussed alongside other acids and triglycerides for this sample in Section 5.2.5.

### 3.11. JFTOT XPS Data

#### 3.11.1. XPS Elemental Quantification

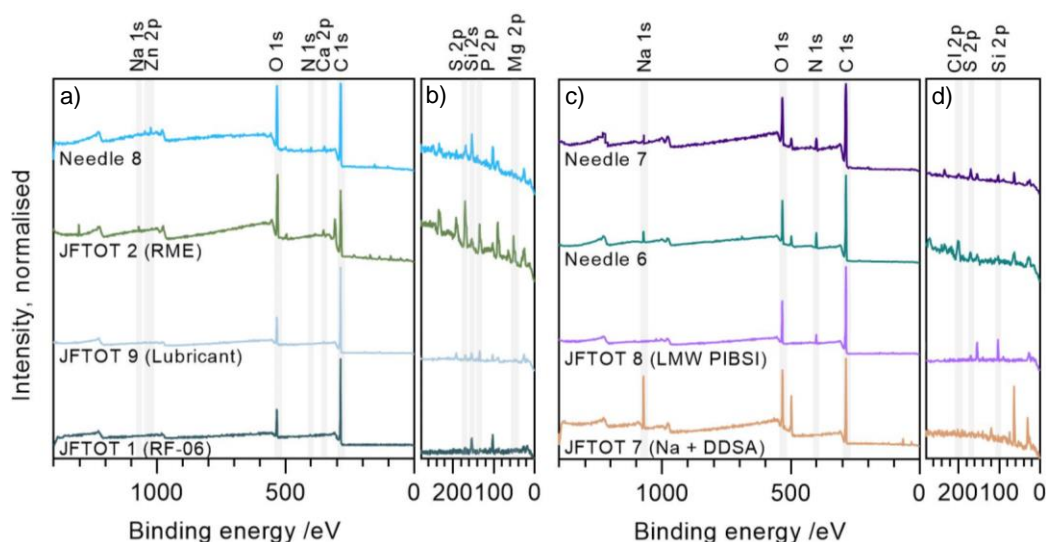


Figure A35: XPS survey spectra examples for JFTOT samples that show varying chemistry and IDID samples (normalised min to max).



Table A43: Elemental XPS relative atomic concentration (at.%) data for JFTOT samples.

Sample, position		C 1s	O 1s	Na 1s	Ca 2p	P 2p	S 2p	Si 2p	Mg 2p	Al 2p	N 1s	Cl 2p
<b>RF-06</b>	<b>3</b>	86.75	11.92	0.00	0.00	0.00	0.00	1.33	0.00	0.00	0.00	0.00
	<b>1</b>	86.41	10.79	0.00	1.53	0.00	0.00	0.28	0.00	0.99	0.00	0.00
	<b>3</b>	68.02	22.41	0.43	1.31	1.31	1.91	0.97	3.63	0.00	0.00	0.00
	<b>5</b>	77.25	16.95	0.35	0.76	0.60	1.56	0.92	1.63	0.00	0.00	0.00
<b>CME</b>	<b>1</b>	80.39	13.31	0.25	1.52	0.00	0.48	0.83	0.00	3.23	0.00	0.00
	<b>3</b>	84.65	13.67	0.36	0.00	0.00	1.02	0.30	0.00	0.00	0.00	0.00
	<b>5</b>	79.96	15.62	0.72	0.57	0.00	1.02	0.79	0.00	1.32	0.00	0.00
<b>HVO</b>	<b>1</b>	84.89	10.40	0.00	0.98	0.00	0.00	0.77	0.00	2.97	0.00	0.00
	<b>3</b>	66.64	19.93	0.00	1.32	0.00	0.96	0.80	1.74	8.62	0.00	0.00
	<b>5</b>	68.69	20.26	0.00	0.54	0.00	0.52	1.11	0.94	7.95	0.00	0.00
<b>HVO50</b>	<b>1</b>	77.32	14.59	0.00	1.02	0.00	0.36	1.10	0.40	4.50	0.71	0.00
	<b>3</b>	76.05	17.79	0.00	0.18	0.00	0.24	1.73	0.38	3.01	0.62	0.00
	<b>5</b>	74.77	18.94	0.00	0.18	0.00	0.42	1.58	0.73	2.76	0.61	0.00
<b>LMW PIBSI</b>	<b>1</b>	81.14	11.36	0.18	1.29	0.00	0.78	1.73	0.00	2.05	1.48	0.00
	<b>3</b>	80.21	13.86	0.00	0.00	0.00	0.12	1.34	0.00	0.00	4.48	0.00
	<b>5</b>	76.10	15.36	0.08	0.73	0.00	0.42	2.58	0.00	0.00	4.74	0.00
<b>Lube</b>	<b>1</b>	63.76	19.79	0.00	0.97	2.09	0.49	2.29	0.91	8.94	0.47	0.28
	<b>3</b>	85.50	12.50	0.00	0.32	0.47	0.22	0.53	0.03	0.37	0.07	0.00
	<b>5</b>	79.71	15.63	0.00	0.77	0.46	0.58	1.29	0.04	1.25	0.05	0.23
<b>Na + DDSA</b>	<b>1</b>	73.17	19.89	5.09	0.00	0.00	0.00	0.00	0.00	1.84	0.00	0.00
	<b>3</b>	69.59	21.03	4.74	0.40	0.00	0.00	0.22	0.86	3.16	0.00	0.00
	<b>5</b>	69.08	18.51	0.58	1.01	0.00	0.00	1.88	0.75	8.19	0.00	0.00
<b>Zinc</b>	<b>3</b>	90.52	9.48	0.00	0.00	0.00	0.00	0.00	0.00	0.00	0.00	0.00

Table A44: Elemental XPS relative atomic concentration Monte Carlo standard deviation errors for JFTOT samples.

Sample, position		C 1s	O 1s	Na 1s	Ca 2p	P 2p	S 2p	Si 2p	Mg 2p	Al 2p	N 1s	Cl 2p
<b>RF-06</b>	<b>3</b>	0.32	0.26	0.00	0.00	0.00	0.00	0.23	0.00	0.00	0.00	0.00
<b>RME</b>	<b>1</b>	0.31	0.20	0.00	0.18	0.00	0.00	0.04	0.00	0.20	0.00	0.00
	<b>3</b>	0.33	0.20	0.06	0.13	0.15	0.10	0.12	0.28	0.00	0.00	0.00
	<b>5</b>	0.29	0.17	0.06	0.11	0.08	0.08	0.09	0.25	0.00	0.00	0.00
<b>CME</b>	<b>1</b>	0.27	0.16	0.06	0.08	0.00	0.07	0.13	0.00	0.21	0.00	0.00
	<b>3</b>	0.18	0.15	0.04	0.00	0.00	0.06	0.09	0.00	0.00	0.00	0.00
	<b>5</b>	0.26	0.17	0.07	0.11	0.00	0.08	0.11	0.00	0.16	0.00	0.00
<b>HVO</b>	<b>1</b>	0.31	0.17	0.00	0.09	0.00	0.00	0.09	0.00	0.26	0.00	0.00
	<b>3</b>	0.36	0.23	0.00	0.09	0.00	0.12	0.11	0.17	0.27	0.00	0.00
	<b>5</b>	0.34	0.20	0.00	0.09	0.00	0.10	0.09	0.15	0.28	0.00	0.00
<b>HVO50</b>	<b>1</b>	0.45	0.26	0.00	0.07	0.00	0.13	0.20	0.18	0.30	0.23	0.00
	<b>3</b>	0.39	0.23	0.00	0.06	0.00	0.09	0.17	0.14	0.28	0.21	0.00
	<b>5</b>	0.23	0.13	0.00	0.04	0.00	0.05	0.09	0.11	0.16	0.11	0.00
<b>LMW PIBSI</b>	<b>1</b>	0.37	0.15	0.04	0.10	0.00	0.10	0.14	0.00	0.22	0.28	0.00
	<b>3</b>	0.26	0.14	0.00	0.00	0.00	0.06	0.10	0.00	0.00	0.25	0.00
	<b>5</b>	0.33	0.17	0.04	0.09	0.00	0.08	0.13	0.00	0.00	0.33	0.00
<b>Lube</b>	<b>1</b>	0.33	0.17	0.00	0.09	0.14	0.13	0.17	0.19	0.20	0.22	0.08
	<b>3</b>	0.24	0.17	0.00	0.09	0.08	0.06	0.11	0.01	0.11	0.01	0.00
	<b>5</b>	0.33	0.19	0.00	0.09	0.09	0.07	0.11	0.01	0.28	0.01	0.08
<b>Na + DDSA</b>	<b>1</b>	0.52	0.38	0.22	0.00	0.00	0.00	0.00	0.00	0.43	0.00	0.00
	<b>3</b>	0.37	0.22	0.14	0.09	0.00	0.00	0.15	0.29	0.22	0.00	0.00
	<b>5</b>	0.45	0.27	0.18	0.23	0.00	0.00	0.19	0.22	0.26	0.00	0.00
<b>Zinc</b>	<b>3</b>	0.81	0.81	0.00	0.00	0.00	0.00	0.00	0.00	0.00	0.00	0.00

## 3.11.2. JFTOT Samples High Resolution C 1s Spectra

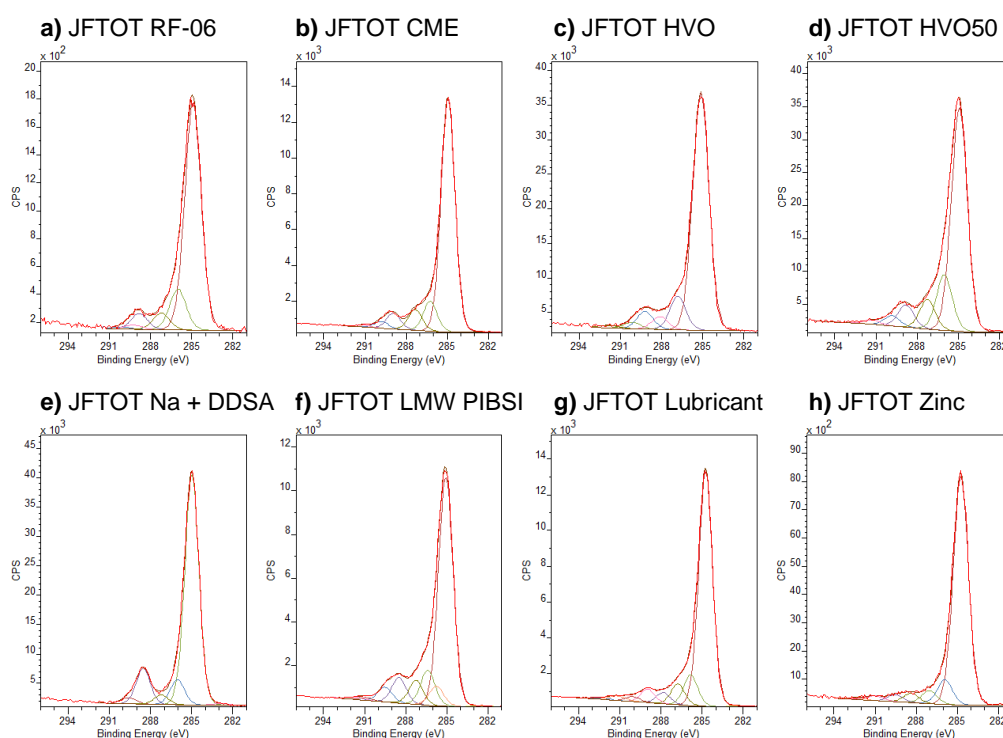


Figure A36: C 1s high-resolution XP spectra for JFTOT samples.

Table A45: C 1s high-resolution XPS component data for fuel JFTOT samples.

Sample		RF-06	CME			HVO	HVO50
Position		3	1	3	5	5	3
FWHM <sup>1</sup>		1.4	1.01	1.18	1.15	1.37	1.35
M-C	Pos	N/A	283.18	282.59	282.86	N/A	N/A
	%	0	0.67	0.27	0.52	0	0
	SD	0	0.16	0.11	0.21	0	0
C-C	Pos	284.90	284.88	284.94	285.04	285.14	284.92
	%	74.76	85.54	75.33	78.9	76.29	64.77
	SD	2.55	0.55	0.43	0.61	1.16	1.34
C-O	Pos	286.00	286.00	286.23	286.34	286.8	286.01
	%	13.55	5.81	9.67	8.51	10.9	16.13
	SD	2.07	0.25	0.25	0.37	0.52	1.16
C=O	Pos	287.20	287.20	287.33	287.41	288.11	287.24
	%	5.5	2.13	6.73	4.95	4.05	8.53
	SD	0.89	0.14	0.22	0.29	0.62	0.59
O-C=O	Pos	288.81	288.55	288.91	288.96	289.2	288.81
	%	5.13	3.97	5.1	5.44	5.65	6.35
	SD	1.55	0.22	0.22	0.22	0.93	0.34
CO <sub>3</sub>	Pos	289.26	289.3	289.8	289.8	290.12	289.8
	%	0.39	1.88	2.18	1.47	2.07	2.92
	SD	0.40	0.23	0.19	0.28	0.66	0.63
$\pi$ - $\pi^*$	Pos	290.1	N/A	291.17	291.42	291.93	291.29
	%	0.67	0	0.72	0.21	1.04	1.29
	SD	0.75	0	0.12	0.14	0.58	0.35

1 – all FWHM for all components in each sample constrained as equal.

Table A46: C 1s HR XPS component data for additive/dopant JFTOT samples. SD from Monte Carlo simulation in CasaXPS.

Sample		Na	LMW PIBSI			Lubricant			Zinc
Position		3	1	3	5	1	3	5	3
FWHM <sup>1</sup>		1.20	1.00	1.22	1.17	1.17	1.18	1.24	1.28
M-C	Pos	282.92	283.51	N/A	283.01	283.44	282.28	282.71	N/A
	%	0.51	0.73	0	0.39	0.62	0.32	0.33	0
	SD	0.34	0.2	0	0.11	0.27	0.11	0.19	0
C-C	Pos	284.98	285.11	285.07	284.99	285.14	284.74	284.97	284.74
	%	74.69	79.99	64.63	69.36	77.57	72.28	72.81	78.82
	SD	1.7	0.99	1.82	1.45	1.04	0.60	0.57	2.23
C-N	Pos	N/A	285.77	285.75	285.84	N/A	N/A	N/A	N/A
	%	0	1.18	5.57	6.22	0	0	0	0
	SD	0	0.48	2.49	0.86	0	0	0	0
C-O	Pos	286.02	285.99	286.38	286.55	286.21	285.82	286.16	285.90
	%	8.15	7.51	9.9	10.4	8.41	9.47	11.69	8.47
	SD	1.26	0.45	1.69	1.14	0.73	0.44	0.45	1.58
C=O	Pos	287.20	287	287.24	287.75	287.2	286.76	287.20	287.03
	%	3.06	4.11	6.8	4.91	5.38	6.44	6.77	4.58
	SD	0.41	0.21	0.68	0.3	0.39	0.29	0.31	0.84
N-C=O	Pos	N/A	288.04	N/A	N/A	N/A	N/A	N/A	N/A
	%	0	1.2	0	0	0	0	0	0
	SD	0	0.15	0	0	0	0	0	0
C-?²	Pos	N/A	N/A	N/A	N/A	288.35	287.82	N/A	N/A
	%	0	0	0	0	2.61	3.41	0	0
	SD	0	0	0	0	0.38	0.22	0	0
O-C=O	Pos	288.53	288.77	288.48	288.68	289.18	288.96	288.47	288.37
	%	11.62	3.39	7.2	6.5	3.22	4.20	4.76	3.21
	SD	0.4	0.23	0.18	0.39	0.55	0.19	0.18	0.62
CO₃	Pos	289.59	289.5	289.5	289.5	289.83	290.05	289.5	289.50
	%	1.97	1.77	4.23	1.86	1.87	1.55	2.90	2.36
	SD	0.41	0.27	0.21	0.27	0.53	0.26	0.21	0.57
π-π* (sum)	%	0	0.12	1.43	0.36	0.31	2.33	0.73	2.56
	SD	0	0.11	0.66	0.21	0.16	0.77	0.13	0.91
π-π* 1	Pos	N/A	290.4	291.67	291.13	291.06	291.18	291.18	291.00
	FWHM	N/A	1.00	1.00	1.26	1.00	1.52	1.59	1.48
	%	0	0.12	0.78	0.36	0.31	1.72	0.73	1.81
	SD	0	0.11	0.56	0.21	0.16	0.47	0.13	0.78
π-π* 2	Pos	N/A	N/A	290.89	N/A	N/A	292.49	N/A	292.46
	FWHM	N/A	N/A	1.40	N/A	N/A	1.60	N/A	1.60
	%	0	0	0.65	0	0	0.61	0	0.75
	SD	0	0	0.34	0	0	0.20	0	0.46

1 – FWHM constrained as equal for all components of each sample except in some cases with more extensive  $\pi$ - $\pi^*$  satellite structures which were uncoupled and constrained 1.00-1.60, with the FWHM noted.

2 – Unknown component, required to achieve good fit.

### 3.11.3. JFTOT 200 °C High Resolution C 1s Spectra

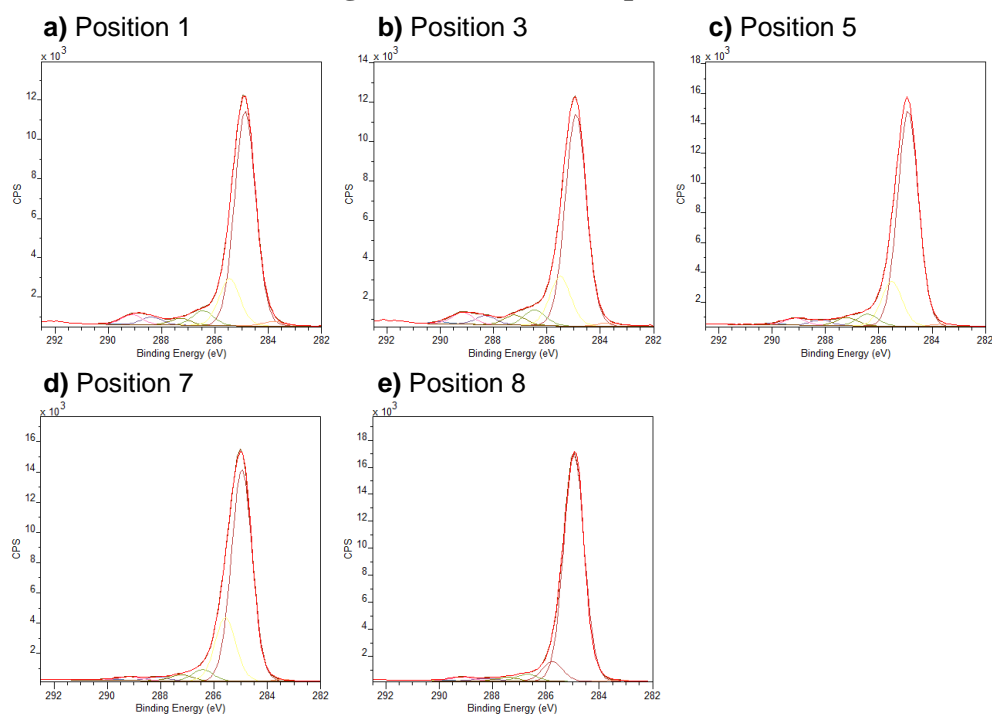


Figure A37: JFTOT 200 °C positions 1-8 as shown in Figure 5.20 C 1s high resolution XP spectra.

Table A47: C 1s HR XPS component data for 200 °C JFTOT sample. Standard deviation from Monte Carlo simulation in CasaXPS.

Position		1	3	5	7	8
FWHM <sup>1</sup>		0.91	0.93	0.90	0.90	0.90
M-C	Pos	283.84	283.67	283.56	283.43	283.29
	%	1.41	1.03	0.80	0.59	0.54
	SD	0.35	0.28	0.12	0.07	0.07
C-C	Pos	284.86	284.91	284.9	284.96	284.94
	%	69.96	67.90	72.49	69.77	85.51
	SD	2.52	3.12	1.46	1.37	0.49
C-?	Pos	285.45	285.50	285.51	285.57	285.76
	%	15.48	15.89	15.16	20.98	7.43
	SD	2.10	2.60	1.21	1.03	0.37
C-O	Pos	286.45	286.44	286.41	286.41	286.71
	%	4.83	4.93	4.00	3.74	2.53
	SD	0.17	0.31	0.24	0.32	0.17
C=O	Pos	287.28	287.20	287.20	287.22	287.43
	%	2.26	3.22	2.76	2.04	1.32
	SD	0.27	0.28	0.21	0.18	0.19
O-C=O	Pos	288.37	288.30	288.17	288.15	288.24
	%	2.56	2.79	1.82	1.18	0.94
	SD	0.25	0.19	0.09	1.18	0.11
CO <sub>3</sub>	Pos	289.11	289.17	289.12	289.15	289.17
	%	3.23	3.69	2.38	1.22	1.43
	SD	0.27	0.24	0.12	0.09	283.29
$\pi$ - $\pi^*$ (sum)	%	0.26	0.56	0.58	0.48	0.30
	SD	0.18	0.22	0.13	0.08	12
$\pi$ - $\pi^*$ 1	Pos	290.00	290.00	290.00	290.00	290.00
	%	0.26	0.56	0.51	0.42	0.23
	SD	0.18	0.22	0.09	0.06	0.09
$\pi$ - $\pi^*$ 2	Pos	N/A	N/A	291.23	291.22	291.00
	%	N/A	N/A	0.07	0.06	0.07
	SD	0	0	0.09	0.05	0.08

1 – FWHM constrained (0.9-1.4) as equal for all components of each sample

### 3.11.4. JFTOT Samples High Resolution O 1s Spectra

O 1s XP spectra are shown here for the JFTOT samples for completeness however were not used to interpret the samples. Component models could be fit with peaks representing C-O and C=O in all samples, with some samples containing other components (including Na KLL). The proportion of C-O/C=O here is generally inconsistent with the C 1s data, so the real components are suggested to be more complex than what is fitted here, where overfitting has been avoided.

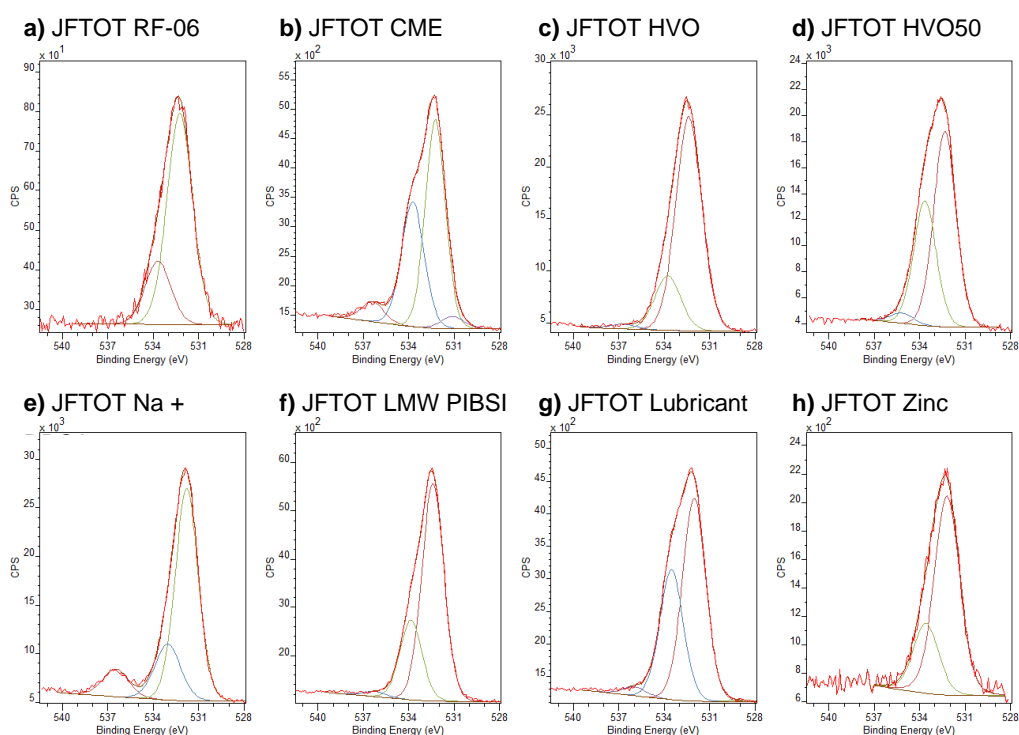


Figure A38: O 1s high-resolution XP spectra for JFTOT samples. All samples are position 3 except HVO which is position 5.

Table A48: O 1s HR XPS component data for JFTOT samples (position 3 for all samples except HVO, position 5). SD from Monte Carlo simulation in CasaXPS.

Position		RF-06	CME	HVO	HVO50	Na	PIB	Lube	Zn
FWHM <sup>1</sup>		1.97	1.61	2	1.74	1.83	1.7	1.81	1.97
M-O	Pos	N/A	530.9	N/A	N/A	N/A	N/A	529.03	N/A
	%	N/A	2.14	N/A	N/A	N/A	N/A	0.46	N/A
	SD	N/A	1.22	N/A	N/A	N/A	N/A	0.49	N/A
C=O	Pos	532.25	532.26	532.38	532.34	531.83	532.4	532.02	532.2
	%	76.95	59.11	79.3	59.17	74.63	71.9	59.16	74.02
	SD	3.85	1.03	1.75	2.26	1.58	0.82	0.79	4.16
C-O	Pos	533.68	533.79	533.76	533.66	533.23	533.85	533.52	533.58
	%	23.05	32.15	20.24	37.72	15.2	26.4	37.78	25.98
	SD	3.85	0.62	1.73	1.47	1.65	0.93	0.85	4.16
O-?	Pos	N/A	N/A	536.71	535.18	N/A	536.21	535.97	N/A
	%	N/A	N/A	0.46	3.1	N/A	1.7	2.6	N/A
	SD	N/A	N/A	0.12	1.33	N/A	0.3	0.37	N/A
Na KLL	Pos	N/A	536.31	N/A	N/A	536.47	N/A	N/A	N/A
	%	N/A	6.61	N/A	N/A	10.17	N/A	N/A	N/A
	SD	N/A	0.43	N/A	N/A	0.49	N/A	N/A	N/A
	FWHM	N/A	2	N/A	N/A	2	N/A	N/A	N/A

<sup>1</sup> – FWHM set equal for all components (except Na KLL) in each sample.



### 3.12. JFTOT 200 °C PAH OrbiSIMS supplementary information

Table A49: Largest PAH ions found at each position of JFTOT 200 °C, 250 °C and Needle 8

Sample	Position	Largest PAH	<i>m/z</i>	Intensity	Intensity (norm to mass decimal <.5)
<b>JFTOT 200 °C</b>	1	C <sub>44</sub> H <sub>16</sub> <sup>+</sup>	544.1248	4.66E-06	2.47E-05
	2	C <sub>59</sub> H <sub>21</sub> <sup>+</sup>	729.1634	3.94E-06	1.78E-05
	3	C <sub>53</sub> H <sub>17</sub> <sup>+</sup>	653.1332	3.31E-06	1.74E-05
	4	C <sub>59</sub> H <sub>19</sub> <sup>+</sup>	727.1491	4.56E-06	1.84E-05
	5	C <sub>76</sub> H <sub>18</sub> <sup>+</sup>	930.1405	7.67E-06	1.58E-05
	6	C <sub>87</sub> H <sub>21</sub> <sup>+</sup>	1065.1634	8.53E-06	1.18E-05
	7	C <sub>91</sub> H <sub>23</sub> <sup>+</sup>	1115.1770	1.38E-05	1.41E-05
	8	C <sub>91</sub> H <sub>19</sub> <sup>+</sup>	1111.1456	2.08E-05	2.11E-05
<b>JFTOT 250 °C</b>	1	C <sub>39</sub> H <sub>15</sub> <sup>+</sup>	483.1167	6.56E-06	1.24E-05
	2	C <sub>60</sub> H <sub>20</sub> <sup>+</sup>	740.1560	9.32E-06	1.25E-05
	3	C <sub>70</sub> H <sub>22</sub> <sup>+</sup>	862.1705	8.87E-06	1.12E-05
	4	C <sub>91</sub> H <sub>21</sub> <sup>+</sup>	1113.1610	9.60E-06	1.06E-05
	5	C <sub>91</sub> H <sub>21</sub> <sup>+</sup>	1113.1612	1.51E-05	1.60E-05
	6	C <sub>91</sub> H <sub>23</sub> <sup>+</sup>	1115.1772	2.41E-05	2.59E-05
<b>Needle 8</b>	1	C <sub>36</sub> H <sub>16</sub> <sup>+</sup>	448.1247	6.42E-07	3.85E-05
	2	C <sub>68</sub> H <sub>18</sub> <sup>+</sup>	834.1406	2.93E-06	1.05E-05
	3	C <sub>62</sub> H <sub>14</sub> <sup>+</sup>	758.1082	9.91E-06	8.54E-05
	4	C <sub>65</sub> H <sub>23</sub> <sup>+</sup>	803.1807	2.23E-05	6.83E-05
	5	C <sub>65</sub> H <sub>17</sub> <sup>+</sup>	797.1328	7.42E-06	1.02E-05
	6	C <sub>72</sub> H <sub>18</sub> <sup>+</sup>	882.1405	1.35E-06	1.56E-05

Table A50: Key PAH ion intensities found at each position of JFTOT 200 °C, 250 °C and Needle 8. Heat map applied to JFTOT 200 °C positions 1-5 and Needle 8 for ease of comparison between these key samples and positions.

Sample, position		$C_{24}H_{12}^+$	$C_{30}H_{12}^+$	$C_{40}H_{16}^+$	$C_{50}H_{18}^+$	$C_{60}H_{16}^+$	$C_{70}H_{16}^+$	$C_{10}^+$
		OrbiSIMS intensities normalised to $C_{12}H_8^+$						
JFTOT 250 °C	1	0.0180	0.0028	0.0000	0.0000	0.0000	0.0000	0.0000
	2	0.0643	0.0250	0.0073	0.0015	0.0000	0.0000	0.0004
	3	0.1131	0.0564	0.0211	0.0075	0.0019	0.0000	0.0027
	4	0.2484	0.1838	0.0928	0.0484	0.0245	0.0107	0.0372
	5	0.2716	0.1837	0.1072	0.0626	0.0344	0.0145	0.0147
JFTOT 200 °C	1	0.0339	0.0082	0.0011	0.0000	0.0000	0.0000	0.0000
	2	0.0486	0.0165	0.0050	0.0013	0.0000	0.0000	0.0000
	3	0.0418	0.0118	0.0013	0.0000	0.0000	0.0000	0.0000
	4	0.0788	0.0298	0.0076	0.0015	0.0000	0.0000	0.0013
	5	0.1676	0.0955	0.0384	0.0152	0.0047	0.0012	0.0093
	6	0.2204	0.1127	0.0556	0.0242	0.0108	0.0035	0.0171
N8	1	0.0259	0.0000	0.0000	0.0000	0.0000	0.0000	0.0022
	2	0.1439	0.0254	0.0063	0.0029	0.0010	0.0002	0.0069
	3	0.0984	0.0257	0.0043	0.0039	0.0000	0.0000	0.0859
	4	0.0583	0.0228	0.0115	0.0058	0.0000	0.0000	0.0086
	5	0.1375	0.0675	0.0113	0.0036	0.0000	0.0000	0.0276
	6	0.0684	0.0480	0.0124	0.0022	0.0009	0.0000	0.0128
		Normalised intensities normalised to largest of each ion in JFTOT 200 or Needle 8						
JFTOT 250 °C	1	0.11	0.03	0.00	0.00	0.00	0.00	0.00
	2	0.38	0.26	0.19	0.10	0.00	0.00	0.00
	3	0.68	0.59	0.55	0.50	0.41	0.00	0.03
	4	1.48	1.92	2.41	3.19	5.22	9.17	0.43
	5	1.62	1.92	2.79	4.13	7.34	12.43	0.17
JFTOT 200 °C	1	0.20	0.09	0.03	0.00	0.00	0.00	0.00
	2	0.29	0.17	0.13	0.09	0.00	0.00	0.00
	3	0.25	0.12	0.03	0.00	0.00	0.00	0.00
	4	0.47	0.31	0.20	0.10	0.00	0.00	0.02
	5	1.00	1.00	1.00	1.00	1.00	1.00	0.11
	6	1.32	1.18	1.45	1.59	2.31	2.97	0.20
Needle 8	1	0.15	0.00	0.00	0.00	0.00	0.00	0.03
	2	0.86	0.27	0.16	0.19	0.22	0.19	0.08
	3	0.59	0.27	0.11	0.25	0.00	0.00	1.00
	4	0.35	0.24	0.30	0.38	0.00	0.00	0.10
	5	0.82	0.71	0.30	0.24	0.00	0.00	0.32
	6	0.41	0.50	0.32	0.15	0.20	0.00	0.15